

2 cys Bulk

FACILITY FORM 602

N66-15267	
(ACCESSION NUMBER)	(THRU)
533	1
(PAGES)	(CODE)
CR 69237	31
(NASA CR OR TMX OR AD NUMBER)	(CATEGORY)

GPO PRICE \$ _____

CFSTI PRICE(S) \$ _____

Hard copy (HC) 8.33

Microfiche (MF) 2.50

ff 653 July 65

**JET PROPULSION LABORATORY
CALIFORNIA INSTITUTE OF TECHNOLOGY
PASADENA, CALIFORNIA**

RE-ORDER NO. 64-523 11

note

CONCEPTUAL DESIGN STUDIES
OF AN ADVANCED MARINER SPACECRAFT

VOLUME III
LANDER DESIGN

Prepared by

RESEARCH AND ADVANCED DEVELOPMENT DIVISION
AVCO CORPORATION
Wilmington, Massachusetts

This work was performed for the Jet Propulsion Laboratory,
California Institute of Technology, sponsored by the
National Aeronautics and Space Administration under
Contract NAS7-100.

RAD-TR-64-36
Contract 950896

28 October 1964

Prepared for

CALIFORNIA INSTITUTE OF TECHNOLOGY
JET PROPULSION LABORATORY
4800 Oak Grove Drive
Pasadena, California

501 PAGES
INCLUDE
(26 ROMAN NUMERALS)
10-1501

RE-ORDER No. 64-523

This document consists of 502 pages,
200 copies, Series A

CONCEPTUAL DESIGN STUDIES
OF AN ADVANCED MARINER SPACECRAFT

VOLUME III
LANDER DESIGN

Prepared by
RESEARCH AND ADVANCED DEVELOPMENT DIVISION
AVCO CORPORATION
Wilmington, Massachusetts

RAD-TR-64-36
Contract 950896

28 October 1964

Prepared for
CALIFORNIA INSTITUTE OF TECHNOLOGY
JET PROPULSION LABORATORY
4800 Oak Grove Drive
Pasadena, California

CONTENTS

1.0 Conceptual Design Synthesis	1
1.1 Payload Analysis	1
1.2 Payload Reliability Analysis	27
1.3 Vehicle Analysis	29
1.4 System Design Summary	42
2.0 Scientific Payload	45
2.1 Instrumentation List	45
2.2 Selected Instrumentation	45
3.0 Design	59
3.1 Landed Shape Generation	59
3.2 Lander Shape Generation	64
3.3 Conceptual Design Description	66
3.4 Weight Summary	75
4.0 Aerodynamic Performance	81
4.1 Effect of Entry Conditions	87
4.2 Effect of Atmosphere	94
4.3 Effect of Vehicle Parameters	95
4.4 Conceptual Design Summary	96
5.0 Aerodynamic Heating	112
5.1 Pressure Distribution	114
5.2 Heating Distribution	114
5.3 Effect of Entry Conditions	114
5.4 Effect of Vehicle Parameters	124
5.5 Effect of Atmosphere	124
5.6 Conceptual Design Summary	124
6.0 Heat Shield System	129
6.1 Material Selection	130
6.2 Entry Condition Effects	140
6.3 Lander Diameter Effects	157
6.4 Shape Modification Effects	161
6.5 Conceptual Design Analysis	162

CONTENTS (Concl'd)

7.0	Descent System.....	175
7.1	Drogue Chute Analysis.....	176
7.2	Main Chute Analysis.....	192
7.3	Snatch and Opening Load Analysis.....	192
7.4	Material Selection.....	196
7.5	Parametric Optimization.....	203
7.6	Conceptual Design Analysis.....	235
7.7	Actuation Systems.....	244
8.0	Impact System.....	256
8.1	Parametric Trade-Off Studies.....	256
8.2	Parametric Design Data.....	268
8.3	Influence Coefficients.....	282
8.4	Optimization Analysis.....	293
8.5	Conceptual Design Analysis.....	302
9.0	Thermal Control System.....	314
9.1	Near Earth.....	314
9.2	Cruise Phase.....	317
9.3	Post-Separation Phase.....	322
9.4	Mars Entry, Parachute Descent and Post Landing Phases.....	327
9.5	Lander Transient Analysis.....	331
9.6	Conceptual Design.....	338
10.0	Communications and Power Supply.....	340
10.1	Assumptions and Constraints.....	340
10.2	Telemetry Link Studies.....	343
10.3	Radar Altimeter Parametric Studies.....	358
10.4	Antennas.....	373
10.5	Power Sources.....	374
10.6	Communications System Hardware.....	390
10.7	Conceptual Design.....	418
10.8	Alternate Concepts.....	432
Appendixes		
A.	Impact Dynamics Analysis.....	439
B.	Wind Dynamics Analysis.....	461
C.	Density Profile Determination.....	468

ILLUSTRATIONS

Figure	1	Relative Expected Yields - Multi-Launches of Alternative Payloads	30
	2	Effect of Payload Weight on Lander Diameter - Payload 9.	33
	3	Effect of Lander Entry and Payload Weight on Diameter - Payload 9	34
	4	Effect of Payload Weight on Lander Diameter - Payloads 10, 11, and 15	37
	5	Effect of Launch Weight on Payload Weight	38
	6	Conceptual Design Lander Diameter Determination	39
	7	Lander Concepts	61
	8	Design Evaluation - "Antenna Deployment"	63
	9	Entry Configuration Design Evaluation "Lander C. G. Control"	65
	10	Advanced Mariner - Lander General Arrangement of Conceptual Design	67
	11	Advanced Mariner - Lander General Arrangement of Conceptual Design	68
	12	Lander Terminology	69
	13	Entry and Landing Sequence Advanced Mariner Lander Concept	72
	14	Advanced Mariner Lander Assembly Sequence	76
	15	Apollo Configuration	83
	16	Estimated Radius of Gyration	84
	17	Drag Coefficient versus Angle of Attack	85
	18	Damping Coefficient versus Angle of Attack	86

ILLUSTRATIONS (Cont'd)

Figure	19	Temperature Profile - Mars Atmospheres	89
	20	Pressure Profile - Mars Atmospheres	90
	21	Density Profile - Mars Atmospheres	91
	22	Effect of Vehicle Moment of Inertia Ratio on Spin Stabilization	92
	23	Effect of Entry Velocity on Angle of Attack Envelope	93
	24	Effect of Entry Angle on Angle of Attack Envelope	98
	25	Effect of Spin Rate on Angle of Attack Envelope	99
	26	Effect of Angle of Attack at Entry on Angle of Attack Envelope	100
	27	Effect of Atmosphere on Angle of Attack Envelope	101
	28	Mach 2.5 Altitude versus m/C_{DA}	102
	29	Mach 2.5 Damping Coefficient on Angle of Attack Envelope	103
	30	Configurations	104
	31	Center of Pressure versus Angle of Attack for Various Shapes	105
	32	Pitching Moment Coefficient versus Angle of Attack for Various Shapes	106
	33	Drag Coefficient versus Angle of Attack for Various Shapes	107
	34	Angle of Attack Envelope versus Time for Various Shapes	108
	35	Conceptual Design Configuration	109
	36	Comparison of Radiation Predictions with Experiment ...	113

ILLUSTRATIONS (Cont'd)

Figure	37	Pressure Distribution for Apollo Shape	115
	38	Laminar Heating Distribution for Apollo Shape	116
	39	Radiation Heating Distribution for Apollo Shape	117
	40	Variation of Radiation Intensity with Shock Wave Angle ..	118
	41	Shock Envelopes for Apollo Shape	119
	42	Effect of Entry Velocity on Peak Heat Rates	120
	43	Effect of Entry Velocity on Integrated Heating	121
	44	Effect of Entry Velocity on Total Heating	122
	45	Effect of Vehicle Dynamics on Stagnation Point Heating ..	123
	46	Heat Pulses for K Atmosphere	125
	47	Variation of Integrated Heating with $m/C_D A$	126
	48	Effect of Atmosphere on Heat Pulses	127
	49	Aluminum Honeycomb Structure Weight Fraction	134
	50	Avco 5026 Heat Shield Weight Fraction	135
	51	Fiberglass Structure Weight Fraction	136
	52	Dielectric Material Heat Shield Weight Fraction	137
	53	Material Comparison of Afterbody Weight Fraction	138
	54	Material Comparison of Heat Shield System Weight Fraction	139
	55	Total Weight Fraction versus Entry Angle	141
	56	Total Heat Shield Weight Fraction versus $m/C_D A$	142
	57	Total Structure Weight Fraction versus $m/C_D A$	143

ILLUSTRATIONS (Cont'd)

Figure	58	Total Shield Systems Weight Fraction as a Function of Entry Angle	145
	59	Total Heat Shield System Weight Fractions of a Function of $m/C_D A$	146
	60	Forebody Structure Weight Fraction versus $m/C_D A$	147
	61	Forebody Heat Shield Weight Fraction versus $m/C_D A$...	148
	62	Forebody Heat Shield - Structure Weight Fraction versus $m/C_D A$	149
	63	Forebody Heat Shield Thickness	150
	64	Forebody Face Sheet Thickness	151
	65	Forebody Honeycomb Thickness	152
	66	Entry Condition Effects on Heat Shield System Weight Fraction	154
	67	Effect or Entry Condition or Heat Shield System Weight Fraction	155
	68	Heat Shield - Structure Weight Fraction versus Entry Velocity	156
	69	Lander Diameter Effects on Heat Shield Weight Fractions	158
	70	Lander Diameter Effects on Structural Weight Fractions	159
	71	Lander Diameters Effects on Total Heat Shield System Weight Fraction	160
	72	Effect of Shape Modifications on Heat Shield System Weight Fraction	163
	73	Conceptual Design Forebody Heat Shield Thickness	165
	74	Temperature History of Beryllium Afterbody	166

ILLUSTRATIONS (Cont'd)

Figure	75	Forebody Structural Thickness in the Area of the Support Ring	168
	76	Face Sheet Meridional Stress Distribution	170
	77	Face Sheet Circumferential Stress Distribution	171
	78	Surface Displacement Distribution (Median Surface)	172
	79	Droge Deployment Altitude versus $m/C_D A$ (γ_e of 90 degrees)	177
	80	Droge Deployment Altitude versus $m/C_D A$ (γ_e of 60 degrees)	178
	81	Droge Deployment Altitude versus $m/C_D A$ (γ_e of 40 degrees)	179
	82	Dynamic Pressure versus $m/C_D A$ (γ_e of 90 degrees)	180
	83	Dynamic Pressure versus $m/C_D A$ (γ_e of 60 degrees)	181
	84	Dynamic Pressure versus $m/C_D A$ (γ_e of 40 degrees)	182
	85	Altitude at Main Chute Deployment versus A_D/A_V and W_D (Nominal Entry Angle of 90 degrees and Droge Chute Deployment of 2.5)	183
	86	Altitude at Main Chute Deployment versus A_D/A_V and W_D (Nominal Entry Angle of 60 degrees and Droge Chute Deployment of 2.5)	184
	87	Altitude at Main Chute Deployment versus A_D/A_V and W_D (Nominal Entry Angle of 40 degrees and Droge Chute Deployment of 2.5)	185
	88	Altitude at Main Chute Deployment versus A_D/A_V W_D (Nominal Entry Angle of 20 degrees and Droge Chute Deployment of 2.5)	186
	89	Altitude at Main Chute Deployment versus A_D/A_V and W_D (Nominal Entry Angle of 60 degrees and Droge Chute Deployment of 3.0)	187

ILLUSTRATIONS (Cont'd)

Figure	90	Altitude at Main Chute Deployment versus A_D/A_V and W_D (Nominal Entry Angle of 60 degrees and Drogue Chute Deployment of 3.5)	188
	91	Altitude at Main Chute Deployment versus A_D/A_V and W_D in the "I" Model Atmosphere (Nominal Entry Angle of 90 degrees and Drogue Chute Deployment of 2.5)	189
	92	Altitude at Main Chute Deployment versus A_D/A_V and W_D in the "K" Model Atmosphere (Nominal Entry Angle of 90 degrees and Drogue Chute Deployment of 2.5)	190
	93	Hyperflo and Ringsail Drag Coefficients versus Mach Number	191
	94	Time to Impact versus Altitude at Main Chute Full Open ..	193
	95	Impact Velocity versus Main Chute Area Over Suspended Weight (A_{mc}/W_s)	194
	96	Dynamic Pressure at Main Chute Deployment Altitude for Various Atmospheres	195
	97	Effect of Dynamic Pressure on Drogue Opening Shock Loads	197
	98	Effect of Dynamic Pressure on Main Chute Opening Shock Loads	198
	99	Mach Number Limits for Nylon Fabric	199
	100	Mach Number Limits for Nomex Fabric	200
	101	Fabric Temperature Limited Mach Number versus Altitude (γ_e of 90 degrees)	201
	102	Fabric Temperature Limited Mach Number versus Altitude (γ_e of 60 degrees)	202
	103	Suspended Weight and Main Chute Weight versus $m/C_D A$ (Impact Velocity of 50 fps and $\gamma_{e\text{ nominal}}$ of 90 degrees)	205

ILLUSTRATIONS (Cont'd)

Figure 104	Suspended Weight and Main Chute Weight versus m/C_{DA} (Impact Velocity of 150 fps and $\gamma_{e\text{nominal}}$ of 90 degrees)	206
105	Suspended Weight and Drogue Chute Weight versus m/C_{DA} (Altitude of 5000 feet at Main Chute Deployment and $\gamma_{e\text{nominal}}$ of 90 degrees)	207
106	Suspended Weight and Drogue Chute Weight versus m/C_{DA} (Altitude of 8000 feet at Main Chute Deployment and $\gamma_{e\text{nominal}}$ of 90 degrees)	208
107	Suspended Weight and Drogue Chute Weight versus m/C_{DA} (Altitude of 10,000 feet at Main Chute Deploy- ment and $\gamma_{e\text{nominal}}$ of 90 degrees)	209
108	Suspended Weight and Drogue Chute Weight versus m/C_{DA} (Altitude of 15,000 feet at Main Chute Deploy- ment and $\gamma_{e\text{nominal}}$ of 90 degrees)	210
109	Suspended Weight and Drogue Chute Weight versus m/C_{DA} (Altitude of 20,000 feet at Main Chute Deploy- ment and $\gamma_{e\text{nominal}}$ of 90 degrees)	211
110	Optimum Suspended Weight and m/C_{DA} versus Main Chute Deployment Altitude (50 fps Impact Velocity and $\gamma_{e\text{nominal}}$ of 90 degrees)	212
111	Suspended Weight and Main Chute Weight versus m/C_{DA} (Impact Velocity of 50 fps and $\gamma_{e\text{nominal}}$ of 60 degrees).	213
112	Suspended Weight and Main Chute Weight versus m/C_{DA} (Impact Velocity of 150 fps and $\gamma_{e\text{nominal}}$ of 60 degrees).	214
113	Suspended Weight and Drogue Chute Weight versus m/C_{DA} m/C_{DA} (Altitude of 5000 feet at Main Chute Deployment and $\gamma_{e\text{nominal}}$ of 60 degrees)	215
114	Suspended Weight and Drogue Chute Weight versus m/C_{DA} (Altitude of 8000 feet at Main Chute Deploy- ment $\gamma_{e\text{nominal}}$ of 60 degrees)	216

ILLUSTRATIONS (Cont'd)

Figure 115	Suspended Weight and Drogue Chute Weight versus m/C_{DA} (Altitude of 10,000 feet at Main Chute Deployment and $\gamma_{e\text{nominal}}$ of 60 degrees).....	217
116	Suspended Weight and Main Chute Weight versus m/C_{DA} (Impact Velocity of 50 fps and $\gamma_{e\text{nominal}}$ of 40 degrees)	218
117	Suspended Weight and Main Chute Weight versus m/C_{DA} (Impact Velocity of 150 fps and $\gamma_{e\text{nominal}}$ of 40 degrees)	219
118	Suspended Weight and Drogue Chute Weight versus m/C_{DA} (Altitude of 5000 feet at Main Chute Deployment and $\gamma_{e\text{nominal}}$ of 40 degrees)	220
119	Suspended Weight and Drogue Chute Weight versus m/C_{DA} (Altitude of 8000 feet at Main Chute Deployment and $\gamma_{e\text{nominal}}$ of 40 degrees)	221
120	Suspended Weight and Drogue Chute Weight versus m/C_{DA} (Altitude of 10,000 feet at Main Chute Deployment and $\gamma_{e\text{nominal}}$ of 40 degrees)	222
121	Optimum m/C_{DA} versus Nominal Entry Angle	223
122	Optimum Suspended Weight versus Nominal Entry Angle .	224
123	Suspended Weight versus m/C_{DA} (Comparison between 90 degrees Nominal Entry Design and Entire Entry Angle Spectrum 20 - 90 degrees)	225
124	Suspended Weight and Main Chute Weight versus m/C_{DA} (Impact Velocity of 50 fps, $\gamma_{e\text{nominal}}$ of 60 degrees and Drogue Deployment at Mach 3.0)	226
125	Suspended Weight and Main Chute Weight versus m/C_{DA} (Impact Velocity of 50 fps, $\gamma_{e\text{nominal}}$ of 60 degrees and Drogue Deployment at Mach 3.5)	227
126	Optimum m/C_{DA} versus Drogue Deployment Mach Number ($\gamma_{e\text{nominal}}$ of 60 degrees and V_{imp} of 50 fps) ...	228

ILLUSTRATIONS (Cont'd)

Figure 127	Optimum Suspended Weight versus Drogue Mach Number ($\gamma_{e\text{nominal}}$ of 60 degrees and V_{imp} of 50 fps)	229
128	Suspended Weight and Main Chute Weight versus m/C_{DA} in the "I" Model Atmosphere (Impact Velocity of 50 fps, $\gamma_{e\text{nominal}}$ of 90 degrees and Drogue Deployment at Mach 2.5)	230
129	Suspended Weight and Main Chute Weight versus m/C_{DA} in the "I" Model Atmosphere (Impact Velocity of 150 fps, $\gamma_{e\text{nominal}}$ of 90 degrees and Drogue Deployment at Mach 2.5)	231
130	Suspended Weight and Main Chute Weight versus m/C_{DA} in the "K" Model Atmosphere (Impact Velocity of 50 fps, $\gamma_{e\text{nominal}}$ of 90 degrees and Drogue Deployment at Mach 2.5)	232
131	Suspended Weight and Main Chute Weight versus m/C_{DA} in the "K" Model Atmosphere (Impact Velocity of 150 fps, $\gamma_{e\text{nominal}}$ of 90 degrees and Drogue Deployment at 2.5)	233
132	Optimum Suspended Weight and m/C_{DA} versus Surface Pressure (Impact Velocity of 50 fps, $\gamma_{e\text{nominal}}$ of 90 degrees and Drogue Deployment at Mach 2.5)	234
133	Optimum Suspended Weight versus Nominal Entry Angle for an 80-Inch Vehicle	236
134	Optimum Suspended Weight versus Nominal Entry Angle for a 90-Inch Vehicle	237
135	Optimum Suspended Weight versus Vehicle Diameter	238
136	Parachute Configuration and Nomenclature	240
137	Drogue Chute Actuation Trajectory Data	245
138	Variation of Lander Axial Deceleration with Mach Number	248

ILLUSTRATIONS (Cont'd)

Figure 139	Variation of Lander Axial Deceleration with Mach Number	249
140	Sensing System Schematic	253
141	Material Properties of Crushable Materials	259
142	Landed Package Shapes	260
143	Lenticular - Impact Attenuator Parameters	261
144	Sphere - Plastic Foam	262
145	Sphere - Balsa Wood - Full Density	263
146	Sphere - Balsa Wood - Low Density	264
147	Sphere - Aluminum Honeycomb - Payload Ratio	265
148	Sphere - Aluminum Honeycomb - Deceleration Parameter	266
149	Sphere - Aluminum Honeycomb - Radius Parameter ..	267
150	Minimax Deceleration versus Payload Mass	270
151	Desired Material Properties - $v_0 = 250$ fps	271
152	Desired Material Properties - $v_0 = 400$ fps	272
153	Desired Material Properties - $v_0 = 600$ fps	273
154	Crushable Material Properties	274
155	Design Data - $v_0 = 210$ fps - Aluminum Honeycomb - Curve Fit	275
156	Typical Design Curve	276
157	Material Properties Based on Curve Fit, - $v_0 = 210$ fps	277
158	Design Data - $v_0 = 250$ fps - Al Honeycomb - Curve Fit.	278

ILLUSTRATIONS (Cont'd)

Figure 159	Material Properties Based on Curve Fit - $v_o = 250$ fps ...	279
160	Design Data - $v_o = 200$ fps - Al Honeycomb - 5052	280
161	Design Data - $v_o = 250$ fps - Al Honeycomb - 5052	281
162	Ratio of Total Landed Mass to Payload Mass versus Impact Velocity - Balsa Wood	283
163	Payload Mass - Outside Radius Factor versus Impact Velocity - Balsa Wood	284
164	Impact G Parameter - versus Impact Velocity - Balsa Wood	285
165	Variation of Payload Weight with Impact Velocity and Packaging Density	287
166	Total Landed Weight versus Outside Radius	288
167	Instrument Package Weight versus n	289
168	Outside Radius versus n	290
169	Maximum Crushing Stress versus n	291
170	Instrument Package Weight and Outside Radius versus m.	292
171	No-Chute Parametric Design Curves	294
172	Optimum W_{PL}/A versus W_{HS}/A for Various Atmospheres	295
173	Optimum W_{PL}/A versus W_{HS}/A for Various Wind Velocities	297
174	Single Chute System Parameters	299
175	Optimization of Single Chute System for Various Descent Velocities - Balsa Wood	300
176	Optimization of Single Chute System - Aluminum Honeycomb	301

ILLUSTRATIONS (Cont'd)

Figure 177	Optimization of Descent Velocity for Two-Chute System - for Various Altitudes	303
178	Optimization of Descent Velocity for Two-Chute System - for Various G Levels	304
179	Typical Shock Spectrum	309
180	Acceleration versus Time for Exponential Pulse	310
181	Acceleration versus Distance for Exponential Pulse	311
182	Maximum Response Factor for Exponential Pulse	312
183	Equilibrium $a_{S/\epsilon}$ Near Earth	315
184	Equilibrium Surface Temperature Near Earth	316
185	Canister Temperatures for Various Bus Temperature during Cruise	318
186	Heat Exchange Between an Enclosed Body and Enclosure and Between Parallel Walls	321
187	Temperature Drop Across a Spherical Wall	323
188	Variation of Illuminated Areas with Solar Aspect Angle ...	324
189	Equilibrium $a_{S/\epsilon}$ to Maintain Temperature	325
190	Equilibrium $a_{S/\epsilon}$ - Various a_{SAB} / a_{SN} Ratios	326
191	Transient Temperature of Beryllium Afterbody During Mars Entry	328
192	Mars Entry, Backface Temperature Heat of Heat Shield ..	329
193	Transient Temperature of Lander Crush-up Due to Radiant Heating from Afterbody during Mars Entry	330
194	Lander Thermal Network	334
195	Transient Temperatures Near Earth	335

ILLUSTRATIONS (Cont'd)

Figure 196	Transient Temperatures at Start of Cruise Near Earth	336
197	Lander Separated from Bus Near Mars	337
198	Telemetry Link Requirements	344
199	Plane Wave Attenuation Coefficient for Various Dielectric Crushup Materials	345
200	Plane Wave Attenuation Coefficient for Various Dielectric Crushup Materials	346
201	Carrier Uncertainty versus Carrier Frequency versus Velocity Uncertainty	350
202	Acquisition Time versus Carrier Loop Noise Bandwidth versus Carrier Uncertainty	351
203	Error Probability versus Signal Energy/Noise Power Density for Coherent PSK	356
204	P. N. Code Acquisition Time versus Noise Bandwidth .	357
205	Pre-entry and Landed Relay Links Transmitter Power/Net Antenna Gain Product versus Slant Range versus Bit Rate ($f_c = 2000$ mc)	359
206	Descent Relay Link Transmitter Power/Net Antenna Gain Product versus Slant Range versus Bit Rate $2 B_{10} = 20$ cps	360
207	Descent Relay Link Transmitter Power/Net Antenna Gain Product versus Slant Range versus Bit Rate $2 B_{10} = 50$ cps	361
208	Descent Relay Link Transmitter Power/Net Antenna Gain Product versus Slant Range versus Bit Rate $2 B_{10} =$ cps	362
209	Descent Relay Link Transmitter Power/Net Antenna Gain Product versus Slant Range versus Bit Rate $2 B_{10} = 200$ cps	363

ILLUSTRATIONS (Cont'd)

Figure 210	AP_{TG} versus Frequency	364
211	Direct Link Transmitter Power/Net Antenna Gain Product versus Slant Range	365
212	Altimeter Range versus Transmitter Power - Antenna Gain versus Pulse Integration Improvement for Re- flectivity Coefficient	370
213	Altimeter Range versus Transmitter Power - Antenna Gain versus Pulse Integration Improvement for Re- flectivity Coefficient	371
214	Gain and Beamwidth of Horn Antennas versus Aperature Size	372
215	Antenna Total Gain* versus Look Angle to Target (From Antenna E)	375
216	Horn Aperture Size in Inches versus Frequency versus Horn Aperture Size in Wavelengths	376
217	Battery Weight versus Operating Time and Power for Communications, Science, and Guidance	377
218	Battery Weight versus Transmitter Operating Time versus Radiated Power	378
219	General Load Profile	383
220	Power System During Data Transmission	383
221	Power System During Data Acquisition	383
222	P_{RTG} Versus $P_C + P_S$	385
223	Added P_{RTG} to Recharge Battery	386
224	Horn Antenna Dimensions in Wavelengths	393
225	Horn Antenna Weight versus Frequency	394

ILLUSTRATIONS (Cont'd)

Figure 226	Solid State Exciter Weight, Volume, Power Conversion Efficiency, and Maximum Power Output versus Frequency	395
227	Amplitron Amplifier Weight versus Output Power	397
228	Amplitron Amplifier Volume versus Output Power	398
229	Amplitron Amplifier Efficiency versus Frequency	399
230	Amplitron Drive Power Required versus Output Power ..	400
231	Amplitron Configurations	401
232	Amplitron Amplifier Efficiency versus Output Power	402
233	Weight versus Storage Capacity for Class 1, 2, 3 Shock Levels	404
234	Volume versus Storage Capacity for Class 1, 2, 3 Shock Levels	405
235	Power versus Storage Capacity for Class 1, 2, 3 Shock Levels	406
236	Budgetary Cost of Storage Capacity for Class 1, 2, 3 Shock Levels	407
237	Weight versus Storage Capacity for 100 g Shock Level ...	408
238	Volume versus Storage Capacity for 100 g, 1500 g, 6000 g Shock Level	409
239	Power versus Storage Capacity for Class 1, 100 g, Class 2, 1500 g, Class 3, 6000 g Shock Levels	410
240	Volume, Power, Weight, versus Storage Capacity at 100 g, 150 g Shock Level	412
241	Generator Weight versus Output Power	416
242	Characteristic Shape of a Thermoelectric Generator ...	417

ILLUSTRATIONS (Concl'd)

Figure 243	Advanced Mariner Lander - Communications and Power Subsystem Shock Diagram	419
244	Slot Antenna	428
245	Typical Radiation Pattern - Slot Antenna	429
246	Circularly Polarized Horn	430
247	Typical Radiation Pattern - Horn Antenna*	431
248	Typical Radiation Pattern - Horn Antenna*	435
249	Impact Dynamics Parameters	441
250	Typical Stress Strain Curve	442
251	Landed Package Geomentry	447
252	Variable Crushing Stress Parameters - General	450
253	Variable Crushing Stress Parameters - Non-Homogeneous Material	452
254	Variable Crushing Stress Parameters - Anisotropic Material	454
255	Crushing Stress versus Angle-Anisotropic Material	456
256	Normalized Acceleration versus Stroke - Non-Homogeneous Impact Absorber	458
257	Normalized Acceleration versus Stroke-Anisotropic Impact Absorber	459
258	"Double-Crushing"	460
259	Wind Dynamics Parameters	462
260	Horizontal Velocity versus Wind Layer Thickness	465
261	Total Descent Velocity versus Vertical Velocity	466
262	Total Descent Velocity versus Wind Layer Thickness ...	467

TABLES

Table 1	Parametric Analysis of Payloads 1 through 7	2
2	Mission Conditions for Payloads 1 through 7	3
3	Mission Conditions for Payloads 10 through 16	4
4	Parametric Payload Characteristics	5
5	Parametric Weights of Communications, Instrumentation and Power Systems	6
6	Payload 9 - Power Usage Breakdown	10
7	Payload 10 - Power Usage Breakdown	11
8	Payload 11 - Power Usage Breakdown	12
9	Payload 15 - Power Usage Breakdown	13
10	Payload 9 - Weight and Volume	14
11	Payload 10 - Weight and Volume	15
12	Payload 11 - Weight and Volume	16
13	Payload 15 - Weight and Volume	17
14	Assumed Geometry at Atmospheric Entry	20
15	Relay Communication - Post Impact Link	24
16	Payload 16 - Weight and Volume	26
17	Relative Expected Yields - Single Launch of Alternative Payloads	28
18	Payload 9 - Vehicle Design Criteria	32
19	Lander System Design Summary	42
20	JPL Instrumentation List for Lander	47
21	Advanced Mariner Lander Scientific Payloads	54

TABLES (Cont'd)

Table 22	Advanced Mariner Payloads	55
23	Weight Summary	77
24	Non - Parametized Weights	80
25	Parametric Study Summary Table	82
26	Mars Model Atmospheres	88
27	Conceptual Design Summary Table	110
28	Convective Heating Program Inputs.....	128
29	Heat Shield Material Properties	131
30	Heat Shield Substructure Material Properties.....	132
31	Weight of Drogue Chute Suspension Lines	239
32	Weight of Main Chute Suspension Lines	243
33	Drogue Chute Actuation Performance.....	247
34	Main Chute Actuation Performance.....	251
35	Flight Trajectory Sequence.....	252
36	Aluminum Honeycomb Properties	305
37	Conceptual Design Parameters	306
38	Surface Absorptivities and Emissivities	333
39	Assumed DSIF Characteristics	341
40	R.F. Component Insertion Losses	349
41	P.N. Bits Per Data Bit Versus P.N. Code Length.....	352
42	Telecommunications Design Control Chart - Lander to Flyby/Bus	353
43	Telecommunications Design Control Chart - Lander to DSIF	366

TABLES (Concl'd)

Table 44	Telecommunications Design Control Chart - Altimeter	368
45	Glossary of Terms	379
46	Lander Power System Contacts.....	380
47	Comparison of Curium 244 and Plutonium 238	389
48	Lander Communication Subsystem Contacts	391
49	Data Handling Subsystem and Programmer Characteristics	413
50	Radar Altimeter Characteristics	414
51	RTG Dimensions - Intact Entry	415
52	Advanced Mariner Lander Communications and Power Subsystem Parts List	420
53	Direct Link Performance Margins	423
54	Post Impact Relay Link.....	424
55	Descent Relay Link	426
56	Payload 16 - Power Usage Breakdown for Landed Payload.....	433
57	Communication Payload - External and Landed.....	434

SUMMARY

This report presents the results of a 4-month parametric analysis and conceptual design study conducted by the Research and Advanced Development Division of the Avco Corporation for the Jet Propulsion Laboratory. The study objectives included a parametric analysis of the unmanned flyby bus/lander concept for scientific investigation of Mars during the 1969 and 1971 launch opportunities, a conceptual design of the selected configuration, and development and cost plan indicating the program leading to development and first flight of the Advanced Mariner vehicle in 1969.

The flyby/lander concept utilizes a 93-pound spacecraft launched on an Atlas Centaur launch vehicle. The scientific capabilities of the lander and flyby bus vehicles were determined to obtain a balance between scientific data and overall systems complexity commensurate with the first landing mission to Mars.

The lander vehicle separates from the flyby bus vehicle prior to planet encounter, enters the planetary atmosphere, and descends to the surface on a parachute. During atmospheric entry, parachute descent, and surface operations, the lander analyzes the Martian atmosphere and, for 5 hours after impact, determines wind velocity, and also performs a simple life-detection experiment. The information is transmitted to Earth via both a direct transmission link to the DSIF and is also relayed through the flyby bus which has been placed on a delayed flyby trajectory for this purpose. The flyby bus also collects interplanetary data and maps the planet. The lander vehicle has been designed to accommodate the minimum projected atmosphere for Mars (11-millibar surface pressure) and surface winds gusting to 200 ft/sec resulting in impact loads of up to 1500 g for a landed payload protected by crushable material. The lander is to be dry-heat sterilized to avoid contamination of Mars with Earth organisms while the flyby bus is placed on a biased trajectory providing a small probability of entering the planetary atmosphere. Therefore it is not required to be sterilized.

The development plan shows that a minimum of three launch attempts are necessary to achieve an 84 percent chance of a successful mission in the 1969 and 1971 launch opportunities, requiring that hardware development begin in early 1965 to meet a 1969 launch date.

INTRODUCTION

The primary objective of the lander study was to conduct parametric evaluations of all pertinent subsystems to such a depth that a conceptual design could be easily synthesized for a given mission objective. In order to do this, a rather detailed parametric study had to be pursued to a depth such that all pertinent design parameters could be evaluated as to their effect on the mission objectives. Each major subsystem within a given lander design was treated as a major discipline so that primary importance could be given each significant tradeoff evaluation in that system and its influences on other interfacing subsystems. In each subsystem, optimization analyses were conducted to fix certain parameters and to aid in the optimization of the complete system.

Such major subsystems as the heat shield system, descent system, impact system, and communication system (including power supply) were given primary emphasis. Other supporting disciplines--aerodynamics, thermal control, scientific instrumentation, and design--provided the final link in the subsystem integration.

With a completely parametric subsystem evaluation, a conceptual design synthesis could be pursued. In order to synthesize a lander design, certain basic mission objectives had to be assigned first. The mission objectives for the lander conceptual design as defined by JPL and Avco RAD are:

1. Define atmospheric model, including (a) surface pressure, (b) surface temperature, (c) density profile, and (d) composition
2. Determine existence of life on Mars
3. Determine surface wind velocities.

With these objectives and the requirement for atmospheric data transmission prior to impact, a system was synthesized. Other basic ground rules established for the study are:

1. Apollo shape (slight modifications)
2. Dry heat sterilization
3. Passive (omnidirectional) impact system
4. Kaplan's atmospheric models (11 to 30 mb)
5. 200 ft/sec winds.

The final conceptual design resulted in a 90-inch-diameter modified Apollo shape (30-degree afterbody), entry weight of 516 lb, and a $m/C_D A = 0.25$ slug/ft². This design is based on landing a 8.5-lb scientific package in the area of Syrtis Major for biological determination and for pressure, temperature, and wind measurements. The design allows for atmospheric sampling of pressure and temperature by direct measurement while on the main parachute and determining the density profile by measuring vehicle performance during entry with a 3-axis accelerometer. Composition of the atmosphere is determined by a multichannel radiometer at the stagnation point during peak heating. All atmospheric data are played out during main chute descent (~ 100 seconds) by an independent communication system prepared for that purpose. All together there are three communication systems included in the lander. The first system plays out engineering and diagnostic data after lander separation and prior to entry, the second plays out descent data prior to impact, and the last, located in the landed payload, plays out the descent data again as well as all post-impact data (biological and wind). Alternate concepts which could possibly eliminate one of these systems could be evaluated in a more detailed system study.

The landed package is a spherical ball with impact attenuation material (aluminum honeycomb) all over. Inside this sphere is the landed payload employing a floatation system for antenna erection after impact. This type of system resulted after an evaluation of many erection methods; however, all others required knowledge of the surface terrain whereas this system did not and could function properly under the most adverse condition. Further details of the lander system are presented in great detail in the following text, subsystem by subsystem, starting with the conceptual design synthesis.

In this volume only the lander from start of atmospheric entry to impact (landing) on the surface will be covered. The phase from flyby/bus separation to entry will be fully covered in the flyby/bus report (volume IV), since this phase involves the flyby bus interface and actuation procedures.

1.0 CONCEPTUAL DESIGN SYNTHESIS

It is the primary objective of this section of the report to discuss the approach and usage of the parametric data in order to synthesize a conceptual design. Two independent paths will be pursued in the approach to a conceptual design synthesis: (1) payload analysis, and (2) vehicle analysis. The first path--payload analysis--will lead to the selected payload through parametric evaluation of the mission objectives in terms of scientific instrumentation and communication requirements. Several payload possibilities will be evaluated for the selected mission objectives described by the systems analysis (Ref. Systems--volume II). The final payload selection will then be discussed in detail, showing the pertinent design features of each subsystem involved. Alternate approaches will also be indicated in areas of possible improvement. The second path--vehicle analysis--will define the vehicle (lander) requirements necessary to accomplish the selected mission objectives. The analysis is confined to the mechanical system design of the lander (i.e., heat shield system, descent system, etc.). Summary parametric curves, based on these systems, were generated in terms of available payload weight as a function of lander diameter for each of the mission objectives defining the payloads. By projecting on these curves the payloads generated in the payload analysis, the final lander design requirements can be established and hence a conceptual design synthesized.

A limited reliability analysis for selected payloads is presented to evaluate the scientific return of these payloads in terms of probability of success.

Finally a complete summary of all pertinent subsystems requirements is presented for the conceptual design selection. This design will be fully evaluated, subsystem by subsystem, in the remaining sections of this report.

1.1 PAYLOAD ANALYSIS

During the early phases of the parametric analyses, various lander payload packages were synthesized utilizing the JPL-supplied instrumentation list and parametric tradeoff curves on communication and power. Section 2.0 describes the approaches to the scientific payload selection. Communication subsystem and power supply subsystem tradeoffs were made versus range, trajectory geometry, antenna geometry, bit rates, and so forth, for application to a relay communication system from lander to bus to DSIF and/or a direct system from lander to DSIF. Section 10 describes the communication and power supply system technology applied.

Seven lander payloads were established, with variations within each, to accomplish several selected missions as shown in table 1. The fixed conditions and parametric data for these first payload determinations are listed in table 2. Payload groupings (number 1 through 7) satisfied the mission objectives and were characterized by landed lifetimes of from 12 to 48 hours duration and by mission total bit content in excess of 1,000,000.

TABLE I
PARAMETRIC ANALYSIS OF PAYLOADS 1 THROUGH 7

Payload	Comm. Systems	Power Source	Scientific Instrument (wt-lb)	Instrument Power (wt-lb)	Comm. System (wt-lb)	Comm. Power (wt-lb)	Payload Total (wt-lb)	Bit Rate (bits/sec)		Comm. Direct (hours)	Time Relay (min.)	Transmitter Power (watts)
								Direct	Relay			
1a	Relay	Batt.	45	74	42	6	167	None	8200	None	0.5	100
b	Relay	Batt.	45	74	42	6	167	None	4850	None	0.8	60
c	Relay	Batt.	45	74	42	7	168	None	800	None	4.5	10
d	Direct	Fuel Cell	45	30	40	72	187	18	None	3.4	None	100
e	Direct	Batt.	45	74	40	178	337	18	None	3.4	None	100
	Direct	Batt.	45	74	40	387	546	5	None	12.1	None	60
2a	Relay	Batt.	45	145	42	7	239	None	8200	None	0.9	100
b	Direct	Fuel Cell	45	58	40	143	286	18	None	6.8	None	100
c	Direct	Batt.	45	145	40	356	586	18	None	6.8	None	100
d	Relay	Batt.	62	74	42	15	193	None	8100	None	8.1	100
3a	D and R	Fuel Cell	62	30	63	77	232	18	8100	3.4	8.1	100
b	D and R	Batt.	62	74	63	192	391	18	8100	3.4	8.1	100
c	Relay	Batt.	62	147	42	15	266	None	8100	None	8.1	100
4a	D and R	Fuel Cell	62	59	63	146	330	18	8100	6.8	8.1	100
b	D and R	Batt.	62	147	63	364	636	18	8100	6.8	8.1	100
5	Relay	Fuel Cell	81	12	42	14	149	None	8100	None	11.2	100
6	D and R	Fuel Cell	92	15	66	29	202	18	8100	0.3	11.2	100
7	D and R	Fuel Cell	92	20	63	43	218	18	8100	0.6	11.2	100

As the parametric study continued it was determined that these payload formulations were too ambitious for the Advanced Mariner concept because of limitations of the state-of-the-art of the complex payloads synthesized and/or because of the allowable landed payload weight and volume. New payload groupings were evolved which satisfied mission objectives ranging from simple "land and survive" to missions of increasing complexity.

This new grouping of payloads was identified numerically as 8 through 15. The mission conditions for payloads 8 and 9 were the same as listed in table 2 except no direct link communications were considered. Mission conditions for payloads 10 through 16 are shown in table 3. The characteristics of each payload are summarized in table 4. Payload 6 of the original grouping is shown on the table to indicate its relative complexity when compared with those payloads in the new grouping. Payload 16 is the conceptual design payload. A parametric weight summary for the payloads listed in table 4 is shown in table 5.

TABLE 2

MISSION CONDITIONS FOR PAYLOADS 1 THROUGH 7

Launch Date	19 February 1969
Communication range - Direct	188×10^6 km
Communication Time - Relay	2 minutes, entry to impact. 1 minute, separation to entry
Communication Range - Relay	75×10^3 km
Approach Velocity	4.34 km/sec
Periapsis Radius	15×10^3 km
Entry Angle	-45 degree
Bit Rate-Direct	18 at 100 w; 6 bps at 60 w
Separation Range	5×10^6 km
Bus Weight	800 lb

TABLE 3

MISSIONS CONDITIONS FOR PAYLOADS 10 THROUGH 16

Launch Window	10 Jan to 11 Feb 1969
Arrival Date	15 Oct to 2 Nov 1969
Communication Range - Direct	176×10^6 km max.
Communication Range - Relay	75×10^3 km max.
Departure Velocity	3.35 to 3.72 km/sec
Approach Velocity	3.74 to 4.20 km/sec
Pariapsis Altitude	
1. Midcourse correction	$32,340 \pm 23,130$ km
2. Midcourse corrections	$6,323 \pm 3,621$ km
Lander Entry Angle (Syrtis Major)	-66 to -74 degrees
Separation Range	1 to 5×10^6 km
Lander Entry Velocity	21,000 ft/sec

A thorough analysis was made of Payloads 9, 10, 11 and 15, according to the following objectives:

<u>Payload</u>	<u>Mission Objectives</u>
9	1. Land and survive
	2. Provide engineering diagnostic data
10	3. Conduct minimum (5 hour) biological experiment, plus 1 and 2.
11	4. Conduct extended (24 hour) biological experiment, plus 1 and 2.
15	5. Provide descent television, plus 1, 2, and 3.

These payloads vary--in landed lifetime from 1 hour to 24 hours, and in size from an entry vehicle that weighs less than 400 lb compatible with nonflooded Atlas payloads and the Surveyor shroud limitation to one that requires 30 percent Atlas flooding and shroud "hammerheading" up to approximately 140 inches in diameter.

TABLE 4

PARAMETRIC PAYLOAD CHARACTERISTICS

PAYLOAD NUMBER	CHARACTERISTIC	POST-IMPACT RELAY LINK	POST-IMPACT DIAGNOSTICS	POST-IMPACT DIRECT LINK	OF PREENTRY TRANSMISSION	PARACHUTE SYSTEM	ENTRY MEASUREMENTS	POST-IMPACT TV TRANSMISSION	POST-IMPACT DESCENT TRANSMISSION	ATMOSPHERIC MEASUREMENTS	POST-IMPACT TRANSMISSION	ATMOSPHERIC MEASUREMENTS WITH DESCENT	MISSION DURATION NOMINAL HOURS
8													< 2
9					*								< 2
10													5
15													5
11													24
12													24
13													24
14													24
6													24
16													5

* BACK UP MODE

64-10023

TABLE 5
PARAMETRIC WEIGHTS OF COMMUNICATIONS, INSTRUMENTATION, AND POWER SYSTEMS

PAYLOAD	COMM. SYSTEM	POWER SOURCE	TRANSMITTER POWER (WATTS)	INST. WT. (LB)	INST. POWER WT. (LB)	COMM. WT. (LB)	COMM. POWER WT. (LB)	PAYLOAD WT. (LB)
8	RELAY	BATT.	60	0.3	0.1	44.5	2.0	46.9
9	DIRECT+RELAY	BATT.	60	1.3	0.2	59.1	14.3	74.9
10	DIRECT+RELAY	BATT.	60	8.3	3.5	59.1	16.7	87.6
15	DIRECT+RELAY	FUEL CELL	30 / 100	32.3	4.1	60.7	13.4	110.5
11	DIRECT+RELAY	FUEL CELL	60	27.3	8.4	59.1	8.6	103.4
12	DIRECT+RELAY	FUEL CELL	60	59.3	37.6	59.1	11.0	167.0
13	DIRECT+RELAY	FUEL CELL	60	76.3	38.2	59.1	28.6	202.2
14	DIRECT+RELAY	FUEL CELL	60	72.6	39.4	64.5	17.0	180.8
6	DIRECT+RELAY	FUEL CELL	100	92.0	15.0	66.5	28.5	202.0
16	DIRECT + RELAY	BATT.	30 / 90	15.8	2.7	86.2	22.7	127.4

64-10022

In formulating these landed payloads, the parametric data presented in section 10 of this volume were used. The communication systems determination was the prime criterion for the selection of the power and subsequent weight of each of these selected four payloads. The results of the selection based on the use of this parametric data is presented on the following pages.

1.1.1 Communications System Determination for Lander Payloads 9, 10, 11, and 15

a. Relay Link--Payloads 9, 10, and 11

1) From section 10, figure 224 and 225: Select "L" equals 7.5 inches for horn antenna based on packaging optimization of antenna weight and volume as well as battery weight and volume.

2) From section 10, figure 216: Relay link frequency for 1.0-wavelength aperture horn antenna is 1.55 kmc at "L" equals 7.5 inches.

3) From section 10, figure 214: -3 db beamwidth point for 1.0 wavelength aperture antenna results in an included angle of 54 degrees and peak antenna gain is + 9.5 db.

4) Assume receiver antenna gain equals transmitter antenna gain results in total gain of twice + 9.5 db equals + 19.0 db.

5) Assume pointing losses for receiver and transmitter antennas equal -3.0 db each resulting in -6.0 db from + 19.0 db or +13.0 db.

6) From section 10, figure 210: Negative gain in power due to selected frequency of 1.55 kmc corrected from 2.0 kmc equals +2.2 dbw, where subscript w refers power to a level of 1 watt, added to + 13.0 db equals 15.2 dbw.

7) From section 10, figure 205: At 14 bps, $P_{TG} = 15.2$ for 2.55×10^4 -km range but desired range is 1.12×10^5 km or $P_{TG} = 28.0$ dbw (desired maximum range based on twice maximum periapsis altitude, 56,000 km, expected from one midcourse correction). Net transmitter power required equals 28.0 less 15.2 or 12.8 dbw.

$$10 \log_{10} \frac{R^P T}{1w} = 12.8 \text{ dbw}$$

$$R^P T = 19.1 \text{ watts}$$

- 8) Assume 1.55 kmc frequency amplifier efficiency equals that at 2.295 kmc, therefore consumed power equals 3.0 R^{PT} or 3.0 times 19.1 equals 57.3 watts.

Payload 15

- 1) Select $\dot{B} = 6300$ bps, based on 1.75 hours post-impact relay transmission.

a. Pressure data	0.026×10^5 bits
b. Radioisotope growth detector	0.012×10^5
c. Anemometer	0.036×10^5
d. Atmosphere mass spect.	0.055×10^5
e. Descent TV (5 pictures)	39.500×10^5
Approximately	39.8×10^5 bits

$$\frac{39.8 \times 10^5 \text{ bits}}{1.75 \text{ hrs} \times 3600 \text{ sec/hr}} = 6300 \text{ bits/sec}$$

- 2) Transmission range: 10^4 km, assumes twice maximum periapsis altitude of 5000 km based on two midcourse corrections and thrust vectoring at bus slowdown.
- 3) Frequency: 1.55 kmc, see payload 9, 10, and 11 considerations.
- 4) From section 10, figure 205: $R^{PTG} = 30.2$ dbw at 2.0 kmc
- 5) From section 10, figure 214: Antenna gain (2 x 9.5 db at 54 degrees beamwidth) + 19.0 dbw.

Pointing loss (2 x - 3db)	-6.0 dbw
	<u>13.0 dbw</u>

From section 10, figure 210: net gain in power due to selection of 1.55 kmc

Total antenna gain	+2.2 db
	<u>+15.2 db</u>

- 6) Net power required for transmission:

$$R^{PT} = R^{PTG} - \text{total antenna gain}$$

$$R^{PT} = 30.2 - 15.2 = 15.0 \text{ dbw}$$

$$10 \log_{10} \frac{R^{PT}}{1w} = 15.0 \text{ dbw}$$

$$R^{PT} = 31.6 \text{ watts.}$$

7) Using efficiency quoted at 2.295 kmc as applicable at 1.55 kmc, consumed power = $3.0 R_{PT}$ or 3.0×31.6 equals 94.8 watts.

b. Direct Link--Payloads 9, 10, 11, and 15

1) Assume $\dot{B} = 7$ bps

$$\begin{aligned} \text{range} &= 200 \times 10^6 \text{ km} \\ f &= 2.295 \text{ kmc} \end{aligned}$$

2) From section 10, figure 211: $P_{TG} = 12.8$ dbw at 5-cps bandwidth for $G = 1$ ($0.0 \text{ db} = G$)

The slot antenna was assumed to have an on-axis gain of +2.5 db. A pointing loss of -2.5 db was assumed to exist at 100 degrees off-axis, Earth-look angle. Thus the net antenna gain $G = +2.5 - 2.5 = 0.0 \text{ db} = G$, and therefore $R_{PT} = 12.8 \text{ dbw} = 19.1$ watts, the transmitter RF power required.

3) At 2.295 kmc, consumed power = $3.0 R_{PT}$ or 3.0×19.1 equals 57.3 w.

1.1.2 Power Usage for Payloads 9, 10, 11, and 15

To accommodate the selected scientific, communication, and data handling requirements established for each of these payloads, a power usage breakdown was calculated to establish the weight and volume required for the power supply subsystems. The summary of these calculations is shown in tables 6 through 9.

1.1.3 Weight and Volume for Payloads 9, 10, 11, and 15

Once the power supply weight and volume determination was completed, these inputs were added to the weight and volume figures selected from the scientific data lists (volume II--Systems) and the communication and data subsystems parametric analysis, section 10, to complete the payload package weight and volume tabulations shown in tables 10 through 13.

1.1.4 Payload 16 Synthesis

The final conceptual design payload requirements established scientific instruments for various phases of the lander operation based on the following JPL objectives:

1. Demonstrate capability of successful landing and survival for several hours

TABLE 6
PAYLOAD 9 -- POWER USAGE BREAKDOWN

Subsystem	Item	Power Usage	Mission Phase	Watts	Hours	Watt-Hr	Multiple Unit Usage Multiplier	Total Watt-Hr
Science Communications	Pressure Sensor	Cont.	Post Imp.	0.1	1.0	0.10	1	<u>0.10</u>
	Relay Link $P_{tot} = 3.0 \text{ Ptrans}$ $B = 14 \text{ bps}$ $P_{trans} = 19.1 \text{ w}$ $f = 1.55 \text{ kmc}$	Cont.	Post Sep.	57.3	0.25	14.33	1	14.33
		Cont.	Post Imp.	57.3	1.0	57.30	1	57.30
						Relay Link Subtotal		<u>71.63</u>
	Direct Link $P_{tot} = 3.0 \text{ Ptrans}$ $B = 7 \text{ bps}$ $f = 2.295 \text{ kmc}$ $P_{trans} = 19.1 \text{ w}$	Cont.	Post Imp.	57.3	0.25	14.33	1	14.33
Data						Direct Link Subtotal		<u>14.33</u>
						Communications Power Total		<u>85.96</u>
	Handling	Cont.	Post Sep.	4.0	0.25	1.0	1	1.00
	Programmer	Cont.	Post Imp.	4.0	1.0	4.0	1	4.00
	Recorder/Storage (3000 bits)	Cont.	Post Sep.	2.0	0.25	0.5	1	0.50
Miscellaneous		Cont.	Post Imp.	2.0	1.0	2.0	1	2.00
		Cont.	Post Imp.	1	1	1.0	1	1.00
						Data Power Total		<u>8.50</u>
	Eng. Data	Cont.	Post Imp.	1.0	1.0	1.0	1	1.00
						Total Power Required		<u>95.56</u>
						at 6.0 watt-hr/lb - Battery Weight = $\frac{95.56}{6.0} = 15.93 \text{ lb}$		
						at 7.66 in ³ /lb - Battery Volume = $15.93 \times 7.66 = 122.0 \text{ in}^3$		

TABLE 7
PAYLOAD 10 POWER USAGE BREAKDOWN

Subsystem	Item	Power Usage	Mission Phase	Watts	Hours	Watt-Hr	Multiple Unit Usage Multiplier	Total Watt-hr
Science	Pres. Sensor Bio. Inst. Anemometer	Cont.	Post Imp.	0.1	5.0	0.5	1	0.50
		Cont.	Post Imp.	3.0	5.0	15.0	1	15.00
		Cont.	Post Imp.	0.07	5.0	0.35	1	0.35
				Science Power Total				15.85
Communications	Relay Link $P_{tot} = 3.0 P_{trans}$ $B = 14 \text{ bps}$ $f = 1.55 \text{ kmc}$ $P_{trans} = 19.1 \text{ w}$	Cont.	Post Sep.	57.3	0.25	14.33	1	14.33
		Cont.	Post Imp.	57.3	1.0	57.3	1	57.30
				Relay Link Subtotal				71.63
		Cont.	Post Imp.	57.3	0.50	28.65	1	28.65
Data	Direct Link $P_{tot} = 3.0 P_{trans}$ $B = 7 \text{ bps}$ $f = 2.295 \text{ kmc}$ $P_{trans} = 19.1 \text{ w}$			Direct Link Subtotal				28.65
				Communications Power Total				100.28
	Handling	Cont.	Post Sep.	4.0	0.25	1.0	1	1.0
	Programmer	Cont.	Post Imp.	4.0	5.0	20.0	1	20.0
		Cont.	Post Sep.	2.0	0.25	0.5	1	0.5
	Recorder/Storage (9000 bits)	Cont.	Post Imp.	2.0	5.0	10.0	1	10.0
		Cont.	Post Imp.	1.7	5.0	8.5	1	8.5
Miscellaneous				Data Power Total				40.0
	Eng. Data	Cont.	Post Imp.	1.0	5.0	5.0	1	5.0
				Total Power Required				161.13
				at 6.0 watt-hr/lb - Battery Weight = 26.86 lb				
				at 7.66 in ³ /lb - Battery Volume = 205.7 in ³				

TABLE 8
PAYLOAD 11 POWER USAGE BREAKDOWN

Subsystem	Item	Power Usage	Mission Phase	Watts	Hours	Watt-Hr	Multiple Unit Usage Multiplier	Total Watt-Hr
Science	Pressure Sensor	Cont.	Post Imp.	0.1	24.0	2.4	1	2.4
	Anemometer	Cont.	Post Imp.	0.07	24.0	1.7	1	1.7
	Bio. Inst.	Cont.	Post Imp.	3.0	24.0	72.0	1	72.0
	Bio. Inst.	Cyclic	Post Imp.	2.0	12.0	24.0	1	24.0
	Sample Coll.	Cyclic	Post Imp.	4.0	0.5	2.0	1	2.0
Science Power Total								
102.1								
Communications	Relay Link	Cont.	Post Sep.	57.3	0.25	14.3	1	14.3
	P _{tot} = 3.0 P _{trans} B = 14/56 bps	Cont.	Post Imp.	57.3	1.0	57.3	1	57.3
	f = 1.55 kmc P _{trans} = 19.1 w	Cont.	Post Imp.	57.3	1.0	57.3	1	57.3
	Direct Link	Cont.	Post Imp.	57.3	1.0	57.3	1	57.3
	P _{tot} = 3.0 P _{trans} B = 7 bps f = 2.295 kmc P _{trans} = 19.1 w	Cont.	Post Imp.	57.3	1.0	57.3	1	57.3
Communication Subtotal								
128.9								
Data	Handling	Cont.	Post Sep.	8.0	0.25	2.0	1	2.0
	Programmer	Cont.	Post Imp.	8.0	24.0	192.0	1	192.0
	Recorder/Storage (18,000 bits)	Cont.	Post Sep.	4.0	0.25	1.0	1	1.0
		Cont.	Post Imp.	4.0	24.0	96.0	1	96.0
		Cont.	Post Imp.	2.5	24.0	60.0	1	60.0
Data Subtotal								
351.0								
Miscellaneous	Eng. Data	Cont.	Post Imp.	1.0	24.0	24.0		24.0
	Total Power Required							606.0
at 15 watt-hr/lb - Fuel Cell Weight = 40.4 lb								
at 25 in ³ /lb - Fuel Cell Volume = 1010.0 in								

TABLE 9
PAYLOAD 15 - POWER USAGE BREAKDOWN

Subsystem	Item	Power Usage	Mission Phase	Watts	Hours	Watt-Hr	Multiple Unit Usage Multiplier	Total Watt-Hr
Science	Pressure Sensor	Cont.	Post Imp.	0.1	5.0	0.5	1	0.5
	Bio. Inst.	Cont.	Post Imp.	3.0	5.0	15.0	1	15.0
	Anemometer	Cont.	Post Imp.	0.07	5.0	0.4	1	0.4
	Descent TV	Cyclic	Post Imp.	30.00	0.33	9.9	1	9.9
	Atm. Mass. Spect.	Cyclic	Post Imp.	4.5	1.0	4.5	1	4.5
Science Power Total						30.3		
Communications	Relay Link	Cont.	Post Sep.	94.8	0.08	7.6	1	12.8
	$P_{tot} = 3.0 P_{trans}$ $B = 6300 \text{ bps}$ $P_{trans} = 31.6$ $f = 1.55 \text{ kmc}$	Cont.	Post Imp.	94.8	1.75	165.9	1	165.9
	Direct Link			Relay Link Subtotal				
	$P_{tot} = 3.0 P_{trans}$ $B = 7$ $f = 2.295 \text{ kmc}$ $P_{trans} = 19.1$	Cont.	Post Imp.	57.3	0.5	28.7	1	28.7
				Direct Link Subtotal				
Data	Handling			Communications Power Total				
	Programmer			28.7				
	Recorder/Storage (4 x 10 ⁶ bits)			202.2				
	Eng. Data			2.0				
				40.0				
Miscellaneous				1.0				
				20.0				
				125.0				
				188.0				
				5.0				
Total Power Required						425.5		
at 15.0 watt-hr/lb - Fuel Cell Weight = $\frac{425.5}{15.0} = 28.4 \text{ lb}$								
at 25 in ³ /lb - Fuel Cell Volume = $28.4 \times 25 = 710 \text{ in}^3$								

TABLE 10

PAYLOAD 9 -- WEIGHT AND VOLUME

Subsystem	Item	Nominal		Number Necessary	Total Used Including Redundants	Final Total	
		Wt. (lb)	Vol. (in. ³)			Wt.(lb)	Vol.(in.)
Science Communications Relay Link	Pressure Sensor	0.3	4	1	1	0.3	4
			Science Subsystem Total			0.3	4
	Power Ampl.	5.1	110	1	2	10.2	220
	Exciter	4.4	76	1	2	8.8	152
Direct Link	7-1/2" horn ant.	3.4	390	1	1	3.4	390
	(1.55 kmc)		Relay Link Subtotal			22.4	762
	Power Ampl.	5.1	110	1	2	10.2	220
	Exciter	4.5	78	1	2	9.0	156
Power	6" Slot Ant.	4.0	300	1	1	4.0	300
	(2.295 kmc)		Direct Link Subtotal			23.2	676
	Battery		Communications Subsystem Total			45.6	1438
	(Ni-Cad, 6w-hr per lb., 7.66 in. ³ lb.)	15.9	122	1	1	15.9	122
Data	Handling		Power Subsystem Total			15.9	122
	Storage (3000 bits)	4.0	60	1	1	4.0	60
	Programming	5.4	68	1	1	5.4	68
		2.0	30	1	2	4.0	60
Miscellaneous	Cabling	3.0				13.4	188
	Eng. Instr.	1.0	---	1	1	3.0	---
	Diagnostic Instr.	1.0	---	1	1	1.0	---
	Brackets, etc.	1.3	---	1	1	1.3	---
Communications*			Miscellaneous			6.3	---
			Subtotal Impact Protected Equipment			81.5	1752
	Power Ampl.	5.1	110	1	1	5.1	110
	Exciter	4.4	76	1	1	4.4	76
	6" Slot Ant.	4.0	300	1	1	4.0	300
	(1.55 kmc)		Subtotal Pre-entry Relay			13.5	486
			Total Payload 9			95.0	2238

*Packaged externally to impact protected equipment

TABLE 11
PAYLOAD 10--WEIGHT AND VOLUME

Subsystem	Item	Nominal		Number Necessary	Total Used Including Redundants	Final Total	
		Wt. (lb)	Vol. (in. 3)			Wt. (lb)	Vol. in.)
Science	Pressure Sensor	0.3	4	1	1	0.3	4
	Simple Bio. Anemometer	6.0	504	1	1	6.0	504
		1.0	19	1	1	1.0	19
Communications Relay Link	Science Subsystem Total					7.3	527
	Power Ampl. Exciter	5.1	110	1	2	10.2	220
	7-1/2" horn ant. (1.55 kmc)	4.4	76	1	2	8.8	152
Direct Link		3.4	390	1	1	3.4	390
	Relay Link Subtotal					22.4	762
	Power Ampl. Exciter	5.1	110	1	2	10.2	220
Power	6" Slot Ant. (2.295 kmc)	4.5	78	1	2	9.0	156
		4.0	300	1	1	4.0	300
	Direct Link Subtotal					23.2	676
Data	Communication Subsystem Total					45.6	1438
	Battery (Ni-Cad, 6w-hr per lb., 7.66 in ³ /lb.)	26.8	205	1	1	26.8	205
	Power Subsystem Total					26.8	205
Miscellaneous	Handling Storage (9000 bits) Programming	4.0	60	1	1	4.0	60
		7.6	94	1	1	7.6	94
		2.0	30	1	2	4.0	60
Communications*	Data System Total					15.6	214
	Cabling	3.0	---	1	1	3.0	---
	Eng. Instr. Diagnostic Instr. Brackets, Etc.	1.0	---	1	1	1.0	---
Communications*		1.0	---	1	1	1.0	---
		1.3	---	1	1	1.3	---
	Miscellaneous Subtotal Impact Protected Equipment					6.3	---
Communications*	Power Ampl. Exciter	5.1	110	1	1	10.2	220
	Slot Antenna (1.55 kmc)	4.4	76	1	1	8.8	152
		4.0	300	1	1	4.0	300
Communications*	Subtotal Pre-entry Relay					13.5	486
	Total Payload 10					115.1	2870
						101.6	2384

*Packaged externally to impact protected equipment.

TABLE 12
PAYLOAD PACKAGE 11 WEIGHT AND VOLUME

Subsystem	Item	Nominal		Number Necessary	Total Used Including Redundants	Final Total	
		Wt. (lb)	Vol (in. ³)			Wt. (lb)	Vol. (in.)
Science	Pressure Sensor	0.3	4	1	1	0.3	4
	Anemometer	1.0	19	1	1	1.0	19
	Radio Isotope	6.0	504	1	1	6.0	504
	Growth Detector	4.0	300	1	1	4.0	300
	Sample Collector	15.0	600	1	1	15.0	600
Science Subsystem Total		26.3	1427				
Communications Relay Link	Power Ampl.	5.1	110	1	2	10.2	220
	Exciter	4.4	76	1	2	8.8	152
	7-1/2" Horn Ant. (1.55 kmc)	3.4	390	1	1	3.4	390
	Power Ampl.	5.1	110	1	2	10.2	220
	Exciter	4.5	78	1	2	9.0	156
Direct Link	6" Slot Antenna (2.295 kmc)	4.0	300	1	1	4.0	300
	Direct Link Subtotal	23.2	676				
	Communication Subsystem Total	45.6	1438				
Power	Fuel Cell (15 w-h/lb 25.0 in. ³ /lb)	40.4	1010	1	1	40.4	1010
	Power Subsystem Total	40.4	1010				
Data	Handling	7.0	120	1	1	7.0	120
	Storage (18,000 bits)	9.4	120	1	1	9.4	120
	Programming	4.0	60	1	2	8.0	120
Miscellaneous	Cabling	3.0	---	1	1	3.0	---
	Eng. Instr.	1.0	---	1	1	1.0	---
	Diagnostic Instr.	1.0	---	1	1	1.0	---
	Brackets, etc.	1.3	---	1	1	1.3	---
	Miscellaneous	6.3	---			6.3	---
Communications*	Subtotal Impact Protected Equipment	143.0	4235				
	Power Ampl.	5.1	110	1	1	5.1	110
	Exciter	4.4	76	1	1	4.4	76
	6" Slot Antenna	4.0	300	1	1	4.0	300
	Subtotal Pre-entry Relay	13.5	486				
Total Payload No. 11		156.5	4721				

*Packaged exclusively to impact protected equipment.

TABLE 13
PAYLOAD PACKAGE 15 WEIGHT AND VOLUME

Subsystem	Item	Nominal		Number Necessary	Total Used Including Redundants	Final Wt. (lb)	Total Vol. (in.)
		Wt. (lb)	Vol. (in. ³)				
Science	Pressure Sensor	0.3	4	1	1	0.3	4
	Radio Isotope	6.0	504	1	1	6.0	504
	Growth Detector						
	Anemometer	1.0	19	1	1	1.0	19
	Descent TV	17.0	505	1	1	17.0	504
Communications Relay Link	Atmospheric Mass Spectrometer	6.0	150	1	1	6.0	150
			Science Subsystem Total			30.3	1181
	Power Ampl.	5.9	116	1	2	11.8	232
	Exciter	4.4	78	1	2	8.8	156
	7-1/2" Horn Ant.	3.4	390	1	1	3.4	390
Direct Link			Relay Link Subtotal			24.0	778
	Power Ampl.	5.1	110	1	2	10.2	220
	Exciter	4.5	78	1	2	9.0	156
	6" Slot Antenna	4.0	300	1	1	4.0	300
			Direct Link Subtotal			23.2	676
Power			Communication Subsystem Total			47.2	1454
	Fuel Cell	28.4	710	1	1	28.4	710
	(15 w-hr/lb., 25 in. ³ /lb)		Power Subsystem Total			28.4	710
	Handling	7.0	120	1	1	7.0	120
	Storage(4x10 ⁶ bits)	45.0	1120	1	1	45.0	1120
Data	Programming	4.0	60	1	2	8.0	120
			Data Subsystem Total			60.0	1360
	Cabling	6.0	---	1	1	6.0	---
	Eng. Instr.	2.0	---	1	1	2.0	---
	Diagnostic Instr.	1.0	---	1	1	1.0	---
Miscellaneous	Brackets, etc.	3.6	---	1	1	3.6	---
			Miscellaneous Total			12.6	---
			Subtotal Impact Protected Equipment			177.9	4705
	Power Ampl.	5.1	110	1	1	5.1	110
	Exciter	4.4	76	1	1	4.4	76
Communications*	Slot Antenna	4.0	300	1	1	4.0	300
			Subtotal Pre-entry Relay			13.5	486
			Total Payload 15			191.4	5191

*Packaged externally to impact protected equipment.

2. Successfully perform a simple biological experiment on the surface for a period of 5 hours.

Avco RAD added the objective to obtain data in support of future missions. A detailed analysis is presented herein for the concept selected to accomplish the above objectives utilizing a representative communication system approach to store and appropriately transmit the data collected during the mission.

Within the brief conceptual design study ground rules, it was not expected that total subsystem optimization could be attained. For instance, further investigations have shown several alternate combinations such as reduction of RF power requirements by reduced data bit rates and/or reduced hardware requirement through RF switching which should be pursued in the preliminary design phase. Also the design presented herein assumes all of the worst case conditions of trajectory geometry and antenna pattern. Analysis of the instrumentation data bit requirements has shown them to be extremely conservative. Such factors as these, when more thoroughly optimized, will reduce the selected communication system power and complexity considerably, as discussed more thoroughly in section 10.8.

a. Systems Approach

The lander mission was divided into three phases after lander-flyby/bus separation:

- 1) Separation to entry
- 2) Entry to impact
- 3) Post-impact (on surface).

Scientific and engineering data requirements (listed in volume III, section 2.0 and volume II, section 2.3) established the type of scientific instruments and engineering instrumentation. Particular scientific instruments were selected to accomplish the data requirements. Total bits of data output from each phase of the mission were tabulated and traded off with the available time for data transmission during each phase of the mission to establish a transmitter bit rate. Data storage versus real time playout was factored into the playout time availability. Transmitter warmup and acquisition tradeoffs versus bandwidth were adjusted to maximize data transmission. The influence of lander transmitter frequency (relating to antenna size) versus bus relay receiver and DSIF command loop compatibility were considered, resulting in the selection of all the systems operating at DSIF frequency at an over-all reduced weight and complexity of the spacecraft system.

The combined design implementation of the above restraints with the trajectory geometry, established the RF power for each phase of the communication system selection. In case of subsystem malfunction during landing entry and descent, data should be played out prior to impact.

This requirement resulted in very high RF power for the 2-minute period of time to play out the large amount of accumulated entry and descent data, while descending on the main chute. The playout time for the separation to entry and on the planet surface is measured in hours; therefore bit rates can be kept low and RF power is reduced accordingly. Hence two separate systems were considered necessary.

For the selected concept the lander communication system operates via a relay link to the flyby/bus for all three phases of post-separation. In addition, a direct link system also transmits the required data during the post-impact phase. In selecting the total lander communication package, those systems which operate prior to impact were packaged external to the protected payload. Wherever possible, common elements were used without the use of any RF switching devices.

It was determined that the entry to impact phase operation required more than three times more RF power than any other phase but for a short operation time. Therefore, this link was designed independent of the others. When considering the other phases, the direct link operating during post-impact required the most RF power. Therefore, the other two relay systems (separation to entry and on surface) were selected at the same power resulting in a large performance margin during these phases. Section 10-7 shows the details of the communication and power systems conceptual design, compatible with the following payload synthesis.

b. Relay Link -- Entry to Impact Phase

1) Subsystem utilization

During atmospheric entry, data are recorded concerning the temperatures, pressures, and accelerations sensed by the lander. These stored data are then played back to the flyby/bus during main parachute descent via a 2.295-kmc relay link. Additional atmospheric data taken during main chute descent are also played out in real time (or with buffer storage, as required). Table 14 shows the geometry at atmospheric entry assumed for communication link design.

TABLE 14
ASSUMED GEOMETRY AT ATMOSPHERIC ENTRY

Planetocentric Latitude (degrees)	Flyby/Bus Inclination (degrees)	Nominal Flyby/Bus Slowdown (ips)	Time from Separation (hr)	Event	Slant Range Bus to Lander (km)	Lander to Bus Angle from Local Vert. at Lander (degrees)	Bus to Lander Angle from Local Vert. at Bus (degrees)
30 N	45	900	68.3	Atmospheric entry*	74,625	17.07	0.77
			71.3	Entry plus 3 hours -- landed	34,339	27.95	2.40
			73.3	Entry plus 5 hours -- landed	11,770	44.45	9.53
40 N	40	900	68.3	Atmospheric entry*	75,041	33.12	1.43
			71.3	Entry plus 3 hours -- landed	34,474	32.87	2.78
			73.3	Entry plus 5 hours -- landed	11,000	2.65	0.63

*Entry altitude is assumed at 800,000 feet.

2) Subsystem selection

From table 14 the communication systems were sized as follows:

a) Flyby/bus antenna (on flyby/bus gimballed payload platform, aimed along local vertical to planet)

<u>1</u>	Antenna type	Horn
<u>2</u>	Antenna frequency	2.295 kmc
<u>3</u>	Beamwidth (at -3 db points)	34°
<u>4</u>	Slant range (see look angle at entry in table 14)	<75,000 km
<u>5</u>	Look angle (from local vertical at bus to lander impact site, table 14)	1.43
<u>6</u>	Bus antenna total gain (section 10, figure 215)	+13.2 db

b) Lander antenna (on lander, external to impact protected package, aimed along local planet vertical)

<u>1</u>	Antenna type	Horn
<u>2</u>	Antenna frequency	2.295 kmc
<u>3</u>	Beamwidth (at -3 db points)	74°
<u>4</u>	Look angle (lander to bus, table 14)	33.12°
<u>5</u>	Assumed parachute sway angle (max)	±10°
<u>6</u>	Total antenna look angle	43.12°
<u>7</u>	Total antenna gain (section 10, figure 215)	+2.8 db

c) Net antenna gain (both antennas) "G" +16.0 db

d) Total data bits (to be transmitted)
(Volume II, section 2.3) 9165

- e) Main parachute descent time, i.e.,
transmission time (min., for $\gamma_E = -90^\circ$, "H"
atm, $m/C_D A = 0.244$) 110 seconds
- f) Total acquisition time (carrier + synch.) ~10.0 sec.
- g) Data transmission time (110 - 10) 100.0 sec.
- h) Bit rate (two total data bit transmissions) 184 bps
- i) Transmitter power/net antenna gain
product "P_TG" (at 75,000 km at 2.295 kmc) 35.45 dbw
- j) Required transmitter power
($P_T = R_P T - G = 35.45 - 16.0$) 19.45 dbw
- From dbw = $10 \log_{10} P_T / W$ 88.10 watts

Use 90-watt transmitter RF power.

c. Direct Link -- Post-Impact Phase

After landing, data generated by the lander scientific instruments and engineering diagnostic information are collected from the lander sub-systems. In addition, the information generated during the entry-to-impact phase has been stored and is transmitted with the landed data.

1) Communications range:

176.2×10^6 km for arrival on 2 November 69 (worst case in selected launch window; all other arrival dates have a shorter communications range).

2) Impact point:

20 degrees North latitude, 280.4 degrees longitude--selection based on 3-sigma dispersion for 150-km tracking error of 3×3.25 degrees = 9.70 degrees latitude dispersion and 3×3.20 degrees = 9.60 degrees longitude dispersion about an aim impact point of 10 degrees N. latitude and 290 degrees longitude (Syrtis Major). See figure 31, Volume I.

3) Earth elevation above Martian equator:

13.2 degrees S. latitude--worst angle possible during launch window.

4) Look angle to Earth:

56 degrees maximum, 33 degrees minimum, during mission with entry at a longitude corresponding to 0.75 hour after sunrise assuming zero time for descent (worst case).

5) Transmitting horn antenna beamwidth:

74 degrees at a 56 degree Earth look angle (limit or horn ability).

6) Antenna gain: (section 10, figure 18).

Look angle 56 degrees = -0.8 db "G"

7) Transmitter power - D^{P_T} :

a) Select 11.5 bps, multiple of 184 bps selected for descent link.

b) Then from section 10, figure 211, $D^{P_T} = 24.54$ watts.

c) Therefore, 30.0 watts was selected to add design performance margin.

d. Relay Link Post-Impact Phase

This link is the backup to the direct link for those data to be transmitted after impact. Parametric analysis showed that the system designed for the direct link would also accomplish the relay transmission with extra margin (ref. section 3.0 and 10.0). Therefore, the post-impact phase communication is accomplished through two modes using a single system.

An analysis was made of the look angles from the lander back to the flyby/bus, which was found to vary from 27.68 degrees N. latitude to 39.79 degrees N. latitude. The minimum flyby/bus trajectory inclination is limited to the same value. Assuming a nominal minimum inclination range of 40 to 45 degrees to allow for the window effect, and with a 900 ft/sec bus slowdown, for a nominal 10^6 km separation distance, table 15 was prepared.

e. Relay Link -- Separation-to-Entry Phase

The separation to entry phase of relay communication will be accomplished by a system similar to the direct/relay system selected for

TABLE 15

RELAY COMMUNICATION -- POST-IMPACT LINK

Margin for relay to bus link (db)		9.1	14.7	20.2	7.1	14.0	26.2
Direct communication selection	D^{PT} (watts)	30.0	30.0	30.0	30.0	30.0	30.0
	G (dbw)	14.8	14.8	14.8	14.8	14.8	14.8
Required R^{PT} at 2.295 kmc and $\dot{B} = 11.5$	R^{PT} (watts)	3.7	1.0	0.3	5.8	1.2	0.1
	G (dbw)	5.65	0.05	-5.45	7.65	0.75	-11.45
Total gain both antennas (db)		19.8	18.6	14.9	17.8	17.9	20.3
34-deg beamwidth total gain ant. (db) (section 10, figure 215)		13.3	13.2	12.4	13.2	13.2	13.3
Look-angle bus antenna C_L to Lander (degrees)		0.77	2.40	9.53	1.87	2.78	0.63
74-deg beamwidth antenna, total gain (db) (section 10, figure 215)		6.5	5.4	2.5	4.6	4.7	7.0
Communications range (km)		74625	34339	11770	75041	34474	11000
Look angle to bus from landed antenna C_L along local vertical at impact point		17.07°	27.95°	44.45°	33.12°	32.87°	2.65°
Periapsis altitude (km)		10^4	10^4	10^4	10^4	10^4	10^4
Time from entry (hr)		0	3	5	0	3	5
Entry trajectory inclination (degrees)		45	45	45	40	40	40
Initial intercept latitude (degrees North)		30	30	30	40	40	40

the post-impact phase, except for the antenna selection. The 30 watts of RF power available are more than adequate to transmit from a low-gain, wide-angle, slot antenna because of the short communication range. View angle constraints between the flyby/bus and lander after separation required the slot antenna to be located on the forebody. See section 10.7.3 for details of the slot antenna.

f. Payload 16 -- Weight and Volume

In synthesizing the lander payload, those scientific instruments and communications subsystems elements used from separation to impact were located external to the landed package except for the accelerometers mounted in the payload sphere at the center of gravity. The single-package power subsystem required for all phases of the mission is also located within the landed package. Weight and volume tabulates shown on table 16 were based on scientific instruments, communications, power, and data subsystems selected from appropriate sections of this volume. The total internal payload (landed) weight is 86.3 pounds, and the total external payload (pre-entry and descent) weight is 41.1 pounds, for a total lander payload weight of 127.4 pounds.

TABLE 16
PAYLOAD 16--WEIGHT AND VOLUME

Subsystem	Item	Reference	Nominal		Number Necessary	No. Incl. Redun- dants	Final Total	
			Weight (lb)	Volume (in. ³)			Weight (lbs)	Volume (in. ³)
Science	Pressure Sensor	Section 3	0.3	4	1	1	0.3	4
	Radioisotope	Table 23	6.0	204	1	1	6.0	204
	Growth Detector							
	Anemometer		1.0	19	1	1	1.0	19
	Accelerometers		0.4	10	3	3	1.2	30
Communications Landed Relay/ Direct	Power Amplifier	Section 10	5.8	115	1	2	8.5	257
	Exciter	Table 52					11.6	230
	34-Inch Horn		4.5	78	1	2	9.0	156
	Antenna		1.6	80	1	1	1.6	80
						Subtotal	22.2	466
Power	Battery	Section 10	25.3	194	1	1	25.3	194
Data	Handling	Table 56	7.0	120	1	1	7.0	120
	Storage	Table 56	8.3	100	1	1	8.3	100
	(12,000 bits)							
	Programming		4.0	60	1	2	8.0	120
						Subtotal	23.3	340
Miscellaneous	Cables	Section 10	3.0	---	1	1	3.0	
	Eng. Instruments	Table 52	2.0	---	1	1	2.0	
	Diagnostic Instruments		2.0	---	1	1	2.0	
						Subtotal	7.0	
						Total Internal	86.3	1257
Science	Radiometer	Section 3	1.5	24	1	1	1.5	24
	Pressure Sensor	Table 23	0.3	4	3	3	0.9	12
	Temp. Sensor		0.3	2	3	3	0.9	6
						Science Subsystem Total	3.3	42
Communications Preentry Relay	Power amplifier	Section 10	5.8	115	1	1	5.8	115
	Exciter	Table 52	4.5	78	1	1	4.5	78
	Slot Antenna		4.0	300	1	1	4.0	300
						Communications Subsystem Total	14.3	493
Descent Relay	Power amplifier	Section 10	9.4	145	1	1	9.4	145
	Exciter	Table 52	4.5	78	1	1	4.5	78
	3.84" Horn Ant.		1.6	80	1	1	1.6	80
						Descent Relay Subsystem Total	15.5	303
Miscellaneous	Cabling	Section 10	4.0	---	1	1	4.0	---
	Eng. Instrument	Table 52	2.0	---	1	1	2.0	---
	Eng. Diagnostic		2.0	---	1	1	2.0	---
							8.0	---
						Total External	41.1	138

1.2 PAYLOAD RELIABILITY ANALYSIS

1.2.1 Introduction

During the parametric evaluation phase, through the selection of the payload, reliability efforts were concerned with the analysis of alternate design concepts and mission approaches. In selecting a particular design concept or mission approach from among several alternatives, such parameters as performance, weight, power requirements, cost, volume, accuracy, information yield, and reliability must be taken into consideration. Depending on the concept or approach being analyzed, the pertinent parameters must be evaluated and factored into a comprehensive systems analysis study of the candidate alternatives. To this end, the purpose of the reliability analyses was to support the overall selection process by providing the necessary reliability inputs.

1.2.2 Analysis of Alternate Mission Payloads

The analysis was concerned with the evaluation of alternate mission payloads to determine which of several being considered has the highest expected yield. Information obtainable from the lander mission can be classified into the following data categories:

- a. Landing/survival data
- b. Diagnostic data
- c. Data for future missions
- d. Minimum biological data
- e. Extended biological data.

A number of payloads were synthesized to acquire these data. However, preliminary analyses reduced the number of prime candidates to five--payloads 9, 10, 11, 15, and 16. Consequently these five mission payloads were subjected to a more detailed evaluation.

This evaluation required the development of mission reliability profiles (from the point of lander separation) to show the success probabilities of significant events occurring during the payload missions. These success probabilities were integrated with relative (importance) values assigned to the above data categories to determine the relative expected yield of each payload.

The relative expected yield for a single launch attempt of alternate mission payloads is summarized in table 17. A review of the results shown in this

TABLE 17
RELATIVE EXPECTED YIELDS
SINGLE LAUNCH OF ALTERNATIVE PAYLOADS

Payload Number	Land and Survive	Diagnostic Data	Data for Future Missions	Minimum Bio	Extended Bio	Total Value	Percentage of Total Achieved ($\frac{\text{Expected}}{\text{Allocated}} \times 100$)
9	Allocated	22	3	1		26	56.6
	Expected	12.4	1.7	0.6		14.7	
10	Allocated	22	3	2	25	52	55.4
	Expected	12.3	1.7	1.1	13.7	28.8	
11	Allocated	22	3	2	25	72	53.8
	Expected	12.3	1.7	1.1	13.1	38.7	
15	Allocated	22	3	30	25	80	54.4
	Expected	12.1	1.6	16.4	13.4	43.5	
16	Allocated	22	3	25	25	75	54.4
	Expected	12.1	1.6	13.7	13.4	40.8	

Expected Yield = (Allocated Event Value) x (Event Success Probability)

5

table reveals that payload 9 returns the highest percent of its total allocated value (56.6 percent), followed in order by payloads 10, 16, 15, and 11. However the spread in percentage between payloads 9 and 11 is only 2.8 percent, indicating that no appreciable difference exists between payloads. In terms of expected yield, payload 15 has the highest yield (43.5), followed in descending order by payloads 16, 11, 10, and 9. A closer examination of the expected yields for payloads 16, 11, 10, and 9 shows that these payloads have yields which range from approximately 9/10 to 1/3 of that expected from payload 15. On this basis, payload 15 very definitely is the most superior payload, since it can be expected to result in the highest expected yield.

The total expected yields from a single launch attempt were extrapolated to the case of multilaunches, specifically two and three attempts. As the bar chart of figure 1 shows, the use of multilaunches has a significant effect in increasing the expected yields for all payloads.

1.2.3 Conclusion

The value of these analyses lies in the methods used by reliability personnel, independent of the remainder of the project study group. The reliability recommendations are, thus, free of the bias sometimes associated with conceptual design selections; i.e., the systems designer might choose, as the most reliable, a concept or approach which is superior for other reasons, but not necessarily reliability. On the other hand, as pointed out in the Introduction, many parameters other than reliability must be evaluated before a final choice can be made. Consequently, the design concepts and mission approaches recommended on the basis of reliability may not always be the concept or approach selected for the conceptual design.

1.3 VEHICLE ANALYSIS

Presented herein is a series of summary parametrics which were generated from the parametric results for specific design conditions. These design conditions were established for the mission objectives defined by payloads 9, 10, 11, 15 and 16 analyzed in section 1.1 -- Payload Analysis. It will be determined in this section what lander diameter, descent system, impact system, and entry weight is required for each of these payloads. Certain design requirements established in the parametric study by subsystem optimization or tradeoff evaluation will be used. These requirements will be called out and referenced as the analysis proceeds.

Only the summary curves will be presented for mission objectives associated with payloads 9, 10, 11, and 15. A detailed discussion and step-by-step calculation of vehicle analysis associated with payload 16 will be presented.

1.3.1 Mission Payload 9

Since the mission objective of payload 9 is a land and survive approach and not a biological mission, it was felt that the equipment associated with this payload could be hardened for high g impact levels (~6000). Therefore, only a balsawood impact attenuator was investigated (see section 8.0). Also the possibility of higher impact velocities was explored by considering

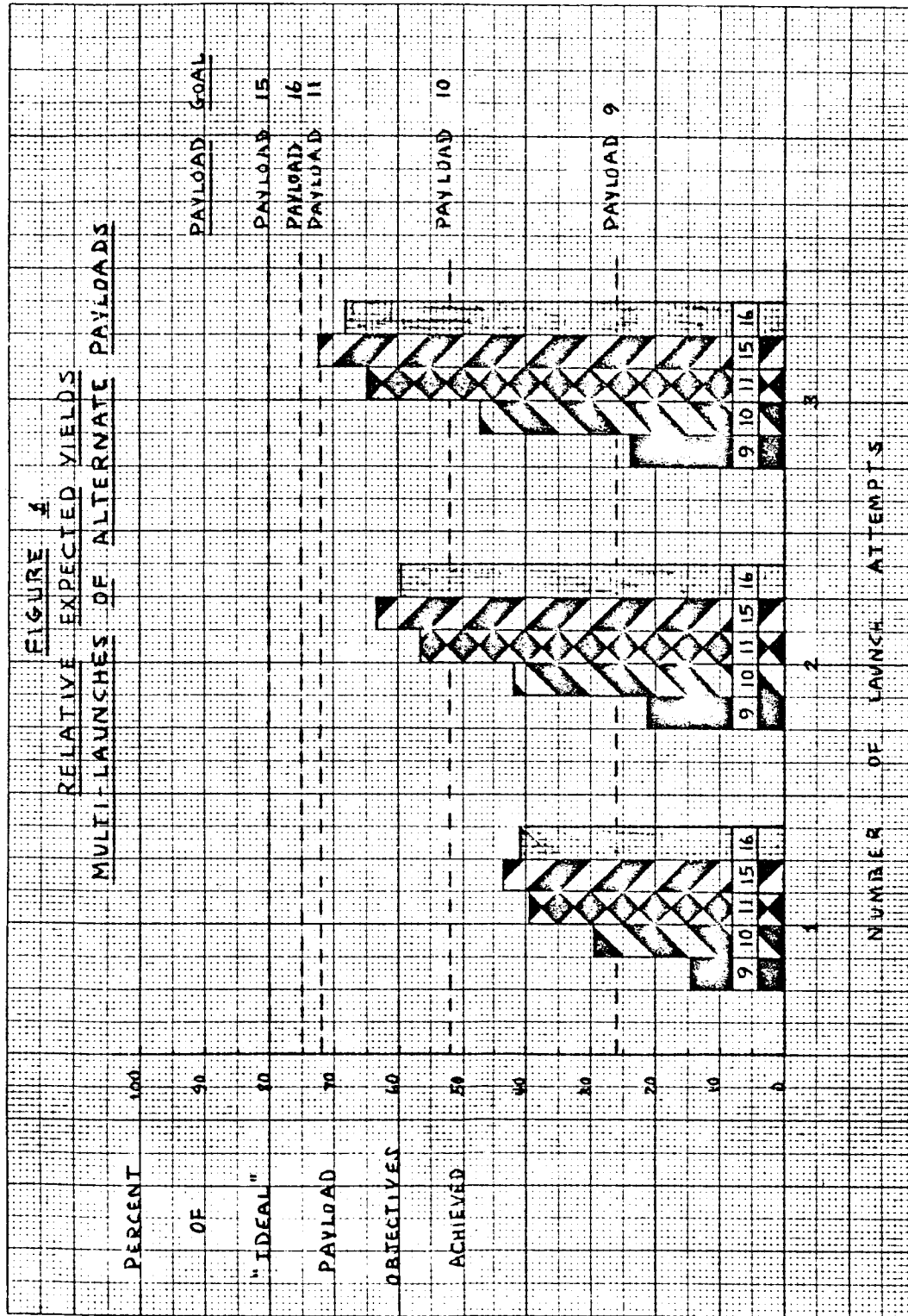


Figure 1 RELATIVE EXPECTED YIELDS - MULTI-LAUNCHES OF ALTERNATE PAYLOADS

64-11506

different descent systems: two-chute systems, single-chute (drogue only), and no chutes at all. In all cases, however, the 200 ft/sec wind velocity (basic ground rule) was root mean squared with the vertical descent velocity to arrive at the impact velocity. Other design conditions established for this analysis are presented in table 18. Note that the entry angle for this mission is $\gamma = 45$ degrees. This results from relaxing the separation angle at flyby/bus-lander separation to remove the slowdown maneuver for relay communication, since the landing location is not a constraint. The 3σ dispersion associated with this entry angle is ± 17 degrees (see Systems--volume II, section 3.2). Coupling all of these conditions together and employing the optimization analysis for m/C_{DA} values and descent velocities, figure 2 was generated.

Notice in figure 2, that there is a small difference in available internal weight (payload plus structure, and so forth) realized between two- or single-chute systems. This is primarily because the 200 ft/sec wind component largely affects the RMS value of the impact velocity, i.e., 210 ft/sec compared to 250 ft/sec. Had the 200 ft/sec wind velocity been neglected, one would have observed much larger available weight differences.

The no-chute system design has two significant criticisms compared to the chute system:

- a. The $m/C_{DA_{opt}}$ required to decelerate the lander to a reasonable impact velocity (resulting in an optimization with the impact attenuator) is extremely low -- 0.165.
- b. The g level associated with this design is twice that of the chute systems.

The low m/C_{DA} value produces large heat shield system and impact attenuator weights, thus significantly reducing the available internal weight.

Now considering payload 9, which is 95 pounds, the required internal weight can be established by adding in the structural, thermal control, and bracketry weights. It was assumed by engineering estimate that this weight would be approximately 40 percent of the payload weight, or 38 pounds. Hence the total required internal weight is 133 pounds. Projecting this value on figure 2, the required lander diameter can be determined. It is evident that a no-chute system is not applicable in the study when considering the maximum available diameter constraint of the Surveyor shroud with the flyby/bus. This is illustrated in figure 3, where only the two-chute design is presented with the entry weight.

1.3.2 Mission Payloads 10, 11, and 15

In the mission objectives for these payloads, simple biological experiments are performed. This has two significant impacts on the lander design:

- a. The landing site must be in an area of possible growth (Syrtis Major).
- b. The instruments are quite fragile, thus requiring low impact g.

TABLE 18

PAYLOAD 9--VEHICLE DESIGN CRITERIA

Shape: Apollo

Heat Shield System;

- (a) Forebody - Avco 5026 Aluminum H/C
- (b) Afterbody - Beryllium

Entry Conditions:

 $\gamma_E = -45$ deg nom., ± 17 deg, 3σ dispersion $\alpha_E = 179$ deg

Spin = Pitch = 0.0

 $V_E = 21,500$ ft/sec

Descent Systems:

2-chute system

Drogue - "Hyperflo" at $M = 2.5$ Z at $M = 2.5 = 10,000$ feetMain - "Ring Sail" at $M = 0.8$ Z at $M = 0.8 = 5000$ feet $V_{\text{descent}} = 65$ ft/sec (opt)

1-chute system

Drogue - "Hyperflo" at $M = 2.5$ Z at $M = 2.5 = 10,000$ feet $V_{\text{descent}} = 150$ ft/secImpact System
System A

Attenuator - Aluminum Honeycomb

Impact $g = 1500$ g

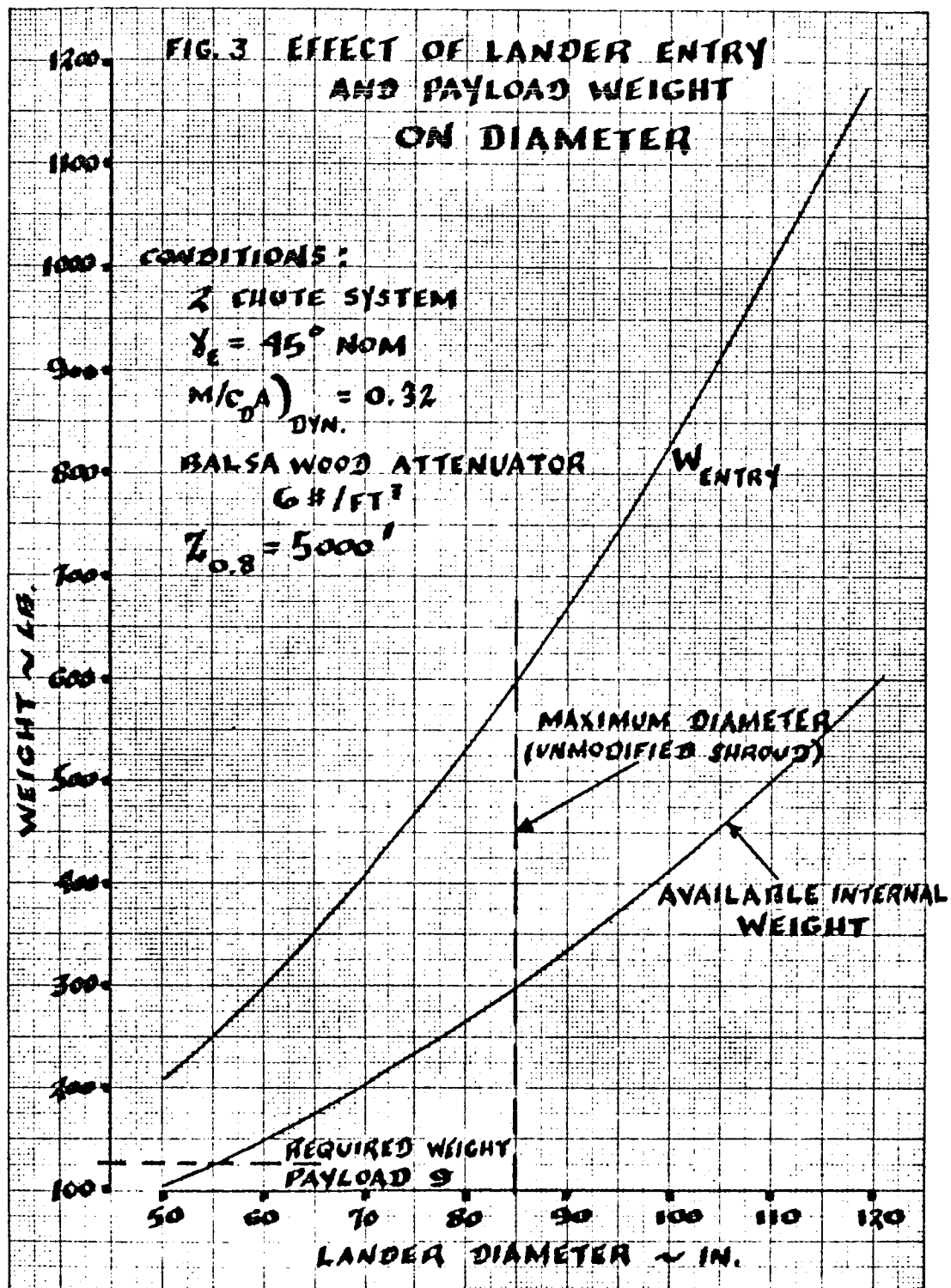
Impact Velocity - 210 ft/sec (opt)

System B

Attenuator - Balsa wood

Impact $g = 3500$ to 6400 g

Impact Velocity - 250 ft/sec (opt)



64-1150F

Figure 3 EFFECT OF LANDER ENTRY AND PAYLOAD WEIGHT ON DIAMETER - PAYLOAD 9

The first condition predicts the entry angle, which is approximately $\gamma_E = 70$ deg nom. For this analysis $\alpha_E = 94$ deg was used as predicted by lander separation, where no despin is applied. All other entry conditions will be exactly the same as in table 18. The second condition, low impact g, restricts the impact attenuation to aluminum honeycomb, which results in approximately 1500 g's (see section 8.0). However, balsa wood was evaluated to show the influence on the available internal weight. Here again two-chute and single-chute systems were investigated for possible fail-safe design considerations. The results of the analysis are plotted in figure 4.

Several significant features are present on figure 4. The first is, as stated previously, the small difference between the two-chute and single-chute system, in particular for balsa wood attenuators. This is due primarily to two reasons:

- a. Small difference in actual impact velocity due to horizontal wind component
- b. The high efficiency of balsa wood.

With aluminum honeycomb this difference is more pronounced due to its low efficiency as an impact material and the restriction to 1500 g's. The use of a single-chute has two bad features:

- a. The drogue chute becomes too large (~ 40 feet in diameter), which is beyond the state-of-art of parachutes deployed at $M = 2.5$
- b. It does not provide a simple system for jettisoning the heat shield system.

Both features have good arguments for not considering single-chute systems in Mars landers, and hence they were not considered in the conceptual design selection.

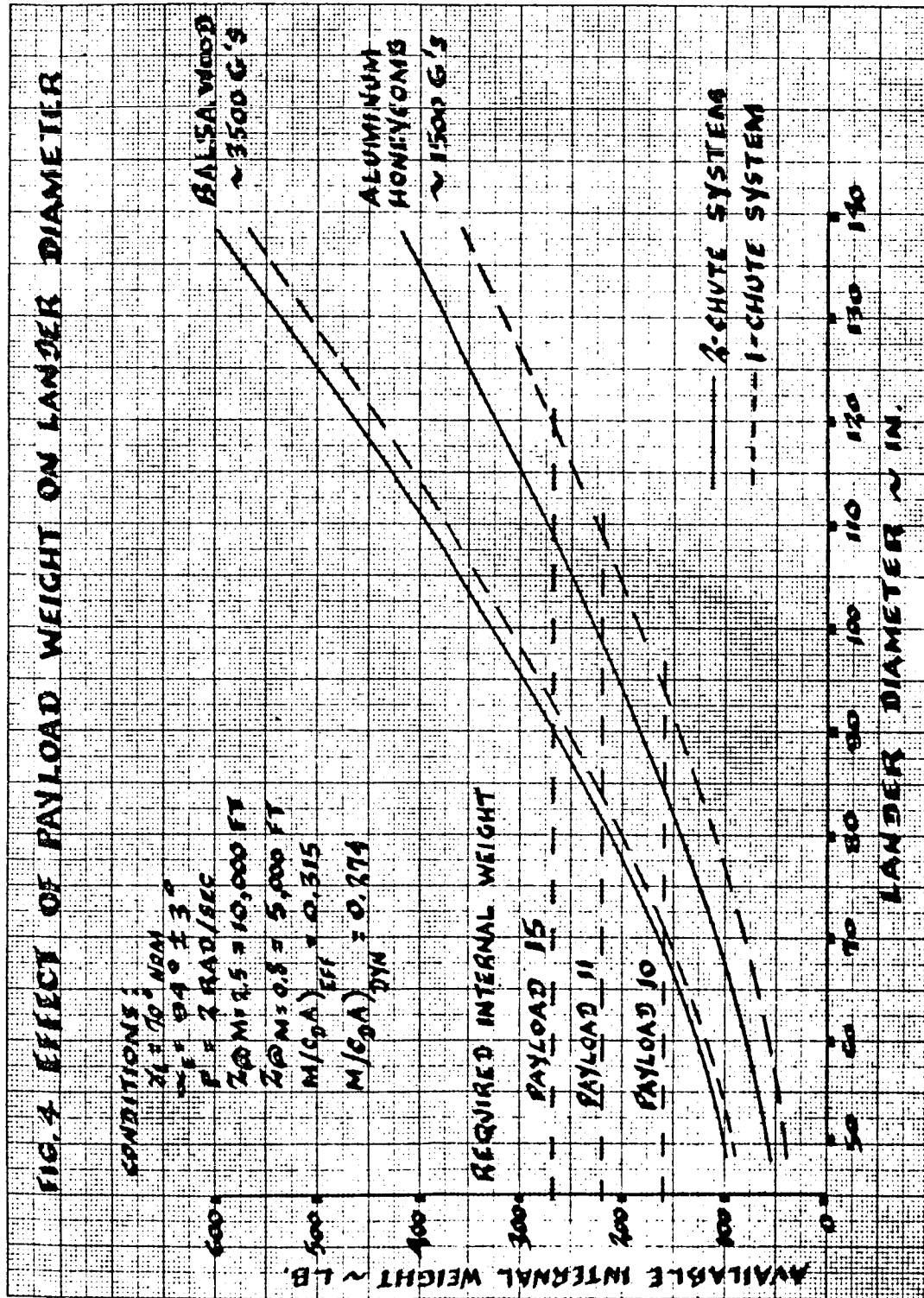
Proceeding now to the payloads 10, 11, and 15, a required internal weight can be estimated. From section 1.1.3 we find payload 10 is 115.1 pounds, payload 11 is 156.5 pounds, and payload 15 is 191.4 pounds. Now applying a factor of 1.4 to these weights to account for structure, etc., we arrive at the required internal weights for these missions; payload 10 is 161.1 pounds, payload 11 is 219.1 pounds, and payload 15 is 268.0 pounds. Crossplotting these internal weights on figure 4, the required lander diameters can be obtained. It is interesting to note that it requires an additional 15- to 20-inch of lander diameter to restrict the g level to 1500 as compared to 3500. Also noted on figure 4, is that only payload 10 is within the maximum lander diameter constraint of 85 inches, (without modifications to the Surveyor shroud). This is noted more clearly on figure 5, where now the entry weight has been added. Only the two-chute system and aluminum honeycomb atten-

uator are represented on figure 5, since they show the final conceptual design selection for the reasons stated above. Also shown on the figure is the maximum lander launch weight of 430 pounds which is constrained by the weight of the flyby/bus (~816 pounds) and separation system (~94 pounds i.e., sterilization shroud, propulsion and fittings), coupled with the maximum launch weight of 1340 pounds (zero floxed) for the launch window under consideration (Systems, volume II, section 3.1). Using this restriction, the maximum lander diameter would be 78 inches, considerably less than what is required for payloads 10, 11, and 15. Hence floxing is required for performance of the mission objectives of these payloads.

1.3.3 Conceptual Design Mission, Payload 16

The conceptual design payload, as synthesized in section 1.1.4, consists of essentially two separate payloads--a descent payload (including pre-entry communication system) and a landed payload. However, in order to pursue the available internal weight analysis independently, the payload is considered as one system and adjustments are made to the descent payload, so that the required internal weight can be obtained. The design requirements for the conceptual design are defined in section 1.1.4 and summarized in section 1.4.0. Using these requirements, an available internal weight curve was generated (figure 6) similar to the preceding curve. On this figure, however, three mainchute deployment altitudes were considered to determine the effect on internal weight. It is evident that going to a lower deployment altitude increases the available internal weight but decreases the descent time significantly. From the communication payload synthesis (section 1.1.4), a long descent time (~100 sec) was required in order not to overpenalize the payload weight. Hence the 8000-foot altitude was selected as a compromise and to ensure that the lander was at a high enough altitude such that surface terrain (mountains) would not jeopardize the mission.

To arrive at the required internal weight, the external (descent payload) weight had to be adjusted to fit figure 6 terminology. Due to this, the descent payload, 41.1 pounds (section 1.1.4, table 11), was multiplied by the ratio of impact attenuator mass to internal mass--0.41--which results in 16.8 pounds. Adding this value to the landed payload weight, 86.3 pounds, gives 103.2 pounds. Now the weight of the internal structure and associated hardware must be accounted for. As before, 40 percent of the payload weight is assumed for these weights. Hence the adjusted required internal weight becomes 144.5 pounds. Crossplotting this value on figure 6 gives a lander diameter of 90 inches and an entry weight of 500 pounds. This then is the conceptual design selection about which more refined analysis will be conducted in the following subsystem sections.



64-11509

Figure 4 EFFECT OF PAYLOAD WEIGHT ON LANDER DIAMETER - PAYLOADS 10, 11, AND 15

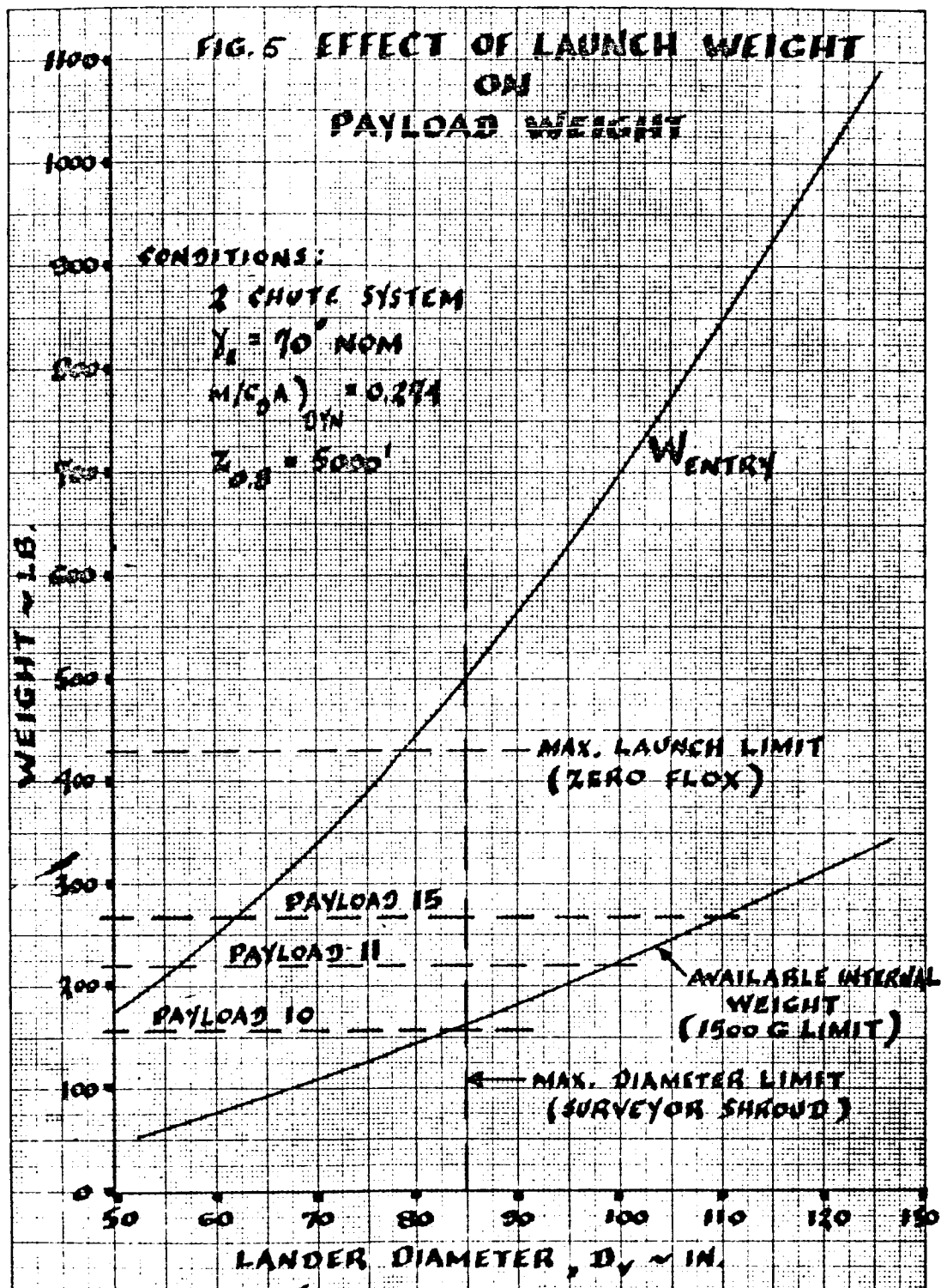


Figure 5 EFFECT OF LAUNCH WEIGHT ON PAYLOAD WEIGHT

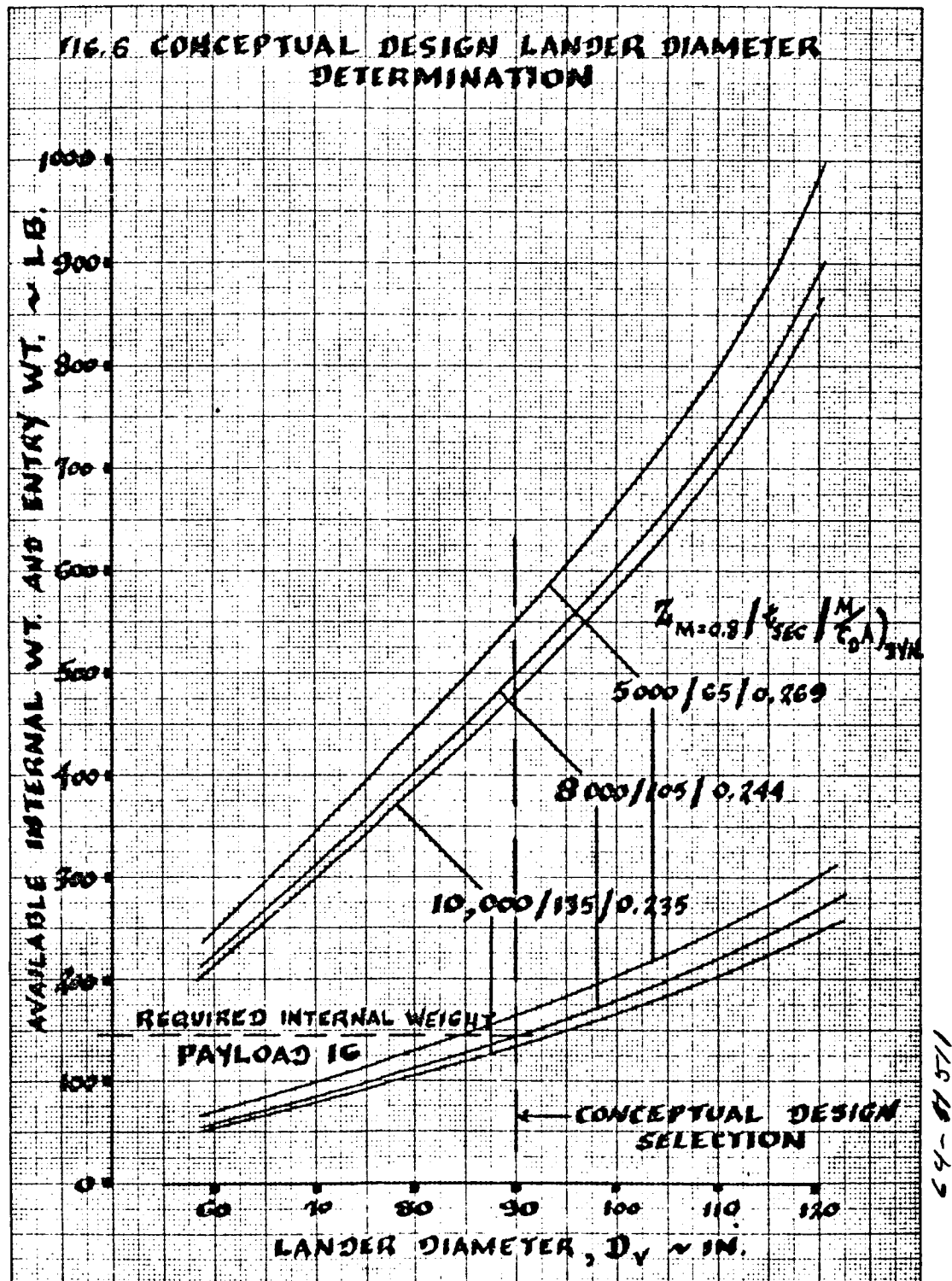


Figure 6 CONCEPTUAL DESIGN LANDER DIAMETER DETERMINATION

Finally, in the following discussion a typical point will be evaluated in the construction of figure 6. This illustrated example is intended to help the reader in understanding the usage of the parametric data presented throughout this report. The analysis is presented in a step-by-step approach showing references to each result.

a. Ballistics Coefficient-- $m/C_D A$

From figure 28 of the Descent System Section (7.5) it is seen that the optimum $m/C_D A$ for an 8000-foot main chute deployment is 0.285 slug/ft². However, note that this result is for a particle trajectory neglecting angle of attack effects. Hence it is necessary to realize a correct $m/C_D A$ based on the actual dynamic motions of the vehicle during entry. From figure 14 in the Aerodynamic Performance Section (4.3), we find that a particle trajectory $m/C_D A$ of 0.285 at 14,000 feet corresponds to a dynamics $m/C_D A$ of 0.244.

b. Entry Angle

A nominal entry angle between -66 degrees and -74 degrees was predicted by the selected launch window (see Systems, volume II, section 3.1). A 3σ (± 14 degrees) entry angle dispersion (Systems, volume II, section 3.2) could result such that an entry angle spectrum of -52 to -88 degrees would be possible. Thus the heat shield (ablator 5026 forebody, beryllium afterbody) will be designed for $\gamma_E = -52$ degrees, while the substructure (aluminum honeycomb) will be designed for -88 degrees, since these conditions represent the worst-worst design. In the same fashion the descent system will be designed for $\gamma_E = -88$ degrees.

c. Entry Weight (w_E)

Using an $m/C_D A = 0.244$, a lander diameter of 90 inches (selected to show a single point calculation in the construction of an available payload curve, figure 6) and a hypersonic $C_D = 1.45$ (zero angle of attack), the entry weight w_E will then equal 500 pounds.

d. Heat shield and Structure Weight

The heat shield is designed on the shallowest possible entry angle of -52 degrees, such that from figure 56 we note by interpolation that the total weight fraction is 0.130, resulting in 65.5 pounds of heat shield. This weight includes 5026 ablator around the entire vehicle except for the afterbody, which utilizes beryllium.

The structure is designed on the steepest possible entry angle of 90 degrees; hence from figure 57 we note that structure weight fraction is 0.130, such that the structural weight (aluminum honeycomb on the nose and toroidal sections) is 66.7 pounds. The combined heat shield and structure weight is 132.5 pounds.

e. Drogue Chute Weight (W_D)

From figure 85 of the Descent System section we note that a drogue area over vehicle area ratio of 6.2 is necessary to decelerate the lander to Mach 0.8 at 8000 feet. Note that this point is at an m/C_{DA} of 0.285 particle trajectory which must be adjusted for $m/C_{DA} = 0.244$ to achieve the same drogue chute performance; hence A_D/A_V must be multiplied by the ratio of m/C_{DA} 's. Thus A_D/A_V now is $6.2 (0.86) = 5.3$. Based on a 90-inch vehicle and a parametric tool that the weight of the drogue system is 0.11 times the area of the drogue ($W_D = 0.11 A_D$), we find the drogue system weight to be 25.0 pounds.

f. Main Chute Weight and/or (A_{MC}/W_S)

Based on a tradeoff between main chute system weight and impact attenuation weight, it was established that 65 ft/sec was an optimum impact velocity (see section 8.4.3). At this point we see on figure 95 in the Descent System section that A_{MC}/W_S is 6.2. Once the suspended weight on the main chute is determined, then the main chute weight can be established noting that W_{MC} is 0.013 times the area, i.e., $W_{MC} = 0.013 A_{MC}$.

g. Suspended Weight, W_S

The suspended weight can be calculated such that (see section 7.0)

$$W_S = \frac{W_E - W_{H/S} - W_C}{1 + \frac{W_{MC}}{W_S}}$$

$$W_S = \frac{500 - 132.2 - 25.0}{1 + 6.2(0.013)} = 317.0 \text{ pounds}$$

h. Available Internal Weight

The internal weight is the suspended weight minus the impact attenuation system weight. The crushable material used for this design is aluminum honeycomb. The vertical descent velocity is 65 ft/sec, and the horizontal wind component is 200 ft/sec. Hence the design impact velocity is 210 ft/sec, resulting in 1500 impact g's. From figure 155 in the Impact System section we find that for suspended weight of 317 pounds, the payload weight is 145 pounds. Hence a single point has been established for figure 6, which also resulted in the conceptual design point. The

impact attenuator weight of 167 pounds is based on a packaging density of 2 slug/ft² and hence must be adjusted for the final design (see section 8.5.1).

i. Main Chute Descent Time

The main chute descent time is a function of the main chute size, the deployment altitude, and the suspended weight. Figure 94 of the Descent System section presents descent times for the thinnest atmosphere (H model). Hence for 8000 feet and a ratio of 6.2 for A_{MC}/W_S , we find the descent time to be 105 seconds.

1.4 System Design Summary

To summarize the selected conceptual design and to aid in the discussion of the forthcoming sections of this report, a complete list of pertinent system requirements are presented in table 19. These requirements evolved out of the analysis and defined mission objectives discussed in the previous sections (1.1 and 1.3). Other requirements evolved from parametric evaluations by basic trade-off studies and optimization analyses. The requirements presented will be used, system by system, throughout this report in the final analysis of the conceptual design. A complete weight summary for the conceptual design is located in section 3.4.

TABLE 19

LANDER SYSTEM DESIGN SUMMARY

Configuration:

Entry Shape - Apollo (Modified Afterbody - 30 degrees) -- 90 in. dia.

Landed Shape - Spherical -- 43 in. dia.

Internal Shape - Spherical -- 15.5 in. dia.

3 slug/ft³ packaging density
Flotation system antenna erection

Entry Conditions:

V_E = 21,500 ft/sec

γ_E = 66 - 74 degrees nominal

α_E = 179 degrees

Spin = Pitch = 0.0

TABLE 19 (Cont'd)

$$W_E = 516.5 \text{ lb}$$

$$M/C_D A = 0.25 \text{ slug/ft}^2$$

Heat Shield System:

Forebody - Ablator - "Avco 5026"
 Aluminum Honeycomb Substructure
 Afterbody - Beryllium (thin shell) heat sink

Descent System:

Drogue chute - "Hyperflo" - 17 ft. dia.
 M = 2.5 nominal deployment
 14,000 ft. min. altitude
 Main chute - "Ringsail" - 50 ft. dia.
 M = 0.8 nominal deployment
 8000 ft. min. altitude

Impact System:

Impact attenuator - aluminum honeycomb
 13 in. stroke
 1500g - impact
 210 ft/sec - impact velocity

Descent Payload:

Science

Radiometer
 Pressure
 Temperature

Communication - Relay

	Preentry	Descent
RF power - watts	30	90
Bit rate - bps	11.5	184
Total bits	1560	16330
Antenna type	Slot	Horn, 74. beamwidth
Design range - km	75×10^3	75×10^3
Frequency - kmc	2.295	2.295
Playout time - sec	136	91

TABLE 19 (Concl'd)

Landed Payload:

Science

5 hr. biological experiment
Surface pressure
Anemometer
Accelerometers (used during descent)
Surface temperature

Communication - direct/relay combined

RF power	- 30 watts
Bit rate	-11.5 bps
Total bits	-13161
Antenna	- Horn 74 degrees beamwidth
Design range	- 1.8×10^8 km
Frequency	- 2.295 kmc
Playout time	- 19 minutes

Power

NiCad battery 28v at 151.8 watt-hr.

2.0 SCIENTIFIC PAYLOAD

2.1 INSTRUMENTATION LIST

The Jet Propulsion Laboratory at the onset of the program furnished Avco RAD with an instrumentation list to be used for the design of scientific payloads. It was deemed necessary to add an anemometer, emission spectrograph, and a six-channel radiometer in order to have greater flexibility in overall mission objectives. The portion of the JPL list that is applicable to lander science is found in table 20.

2.2 SELECTED INSTRUMENTATION

2.2.1 Generation of Payloads

During this current study, full advantage was taken of the extensive optimization and evaluation of instrumentation that was performed under a prior Voyager study. Volume II of the Voyager study, Scientific Mission Analysis (pages 167 through 192) gives a thorough treatment of the problem of instrumentation choice.

Table 21 was derived as a result of this approach and lists those instruments determined by the evaluation procedure to be most useful in the Advanced Mariner lander. These instruments were then used in the parametric design of the many payloads studies.

Seven lander payloads were initially established (1 through 7, table 22), with variations of the communications, instrumentation, and power systems to accomplish several selected missions. These payload groupings (1-7) satisfied ambitious mission objectives and were characterized by landed lifetimes of from 12 to 48 hours duration and by mission total bit content in excess of 1,000,000.

It was later determined that these mission and payload formulations were too ambitious for the Advanced Mariner concept; therefore new payload groupings were evolved which satisfied mission objectives ranging from simple "land and survive" missions to missions of increasing reasonable complexity (8 through 15, table 22).

Working toward the goal of the choice of a final conceptual design, four payloads were more actively studied. Payload 9 was chosen to designate a successful landing with notification of survival. The instrument chosen was the simplest and yet furnished pressure data so important to future flights. Payload 10 was chosen to furnish the same data obtained with payload 9 with further information on wind speeds. A 5-hour biological experiment was included to answer the prime scientific question: Does life exist on Mars?

Payload 11 was identical to payload 10 but had a 24-hour mission life. Payload 15 was the most ambitious of the payloads studied. This payload was in essence payload 10 with the addition of descent television. This final payload was chosen by Avco as a serious candidate for the conceptual design portion of this study.

Jet Propulsion Laboratory felt that the descent TV experiment added unacceptable complexities and legislated against it. An atmospheric composition experiment was substituted which was to acquire and transmit its data prior to impact. This is the basis of the formulation of payload 16.

TABLE 20

JPL INSTRUMENTATION LIST
for Lander

Instrument	Experimental Objectives	Wt (lb)	Power (w)	Volume or Dimensions (in.)	Bits/Sample	Total Bits	Additional Constraints
<u>Aerometeorometer</u>							
Static temperature	100 to 300°K; accuracy 1%	0.31	0.070	1 (dia) x 3 (length)	7; measure every 500 m		
Static pressure	100-15 x 10 ³ newtons/m ² ; accuracy ± 50 newtons/m ²	0.31	0.10	1.6 (dia) x 2 (length)	9 Measure every 500 m		Sampling mechanism must provide free-stream conditions to the sensor during capsule descent
Density	2 x 10 ⁻⁵ to 2 x 10 ⁻⁴ gm/cm ³ ; accuracy 1%	0.75 (β ray) 1.5 (γ ray)	0.25 2.0		8; measure every 500 m		
Velocity of sound	250 to 380 m/sec; accuracy 1%	0.625	0.30	2.3 (dia) x 2 (length)	7; measure every 500 m		
Mass spectrometer	Determination of the composition of the atmosphere in the mass range of 12 to 50 amu	6.0	6.0	10 x 5 x 3	1100	5500	Representative sample of the atmosphere is required
Gas chromatograph	Determination of the composition of the atmosphere	7	4.5	5 x 5 x 8	200	800	

TABLE 20 (Cont'd)

Instrument	Experimental Objectives	Wt (lb)	Power (w)	Volume or Dimensions (in.)	Bits/Sample	Total Bits	Additional Constraints
Simple Composition							
H ₂ O (vapor)	(0.1 atm): dynamic range 1 to 1000 ppm; 190 to 240°K	1.5	1	3 x 3 x 3	7	105	Representative sample of the atmosphere is required
O ₂	(0.1 atm): dynamic range 0.01 ppm (3 orders of magnitude per sensor)	1.5	1	5 x 3 x 3	7	35	
O ₃	(0.1 atm): dynamic range 10 ⁻² to 10 ppm	1.5	1	3 (dia) x 6	7	105	Representative sample of the atmosphere is required
A	(0.1 atm): dynamic range 3 to 100%	1.5	1	10 x 2 x 2	7	35	
N ₂	(0.1 atm): dynamic range 0.1 to 100%	1	1	4 x 3 x 4	7	35	
CO ₂	(0.1 atm): dynamic range 1 to 100%	1	1	4 x 3 x 4	7	70	
Radioisotope growth detector	Uses radioisotope techniques for detection of metabolic and growth process. Carbon 14 included in a liquid media is converted to C ¹⁴ O ₂ which is	6	3	8 x 10 x 6 plus four 1 x 2 x 3	Sample at 20 bits/30 min.	600 for 12 hours	Up-down orientation required. Soil samples required.

TABLE 20 (Cont'd)

Instrument	Experimental Objectives	Wt (lb)	Power (w)	Volume or Dimensions (in.)	Bits/Sample	Total Bits	Additional Constraints
Reduction-oxidation potential experiment	detected with a geiger-mueller tube or solid-state detector. Control experiments are performed as a contrast to the actively metabolizing experiment						
	Multiple experiment designed to measure changes in eH (redox potential) in a medium which organisms are actively metabolizing and therefore changing the redox potential of that media. Large number of samples can be run simultaneously	3	1	8 (dia) x 4	700 with 100 chambers; 2800 with 400 chambers	2800 sampled once every hour for 8 hours; 3400 sampled every hour for 12 hours	Aerosol or soil sample; orientation required.
Microscope	Visual observations of morphology and optical characteristics of small organisms. This could be used as a specialized instrument for microcolorimetry, spectrophotometry, and fluorescence	5	2 (10 min.) 1 (cont)	3 (dia) x 10	10 ⁶ bits/picture.	To be maximized	Aerosol or soil sample required

TABLE 20 (Cont'd)

Instrument	Experimental Objectives	Wt (lb)	Power (w)	Volume or Dimensions (in)	Bits/Sample	Total Bits	Additional Constraints
Organic gas chromatograph	Detection of organic compounds and possibly organisms by measurement of the volatile organic substances and degradation substances from pyrolyzed samples. Characteristic "fingerprint" of microorganisms may be found	7	4.5	5 x 5 x 8	300 bits/scan	900 minimum	Soil sample required
Turbidity and pH and growth detector	Changes in optical density and other light scattering phenomena plus changes in pH are used to detect growing organisms in a transparent liquid culture medium	4	1	6 x 6 x 6	7	Sample 2 times/hour continuously	Aerosol sample orientation required
Multiple chamber biochemical experiment	Multiple versatile miniaturized biochemical laboratory capable of performing	4	2		100	1500 hours 2250 hours 12 hours	Vertical orientation. Soil or aerosol sample required

TABLE 20 (Cont'd)

Instrument	Experimental Objectives	Wt (lb)	Power (w)	Volume or Dimensions (in.)	Bits/Sample	Total Bits	Additional Constraints
	reactions characteristics of biological life. At present, it is used to measure enzymatic hydrolysis using a sensitive fluorescent technique. Capable of carrying out growth and control experiments.						
Stain experiment	Stain soil particles selectively to provide a positive identification of organic materials present. The capability may be extended to determining whether or not the organic material is living.	5	5	3 x 10 x 8 plus 2 (dia) x 6	30	2000 10 hours approx. 7 samples/hour	Soil sample required
X-ray diffractometer	Identification of minerals and determination of relative quantities and precise composition of mineral assemblages.	10	15	10 x 10 x 10	5000 maximized	To be maximized	Prepared soil sample required
Alpha scattering	Compositional analysis of surface material.	7	2	3 x 3 x 3 (sensor) 5 x 7 x 7 (elec.)	1000 bit/spectra requires storage	10 spectra	Placement of sensor head slightly above planetary surface

TABLE 20 (Cont'd)

Instrument	Experimental Objectives	Wt (lb)	Power (w)	Volume or Dimensions (in.)	Bits/Sample	Total Bits	Additional Constraints
Soil mechanics experiment	Measurement of load-bearing strength, shear strength, cohesive modulus, and bearing stability of surface.	13	13	12 (dia) x 24		10^3	Axis vertical held 4 inches above surface
Seismograph (Single axis)	Study of the internal activity and heterogeneity of the planet	8	1	5 (dia) x 6	Less than 20 cps	Continuous, to be maximized	Emplacement on planetary surface several months lifetime required
Seismograph (three axis)	Study of the internal activity and heterogeneity of the planet	34	4	10 (dia) x 15	Less than 20 cps	Continuous	Emplacement on planetary surface
Petrographic microscope	Textural analysis of rock units.	14	7	12 x 12 x 4	10^6 bit/picture	To be maximized	Prepared soil sample required
Surface and approach photography							
Neutron analysis	Surface compositional studies, major, minor, and trace elements (possibly isotopic ratio determination).	20	20	4 (dia) x 36" detector and generator plus 4 x 4 x 3 analyzer	2000 bits/spectra.	4 times/minute initially every 10 minutes	Prepared soil sample desired. Can be direct surface analysis. RTG required.

TABLE 20 (Concl'd)

Instrument	Experimental Objectives	Wt (lb)	Power (w)	Volume or Dimensions (in.)	Bits/Sample	Total Bits	Additional Constraints
γ -ray spectrometer	Gross compositional analysis for naturally radioactive materials. Interplanetary γ -radiation analysis.	8	2	200 in. ³	1000 bits spectra	Sampled every 500 seconds	No radioactive sources on lander
Advanced mass spectrometer	Solid analysis for elemental and isotopic composition.	20	30	14 x 3 x 8	5000/sample	5 x 10 ⁴	Requires surface soil sample
Seismic refractometer	Active seismic experiment to establish time-distance relationships giving the nature of the upper surface layers to a depth of one-third the shot-to-receiver distance	40	Minimal	300 in. ³	N/A	6000	Precise dispersal of explosive charges and geophones to 500 feet
Fluorescent spectrometer	Analysis of surface for elements from sodium through iron.	25	25	5 (dia) x 15 3 boxes 8-inch cubes	1000	Several samples	Requires a prepared soil sample. This is a Surveyor instrument, and much adaptation is required

TABLE 21
ADVANCED MARINER LANDER SCIENTIFIC PAYLOADS

Instrument	Wt. (lb.)	Dimen- sions (in.)	Power (w)	Input/ Duty Cycle (min)	Input/ Output No. of Sam- ples	Total Energy (24 hr. / 48 hr.) (w-hr)	Total Bits (10 ⁵)
1. Organic plus biological gas chromatograph	7.0	5 x 5 x 8	4.5	240/480	2/	36	0.02
2. Inorganic X-ray diffractometer	10.0	10 x 10 x 10	15.0	360/1440	4/	360	2.00
3. Sample collector	15.0		4.0	30	4	8	---
4. Atmosphere mass spectrometer	6.0	10 x 5 x 3	4.5	12/60	5/	4.5	0.055
5. Wind velocity anemometer	1.0	2 (dia) x 6	0.07	Cont.	---	2.4/4.8	0.026
6. Temperature	0.3	1 (dia) x 3	0.07	Cont.	---	1.7/3.4	0.026
7. Pressure	0.3	1.6 (dia) x 2	0.1	Cont.	---	2.4/4.8	0.026
8. Cell growth multiple chamber	4.0		2.0	720/	1/720	24	0.026
9. IR spectrometer	40.0	12 (dia) x 15	100.0	47/94	2/	157	15.00
10. Emission spectrom- eter	6	8 x 4 x 2	12.0	12/24	2/	4	0.10
11. Television	17.0	12 x 6 x 7	30.0	5 min. warmup 20 sec/pix	5/	3	39.95
12. Radioisotope growth detector	6.0	8 x 10 x 6 plus 4 1 x 2 x 3	3.0	300/1400	1/48	72	0.012
13. Three axis accel- erometer - Palomer Co.	1.2	10 in. ³ 2 x 2 x 2.5	3.0	5 min.	1240	.3	.62
14. Radiometer - Avco	1.5	24 in. ³	7.0	1.2 min.	2	.14	.72

TABLE 22

ADVANCED MARINER PAYLOADS

<u>Payload 1</u> - Instruments 1 through 8	<u>Payload 6</u> - Instruments 1, 3 through 11
Mission duration - 24 hours	Mission duration - 24 hours
Instrument weight - 45 lb	Instrument weight - 92 lb
Total bits - 217,900 direct	Total Bits - 17,900 direct
Total energy - 439 w-hr	5.445 x 10 ⁶ relay
Peak power - 30.27 w	Total energy - 225 w-hr
	Peak power - 157 w
<u>Payload 2</u> - Instruments 1 through 8	<u>Payload 7</u> - Instruments 1, 3 through 11
Mission duration - 48 hours	Mission duration - 48 hours
Instrument weight - 45 lb	Instrument weight - 92 lb
Total bits - 435,800 direct	Total bits - 35,800 direct
Total energy - 878 w-hr	5.445 x 10 ⁶ relay
Peak power - 30.27 w	Total energy - 286 w-hr
	Peak power - 157 w
<u>Payload 3</u> - Instruments 1 through 8 and 11	<u>Payload 8</u> - Instrument 7
Mission duration - 24 hours	Mission duration - 2 hours
Instrument weight - 62 lb	Instrument weight - 0.3 lb
Total bits - 217,900 direct	Total bits - 250 direct and relay
3.925 x 10 ⁶ relay	Total energy - 0.2 w-hr
Total energy - 422 w-hr	Peak Power - 0.1 w
Peak power - 60.27 w	
<u>Payload 4</u> - Instruments 1 through 8 and 11	<u>Payload 9</u> - Same as 8 plus diagnostics (see next page)
Mission duration - 48 hours	Mission duration - 2 hours
Instrument weight - 62 lb	Instrument weight - 1.3 lb
Total bits - 435,800 direct	Total bits - 2,670 direct and relay
3.935 x 10 ⁶ relay	Total energy - 2.2 w-hr
Total energy - 881 w-hr	Peak power - 0.1 w
Peak power - 60.27 w	
<u>Payload 5</u> - Instruments 3 through 7, 9, 10, and 11	<u>Payload 10</u> - Instruments 5, 7, and 12
Mission duration - 2.5 hours	Mission duration - 5 hours
Instrument weight - 81 lb	Instrument weight - 6.3 lb
Total bits - 5,451,314 relay	Total bits - 3,420 direct
Total energy 177.3 w-hr	2,670 relay
Peak power - 151 w	Total energy - 15.5 w-hr
	Peak power - 3.1 w

TABLE 22

ADVANCED MARINER PAYLOADS (Cont'd)

<u>Payload 11</u> - Instruments 5, 7, 8, and 12	<u>Payload 15</u> - Instrument 6, 7, 8, 11, and 12
Mission duration - 24 hours	Mission duration - 5 hours
Instrument weight - 10.3 lb	Instrument weight - 30.3 lb
Total bits - 9,000 direct	Total bits - 12,600 direct
2,670 relay	45.4 x 10 ⁶ relay
Total Energy - 120.4 w-hr	Total energy - 425 w-hr
Peak power - 5.1 w	
<u>Payload 12</u> - Instruments 3, 5, 7, through 10, and 12	
Mission duration - 24 hours	
Instrument weight - 59.3 lb	
Total bits - 9.0 x 10 ³ direct	
1.5 x 10 ⁶ relay	
Total energy - 292.4 w-hr	
Peak Power - 121.1 w	
<u>Payload 13</u> - Instruments 3, 5, 7, through 12	
Mission duration - 24 hours	
Instrument weight - 76.3 lb	
Total bits - 9.0 x 10 ³ direct	
5.45 x 10 ⁶ relay	
Total energy - 295.4 w-hr	
Peak power - 121.1 w	
<u>Payload 14</u> - Instruments 1, 3, through 10, and 12	
Mission Duration - 24 hours	
Instrument weight - 72.6 lb	
Total bits - 21,550 direct	
1.5 x 10 ⁶ relay	
Total energy - 337 w-hr	
Peak power - 129.5 w	

2.2.2 Conceptual Design Payload

Payload 16, used for the conceptual design, is divided into two packages:

1. A six-channel radiometer, pressure sensor, and temperature sensor, are mounted external to the landed package. They function during entry and are jettisoned along with the heat shield upon opening of the parachute.
2. Located internal to the landed payload are pressure and temperature sensors, the Gulliver biological experiment, an anemometer, and three single-axis accelerometers. All of these instruments function after landing except the accelerometers, which operate during entry and are packaged internally in order to place them on the c. g.

The anemometer, with the temperature sensor, is deployed external to the package after landing. The "sticky" string portion of the biological experiment is fired to a distance of 25 feet from the vehicle, retrieved, and thus furnishes samples for the experiment.

A functional description of the instrumentation of payload 16 follows:

1. During entry, the acquisition of atmospheric data is the prime function of the science payload. A pressure sensor, a temperature sensor, and the accelerometers will gather data to be used for the computation of the density profile of the atmosphere.

A six-channel radiometer will be used to measure the chemical composition of the atmosphere. As its source of optical spectral data, this instrument uses the shock-heated atmosphere behind the shock front in the stagnation point region. * Measurements of preselected emission bands will make possible the quantitative determination of the ratios of carbon dioxide, nitrogen, and argon. This determination of chemical composition will also be used in the density calculation.

A three axis accelerometer package was chosen to measure the lander performance from 1 g ascending on the g-pulse to drogue chute deployment (~10 descending). Sampling rates of 4 samples/sec (from 1 g to 10 g ascending) and 20 samples/sec (from 10 g ascending to chute deployment) were used in the payload analysis to predict the lander dynamic and hence deduce pressure and density profiles. Later studies, however, indicate that 1 sample/sec may be all that is necessary (throughout the pulse) to predict these profiles and at least a three-axis accelerometer is required to deduce the density profiles, unless only the

* The use of shock layer spectroscopy for the determination of atmospheric composition was first suggested by A. Seiff, NASA TN D-1770.

scale height is all that is desired. In this case only a peak g measurement is required, since the lander angle of attack at peak-g varies little over a complete range of entry condition. A more detailed analysis of the pressure and density profile determination is presented in appendix C.

The determination of surface pressure and temperature can be accomplished directly with a pressure transducer. The difficulty of the task is dependent on the knowledge of the vehicle's speed and dynamic motion prior to impact. For the conceptual design, where a parachute is used, the descent velocity is sufficiently small such that a pressure sensor located in the vicinity of the stagnation point indicates the atmospheric pressure directly.

2. Once the lander has been anchored by the jettisoned crushable material, the rotating cup anemometer is deployed on a small staff to which is also attached the temperature sensor. Estimate of surface wind speeds are so controversial today and are of such exceptional importance to the engineering design of future Martian landings that inclusion of an anemometer was considered essential.

Another controversial dimension is the atmospheric pressure existing on Mars. Thus the inclusion of a pressure sensor on the landed vehicle was also considered a must.

The biological experiment chosen has a simple and easily accommodated sample acquisition system. A "sticky string" is fired or spring propelled from the vehicle and, when retrieved, deposits the adhered soil in a complex culture medium tagged with C^{14} atoms. The expectation is that the metabolic cycle of viable organisms will liberate radioactive carbon dioxide which will be measured in its gaseous stage by a Geiger counter, thus giving evidence of activity and its attendant rate.

8-1

3.0 DESIGN

Design studies of the lander were involved in generating the best functional scheme to do the job established by the mission objectives. The design analysis presented in this section will be centered around this task with primary emphasis on subsystem integration and mechanical systems designs. In order to proceed on any one concept, several geometrical shape evaluations had to be pursued. These evaluations involved many aspects from the design of the basic landed package to the modification of the entry configuration. The first step in the landed package configuration was to evaluate the desired shape from the standpoint of the basic ground rule of complete passive protection at impact under 200 ft/sec wind conditions and secondly, from the viewpoint of erection of the landed antenna for relay and direct communication. These design studies coupled with the impact system studies produced a spherical shape, employing a flotation system for antenna erection, as the best approach for both the impact attenuator and the landed payload. The next problem that faced the lander design studies was center of gravity control. Since the Apollo shape has a critical center of gravity location (i. e., it is located close to the forebody) due to the rearward entry center of pressure constraint, it became necessary to modify the shape to relax this problem. Several modifications were analyzed and judged on many arguments. A slight afterbody cone angle modification was determined to be the most desirable solution to meet the c. g. constraint.

Other design evaluations were conducted in conjunction with the above studies; among these were the optimization of the antenna size, landed sphere size, and landed weight. This study indicated that a low communication frequency for relay produced too large an antenna, thus penalizing the size of the landed sphere and hence lander c. g. location. The optimization study indicated that a frequency slightly less than S-band frequency, using horn antennas, would be desirable from the standpoint of communication weight and landed sphere size. Therefore, since the direct link is S-band (DSIF requirements), it was apparent that the relay link should also be S-band and thus eliminate one system completely. Further analysis and discussion of these pertinent evaluations will be covered in greater depth in the following text.

Finally, a complete description of the conceptual design was established with working layouts. A preliminary weight summary is included showing one complete iteration in design from conceptual design selection (using the parametric analysis) to the final preliminary design (using a more rigorous approach, where possible). Weights that were analyzed from design layouts (nonparametized) and could not be included in the parametric study are also summarized.

3.1 LANDED SHAPE GENERATION

In the initial design studies the primary effort was devoted to the landed package configuration and arrangement. Studies of many concepts were evaluated in con-

junction with the impact system analysis. Several of these concepts are presented in figure 7. Notice that in the first column only spherical shapes are considered. In the impact system analysis the use of a spherical shape proved to be the desirable approach from the standpoint of a low g level and impact attenuator weight (reference Section 8.0). However, the other concepts presented in figure 7 have interesting design features that could be expanded on. The lenticular shape has one very good asset in that it affords a low (forward) center of gravity location in the entry vehicle (more simply, it fits the shape very well). This shape also is desirable after landing because the probability of landing on one of the two blunt sides is very high, thus making the antenna erection problem simpler. The tetrahedron concept also is very attractive as a landed configuration. Its payload packaging and erectability are the significant design features. The shape also will land on one of four sides and hence the antenna gimbaling problem becomes greatly reduced, in particular if erectable legs are part of the design as illustrated in this figure. The other concepts have equally attractive features of some sort or other but result in very complex impact dynamics and hence were not pursued in the final parametric or conceptual design studies.

Once a landed configuration (i. e., a sphere) was selected, primarily through the analysis conducted on the impact system (reference section 8.0), the problem arises of how to erect the communication antenna after impact. Before this can be pursued to any great depth, the design requirements must be established. The first approach to the communication system was to employ VHF frequency (large antenna requirements) for the relay link. This frequency proved to be the optimum approach for other design studies, in particular project Voyager, where packaging volume was not the critical constraint and large antennas could be handled. However, in the Advanced Mariner studies the packaging volume (size) is a very critical constraint, and hence large antennas are prohibited. An optimization study was conducted on the sphere size, considering a range of antenna sizes (using both slot and horn antennas), and hence a range of frequencies. The study showed that an antenna size or frequency slightly less than S-band (frequency of the DSIF direct link) was optimum in size and a slightly larger antenna was optimum in weight. This conclusion immediately led to the use of S-band frequency for both relay and direct links, and hence removed one set of communication systems hardware and added a redundant scheme, since both relay and direct telecommunication can be sent out at the same bit rate and time. The resulting antenna is a 4-in. horn.

It has been established that aluminum honeycomb material (of the available state-of-the-art energy absorbers) best satisfies the impact attenuator design requirements (i. e., low impact g level, where 1500 is feasible). This, however, imposes a critical design requirement on the landed sphere, since aluminum is not radio frequency transparent and hence must be jettisoned after impact. The jettisoning procedure may very well include the erection technique utilized for antenna deployment. Several erection schemes of this nature and others were evaluated to arrive at the reference erection method. These schemes, along with

LANDER CONCEPTS

SPHERES					OTHERS				
	IN ENTRY VEHICLE	DESCENDING	LANDED			IN ENTRY VEHICLE	DESCENDING	LANDED	
SOLID SPHERE IN SPHERE					LENTICULAR				
ECCENTRIC SPHERES					TETRAHEDRON				
FOLDING HEMI-SPHERES					DOUBLE CONE HORIZONTAL AXIS				
FOLD-OUT LOOPS					DOUBLE CONE VERTICAL AXIS				
SLIDING SEGMENTS					LENTICULAR WITH ROLL BARS				

64-11612

Figure 7 LANDER CONCEPTS

some of the pertinent arguments used in projecting the selected systems, are presented in figure 8.






System 1 is simply deploying one half of the impact attenuator. The system has many drawbacks in design philosophy. In the first place the attenuator is being used as the erection method; however, since it is used for impact, it may be partially destroyed, and hence it is unlikely to be too useful in the erection process. If a gimbaling method can be designed (which seems unlikely), the antenna would also have to be gimbaled as well. This is due to the unknown terrain, which would require a certain design criterion for terrain slope, say 30 degrees. Thus the antenna would require a 30-degree gimbal system, since local vertical is very critical on communication power supply (due to a large db loss in antenna pattern).

In system 2 the attenuator is jettisoned after impact, and the landed internal sphere (payload package) is actuated into two halves. Here again the design depends on the terrain and hence requires that the antenna be gimbaled as well. It is also evident that two antennas are required to acquire the vertical direction in the event that the two halves end up upside-down. This in turn produces a large landed sphere and hence penalizes the lander (entry vehicle) center of gravity location. Two operational sequences are required after impact: (1) jettison of the attenuator and (2) actuation of the internal sphere. The latter operation is considered difficult due to the electrical wiring and switching (namely, the antenna cabling) from one half to the other. In addition to the above critical arguments, this concept would have very difficult thermal control requirements, since now the internal payload will be exposed to the Martian surface environment (which is extremely cold). System 3 deploys just the antenna from the landed sphere. It is obvious that a 360-degree gimbaling scheme would be required for the antenna, which is most difficult (if not impossible) due to electrical wiring. This system would require a rather large sphere and hence would produce poor lander c.g. location. After impact certain scientific equipment must be deployed (namely, the biological "sticky string"). With the impact attenuator still in place, the deployment method becomes very difficult.

In System 4 the attenuator is again used as the erection scheme by using spring-loaded impact attenuator segments (like stripping an orange back in segments). This system has the same objectionable features as described for System 1. Here again the antenna must be gimbaled as well, since its orientation depends on the terrain. In addition to all of these arguments, it is felt that this scheme is very complex and would require extensive development effort to prove reliability.

The final system (number 5) is the selected design concept. The impact attenuator is jettisoned after impact and is used to stabilize the internal sphere by means of elastic lines attached to each segment of attenuator. The exposed sphere encases a flotation system of fluid and an inner sphere housing the payload

**DESIGN EVALUATION
"ANTENNA DEPLOYMENT"**

SYSTEMS ARGUMENT	1 2 3 4 5				
					
NO. OF ANTENNAS	1	2	1	1	1
ANTENNA GIMBAL METHOD	FAIR	FAIR	POOR	POOR	GOOD
ANTENNA LOCAL VERTICAL	POOR				GOOD
SPHERE SIZE	GOOD	LARGE	LARGE	GOOD	GOOD
LANDER C. G.	OK	POOR	POOR	OK	OK
SCIENCE DEPLOYMENT	GOOD	GOOD	POOR	GOOD	FAIR
THERMAL CONTROL	OK	POOR	OK	OK	OK
OPERATIONAL SEQUENCE	1	2	2	1	1
COMPLEXITY	MODERATE	HIGH	HIGH	HIGH	MODERATE

64-9949

Figure 8 DESIGN EVALUATION - "ANTENNA DEPLOYMENT"

and antenna system. This system allows for an excellent antenna gimbaling method, since it does not depend on surface terrain for erection. The antenna itself is fixed to the inner sphere, thus making the sphere minimum size (large packaging density), which in turn helps the lander c. g. control and minimizes the attenuator weight. One drawback of this concept is the deployment of the scientific equipment, which must be deployed through the flotation shell. However, it is felt that by proper design, this drawback can easily be overcome as will be described later.

3.2 LANDER SHAPE GENERATION

Once the landed configuration was established, the next problem in the generation of a conceptual design was to control the entry vehicle center of gravity. Due to the large stroke requirement of the impact attenuator (~13 inches in the conceptual design), it became apparent immediately that the lander c. g. using the Apollo shape (which is $<0.19D$) could not be met without some modifications either in the Apollo shape or in the landed shape. An extensive evaluation was conducted to determine which of many possible approaches was desirable. These approaches are presented in figure 9 with the represented arguments used in the evaluation.

The first approach would be to simply move the internal (i. e., weight inside the impact attenuator) weight as close to the forebody of the lander as possible. In configuration 1 two methods are proposed: (1) split the impact attenuator into halves and at main chute deployment, retract the internal weight back into the attenuator, then lock in place, and (2) remove a portion of the impact attenuator, thus reducing the stroke on one segment. Both approaches seemed very complex. In the first approach the impact attenuator had to be locked back into place around the internal weight, and in the second approach the landed package had to be rotated at main chute deployment so that the shortened stroke segment was at the top at impact, thus ensuring maximum stroke at initial impact. Configurations 2, 3, and 4 involved modifications to the forebody. In 2 the landed package was protruded out of the original contour, causing a bubble on the forebody. In 3 a shallow cone was constructed about the landed package in place of the spherical forebody. Both of these configurations presented a significant decrease in aerodynamic performance (~6 percent in C_D and C_{mq}) and hence were dropped from consideration. The fourth configuration is similar to a NASA Langley concept except for the afterbody. This concept employs a reverse curvature forebody, thus putting the substructure in tension, which will decrease the structure weight since the structure can be operated at a much higher stress level as compared to a blunt spherical cap, which is in compression under a buckling mode of failure. The aerodynamic performance of this shape should greatly increase with only slight changes in the aerodynamic heating. The configuration was dropped due to lack of structural and aerodynamic development. However, this shape looks promising for the future. In configuration 5 a conical (15-degree) afterbody extension was added to move the c. g. back

ENTRY CONFIGURATION DESIGN EVALUATION "LANDER C.G. CONTROL"

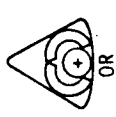



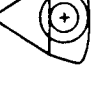


CONFIGURATION ARGUMENT	1	2	3	4	5	6	7
							
INTERNAL PAYLOAD DESIGN	COMPLEX	OK	OK	OK	OK	OK	OK
AERODYNAMIC HEATING	OK	INCREASE	INCREASE	SLIGHT INCREASE	OK	OK	SLIGHT INCREASE
AERODYNAMIC PERFORMANCE	OK	DECREASE	INCREASE	OK	IMPROVED	IMPROVED	SLIGHT INCREASE
HEAT SHIELD WEIGHT	UNAFECTED	SLIGHT INCREASE	SLIGHT INCREASE	SLIGHT INCREASE	LARGE INCREASE	LARGE DECREASE	SLIGHT INCREASE
STRUCTURAL WEIGHT	UNAFECTED	SLIGHT INCREASE	SLIGHT DECREASE	DECREASE	LARGE INCREASE	LARGE DECREASE	SLIGHT INCREASE
ENTRY CONDITIONS	UNAFECTED					$q_c < 90^\circ$	UNAFECTED
EFFECT ON PARAMETRIC EVALUATION	UNAFECTIVE	CHANGED	CHANGED	CHANGED	UNAFECTIVE	UNAFECTIVE	SLIGHT CHANGE
FUTURE OUTLOOK	GOOD	POOR	POOR	PROMISING	POOR	PROMISING	GOOD

Figure 9 ENTRY CONFIGURATION DESIGN EVALUATION
"LANDER C. G. CONTROL"

64-9948

($\sim 1/2$ AX extension). This extension, however, added significant weight (~ 10 percent) to the afterbody in the worst possible place. Even though the aerodynamic performance improved, it was felt that the weight loss to the afterbody was too severe; hence the configuration was not pursued. Configuration 6 is an Apollo shape with the afterbody completely removed. This is a drastic modification to the Apollo shape but offers several significant features. Since the afterbody is only utilized during rearward entry to turn the vehicle around and actually hinders the aerodynamic performance after initial entry, then why have it at all? The only critical objection is that the entry angle of attack must be held below 90 degrees, since the shape is stable backward. Lander flyby/bus separation analysis indicated that this could not be met, and coupled with the lack of aerodynamic test data, the configuration was dropped. However, the future outlook for this configuration is very promising for Mars landers.

The final configuration (Number 7) was the selected approach for this conceptual design. In this concept the after body cone angle was decreased slightly from 33 degrees (Apollo shape) to 30 degrees. This change allowed the center of pressure location to move from 0.19 D to 0.25D, giving sufficient static margin on the center of gravity locations (in the conceptual design the c.g. is at 0.21D). Only a slight increase in the afterbody weight (~ 10 percent) was noted with a slight increase in aerodynamic performance.

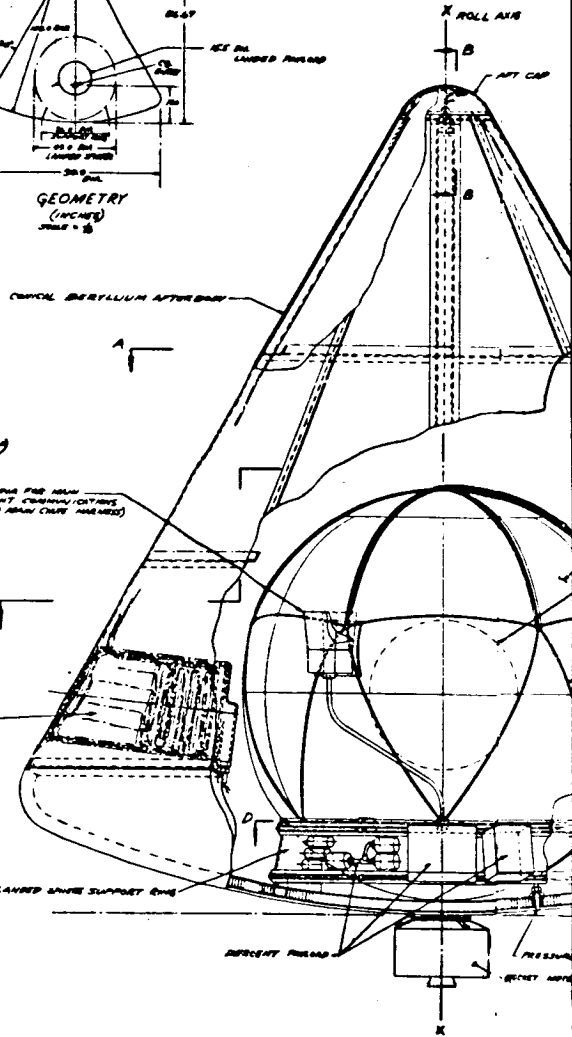
3.3 CONCEPTUAL DESIGN DESCRIPTION

In general, the lander configuration and pertinent design details are described in figures 10 and 11. Other major dimensions and functional sequences are described in the following text. Figure 10 presents the overall arrangement of the lander in the entry configuration, whereas figure 11 presents the landed sphere arrangement with particular emphasis on the internal sphere scientific payload deployment and actuation devices. Most of the subsystems analysis and description involved in making up the lander design have been established in other sections of this report. It is the primary purpose of this section to present briefly the conclusions of the subsystem design and to tie the complete lander design together by covering those areas not specified elsewhere in the general design description. In order to clarify the lander description and weight summary, a chart is presented in figure 12, which lists the terminology used throughout the lander report.

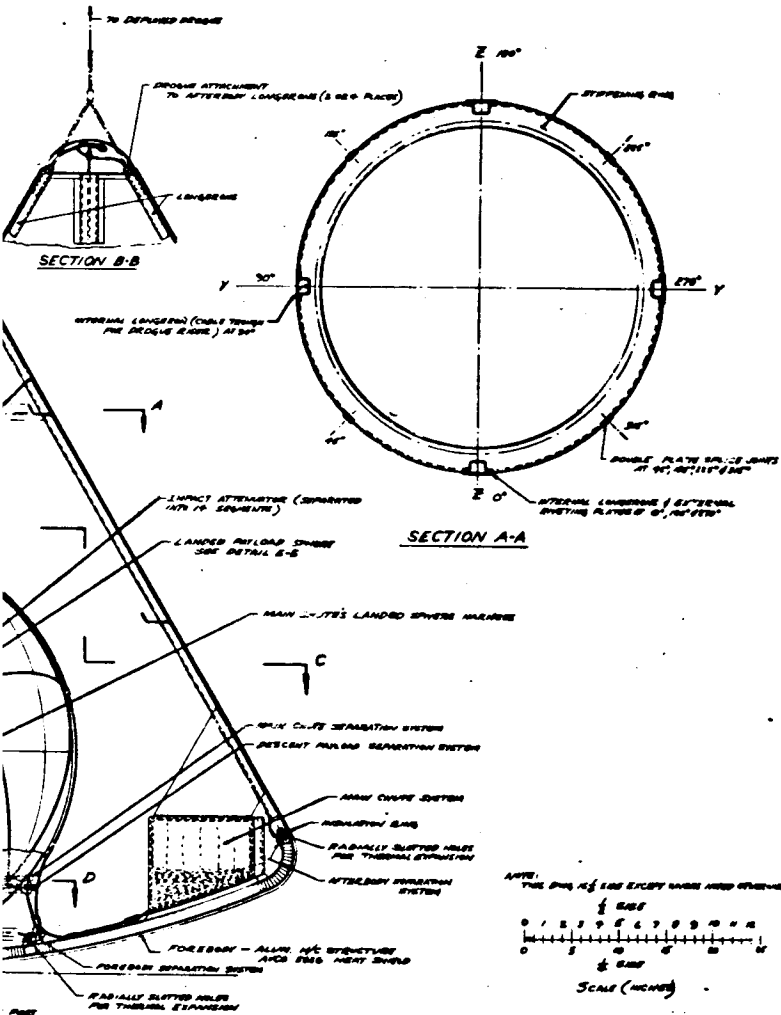
1. External-Configuration

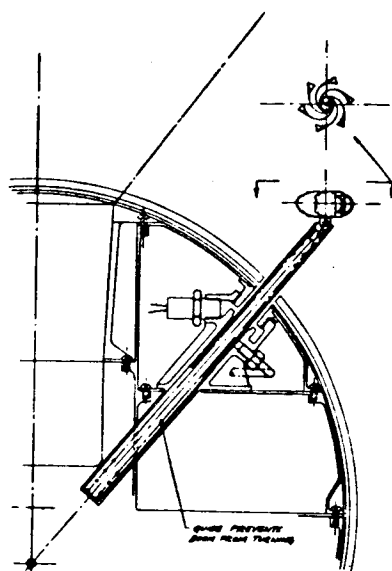
Basically the lander is a scaled down Apollo shape 90 inches in diameter. The afterbody is modified slightly by changing the cone angle from 33 degrees (Apollo) to 30 degrees. This modification was brought about by the necessity for moving the lander center of gravity rearward as described in the previous Section. The external configuration is composed of a fore-

PRE-ENTRY COMMUNICATION ANTENNA ON PLATE BODY
 CHAIRMAN'S ROOM
 AGONY CHAIRS
 AGONY CHAIRS PRESENT COMMUNICATIONS & SERVICE
 ANTENNA ON LAMINATED STRESS SUPPORT RING
 AGONY CHAIRS

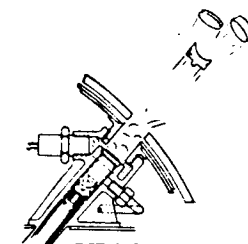


12

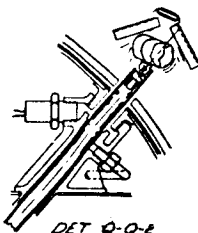




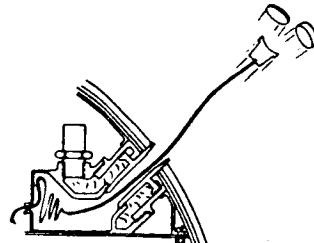
DETAIL Q-Q-3
ANEMOMETER & THERMOCOUPLE DEPLOYED



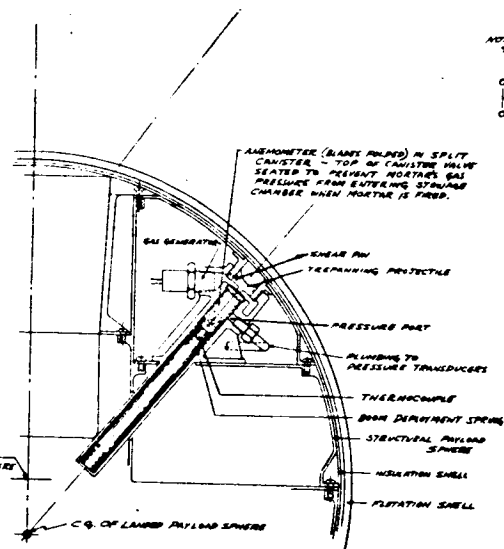
DET Q-Q-1
MORTAR FIRES - TREPPANNING PROJECTILE
CUTS HOLE THROUGH FLOTATION & INSULATION
SHELL FOR ANEMOMETER DEPLOYMENT.



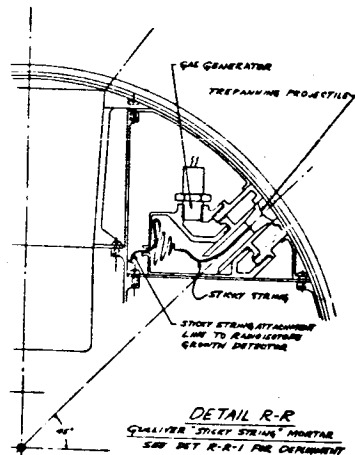
DET Q-Q-2
SPRING DEPLOY ANEMOMETER BOOM
SEGMENTS OF CANISTER SEPARATED BY UNFOLDING
OF ANEMOMETER SPRING BLADES



DETAIL R-R-1
MORTAR FIRES - STICKY STRING DEPLOYS



DETAIL Q-Q-2 SCALE 1/4
MORTAR & BOOM FOR DEPLOYMENT OF ANEMOMETER & THERMOCOUPLE
SEE DETAILS Q-Q-1, Q-Q-2 & Q-Q-3 FOR DEPLOYMENT SEQUENCE



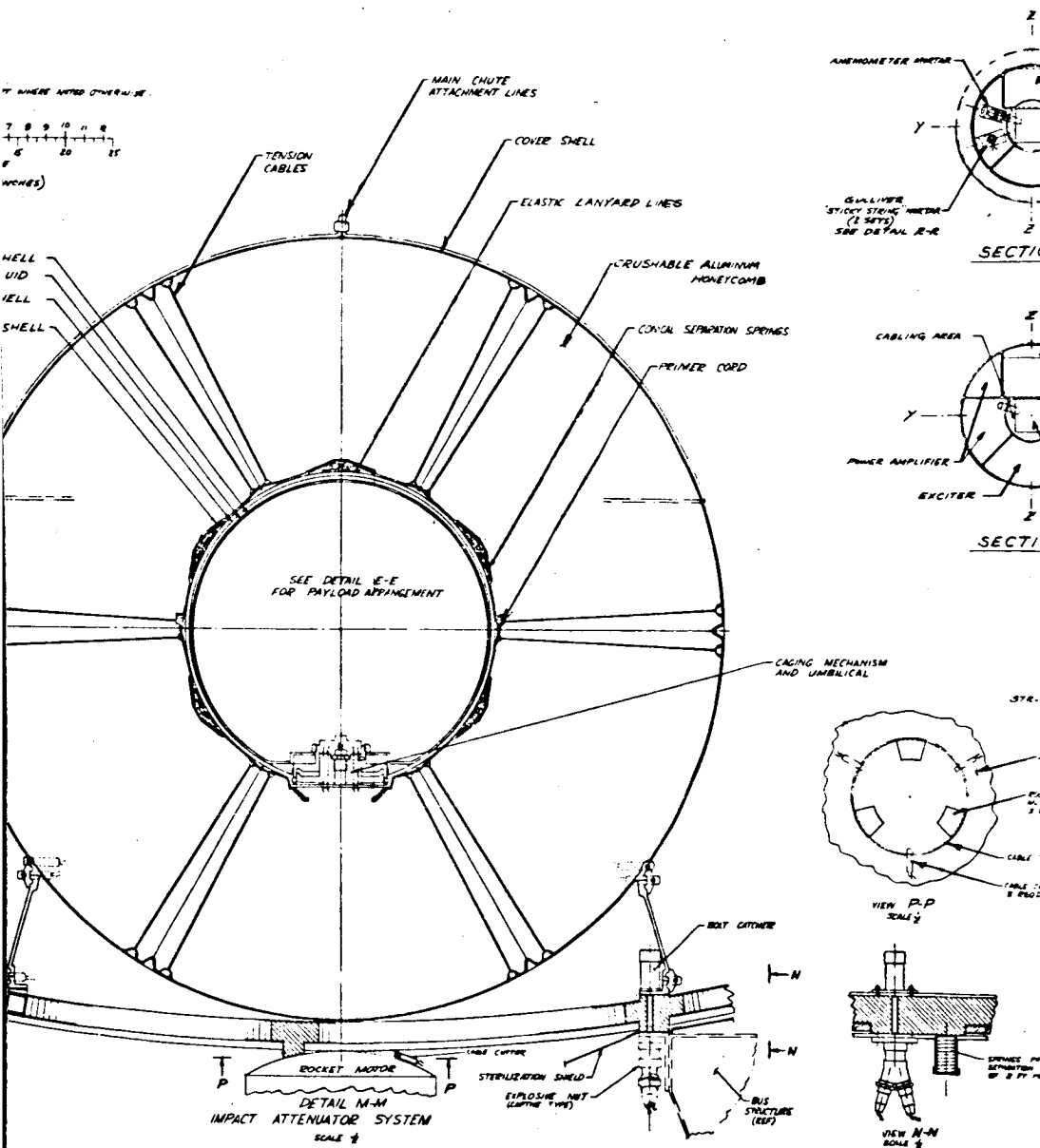
DETAIL R-R
QUALIFIER "STICKY STRING" MORTAR
SEE DET R-R-1 FOR DEPLOYMENT
SCALE 1/4

NOTE
THIS DRAWING IS NOT TO SCALE
0 1 2 3 4 5 6
10 20 30 40 50 60
SCALE (INCHES)

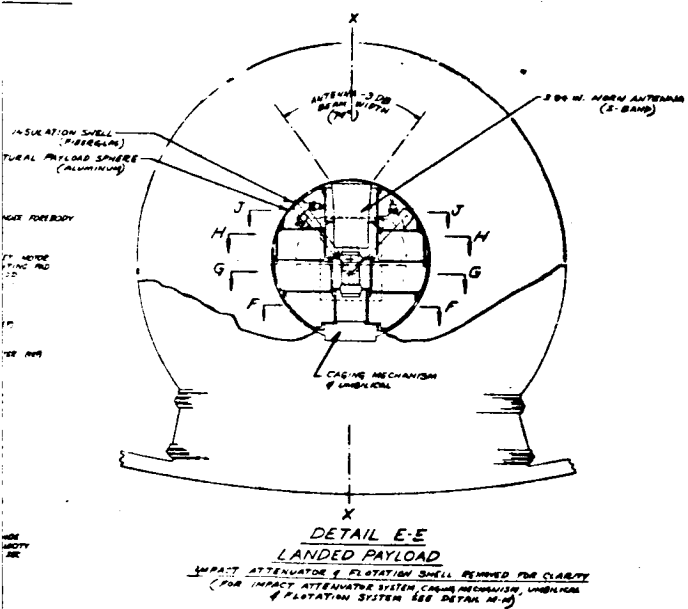
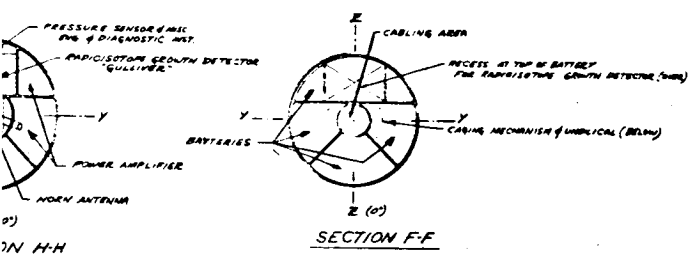
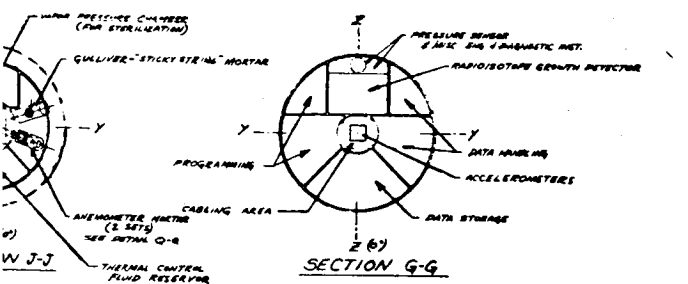
INSULATION
FLOTATION F
FLOTATION S
SEPARATION

Figure 11 ADVA

#1



UNCEDED MARINER - LANDER GENERAL ARRANGEMENT OF
CONCEPTUAL DESIGN



#3

94

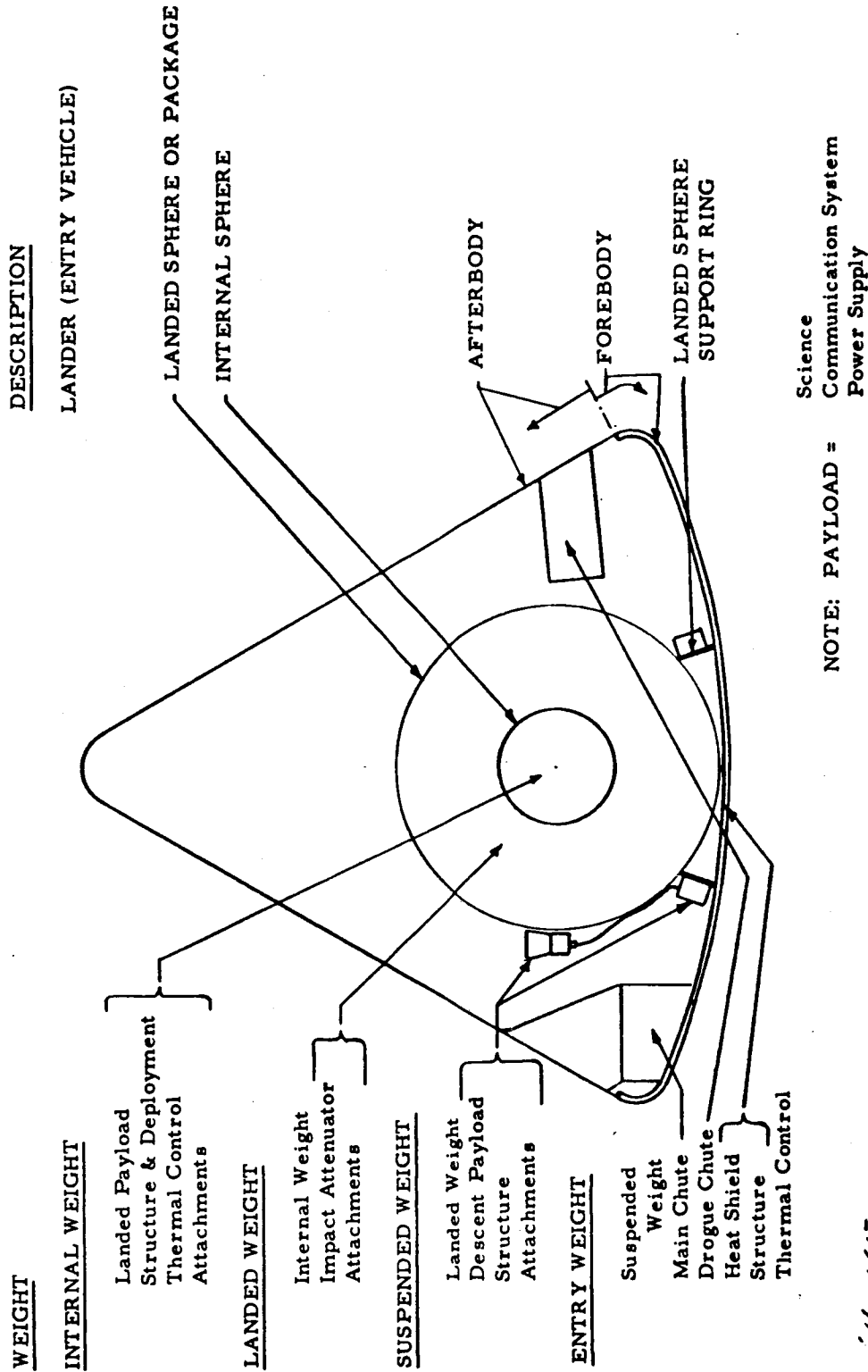


Figure 12 LANDER TERMINOLOGY

64-11575

body heat shield system and an afterbody heat shield system. In the forebody design the heat shield system consists of a high temperature charring ablator (Avco 5026) and an aluminum honeycomb (sandwich) substructure. The ablator is 0.23 inch thick at the stagnation point, and the substructure is 1.25 inches thick (i. e., the core) with 0.011-inch face sheets, except in local concentrations around ring locations. A ring is embedded in the forebody at the location of and for mounting of the landed sphere support ring. This ring also supports the separation joints for lander tie-down to the flyby/bus (at three locations, view N-N of figures 10 and 11). Thermal expansion joints are required on the forebody at two locations: at the support ring and at the afterbody interface. These thermal expansion joints provide a twofold purpose: (1) they supply thermal expansion growth capability due to both space and entry thermal sterilization and (2) they supply expansion growth capability due to both space and entry thermal environments. The first was necessary since the time constant of the lander is very high and hence the sterilization process could require an extended time which could be detrimental to the function sequence if expansion growth is not provided. In the latter case the temperature gradients around the lander under both of these environments, in particular, entry, could result in significant expansion incompatibilities, particularly between the afterbody and forebody. To reduce the discontinuity stresses due to these incompatibilities, thermal expansion is required.

Also included in the forebody construction are three pressure port holes located symmetrically about the center of the forebody. These pressure intakes are fed back to the landed sphere support ring to the pressure transducer. Located approximately 5 degrees off the center line of the forebody is the multichannel radiometer, used during the peak heating pulse to determine atmospheric composition. Details of this instrument are defined in section K-K of figure 10.

At the stagnation point on the forebody the main propulsion unit is mounted. This unit is strapped to the forebody by a cable around three symmetrical mating mounting pads on the forebody and propulsion unit (See detail M-M of figures 10 and 11).

The remaining equipment mounted to the forebody is the pre-entry communication system. It consists of a 2-inch slot antenna embedded into the forebody and flush with the outer surface (see detail K-K). Adjacent to the antenna are mounted the communication power amplifier and exciter.

The afterbody design is a beryllium thin-skin shell (hot structure design) with two rings and four longeron stiffeners (so called semimonocoque). The rings are made integral with the skin construction; however, the longerons are insulated from the skin, since they must be capable of reacting the high snatch loads at drogue chute openings. Since they are insulated, thermal expansions also must be provided to reduce thermal stresses. Beryllium

can only be manufactured in 3 x 8 foot sheets (present state-of-the-art); hence the afterbody skin is spliced at eight points (four of which are at the longerons). On one longeron the drogue chute mortar canister is mounted. Embedded in this longeron and well insulated is the drogue chute riser line. At drogue deployment the line is ripped out by the opening loads and attached to the end of 2 (or possibly 4) of the longerons. An aft cap is kicked off at drogue deployment, thus exposing the attachment points.

The main chute canister is also mounted to the afterbody (note that the main chute rests on the forebody and is not attached to the canister). At the time of main chute deployment the afterbody is cut loose by a linear shaped charge at the forebody-afterbody interface ring, thus deploying the main chute. This is best seen by the operation sequence presented in figure 13 (Ref. section 2.3.3.).

2. Internal Configuration

The internal configuration is primarily composed of the landed sphere and the landed sphere support ring (excluding the parachute system, pre-entry communication system, and radiometer). The landed sphere support ring is a short truncated cone. In addition to supporting the landed sphere the ring also supports the descent payload communication system and science except for the descent communication antenna (a 4-inch horn), which is mounted on the main parachute harness. The support ring incorporates two release systems: (1) forebody release at main chute deployment and (2) the support ring release system. Both systems are similar in that they use a cable strap technique with simple cable cutters. Each system is armed with three cable cutters, of which any given one will cause release; hence complete redundancy is obtained. The main parachute is attached to the landed sphere by a 6-lead bridle harness strapped around the sphere and secured by a single cable release system exactly the same as the support ring release systems. Elastic cords are stretched around the top of the sphere, so that at the harness release (initiated at impact by an impact fuse) the harness is jettisoned clear of the landed sphere.

The landed sphere is 43 inches in diameter and consists of an impact attenuator and an internal sphere (housing the landed payload). The impact attenuator is primarily aluminum honeycomb core (5052 1/8 cell - 4.5 lb/ft³, see section 8.5.1) constructed of 14 segments with a thin fiberglass cover on the outside and a thin fiberglass shell on the inside. The fiberglass cover tends to support the honeycomb segments during fabrication and impact (by overlapping grooves). The intershell is used to fasten the assembly to the internal sphere and provide the separation system after impact. Separation of the attenuator (required, since it is not rf transparent) is accomplished by a linear charge cutting the separation (inter) shell into 14 segments and jettisoning the segments by conical springs. Each segment, however, is

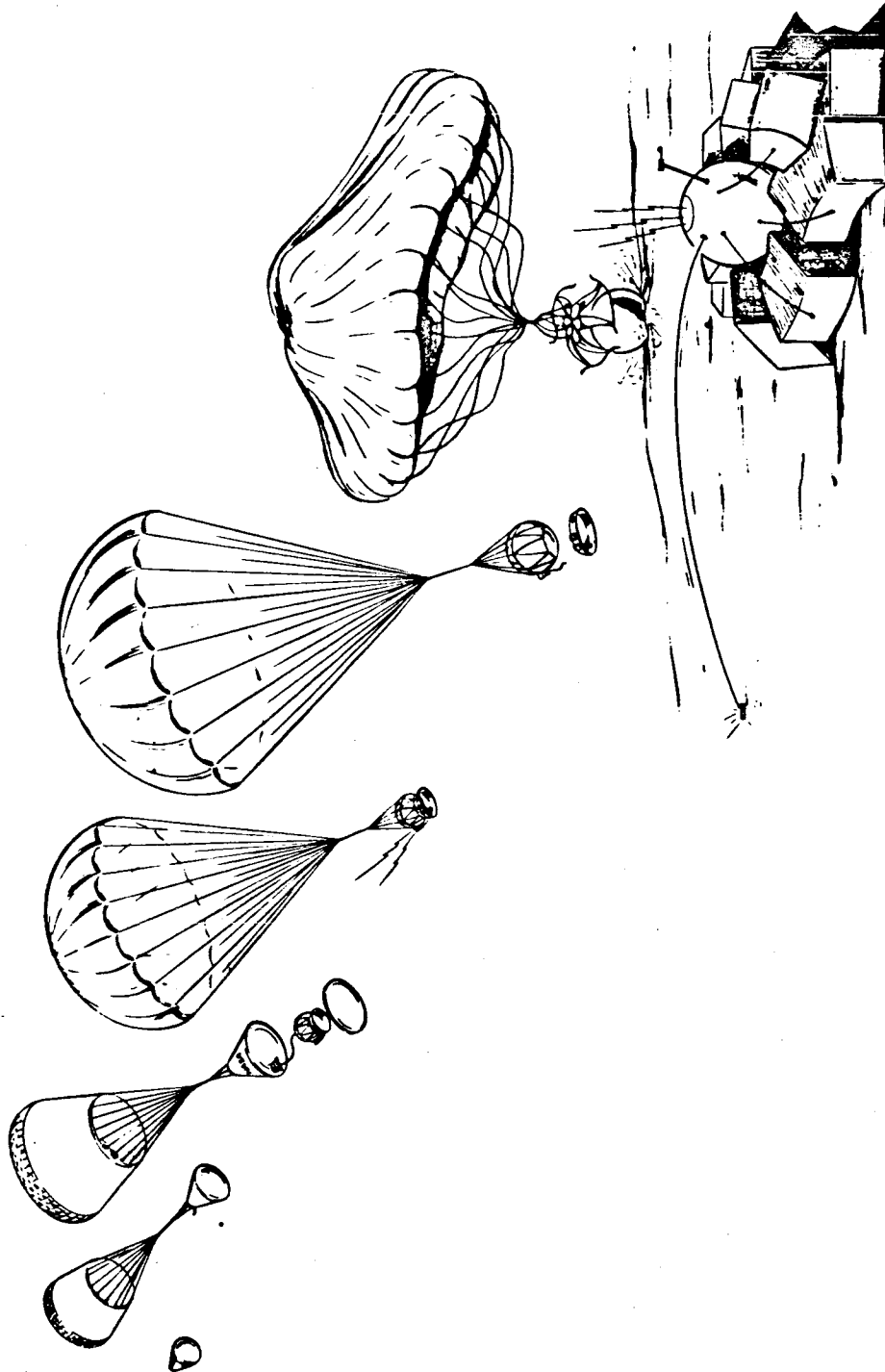


Figure 13 ENTRY AND LANDING SEQUENCE ADVANCED MARINER
LANDER CONCEPT

64-9012

attached to the internal sphere by elastic lanyard lines that stabilize the internal sphere; this then eliminates the necessity of anchoring the internal sphere by other means.

The internal sphere is constructed of a flotation shell, flotation fluid, and an intersphere covered with an insulator-sealer. The flotation shell and fluid provide the erection technique for the communication antenna, since the intersphere (which is housing the fixed antenna and payload) is free to float to an upright position. The center of gravity of the intersphere is ~1.5 inches from the center of buoyancy, hence allowing sufficient static margin. The flotation shell is fiberglass, (~0.25 inches thick), since it must also be rf transparent. The selection of a flotation fluid is predicated on meeting several design requirements:

- a. It must be dielectric, rf transparent,
- b. It must have a high boiling point $>300^{\circ}\text{F}$, due to the sterilization,
- c. It must have a low freezing point $<0^{\circ}$, due to space environment,
- d. It must have a low viscosity and finally,
- e. It must have the exact density of the intersphere, $\sim 3.2 \text{ slugs/ft}^2$.

For the conceptual design Freon - E3 (a fluorocarbon-developed by DuPont) was selected. It satisfies all these design requirements.

The insulation shell serves three important purposes: (1) provides an insulation barrier for thermal control, (2) acts as a sealer against the flotation fluid, and (3) provides a smooth surface for the intersphere. The intersphere is constructed in a series of layers, where each layer houses a portion of the payload in an aluminum shell (this is illustrated in figure 10, detail E-E). These layers of payload equipment are so arranged that ease of fabrication and weight distribution are achieved. Details of the biological experiment (Gulliver - "sticky string") and anemometer deployment schemes are also presented in figures 10 and 11. Finally a detail is presented in this layout of the caging mechanism. The purpose of the caging mechanism is twofold: (1) it secures the intersphere to the flotation shell and consequently, to the lander during launch, space cruise, and entry, and (2) it provides an umbilical connection for all electrical wiring to and from the landed payload for ground checkout, storage of engineering and scientific data during flight, and command of release mechanisms.

3. Operational Sequence

After the entry vehicle has successfully survived the atmospheric entry environment, descent and landing operations must occur in the following chron-

ological order: drogue chute deployment at $M = 2.5$, separate the landed sphere (with descent payload) from the entry vehicle, deploy main parachute at $M = 0.8$, jettison descent payload, jettison main parachute at impact, and jettison impact attenuator after sphere rolls to rest. In order to facilitate their operation, the main and drogue parachutes are packaged within the entry vehicle but external to the landed sphere. This is illustrated in figure 13.

The drogue parachute, in its mortar with insulated cover, is located as far forward as possible in the conical afterbody (a vehicle center of gravity consideration) with its cylindrical axis aligned through the vehicle center of gravity. This prevents an overturning or tumbling motion from being imparted to the vehicle at mortar firing. The drogue attachment line lies in an insulated, covered trough, formed by one of the afterbody longerons, which extends from the mortar to the after cap, and is attached to the aft end of the afterbody on two or more longerons by a bridle designed so that the drogue loads will be carried axially along the neutral axes of the longerons.

At mortar firing (initiated by a peak g switch and a programmer timer for Mach 2.5, see section 7.7) and drogue injection, the insulated mortar cover is jettisoned and the attachment line trough cover and aft cap are pulled free of the vehicle afterbody by the taut drogue attachment line. The trough cover and aft cap remain captivated to the afterbody after drogue deployment in order to prevent them from damaging the deployed drogue canopy.

The main parachute (canopy, shrouds, and riser) is packaged in a cloth bag secured to the inside of a canister which in turn is fastened to the entry vehicle afterbody. The bottom or forward end of this canister is open, allowing the main parachute, in the cloth bag, to rest directly on an insulated area of entry vehicle forebody. The main parachute attachment line is fastened to the landed sphere harness by a six-lead bridle.

The landed sphere (with descent payload) is separated from the entry vehicle, and the main parachute is deployed by simultaneously initiating (at Mach 0.8 by a timer) the releasing of the landed sphere from the forebody and firing the shaped charge that separates the vehicle's fore - and afterbodies. The forebody falls free. The landed sphere falling below the drogue-supported afterbody, pulls the main parachute's riser, shroud, and canopy from the cloth bag and canister attached to the afterbody. The drogue-supported afterbody, with empty main parachute cloth bag and canister, floats to the planet's surface as the landed sphere descends supported by the deployed main parachute.

Prior to landing and after descent data payout (~100 seconds) the descent payload is jettisoned from the parachute-supported landed sphere. Upon

impact with the planet's surface, the parachute and its harness are jettisoned from the landed sphere, at initiation by an impact fuse. After the landed sphere has come to a complete rest, the impact attenuator is jettisoned by a linear charge into fourteen segments. These segments are attached to the internal sphere by elastic lanyard lines, thus stabilizing the sphere. The caging mechanism has previously been released during jettisoning of the descent payload and hence the intersphere (housing the payload and antenna) is free to rotate to an upright position. After all oscillations have dampened out, the "sticky string" and anemometers (two each) are jettisoned out in sequence, thus recaging the intersphere to the flotation shell, hence fixing the antenna in an upright position for communication.

4. Assembly Sequence

In order to clarify the lander design and to understand the assembly operation required to build the lander concept, a cursory estimate of the assembly sequence is presented in figure 14. Included in the assembly sequence is a parts list for each chronological step in the assembly. The development and cost plan associated with volume V of the Advanced Mariner final report was based on this sequence in conjunction with the preceding design layouts, figures 10 and 11.

3.4 WEIGHT SUMMARY

Included in table 23 is a complete weight summary of the lander. Two sets of weights are presented. The first columns (not in parentheses) are those weights generated in the conceptual design synthesis from parametric data. The second column (those in parentheses) are the final lander weights resulting from the conceptual design analysis. In the conceptual design synthesis, engineering estimates were used to account for weights that are nonparametrized in the parametric study (such as thermal control, internal structure, wiring, pyrotechnics, and hardening effects). As the conceptual design proceeded, certain additional systems were added and more rigorous analyses were conducted. These effects are illustrated by the change in weights shown in the parentheses. The significant changes were realized in the addition of umbilicals, wiring, and pyrotechnics due to the large number of separation systems incorporated in the design.

Another significant change was noted in the impact attenuation weight (~20 pounds). This change was due to the use of a curve fit to cover a series of crushable material in the parametric study, whereas in the conceptual design a specific aluminum honeycomb material was used (see section 8.5.1), which resulted in greater efficiency.

Notice that the payload weights (both landed and descent) did not change from the conceptual design synthesis. The weights used for these systems employed state-of-the-art hardware in the parametric study, and hence could not be improved.

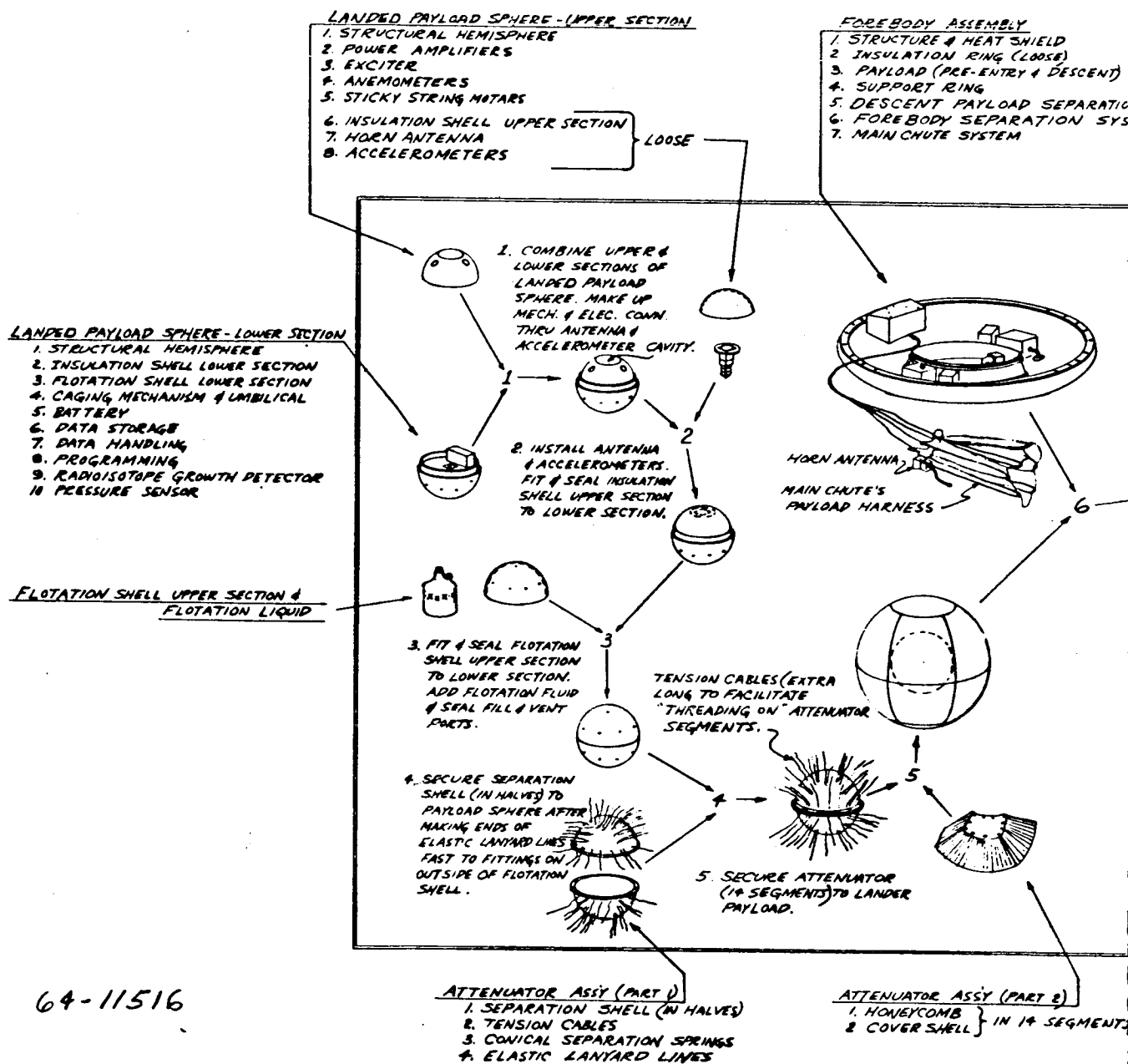
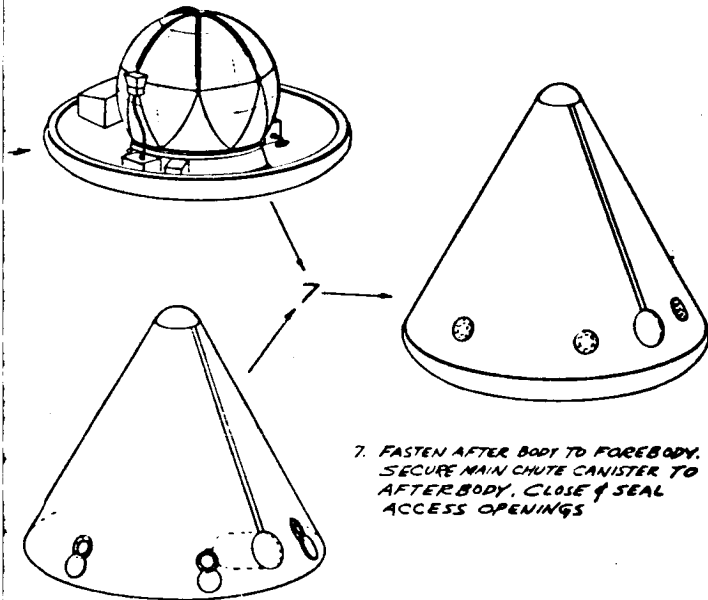


Figure 14 ADVANCED MARINE

N SYSTEM (LOOSE)
 TEM

MULTI-CHANNEL RADIOMETER
 PRESSURE SENSORS
 TEMPERATURE SENSORS
 PRE-ENTRY POWER AMPLIFIER
 PRE-ENTRY EXCITER
 PRE-ENTRY SLOT ANTENNA
 DESCENT POWER AMPLIFIER
 DESCENT HORN ANTENNA

6. SECURE LANDER TO SUPPORT RING
 ON ENTRY VEHICLE FOREBODY.
 FASTEN MAIN CHUTE HARNESS TO
 LANDER & COMPLETE ALL MECHANICAL
 & ELECTRICAL CONNECTIONS.



7. FASTEN AFTER BODY TO FOREBODY.
 SECURE MAIN CHUTE CANISTER TO
 AFTERBODY, CLOSE & SEAL
 ACCESS OPENINGS

0 10 20 30 40 50 60 70 80 90
 APPROX. SCALE (INCHES)

AFTERBODY ASSEMBLY

1. CONICAL SHELL
2. AFT CAP
3. DROGUE CHUTE SYSTEM (COMPLETE)
4. COVERS FOR ACCESS OPENINGS (LOOSE)
5. ATTACHMENT BRACKETS FOR MAIN CHUTE CANISTER

NOTES:

1. ITEMS MAKING UP SUB-ASSEMBLIES ARE LISTED OUTSIDE OF THE DOUBLE LINED BORDER. SOME ITEMS LISTED SEPARATELY MAY BE MADE AS COMBINED UNITS TO SUIT MANUFACTURING TECHNIQUES. HARDWARE & WIRING, IN GENERAL, HAS NOT BEEN SHOWN OR LISTED.
2. ITEMS OUTSIDE OF THE ENTRY VEHICLE (PROPULSION MOTOR, DE-SPIN YO-YO, STERILIZATION CAN ETC.) ARE NOT SHOWN.

R LANDER ASSEMBLY SEQUENCE

TABLE 23

WEIGHT SUMMARY

<u>Internal Weight</u>		<u>124.1</u>	(126.3)
Landed Payload		<u>86.3</u>	
Communication	52.5		
Science	8.5		
Power	25.3		
Structure and Deployment		<u>28.8</u>	(27.9)
Thermal Control		<u>7.0</u>	(2.1)
Umbilicals and Wiring (est)		<u>2.0</u>	(8.0)
Pyrotechnics (est)			(2.0)
<u>Landed Weight</u>		<u>272.0</u>	(258.0)
Attenuator		<u>146.4</u>	(126.7)
Support Structure	16.7		
Aluminum H/C	129.7		(110)
Umbilicals and Wiring (est)		<u>1.0</u>	(3.0)
Pyrotechnics and Release (est)		<u>0.5</u>	(2.0)
<u>Suspended Weight</u>		<u>317.1</u>	(312.3)
Descent Payload		<u>41.1</u>	
Communication	37.8		
Science	3.3		
Structure		<u>4.1</u>	(9.2)
Pyrotechnics and Release (est)			(1.0)
Umbilicals and Wiring (est)			(3.0)

TABLE 23 (Concl'd)

<u>Entry Weight</u>		<u>500.0</u>	(516.5)
Heat Shield	<u>65.5</u>	(70.1)	
Structure	66.7		
Drogue Chute	<u>25.0</u>	(30.1)	
Main Chute	<u>25.6</u>	(26.7)	
Thermal Control (Insulation)		(10.3)	
<u>Thrusted Weight</u>		<u>536.0</u>	(554.5)
Propulsion System	<u>25.0</u>	(23.0)	
Bracketry	<u>6.0</u>	(5.5)	
Yo-Yo Despin	<u>5.0</u>	(9.5)	
<u>Separated Weight</u>		<u>601.0</u>	(627.1)
Sterilization Canister	<u>60.0</u>	(66.5)	
Spin Rockets	<u>5.0</u>	(2.8)	
Separation Joints		(3.3)	

104

Finally it is interesting to note the sum of weights that are nonparametized (i. e., not included in the parametric studies), weights that do not have a single criterion to parametrize against and depended entirely on the conceptual design selection. These weights are listed in table 24 and result in approximately 18 percent of the total lander (entry vehicle) weight. Summarized in the following table are the moments of inertia of the lander at flyby bus separation and at entry. These inertias were calculated using the conceptual design layouts and weight summary in table 23.

	At Separation	At Entry
I_x (Roll) slugs/ft ²	45.62	40.76
I_y (Pitch) slugs/ft ²	36.17	26.16
I_z (Yaw) slugs/ft ²	43.33	35.44
$x_{c.g.}$ inch/inch of dia.	0.18D	0.19D

The large value of I_z is due primarily to the parachutes located on the opposing axis. Notice that this value is close to the roll moments of inertia. This result necessitated that the lander be despun at entry since spin stabilization could not be guaranteed (see section 4.1).

TABLE 24

NON-PARAMETIZED WEIGHTS

	Pounds	Percent
Engineering Instrumentation & Diagnostic	4.0	(0.8)
Descent Payload Structure	9.2	(1.8)
Internal Payload Structure	27.9	(5.5)
Attenuator Support Structure	16.7	(3.2)
Umbilicals & Wiring	17.0	(3.3)
Pyrotechnics	5.0	(1.0)
Thermal Control	<u>12.4</u>	<u>(2.4)</u>
Total	92.2	(18.0)

4.0 AERODYNAMIC PERFORMANCE

The reference lander shape for the Advanced Mariner Design Study has been the Apollo configuration shown in figure 15. A nominal diameter of 8 feet and $m/C_D A = 0.20$ were chosen for the initial parametric trajectory study. Nominal moments of inertia of $I_X = 95$ and $I_Y = I_Z = 65$ were computed based on the center of gravity location and an assumed density distribution. Figure 16 shows the variation of longitudinal and transverse radii of gyration versus vehicle diameter for the assumed $X_{CG}/D = 0.175$.

The trajectory studies were performed for the most part with a four-degree-of-freedom digital program, and compared at critical conditions with a full 6-degree-of-freedom program. The four-degree program has the advantage of providing both heating and dynamic data at a lower cost than the six-degree program can provide dynamics alone. The main disadvantage of the four-degree-of-freedom program is the fact that it can accommodate angle-of-attack variation of aerodynamic coefficients at only one Mach number. However, it was possible to obtain excellent simulation of the trajectory down to peak dynamic pressure and qualitative effects to Mach 2.5. Mach 2.5 is a convenient reference because it is the nominal Mach number for drogue chute deployment.

The aerodynamic coefficients used in the study were obtained from references 1, 2, 3, 4, 5. Newtonian variations of C_D and C_{mq} with angle of attack are plotted in figures 17 and 18. Reliable experimental values of all static aerodynamic coefficients were found, but data on the damping coefficient, C_{mq} , were rather limited and inconsistent. Based on data from several sources, values of this coefficient were estimated for the complete range of Mach number and angle of attack. These are believed to be conservative, but to evaluate the sensitivity of the performance to damping, C_{mq} was treated as a parameter and varied over the range from zero to Newtonian. The poor transonic and subsonic dynamic stability of the Apollo Shape results in reduced drag (owing to the large average angle of attack) and consequently high impact velocities in the rarer atmospheres. This forced the decision to use a drogue chute to assure survival of the payload after impact.

The results of the parametric trajectory study are summarized in table 25. This table is arranged to show the effect of varying only one parameter while holding all other conditions the same as a reference trajectory obtained with the Apollo shape. A reference trajectory was computed using both zero and the estimated values for the damping coefficient, C_{mq} . These are both given at the top of the table together with the results of the 6-degree-of-freedom program for the same nominal conditions. Care should be taken in observing the effects of the variables to compare with the proper reference trajectory according to the C_{mq} specified in the second column. A detailed discussion of the effect of each of the variables is given below.

TABLE 25

PARAMETRIC STUDY SUMMARY TABLE
(Four-degree-of-freedom Results)

Variable	C_{mq}	Peak Heating			Integ. Heating			Peak Deceleration		M = 2.5			NOTE
		a_E deg	q_c Btu $ft^2 \cdot sec$	q_R Btu $ft^2 \cdot sec$	Q_c Btu/ ft^2	Q_R Btu/ ft^2	Q_{tot} Btu/ ft^2	a_E deg	X/W g	a_E deg	h ft	t sec	
*Reference Trajectories 0 6° Freedom	Est. 0 Est.	22.7 26.8 22.8	67 70 --	17 19 --	608 641 --	62 67 --	670 780 --	19 26 19	75 75 75	22 52 29	22K 11K 20K	45 47 45	See nominal conditions below Average envelope values
$V_e = 25,500$ 28,000	Est. Est.	21.5 20.8	107 139	41 60	827 982	127 227	954 1209	18 18	103 123	22 22	20K 19K	39 36	
$\gamma_e = -40^\circ$ -40°(6° F)	Est. Est.	24.8 25.9	54 --	11 --	797 --	66 --	863 --	21 23	46 46	23 41	41K 37K	72 73	
-20° -45°	0 0	35.8 28.7	37 59	6 13	1480 797	92 70	1572 862	33 28	17 52	48 49	63K 25K	174 67	
P = 0 1 4	0 0 0	15.0 21.4 34.4	60 64 79	14 16 25	568 603 701	51 57 85	619 660 786	16 22 32	67 71 82	62 58 48	21K 15K 7K	46 47 47	
$\epsilon_e = 0^\circ$ 5° 45° 179° 179°	-- 0 0 0 Est.	0.0 1.9 15.9 39.4 32.2	-- 58 62 69 66	-- 13 14 18 17	-- 550 582 651 606	-- 48 53 66 61	-- 598 635 717 667	0 2 16 40 27	68 68 70 60 68	0 5 32 178 34	28K 27K 19K 7K 22K	45 45 46 47 45	(Particle) P = 0 P = 0
Atm = G I J K	Est. Est. Est. Est.	21.4 22.4 22.3 24.6	87 71 71 54	31 154 247 144	448 548 489 668	60 534 836 885	508 1082 1325 1553	19 19 19 20	125 87 96 55	19 22 22 22	26K 32K 60K 87K	43 44 42 44	
m/C _D A = 0.15 0.25 0.30 0.30	Est. Est. Est. 0	22.7 22.7 22.7 24.6	58 75 82 28	13 22 26 28	527 679 743 765	46 78 95 97	573 757 838 862	19 19 19 24	75 76 76 74	22 22 22 48	34K 14K 6K 0	44 45 45 46	Cmq effects
Shape A-1 Concept. Des.	Est. Est.	20.6 21.5	66 73	17 18	598 668	60 67	658 735	16 17	75 72	12 13	25K 17K	45 45	m/C _D A = 0.25

*Apollo Shape, (D = 8', Xcg/D = .175, Ix = 95, Iy = Iz = 65)
 $V_e = 21,500$ $\epsilon_e = 90$ degrees
 $\gamma_e = -90$ degrees H atm } Nominal Conditions
 $P = Z$ m/C_DA = .2

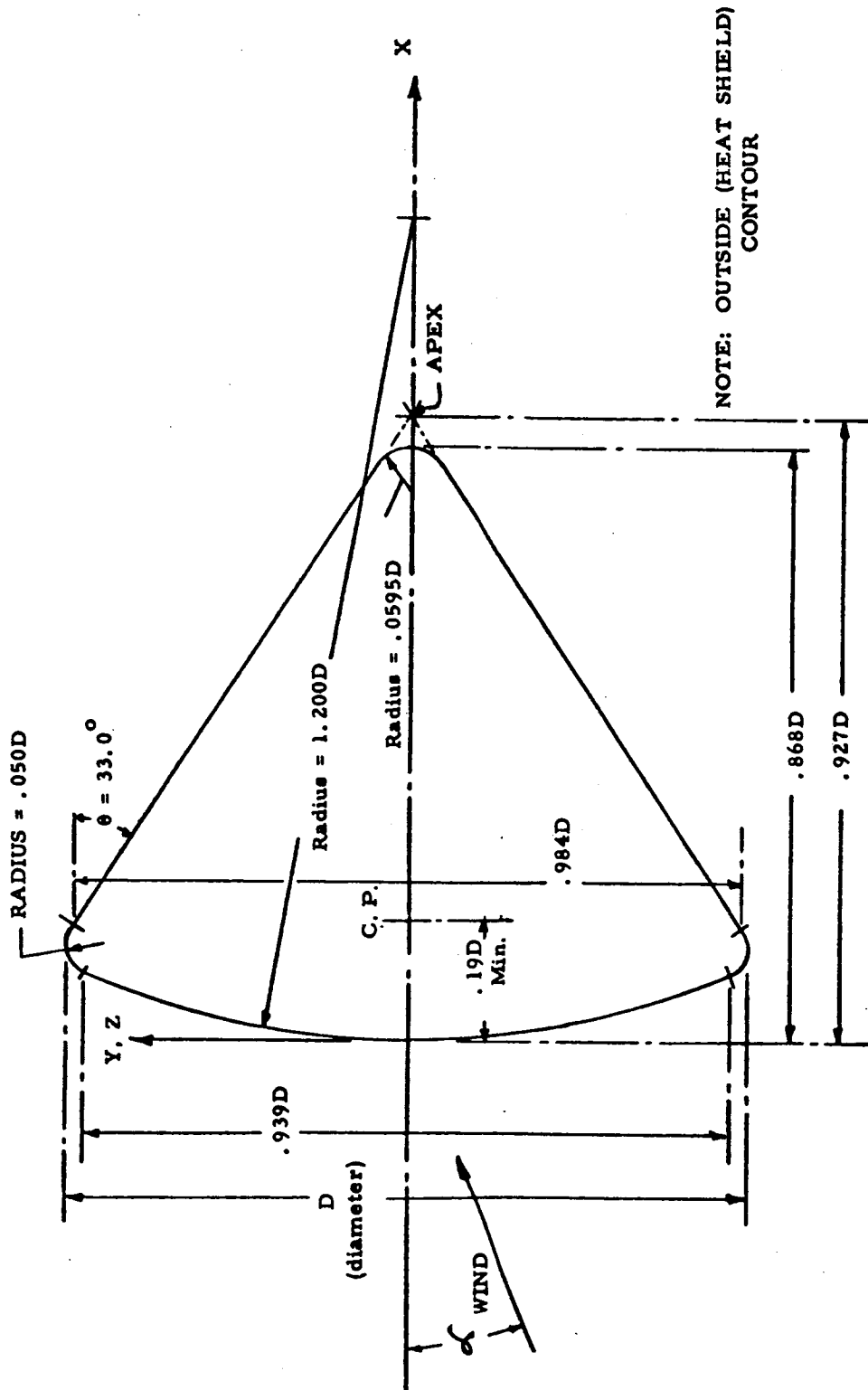


Figure 15 APOLLO CONFIGURATION

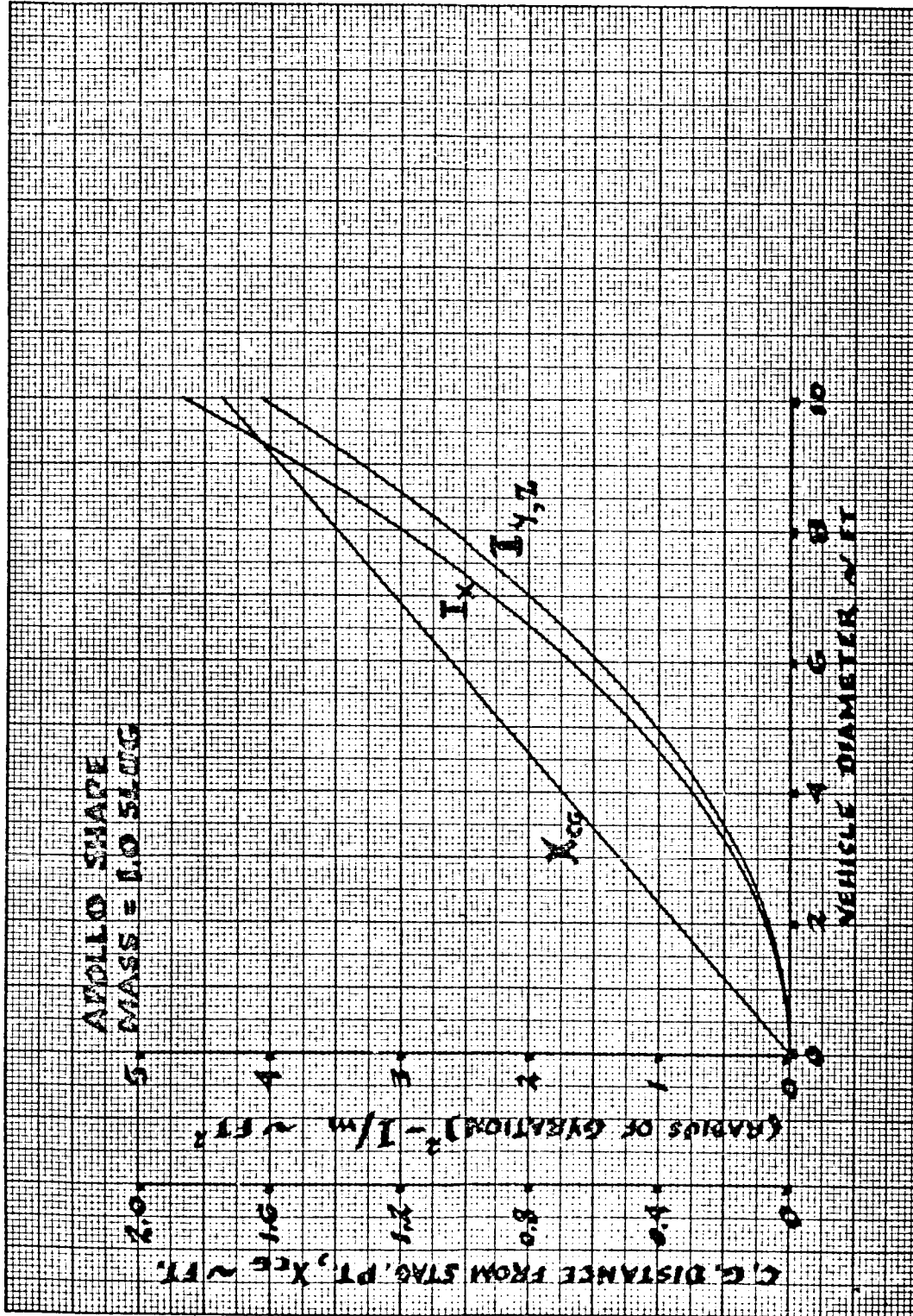
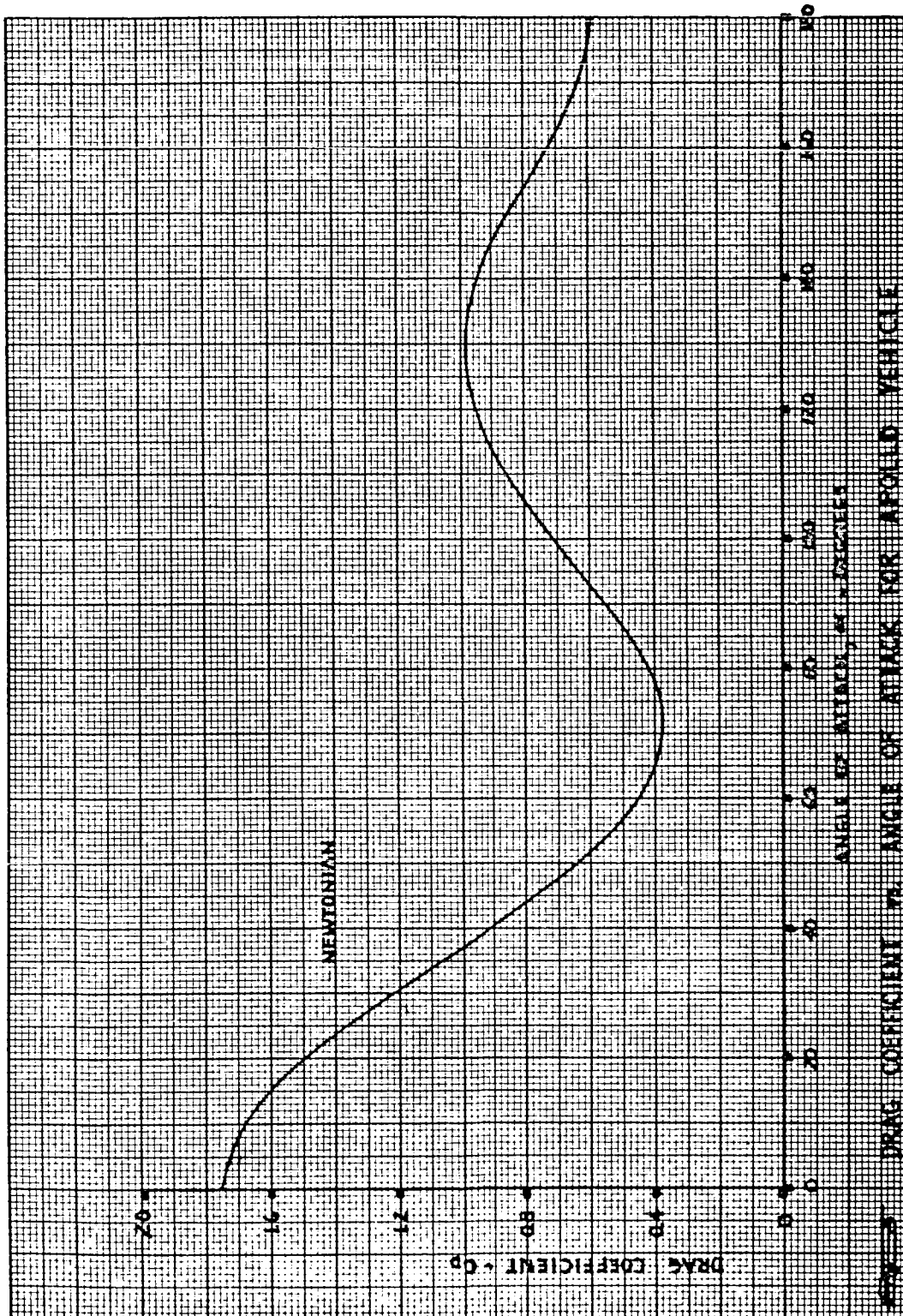


Figure 16 ESTIMATED RADIUS OF GYRATION

81511-49



64-115-19

Figure 17 DRAG COEFFICIENT VERSUS ANGLE OF ATTACK

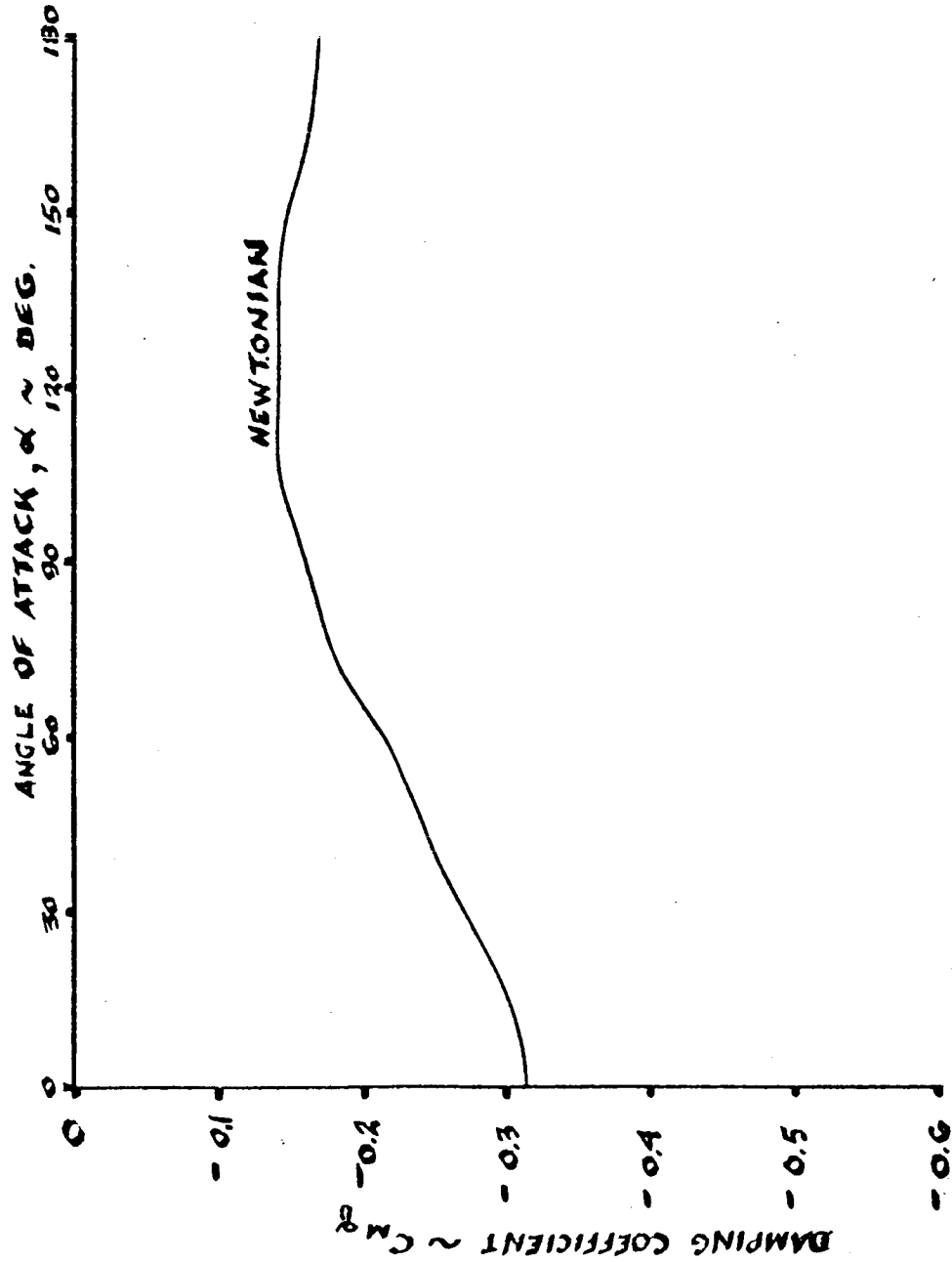


Figure 18 DAMPING COEFFICIENT VERSUS ANGLE OF ATTACK

The Mars atmospheric models considered in the study have the characteristics tabulated in table 26, and the temperature, pressure and density profiles plotted in figures 19 thru 21, as specified for the Advanced Mariner Study (reference 1 section 6.0). The H atmosphere was chosen for the aerodynamic parametric studies because it was the most critical atmosphere for chute deployment, due to low pressure and high temperature.

4.1 ENTRY CONDITIONS

The entry conditions considered were based on the analysis of bus lander separation conditions. Entry velocities ranged from 19,000 to 24,000 ft/sec with flight path angles from -90 to -20 degrees. The angle of attack could be either random (e. g. up to 179°) with negligible rates of spin, pitch, and yaw, or held to approximately 90 degrees with spin stabilization. The proposed spin rate for this purpose is 2 rad/sec, which is the required spin rate for thrust vector control. Since the latter combination ($\alpha_r = 90$ degrees $P = 2$ rad/sec) resulted in acceptable trajectories and would not require despin, it was selected for the nominal parametric entry conditions. The mean entry velocity of 21,500 ft/sec and a flight path angle of 90 degrees also were chosen for the nominal entry conditions.

A study was made of the limitations on spin stabilization of the lander during the period between separation from the bus and entry into the Martian atmosphere. A relationship is given in reference 6 for the maximum precession angle as a function of the moment caused by misalignment of the separation thrust axis, the kinetic energy of spin, and the ratio of longitudinal to transverse moments of inertia. A chart for determining the required spin kinetic energy for any given case is reproduced in figure 22. For the assumed inertial properties of the lander, a spin of 2 rad/sec was found adequate. The effect of solar pressure was also investigated and found to be negligible for the proposed design with the spin rate of 2 rad/sec. Not investigated, and unknown in this case, are the effects of internal damping, gravity and magnetic fields, and impact of micrometeoroids.

1. Entry Velocity, V_e

The entry velocity determines the kinetic energy which must be dissipated. Figure 23 shows that varying entry velocity has a negligible effect on the angle of attack envelope at peak g and at Mach 2.5. However, as expected, there is a large effect on loads. It can be seen in table 25 that peak deceleration varies approximately as the square of the entry velocity at constant entry flight path angle.

TABLE 26

MARS MODEL ATMOSPHERES*

Interim Low Pressure Models
With 13.3 gm/cm² Argon

Property	Symbol	Dimensions	G	H	I	J	K
Surface pressure	P_o	mb	11	11	15	30	30
		lbs/ft ²	23.0	23.0	31.3	62.6	62.6
Stratosphere temperature	T_s	*K	130	230	180	130	230
		*R	234	414	324	234	414
Surface Temperature	T_o	*K	260	260	230	210	230
		*R	468	468	414	378	414
Acceleration of gravity at surface	g	cm/sec ²	375	375	375	375	375
		ft/sec ²	12.3	12.3	12.3	12.3	12.3
Composition (Volume)		%					
CO ₂			64.8	64.8	43.3	10.5	10.5
A			35.2	35.2	32.2	13.0	13.0
N ₂			0	0	24.5	76.5	76.5
Molecular weight	M	mol ⁻¹	42.6	42.6	38.8	31.3	31.3
Specific heat ratio	γ		1.37	1.37	1.39	1.40	1.40
Adiabatic temperature lapse rate	Γ	*K/km	5.18	5.18	4.91	4.05	0
		*R/ft x 10 ³	2.84	2.84	2.69	2.22	
Tropopause altitude	h_T	km	25.09	5.79	10.19	19.75	0
		ft	82300	19000	33400	64800	
Inverse scale height (stratosphere)	β	km ⁻¹	0.1478	0.0835	0.0972	0.1085	0.0613
		ft ⁻¹ x 10 ⁵	4.506	2.546	2.963	3.308	1.869
Surface density	ρ_o	(gm/cm ³) 10 ⁵	2.17	2.17	3.04	5.37	4.91
		(sl/ft ³) 10 ⁵	4.21	4.21	5.90	10.42	9.54
Artificial surface density	ρ_1	(gm/cm ³) 10 ⁵	13.60	2.52	4.35	14.20	4.91
		(sl/ft ³) 10 ⁵	26.40	4.89	8.44	27.55	9.54
Density at tropopause	ρ_T	(gm/cm ³) 10 ⁵	0.332	1.55	1.62	1.66	4.91
		(sl/ft ³) 10 ⁵	0.643	3.02	3.14	3.23	9.54

*Based on L. Kaplan's (JPL) measurements of surface pressure and mass of CO₂.

117

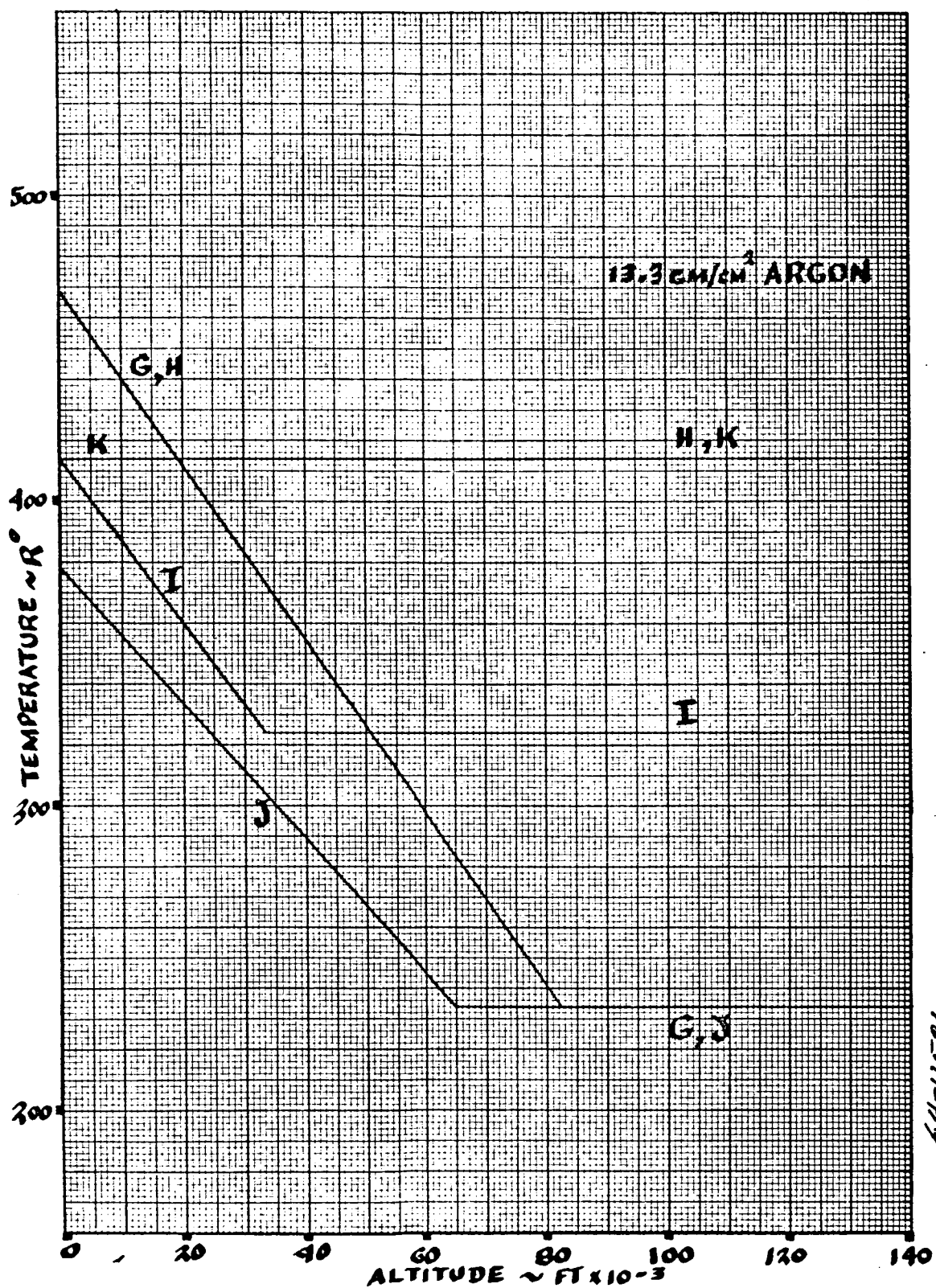
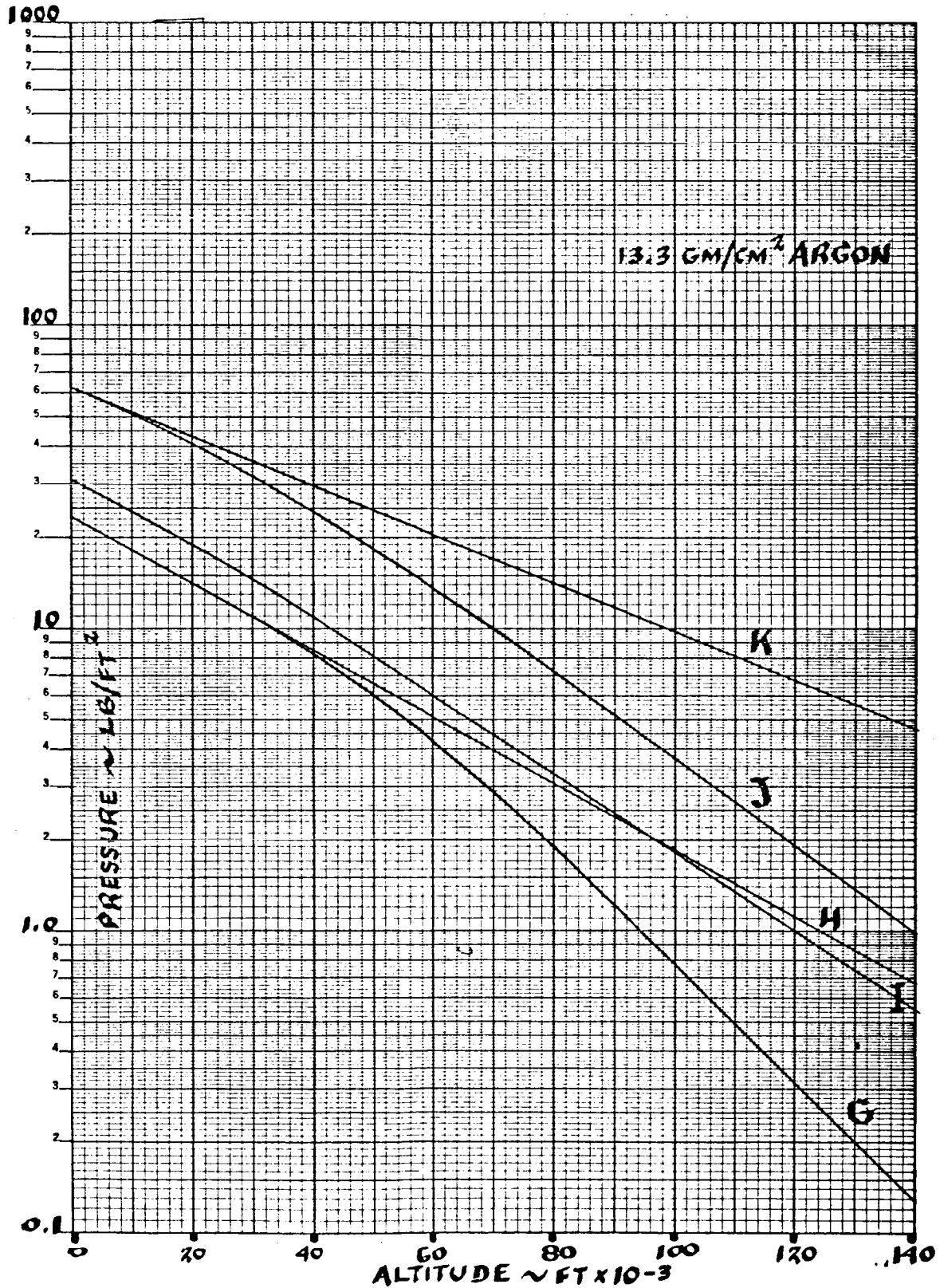


Figure 19 TEMPERATURE PROFILE - MARS ATMOSPHERES

115



64-11522

Figure 20 PRESSURE PROFILE - MARS ATMOSPHERES

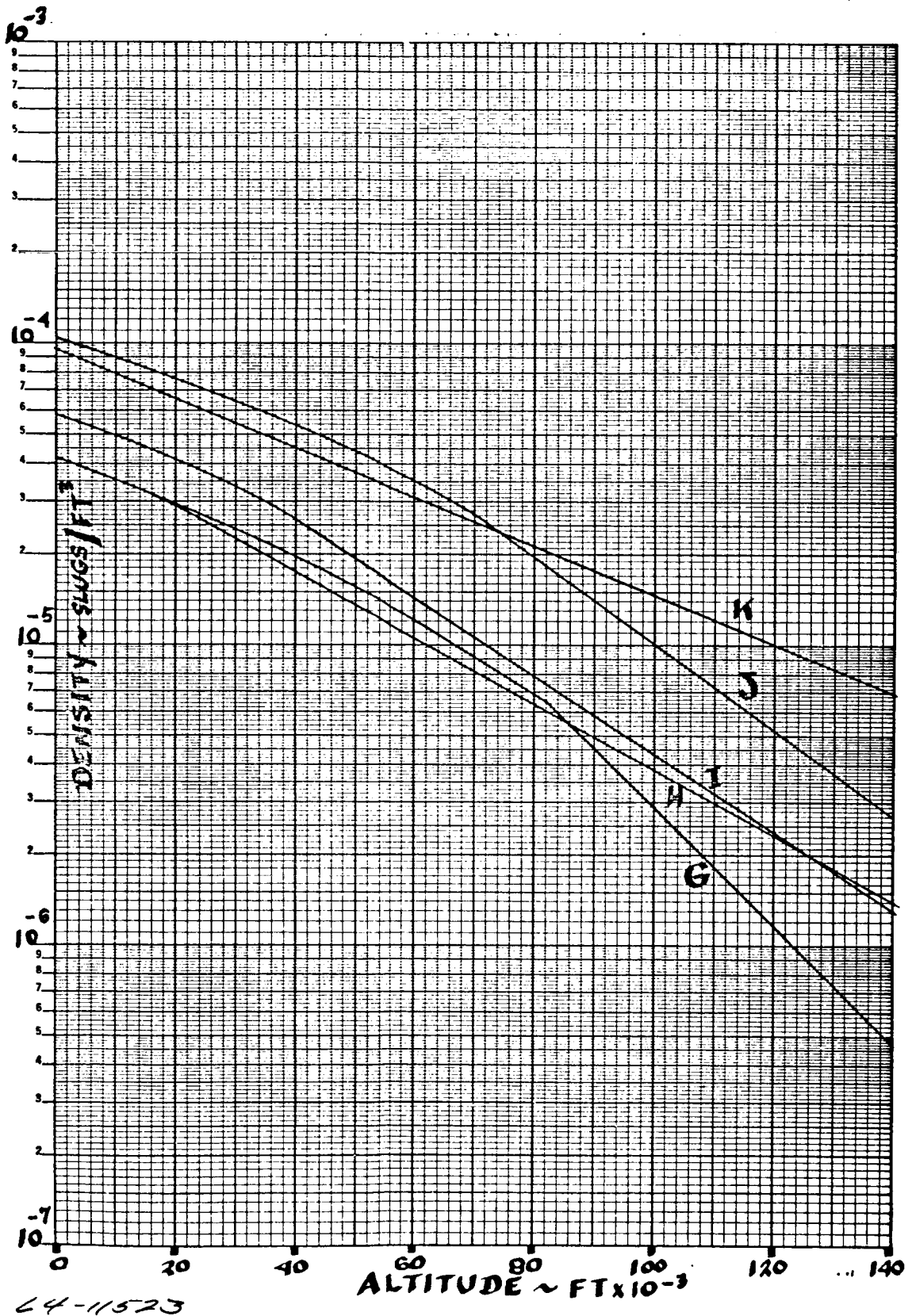


Figure 21 DENSITY PROFILE - MARS ATMOSPHERES

117

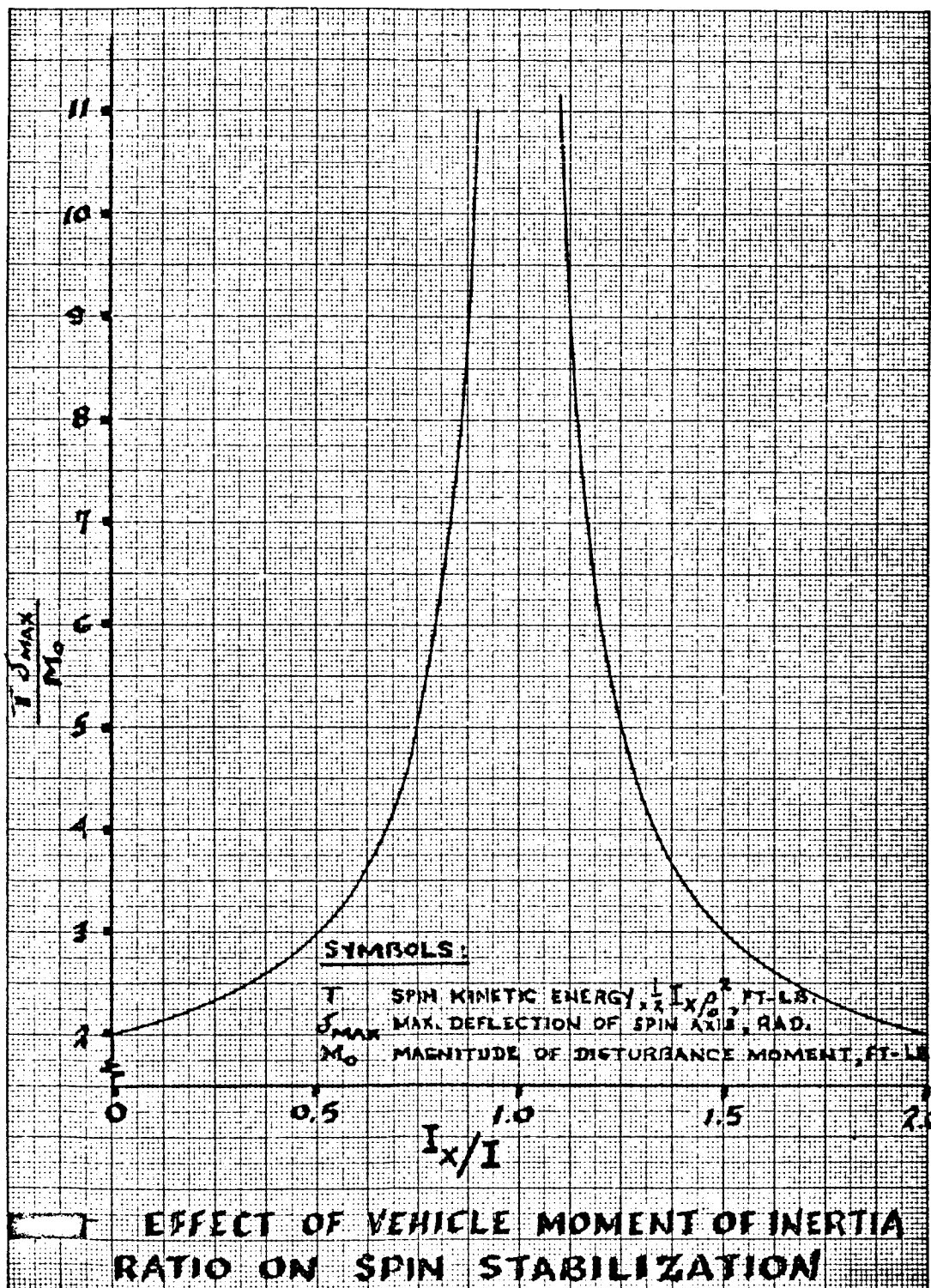


Figure 22 EFFECT OF VEHICLE MOMENT OF INERTIA RATIO ON SPIN STABILIZATION

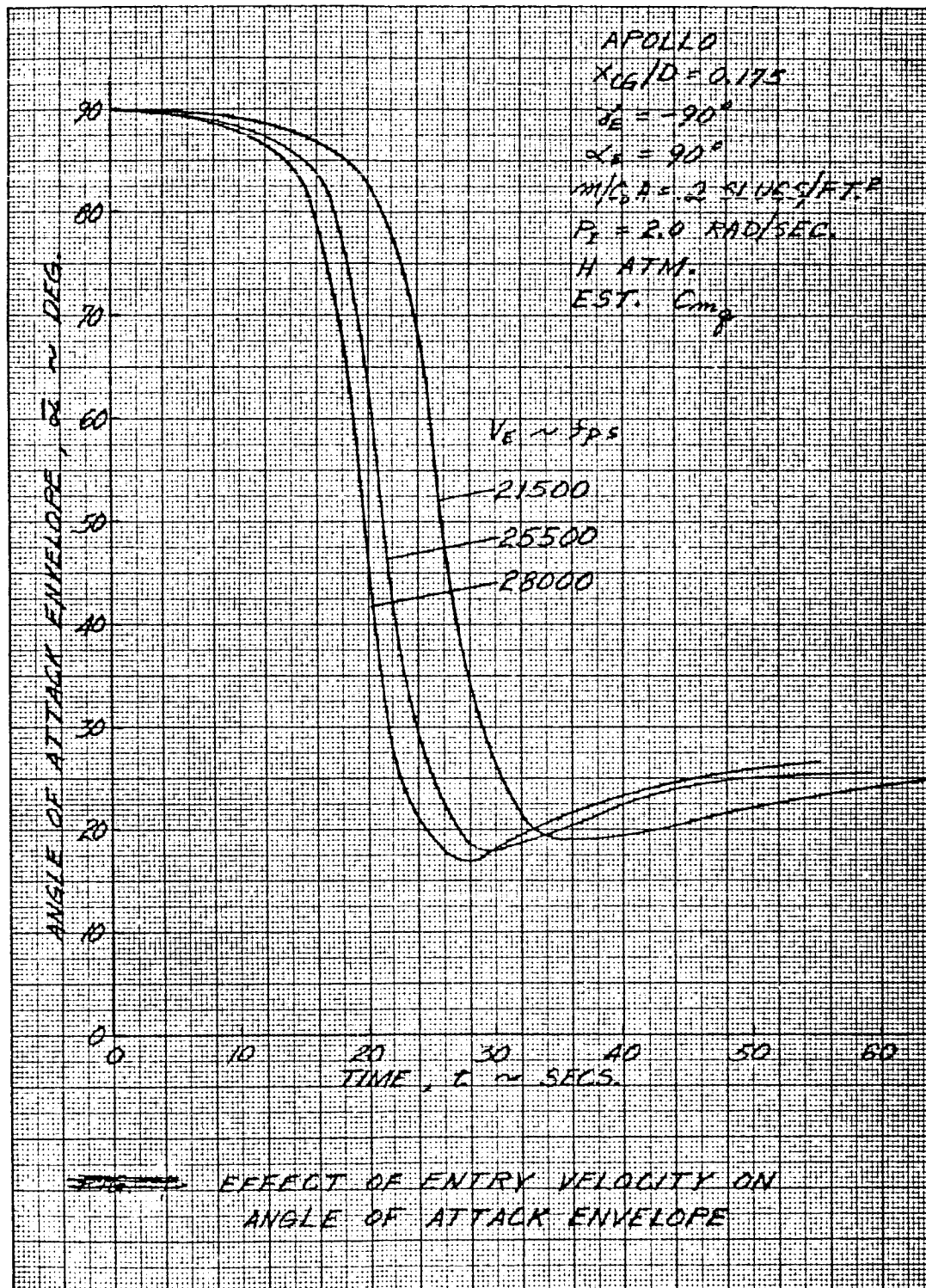


Figure 23 EFFECT OF ENTRY VELOCITY ON ANGLE OF ATTACK ENVELOPE

2. Flight Path Angle, γ_e

The flight path angle governs the capture and the relative magnitudes of heating and loads incurred during entry. A minimum capture angle of $\gamma_e = -20$ degrees was used for this study. (Note minimum entry angle analysis, System Volume 1, 3.3).

Figure 24 shows the effect of entry flight path angle, γ_e , on the dynamics. It can be seen that the greatest effect other than the time scale is the change in angle of attack envelope at peak g and Mach 2.5. Referring to table 25, the magnitude of peak deceleration varies approximately as the sine of the entry angle. The six-degree-of-freedom results given on the table for $\gamma_e = -40$ degrees illustrate that the four-degree results are very good at peak g, but are optimistic at Mach 2.5.

3. Spin Rate, P

Angle of attack envelopes for various spin rates are presented in figure 25 for $C_{mq} = 0$.

The effect of increasing spin rate is to gyroscopically stabilize the vehicle, reducing both the convergence and divergence of the envelope of oscillations. Referring to table 25, it can be seen that increasing the spin beyond 2 rad/sec does not improve the envelope significantly but results in loss of too much altitude at Mach 2.5, due to the decrease in average drag, which is a function of angle of attack.

4. Angle of Attack, α_e

Figure 26 shows that the performance of the lander is very sensitive to entry angle of attack. Note that a spin of 2 rad/sec. has been used for this study, and that the $C_{mq} = 0$. In addition to the large amplitudes of oscillation obtained with large entry angles of attack, the average drag is reduced, resulting in loss of altitude at Mach 2.5. This latter effect is evident in table 25. In this table, a comparison is provided for both a particle trajectory (zero angle of attack) and the unspun 179 degrees case. It can be seen that if C_{mq} is much smaller than estimated, an improvement in performance is possible by spin stabilizing at $\alpha_e = 90$ degrees. Or stated another way, there is less sensitivity to C_{mq} for entry conditions of $\alpha_e = 90$ degrees and spin rate of 2 rad/sec.

4.2 EFFECT OF ATMOSPHERE

Figure 27 shows the effect on performance of the various atmospheric models considered. It can be seen the atmosphere has practically no effect on either

the time or angle of attack at peak g. The main effect is on the envelope after peak g, and the time to impact. The greatest peak deceleration (see table 25), occurs in the G atmosphere. The greatest altitude at Mach 2.5 occurs in the K atmosphere.

4.3 EFFECT OF VEHICLE PARAMETERS

1. Ballistic Coefficient, $m/C_D A$

The first vehicle parameter to be studied was $m/C_D A$ because this is probably the most important single characteristic of the lander. Through this parameter, the performance of the vehicle will ultimately determine the payload.

It has already been observed that since the drag of the reference shape varies with angle of attack, the smaller the average angle of attack, the greater the deceleration, and consequently the lower the impact velocity and the greater the altitude at Mach 2.5. Effective $m/C_D A$ is the parameter which compares the performance of the vehicle in a dynamic trajectory with the performance possible at zero angle of attack (particle trajectory). The effective $m/C_D A$ is thus always higher than the static hypersonic $m/C_D A$ at zero angle of attack used to describe the vehicle, and is defined in this study as the $m/C_D A$ required in a particle trajectory to achieve a given altitude at Mach 2.5. Figure 28 compares dynamic and particle trajectory performance at Mach 2.5 as a function of hypersonic $m/C_D A$.

The overall effect of $m/C_D A$ on entry dynamics is illustrated in table 25. The envelopes are almost identical down to $M = 2.5$ for the range considered. The only difference appears to be the altitude at $M = 2.5$ as discussed above.

2. Damping Coefficient, C_{m_q}

The effect of the damping coefficient, C_{m_q} , on the angle of attack envelope is shown in figure 29. It can be seen that the aerodynamic performance is rather sensitive to this parameter, and that more data should be obtained to verify or refine the estimated values. As pointed out earlier, the effect of C_{m_q} can be minimized through the use of spin.

3. Configuration

A shape study was undertaken to determine what modifications to the Apollo shape might improve the effective $m/C_D A$ and increase the payload. The variations considered are shown in figure 30, and associated aerodynamic characteristics are compared in figures 31, 32, and 33. The effect on the angle of attack envelope is shown in figure 34.

The first modification considered was the addition of fins to the Apollo shape, in an attempt to increase both damping and drag at large angles of attack without changing the desirable characteristics at small angles of attack. The disadvantage of this configuration is the possibility that the large fins might impart a high spin rate.

Shape E-5 was investigated because of its high drag at all angles of attack and the greater latitude on center of gravity location as compared to the Apollo. However, the weight of the heat shield required would more than offset the drag benefits.

The sphere was also considered because of the constant drag at all angles of attack. However, the decrease in drag and increase in surface area made this configuration unacceptable.

The most promising shape was A-1, because it not only significantly lowered the effective $m/C_D A$, but allowed reduction in the heat shield weight. However, within the scope of this study, it was rejected because of the need for greater control of entry angle of attack.

4.4 CONCEPTUAL DESIGN SUMMARY

The results of the parametric study and the final internal design requirements combined in the determination of the conceptual design. A new center of gravity location of 0.21 D necessitated a change in the afterbody design to prevent rearward stability during entry. Using Newtonian theory, it was found that changing the cone angle from 33 to 30 degrees moved the center of pressure rearward sufficiently to maintain a satisfactory static margin. The conceptual design configuration is shown in figure 35.

The $m/C_D A$ for the conceptual design was selected based on a required minimum altitude for drogue chute deployment of 14,000 feet. This corresponds to an effective $m/C_D A$ of 0.285 or an actual hypersonic $m/C_D A$ of 0.244 at zero angle of attack indicated by the parametric study (see figure 28). Final conceptual design analysis resulted in an $m/C_D A$ of 0.25.

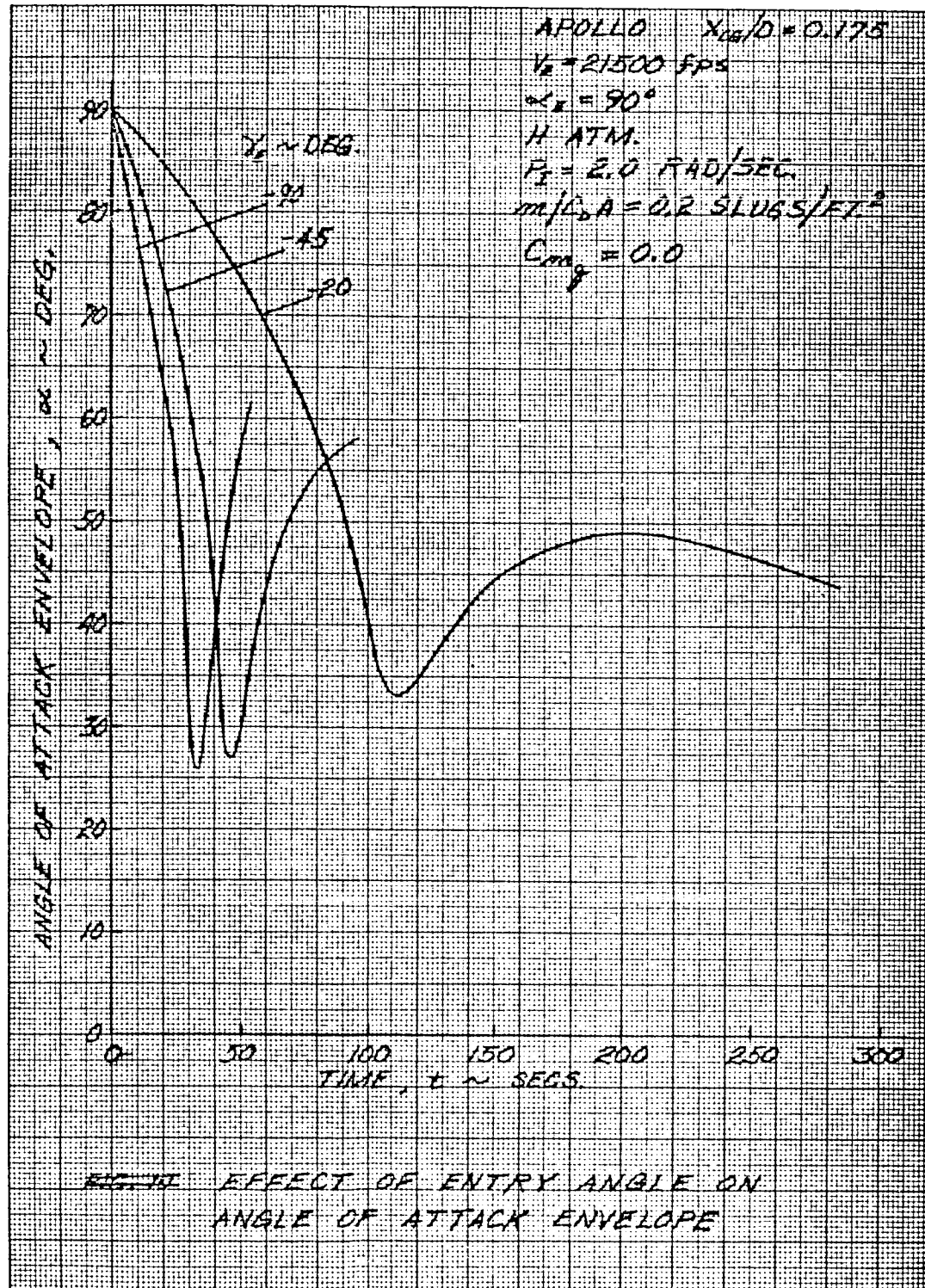
The final moments of inertia were less than predicted (see section 3.4) and the difference between axial and transverse moments of inertia became too small for effective spin stabilization. It was therefore decided to despin prior to entry, to improve the performance for large angle of attack at entry. A beneficial effect of the reduced moments of inertia is increased damping, with resultant improvement in the effective $m/C_D A$ (see section 4.3).

An abbreviated parametric study was conducted with the conceptual design as the reference to confirm the conclusions from the previous studies, as applied to this specific combination of the variables. For this study, the K atmosphere was used as the nominal model, because of the additional information which

could be obtained on heating. The coefficients used for the conceptual design were based on the Apollo coefficients adjusted for the theoretical changes due to new center of gravity location and afterbody change. The nominal angle of attack at entry was 179 degrees with no spin.

The results of the study are presented in table 27. It is interesting to note that for this design there is a smaller effect of entry angle of attack on peak g and altitude at Mach 2.5 than observed with the original reference design. This is evidenced in the location of the conceptual design point on Figure 28.

The maximum loading encountered (112g) occurs in the G atmosphere at an entry flight path angle of -90 degrees. The minimum altitude at Mach 2.5 (15,000 feet) now occurs slightly lower in the G than the H atmosphere, but still above the required minimum for chute deployment.



64-11526

Figure 24 EFFECT OF ENTRY ANGLE ON ANGLE OF ATTACK ENVELOPE

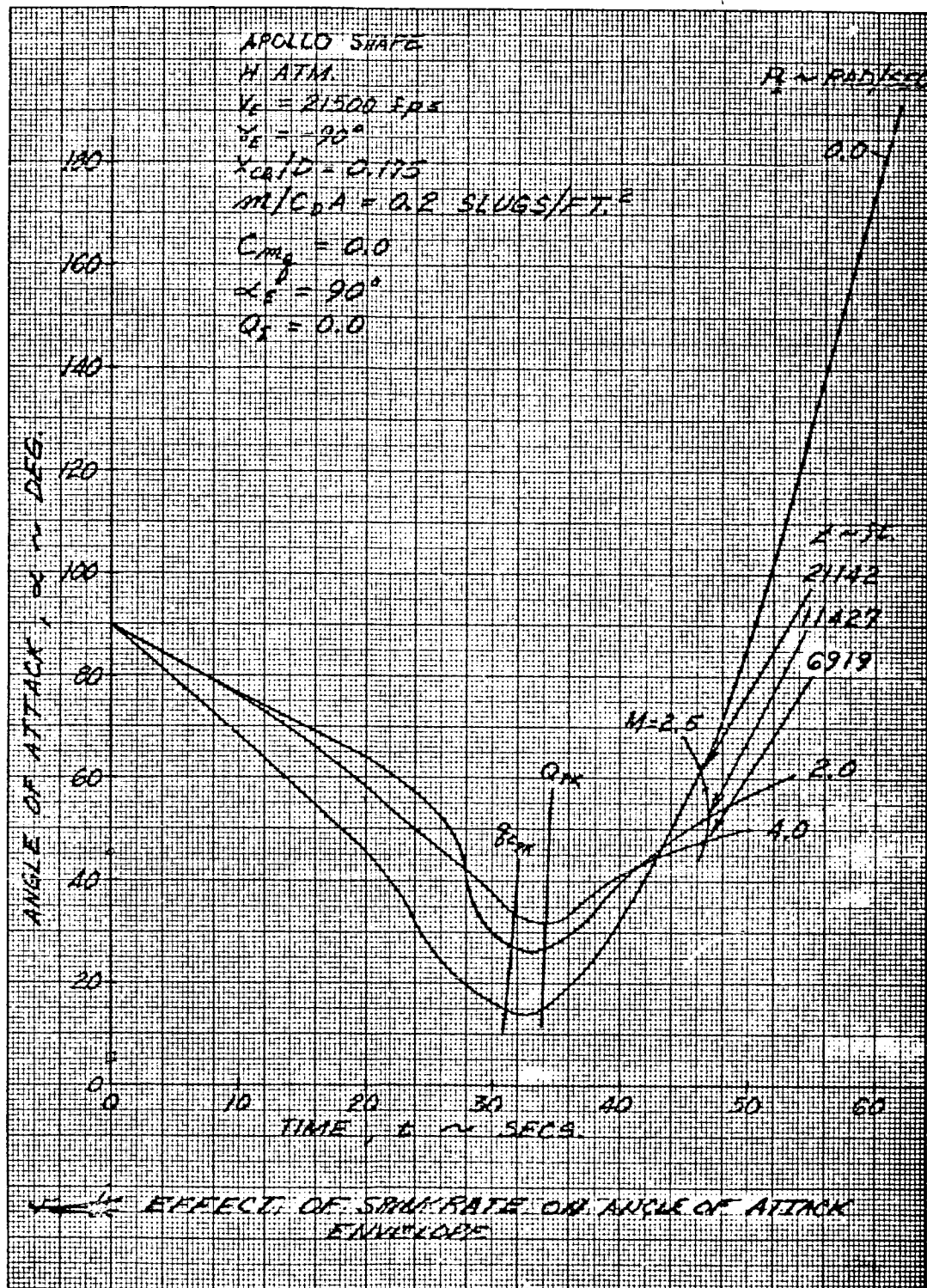


Figure 25 EFFECT OF SPIN RATE ON ANGLE OF ATTACK ENVELOPE

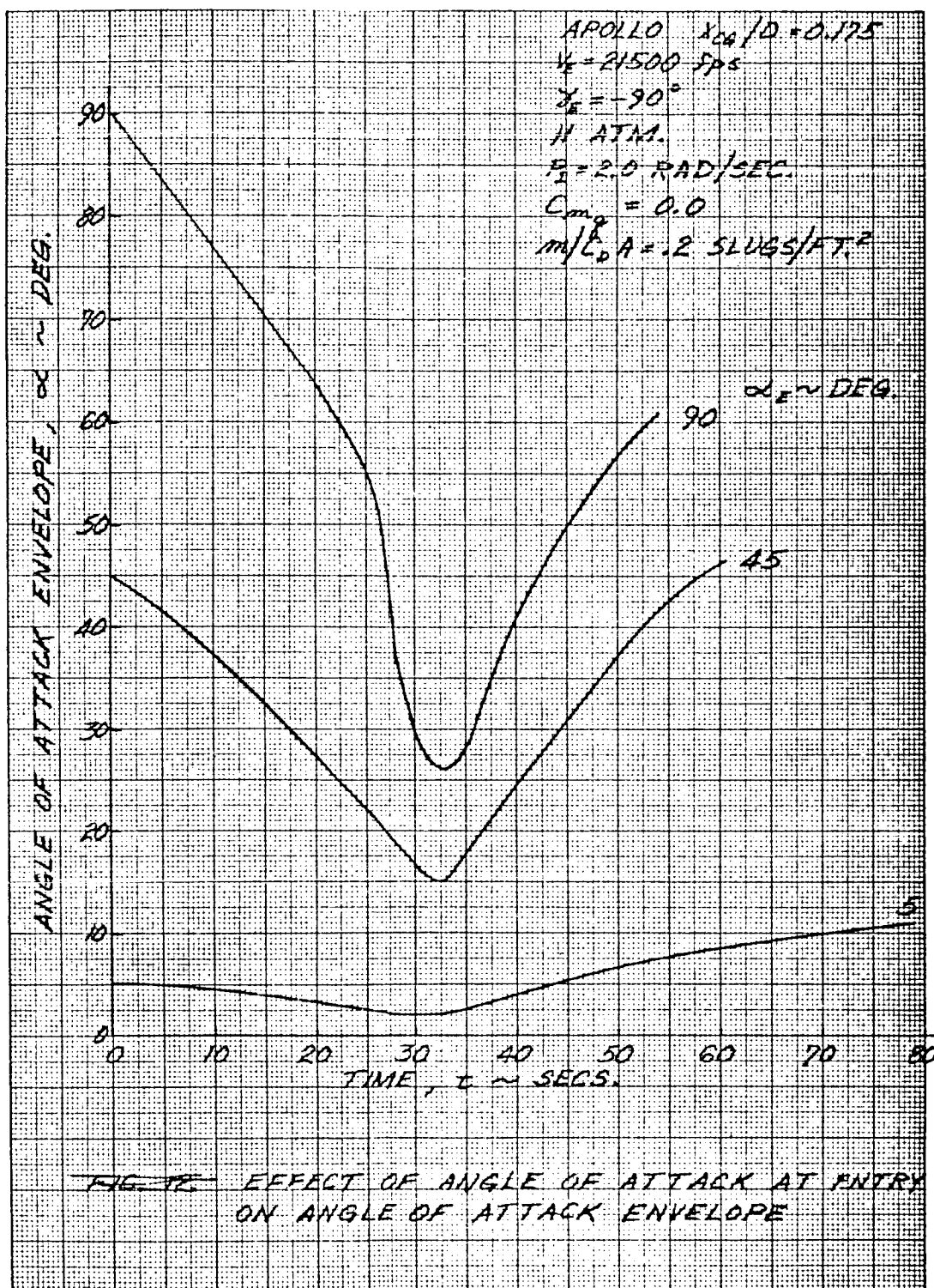


Figure 26 EFFECT OF ANGLE OF ATTACK AT ENTRY ON ANGLE OF ATTACK ENVELOPE

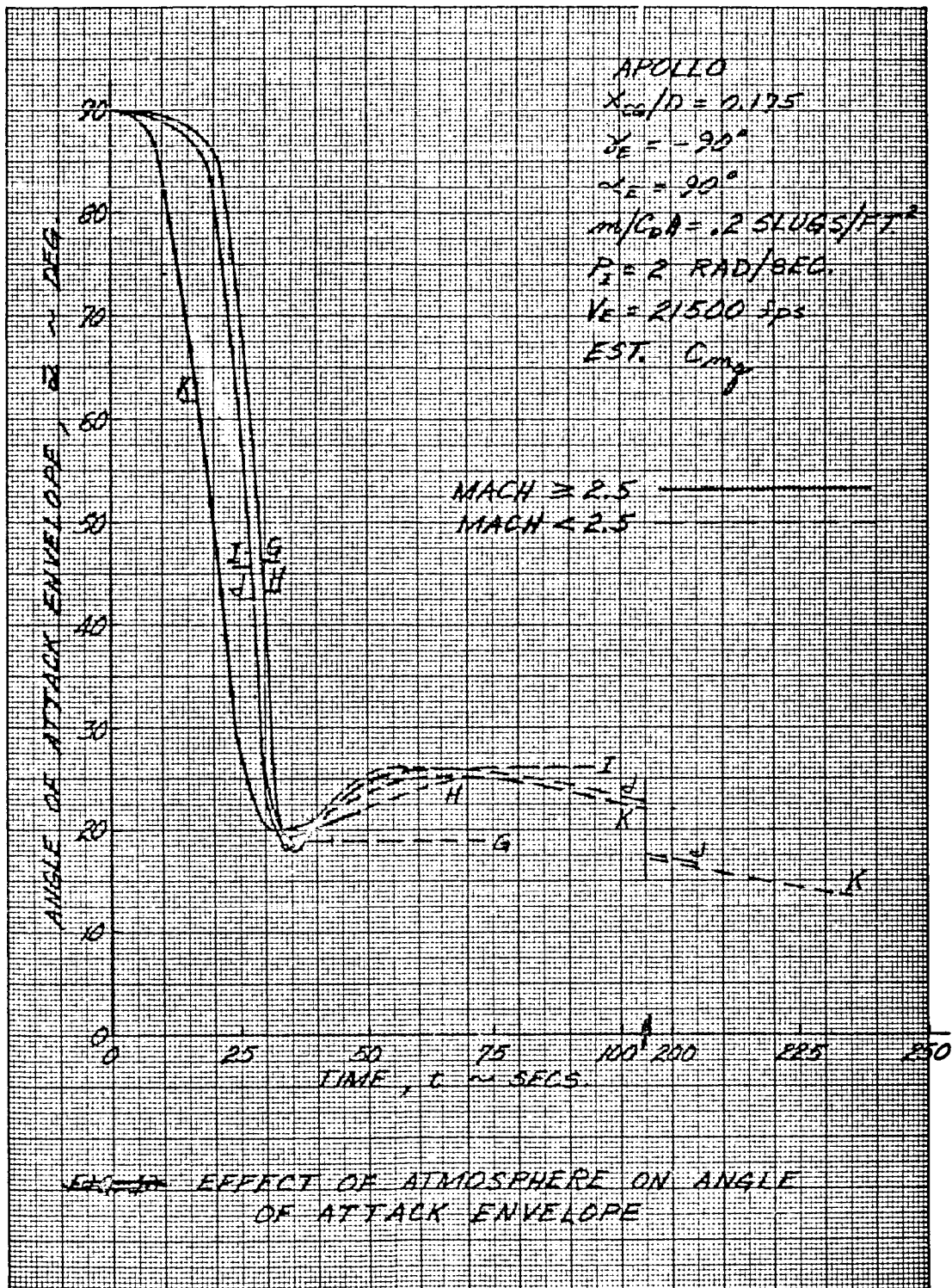
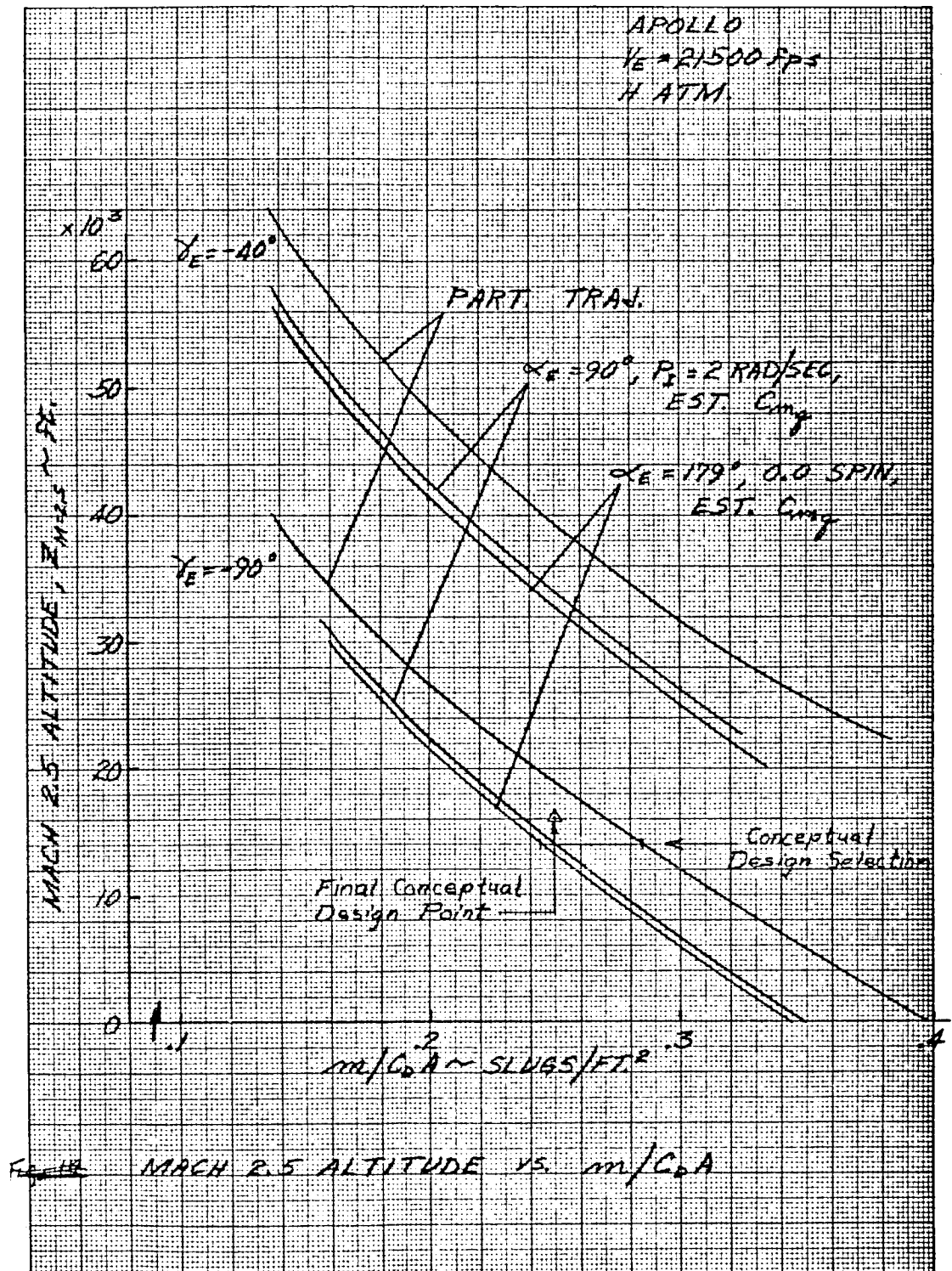
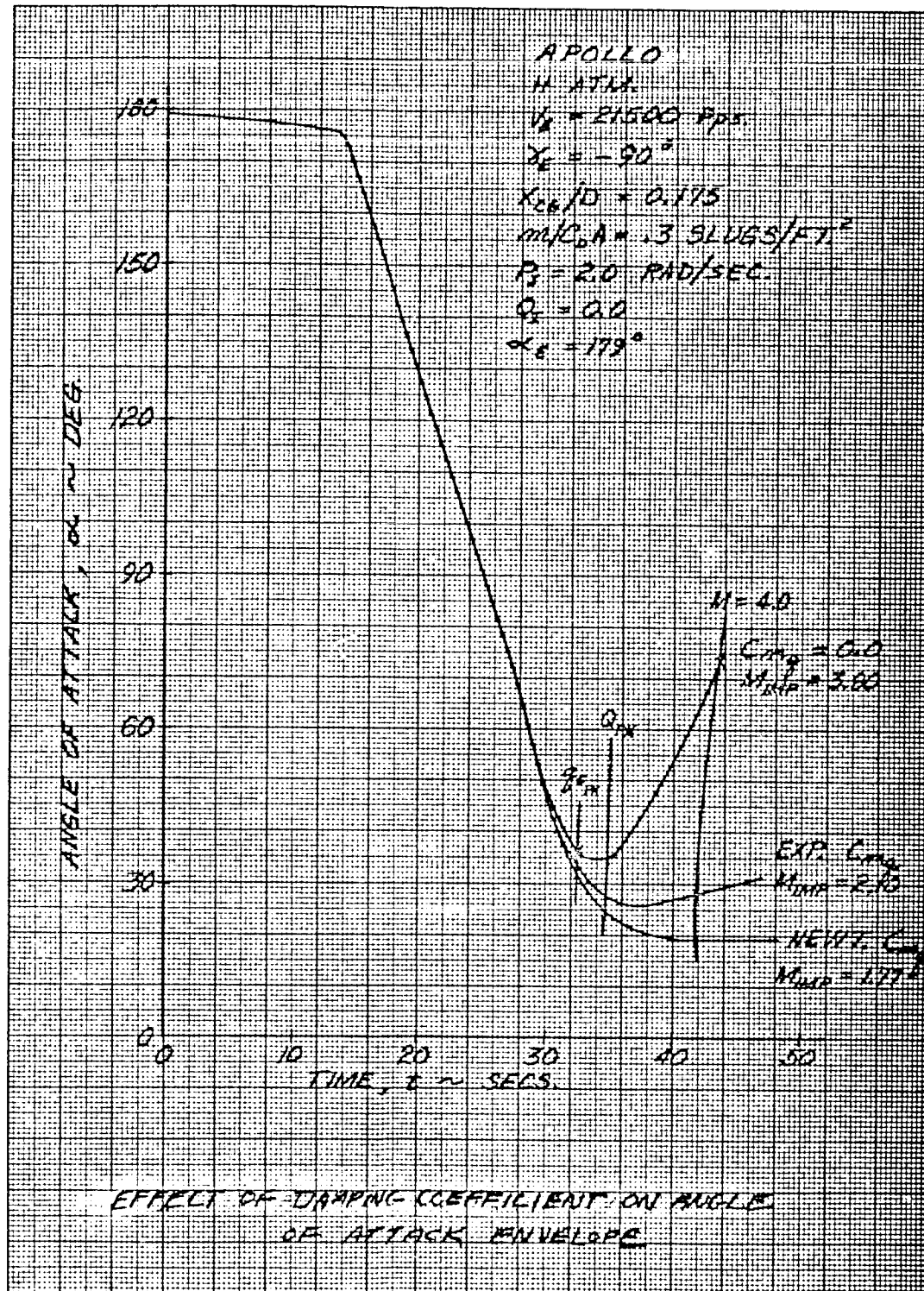


Figure 27 EFFECT OF ATMOSPHERE ON ANGLE OF ATTACK ENVELOPE


Figure 28 MACH 2.5 ALTITUDE VERSUS $m/C_D A$



64-11531

Figure 29 MACH 2.5 DAMPING COEFFICIENT ON ANGLE OF ATTACK ENVELOPE

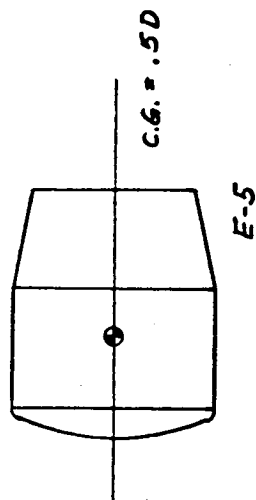
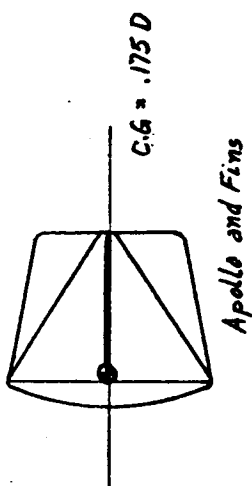
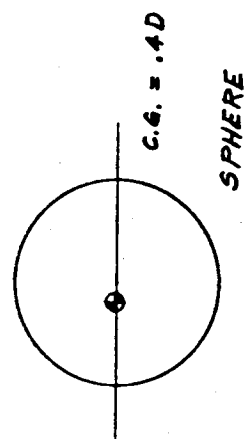
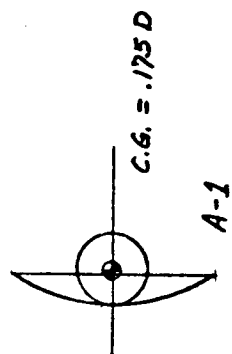


Figure 30 CONFIGURATIONS

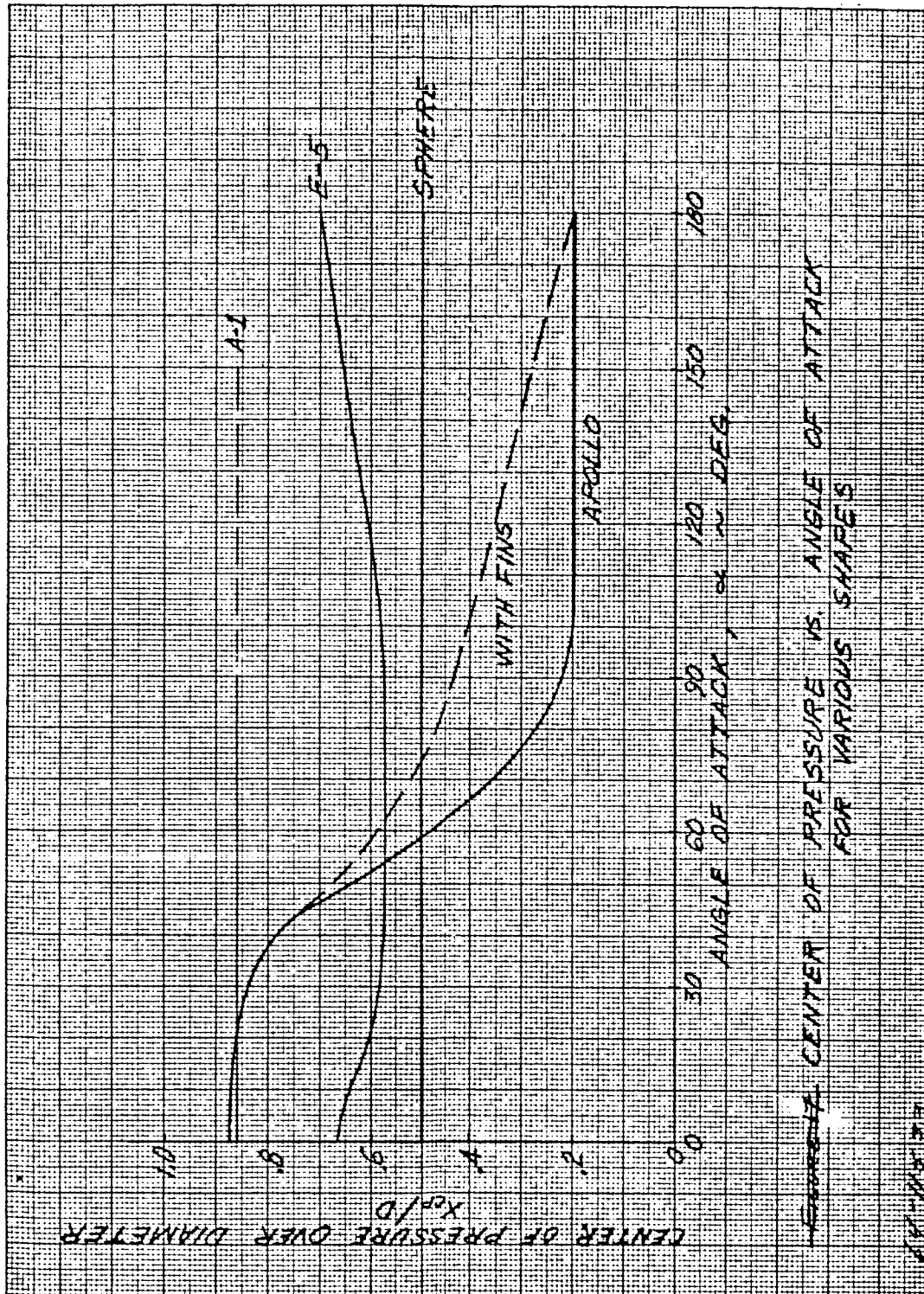


Figure 31 CENTER OF PRESSURE VERSUS ANGLE OF ATTACK FOR VARIOUS SHAPES

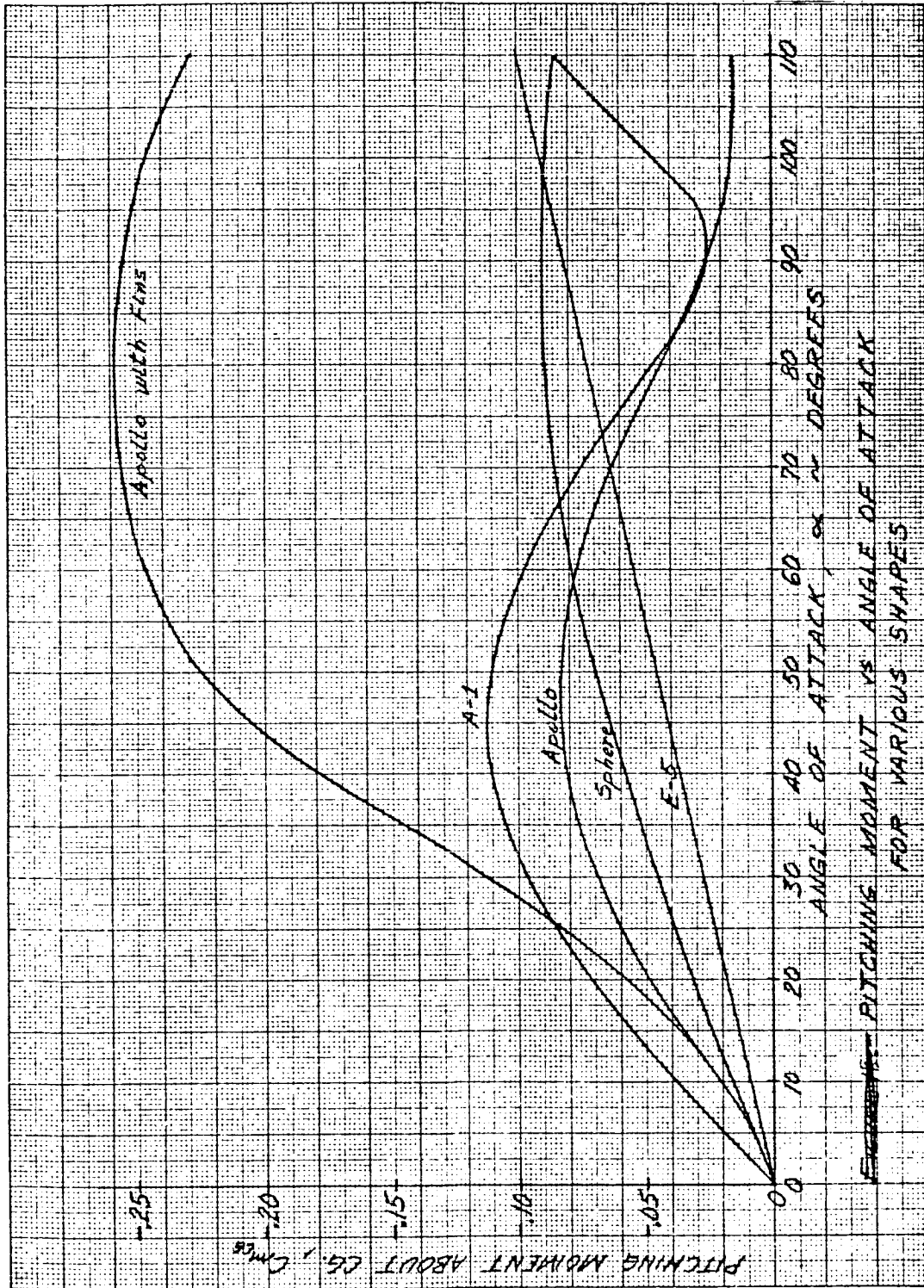


Figure 32 PITCHING MOMENT COEFFICIENT VERSUS ANGLE OF ATTACK FOR VARIOUS SHAPES

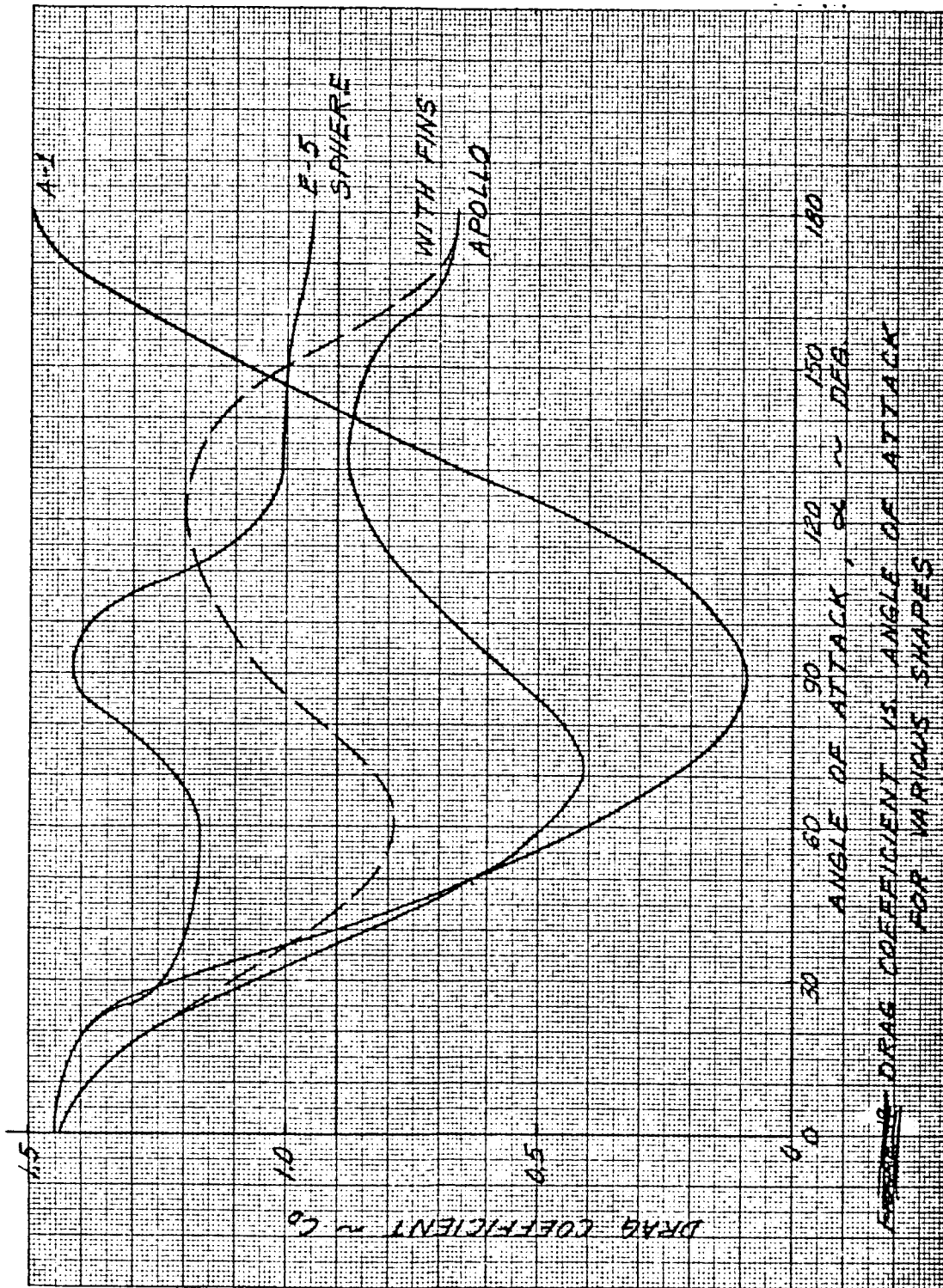
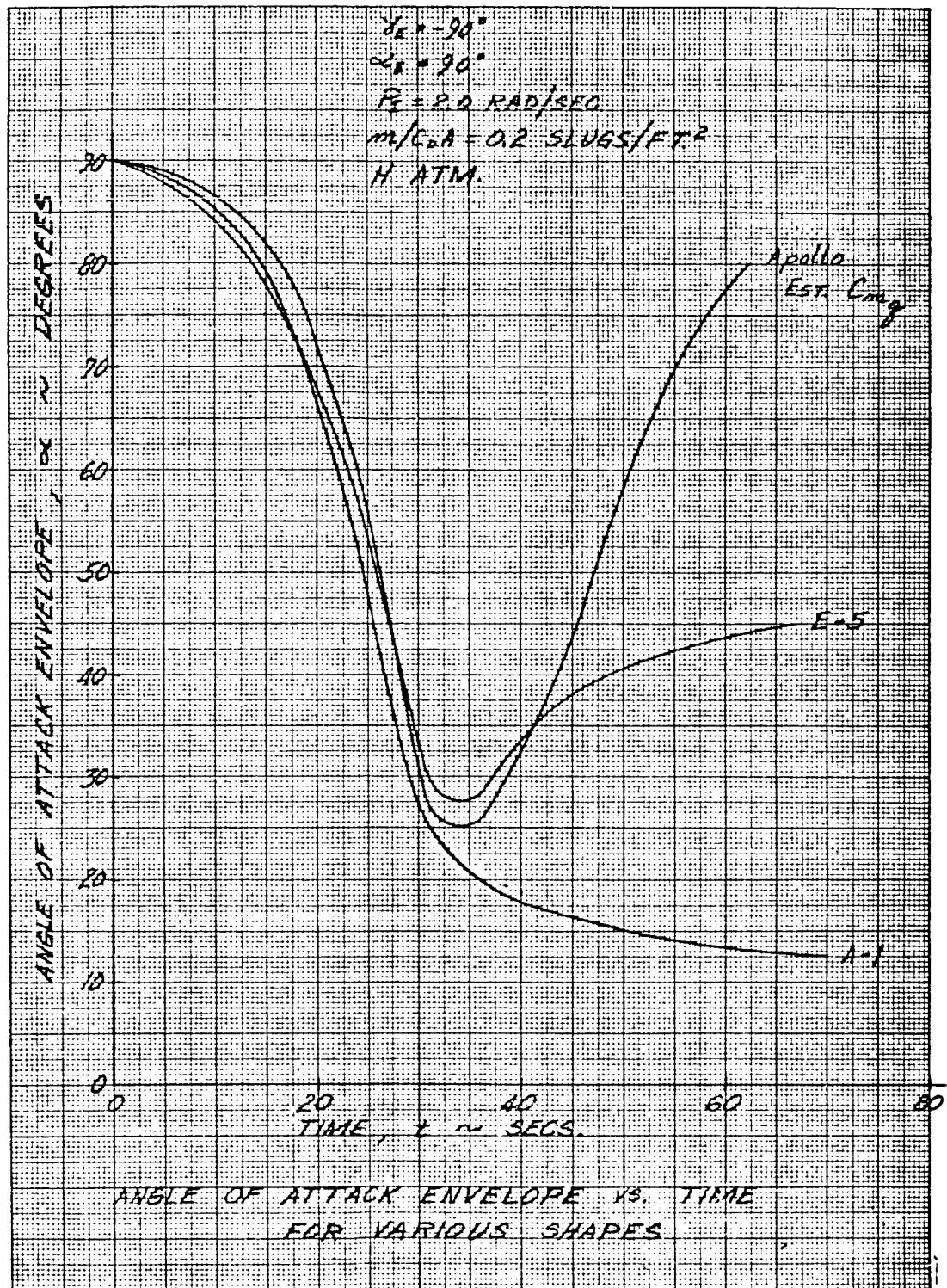


Figure 33 DRAG COEFFICIENT VERSUS ANGLE OF ATTACK FOR VARIOUS SHAPES



64-11536

Figure 34 ANGLE OF ATTACK ENVELOPE VERSUS TIME FOR VARIOUS SHAPES

134

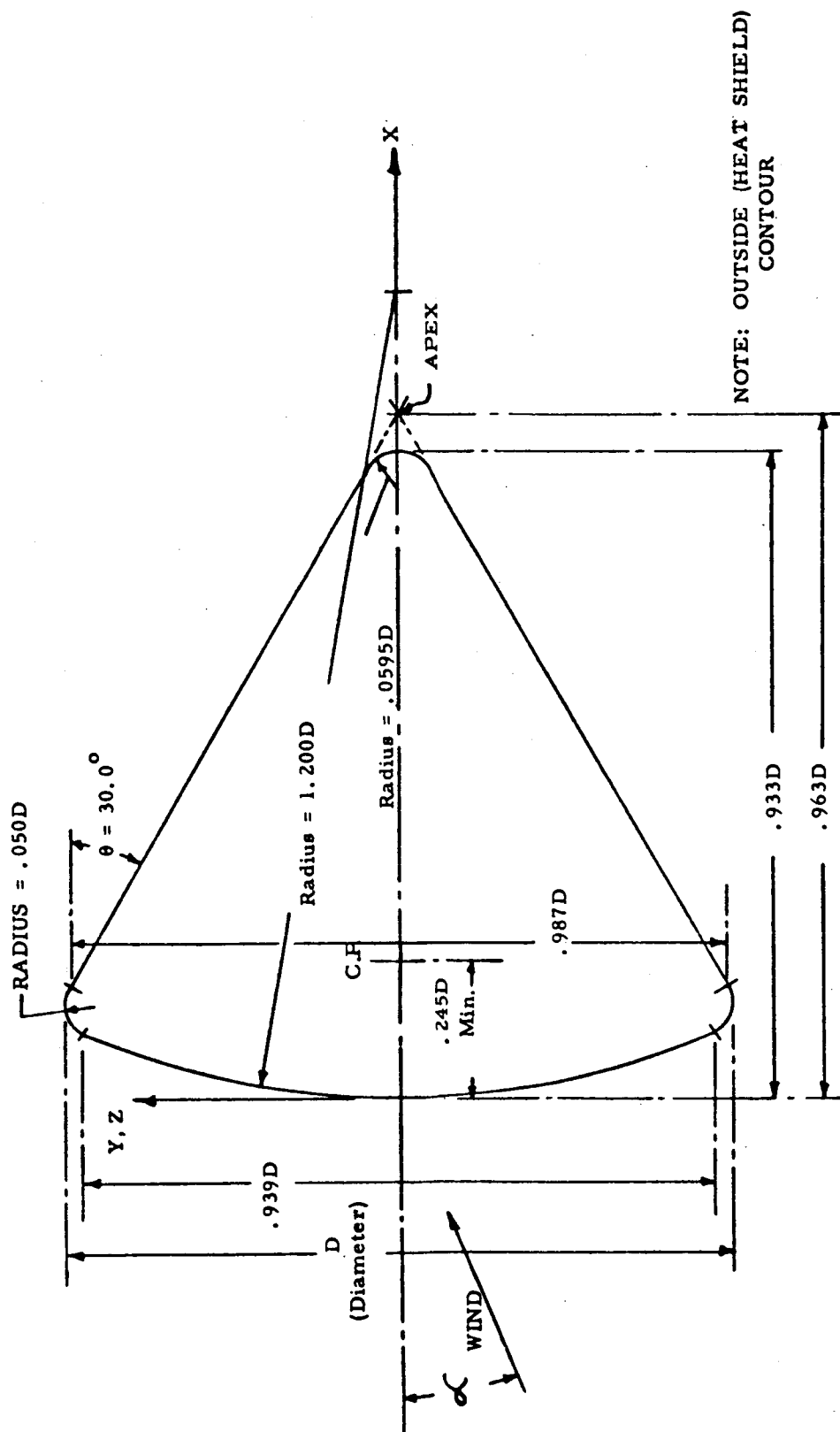


Figure 35 CONCEPTUAL DESIGN CONFIGURATION

64-11537

135

TABLE 27
CONCEPTUAL DESIGN SUMMARY TABLE
(Four-degree-of-freedom Results)

Variable	Peak Heating				Integ. Heating			Peak g		M = 2.5			NOTE
	σ_F deg	q_c Btu/ ft ² sec	q_R Btu/ ft ² sec	\dot{w} lbs/ ft ²	Q_c Btu/ ft ²	Q_R Btu/ ft ²	Q_{tot} Btu/ ft ²	σ_F deg	X/W g	σ_F deg	h ft	t sec	
*Reference trajectory	24	60	148	1.9	770	935	1705	19	50	14	80K	44	See nominal conditions listed below.
m/CDA = 0.20 0.30	24	54	118	1.7	685	750	1435	19	50	14	92K	44	
	24	67	181	2.1	844	1120	1964	18	50	14	70K	45	
	24	61	143	1.9	795	905	1700	19	50	14	80K	44	
D = 84" 96" 100"	24	59	153	1.8	746	966	1702	19	50	14	80K	44	
	25	58	157	1.8	729	986	1715	19	50	14	80K	44	
	30	101	39	4.2	530	76	606	25	112	19	15K	44	
Atm = G H H (6°F) J	26	73	19	2.9	674	68	742	20	70	15	16K	45	
	26	--	--	--	--	--	--	19	74	16	16K	45	
	28	80	288	3.2	552	975	1527	21	90	16	55K	42	
	21	29	44	0.9	1470	1081	2551	17	12	13	155K	151	
$\gamma = -20^\circ$ -52°	23	53	112	1.6	870	934	1804	18	38	14	94K	56	
	0	55	126	1.4	726	817	1543	0	49	0	83K	44	(Particle Traj.)

*Conceptual Design (D = 90 inches, Xcg/D = 0.20, $\dot{X} = 41.8$, $\dot{Y} = 36.4$, $\dot{Z} = 26.9$)

m/CDA = 0.25 $\alpha_c = 179$ degrees
 $V_c = 21,500$ P = 0
 $\gamma_c = -90$ degrees K atm.

Nominal conditions

REFERENCES

1. Mosely, W.C., Jr., and R.H. Moor, Jr., Unpublished Data on Apollo Command Module (September 1962).
2. Kilgore, A., and R.L. Barton, Aerodynamic Damping and Oscillatory Stability in Pitch of Two High-Drag Bodies of Revolution of Transonic Speeds, NASA-TM-X-906.
3. Kilgore, R.A., and B.T. Averett, Wind-Tunnel Measurements of Some Dynamic Stability Characteristics of 0.055 Scale Models of Proposed Apollo Command Module and Launch-Escape Configurations at Mach Numbers from 2.40 to 4.65, NASA-TM-X-769.
4. Averett, B.T., and R.A. Kilgore, Dynamic-Stability Characteristics of Models of Proposed Apollo Configurations at Mach numbers from 0.30 to 1.20 NASA-TM-X-914.
5. Wiley, Kilgore, and Hilje, Dynamic Directional Stability Characteristics for a Group of Blunt Reentry Bodies at Transonic Speeds, NASA-TM-X-337.
6. Suddath, J. H., A theoretical Study of the Angular Motions of Spinning Bodies in Space, NASA-TR-R-83.

5.0 AERODYNAMIC HEATING

The objective of this portion of the parametric study was to determine the critical or design conditions from the range of possible atmospheres and entry conditions and to obtain a correlation between the vehicle parameters and required heat shield weight. This information, combined with the results of the performance study, will lead to the choice of a conceptual design and influence the selection of some of the entry conditions.

The heating studies were performed with a digital computer program. This program, which was described fully in reference 2 (section 6.0), computes the laminar stagnation point convective heating using the formula

$$q_s = K \sqrt{\rho_\infty} \left(\frac{V_\infty}{10^4} \right)^b$$

in which

$$K = \frac{(1.1 + 0.075M) 10^4}{\sqrt{R}} \sqrt{\frac{R}{V_\infty} \left(\frac{du}{ds} \right)_s}$$

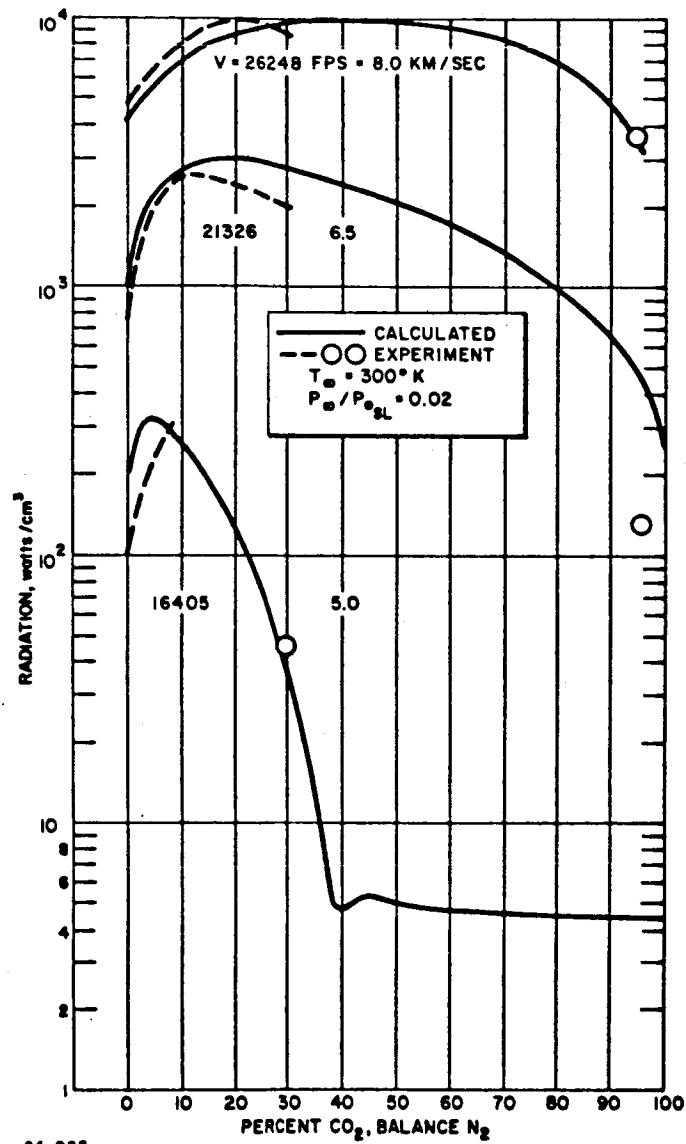
and

$$b = 3.909 - 0.0229M$$

where M is the molecular weight determined from the atmospheric composition, R is the vehicle radius, and $\frac{R}{V_\infty} \left(\frac{du}{ds} \right)_s$ is the non dimensional velocity gradient at the stagnation point. Table 28 presents values of M , $K\sqrt{R}$, and b for each of the atmospheres considered.

An equilibrium radiative heat pulse was computed by evaluating the state of the gas at the stagnation point and computing its emissivity. A radiative heat pulse including the estimated effects of nonequilibrium was also computed. The stagnation point heating was computed along the actual flight path, which accounted for angle of attack effects. A comparison of radiation computed in this program with experimental results is shown in figure 36 which is reproduced from reference 2 (section 6.0). The change in location of the stagnation point with angle of attack was accounted for in the heating distributions, which provide the heating at all points on the body as a ratio to the value at the center line at zero angle of attack.

The results of the parametric studies are summarized in tables 25 and 27, section 4.1, and figures illustrating the effects of varying the parameters are discussed below.



64-228

Figure 36 COMPARISON OF RADIATION PREDICTIONS WITH EXPERIMENT

5.1 PRESSURE DISTRIBUTION

Presented in figure 37 is the pressure distribution for the Apollo shape as a function of angle of attack. The forebody pressures are based on Newtonian predictions, and the afterbody pressures are from test data. These pressures are used to compute the loading for structures, and the heating distribution.

5.2 HEATING DISTRIBUTION

The laminar convective heating distributions for the Apollo shape are plotted in figure 38. At zero angle of attack the distribution was computed by the method described in reference 2 (section 6.0). Wind tunnel data were available for the distributions at angles of attack up to 50 degrees.

The radiative heating distributions for each of the atmospheres considered are presented in figure 39. These are based on a shock envelope at zero angle of attack assumed to be concentric with the spherical face of the vehicle and a theoretical variation of intensity with wave angle plotted for each atmosphere in figure 40. The greatest amount of radiative heating across the face of the vehicle is experienced in the J atmosphere. The zero angle of attack values were applied conservatively to the entire spherical face at angles of attack up to approximately 23 degrees, which is close to the maximum encountered at peak heating.

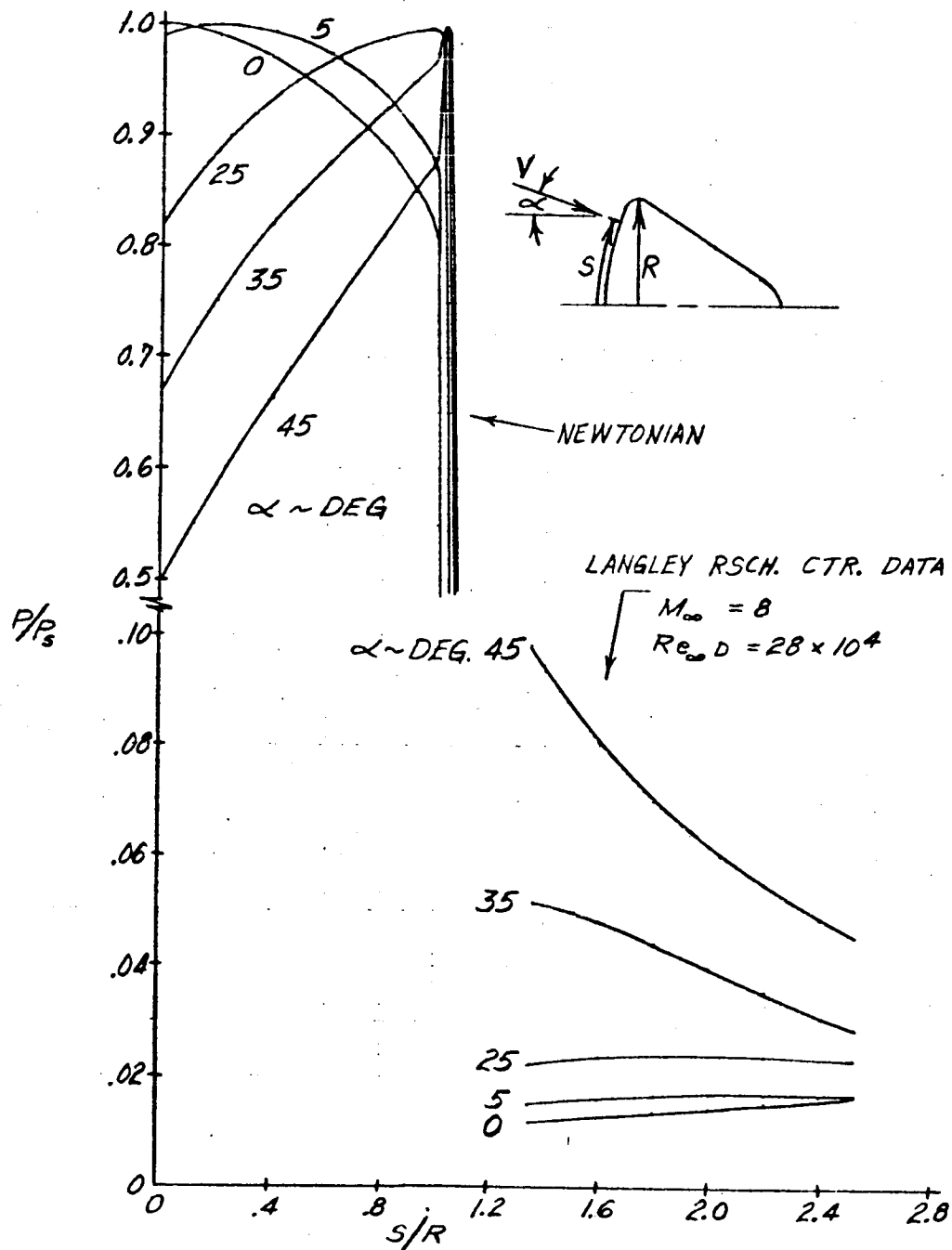
The approximate shock envelopes about the Apollo shape at angles of attack of zero and 27.5 degrees are shown in figure 41. The envelope at zero angle of attack is conservatively estimated to be a spherical surface concentric with the spherical face of the vehicle and the shock at angle of attack was estimated from data provided in reference 2. These shock shapes were used to estimate the radiative heating contributions to the torus and afterbody at angle of attack.

5.3 EFFECT OF ENTRY CONDITIONS

The effects of both entry velocity and flight path angle on stagnation point heating are shown in figures 42, 43, and 44. These results are based on particle trajectories in the K atmosphere, which was found to be the worst atmosphere from the point of view of total heating.

Peak rates of both convective and radiative (nonequilibrium) heating increase with higher entry velocities and steeper entry angles. Integrated heating also increases with increasing velocity, but the trend with entry angle is reversed due to the longer heat pulse at the smaller entry angles.

The effect of dynamics on heating is shown in figure 45 which compares the radiative and convective heat pulses obtained with a particle ($\alpha = 90$ degrees) trajectory with those obtained with an entry angle of attack of 179 degrees. It can be seen that as a result of the oscillations, the peak rates increase about 15 percent, while the total heating increases by only 9 percent.



, PRESSURE DISTRIBUTION FOR APOLLO SHAPE

Figure 37 PRESSURE DISTRIBUTION FOR APOLLO SHAPE

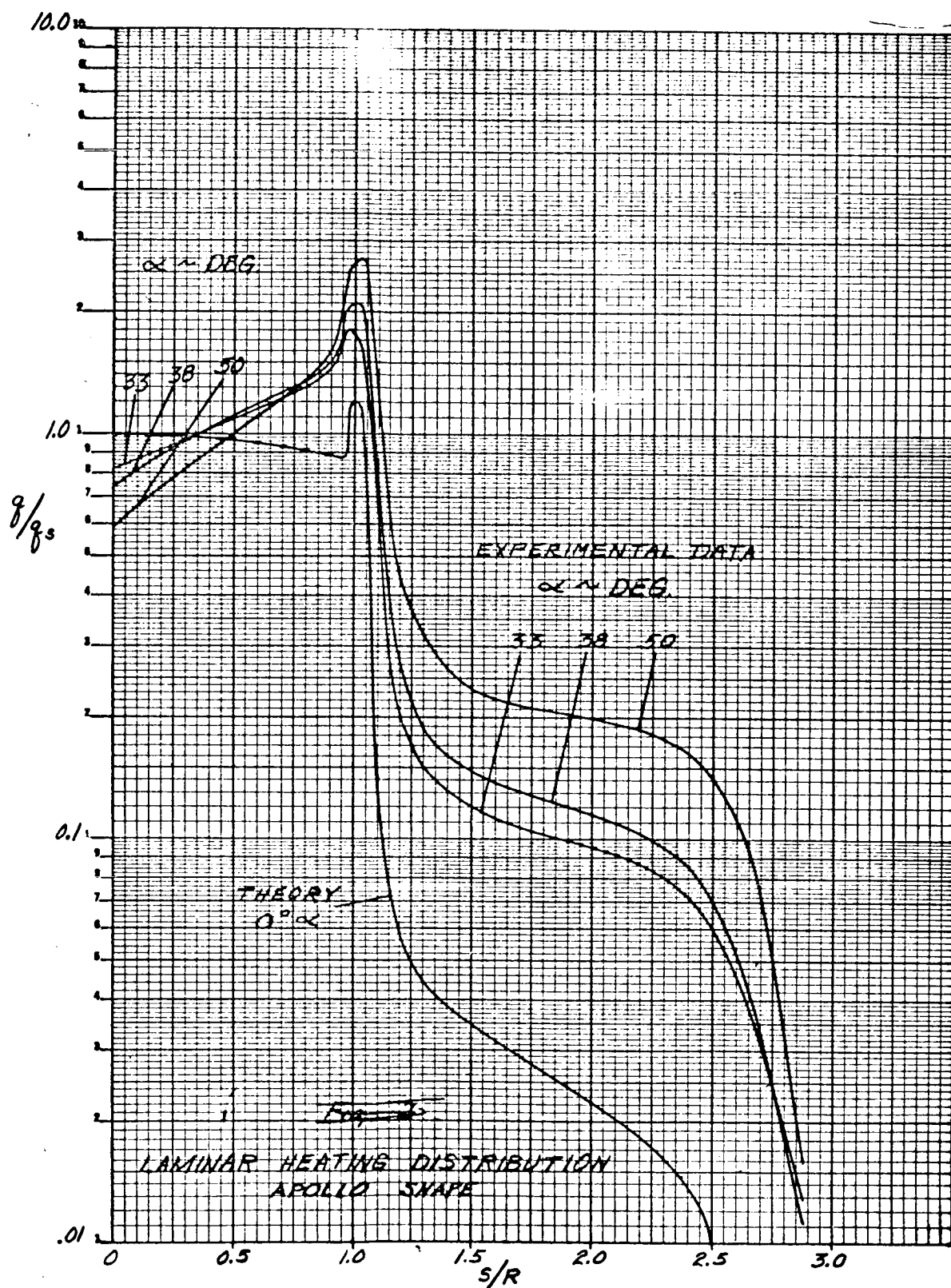
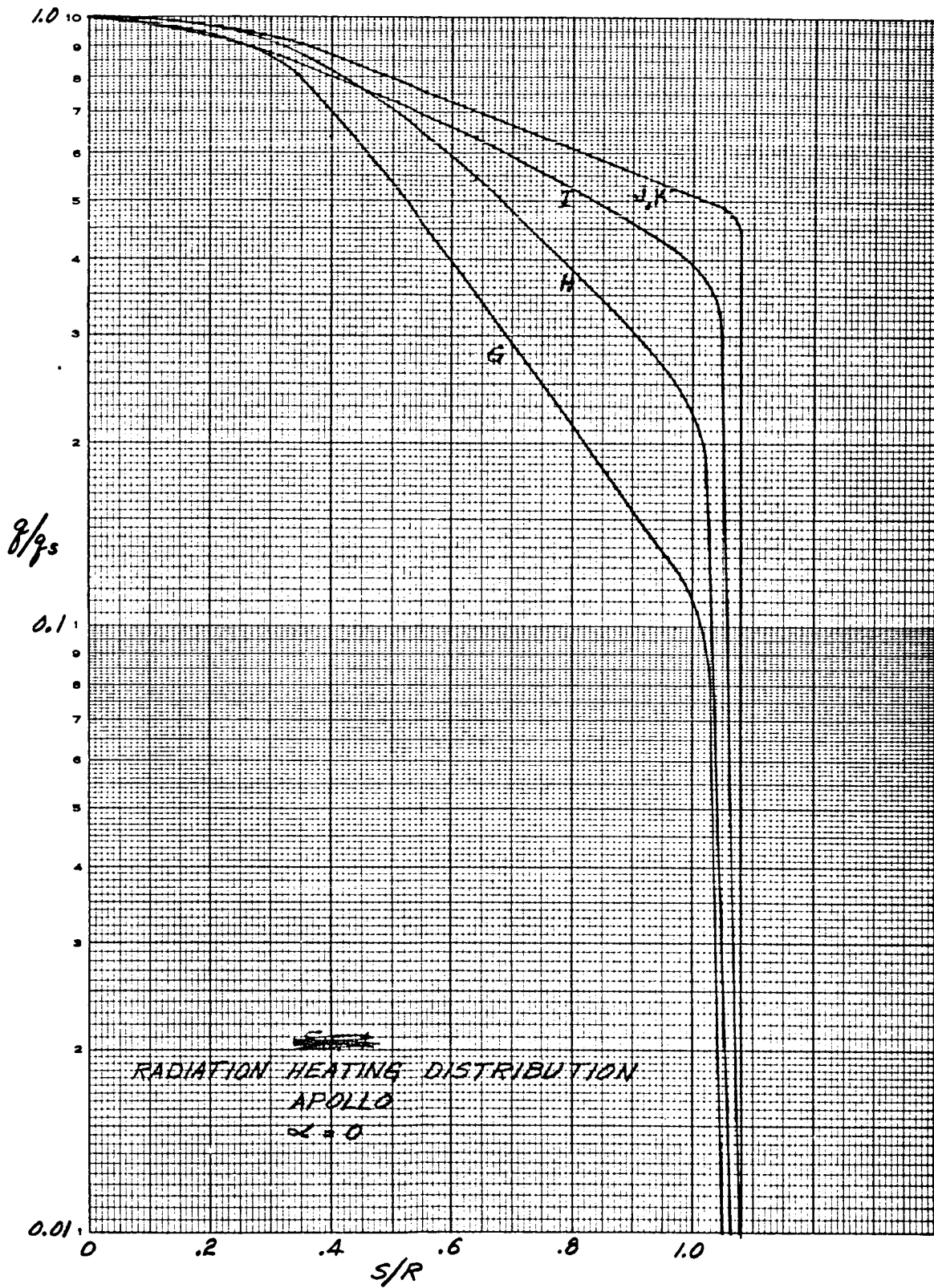


Figure 38 LAMINAR HEATING DISTRIBUTION FOR APOLLO SHAPE

64-115-39

142



64-11540

Figure 39 RADIATION HEATING DISTRIBUTION FOR APOLLO SHAPE

143

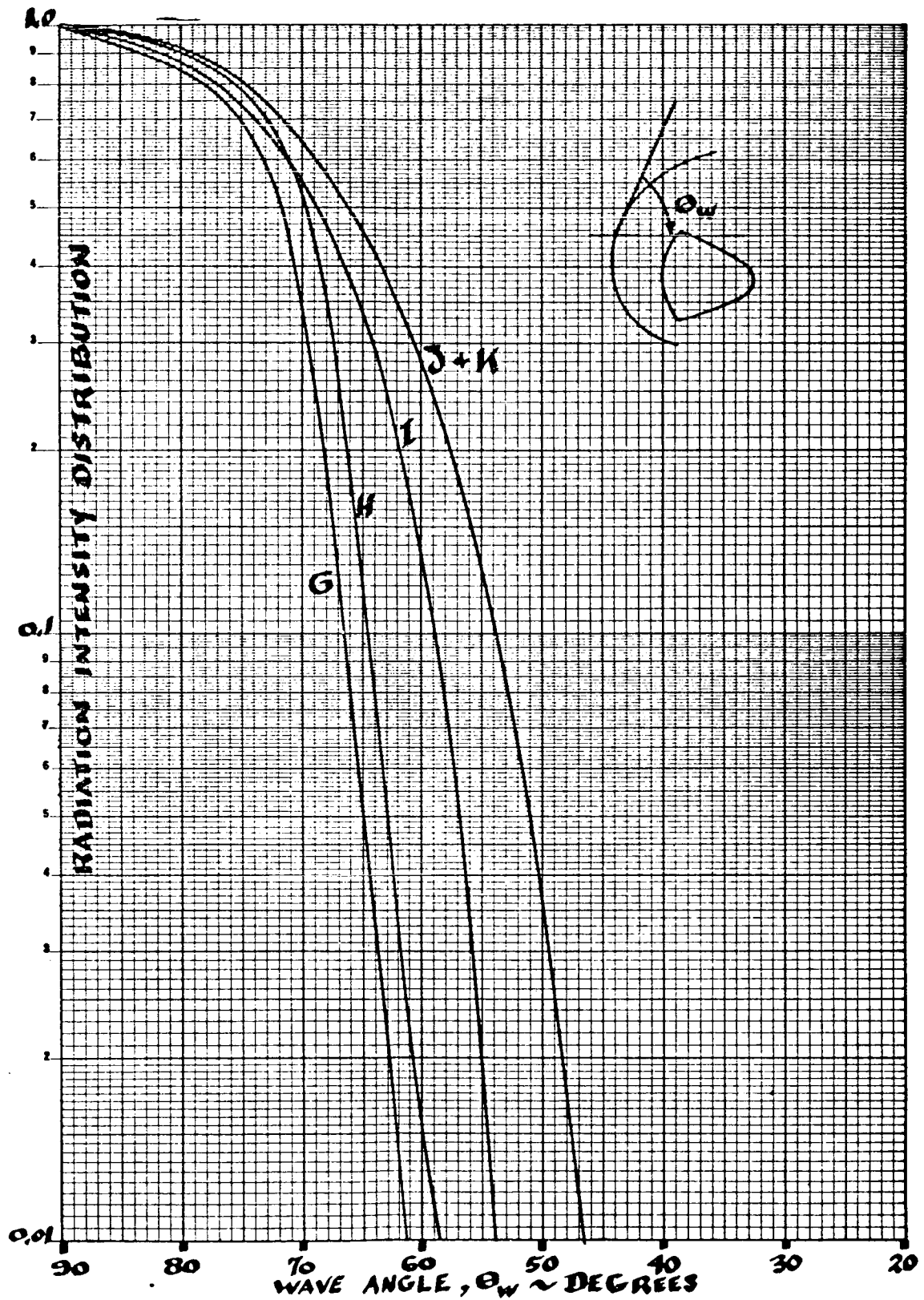


Figure 40 VARIATION OF RADIATION INTENSITY WITH SHOCK WAVE ANGLE

64-11541

144

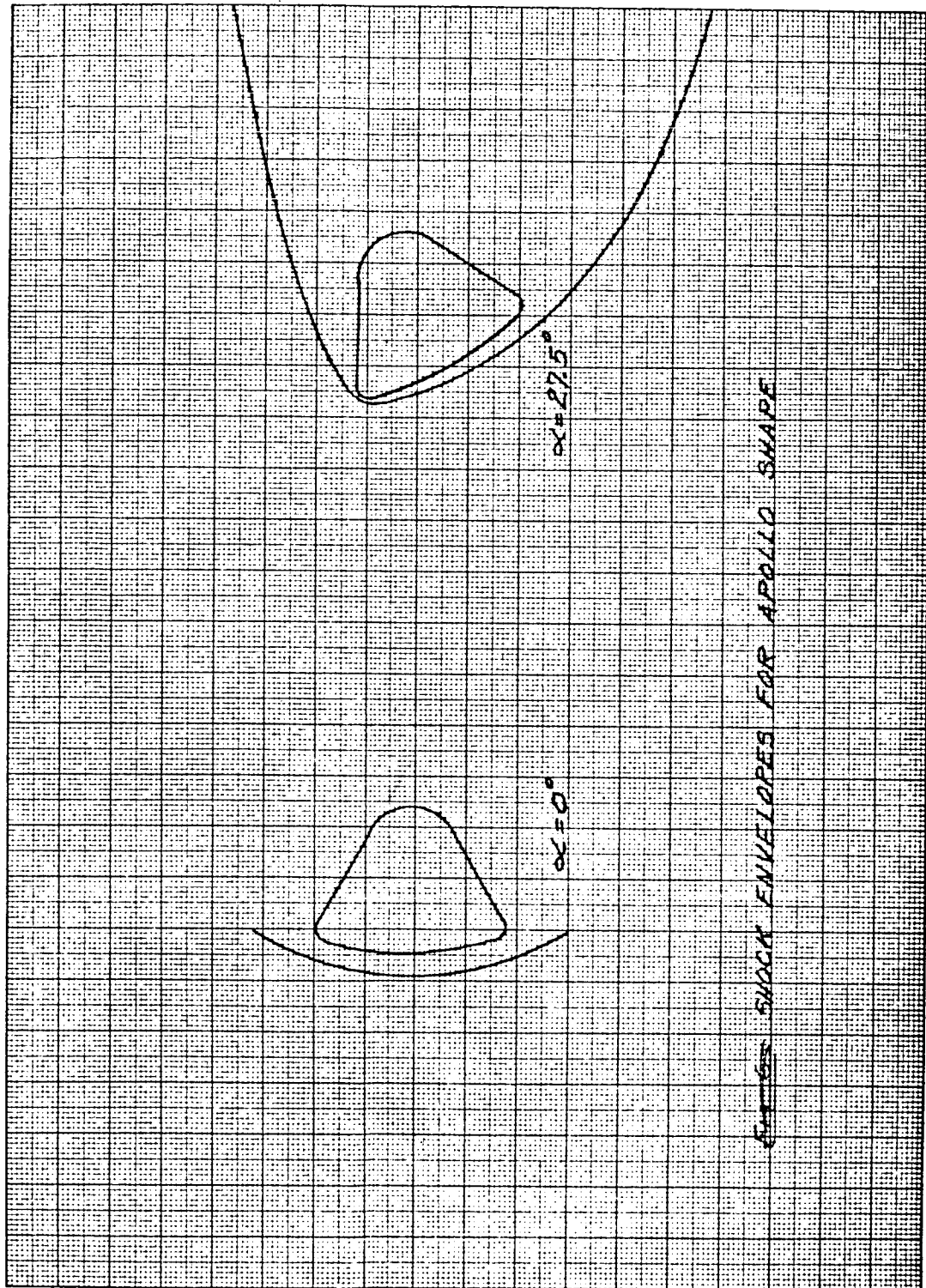


Figure 41 SHOCK ENVELOPES FOR APOLLO SHAPE

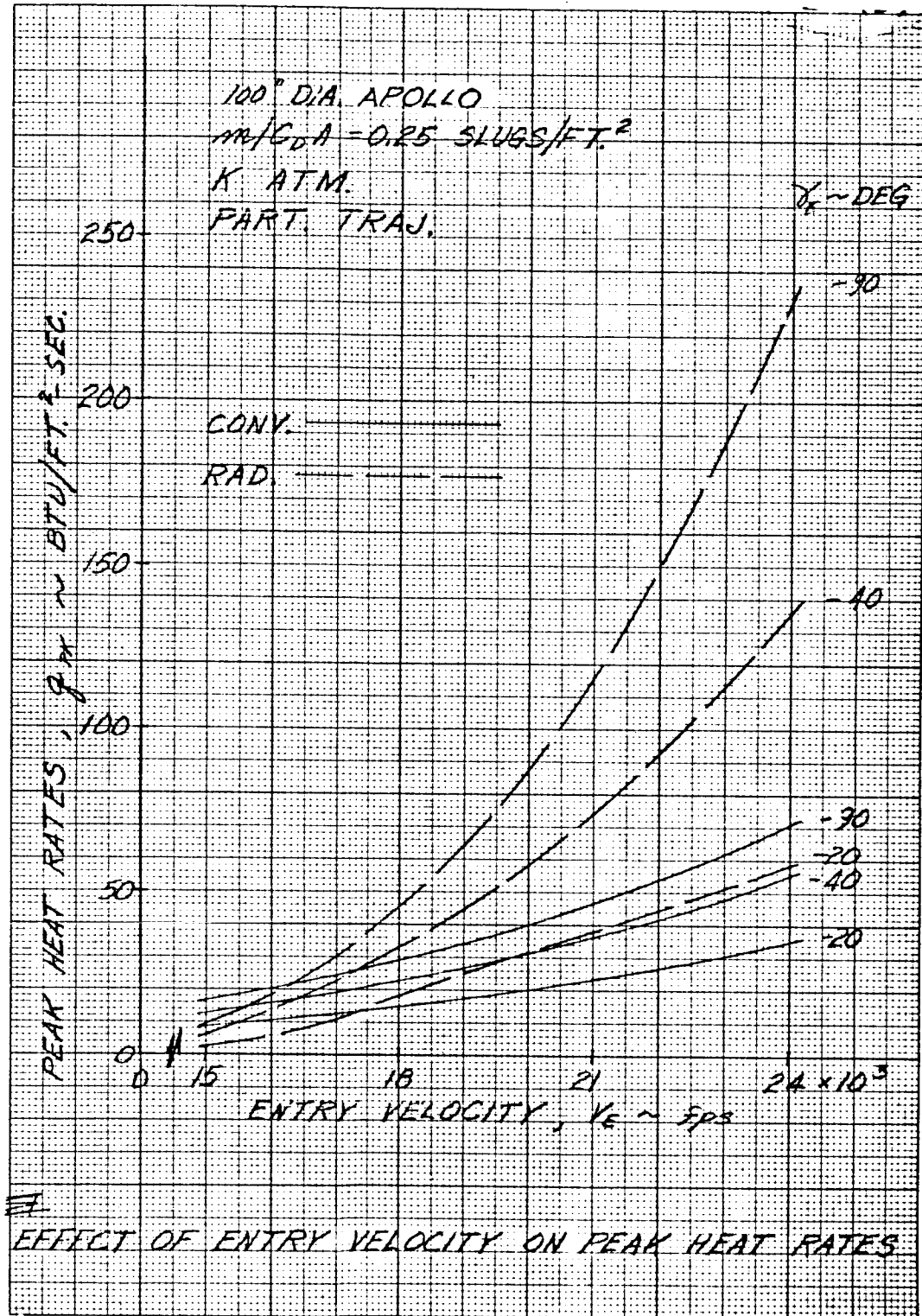


Figure 42 EFFECT OF ENTRY VELOCITY ON PEAK HEAT RATES

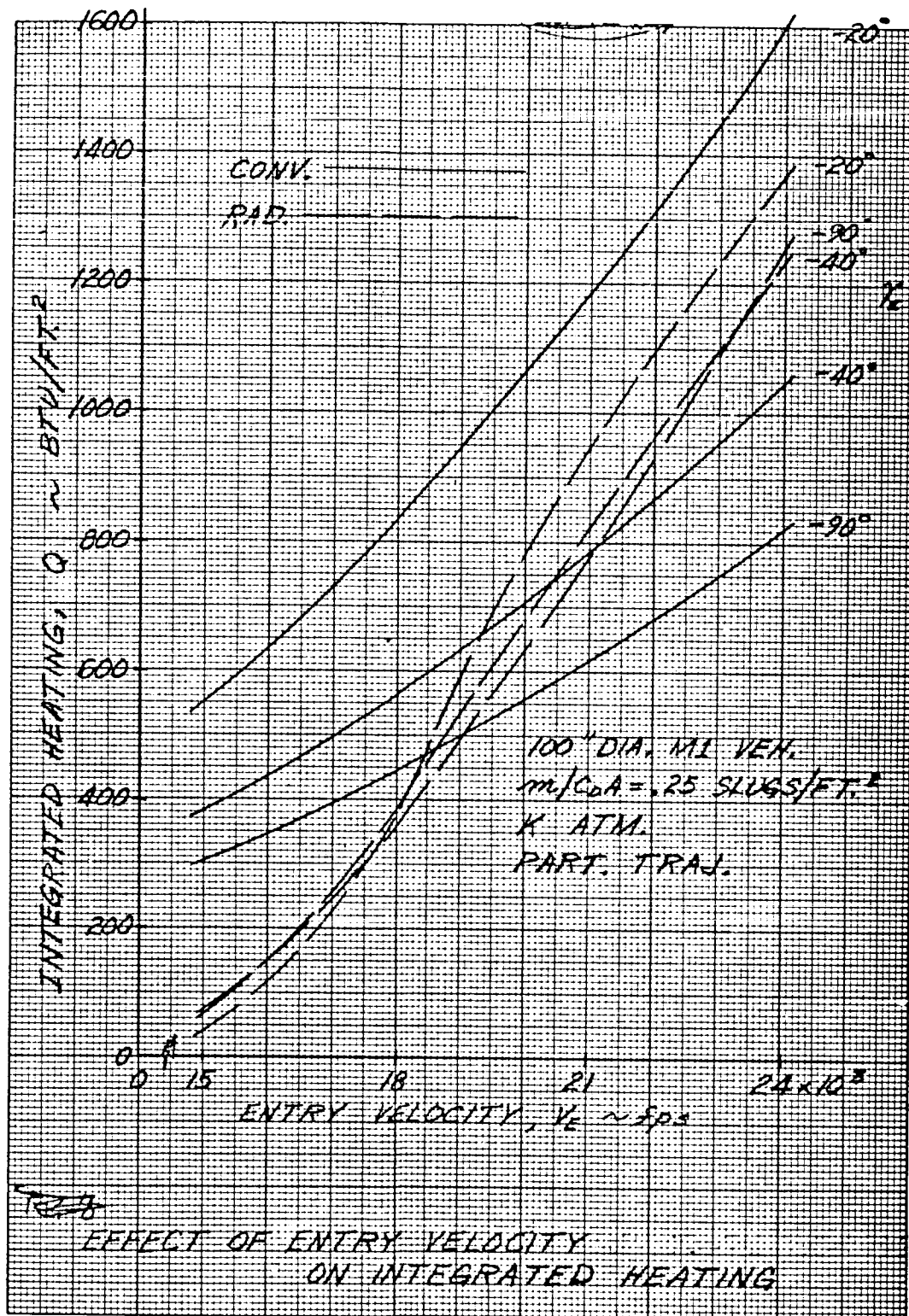


Figure 43 EFFECT OF ENTRY VELOCITY ON INTEGRATED HEATING

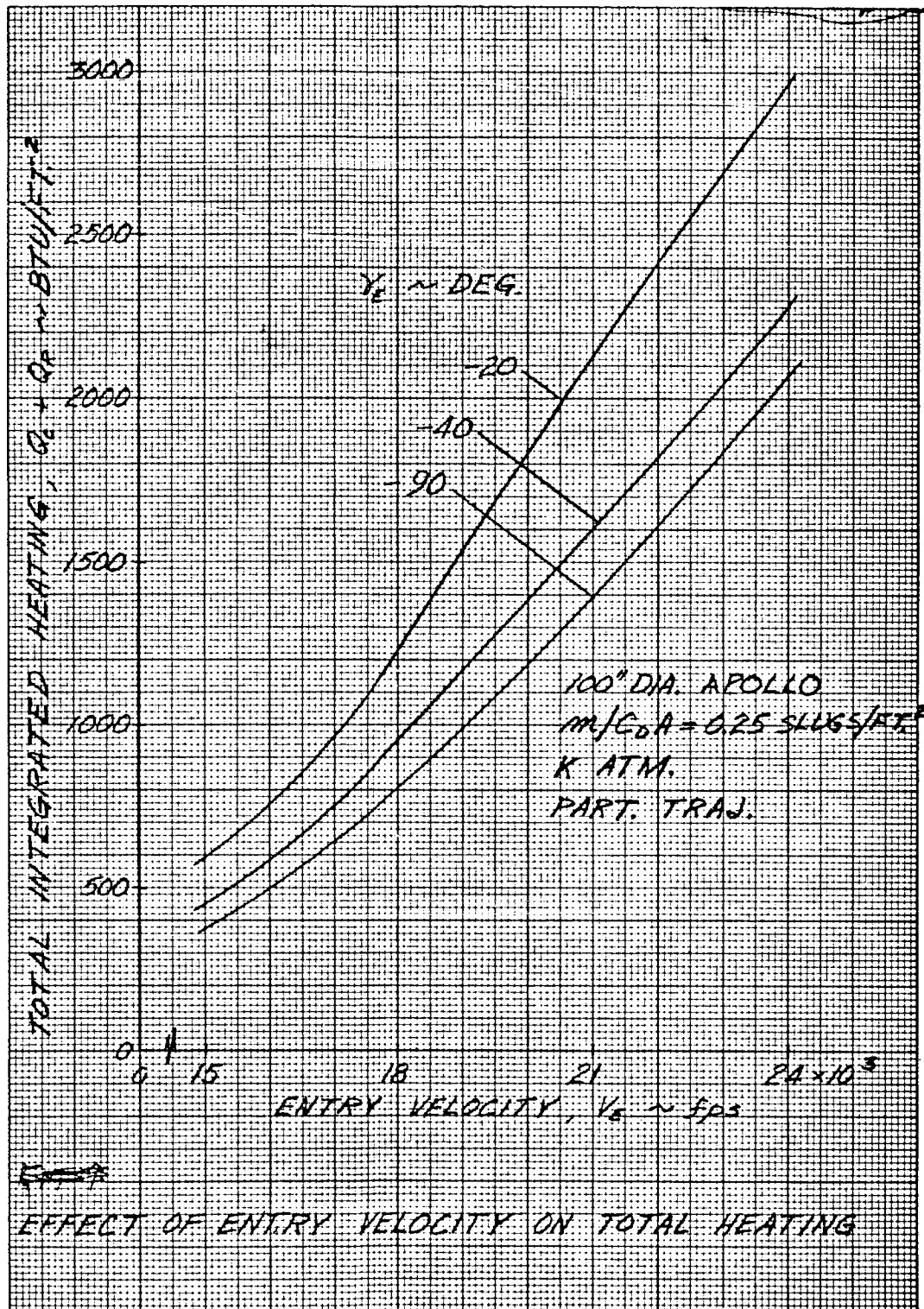


Figure 44 EFFECT OF ENTRY VELOCITY ON TOTAL HEATING

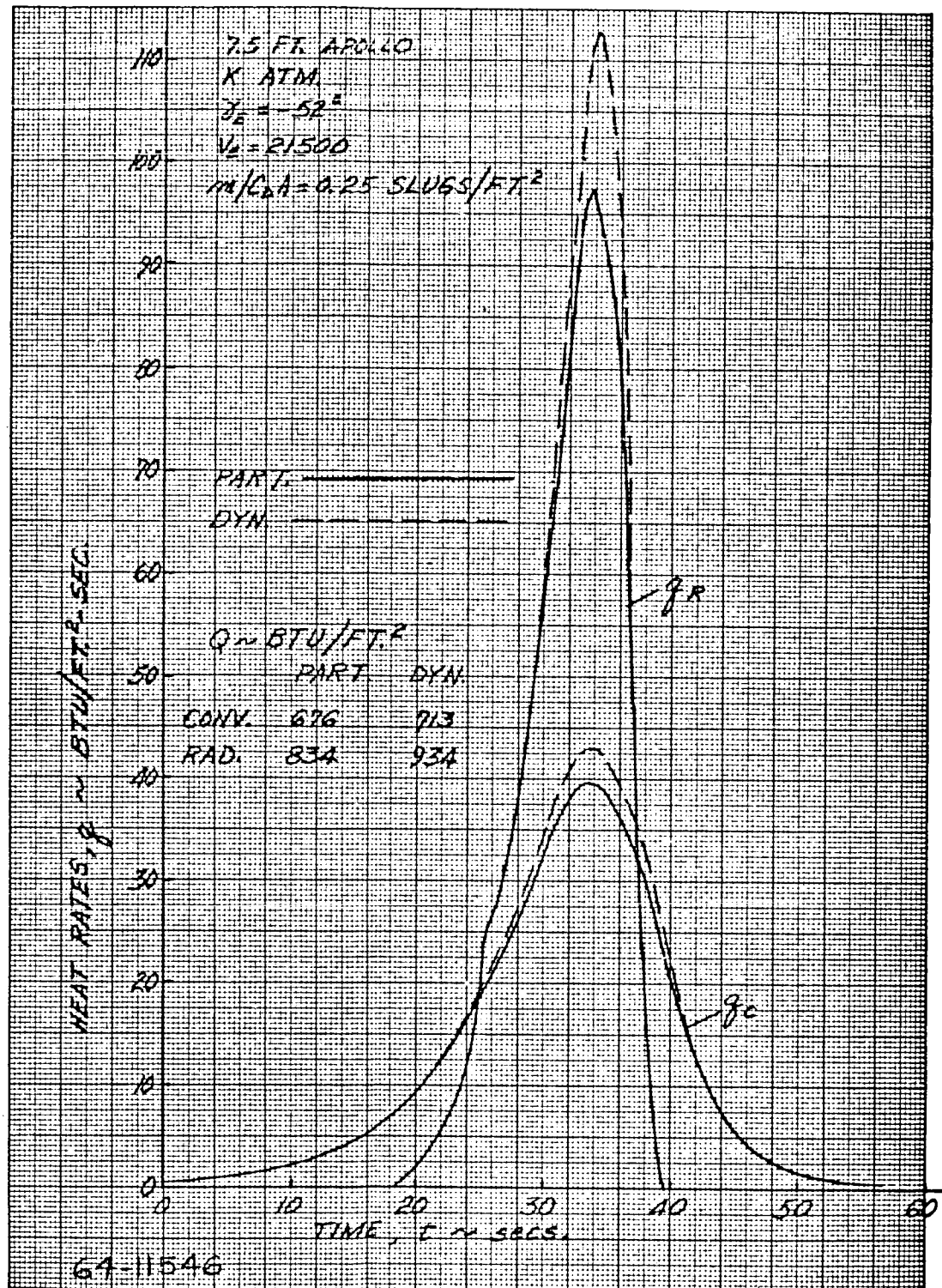


Figure 45 EFFECT OF VEHICLE DYNAMICS ON STAGNATION POINT HEATING

The effect of flight path angle on the convective and radiative heat pulses is shown in figure 46. It can be seen that although the rates are lower for a 52-degree entry angle, the pulses are longer than for the 90-degree entry, resulting in no change in integrated radiative heating but an increase in convective heating for the shallower entry case.

5.4 EFFECT OF VEHICLE PARAMETERS

The effect of increasing the ballistic coefficient, $m/C_D A$, is to increase both radiative and convective heating. Figure 47 shows that total heating varies approximately linearly with $m/C_D A$.

The effect of damping coefficient, C_{mq} , on heating can be seen to be slight on table 25 (section 4.0). This was to be expected because of the small effect observed on the envelope of oscillations during the period of maximum heating.

The effect on heating of varying diameter was also studied and table 27, section 4.0, shows that increasing the diameter results in a decrease in convective heating and an increase in radiative heating. The net effect is a negligible change in total heating.

5.5 EFFECT OF ATMOSPHERE

The effects of varying the atmospheric model on heating are shown on table 25, section 4.0. The highest convective heating rate (associated with low scale height) occurs in the G atmosphere, while the highest radiative heating rate occurs in the J atmosphere. However, the K atmosphere results in the greatest integrated heating due to combined convection and radiation. Figure 48 shows the variation of heat pulse shape with atmospheric model for three atmospheres.

Referring back to the discussion of radiative heating distribution, it was found that the highest level of radiation over the face of the vehicle occurred in the J atmosphere.

5.6 CONCEPTUAL DESIGN SUMMARY

The conceptual design which evolved from the parametric studies differs from the reference design in that it has a 30-degree conical afterbody, the $m/C_D A$ increases to 0.25, the diameter decreases to 7.5 feet, the center of gravity moves aft to 0.21 D, and the moments of inertia are reduced to about half the predicted values (see section 3.4).

Table 27 section 4.0, summarizes the results of the additional parametric study conducted for the conceptual design to investigate the effects of further changes which might be made in the final design and to determine the severest heating conditions which might be encountered within the known limits of entry conditions. Note that the nominal entry angle of attack for this study was 179 degrees with no spin.

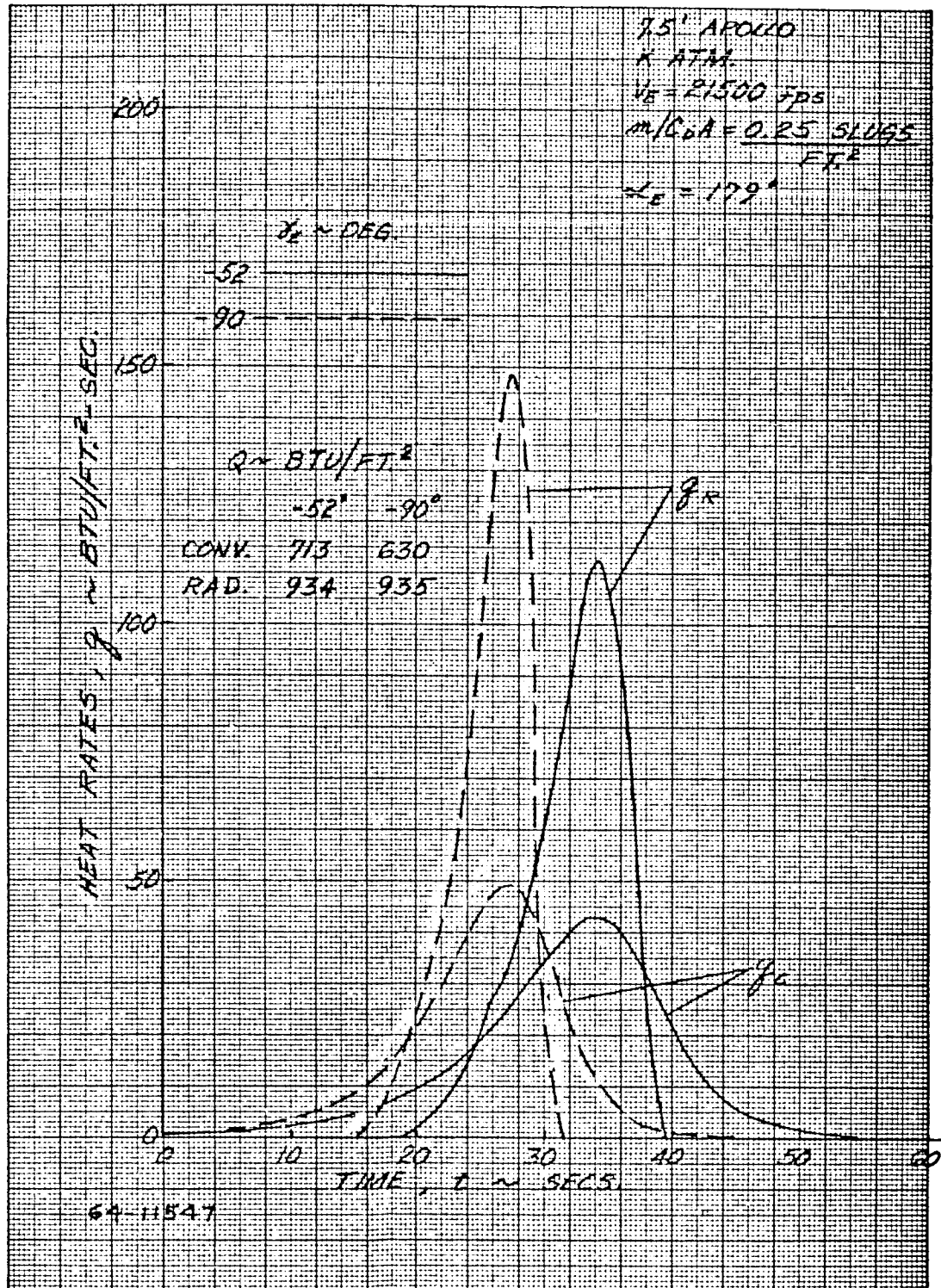


Figure 46 HEAT PULSES FOR K ATMOSPHERE

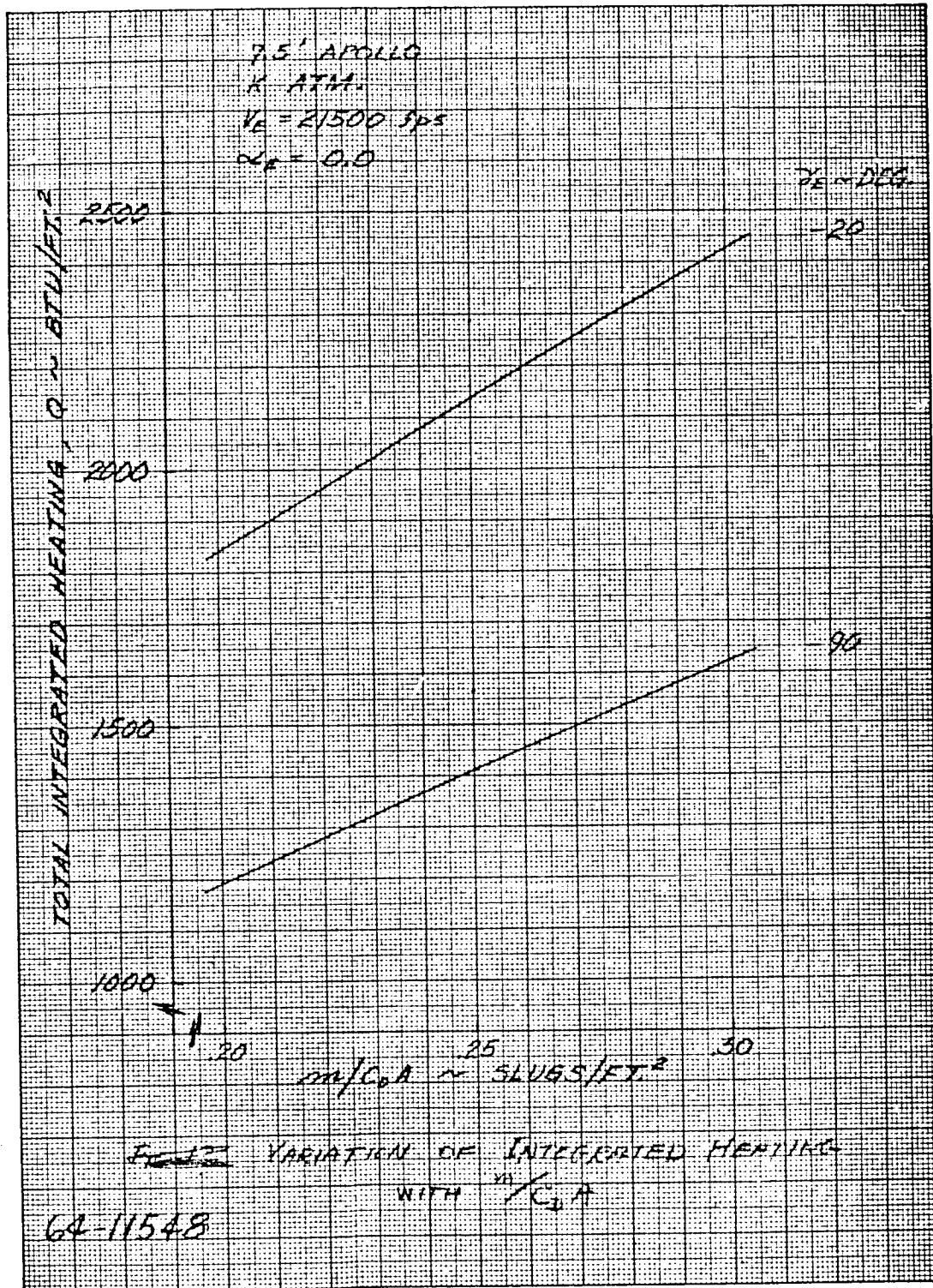


Figure 47 VARIATION OF INTEGRATED HEATING WITH $m/C_D A$

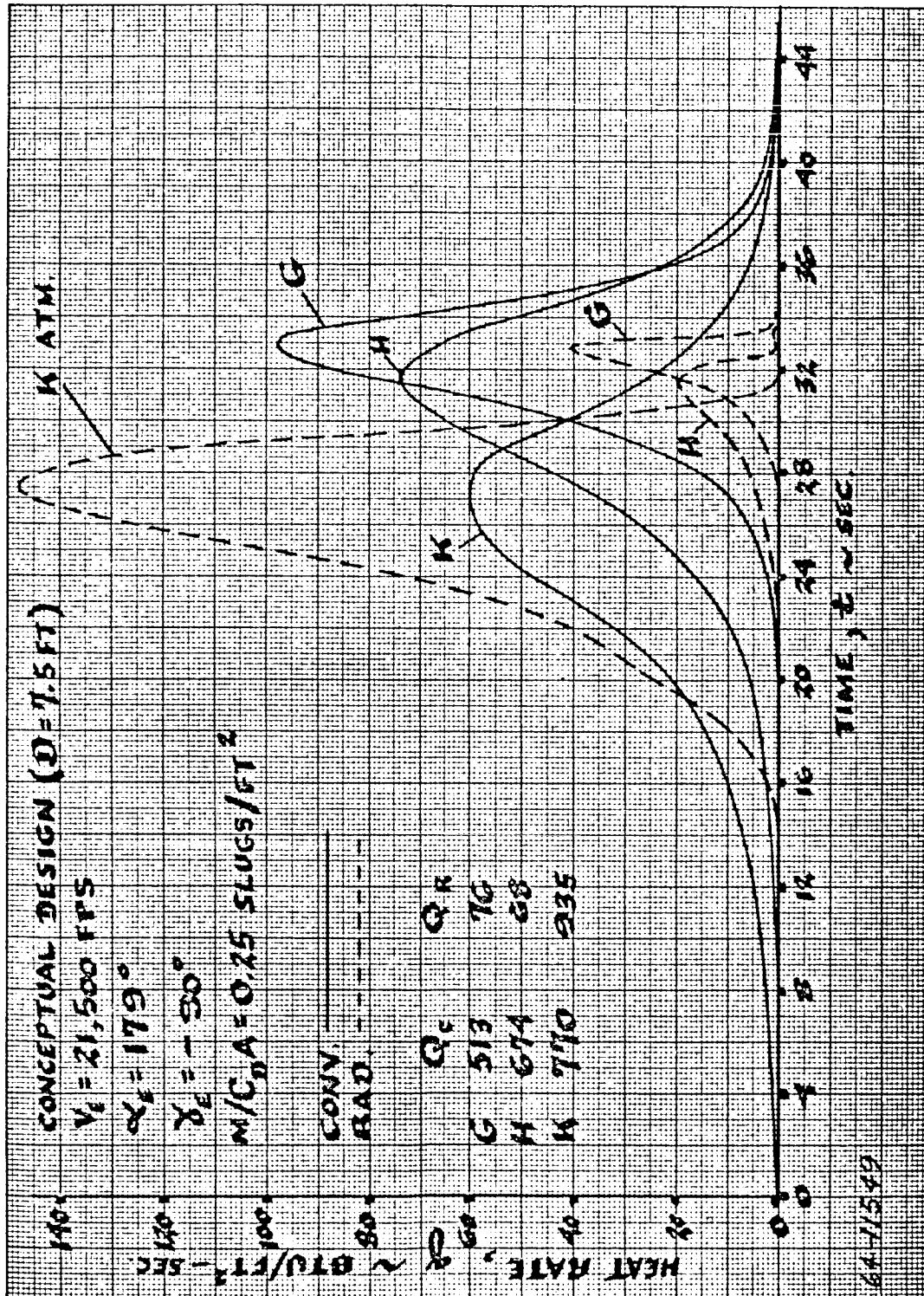


Figure 48 EFFECT OF ATMOSPHERE ON HEAT PULSES

The most critical entry conditions for design of the heat shield are a flight path angle of -52 degrees in the K atmosphere, which results in a total heating of 1804 Btu/ft². The entry angle of -52 degrees represents the dispersion limit associated with the proposed separation conditions. The velocity can be held very close to 21,500 ft/sec.

The maximum convective heating rate of 101 Btu/ft²-sec is reached in the G atmosphere, and a maximum radiative heating rate of 288 Btu/ft²-sec is obtained in the J atmosphere, both occurring at the steepest entry flight path angle of 90 degrees.

TABLE 28
CONVECTIVE HEATING PROGRAM INPUTS

Atmosphere	M	K \sqrt{R}	b
G	42.6	14861	2.933
H	42.6	14861	2.933
I	38.8	13876	3.020
J	31.3	11928	3.192
K	31.3	11928	3.192

1. Jones, R., Preliminary Langley Research Center Data on the Apollo Configuration.
2. Walters, E.E., Free Flight Measurements of Radiative Heating to the Front Face of the Apollo Reentry Capsule as a Function of Angle of Attack, NASA TM X-851, 1964.

154

6.0 HEAT SHIELD SYSTEM

The heat shield system is defined as the thermal protection system of the lander during entry and will consist of an ablator with a substructure. In some cases, however, a radiating (heat sink) design will be employed (e.g., for the afterbody). The heat shield system study is broken down into a parametric evaluation and a conceptual design verification. In the parametric evaluation, pertinent parameters were varied over the most likely combinations of entry conditions, materials, and shapes. The heat shield and substructure are plotted as weight fractions of the entry weight in terms of these pertinent parameters.

Design analyses were conducted for the conceptual system considering a more rigorous analytical approach than was used in the parametric study. These analyses were then compared to the parametric analysis to determine the degree of accuracy. In cases where the conceptual design analyses indicated non-conservative results, the parametric analyses were reworked.

The primary constraints imposed on the heat shield system study were the atmospheric models, vehicle shape, and sterilization requirement. The Mars atmospheric models are defined in reference 1 and presented in section 4.0. The atmospheric models consist of five separate sets varying from a surface pressure of 11 mb to 30 mb (defined as G through K in reference 1). Previous in-house and contracted studies (Reference 2) on planetary entry employing these atmospheric models indicated that the G-model is the most severe from the loading standpoint and hence, was the only atmospheric model used in the substructure analysis. The K model atmosphere proved to be the most severe from the heating (total integrated convective and radiative heating) standpoint, therefore only this model was employed in the heat shield (ablator and heat sink) studies.

It was established early in the study that a blunt aerodynamic shape was required to adequately aerodynamically brake the lander for parachute deployment. More particularly, a low $m/C_D A$ vehicle would be required. Hence, the Apollo configuration was chosen as the lander shape because of the extensive development in terms of aerodynamic testing which has been accomplished for this shape. Several variations in the shape were considered to evaluate fully the designed and performance requirements. These modifications were mainly performed on the afterbody, ranging from small angle changes to large conical extensions.

The third constraint on the heat shield system is the sterilization requirement. As established by NASA, all planetary probes must undergo a dry heat sterilization of 145°C for 36 hours three times. This puts a very severe criterion on the material selection of both the heat shield and the substructure. The materials selected must not only be compatible with this criterion by itself but also must be compatible with other adjacent materials since the composite must be also

capable of surviving the sterilization criteria without detrimental effects. Hence, all materials selected in this study were evaluated for their capability to survive this sterilization criteria.

6.1 MATERIAL SELECTION TRADE-OFFS

In this section, several heat shield systems will be investigated to assess the relative merits of each particular system in terms of weight efficiency to accomplish the desired mission objective. Three types of heat shield systems will be investigated; (1) a high temperature (charring) ablator-aluminum honeycomb substructure, (2) a dielectric design using low temperature ablators and fiberglass honeycomb substructure and (3) a heat sink afterbody design. The first and last design systems will be evaluated for overall weight efficiency, while the second system will be evaluated in terms of weight penalty to obtain a completely transparent design for communication during entry and after impact.

1. Ablator-Aluminum Honeycomb

The ablator considered will be Avco 5026, a high temperature charring ablator under development for the Apollo project. It is formulated from organic resins and silica fiber and contains phenolic microballoons. This material has been developed specifically for the Apollo heat shield, which is subjected to some of the same environmental problems as will be experienced by the Advanced Mariner, and will be quite suitable. Typical thermal properties of this material are shown in table 29.

Preliminary tests of this ablator under the sterilization environment indicated a loss in both mechanical and physical properties. However, further testing resulted in a stabilization method in the curing cycle which led to no reduction in properties. Thus, this particular material will meet the sterilization requirements. Now a substructure must be obtained that will be compatible with the selected heat shield under both the sterilization and entry environments. An aluminum honeycomb structure was selected. This material can easily meet the sterilization criterion and is completely compatible with the selected ablator since the coefficients thermal expansion are approximately equal. However, during entry, the backface temperature must be limited to 600° F, which is also the temperature limit of most state-of-the-art bonding materials. Structural properties of aluminum and other substructure materials are presented in table 30.

Using the design model, heat shield-structure weight curves were generated as a function of the ballistic coefficient $m/C_D A$ for a 90 inch diameter Apollo shape lander. The analysis is based on a computer program described in reference 2. The program employs a 4-degree-of-freedom performance trajectory analysis for heating and pressure loading histories; then it combines a one-dimensional thermal model for heat shield analysis, and a hydrostatic buckling analysis for the substructure in determining the weight components.

TABLE 29

HEAT SHIELD MATERIAL PROPERTIES

	Delrin	5026	Teflon	LT-a	Beryllium
Density (ρ), (lb/ft ³)	89.4	37.00	136.00	66.4	115.00
Specific Heat, (C _p), (Btu/lb)	0.42	0.37	0.20	0.52	0.475
Thermal Conductivity (K), (Btu/ft/hr °F)	0.17	0.068	0.14	0.11	93.00
Ablation Temperature (T _A) (°F)	800.00	4950.00	1340.00	836.00	---
Transpiration Factor (η)	0.36	0.57	0.43	0.57	---
Emissivity (ϵ)	0.15	0.75	0.15	0.70	0.50
Heat Absorbed by Phase Change (H _v) (Btu/lb)	1220.00	85.00	600.00	207.00	85.00

TABLE 30
HEAT SHIELD SUBSTRUCTURE MATERIAL PROPERTIES

	Aluminum (Honeycomb)	Fiberglass (Honeycomb)	Beryllium
Face Sheet Density (ρ_f) (lb/ft ³)	170.0	112.3	115.0
Minimum Core Density (ρ_c) (lb/ft ³)	3.0	3.0	---
Yield Stress (σ_y) (psi)	40,000.0	20,000.0	50,000.0
Temperature Limit (T_R) (°F)	600.0	600.0	1,500.0
Modulus of Elasticity, (E) (psi)	10×10^6	3×10^6	40×10^6
Minimum Gage Thickness (t_t) (in)	0.008	0.020	0.020

Figures 49 and 50 give the results of these analyses for the structure and heat shield weight fractions, respectively. Also, shown on these curves is the comparison of forebody and afterbody. Notice that the structure is designed for an entry angle of -90 degrees while the heat shield is designed for -20 degrees. These entry angle combinations represent the worst conditions for each design for comparison purposes.

2. Dielectric Designs

The purpose for a dielectric design, in particular on the afterbody, was to ease the communications antenna design and to create a fail safe mode in case the antenna is not exposed during descent or after landing. In order to produce a dielectric design, low temperature (noncarbon, charring) ablators must be employed with a dielectric substructure. For this study Teflon, Delrin, and LT_a ablators were selected because of the good dielectric properties and compatibility with other environments. The thermal properties of these materials are shown in table 29. As a substructure design for the ablators a phenolic base laminated honeycomb will be used.

Here again the same computer program was employed as in the previous analyses. The results are depicted in figures 51 and 52 for the structure and heat shield weight fraction respectively. All conditions are exactly the same as stated in the previous analysis for ablator-aluminum honeycomb design. It can easily be seen that the LT_a design is the minimum weight design for the afterbody, but Delrin proved more efficient on the forebody. Figures 53 and 54 show comparisons of total heat shield systems which again which shows the same results.

A cursory evaluation of heat sink designs indicated, for the magnitude of heat occurring (reference section 5.0), that only an afterbody design could be considered in terms of weight efficiency since it would not compare to an ablator design of the forebody. Only beryllium heat sink material was considered in the study because of its high temperature and specific heat capability, coupled with its superiority in structural properties over other candidates. In all cases the thickness of material required for the design was determined by the structural minimum gage requirements and resulted in 0.020 inch thickness for a 90-inch diameter Apollo vehicle over the complete range of $m/C_D A$ considered. The heat shield-structure weight fraction for a beryllium afterbody design is shown in figure 53. The figure also includes a 1.7 factor for rings, fittings, and bracketry.

Finally, a comparison of all designs is made in figures 53 and 54 for just the afterbody design and the complete lander, respectively. One can easily see that the beryllium afterbody design results in the minimum weight. Going to a dielectric design, considering the minimum design of LT_a - fiberglass, the weight penalty is very severe. Hence, in the following parametric analysis, only the beryllium afterbody/5026-aluminum forebody design will be considered.

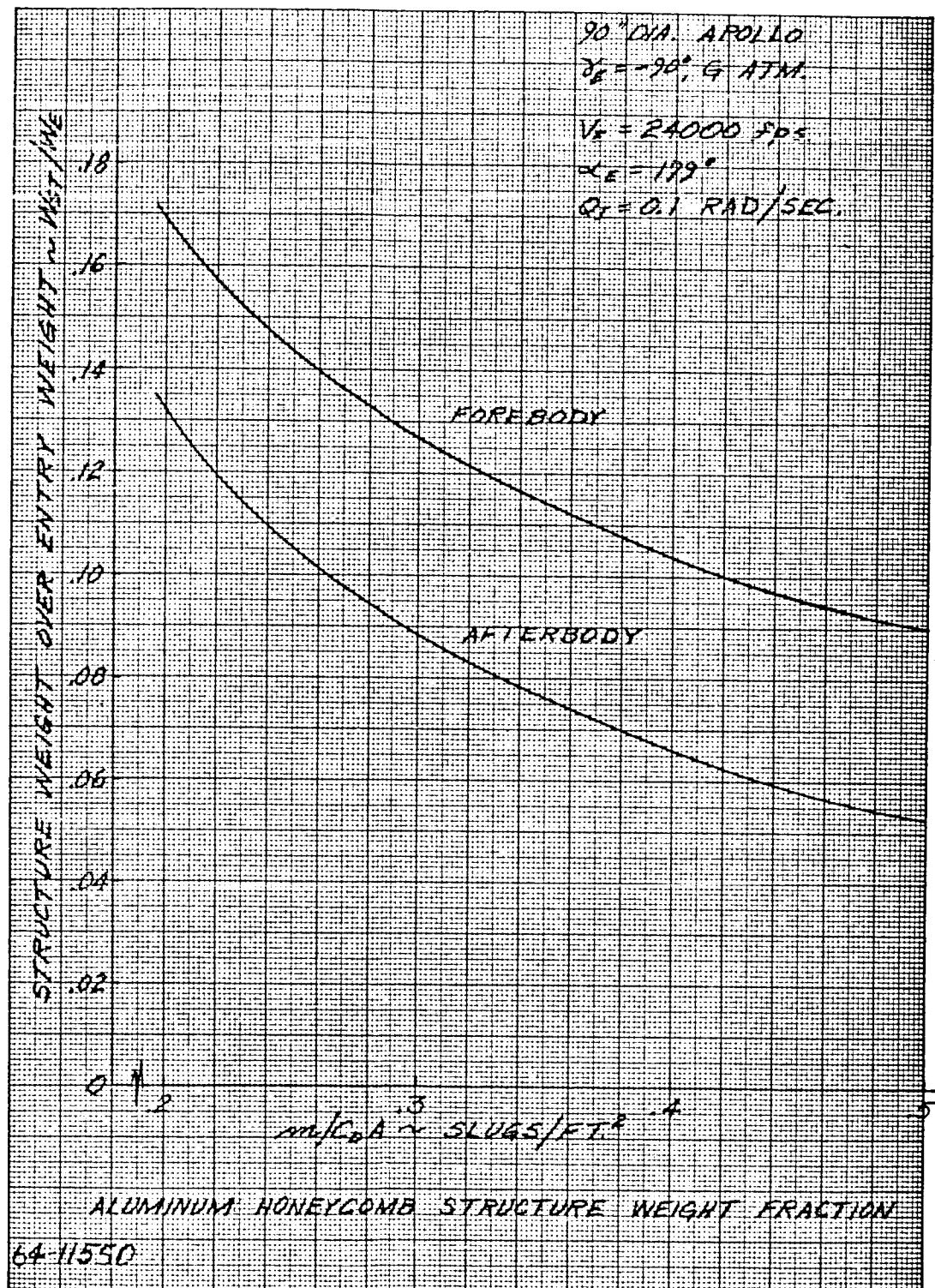


Figure 49 ALUMINUM HONEYCOMB STRUCTURE WEIGHT FRACTION

160

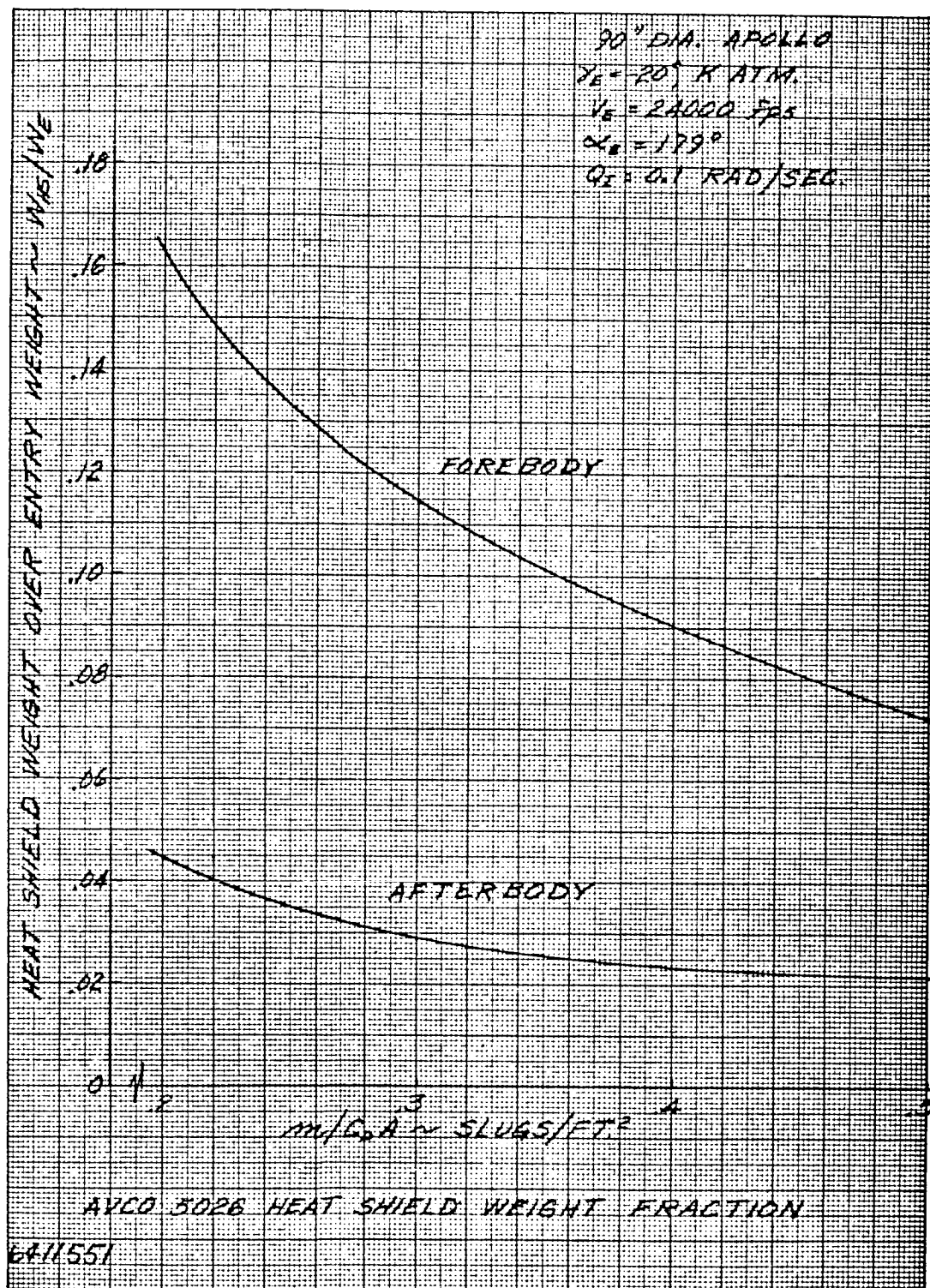


Figure 50 AVCO 5026 HEAT SHIELD WEIGHT FRACTION

161

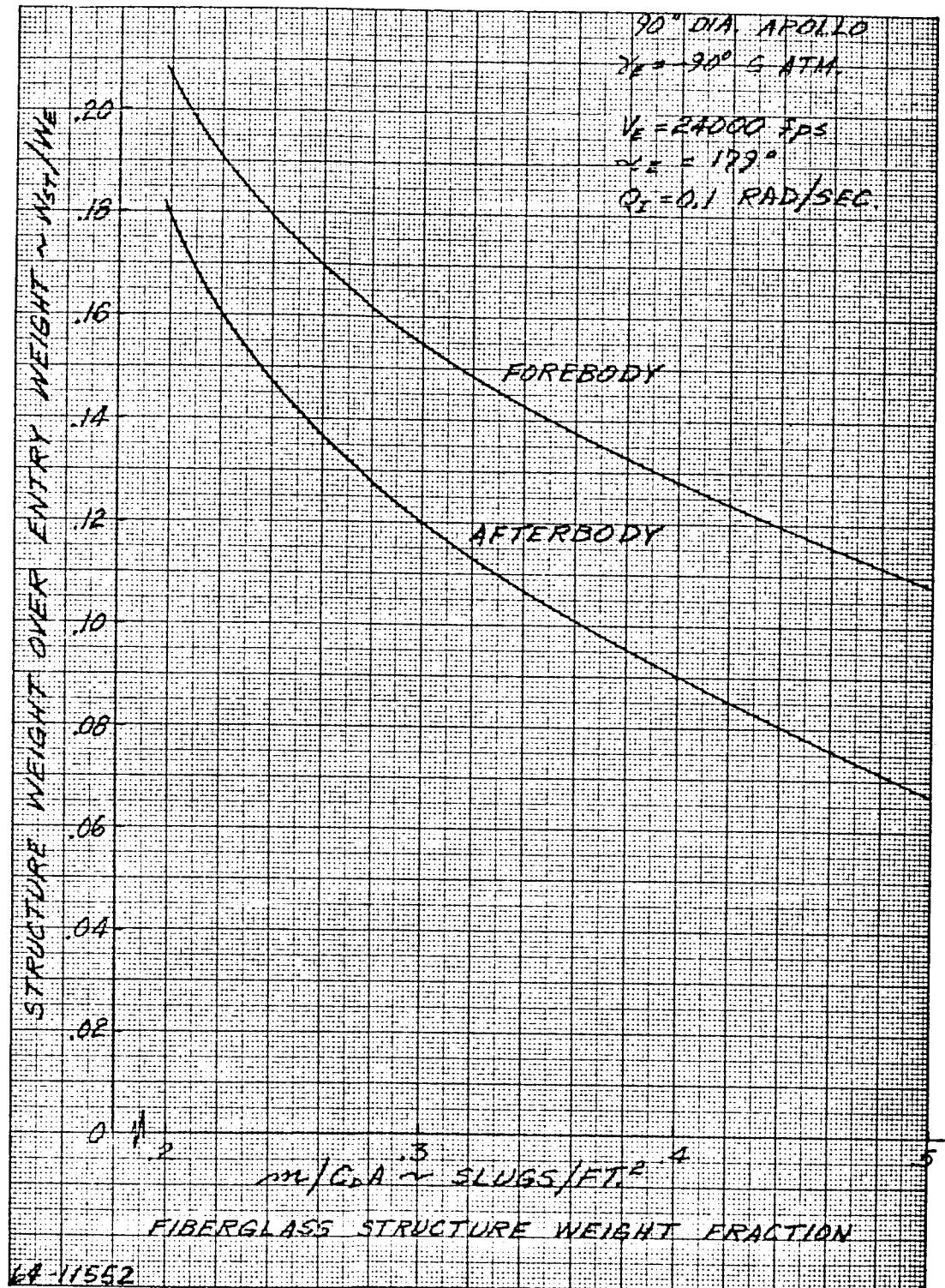


Figure 51 FIBERGLASS STRUCTURE WEIGHT FRACTION

112

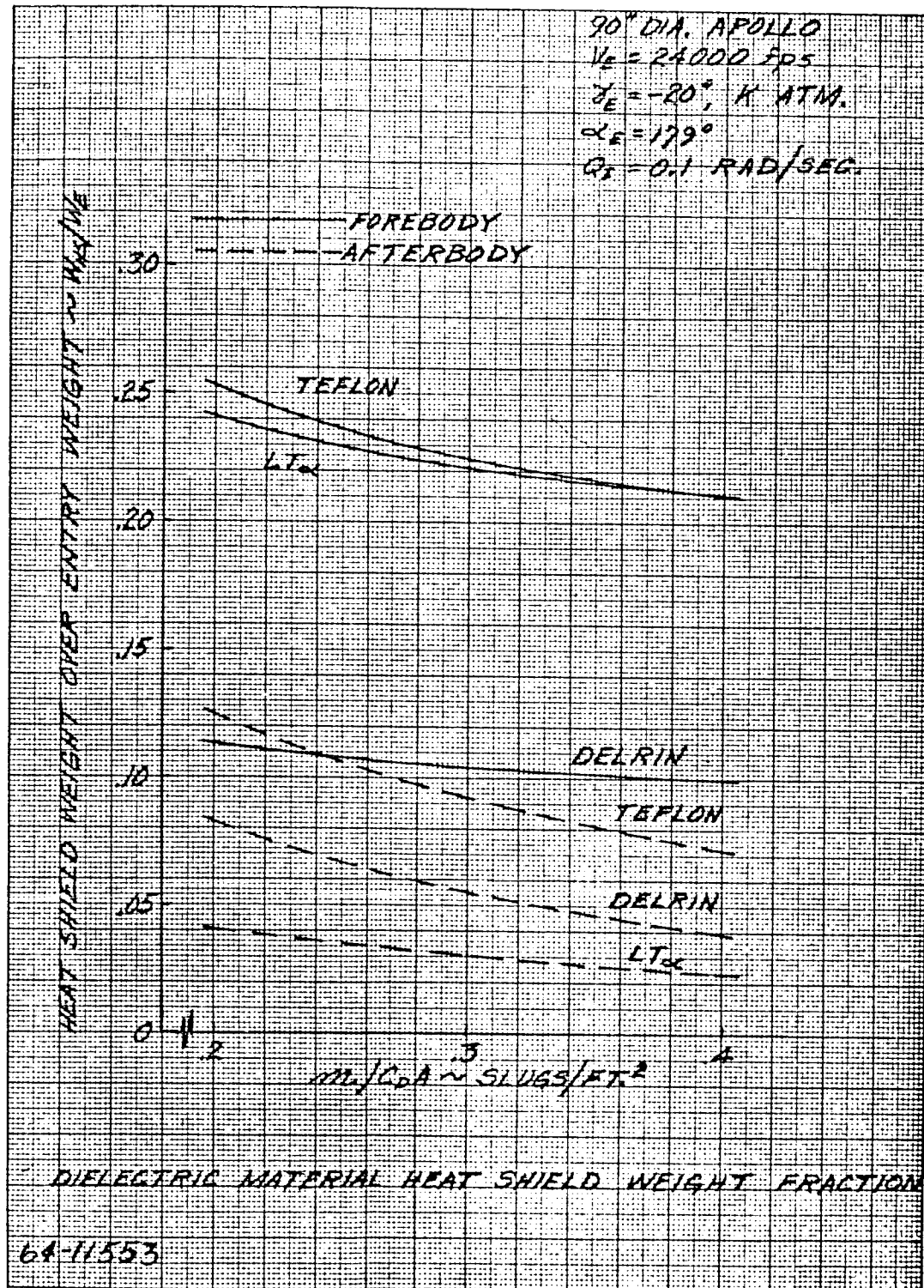


Figure 52 DIELECTRIC MATERIAL HEAT SHIELD WEIGHT FRACTION

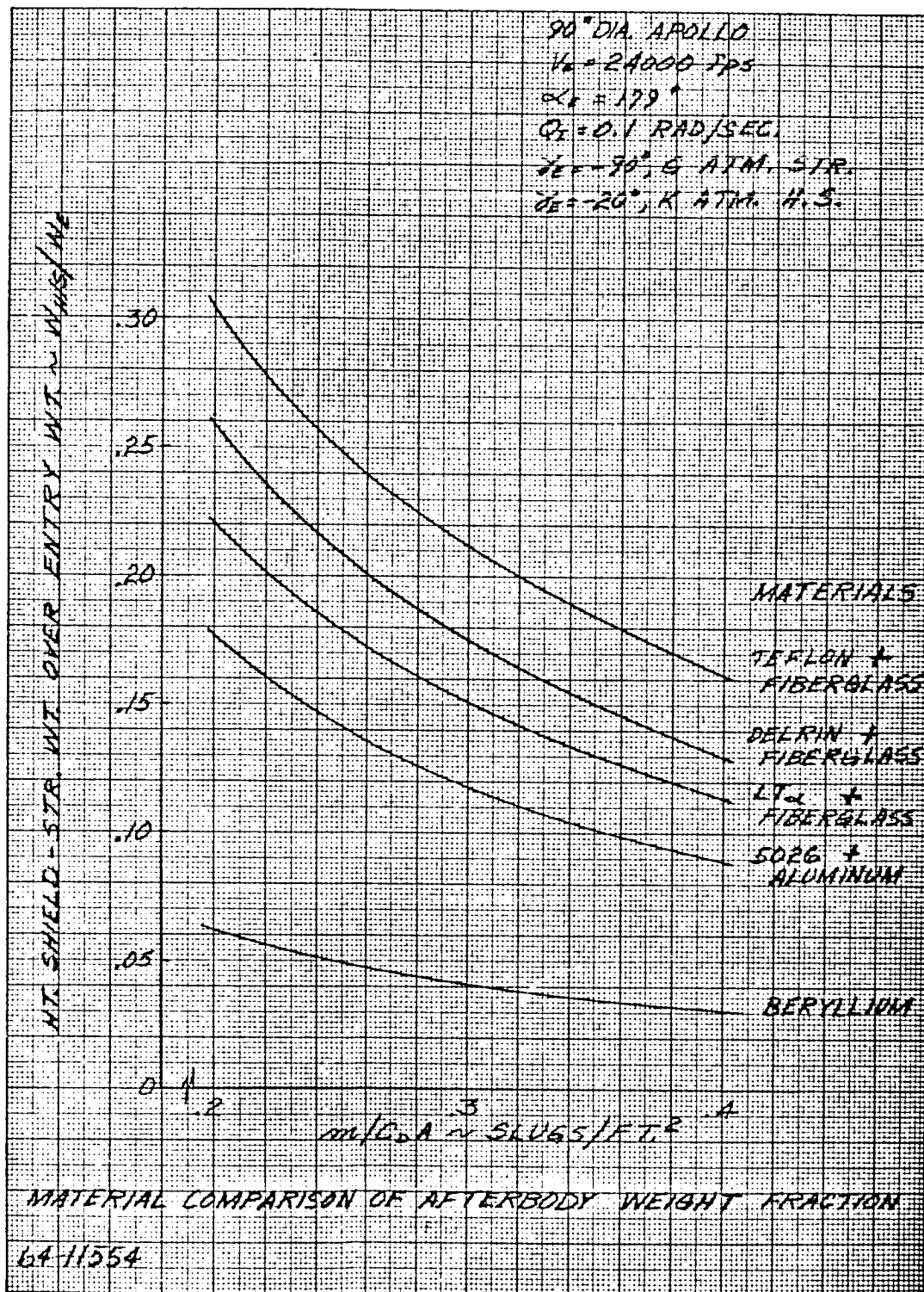


Figure 53 MATERIAL COMPARISON OF AFTERBODY WEIGHT FRACTION

164

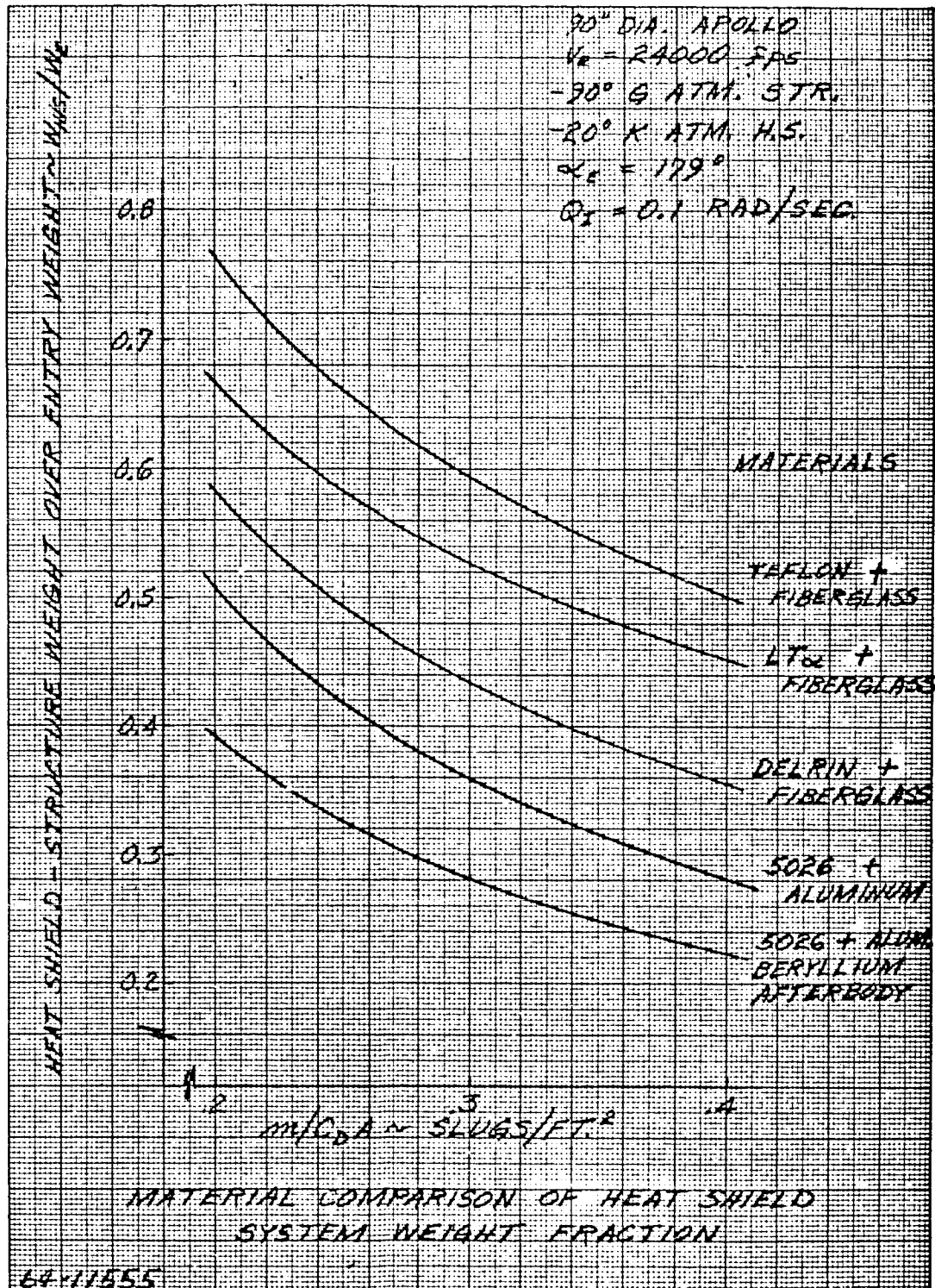


Figure 54 MATERIAL COMPARISON OF HEAT SHIELD SYSTEM WEIGHT FRACTION

165

6.2 ENTRY CONDITION EFFECTS

Since the entry conditions greatly affect the performance of the lander, and consequently the heating and pressure loading histories, then these conditions must be fully parametrized to assess their effects on the heat shield systems. In this section, the pertinent entry parameters will be evaluated. Among these will be entry angle (γ_E), ballistic coefficient (m/C_{DA}), lander pitch rate (Q), spin (P), angle of attack (α_E), and entry velocity (V_E). From these parametric evaluations, one can easily determine the heat shield system weights and assess the effects of entry conditions on the overall mission objectives.

1. Entry Angle (γ_E) and m/C_{DA}

In this section both the entry angle (γ_E) and the ballistic coefficient (m/C_{DA}) will be varied. The entry angle parameter will vary from -20 to 90 degrees where the low value is the minimum angle before skip-out would occur and -90 degrees is the obvious maximum value. The ballistic coefficient range of values ($m/C_{DA} = 0.2 - 0.5$) was determined from a cursory evaluation of the required aerodynamic deceleration necessary for Mach 2.5 parachute deployment under the atmospheric models proposed for this study. Also, previous studies considering these atmospheric models suggested this range of values.

The first parametric curve, figure 55, is a plot of total heat shield system weight fraction versus entry angle (γ_E) as a function of m/C_{DA} . In this figure the forebody is Avco 5026 - aluminum honeycomb (including the toroidal corner) and the afterbody is beryllium. It is evident that entry angle has a small effect on the fraction above -40 degrees. This is due to the resulting summation of an increasing heat shield fraction and a decreasing structural fraction with decreasing entry angle, since both the heating and pressure loadings are sine functions of opposite sign with γ_E . This effect is noted on figures 56 and 57 for the total heat shield and total structural weight fractions. Note that the beryllium afterbody is included as a heat shield weight in these curves. In the generation of the above curve, it must be noted that the heat shield design is for the K-atmosphere and the structure design is for G-atmosphere as stated previously.

In an actual design, it is unlikely that the heat shield system would be designed for a single entry angle as presented in figure 55, but would more likely be designed over a range of angles. The range of entry angles used in designing a heat shield system is usually determined about a nominal entry angle by considering the 3σ error dispersion about the nominal condition. As presented in the system trajectory analysis (volume II, section 3.2), the dispersion becomes very significant at low values of entry angle. One now designs the heat shield weights using the low entry angle, which gives the highest integrated heating, and the structural weights using

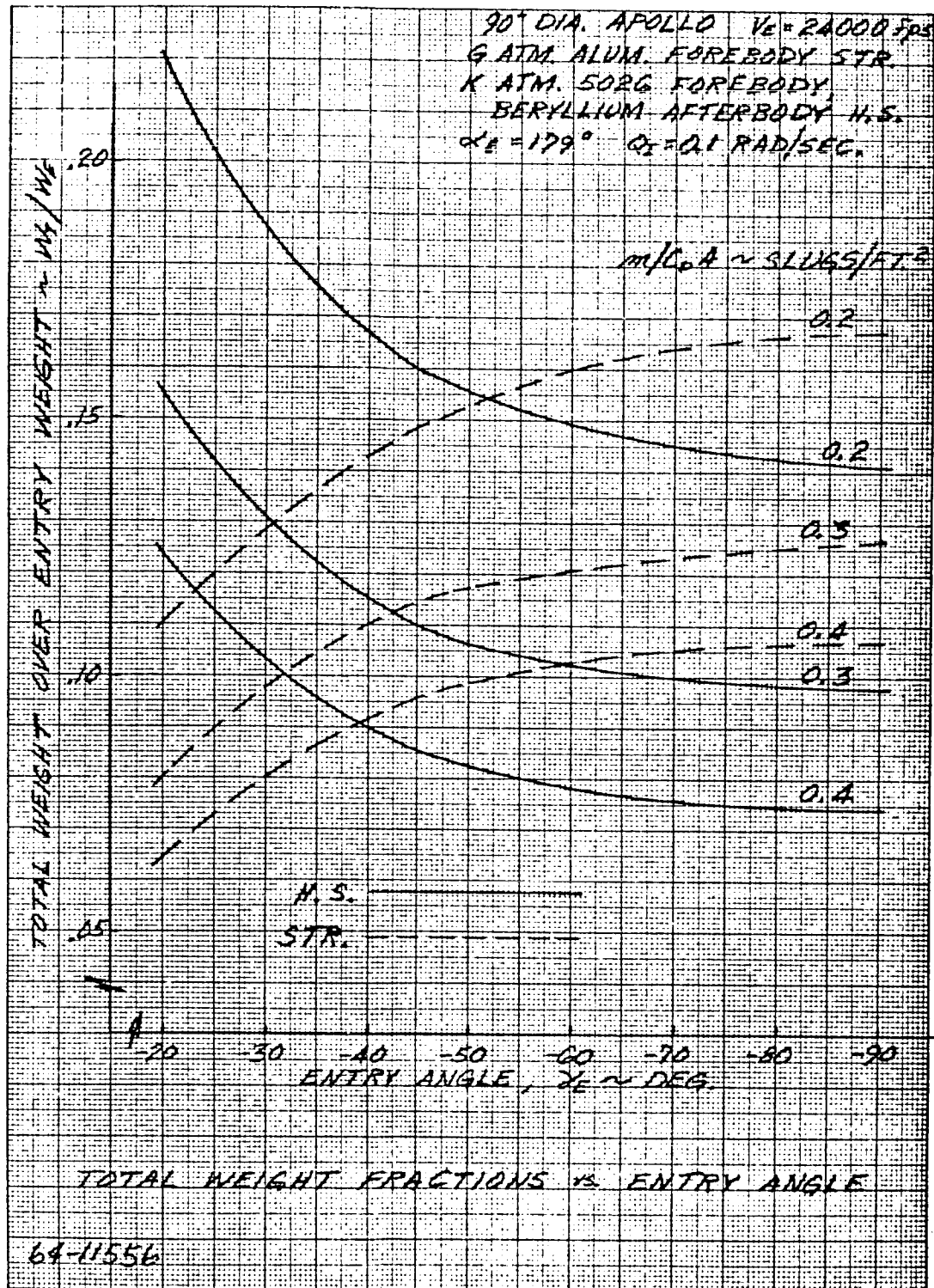
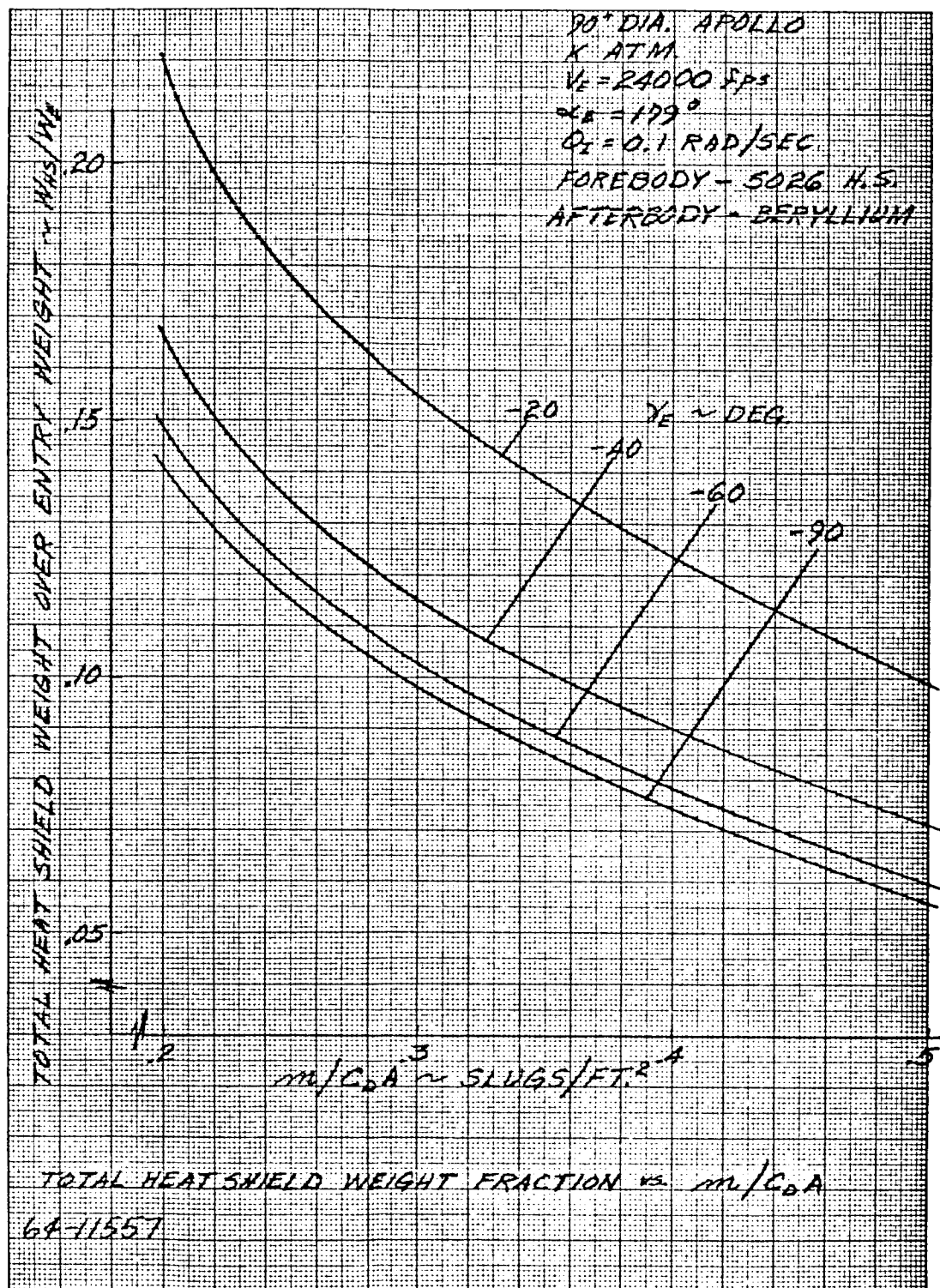


Figure 55 TOTAL WEIGHT FRACTION VERSUS ENTRY ANGLE


Figure 56 TOTAL HEAT SHIELD WEIGHT FRACTION VERSUS $M/C_D A$

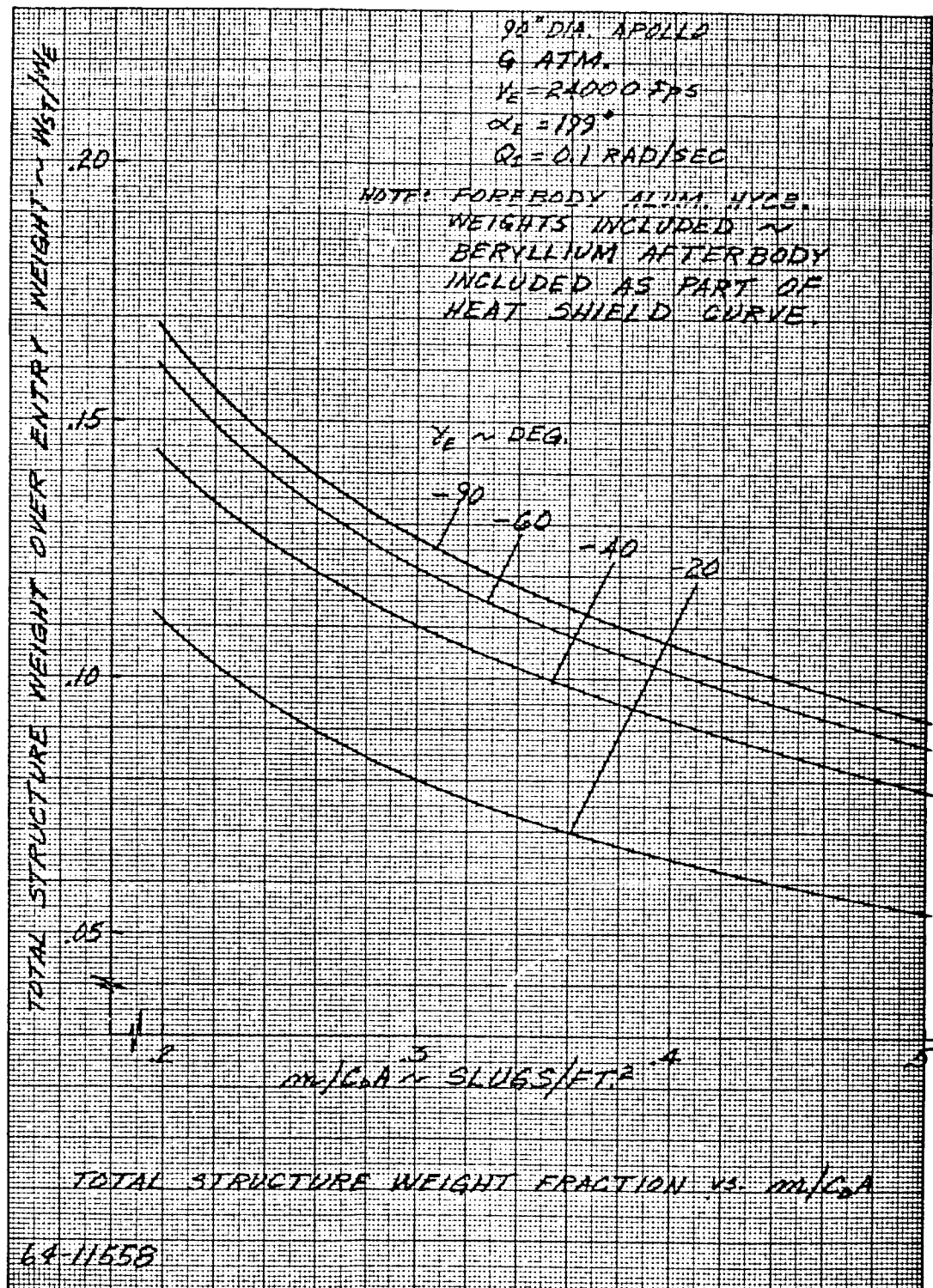


Figure 57 TOTAL STRUCTURE WEIGHT FRACTION VERSUS m/C_{DA}

the high entry angle, which results in the highest pressure loading. This is best illustrated by the following table which was generated using 3σ dispersion about the nominal:

γ_E) Nominal	Design Range	
	γ_E) Heat Shield	γ_E) Structure
-40	-21.3	-58.3
-60	-45.6	-74.4
-90	-77.1	-90.0

Combining the nominal entry angle results with the previous plots of weight fractions, a curve of total heat shield system weight fraction versus γ_E)_{NOM} can be constructed as depicted in figure 58. Now the true effect of entry angle can be evaluated as illustrated by this figure.

It is often desirable to find a simple expression for the heat shield system weight fraction. This can be accomplished by cross plotting figure 58 as a function of m/C_{DA} instead of γ_E . Now a curve fit can be obtained to satisfy all entry angles and the range of m/C_{DA} . Such an expression is,

$$\frac{w_{HS} + w_{ST}}{w_E} = K (m/C_{DA})^{-0.8}$$

where the constant K depends on the nominal entry angle $(\gamma_E)_{NOM}$ as presented in the table on figure 59. In the following sections we will establish another expression coupling in the effect of lander diameter to the above expression.

To facilitate design tradeoffs and to illustrate entry angle effects on forebody design, curves have been added showing the forebody heat shield, structure, and total heat shield system weight fractions. These curves are presented in figures 60, 61, and 62. In addition, the heat shield thicknesses and structural thicknesses for the forebody are also presented to support design layouts and lander center of gravity locations. These data are presented as a function of both m/C_{DA} and γ_E in figures 63 through 65.

2. Angle of Attack, Spin and Pitch

The entry angle of attack, spin rates, and pitch rates could have a significant effect on the total heat shield system weight, in particular on the heat shield (ablator) weight. This effect is due primarily to the angle of attack history of the lander during peak heating pulse (reference section 4.0). The heat shield and structure computer programs used in these analyses account for

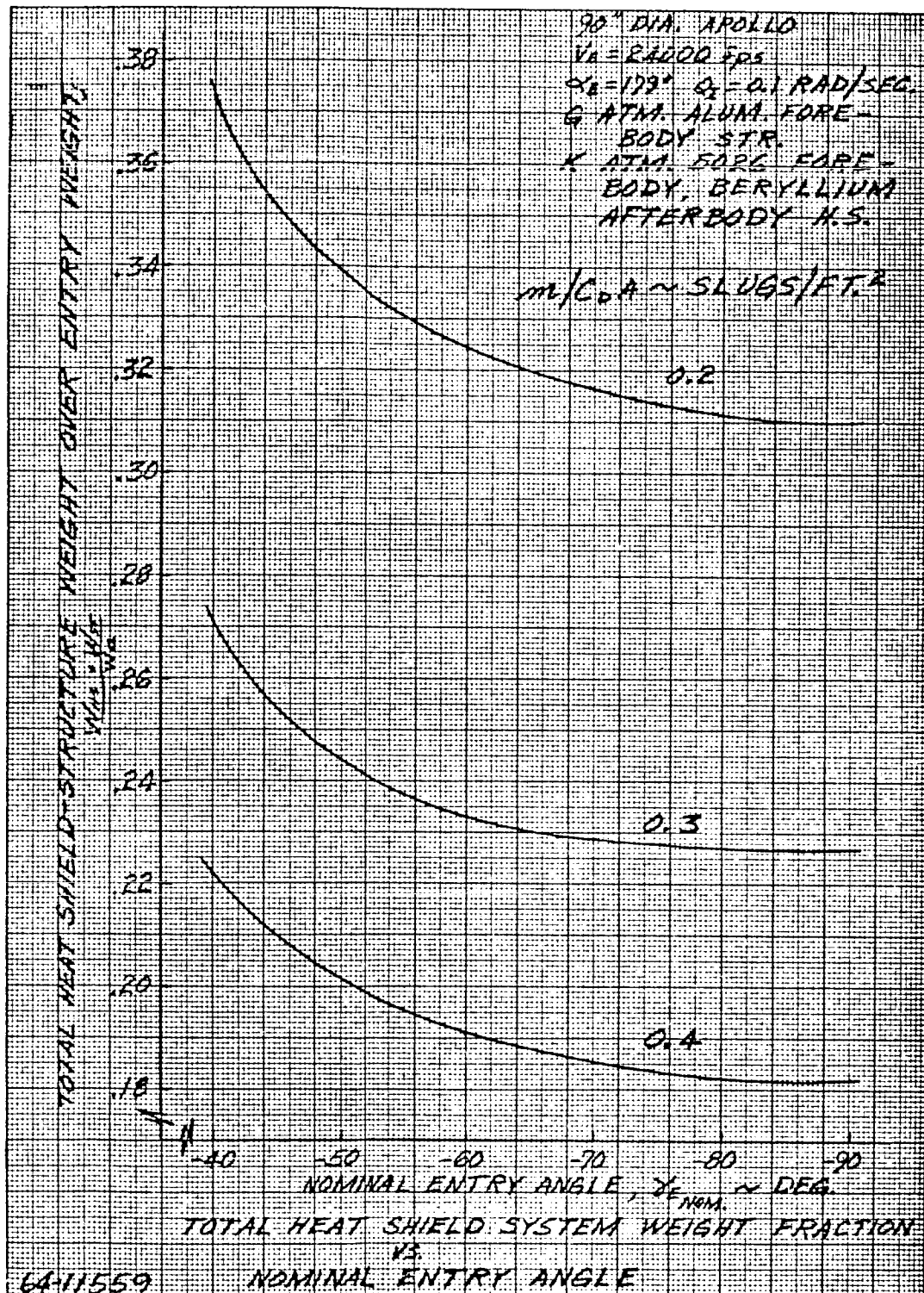


Figure 58 TOTAL SHIELD SYSTEMS WEIGHT FRACTION AS A FUNCTION OF ENTRY ANGLE

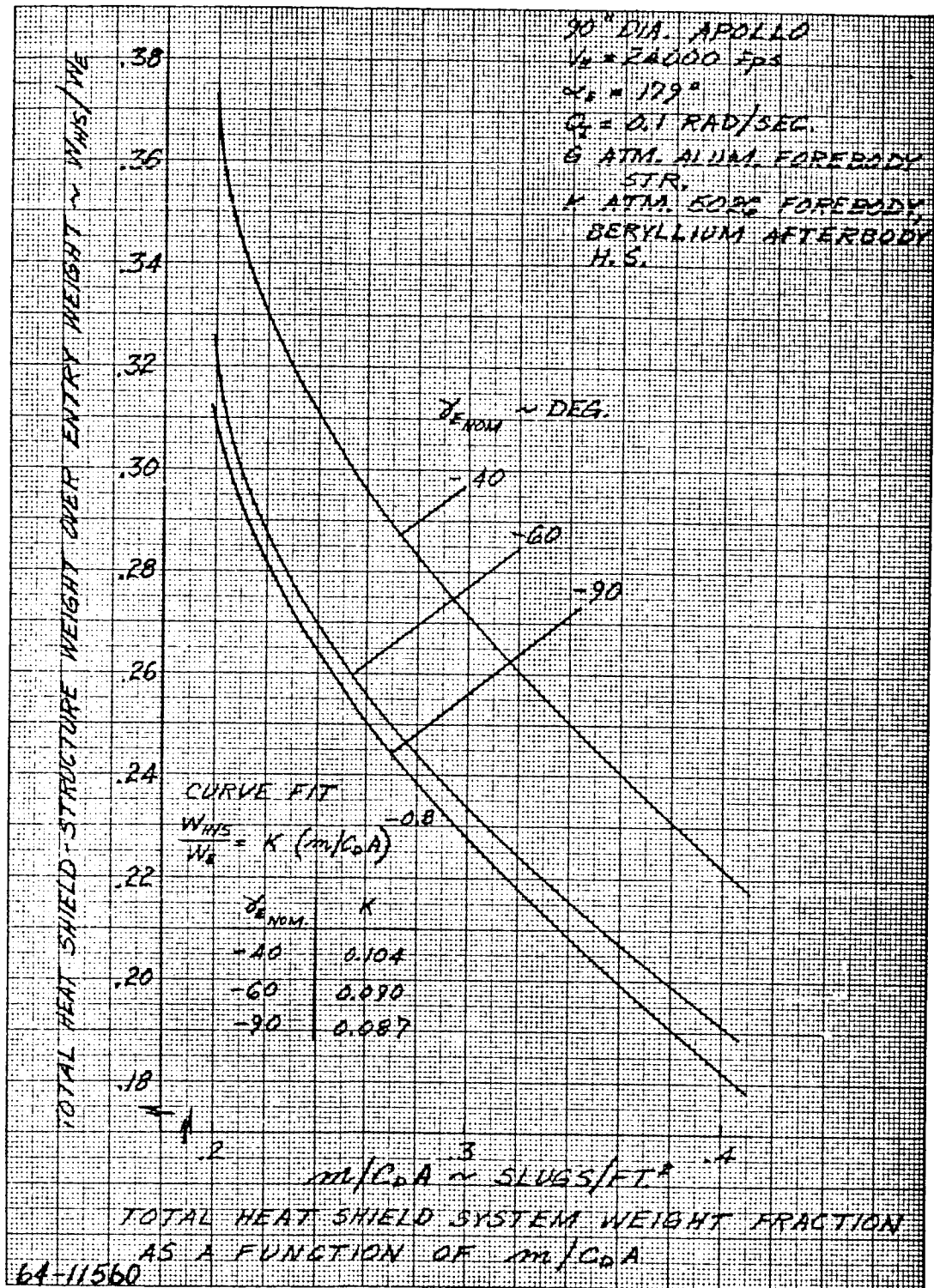
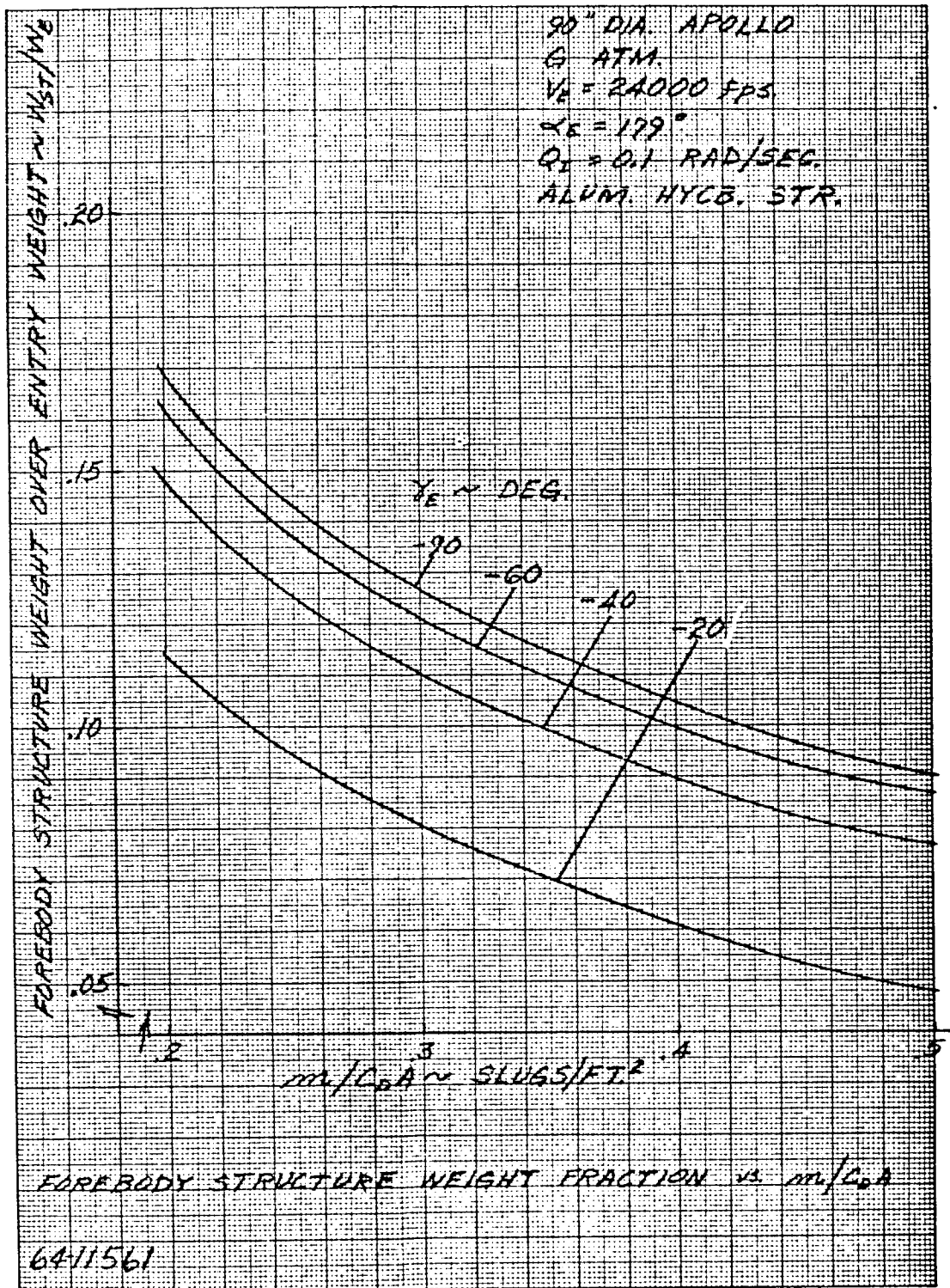


Figure 59 TOTAL HEAT SHIELD SYSTEM WEIGHT FRACTIONS OF A
FUNCTION OF $m/C_D A$


Figure 60 FOREBODY STRUCTURE WEIGHT FRACTION VERSUS $m/C_D A$

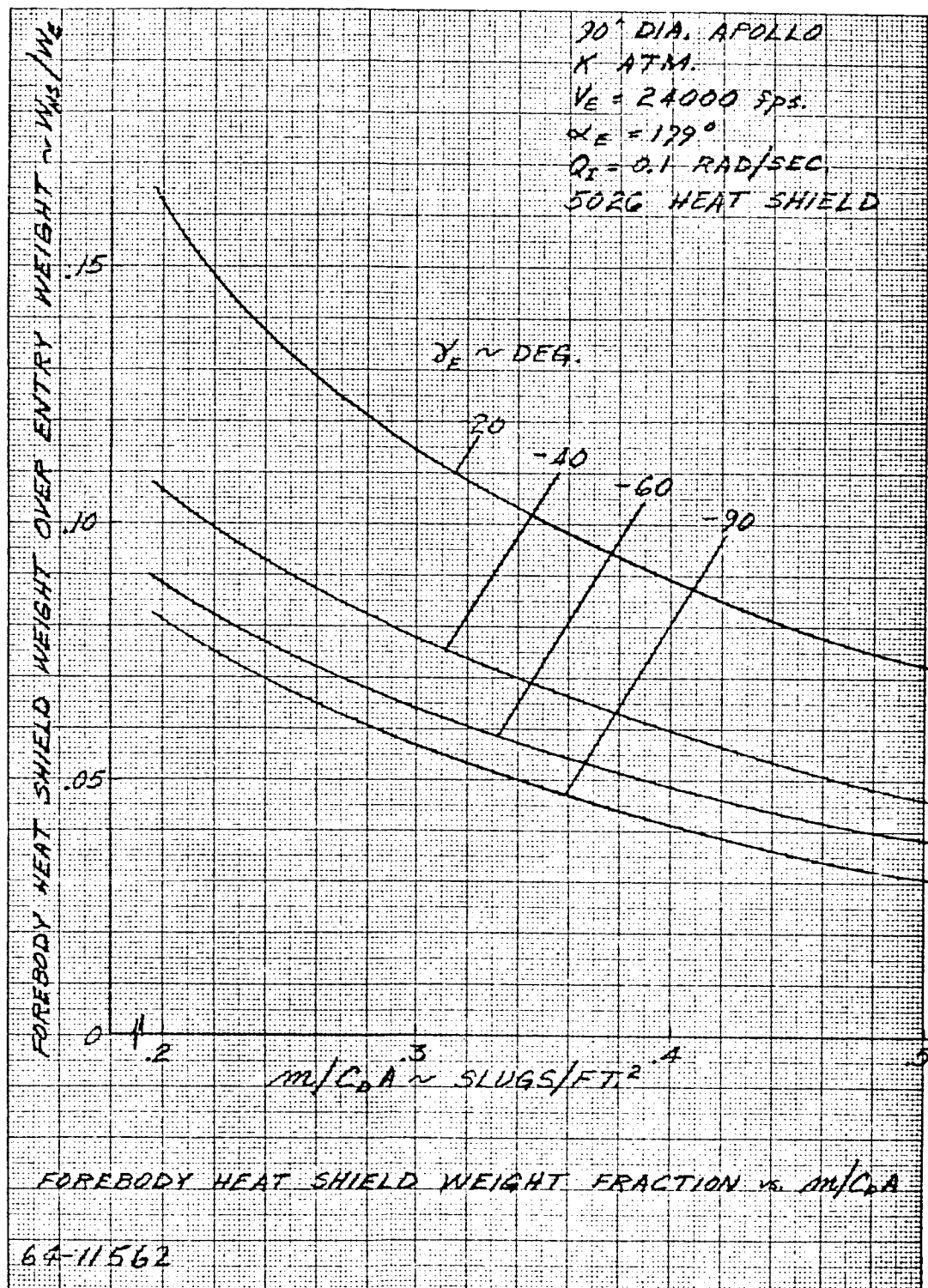


Figure 61 FOREBODY HEAT SHIELD WEIGHT FRACTION VERSUS $m/C_D A$

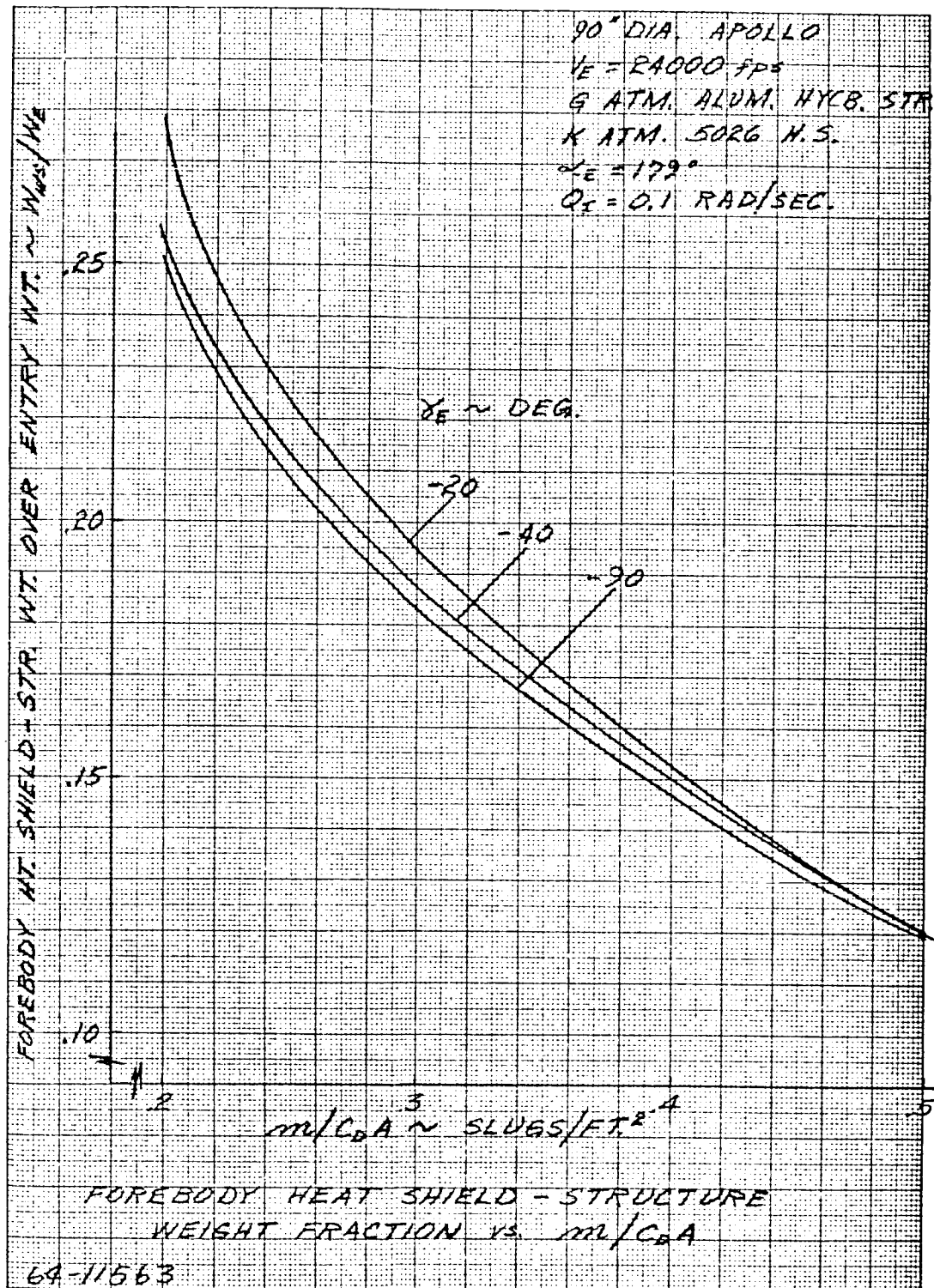


Figure 62 FOREBODY HEAT SHIELD - STRUCTURE WEIGHT FRACTION
 VERSUS $m/C_D A$

175

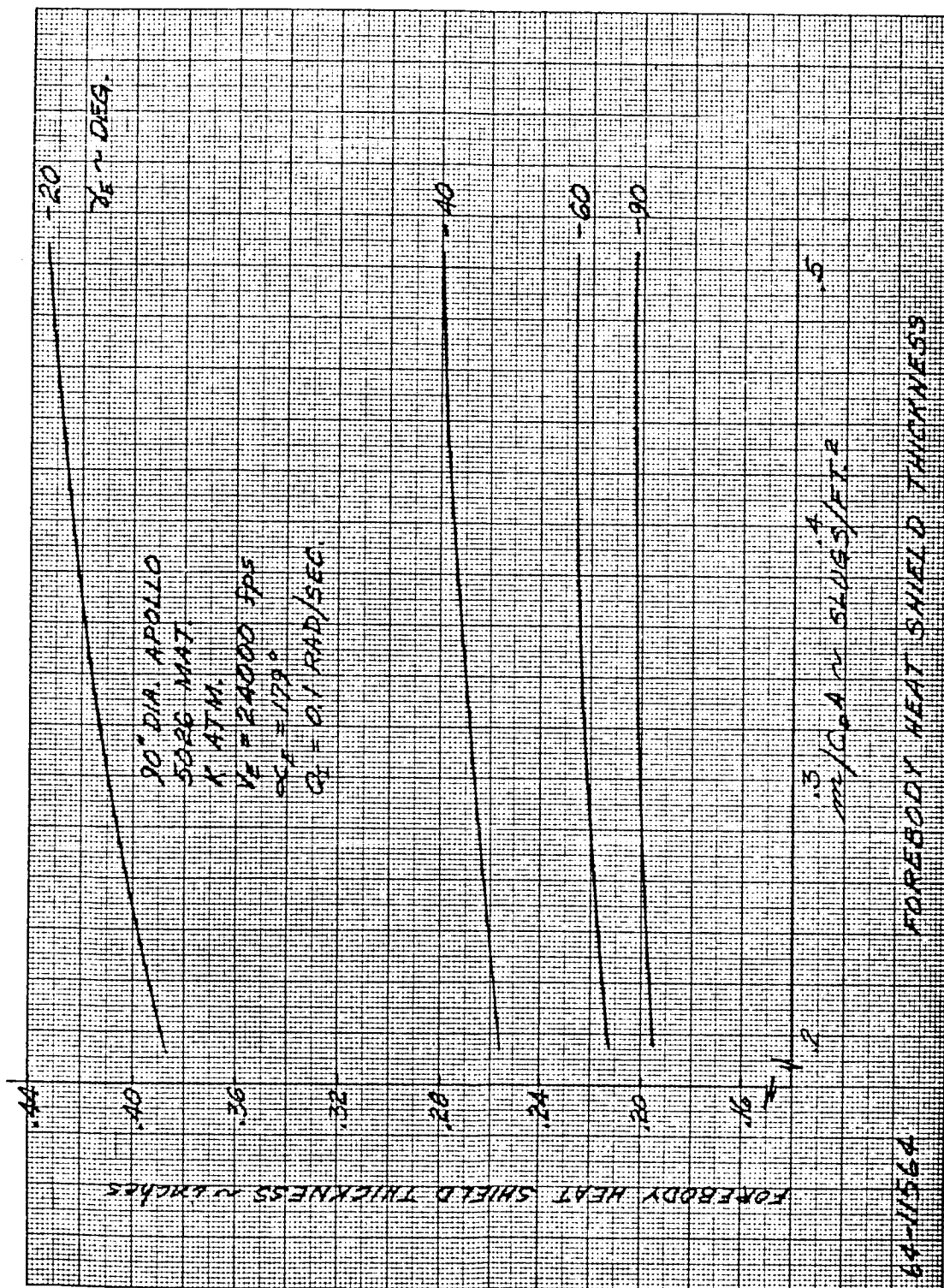


Figure 63 FOREBODY HEAT SHIELD THICKNESS

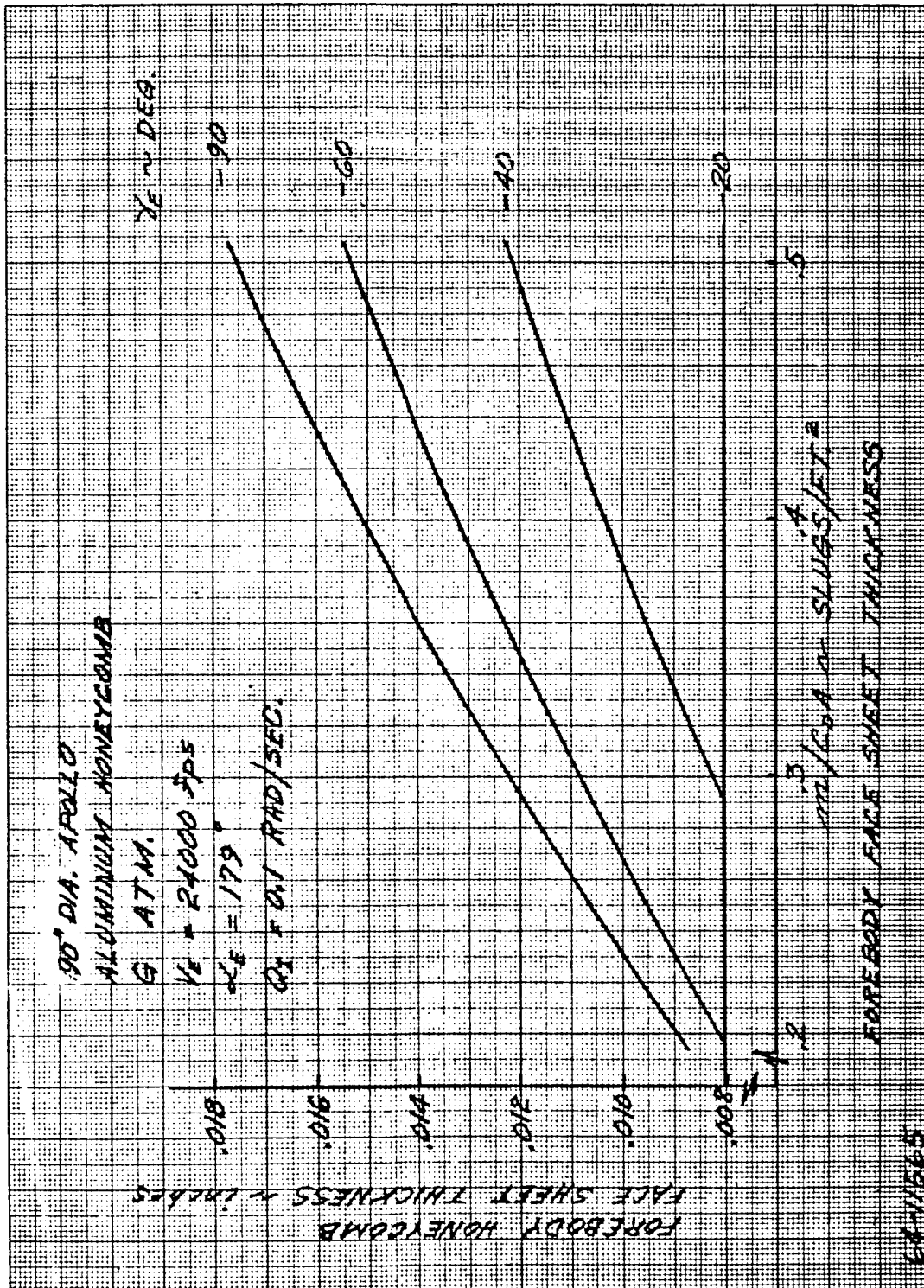


Figure 64 FOREBODY FACE SHEET THICKNESS

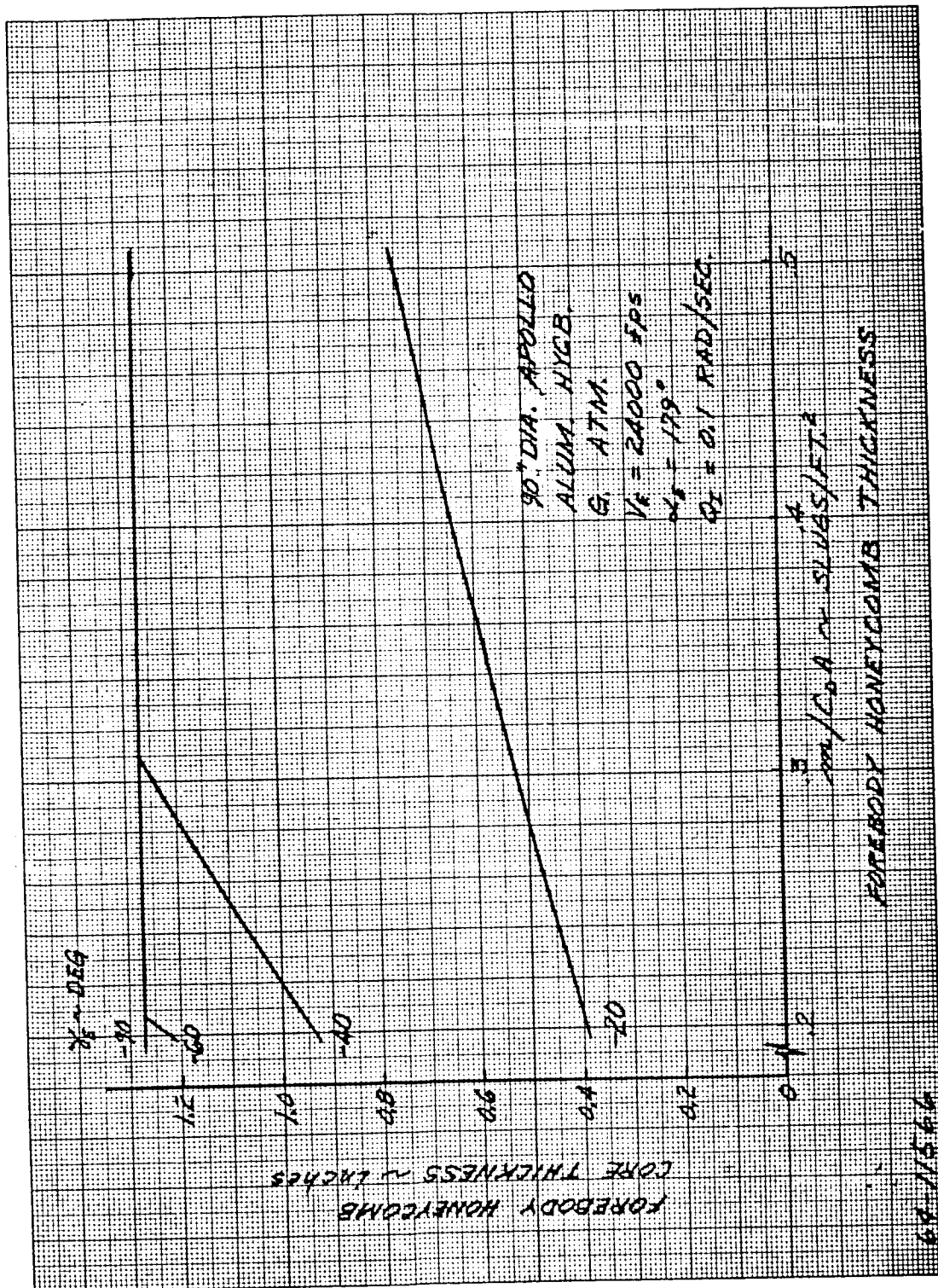


Figure 65 FOREBODY HONEYCOMB THICKNESS

this angle of attack history in their weight predictions. The angle of attack effect is particularly noticeable on the afterbody heat shield weights as can be seen in figure 66. In this figure an ablative heat shield (Avcoat 5026) was used and a notable weight penalty is realized as the entry condition becomes more severe ($\alpha_E = 179$ degrees, $P = 0$, $Q = 0$). However, when a hot structure (heat sink) design is employed on the afterbody, such as beryllium, a small effect with entry condition is noticable, as illustrated in figure 67. This is due to the low integrated heating experienced on the lander during entry. Even with the worst condition, the beryllium thickness required to operate at 1300°F is well below the minimum gage constraint. Only a small difference in heat shield weight (~ 1 percent) will be noticed on the forebody due to the non-uniform heating distribution, even at large angle of attack.

In conclusion, if a hot structure design is used for the afterbody, entry conditions will have little effect on the heat shield system weight; however, if an ablator design is used, entry conditions will have a large effect.

3. Entry Velocity

The results of a study to ascertain the feasibility of using a beryllium hot structure (for both forebody and afterbody) and to determine the effect of entry velocity on the heat shield system is presented herein. A range of entry velocities between 15,000 and 24,000 ft/sec was considered. This range of velocities is considered to give the practical bounds for the 1969 launch opportunity.

The design heat pulses are based on a ballistic coefficient of 0.25 slug/ft^2 using the Mars K-atmosphere model⁽¹⁾ and a 100 inch diameter Apollo vehicle. The study was conducted for a range of entry angles between $\gamma_e = -20$ to 90 degrees (combining both structural and heat shield analysis at each entry angle).

In figure 68 the relative heat shield system weight fractions are compared for three possible combinations of heat shield system designs:

- a. Avco 5026 and aluminum honeycomb structure all over.
- b. Avco 5026 and aluminum honeycomb structure forebody, beryllium hot structure afterbody.
- c. Beryllium hot structure all over.

The results presented in figure 68 clearly indicate that combination 2 (using beryllium afterbody) represents the minimum weight design over

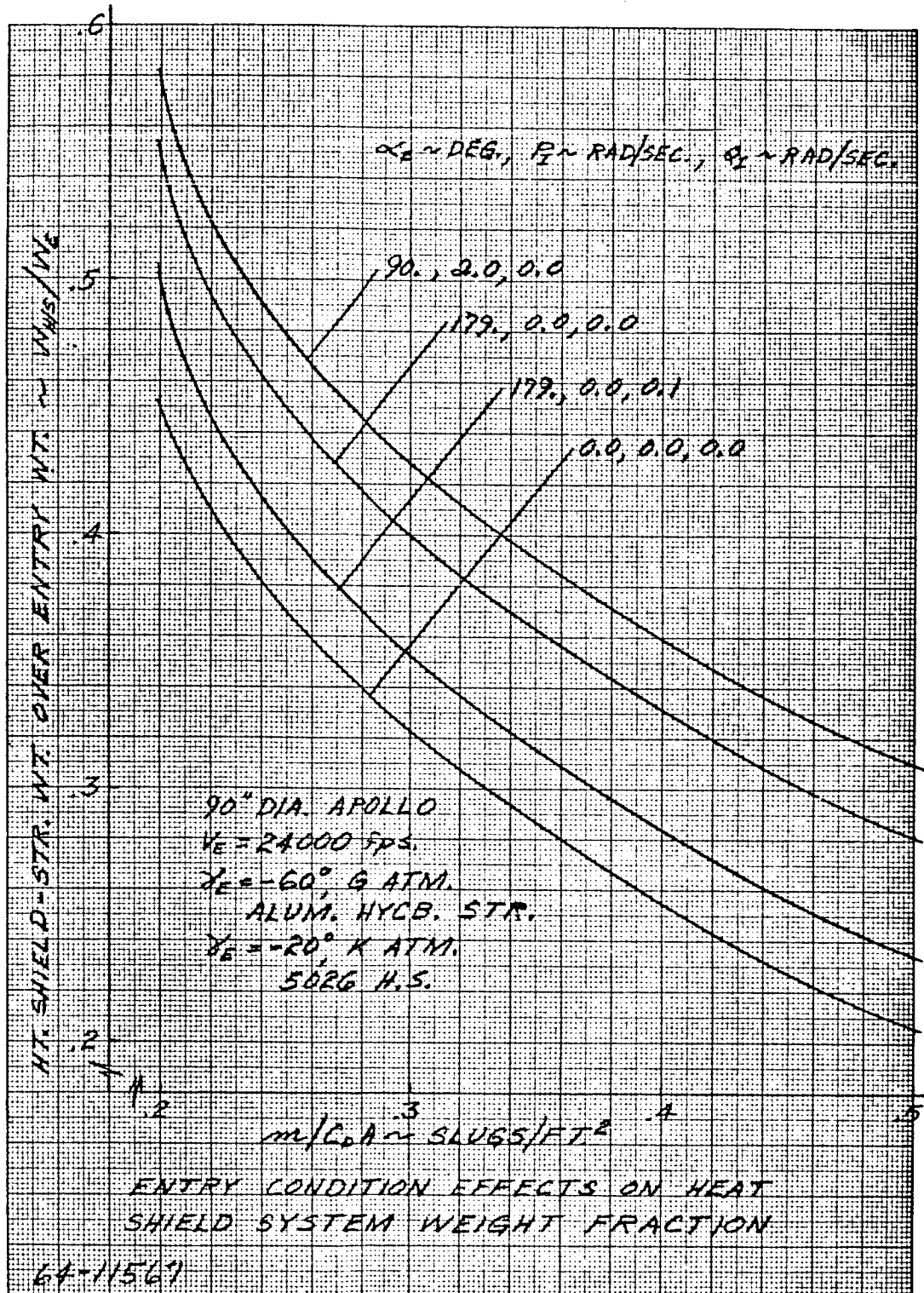


Figure 66 ENTRY CONDITION EFFECTS ON HEAT SHIELD SYSTEM WEIGHT FRACTION

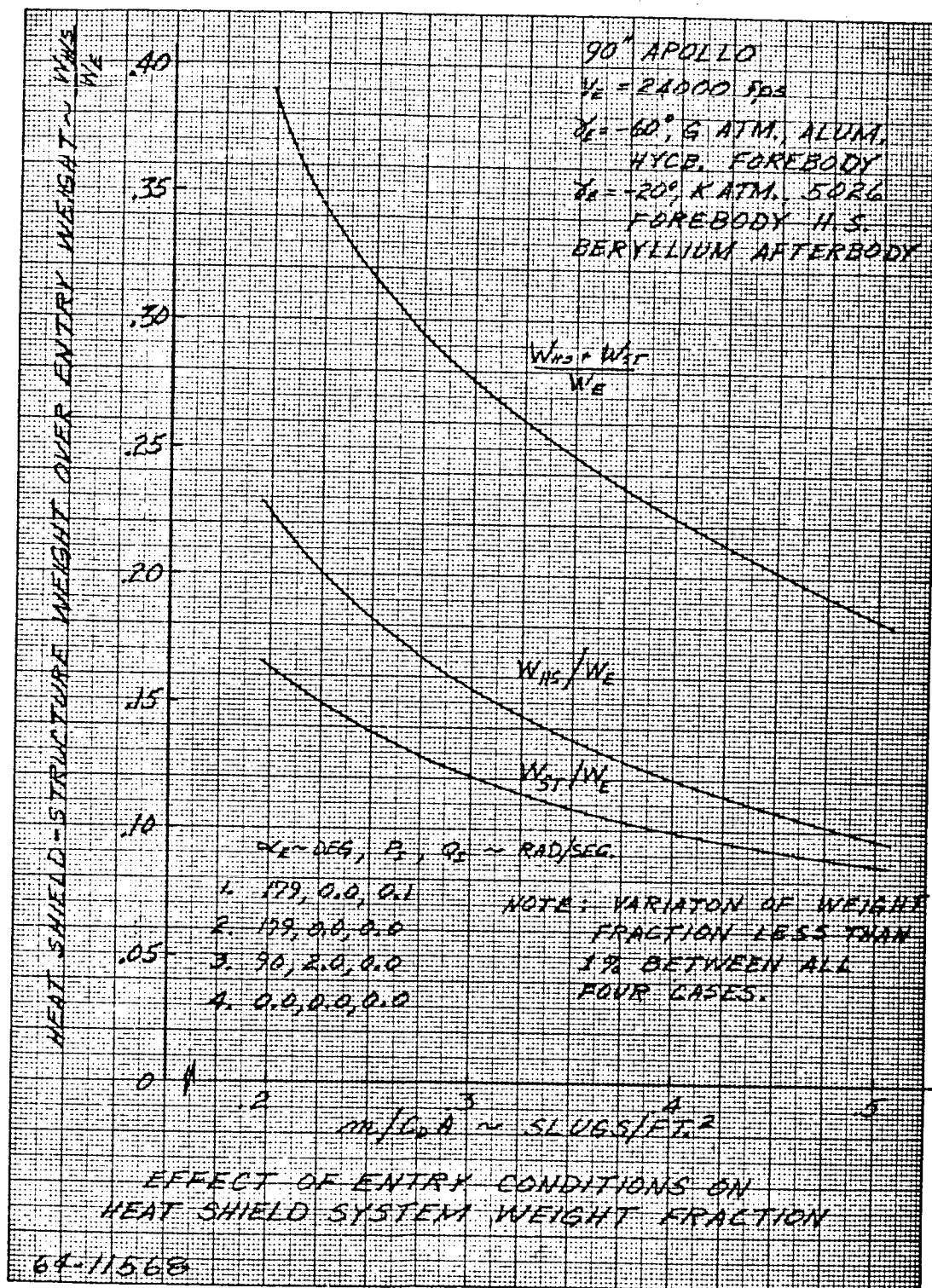


Figure 67 EFFECT OF ENTRY CONDITION ON HEAT SHIELD SYSTEM WEIGHT FRACTION

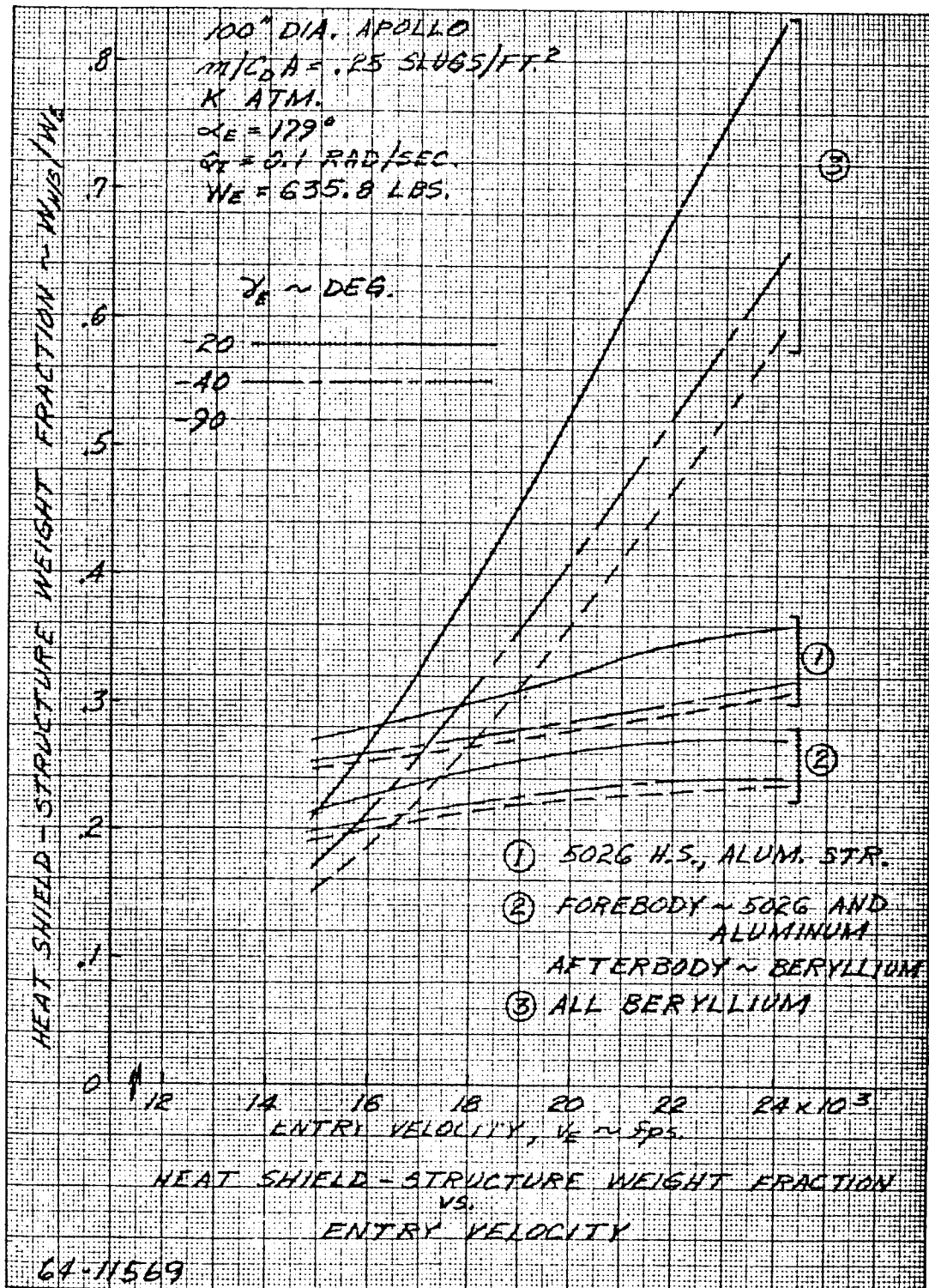


Figure 68 HEAT SHIELD - STRUCTURE WEIGHT FRACTION VERSUS ENTRY VELOCITY

almost the entire velocity range. This conclusion supports the selection previously made in the material trade-off section. Combination 3 (beryllium hot structure all over) would only produce minimum weight design at very low velocities which require a retro-maneuver prior to entry to bring the velocity down to this range; hence the weight required for retro would greatly overshadow the heat shield system weight savings.

6.3 LANDER DIAMETER EFFECTS

In all of the previous analyses of the heat shield system, only a 90 inch-diameter Apollo lander was considered. It will be the attempt of this section to establish the effect of lander diameter on the heat shield system weight. The analysis will be limited to one $m/C_D A$ (0.30) and will be studied over the complete range of entry angles with all other parameters held fixed. All analyses presented in this section will be based on the same computer program ² used in the previous sections.

In the first parametric curve, figure 69, heat shield weight fraction versus entry angle, there is a small effect of lander diameter on the heat shield weight fraction but a significant effect with γ_E . Since the total convective heat load

decreases with increasing diameter ($\propto \frac{1}{D^{1/2}}$) and at the same time the surface area and entry weight are increasing with diameter ($\propto D^2$). Then

$$\frac{w_{HS}}{w_E} = \frac{t_{HS} A_S}{A_V} = \frac{t_{HS} D^2}{D^2} = t_{HS} \propto \frac{1}{D^{1/2}}$$

Hence this result would be expected.

However, a look at the structural weight fraction indicates a reverse trend and a large effect on the weight fraction with diameter and γ_E (figure 70). This is attributed to the fact that the structural thickness is increasing with increased diameter ($\propto D^m$, where $1.5 \leq m \leq 2$; see reference 2) and hence an increasing weight fraction with diameter; i. e.,

$$\frac{w_{ST}}{w_E} = \frac{t_{ST} A_S}{A_V} = \frac{t_{ST} D^2}{D^2} = t_{ST} \propto D^m$$

Combining these two results (on figure 71) shows a small effect with entry angles from -40 to -90 degrees but a significant effect with diameter.

Now, combining the diameter effects with the entry angle and $m/C_D A$ effect established in section 6.2, a simple expression can be obtained for the heat

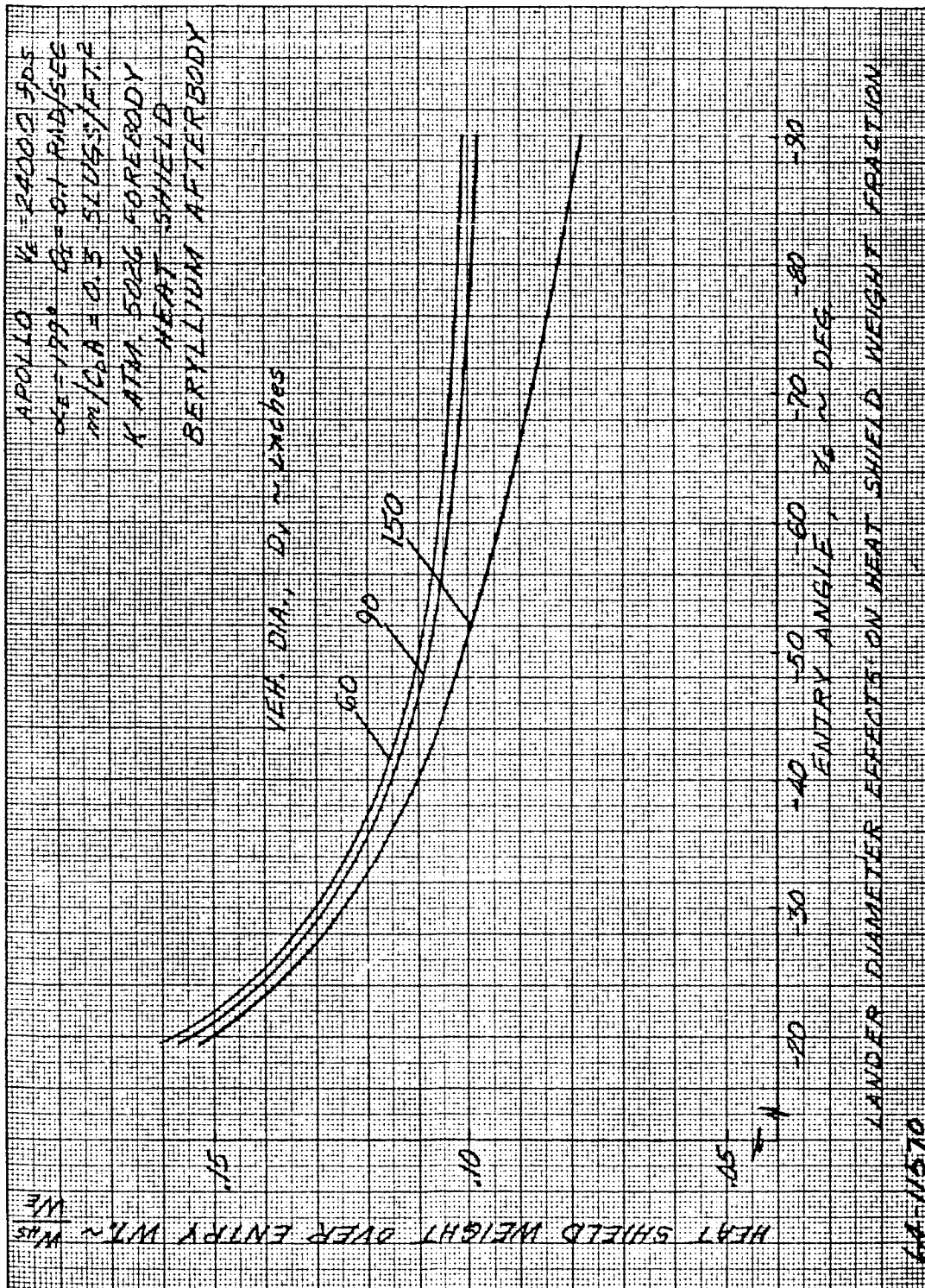


Figure 69 LANDER DIAMETER EFFECTS ON HEAT SHIELD WEIGHT FRACTIONS

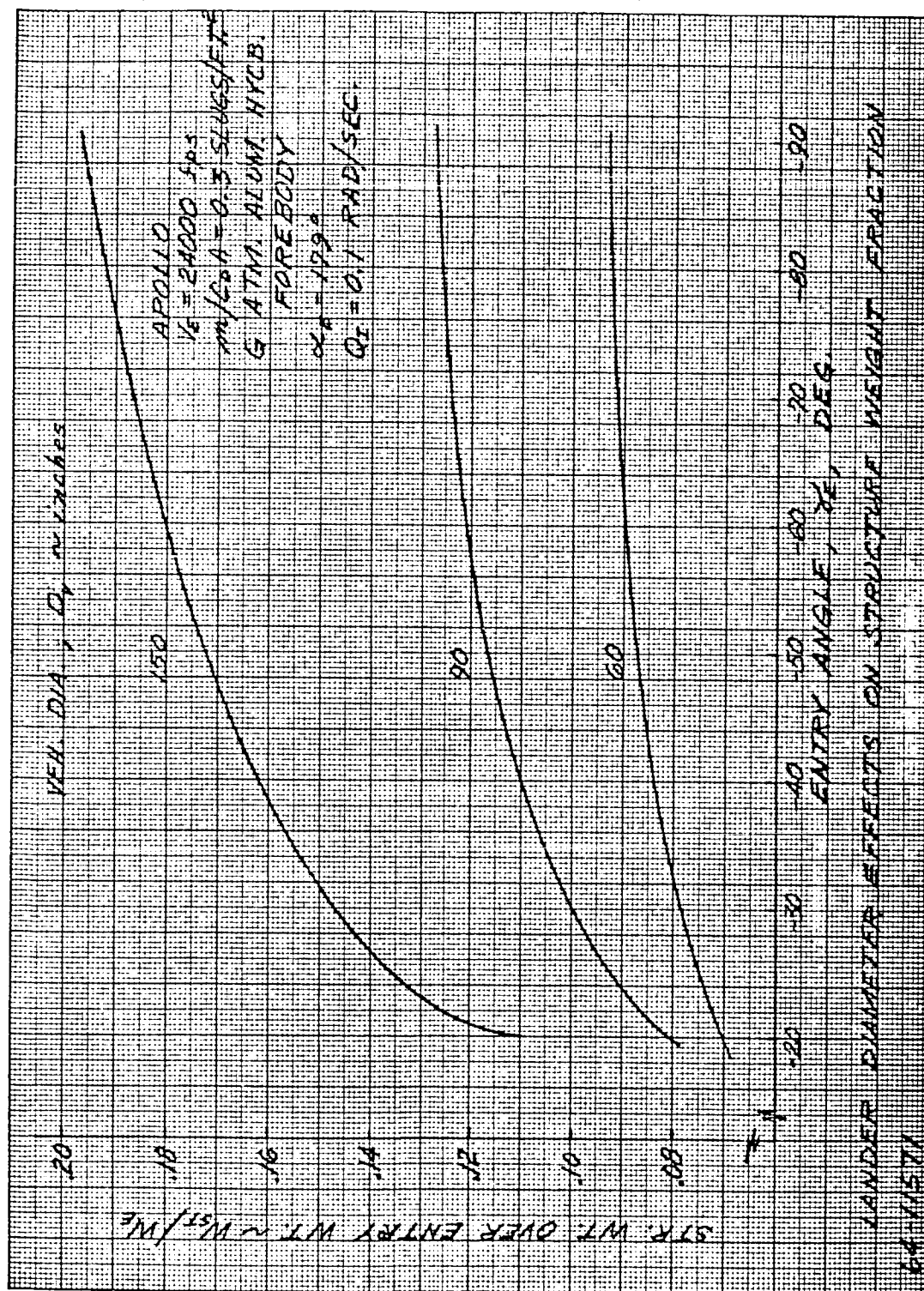


Figure 70 LANDER DIAMETER EFFECTS ON STRUCTURAL WEIGHT FRACTIONS

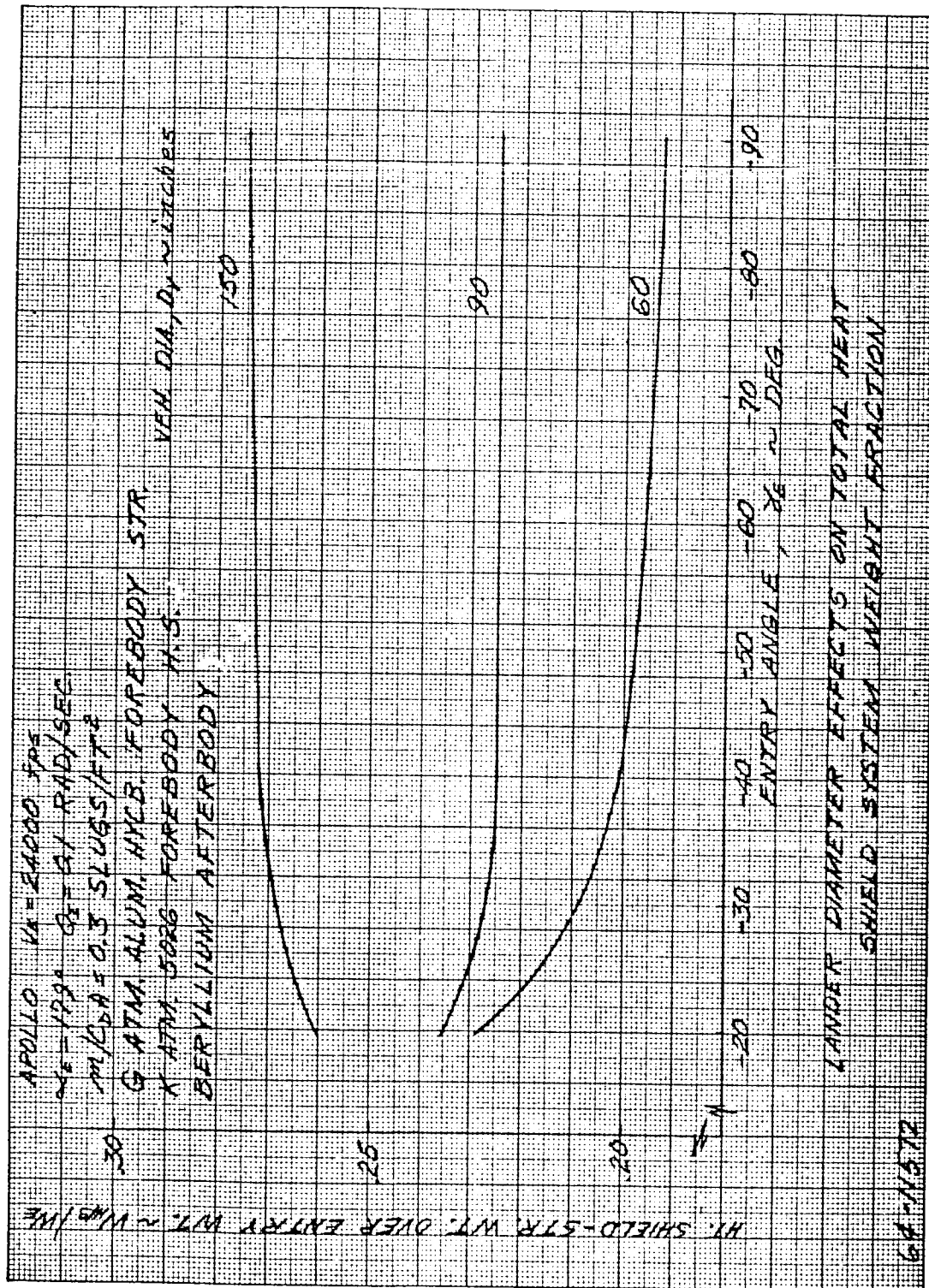


Figure 71 LANDER DIAMETERS EFFECTS ON TOTAL HEAT SHIELD SYSTEM WEIGHT FRACTION

shield system weight fraction as a function of lander diameter m/C_{DA} and entry angle α ,

$$\frac{W_{HS} + W_{ST}}{W_E} = K_1 (D)^{(0.3)} (m/C_{DA})^{-0.8}$$

where

D = Lander diameter, inches.

m/C_{DA} = Ballistic coefficient, slugs/ft²

K_1 = Constant dependent on $\gamma_{E_{nom}}$ as shown in following table.

$\gamma_{E_{nom}}$	$= K_1$
-40	0.029
-60	0.024
-90	0.022

6.4 SHAPE MODIFICATION EFFECTS

In the initial preliminary design studies, it becomes apparent that the required center of gravity location for the Apollo shape (rearward entry center of pressure location) would be difficult to obtain, coupled with the large stroke requirements required by the impact attenuation system. Therefore, some modifications in the Apollo shape would be required to relax the center of gravity constraint. Among the shape modifications considered, as presented in figure 9, only the afterbody extension and afterbody cone angle decrease seem practical at this time, due to lack of aerodynamic performance data on the other shape modifications.

In the latter case, afterbody cone angle decreases from the Apollo 33 degrees cone angle, if the change in cone angle is quite small (less than 5 degrees, would not greatly affect the parametric results, since the use of beryllium would most likely be limited to minimum gage. In the final conceptual design the cone angle only changes by 33 to 30 degrees, which results in approximately a 10 percent increase in surface area or ~ 10 percent increase in afterbody weight. If, however, a large decrease in cone angle is required, then an evaluation of the aerodynamic heating on the afterbody would be required and parametric studies conducted on afterbody weight fractions. Time did not permit this type of an evaluation in this study.

Referring back to the afterbody extension modification it is obvious that an extension of ΔX at the maximum diameter would result in a large increase in the weight fraction because of two reasons (a) higher heat and pressure loading, thus large heat shield and structural weights and (b) large surface area. However, the aerodynamic performance increases significantly and the center of gravity moves back approximately $\Delta X/2$, which greatly relieves the center of gravity constraint.

The effects of an afterbody extension were evaluated and are presented in figure 72. This figure was generated for 90-inch diameter vehicle combining the worst-worst conditions of heat shield and structural design. (i.e., -90 degrees G atmosphere structure, -20 degrees, K atmosphere heat shield.) The afterbody was extended by elements ΔX equal to 0.2D and 0.5D. Note that a 15 degree cone angle was used in these designs. This resulted from the restriction of the surveyor shroud envelope which is also 15 degrees. Using a cylindrical element would reduce the maximum lander diameter (i.e., E-5 shape) and hence, would reduce the lander weight for a fixed $m/C_D A$. For the 15 degree conical element extension, an ablator heat shield - aluminum substructure design had to be employed due to the high heating experienced at this cone angle.

Comparison of the results presented in figure 72 clearly indicates a severe weight penalty by adding an extension to the afterbody. The afterbody extension approach to the center of gravity problem appears not the way to go unless a significant increase in entry performance can be obtained such that it will outweigh the weight penalty in heat shield system.

6.5 CONCEPTUAL DESIGN ANALYSIS

As the result of the parametric evaluation study it was concluded that Avco-5026-aluminum honeycomb structure forebody and beryllium afterbody design yielded the minimum weight heat shield system, providing rf transparency requirements are not necessary. In the conceptual design synthesis, section 1.0, the use of rf transparent heat shield system was eliminated in order to meet the mission payload requirements. Thus, the above heat shield system will be considered as the conceptual design.

In the following sections, this design will be evaluated employing a more rigorous approach than was used in the parametric study. The attempt here will be to determine the degree of accuracy and to improve the parametric result. The analysis will still be limited to a cursory evaluation rather than a detailed analysis since a detailed design was not the objective of the conceptual design study. Each of the major subsystems, heat shield (ablator or heat sink) and substructure, will be analyzed employing the most refined analytical approach feasible. In all analyses, the results of the parametric design will be used as the bases for comparison.

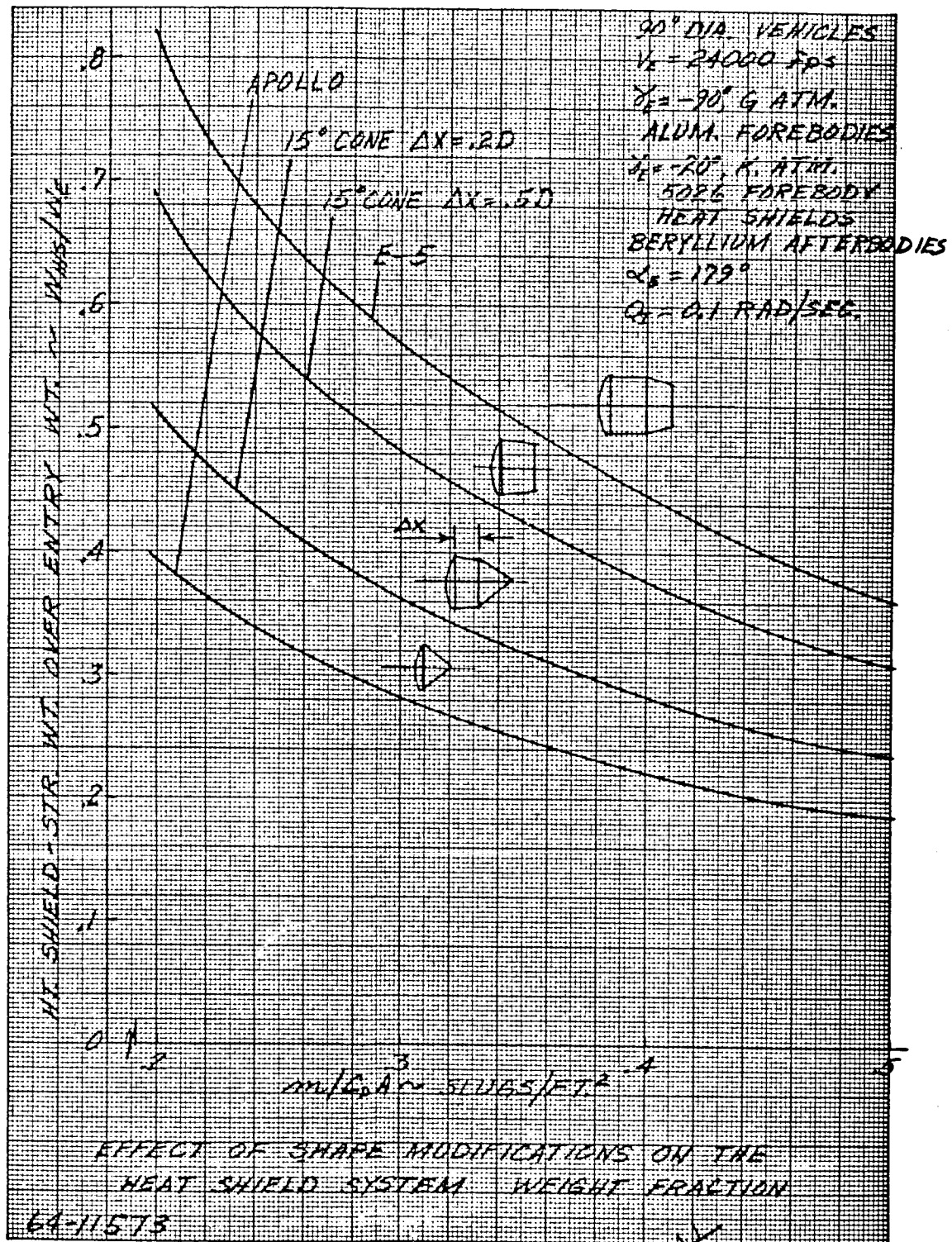


Figure 72 EFFECT OF SHAPE MODIFICATIONS ON THE HEAT SHIELD SYSTEM WEIGHT FRACTION

1. Heat Shield Analysis

In the parametric evaluation analysis, the heat shield was analyzed using the digital computer program in reference 2. This program is limited in its approach to the analytical model due to the constraint on computation time. A more rigorous analytical program is available which uses a more exact heat shield model but still is limited to a numerical solution. Using this program, the heat shield (Avco 5026) was analyzed as a function of back face temperature (T_R). The heating load used in this analysis was generated considering the final conceptual design parameters;

$$m/C_D A = 0.25 \text{ slugs/ft}^2$$

$$V_E = 21,500 \text{ ft/sec}$$

$$\alpha_E = 179 \text{ degrees}$$

$$\gamma_E = -52 \text{ degrees min.}$$

$$D = 90 \text{ inches}$$

The heating load analysis is presented in section 5.6.

In figure 73 the results of the heat shield analysis are presented. This curve presents the back face temperature (rear, T_R) as a function of heat shield thickness. Comparing this result at $T_R = 600^\circ\text{F}$ and $t_{HS} = 0.17$ inch to the parametric study (figure 63) at $m/C_D A = 0.25$ and $\gamma_E = -52$ degrees, we find $t_{HS} = 0.23$ which indicates a considerable amount of conservatism in the parametric analysis (~ 30 percent). This is attributed to several pertinent influences; 1) decrease in entry velocity from 24,000 to 21,500 ft/sec, 2) increased aerodynamics performance (as evident in section 4.4) due to decreased moments of inertia by a factor of two over parametric study which resulted in low angle of attack history and reduced heat load, and 3) more exact analytical heat shield model, primarily in the method of adjusting for the structural capacitance. However, it was felt that the degree of conservatism should be left in the parametric study due to the uncertainties in how this material will behave under an unknown atmosphere.

Finally, a temperature history analysis was conducted on the beryllium hot structure afterbody. The results of this analysis are presented in figure 74 for two beryllium thicknesses. It is evident that the thickness will not be dictated by the heating pulse since beryllium is capable of 1500°F max temperature and the highest temperature with 0.020 thickness (min. gage) is $\sim 800^\circ\text{F}$ which also supports the conclusion of the parametric study.

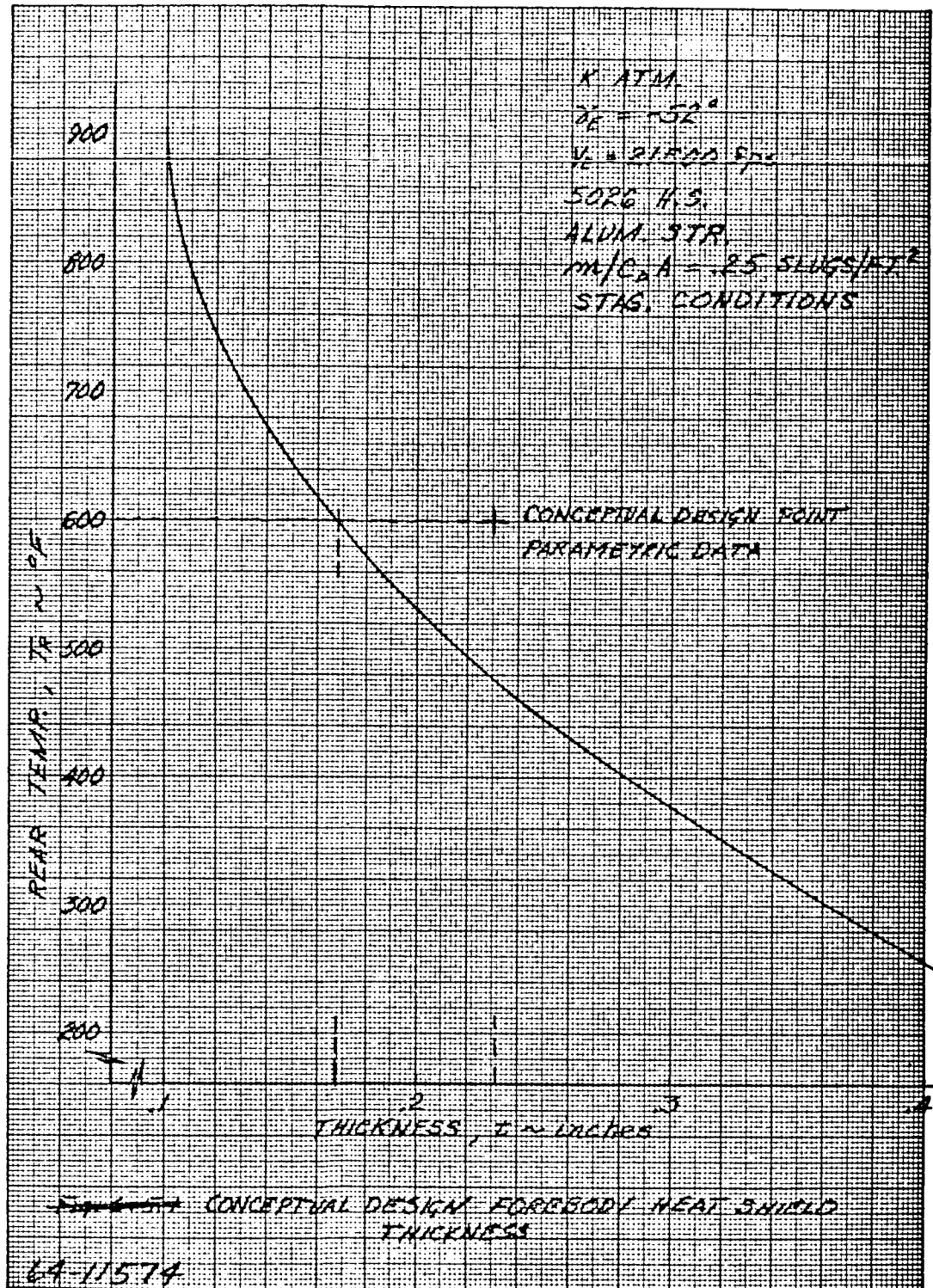


Figure 73 CONCEPTUAL DESIGN FOREBODY HEAT SHIELD THICKNESS

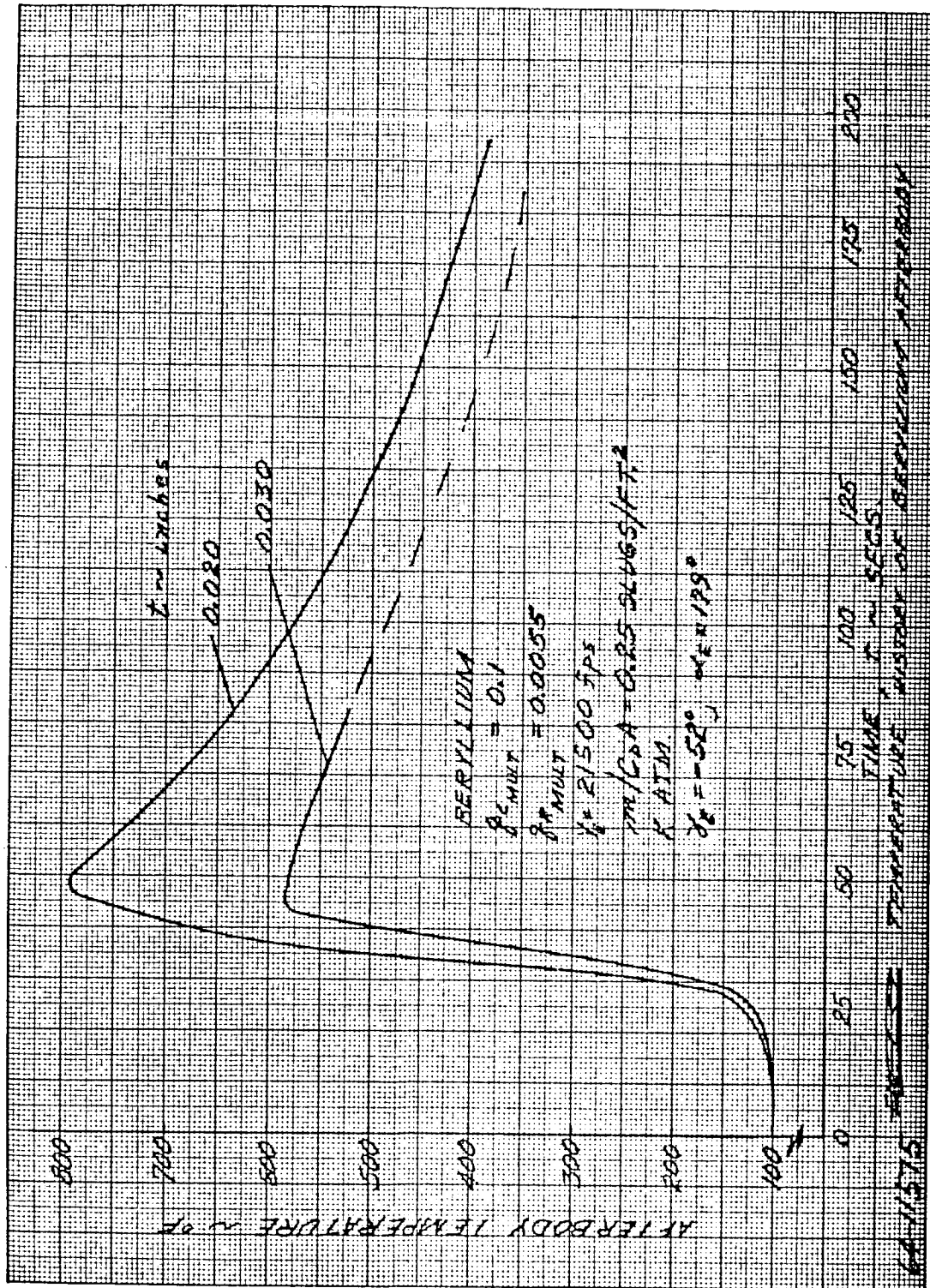


Figure 74 TEMPERATURE HISTORY OF BERYLLIUM AFTERBODY

2. Aluminum Honeycomb Forebody Analysis

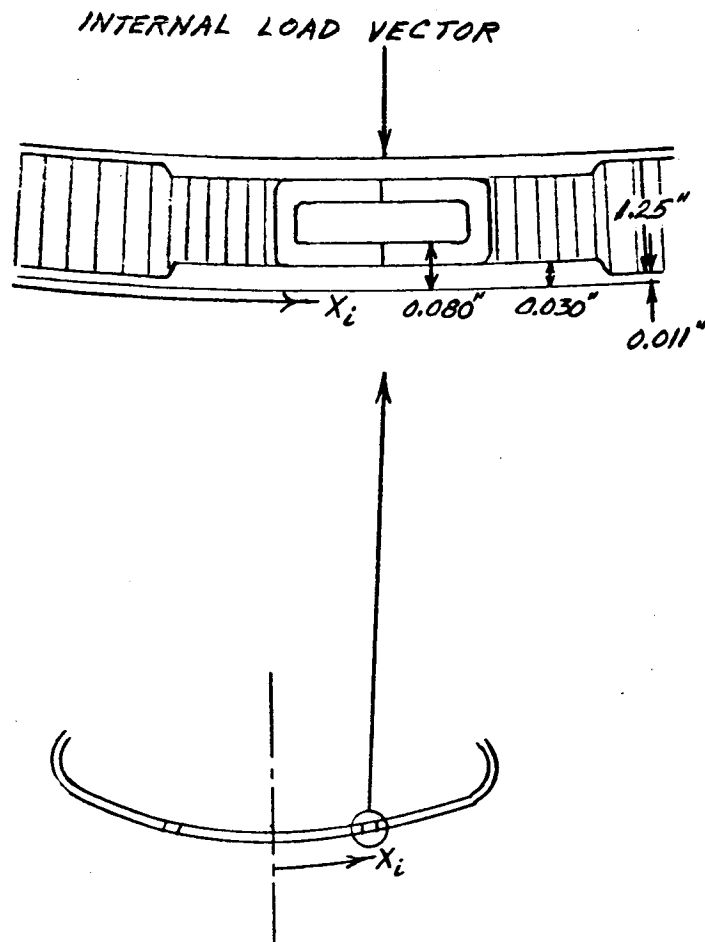
The initial emphasis in the conceptual design of the forebody was given towards preventing the elastic buckling of the composite shell as a shallow spherical cap. This was accomplished by designing the facing sheets of the honeycomb structure to withstand the peak membrane forces and then, selecting a core depth which would prevent general instability of the composite structure.

Although this study was preliminary in nature, it did serve several useful purposes. First, it provided a means for assessing a primary mode of failure which would influence, or perhaps, even govern the final design of the structure. Secondly, it provided for an initial sizing of structure and subsequently, led to a first estimate for the residual weight of the composite. This estimate permitted detailed calculations to be performed on the inertial forces acting on the structure and moreover, allowed for parametric studies to be conducted on the effects of axial and bending stresses associated with support ring.

The results of one such study on the effect of payload attachment is given in the subsequent sections. The major purpose for presenting these results is to indicate the relative magnitudes of the peak axial and bending stresses, and further, to insure that the design configuration selected for the Mariner mission is structurally adequate to sustain these stress levels.

Before proceeding with a general description of the results, it is worthwhile mentioning that the analysis is based on an existing shells program. The equations utilized in the program are based on the formulation of the first order, linear theory of elasticity. The computer program is used to solve for the elastic strains, stresses, and displacements for a multilayered, multiregion orthotropic shell of revolution subjected to rotationally symmetric surface loads and temperature distributions. Both the loading and temperature distributions are arbitrarily varied along the meridian of the shell with the temperature also varying radially. Shell thicknesses can be varied along the meridian and material properties allowed to be temperature dependent.

Figure 75 gives a graphical illustration of the details for the final forebody design which consists of a shallow spherical cap intersecting a toroidal corner. The thickness of the facing sheets remains constant except in the region of the support ring where the thickness is increased significantly. The reason for this increase is to provide a means for distributing the inertial forces at lower stress levels and, also, to aid in minimizing any large shear deformation effects which might occur. For purposes of programming, the shell structure was subdivided into 15 regions along the meridian, and into three layers through the depth. The inner and outer layers of the composite consisted of aluminum 7075-T6 facing sheets with a modulus of elasticity



64-11576

Figure 75 FOREBODY STRUCTURAL THICKNESS IN THE AREA OF THE SUPPORT RING

of 10×10^6 psi. The central layer, or core, was considered to be an aluminum honeycomb which held the facing sheets at a fixed depth, but one which had a negligible effect on the bending rigidity of the shell.

In the present investigation, the shell structure was considered to be at zero-angle of attack and subjected to a Newtonian pressure distribution applied over the spherical segment. The pressure distribution at the toroidal corner was obtained from wind-tunnel simulation tests and varied from the Newtonian value at the sphere-torus intersection to zero at the junction of the aft-and forebody.

The results obtained from the computer program are plotted in figures 76 to 78 as a function of the surface coordinate, X_i , measured along the meridian of the shell. In figure 76, the inner and outer fiber meridional stresses are shown; figure 77 depicts the circumferential stresses at the two extreme surfaces; figure 78 shows the variation of the displacement, u , directed parallel to the axis of revolution and measured from the undeformed position, and w , which is directed normal to the axis of revolution and is also measured from the undeformed position. In all instances, the results have been normalized to a one-g loading condition. (In the conceptual design $G_{MAX} = 110$, $\gamma_E = 90^\circ$, G-atmosphere).

From an inspection of figure 76 it is observed that the inner, meridional fiber of the honeycomb shell is in tension at the pole of the spherical cap. This tension diminishes rapidly as one proceeds from the pole until a maximum compressive stress is reached just prior to the increase in facing sheet thickness. Within the region where the thickness has been substantially increased, the stress level is lowered but still remains compressive in nature. The meridional stress continues to be compressive for a small distance outside this region and then reverts to a tensile state with a maximum peaking at the sphere-torus intersection.

It is of interest to note that the sharp rises and drops in the stress level at the support ring are attributed to the abrupt changes assigned for the thickness of the shell. A more consistent design would, of course, have a gradually tapering thickness such that the stress would flow uniformly across the region and, thus eliminate any sharp, localized changes. Another point of interest relates to the small compressive level of stress which exists at the intersection of the fore and afterbodies. It is briefly mentioned that the existence of the compressive stress is due to the support conditions assumed for the present investigation. That is, the honeycomb structure was taken as simply supported at the junction. This condition permitted arbitrary movement of the shell in the radial direction by insuring that the meridional moment and shear were identically equal to zero. Consequently, the only force acting on the shell cross-section at the junction was a uniform compressive axial thrust which represents the unbalance between the pressure loading and the reactive inertial forces.

145

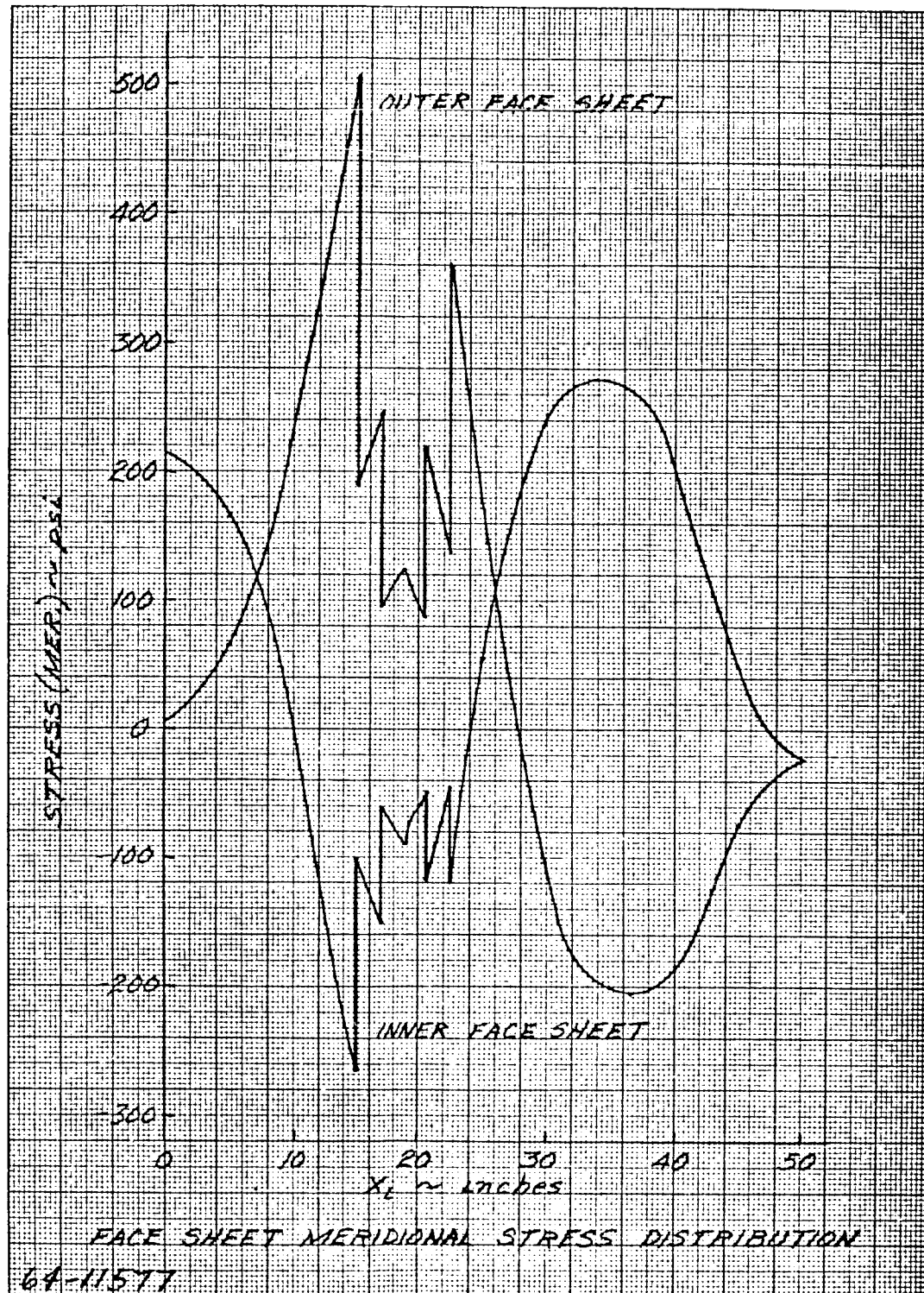


Figure 76 FACE SHEET MERIDIONAL STRESS DISTRIBUTION

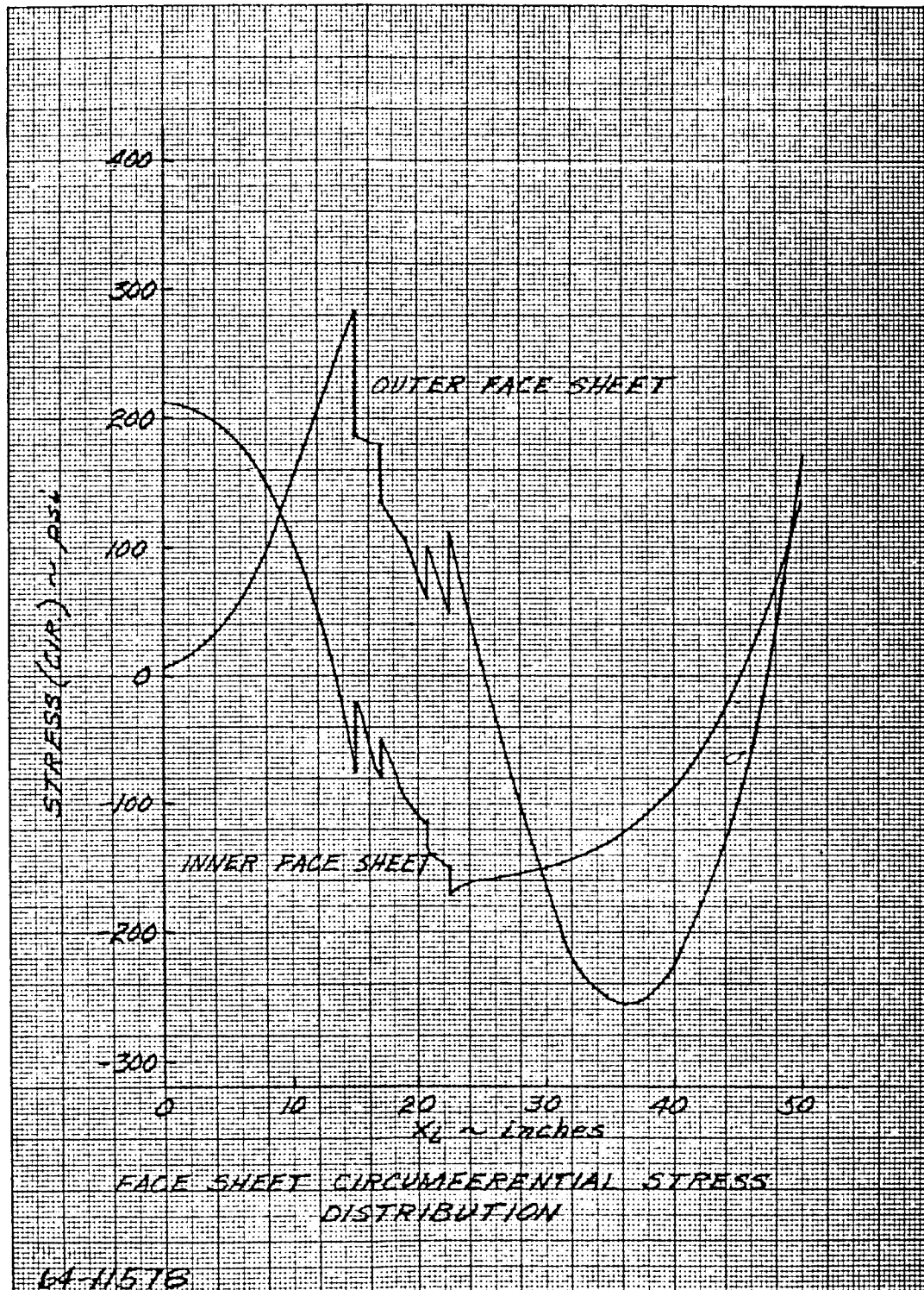


Figure 77 FACE SHEET CIRCUMFERENTIAL STRESS DISTRIBUTION

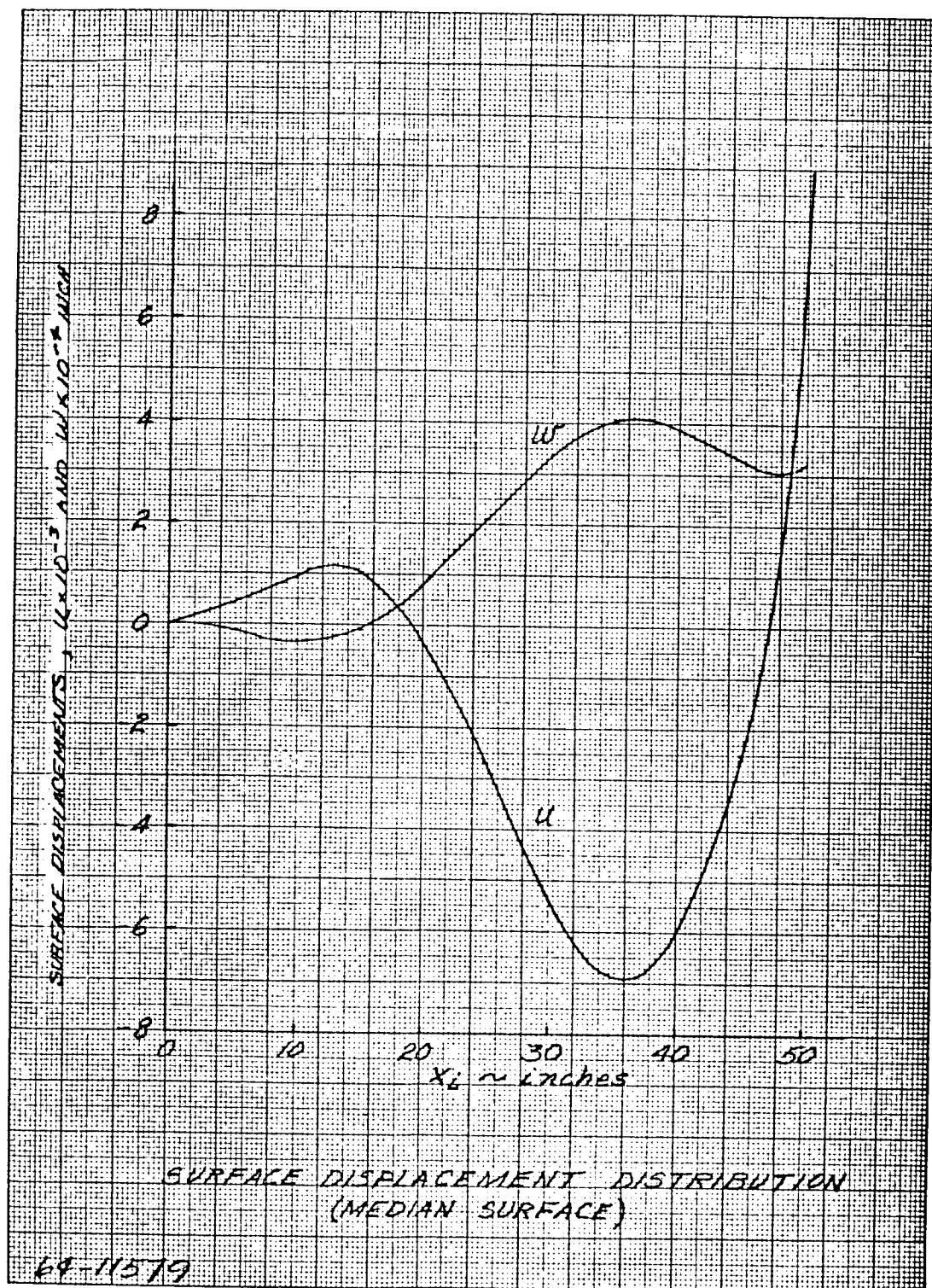


Figure 78 SURFACE DISPLACEMENT DISTRIBUTION (MEDIAN SURFACE)

The gross behavior for the meridional stress at the outer fiber is also shown in figure 76. The behavior essentially represents the same type of behavior as the inner layer except that the present curve is inverted and translated.

The reason for the inversion is due mainly to the change in sign of the bending movement, whereas the translation accounts primarily for the variations in the axial stress. This result was expected and led to a maximum compressive stress of 500 lb/in^2 . Based on the expected 120 g loading for the Mariner mission, it is seen that the maximum stress level becomes $60,000 \text{ lb/in}^2$. This level is well within the yield limit range given for 7075-T6 Aluminum.

In figure 77 are shown the inner and outer circumferential fiber stresses. The only significant point worthwhile mentioning here is that the effects of the abrupt thickness changes are considerably dampened. Also, in the vicinity of the assumed simply-supported boundary, both the inner and outer circumferential fiber stresses remain in tension, indicating that the surfaces are undergoing stretching at the support.

Figure 78 shows the magnitudes of the displacement, u , which is directed parallel to the axis of revolution and considered positive when directed outward. The pole of the spherical cap is taken as a reference point of zero displacement. As shown, the displacement is directed outward up to the point where the payload attachment load is acting, i. e., $X_i = 19$ inches. At that point, the displacement is approximately equal to zero and then, continues to be directed inward for small distances past the sphere-torus intersection. In the subsequent region, the median surface of the shell is displaced outwardly and reaches a maximum value at the boundary.

The peculiar behavior of the displacement at the payload attachment ring is attributed to the fact that the external force system is completely balanced at that point. This condition permits only a uniform, radially expansion of the ring.

In figure 78 the displacement, w , is shown plotted as a function of the meridional surface coordinate, X_i . This displacement represents the amount of expansion or contraction of the shell element, normal to the axis of revolution. The sign convention adopted for the present study is positive for expansion of the element and negative for contraction. Again, the pole of the spherical cap is taken as a fixed reference.

As seen from an inspection of the graph, a large portion of the shell's median surface is undergoing extension. This is true even in the vicinity of the payload attachment load. The only contractive areas which exist occur in the region near the pole of the spherical cap. Also, note that the

maximum extension of the shell occurs just prior to the junction of the sphere and torus.

In summary, it is remarked that the present analysis has demonstrated some of the displacement characteristics and stress levels which are to be expected in the Mariner forebody. In addition, the study has clearly indicated that additional thickness increases are only required in the vicinity of the payload attachment load. For distances slightly removed from the application of the load, the stress levels are reduced considerably and are adequately sustained by the shell thickness and core depth obtained from elastic stability analyses. The weight increase due to the additional structure in the vicinity of the payload attachment has been adequately taken account of by the 1.7 factor which has been applied to the basic structural weights in the parametric study.

REFERENCES

1. Harulan, P. N. and D. Joslyn, JPL Inputs to Avco Study Contract 950896 (8 May 1964).
2. RAD, Mars-Venus Capsule Parameter Study, Avco-RAD-TR-64-1, JPL Contract 950626 (21 March 1964).

7.0 DESCENT SYSTEM

Several parachute systems were investigated using one or two chutes. The results presented herein are parametric curves which permit rapid estimation of a descent system weight for specific design conditions. The goal of the parametric evaluation was to optimize suspended weight (payload plus impact system) as a function of ballistics coefficient, main chute deployment altitude, nominal entry angle, and impact velocity. All of the suspended weight curves reflect incorporation of heat shield and structure weights which were designed for particular nominal entry angles.

One should note that in order to calculate the main parachute system weight it is essential to know the weight of heat shield and structure since they are jettisoned at main chute deployment. Both of these weights are highly dependent upon entry angle while interplanetary trajectory analysis has indicated that a 3σ dispersion (see Systems, volume I, 3.1.2) is possible on the nominal entry angle. Hence, the parachute design must include heat shield and structure weights based on this dispersion. Listed below is a table of heat shield and structure design entry angles for various nominal entry angle trajectories.

(γ_e) Nominal (degrees)	Heat Shield Design Entry Angle	Structure Design Entry Angle	Parachute Trajectory Design
90	75	90	90
60	47	73	73
40	21	59	59

The basic weight components of the lander are expressed as follows:

$$W_E = W_D + W_{H/S} + W_S + W_{MC}$$

where

W_E , gross entry weight

W_D , drogue chute system weight

$W_{H/S}$, heat shield and structure weight

W_S , suspended weight (payload + crushup)

W_{MC} , main chute system weight

The primary objective of this parametric study is to obtain the optimum ballistics coefficient and/or suspended weight. Hence rearranging the above expression for suspended weight we find that

$$W_S = \frac{W_E - W_{H/S} - W_D}{1 + \frac{W_{MC}}{W_S}}$$

On figures 79 through 84 is shown trajectory data relating altitude, dynamic pressure, and ballistics coefficient.

All of the parachute trajectory analysis presented herein are evolved from a three degree of freedom compute program. The drag coefficient of both the vehicle and the parachutes are combined and utilized in such a way as to predict the correct trajectory from entry to impact.

7.1 DROGUE CHUTE ANALYSIS

A Hyperflo type drogue chute was selected as the reference design based on its good stability and drag characteristics at the desired deployment Mach numbers. A nominal deployment of Mach 2.5 was chosen in order to leave enough leeway in the actuation system to accommodate variations due to entry angle and atmosphere uncertainties while remaining within fabric temperature and loading limitations.

The drogue chute trajectory data shown on figures 85 through 92 assume drogue chute deployment at the indicated Mach number and main chute deployment at Mach 0.8. The curves presented demonstrate the required drogue area/vehicle area ratio such that for a given m/CDA the vehicle will decelerate to Mach 0.8 at a given altitude. The trajectory curves utilize an effective drag coefficient such that,

$$C_{D_{eff}} = \frac{(C_D A)_V + (C_D A)_D}{A_V}$$

where the subscripts D and V refer to drogue and vehicle, respectively. The drag coefficient of the Hyperflo chute is shown on figure 93 (these data were obtained from reference 1). For this drogue chute parametric analysis the following assumptions were made.

1. Time delay of 1.0 seconds for drogue chute opening.
2. Particle Trajectory.
3. $W_{DROGUE} = 0.11 A_{DROGUE}$
4. Deployment at Mach number as indicated.

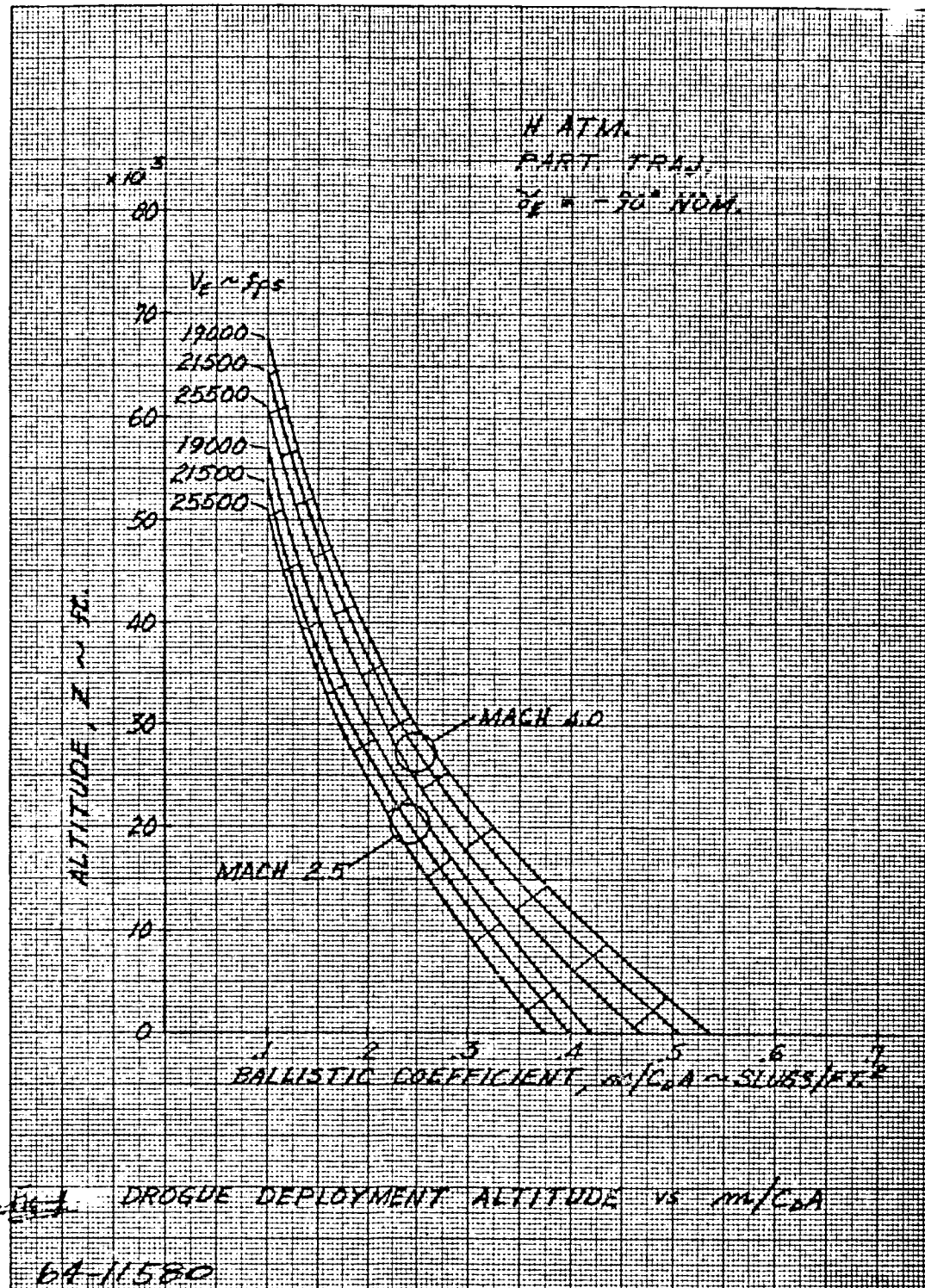


Figure 79 DROGUE DEPLOYMENT ALTITUDE VERSUS m/C_{DA}
 (γ_e OF 90 DEGREES)

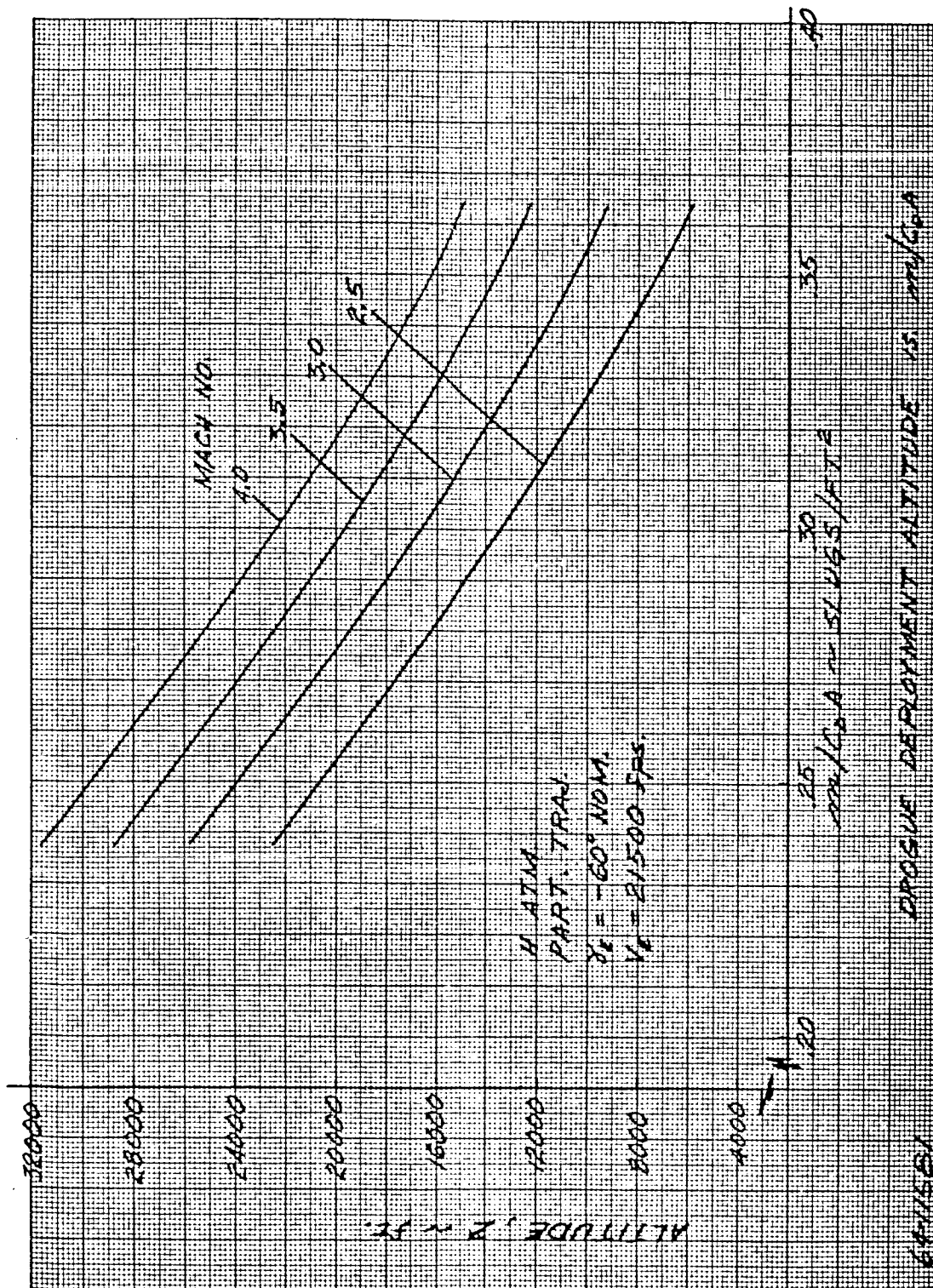


Figure 80 DROGUE DEPLOYMENT ALTITUDE VERSUS M/CD
(γ OF 60 DEGREES)

204

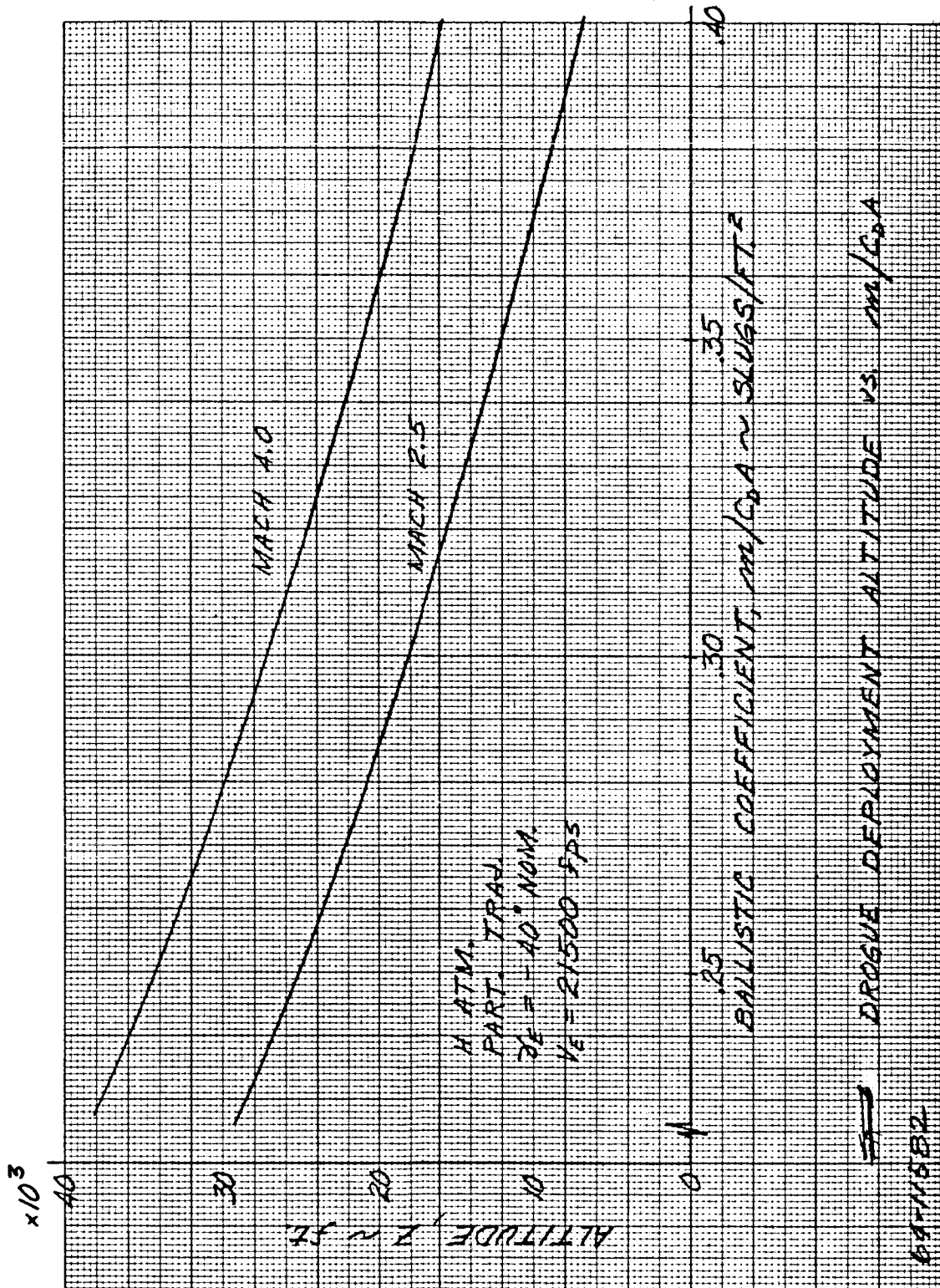


Figure 81 DROGUE DEPLOYMENT ALTITUDE VERSUS M/C_{DA}
 (γ OF 40 DEGREES)

2-05-

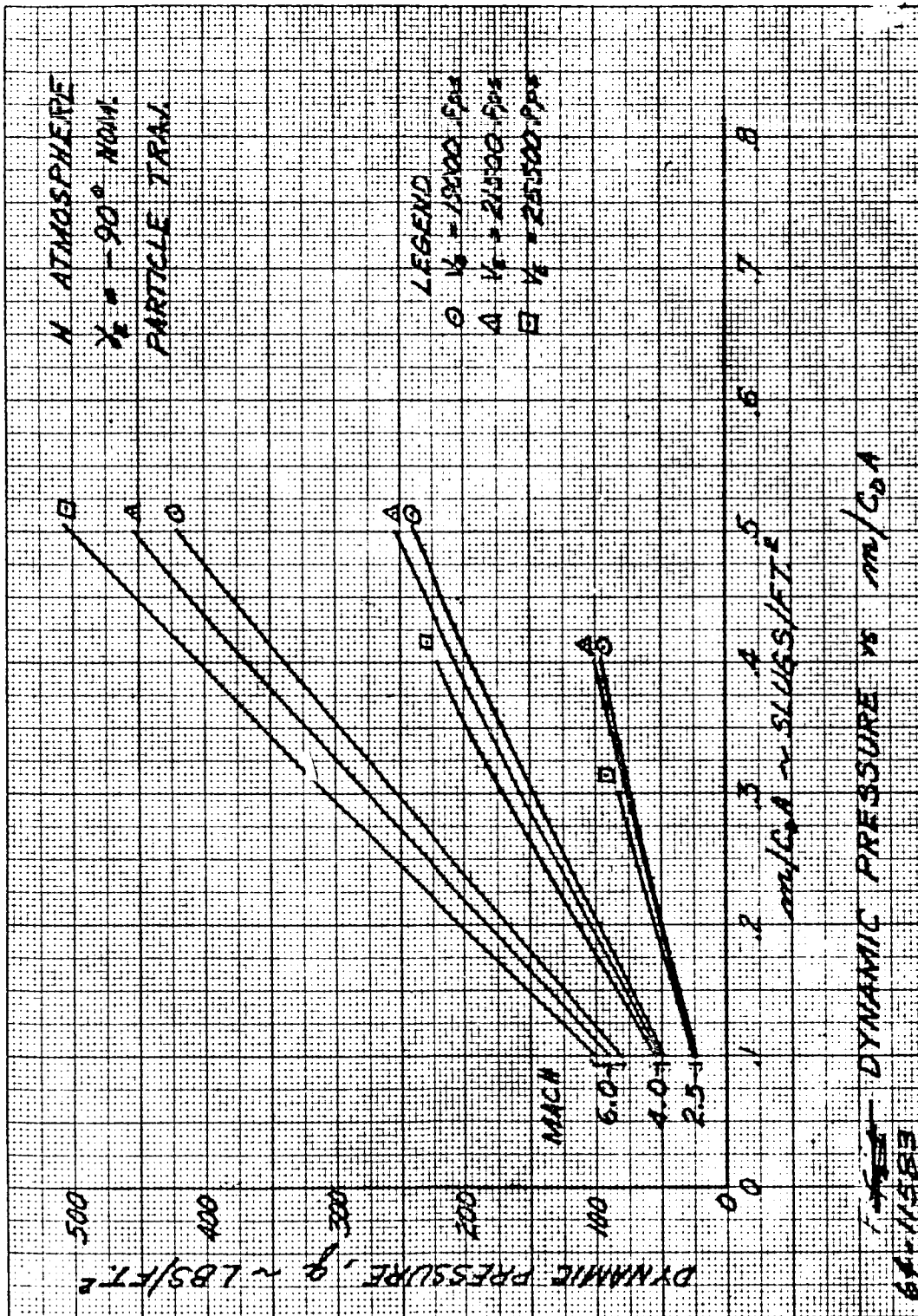


Figure 82 DYNAMIC PRESSURE VERSUS $m/C_D A$ (γ_c OF 90 DEGREES)

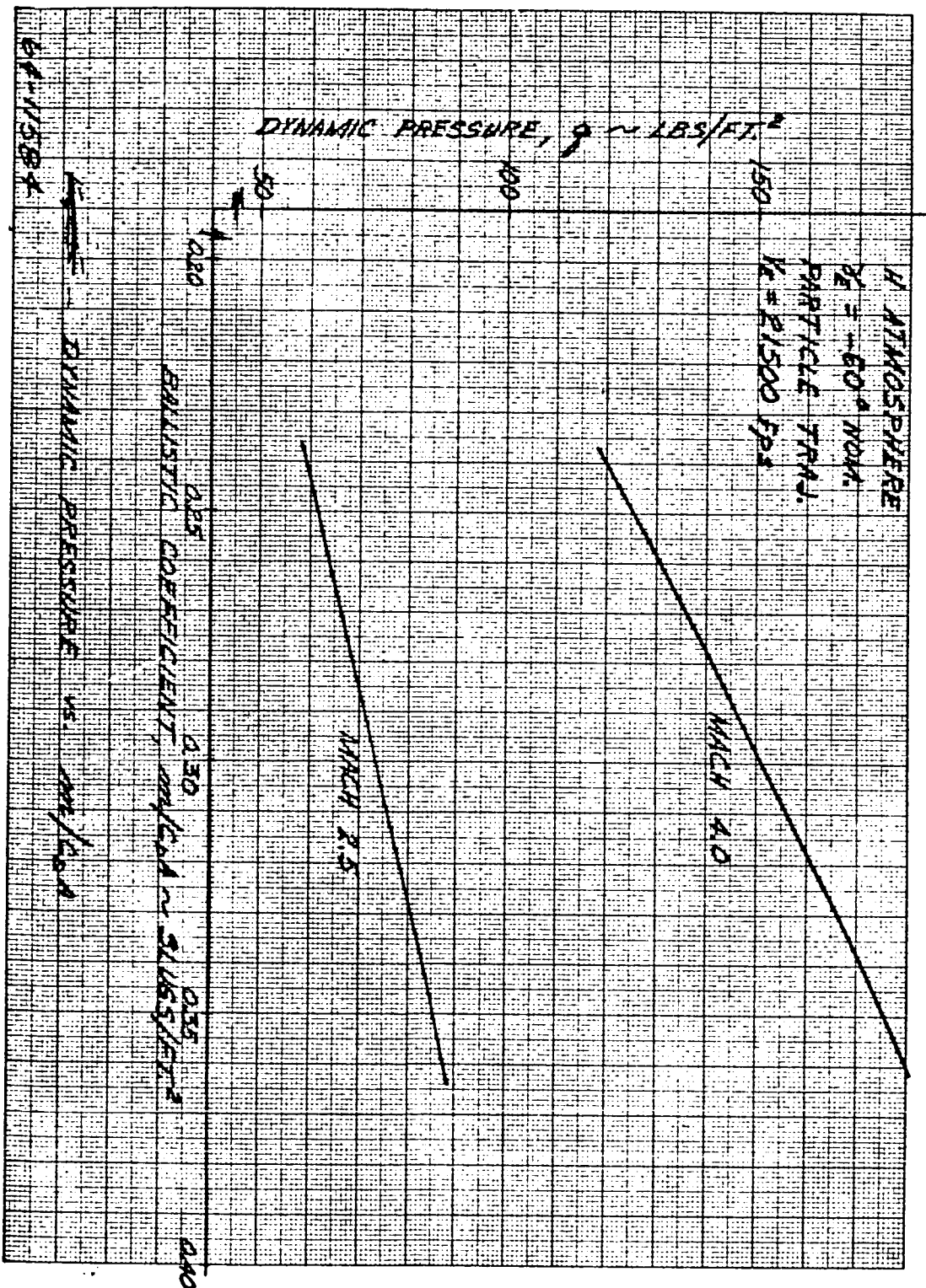


Figure 83 DYNAMIC PRESSURE VERSUS M/C_D (α OF 60 DEGREES)

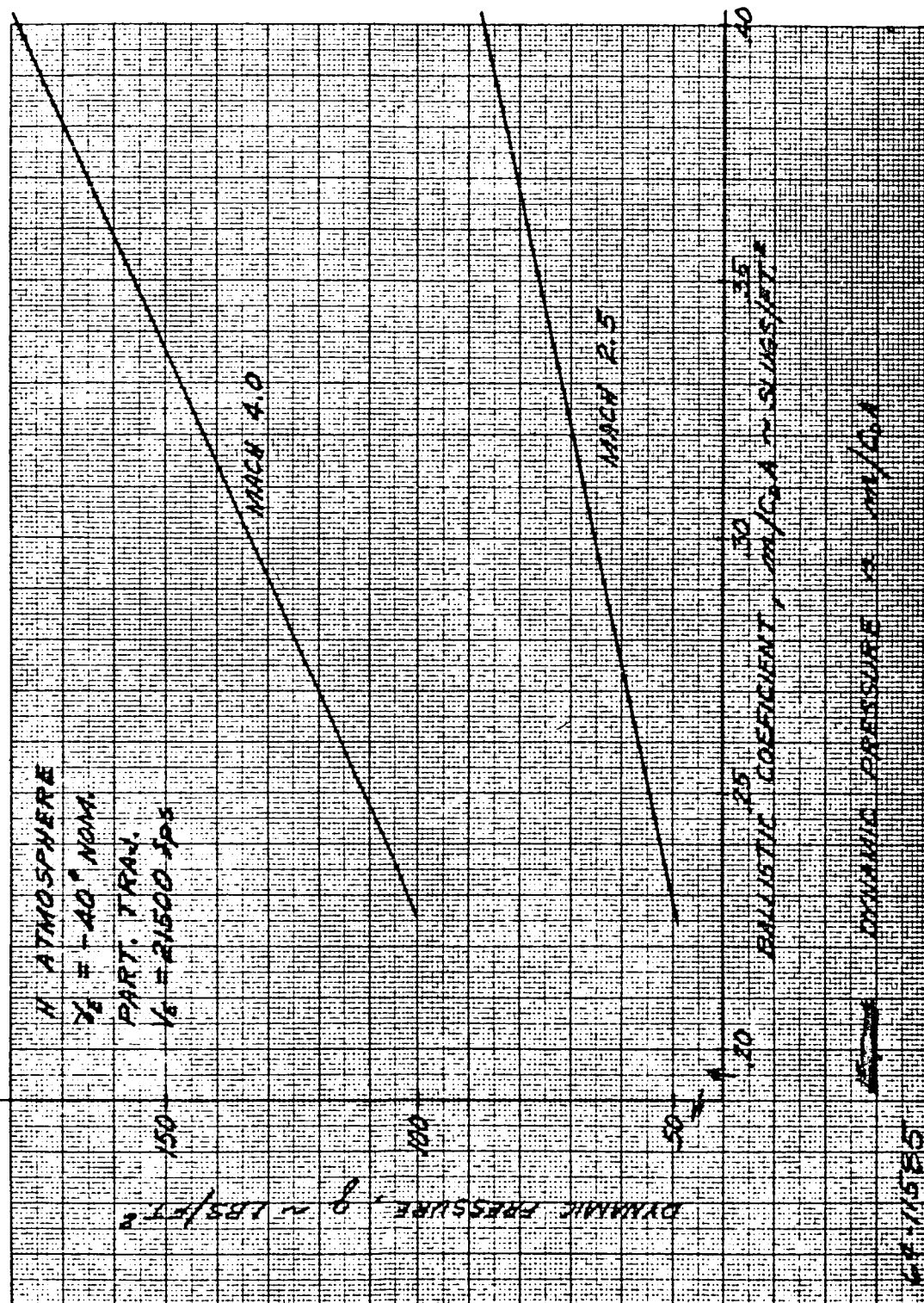


Figure 84 DYNAMIC PRESSURE VERSUS M/C_{DA} (γ_c OF 40 DEGREES)

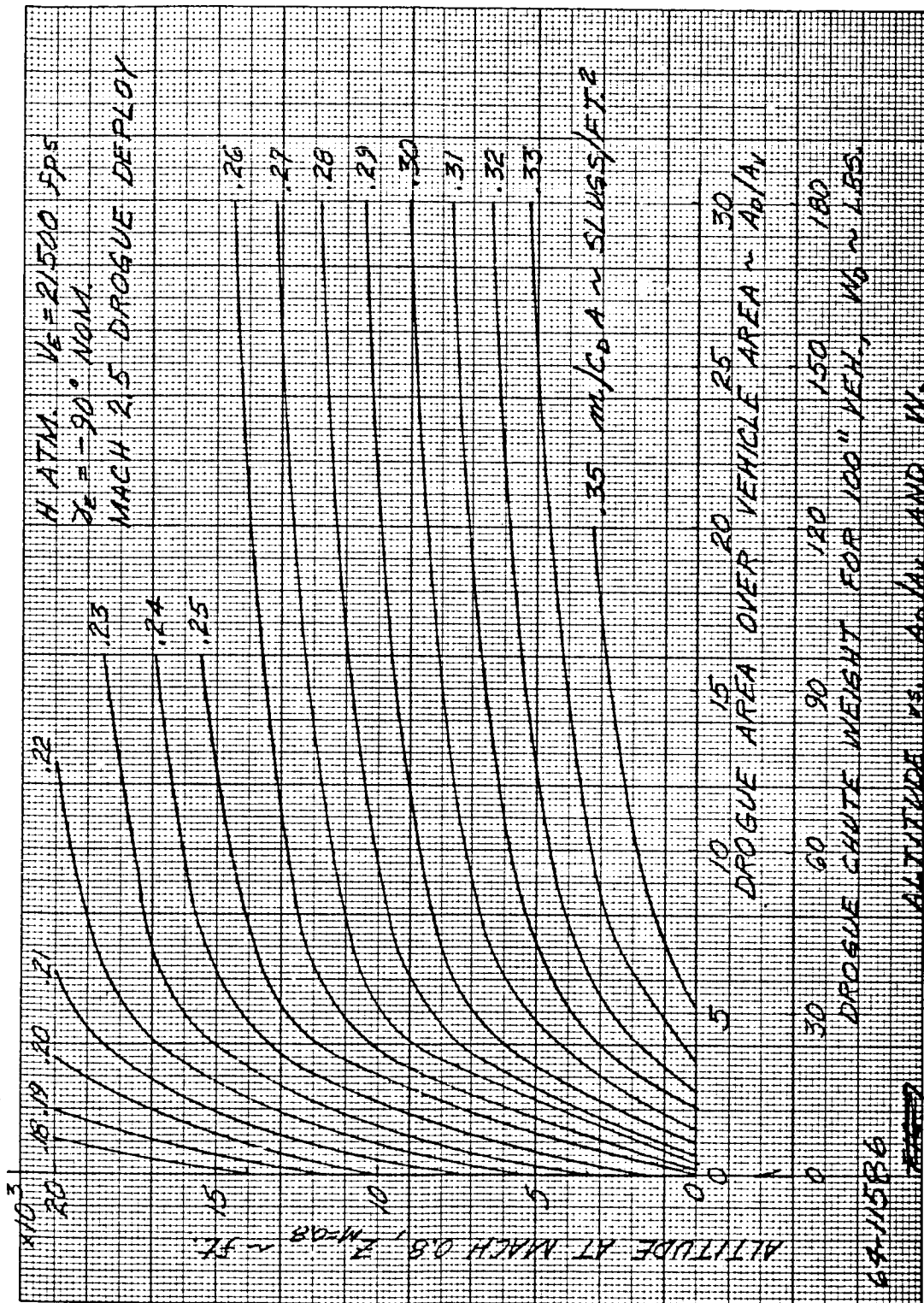


Figure 85 ALTITUDE AT MAIN CHUTE DEPLOYMENT VERSUS A_D/A_V AND W_D
(NOMINAL ENTRY ANGLE OF 90 DEGREES AND DROGUE CHUTE
DEPLOYMENT OF 2.5)

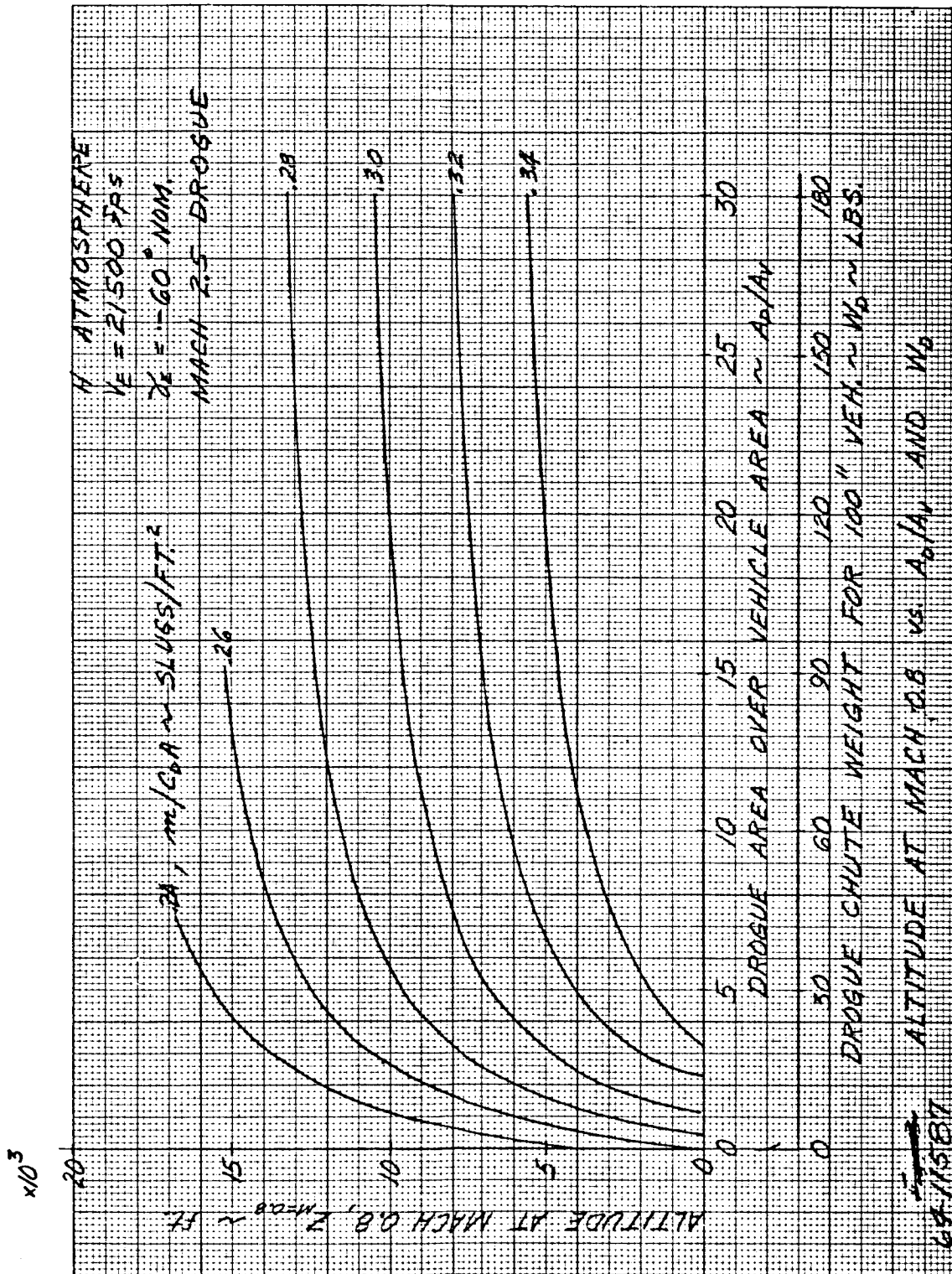


Figure 86 ALTITUDE AT MAIN CHUTE DEPLOYMENT VERSUS A_D/A_V AND W_D
 (NOMINAL ENTRY ANGLE OF 60 DEGREES AND DROGUE CHUTE
 DEPLOYMENT OF 2.5)

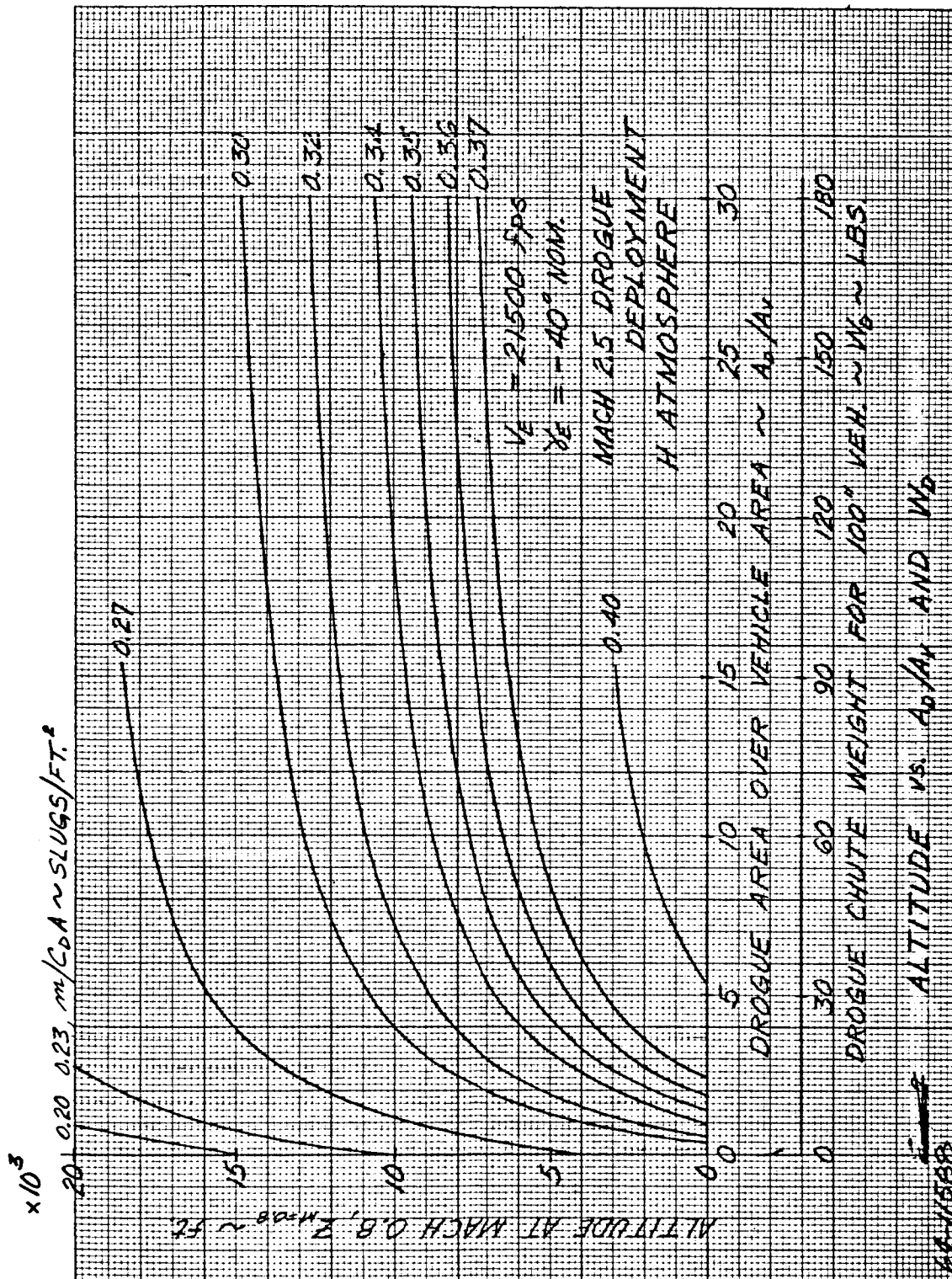


Figure 87 ALTITUDE AT MAIN CHUTE DEPLOYMENT VERSUS A_D/A_V AND W_D
(NOMINAL ENTRY ANGLE OF 40 DEGREES AND DROGUE CHUTE
DEPLOYMENT OF 2.5)

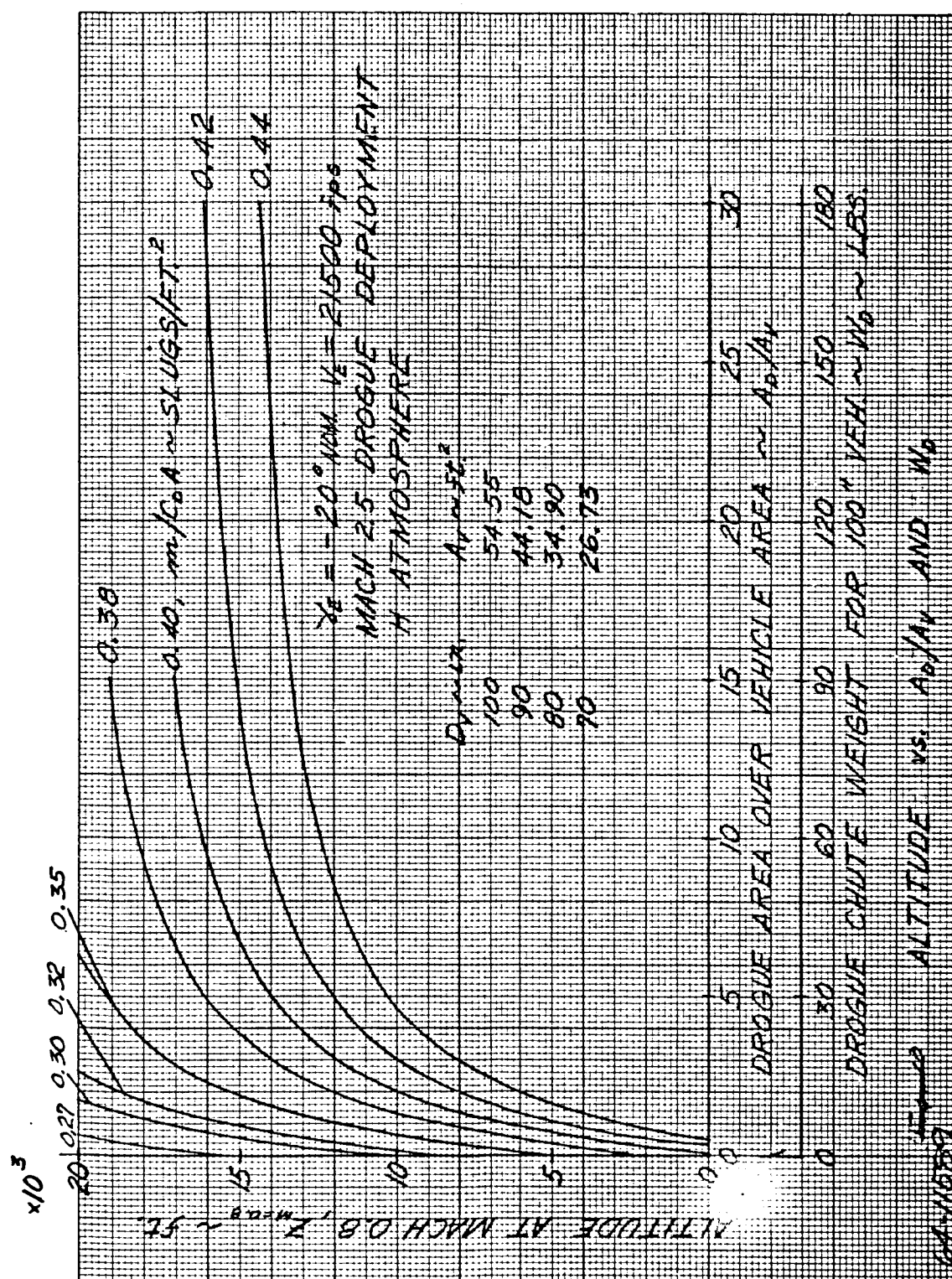


Figure 88 ALTITUDE AT MAIN CHUTE DEPLOYMENT VERSUS A_0/A_V AND W_0
(NOMINAL ENTRY ANGLE OF 20 DEGREES AND DROGUE CHUTE
DEPLOYMENT OF 2.5)

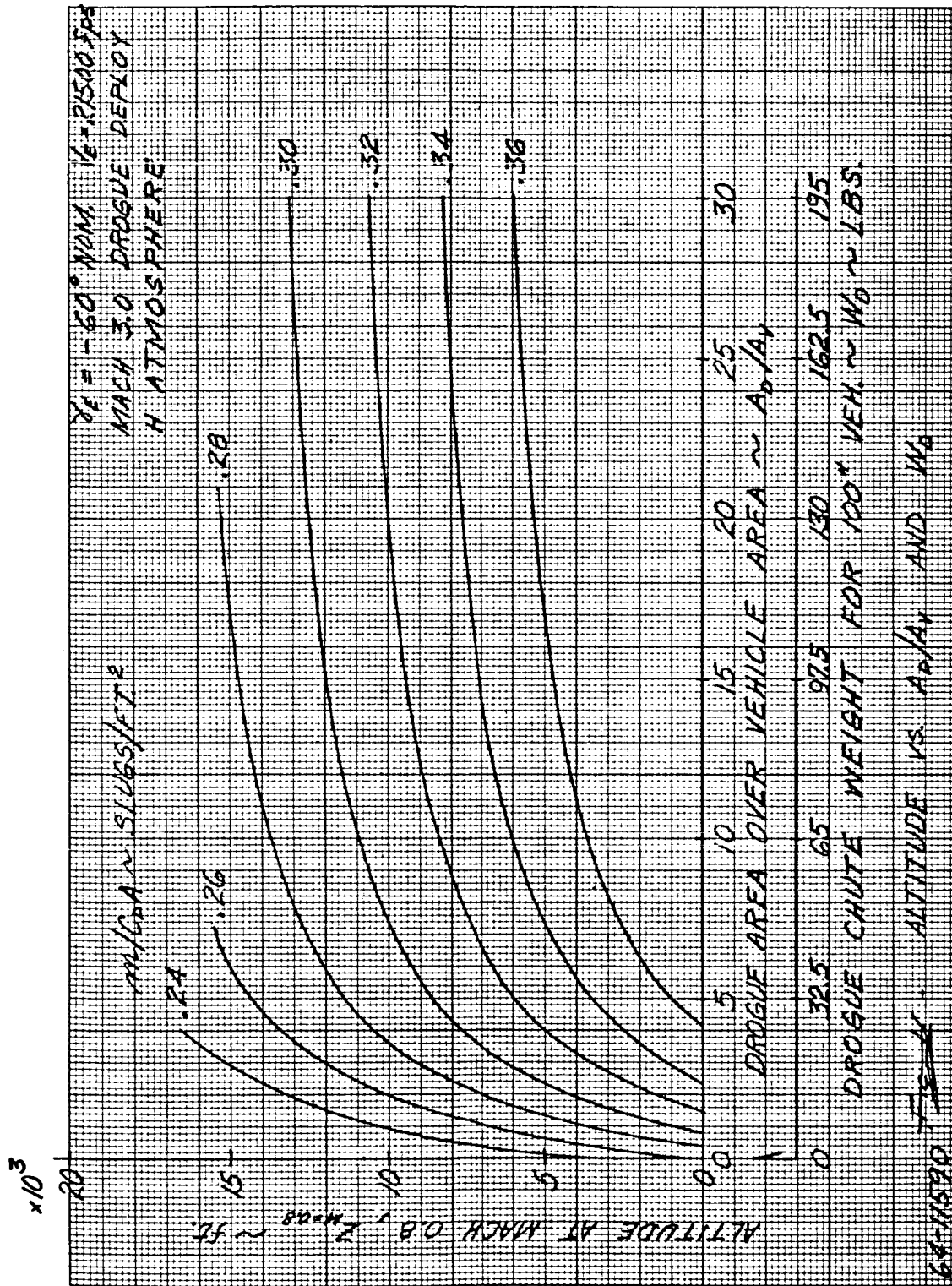


Figure 89 ALTITUDE AT MAIN CHUTE DEPLOYMENT VERSUS A_D/A_V AND W_D
(NOMINAL ENTRY ANGLE OF 60 DEGREES AND DROGUE CHUTE
DEPLOYMENT OF 3.0)

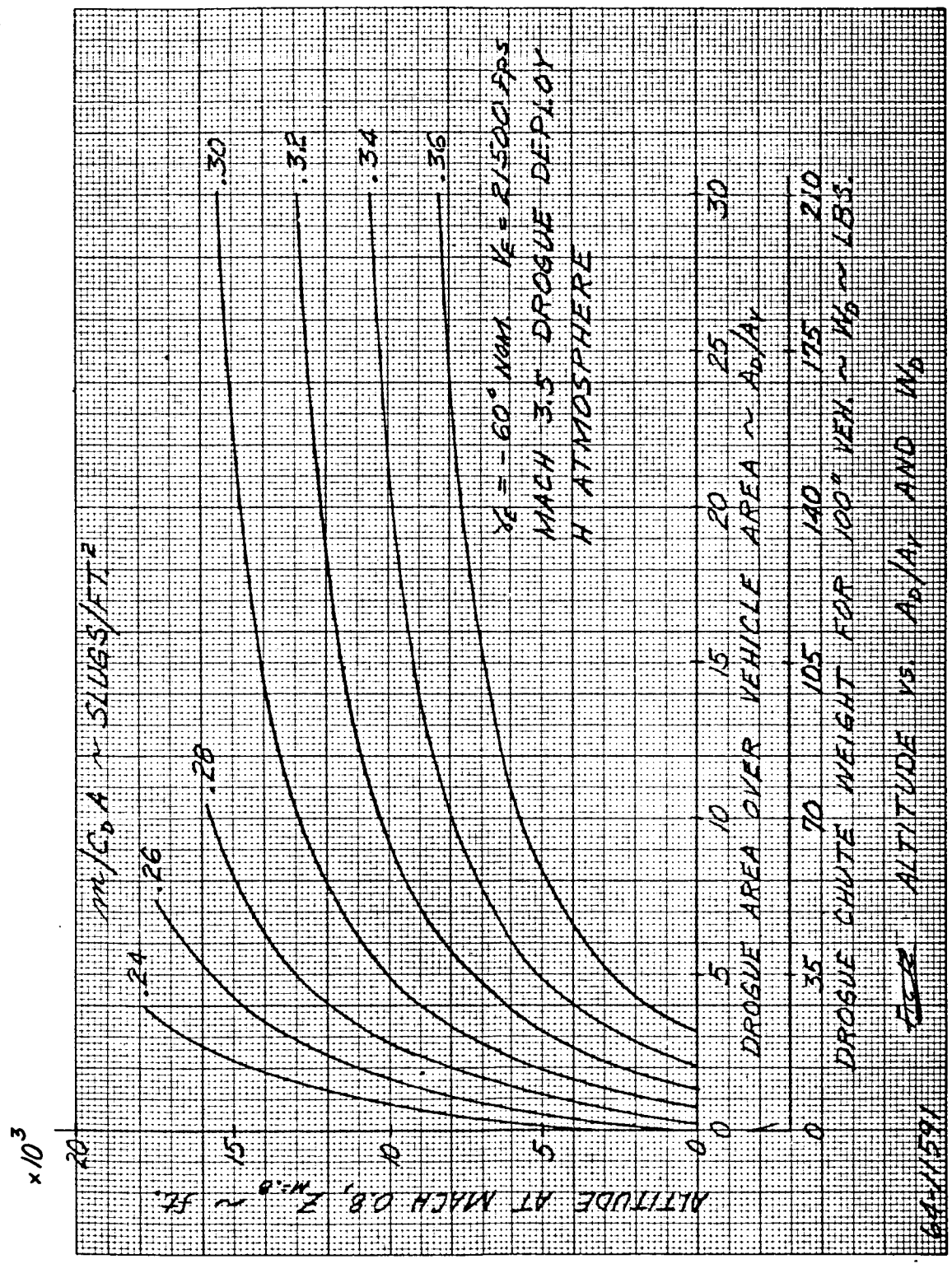


Figure 90 ALTITUDE AT MAIN CHUTE DEPLOYMENT VERSUS A_0/A_V AND W_D
(NOMINAL ENTRY ANGLE OF 60 DEGREES AND DROGUE CHUTE DEPLOYMENT OF 3.5)

214

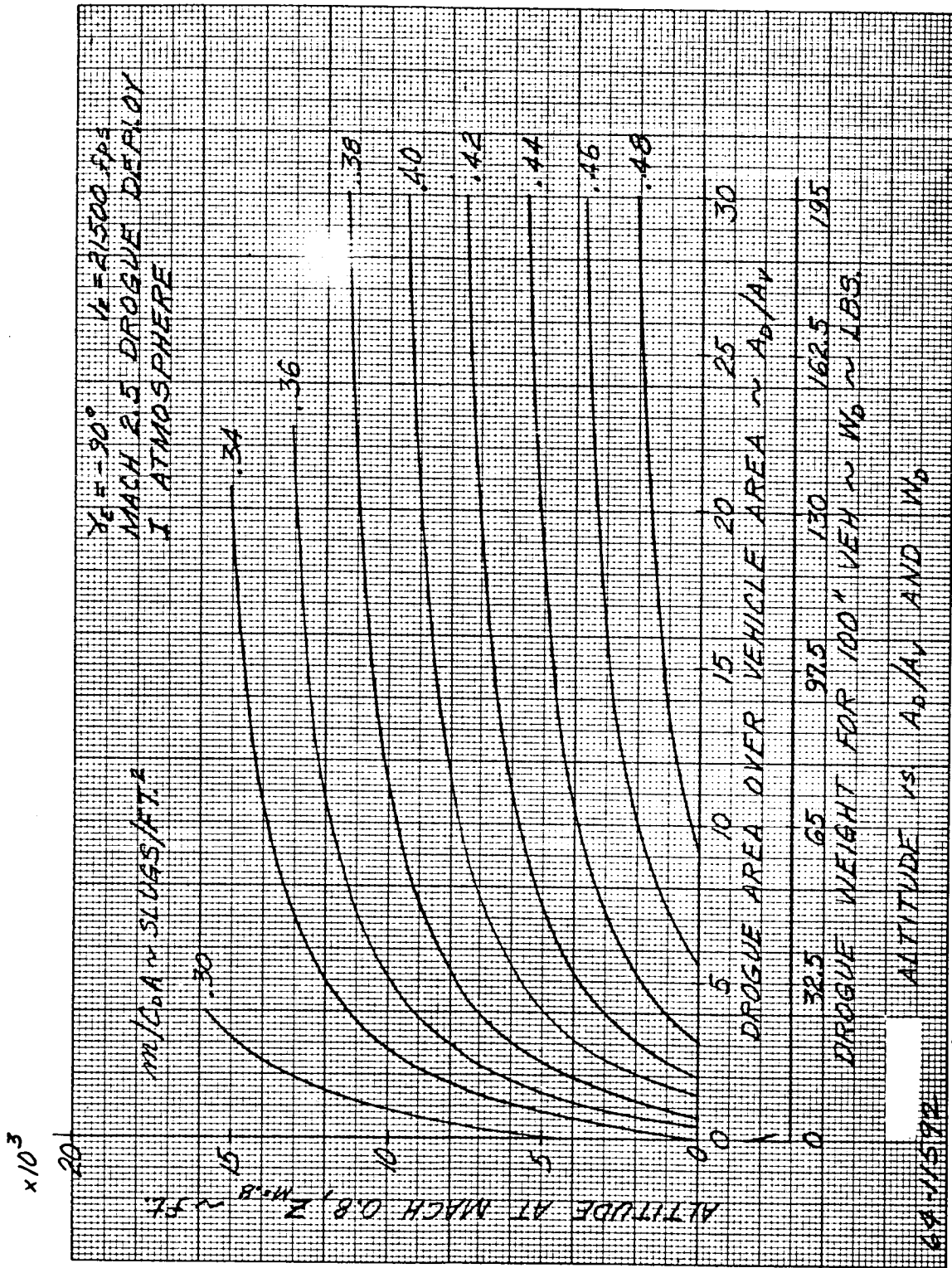


Figure 91 ALTITUDE AT MAIN CHUTE DEPLOYMENT VERSUS A_D/A_V AND W_D IN THE "I" MODEL ATMOSPHERE (NOMINAL ENTRY ANGLE OF 90 DEGREES AND DROGUE CHUTE DEPLOYMENT OF 2.5)

215

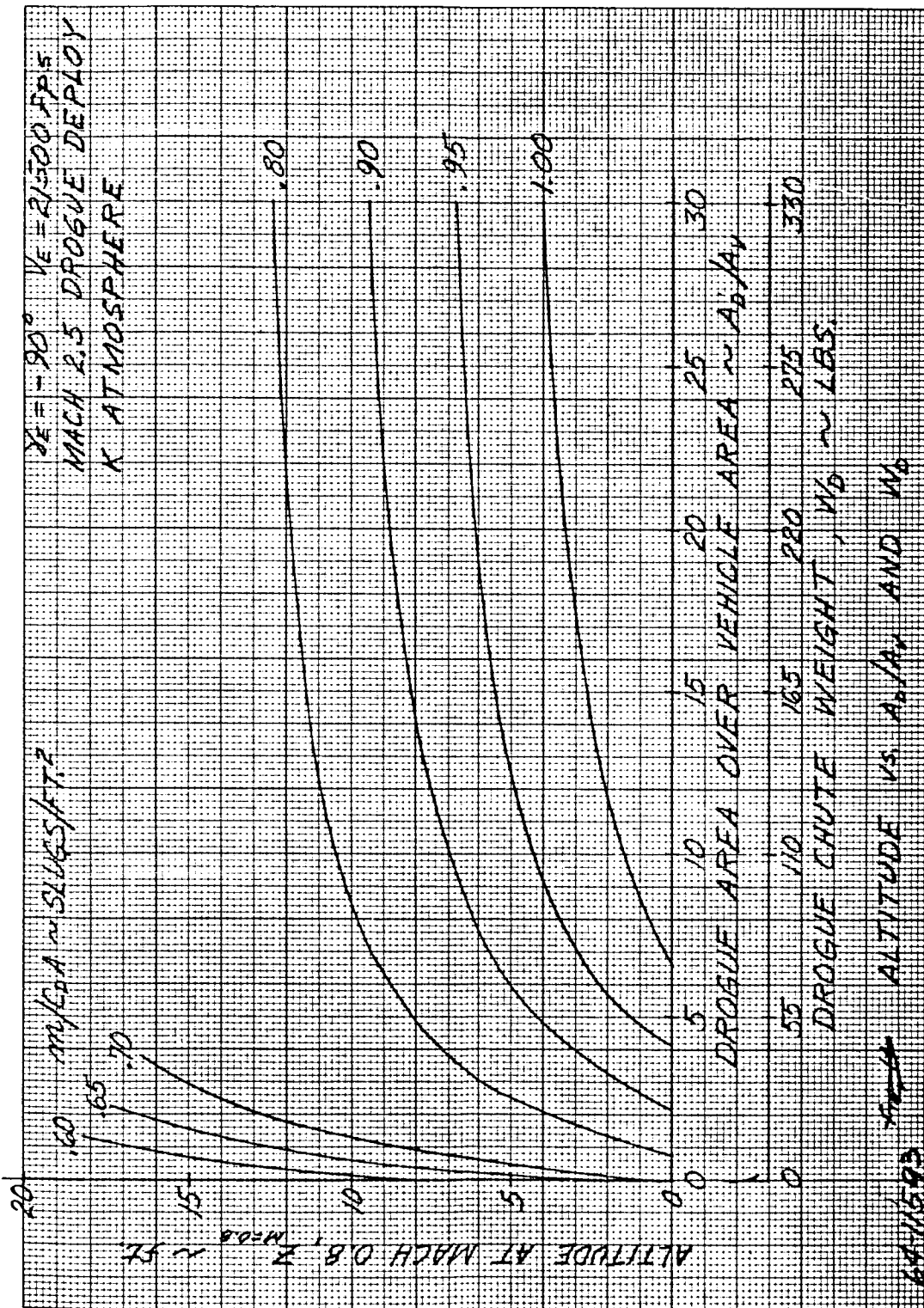


Figure 92 ALTITUDE AT MAIN CHUTE DEPLOYMENT VERSUS A_D/A_V AND W_D IN THE "K" MODEL ATMOSPHERE (NOMINAL ENTRY ANGLE OF 90 DEGREES AND DROGUE CHUTE DEPLOYMENT OF 2.5)

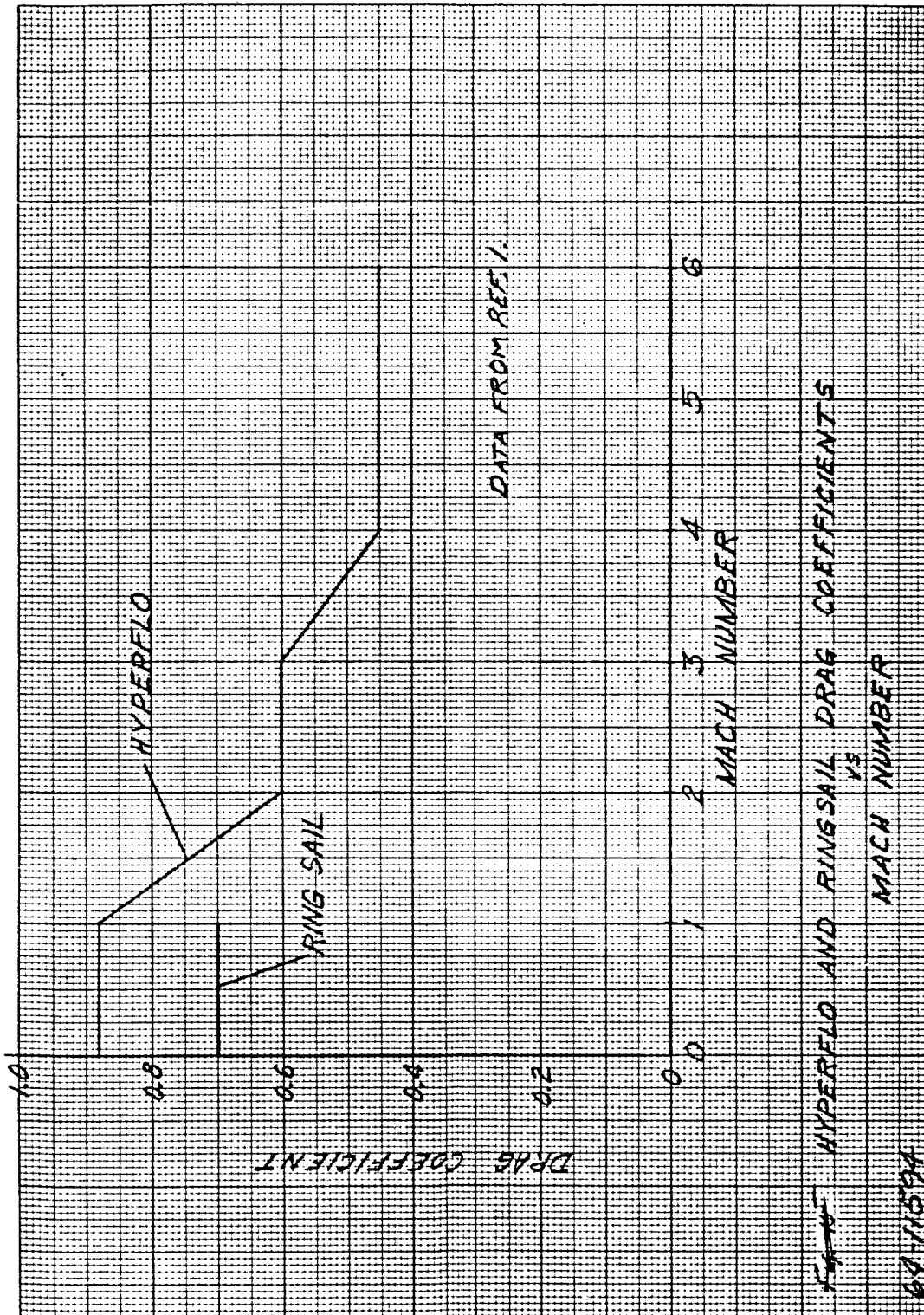


Figure 93 HYPERFLO AND RINGSAIL DRAG COEFFICIENTS VERSUS MACH NUMBER

7.2 MAIN CHUTE ANALYSIS

A Ring-Sail type main chute was selected as the reference design based on its good stability and drag characteristics as well as the state-of-the-art development in the subsonic regime. A nominal deployment Mach number of 0.8 was chosen in order to assure subsonic actuation. Figure 94 presents the time to impact from a given altitude for a range of the ratio, main chute area/suspended weight (A_{MC}/W_S). One should note that initial entry angle had little effect on impact time. Figure 95 presents impact velocity versus A_{MC}/W_S . Both figures 94 and 95 are for the H model atmosphere because this is the most critical design atmosphere from a parachute descent standpoint. Figure 96 shows dynamic pressure versus altitude at main chute deployment.

The following assumptions were made in generating the above mentioned curves:

1. Zero time delay for chute opening.
2. Drag coefficient of 0.7
3. $W_{\text{main chute}} = 0.013 A_{\text{main chute}}$

7.3 SNATCH AND OPENING LOAD ANALYSIS

In order to adequately determine the weight of a parachute canopy, its suspension lines, and riser line, it is necessary to establish the maximum opening shock loads sustained by the entire parachute system. The opening shock or opening force is expressed as

$$F_o = kq (C_D A) \text{ Reference 2}$$

where

k = Experimental dimensionless factor

q = Dynamic pressure - psf

$(C_D A)$ = Drag coefficient times projected area of chute - ft²

The dimensionless parameter k is an amplification factor denoting the relationship between maximum opening force F_o and the constant drag force F_c expressed as

$$k = \frac{F_o}{F_c}$$

The dimensionless factor k has been established experimentally for various types of canopies, a few of which are listed below:

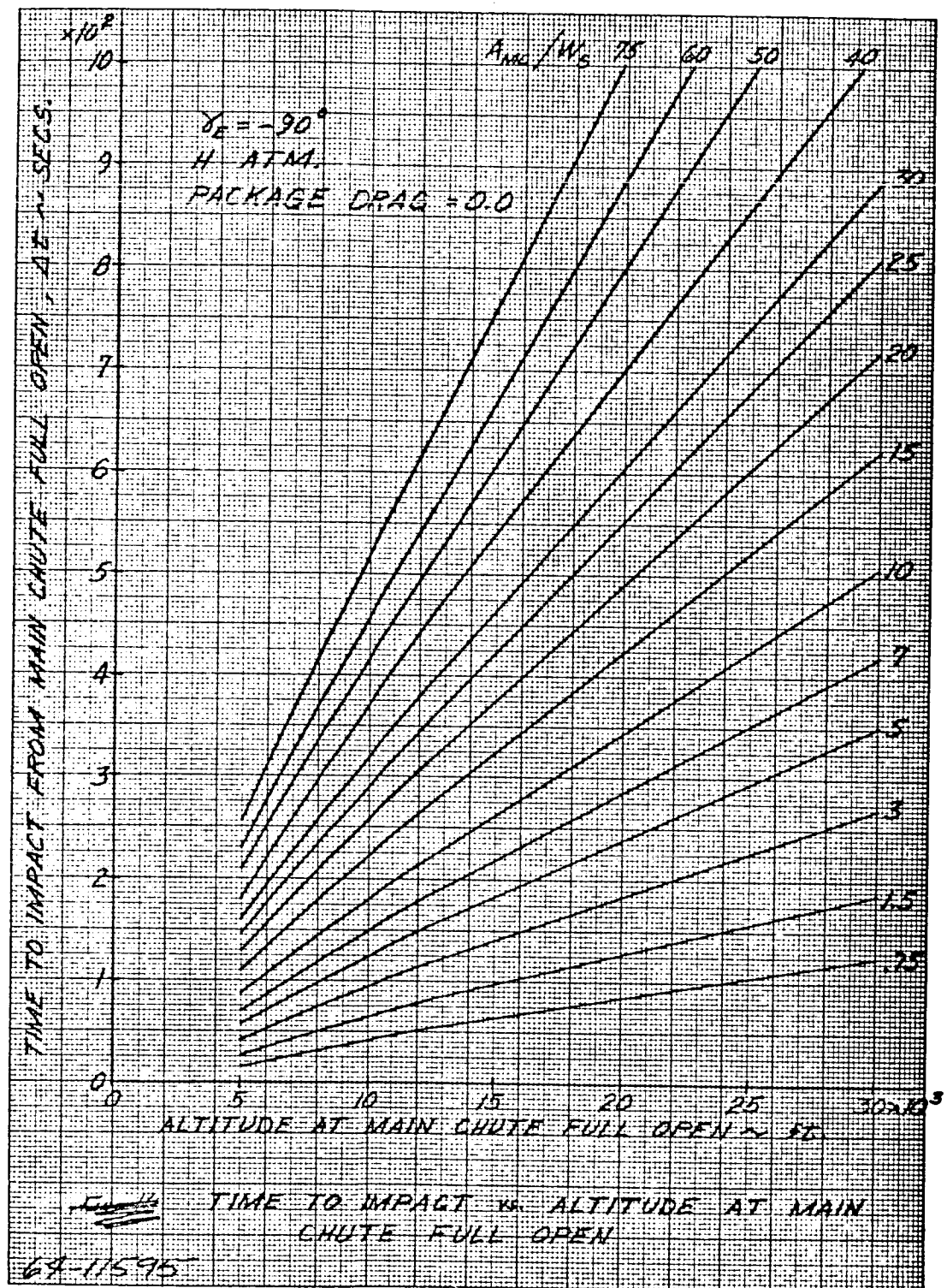


Figure 94 TIME TO IMPACT VERSUS ALTITUDE AT MAIN CHUTE FULL OPEN

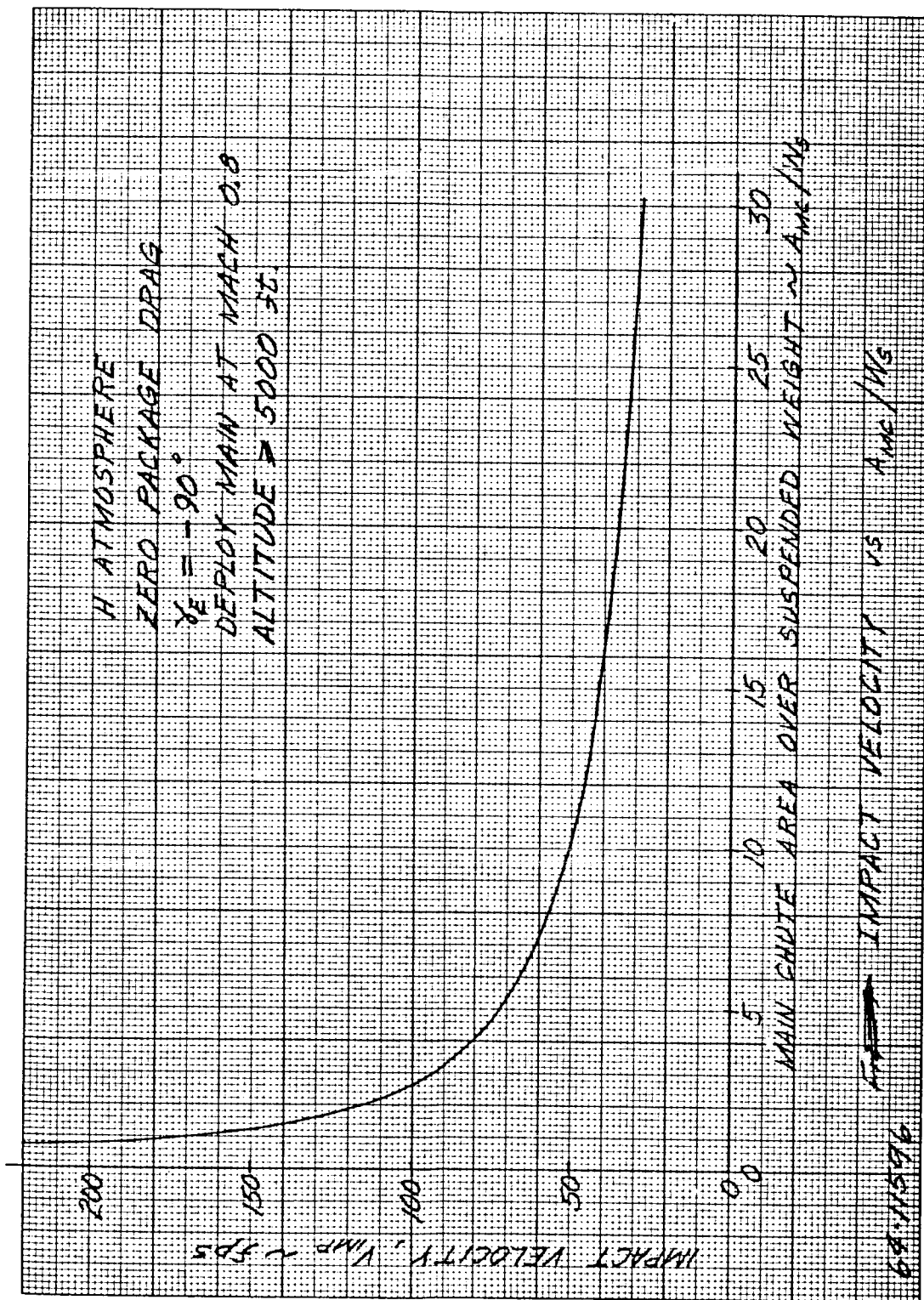


Figure 95 IMPACT VELOCITY VERSUS MAIN CHUTE AREA OVER SUSPENDED WEIGHT (A_{MC}/W_0)

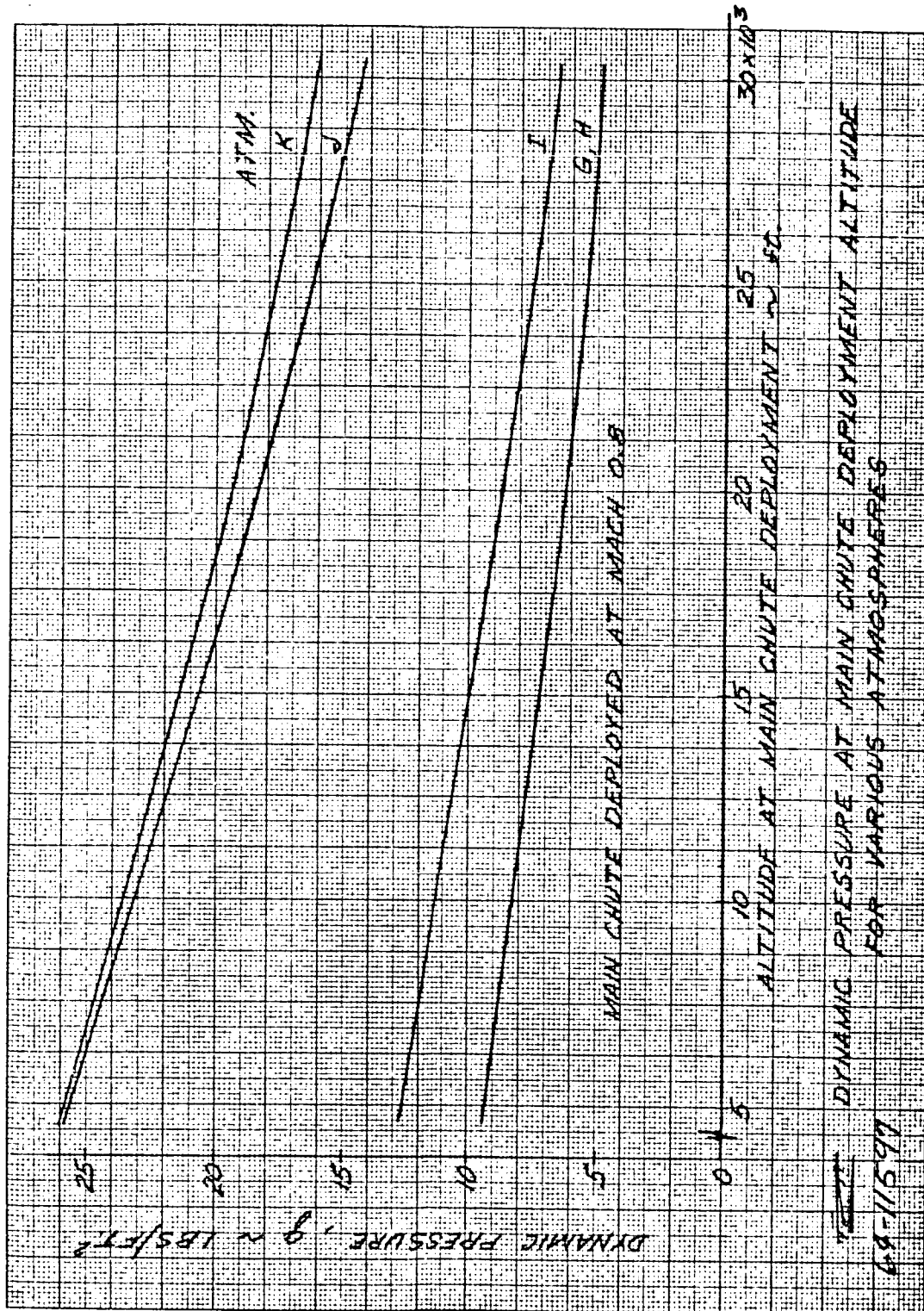


Figure 96 DYNAMIC PRESSURE AT MAIN CHUTE DEPLOYMENT ALTITUDE FOR VARIOUS ATMOSPHERES

(a) Solid Cloth, Flat Circular	$k \geq 2.0$	} Reference 2
(b) Solid Cloth, Extended-Skirt	$k \geq 1.9$	
(c) Ribbon	$k \geq 1.1$	
(d) Hyperflo	$k \geq 1.85$	
(e) Ring-Sail	$k \geq 1.05$	

The maximum opening shock loads for various dynamic pressure levels and chute diameters are shown on figures 97 and 98 for the Hyperflo drogue chute and the Ring-Sail main chute, respectively. A maximum value of 2.0 was used for the amplification factor k in calculating the shock loads for the Hyperflo drogue chute. This was done due to some present uncertainty in the experimental value of 1.85 and also to build some added conservatism into the system design.

7.4 MATERIAL SELECTION

Parachute fabrics are selected on the basis of load and temperature limitations. The load criterion is set by the breaking strength of the fabric and is a function of the dynamic pressure and the diameter of the chute. The stress on the canopy can be calculated by utilizing a thin-wall hemisphere approach, the expression for which is

$$S = \frac{qD_0}{4t} \text{ lbs/in}^2 \quad (\text{Reference 2})$$

where q is the pressure acting uniformly on the hemisphere, t is the thickness of the material, and D_0 the diameter of the parachute.

The temperature limitation is set by the maximum wall temperature a particular fabric is able to withstand and is a function of the ratio of specific heats (γ), static free stream temperature (T_∞), and the free stream Mach number at a given altitude (M_∞). Hence, the canopy wall temperature can be expressed as

$$T_S = T_\infty \left[1 + \eta \frac{(\gamma - 1)}{2} M^2 \right] \quad (\text{Reference 2})$$

where η is the temperature Recovery Factor assumed as 1.0 throughout the study. Nylon and Nomex (HT-1) were the two fabrics investigated and have maximum temperature limitations of 1260° and 1760°R, respectively. Based on these temperature limitations figures 99 and 100 present the maximum possible deployment Mach numbers for all the model atmospheres and a range of altitudes. Figures 101 and 102 show the fabric temperature limited Mach numbers for Nylon and Nomex materials in the H atmosphere. The curves are for a 90- and 60-degree entry, respectively.

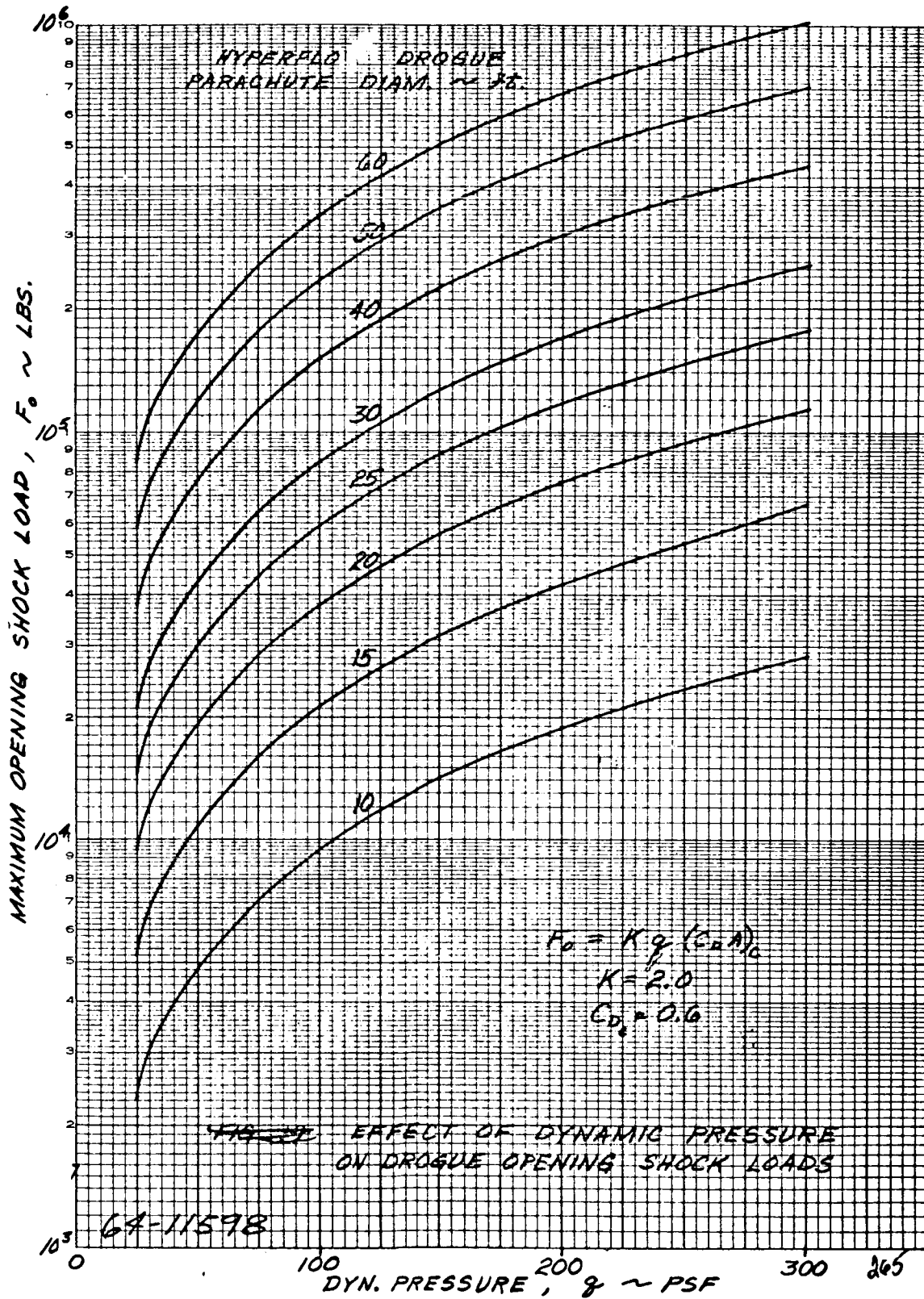


Figure 97 EFFECT OF DYNAMIC PRESSURE ON DROGUE OPENING SHOCK LOADS

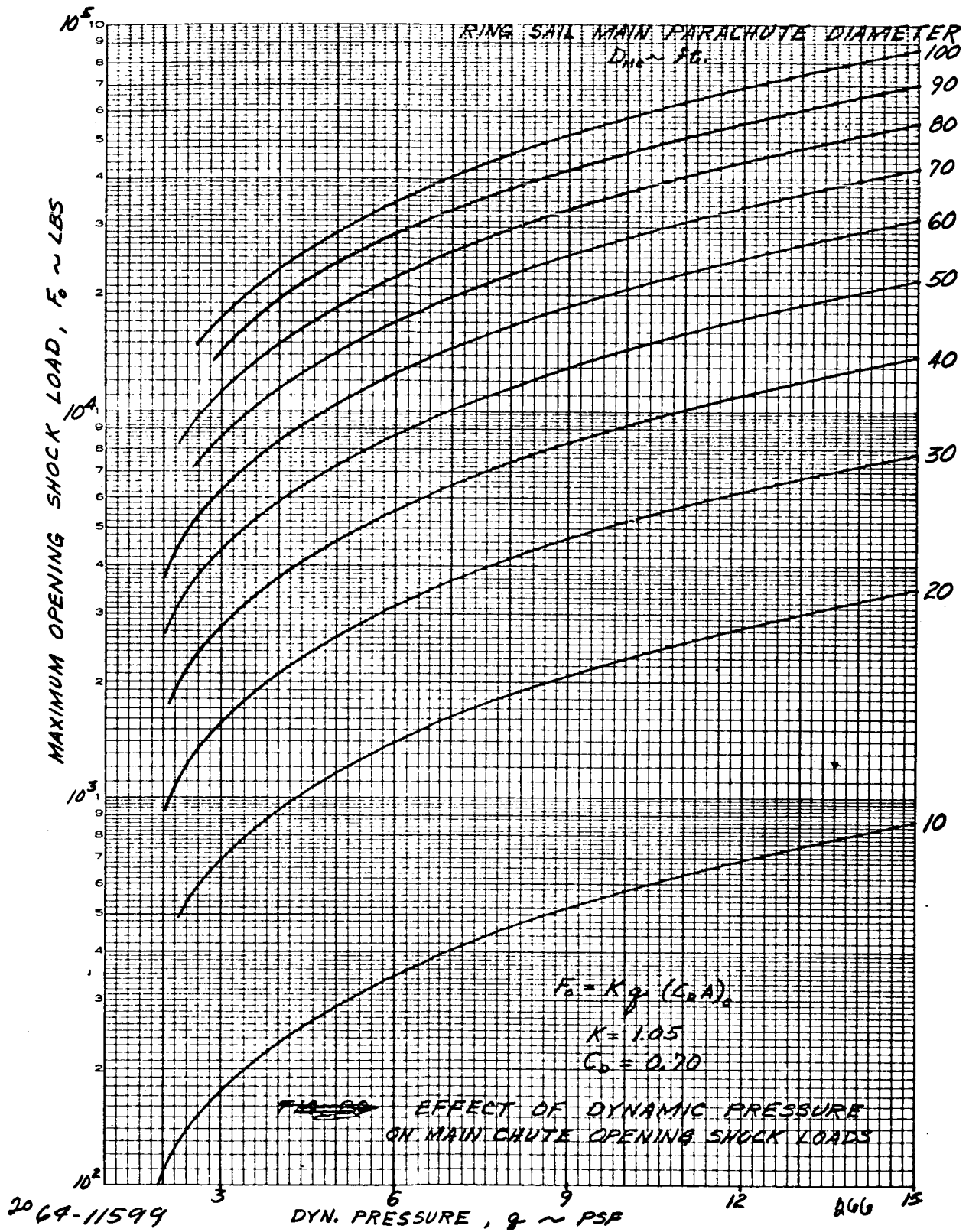


Figure 98 EFFECT OF DYNAMIC PRESSURE ON MAIN CHUTE OPENING SHOCK LOADS

2.24

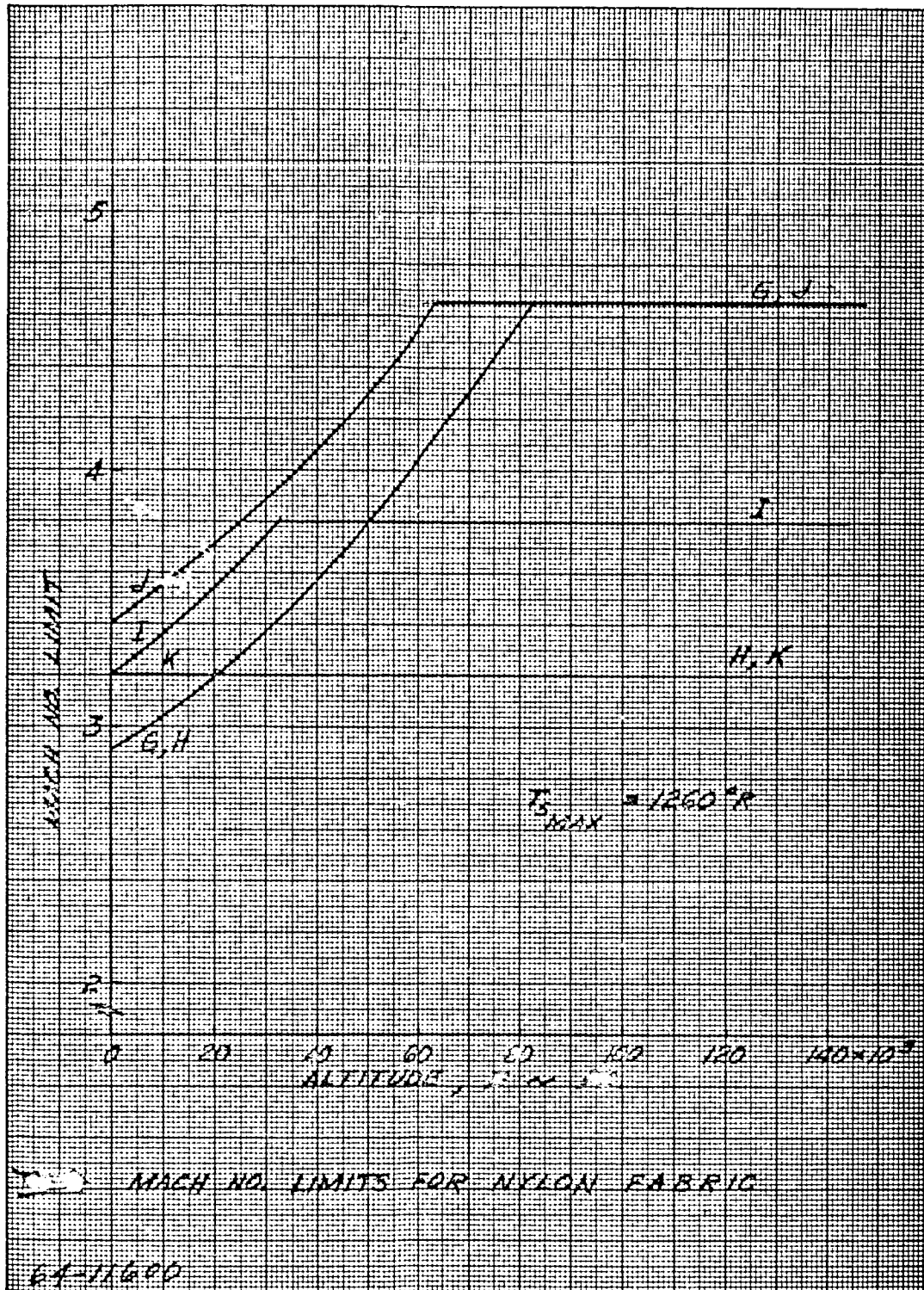


Figure 99 MACH NUMBER LIMITS FOR NYLON FABRIC

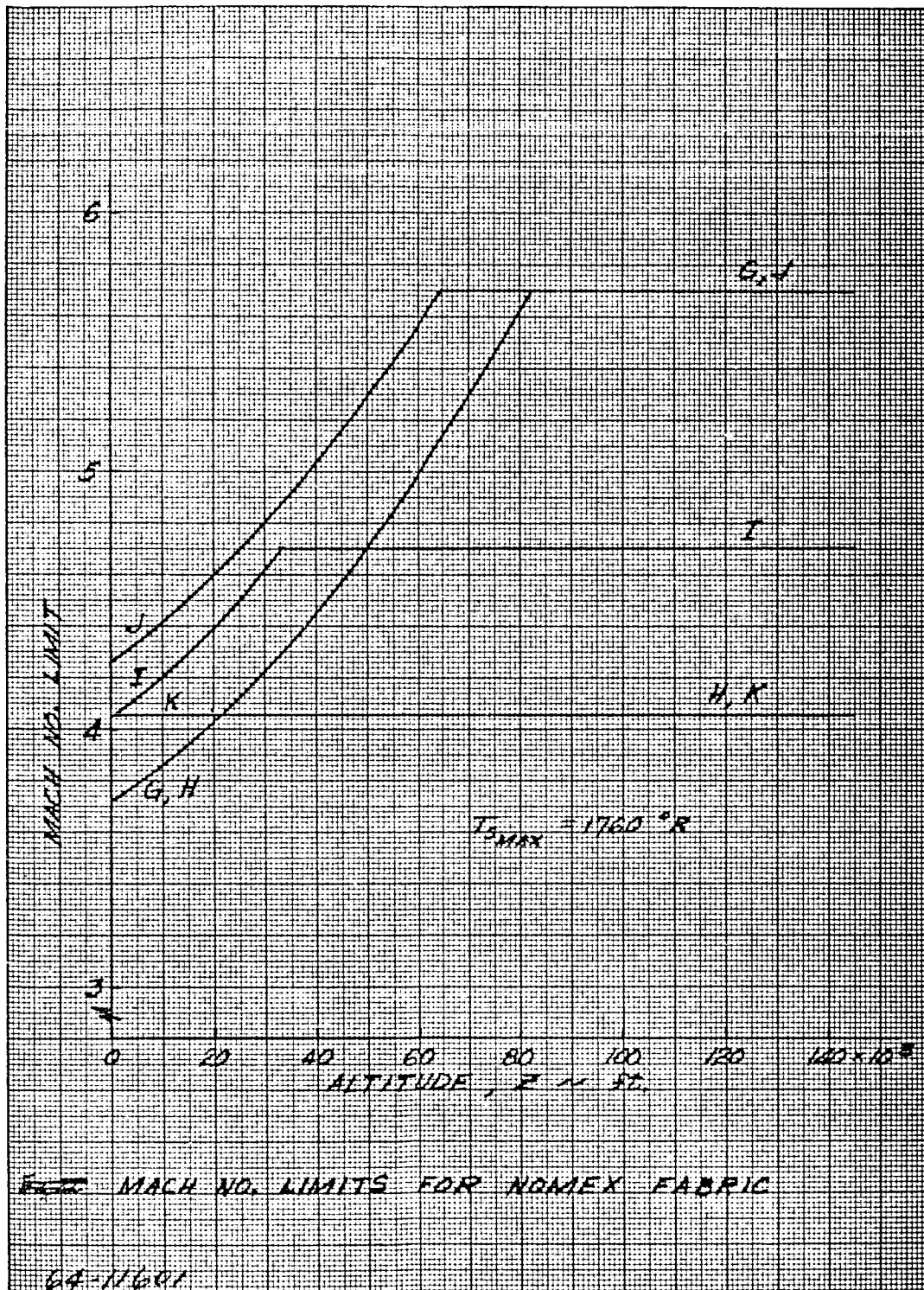


Figure 100 MACH NUMBER LIMITS FOR NOMEX FABRIC

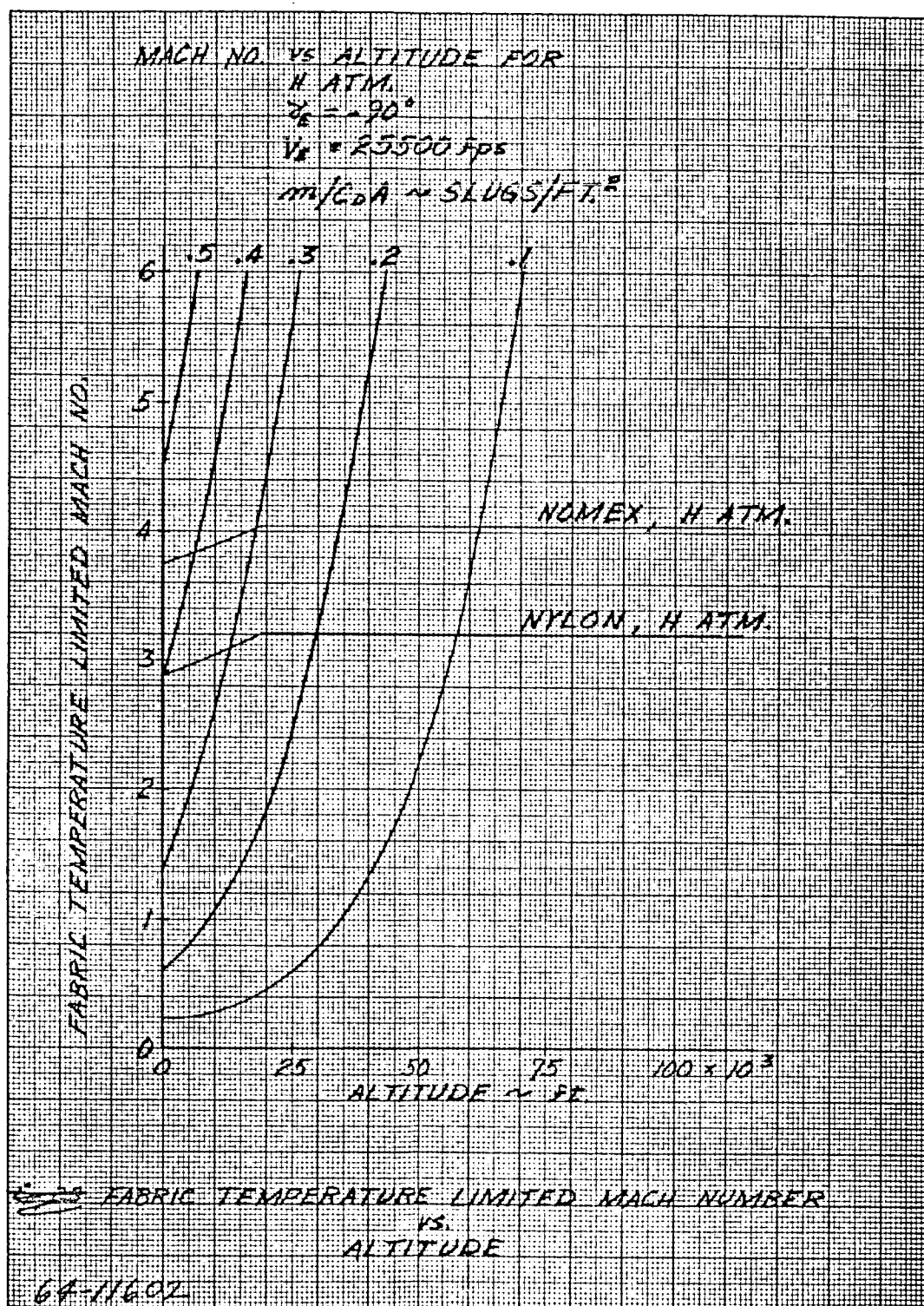


Figure 101 FABRIC TEMPERATURE LIMITED MACH NUMBER VERSUS
ALTITUDE (γ_e OF 90 DEGREES)

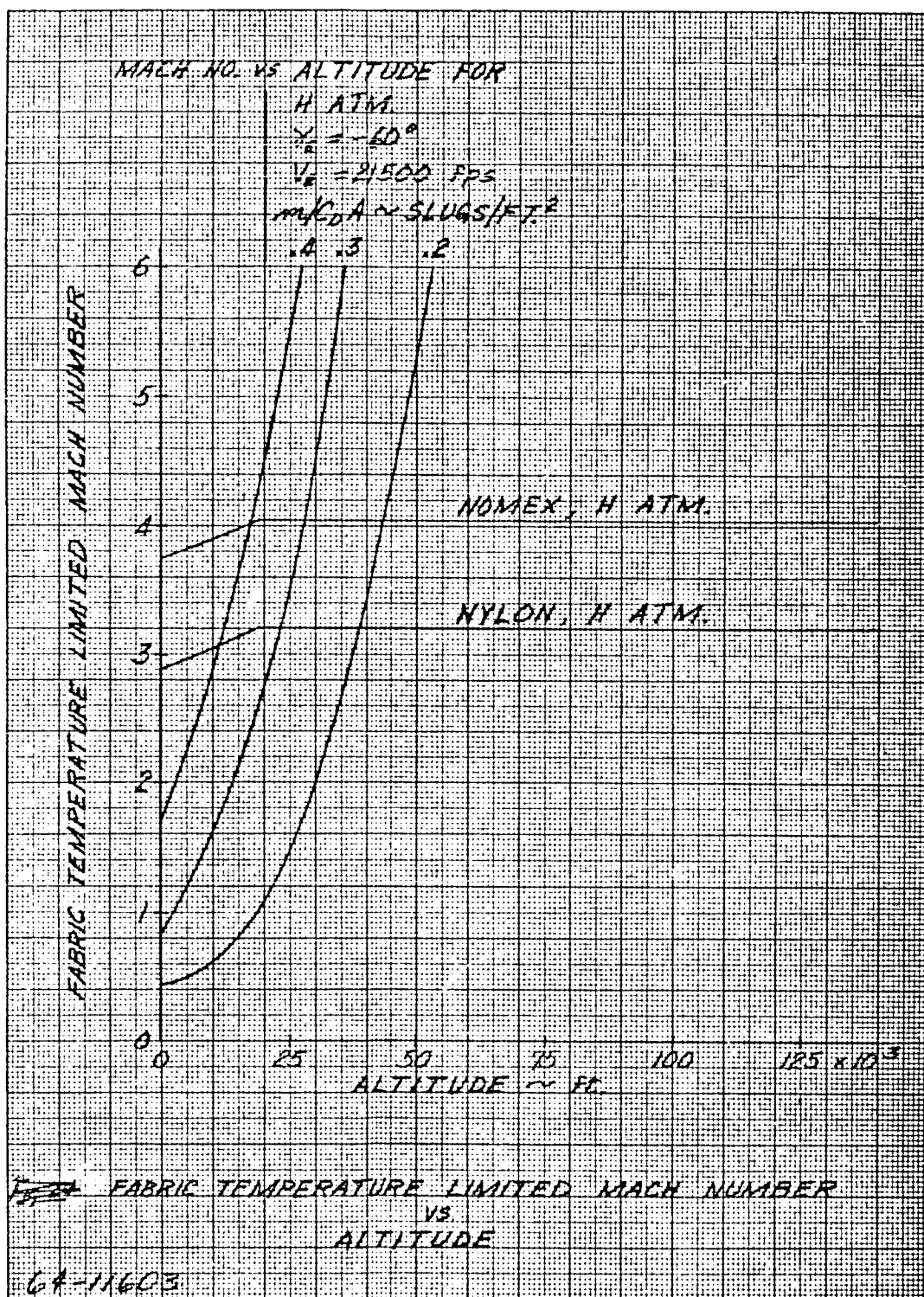


Figure 102 FABRIC TEMPERATURE LIMITED MACH NUMBER VERSUS
ALTITUDE (γ_e OF 60 DEGREES)

7.5 PARAMETRIC OPTIMIZATION

One of the primary objectives of the parametric study was to optimize the ballistics coefficient and/or the suspended weight. As mentioned previously the suspended weight is expressed as

$$W_S = \frac{W_E - W_{H/S} - W_D}{1 + \frac{W_{MC}}{W_S}}$$

For a given set of conditions and a range of m/C_{DA} 's the above expression can be maximized. The controlling parameter in this expression is the drogue chute weight (W_D). This is the parameter that forces an optimum m/C_{DA} . As the ballistics coefficient increases, it becomes increasingly more difficult to achieve Mach 0.8 (main chute deployment) at the given main chute deployment altitude. In order to decelerate to Mach 0.8 at the given deployment altitude (for increased m/C_{DA} 's) the drogue chute diameter must increase. Finally we reach an m/C_{DA} such that the drogue weight becomes greater than the increased entry weight; hence the suspended weight starts to decrease and an optimum design point is reached.

Figures 103 through 110 are all for a 90 degree entry angle. Presented are parametric curves for main chute deployment altitudes of 5,000 through 20,000 feet and impact velocities of 50, 100 and 150 ft/sec. One can note that as the main chute deployment altitude increases, the optimum m/C_{DA} decreases quite rapidly. This effect is summarized on figure 110. Impact velocity has no effect on the optimum m/C_{DA} but does influence the amount of suspended weight, the differences being in the main chute weight. This result is seen on figure 105.

1. Entry Angle Effects

Parametric curves of suspended weight versus m/C_{DA} are presented for entry angles of 60 and 40 degrees on figures 111 through 122. A summary curve of optimum m/C_{DA} versus entry angle is shown on figure 121 and indicates that the optimum m/C_{DA} increases as the entry angle decreases. On figure 122 is a summary curve of optimum suspended weight versus entry angle for main chute deployment altitudes of 5000, 8000, and 10,000 feet and impact velocities of 50 and 150 ft/sc.

Figure 123 is a plot of suspended weight versus m/C_{DA} . Two distinct sets of curves are presented for comparison purposes. The upper set of curves optimize suspended weight based on a nominal entry angle of 90 degrees which would include design for structure of 90 degrees entry and heat shield of 75 degrees entry. This variation is based on a 3σ entry angle dispersion. The lower set of curves reflect optimum

suspended weight utilizing heat shield and structure weights designed for the entire entry angle spectrum of 20 to 90 degrees, i.e., design heat shield for 20 degrees and structure for 90 degrees. Hence, figure 123 readily demonstrates the loss in suspended weight due to designing for the entire entry angle spectrum.

2. Mach Number Effects

Studies were conducted to evaluate the results of increased drogue chute deployment Mach number. Parametric optimization curves for Mach 3.0 and 3.5 are presented on figures 124 and 125, respectively. Figure 126 presents curves of optimum m/CDA versus drogue deployment Mach number and figure 127 shows curves of optimum suspended weight versus drogue deployment Mach number. One should note that all of the above mentioned curves were generated for a 60-degree entry angle. The above curves should be used in conjunction with the data in the materials selection section so as to ascertain what the maximum drogue chute deployment Mach number is for a particular set of conditions and type fabric. The design should also be such so as to allow for dispersion in the deployment Mach number due to the actuation system.

3. Surface Pressure Effects

The effect of surface pressure on landed weight was determined. The range of surface pressures studied were 11 to 30 mb which are the G through K model atmospheres. A nominal set of conditions was chosen just to demonstrate the effects of surface pressure. The assumptions are as follows:

- a. γ_e nominal -90 degrees
- b. Diameter of Vehicle 100 inches
- c. Drogue Chute Deployment Mach 2.5
- d. Main Chute Deployment Mach 0.8
- e. Altitude at Main Chute 5000 feet
 deployment
- f. Impact Velocity 50 ft/sec

Parametric curves similar to previous results are presented on figures 128 through 131. Results for the 15 and 30 mb atmospheres are presented therein. Figure 132 is a summary of optimum m/CDA and optimum suspended weight versus surface pressure. Note that if the minimum surface pressure were 30 mb, then a vehicle design with an m/CDA in the order of 0.90 slugs/ft² would be possible.

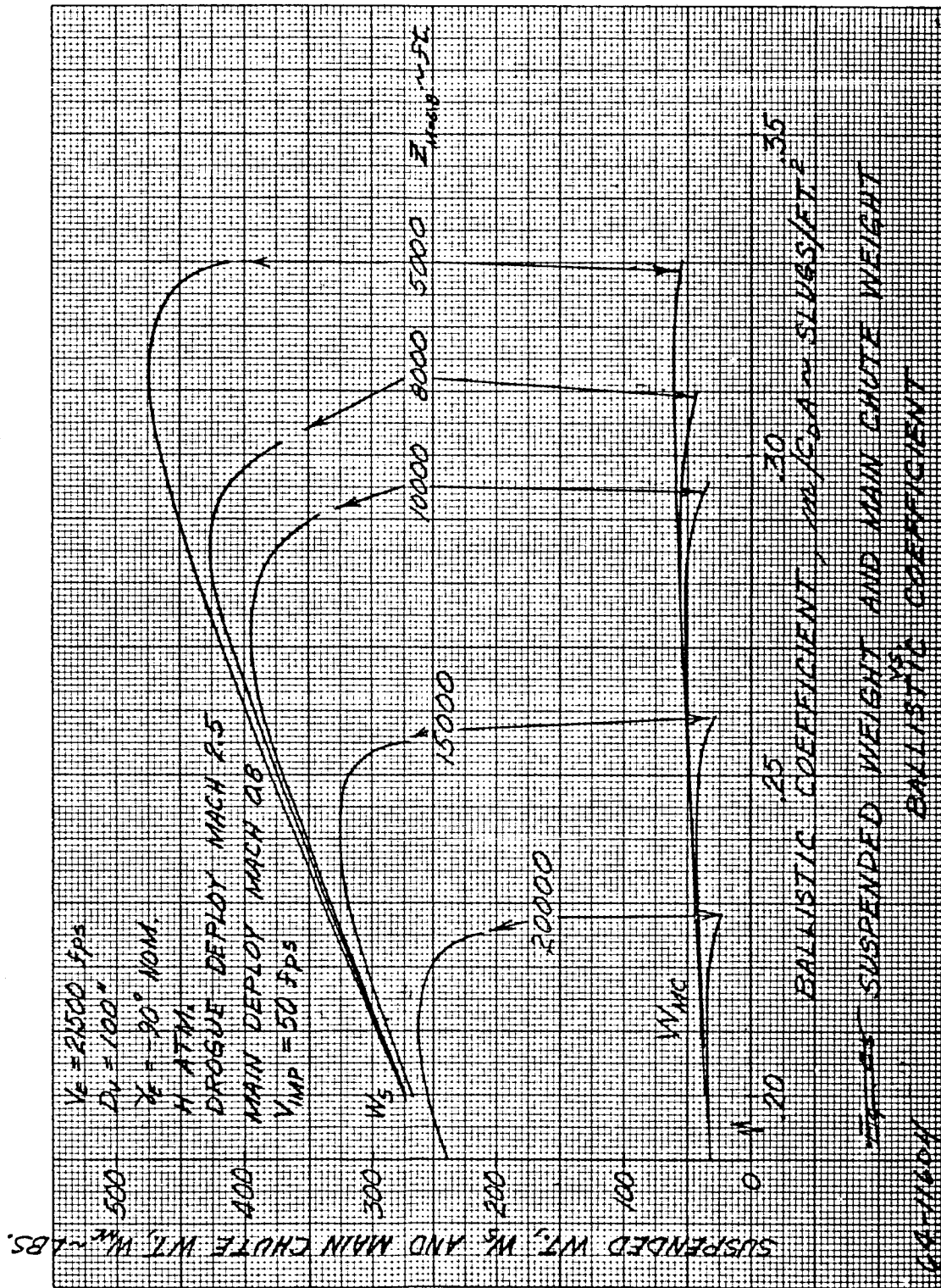


Figure 103 SUSPENDED WEIGHT AND MAIN CHUTE WEIGHT² VERSUS $m/C_D A$
(IMPACT VELOCITY OF 50 FPS AND γ_c nominal OF 90 DEGREES)

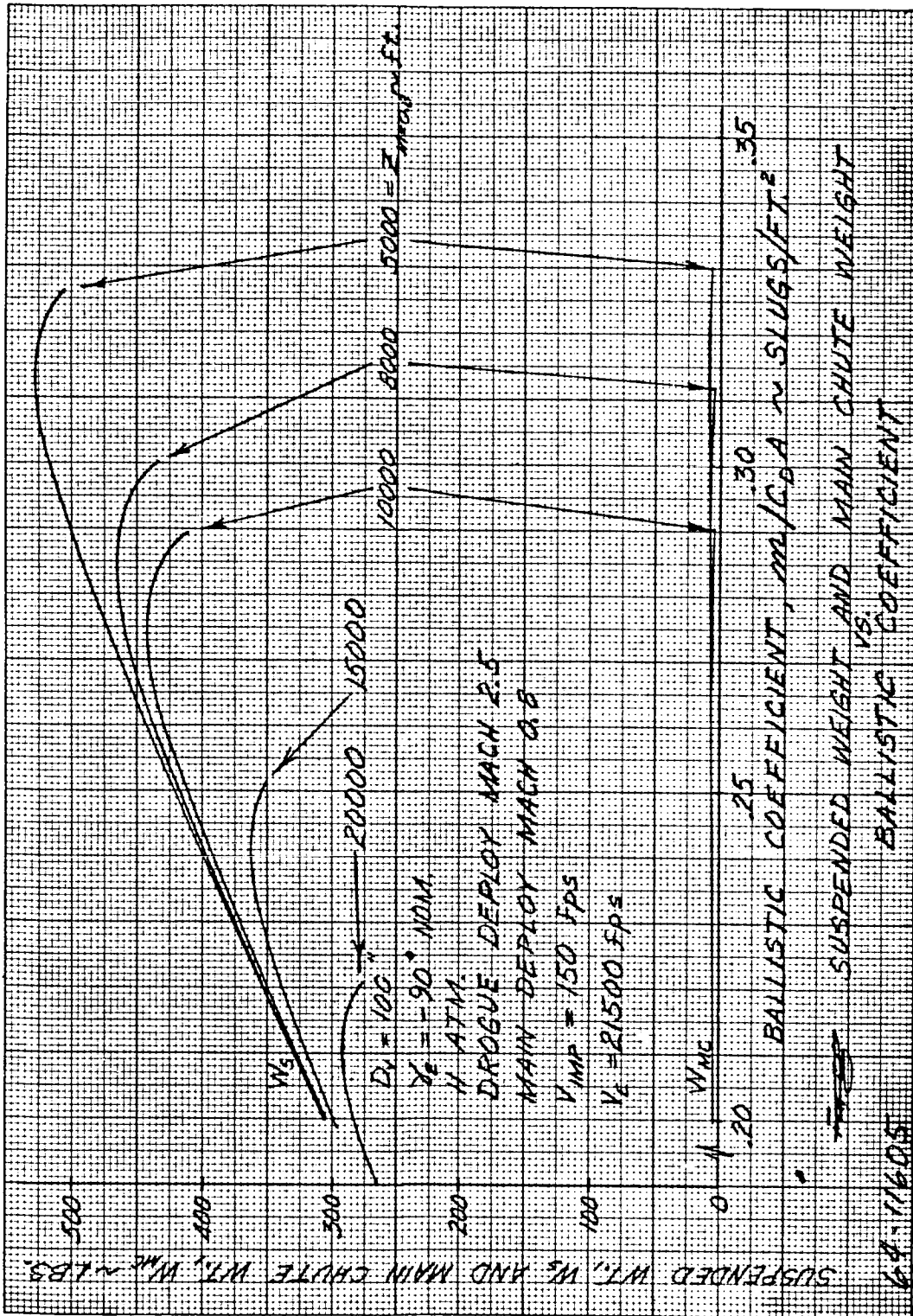


Figure 104 SUSPENDED WEIGHT AND MAIN CHUTE WEIGHT VERSUS m/C_{DA}
(IMPACT VELOCITY OF 150 FPS AND $\gamma_{e\text{nominal}}$ OF 90 DEGREES)

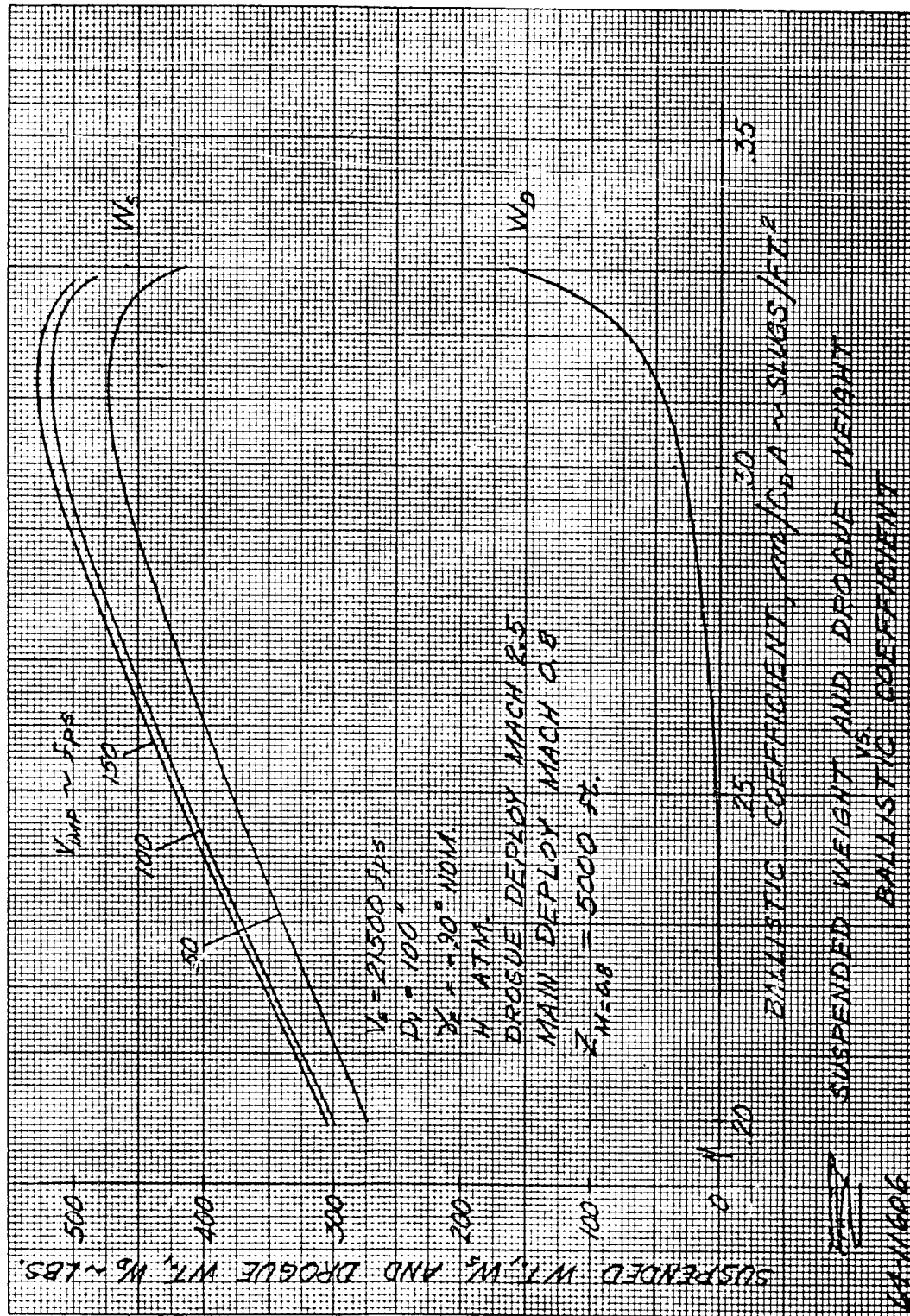


Figure 105 SUSPENDED WEIGHT AND DROGUE CHUTE WEIGHT VERSUS M/C_{DA} (ALTITUDE OF 5000 FEET AT MAIN CHUTE DEPLOYMENT AND γ_{nominal} OF 90 DEGREES)

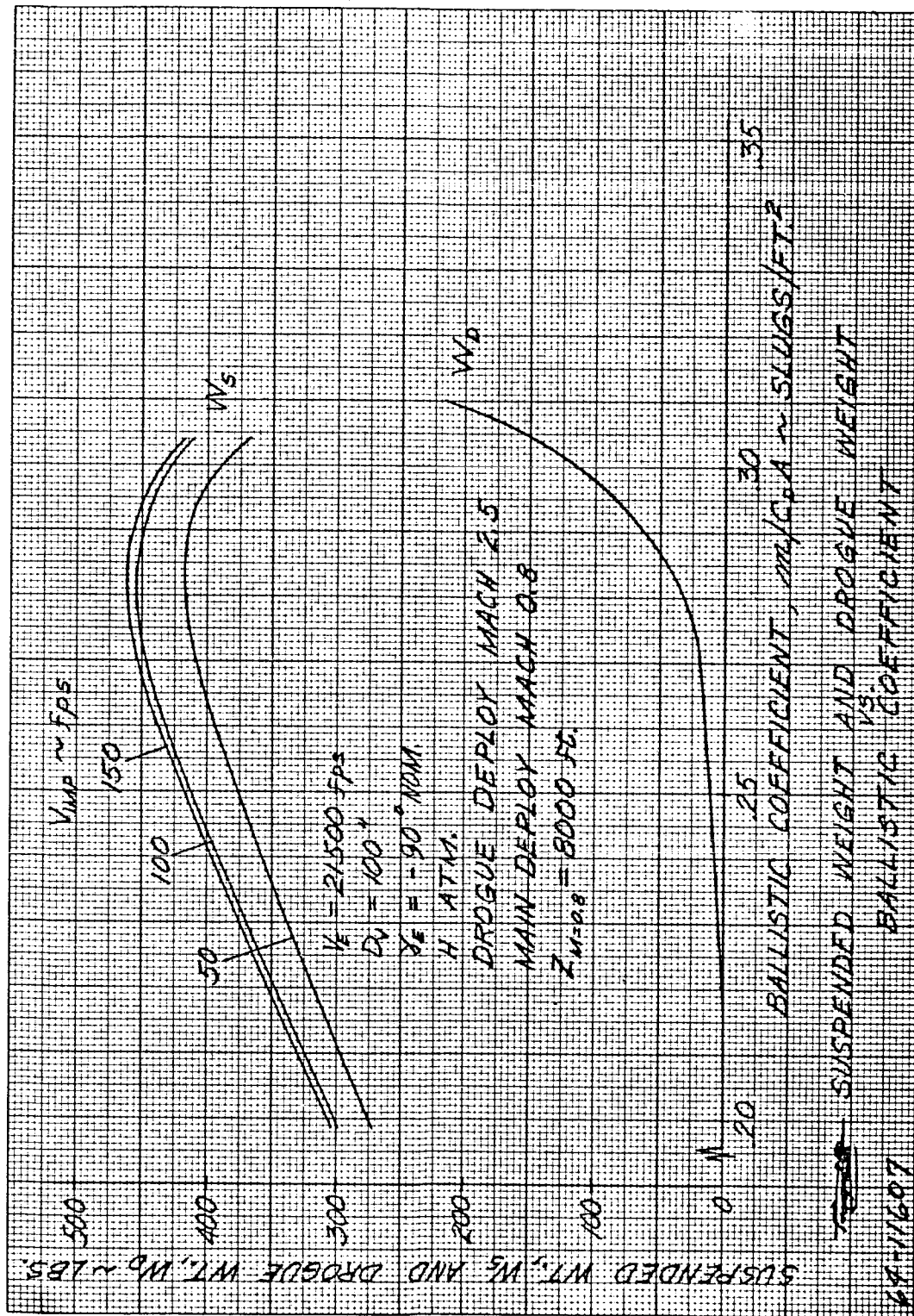


Figure 106 SUSPENDED WEIGHT AND DROGUE CHUTE WEIGHT VERSUS
 M/CDA (ALTITUDE OF 8000 FEET AT MAIN CHUTE DEPLOYMENT
 AND $\gamma_{c \text{ nominal}}$ OF 90 DEGREES)

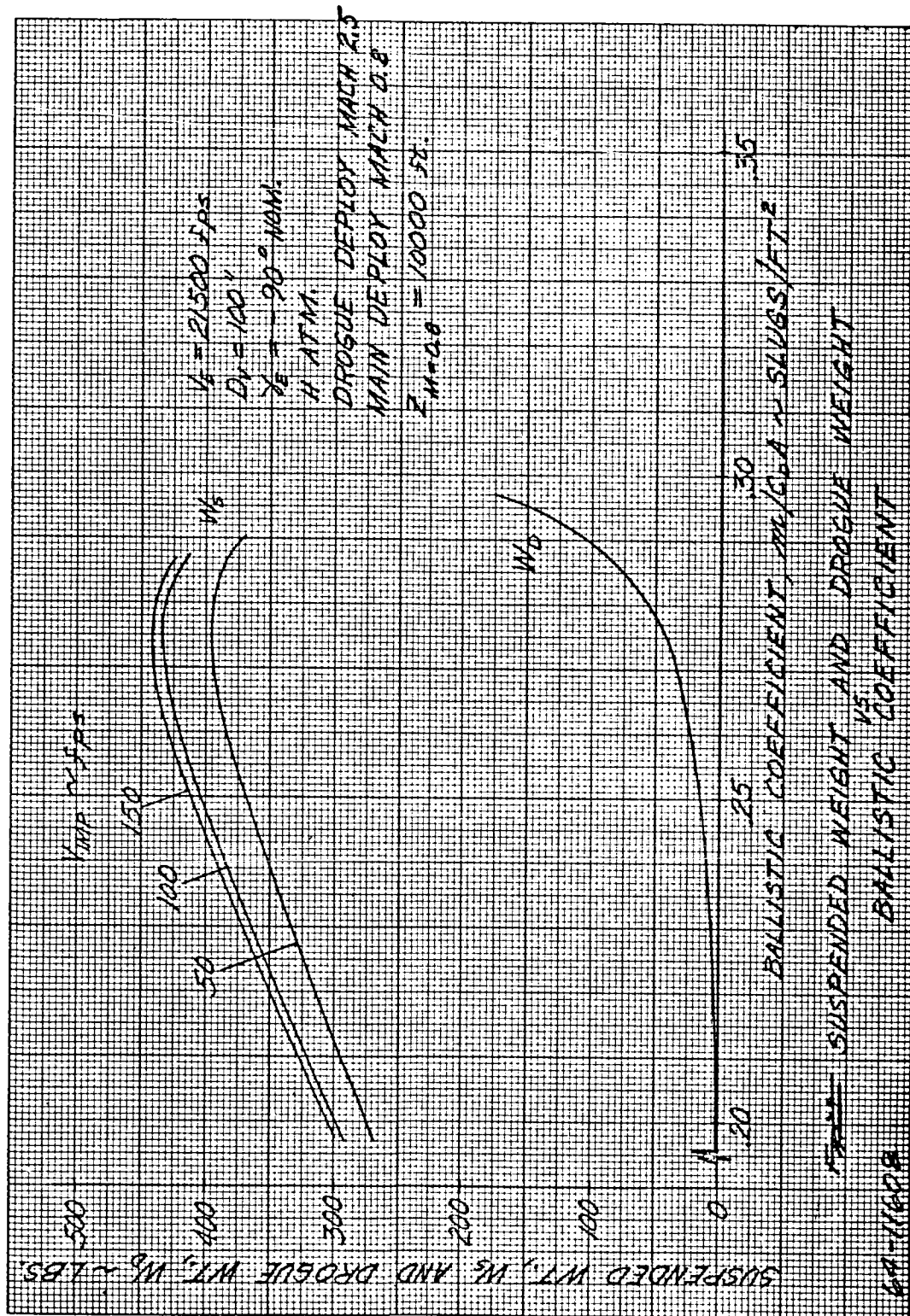


Figure 107 SUSPENDED WEIGHT AND DROGUE CHUTE WEIGHT VERSUS M/CDA (ALTITUDE OF 10,000 FEET AT MAIN CHUTE DEPLOYMENT AND $Y_{nominal}$ OF 90 DEGREES)

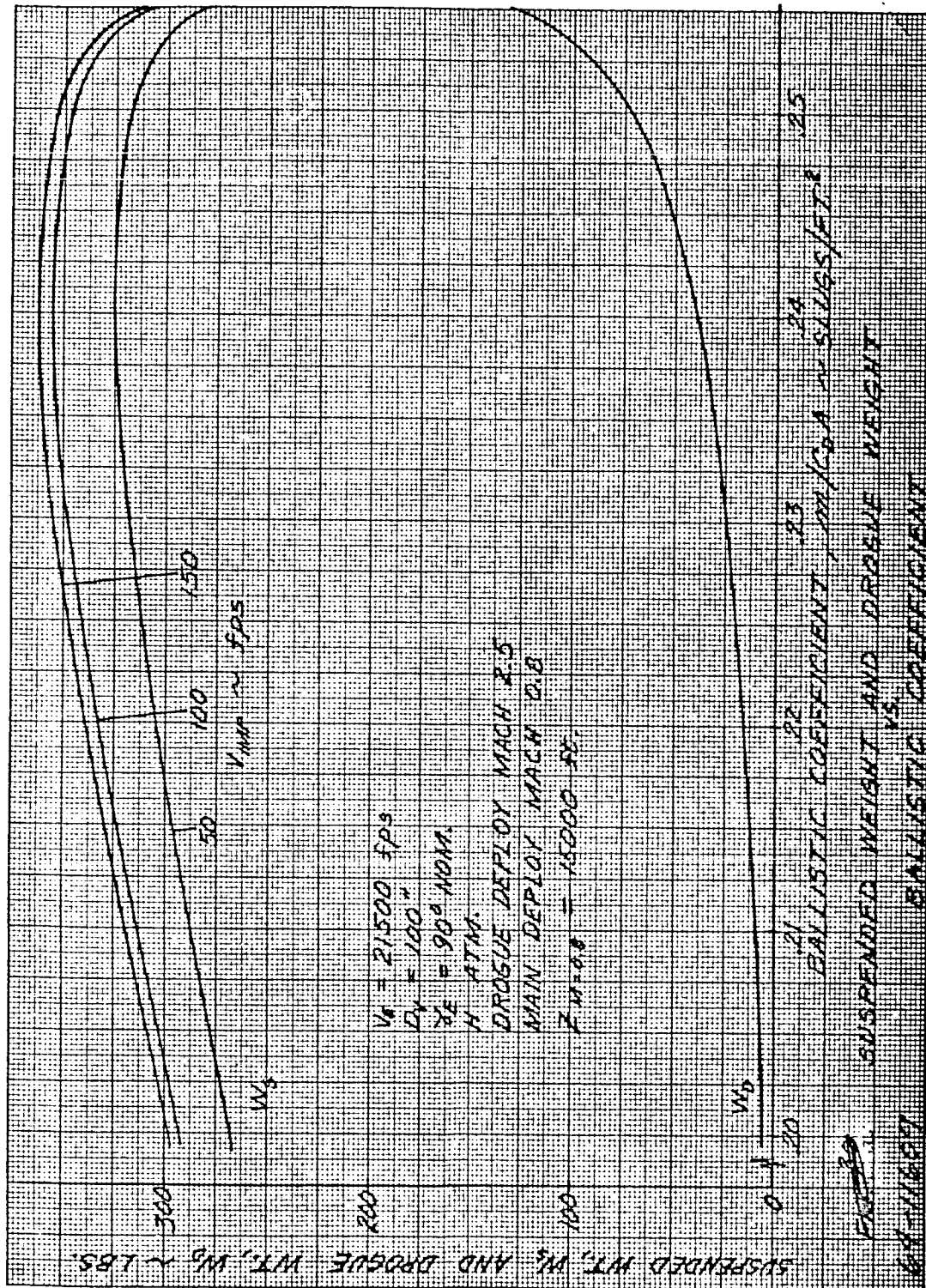


Figure 108 SUSPENDED WEIGHT AND DROGUE CHUTE WEIGHT VERSUS
M/CDA (ALTITUDE OF 15,000 FEET AT MAIN CHUTE DEPLOYMENT
AND $Y_{nominal}$ OF 90 DEGREES)

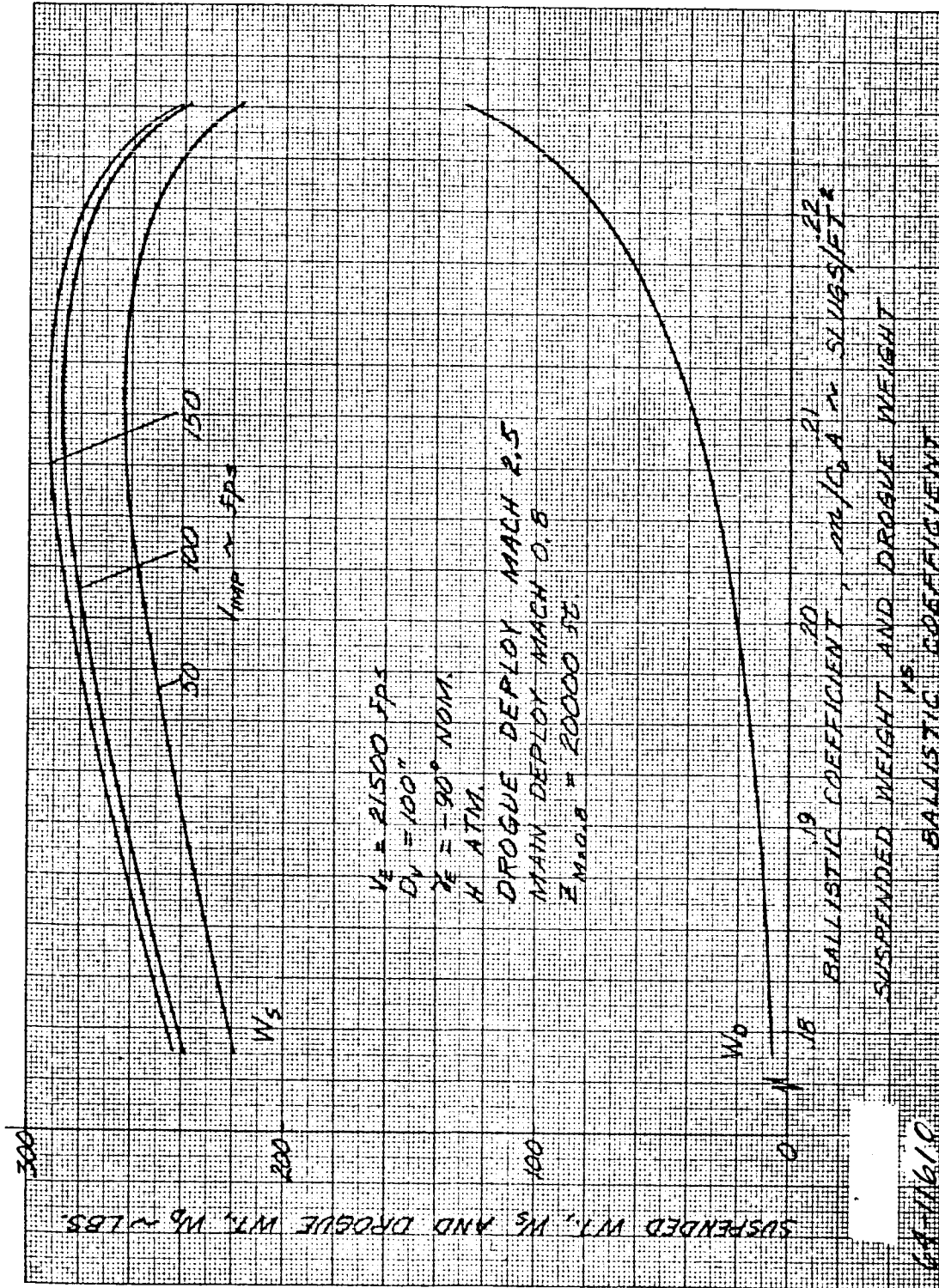


Figure 109 SUSPENDED WEIGHT AND DROGUE CHUTE WEIGHT VERSUS M/C_{DA} (ALTITUDE OF 20,000 FEET AT MAIN CHUTE DEPLOYMENT AND $\gamma_{nominal}$ OF 90 DEGREES)

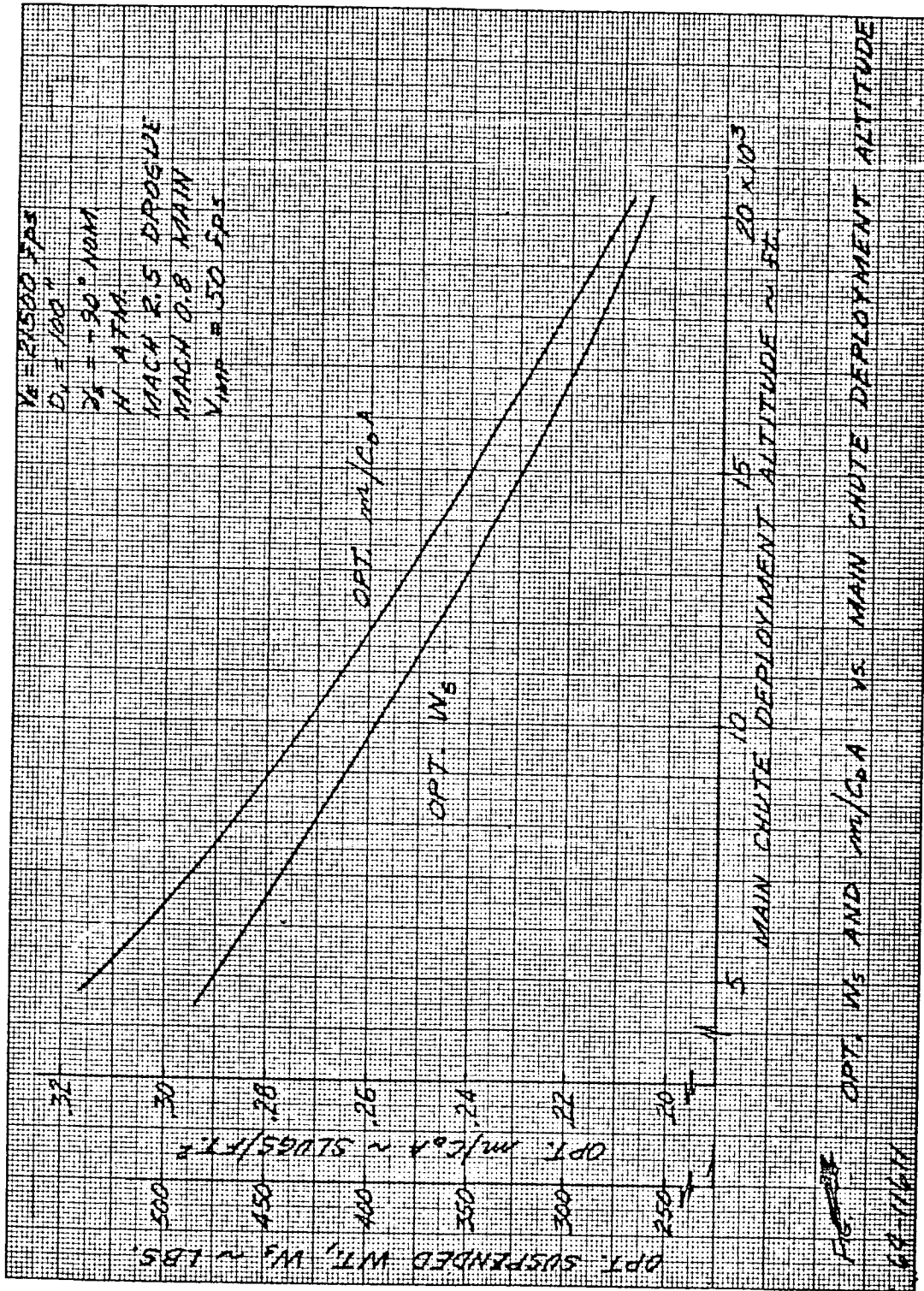


Figure 110 OPTIMUM SUSPENDED WEIGHT AND $m/c o/a$ VERSUS MAIN CHUTE DEPLOYMENT ALTITUDE (50 FPS IMPACT VELOCITY AND $\gamma_{c \text{ nominal}}$ OF 90 DEGREES)

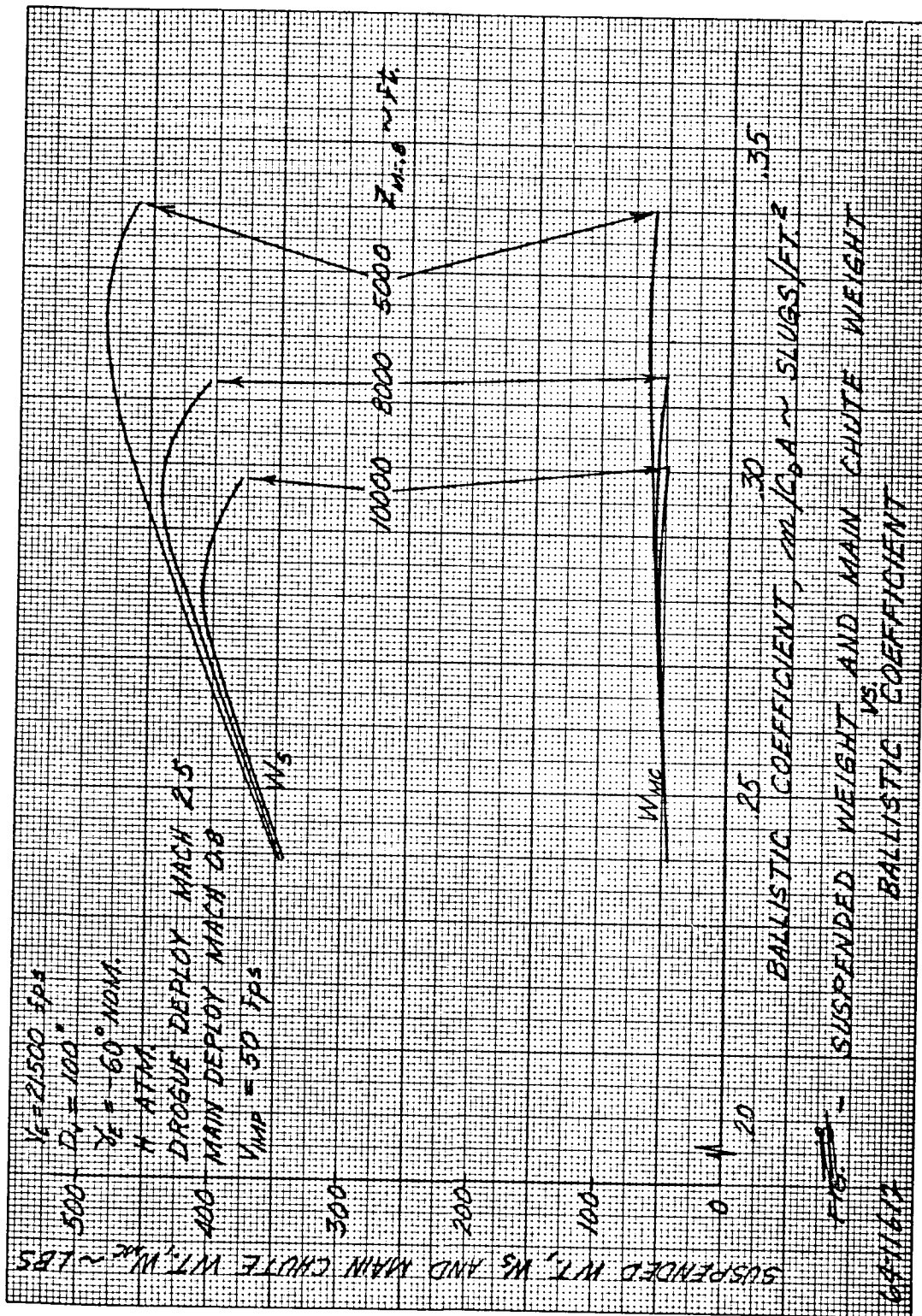


Figure 111 SUSPENDED WEIGHT AND MAIN CHUTE WEIGHT VERSUS $m/C_D A$ (IMPACT VELOCITY OF 50 FPS AND $\gamma_{e nominal}$ OF 60 DEGREES)

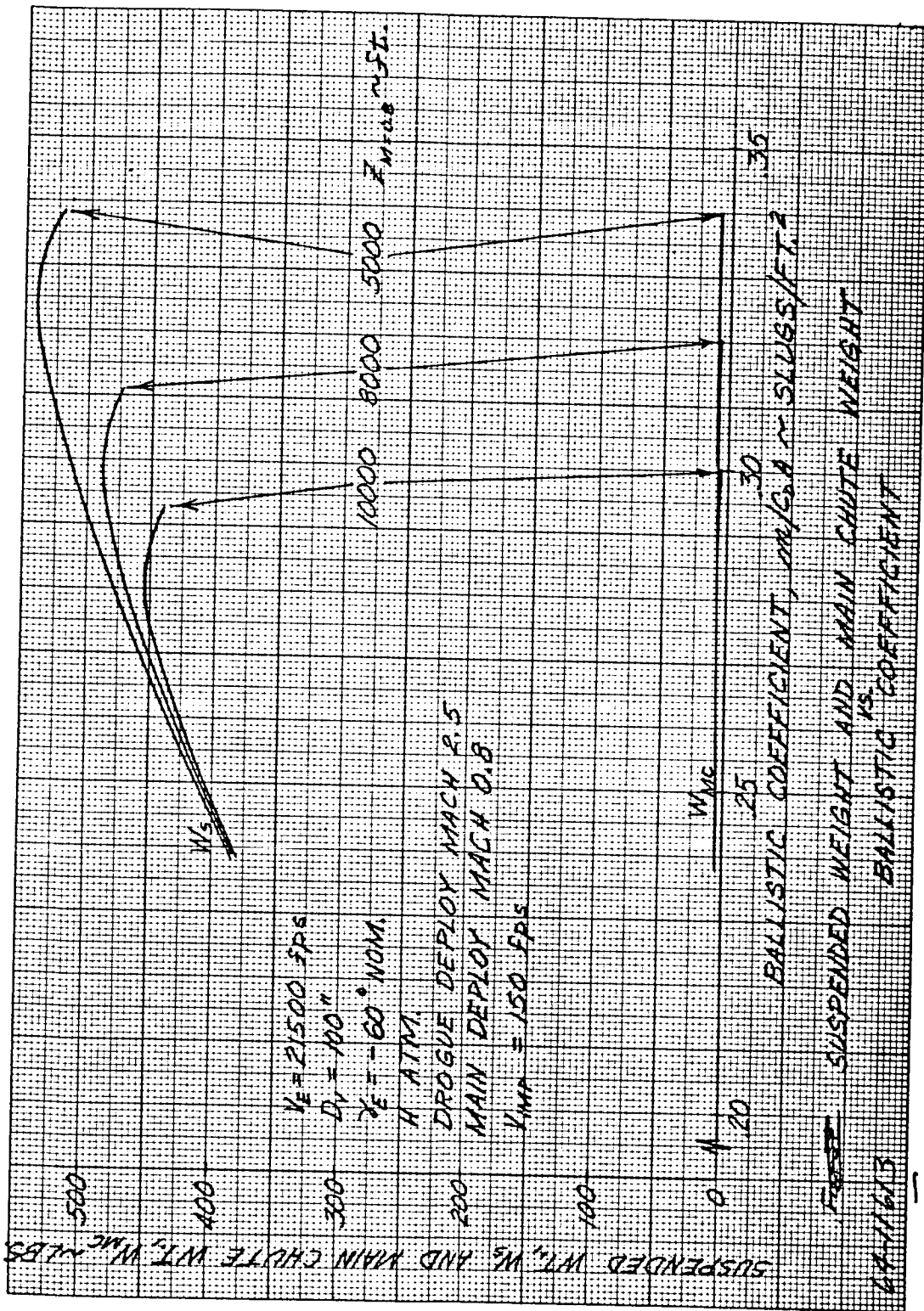


Figure 112 SUSPENDED WEIGHT AND MAIN CHUTE WEIGHT VERSUS M/CDA (IMPACT VELOCITY OF 150 FPS AND $\gamma_{nominal}$ OF 60 DEGREES)

240

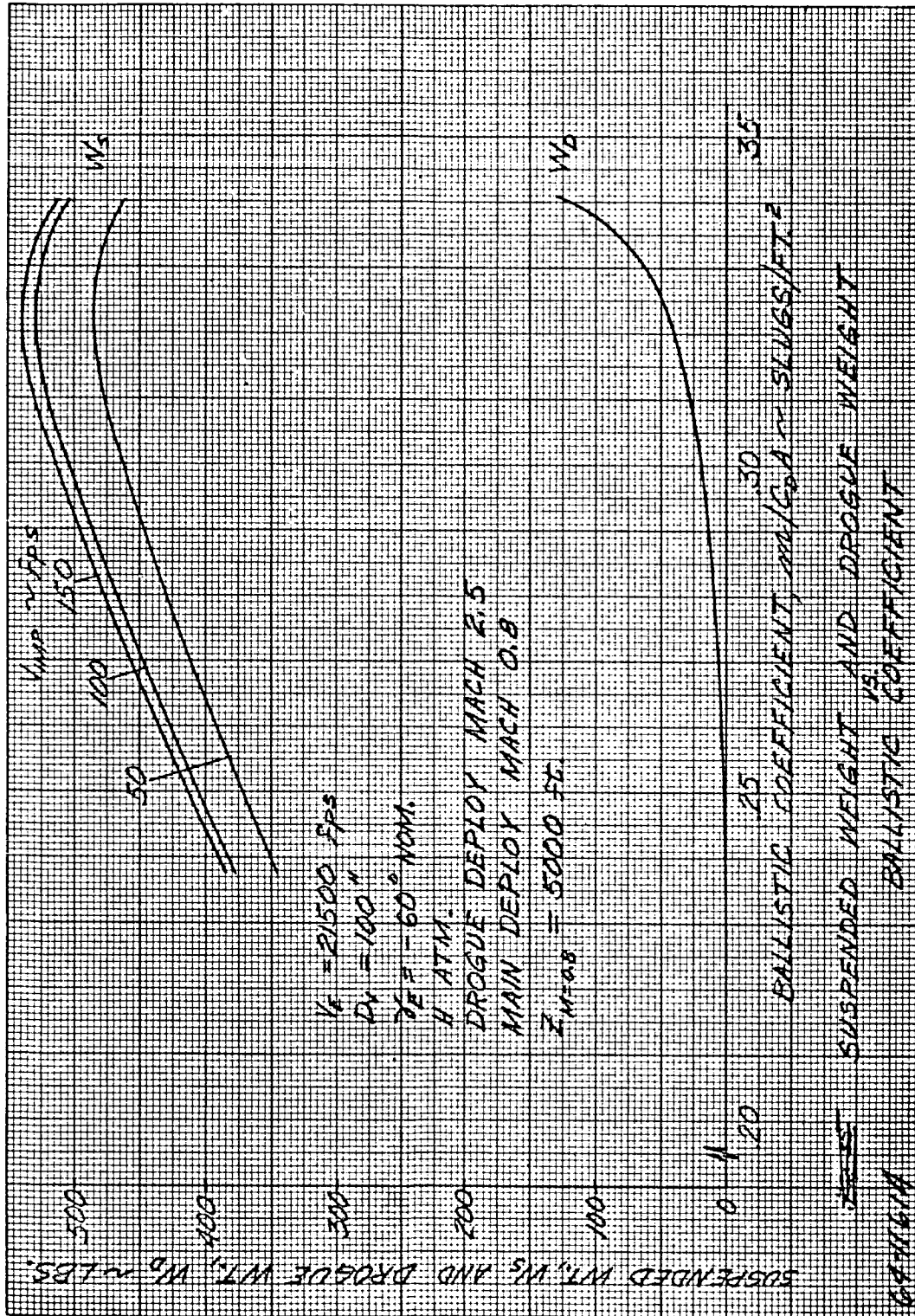


Figure 113 SUSPENDED WEIGHT AND DROGUE CHUTE WEIGHT VERSUS M/C_{DA} (ALTITUDE OF 5000 FEET AT MAIN CHUTE DEPLOYMENT AND γ_{nominal} OF 60 DEGREES)

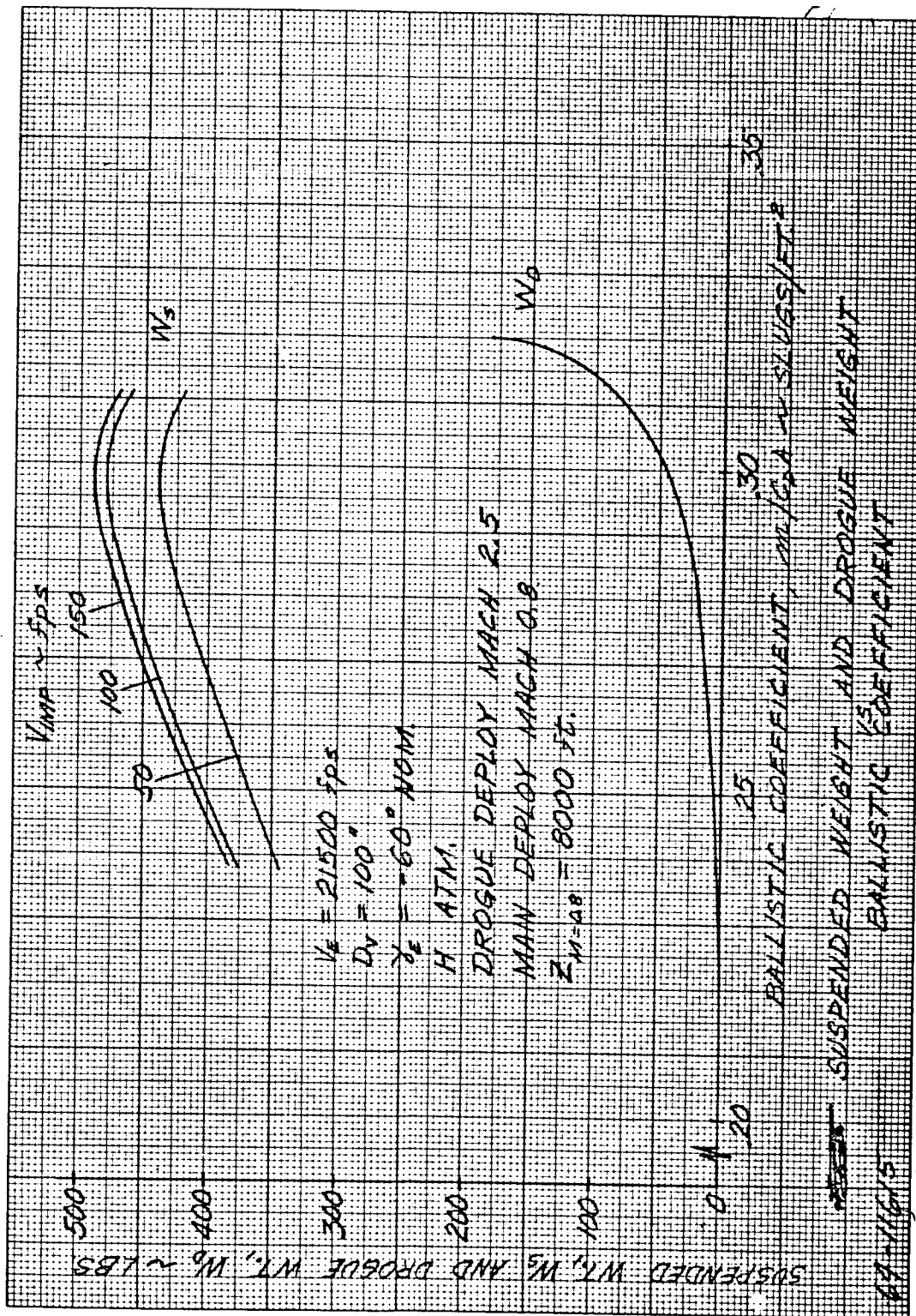


Figure 114 SUSPENDED WEIGHT AND DROGUE CHUTE WEIGHT VERSUS M/CDA (ALTITUDE OF 8000 FEET AT MAIN CHUTE DEPLOYMENT AND $\gamma_{c \text{ nominal}}$ OF 60 DEGREES)

1002

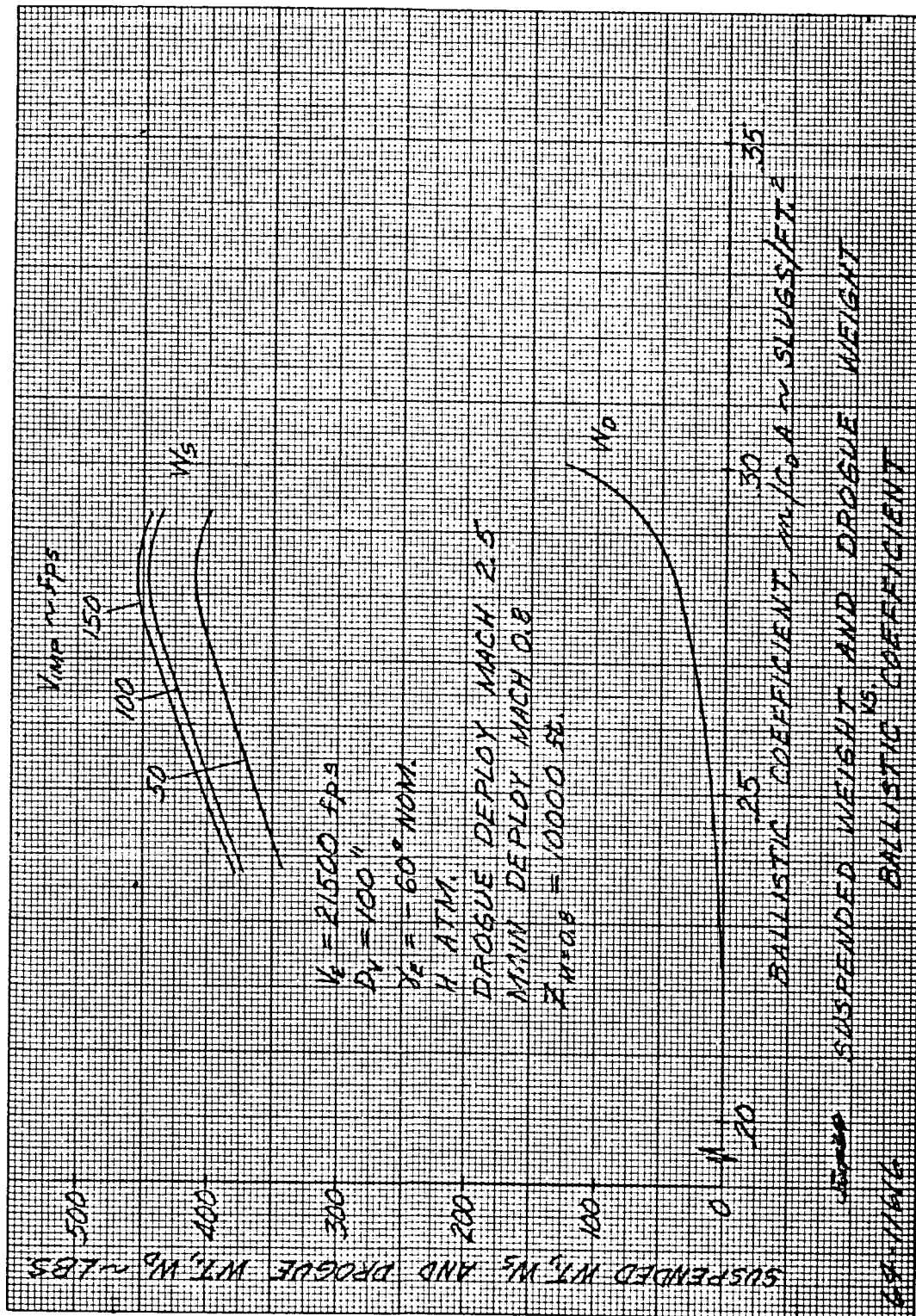


Figure 115 SUSPENDED WEIGHT AND DROGUE CHUTE WEIGHT VERSUS M/CDA (ALTITUDE OF 10,000 FEET AT MAIN CHUTE DEPLOYMENT) AND $Y_{c \text{ nominal}}$ OF 60 DEGREES

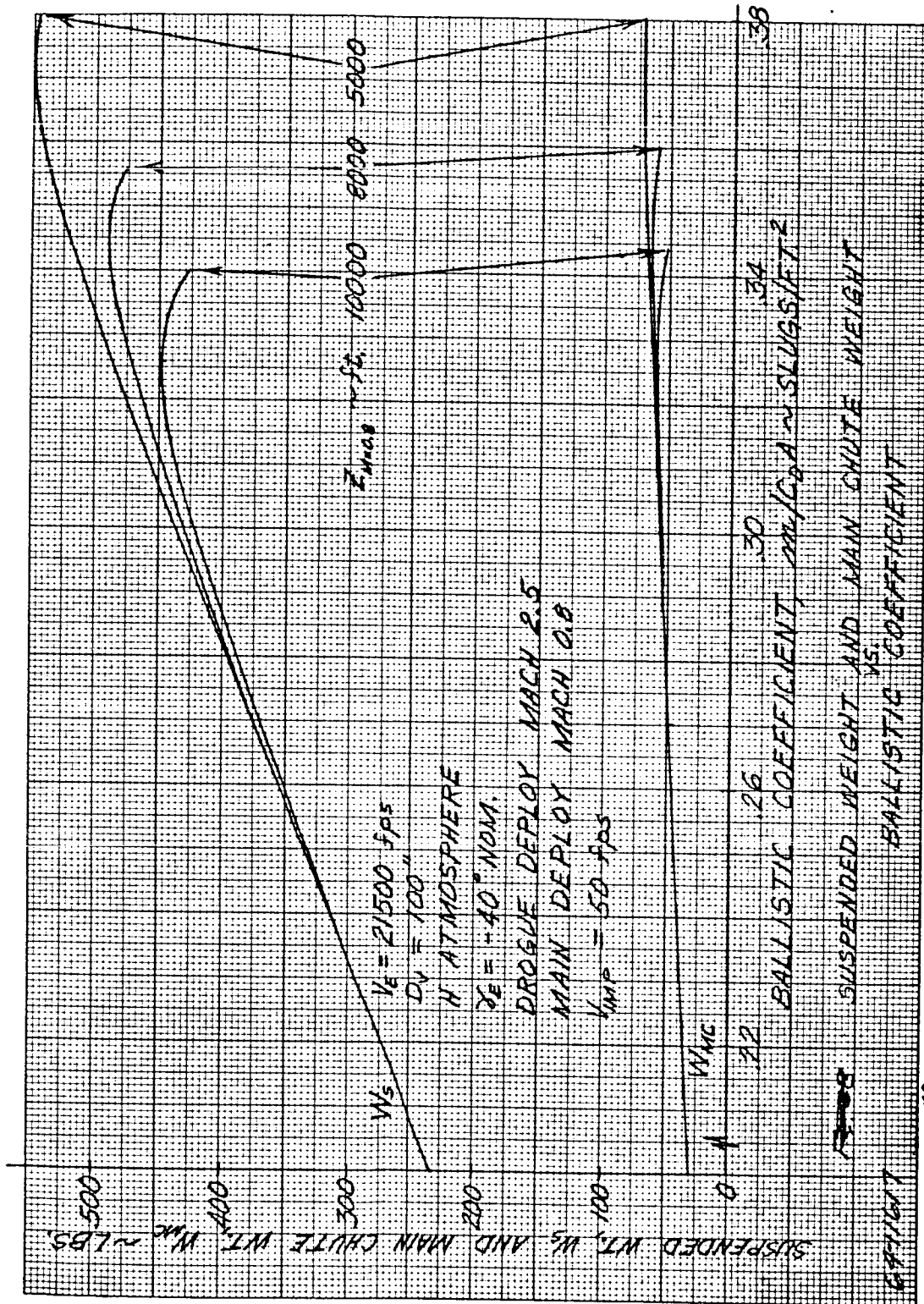


Figure 116 SUSPENDED WEIGHT AND MAIN CHUTE WEIGHT VERSUS M/CDA
(IMPACT VELOCITY OF 50 FPS AND $V_{e \text{ nominal}}$ OF 40 DEGREES)

244

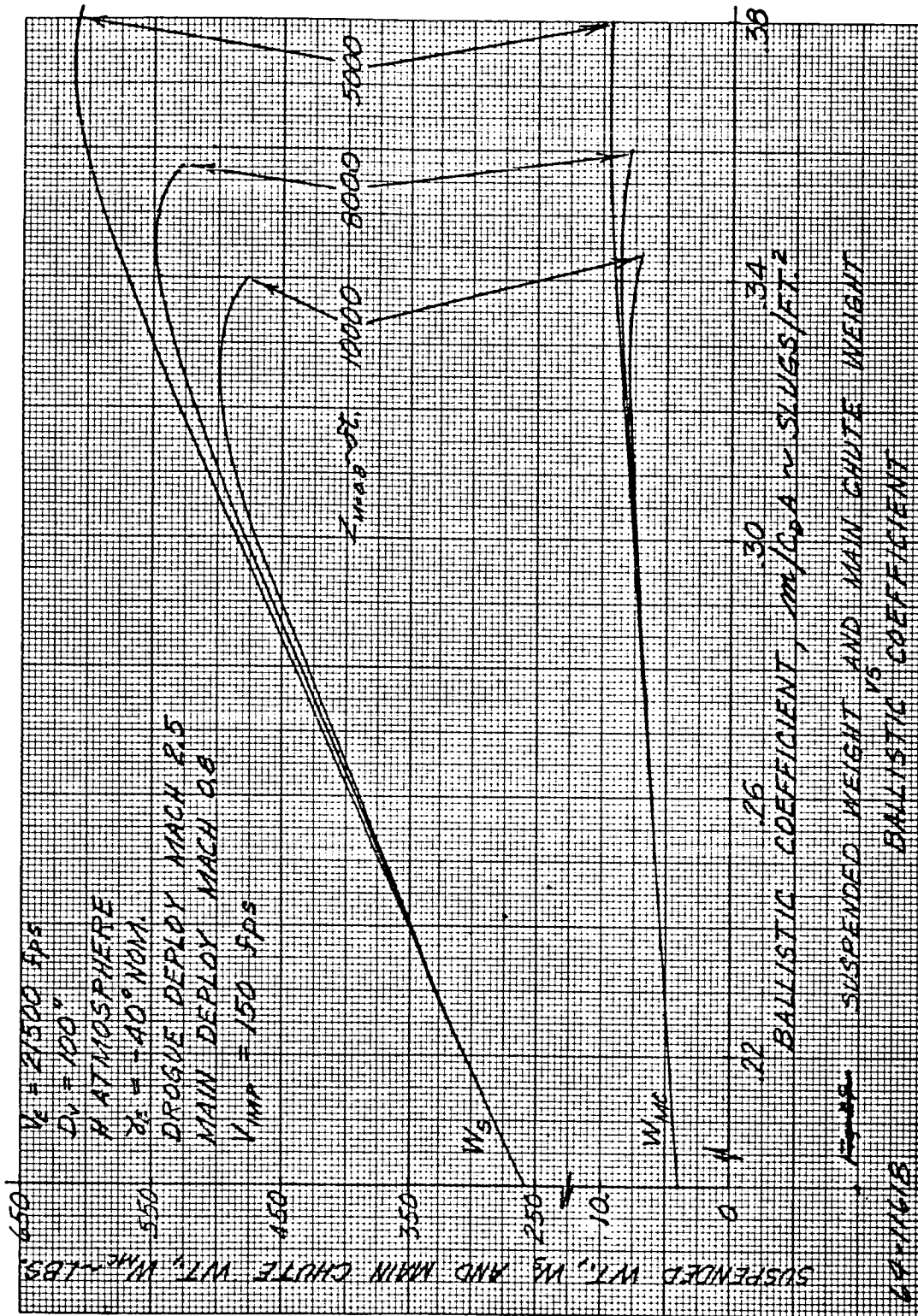


Figure 117 SUSPENDED WEIGHT AND MAIN CHUTE WEIGHT VERSUS M/CDA (IMPACT VELOCITY OF 150 FPS AND $\gamma_{e \text{ nominal}}$ OF 40 DEGREES)

245

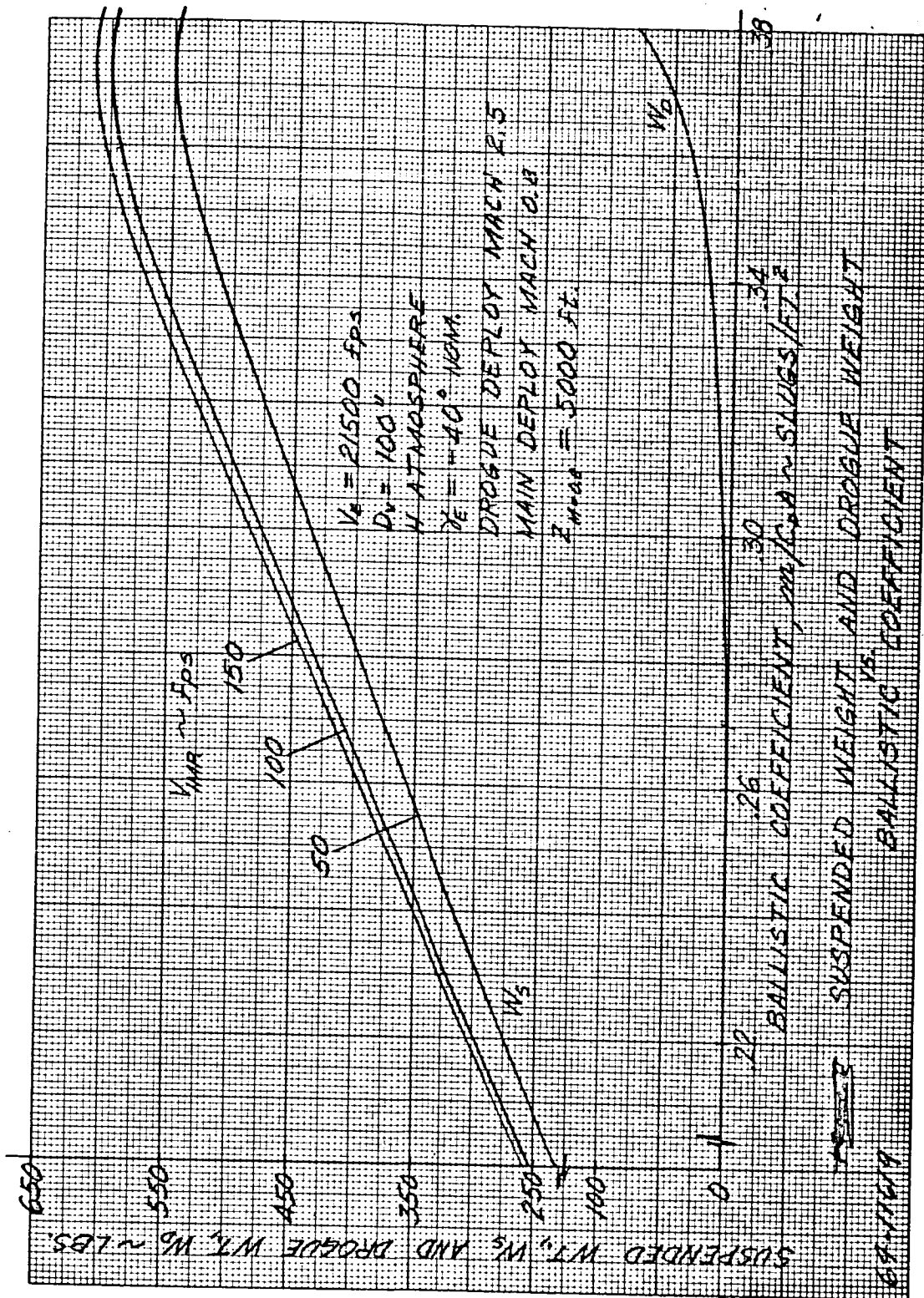


Figure 118 SUSPENDED WEIGHT AND DROGUE CHUTE WEIGHT VERSUS
 M/CDA (ALTITUDE OF 5000 FEET AT MAIN CHUTE DEPLOYMENT
 AND Y_{nominal} OF 40 DEGREES)

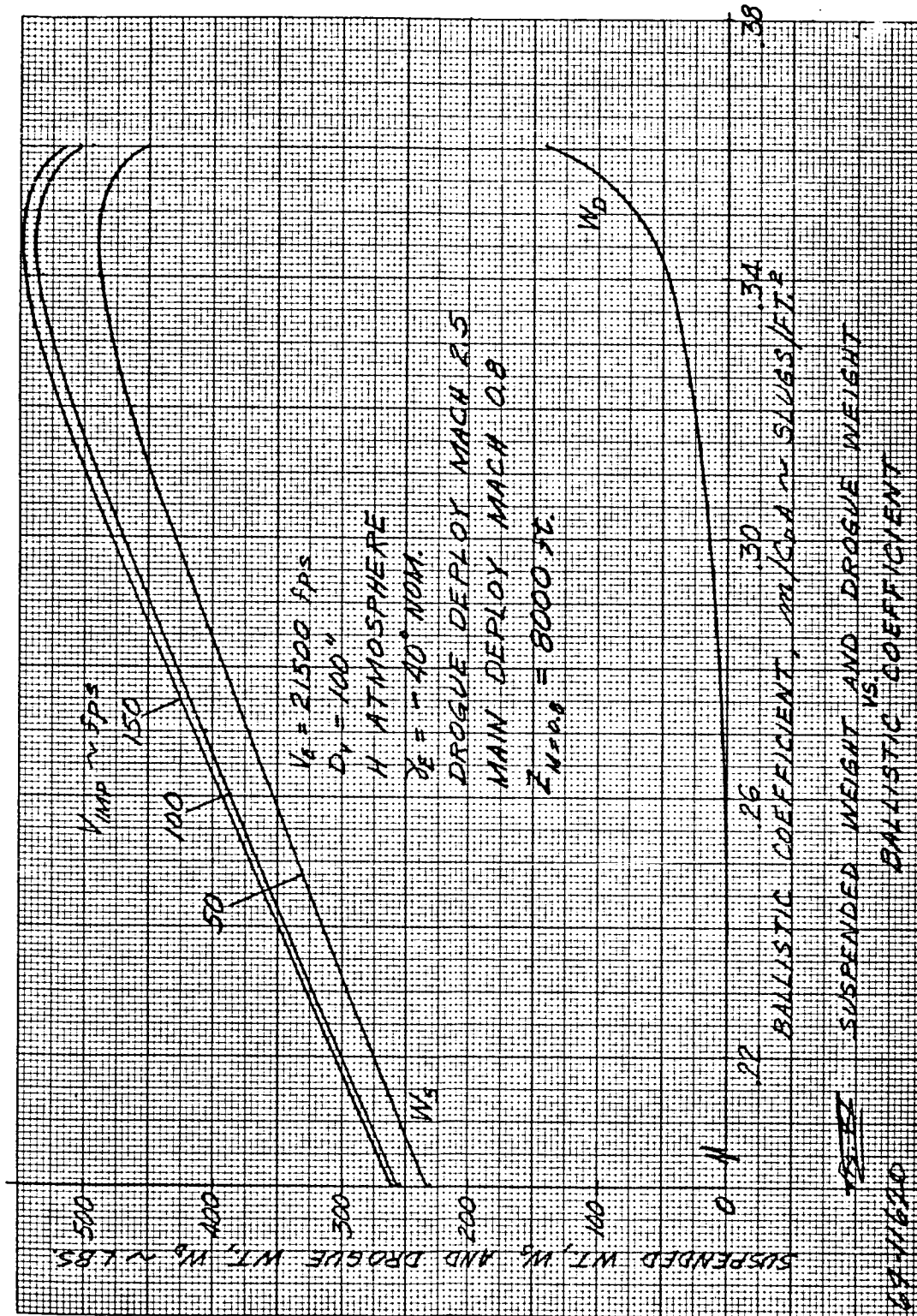


Figure 119 SUSPENDED WEIGHT AND DROGUE CHUTE WEIGHT VERSUS M/CDA (ALTITUDE OF 8000 FEET AT MAIN CHUTE DEPLOYMENT AND $\gamma_{c_{nominal}}$ OF 40 DEGREES)

247

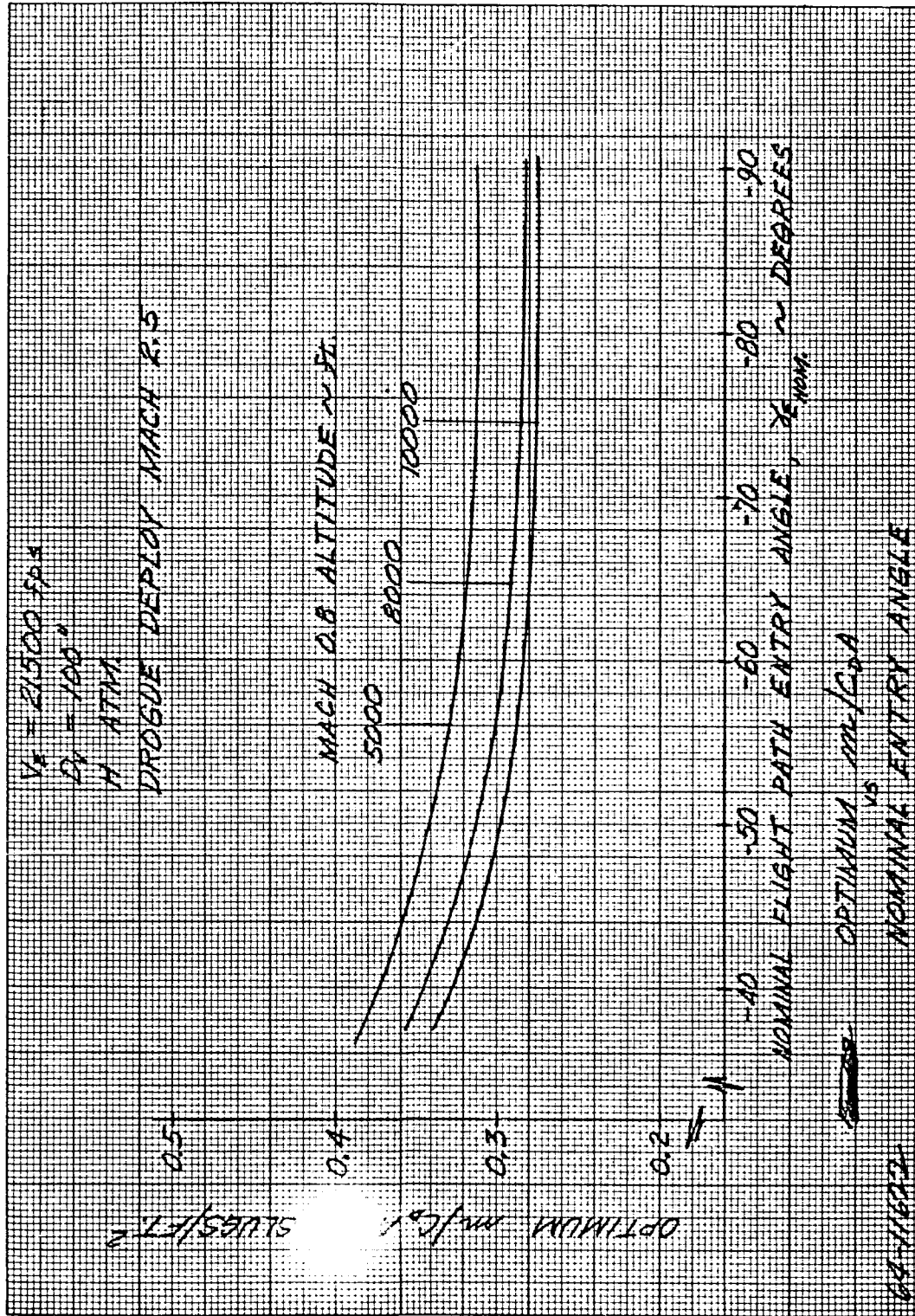


Figure 121 OPTIMUM m/C_{DA} VERSUS NOMINAL ENTRY ANGLE

2.19

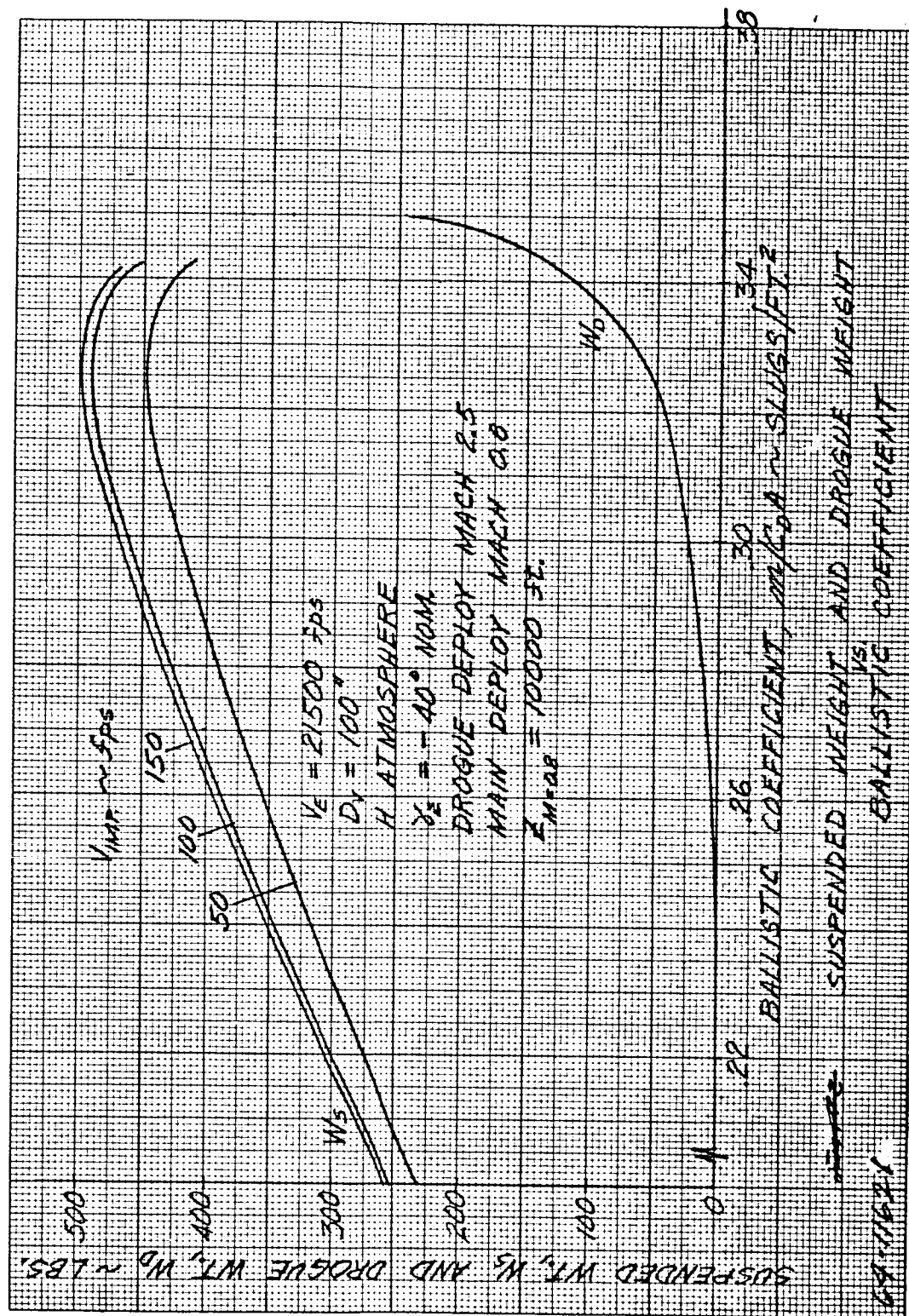


Figure 120 SUSPENDED WEIGHT AND DROGUE CHUTE WEIGHT VERSUS
 M/CDA (ALTITUDE OF 10,000 FEET AT MAIN CHUTE DEPLOYMENT
 AND $\gamma_{c \text{ nominal}}$ OF 40 DEGREES)

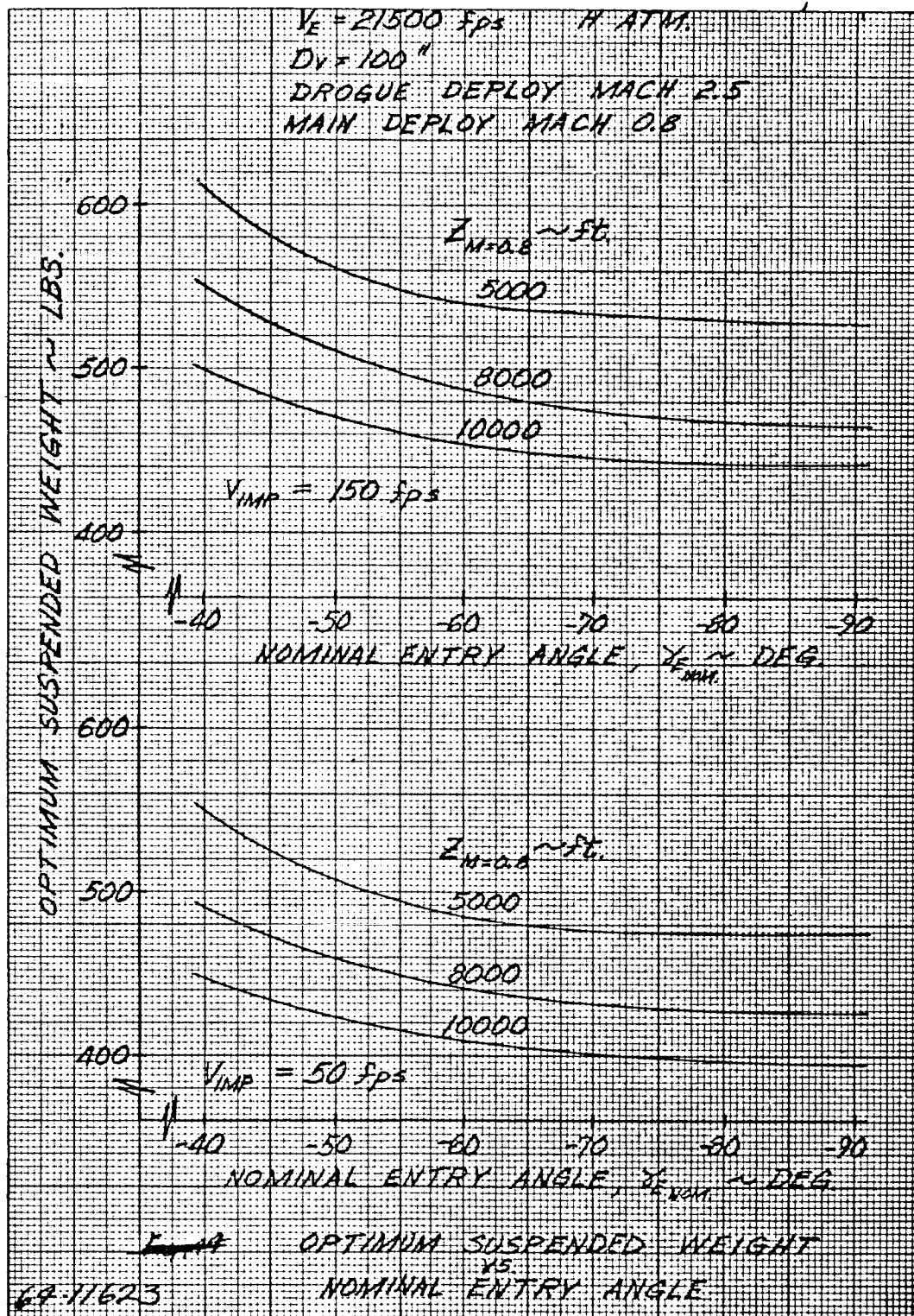


Figure 122 OPTIMUM SUSPENDED WEIGHT VERSUS NOMINAL ENTRY ANGLE

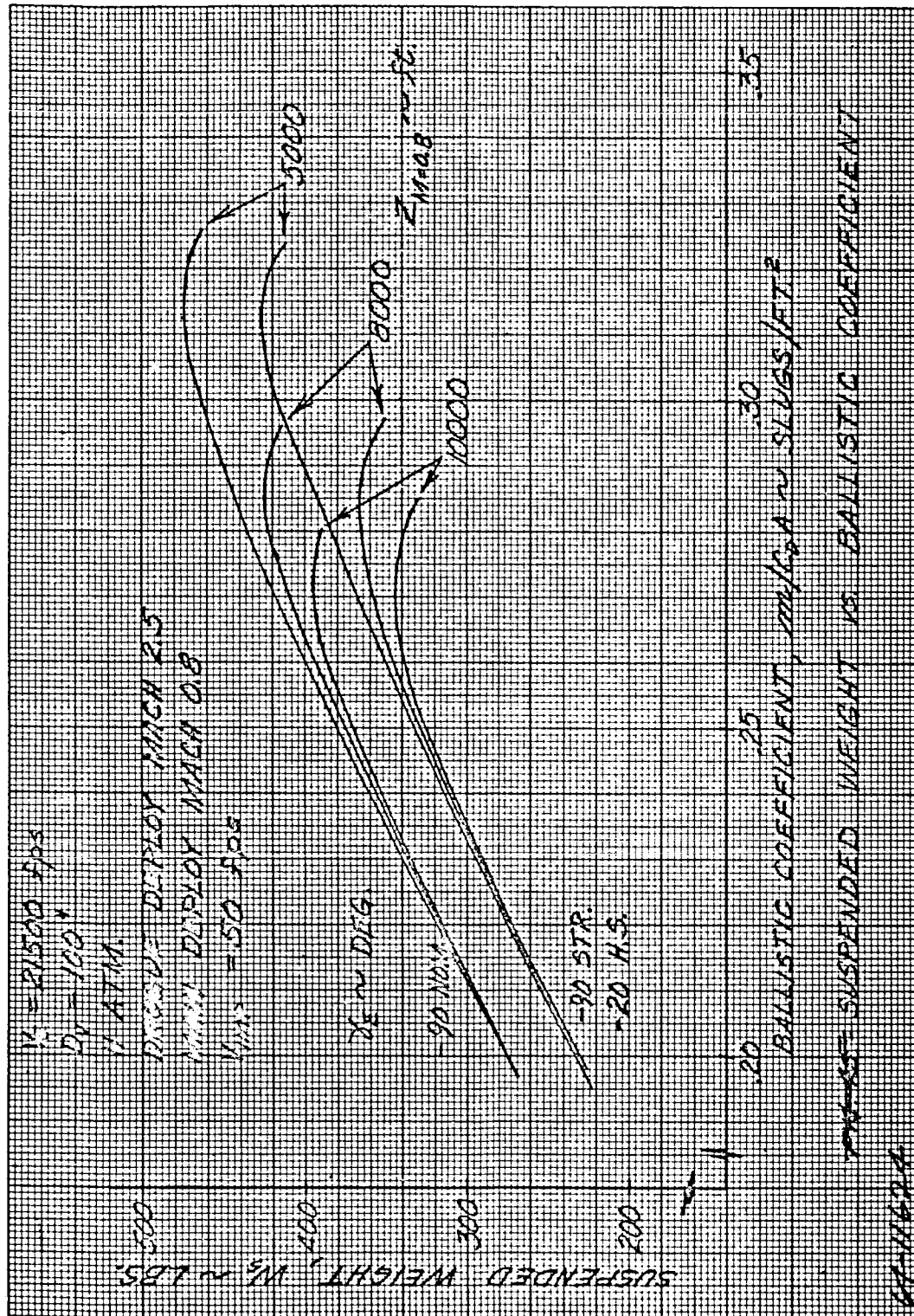


Figure 123 SUSPENDED WEIGHT VERSUS m/C_{DA} (COMPARISON BETWEEN 90 DEGREES NOMINAL ENTRY DESIGN AND ENTIRE ENTRY ANGLE SPECTRUM 20 DEGREES - 90 DEGREES)

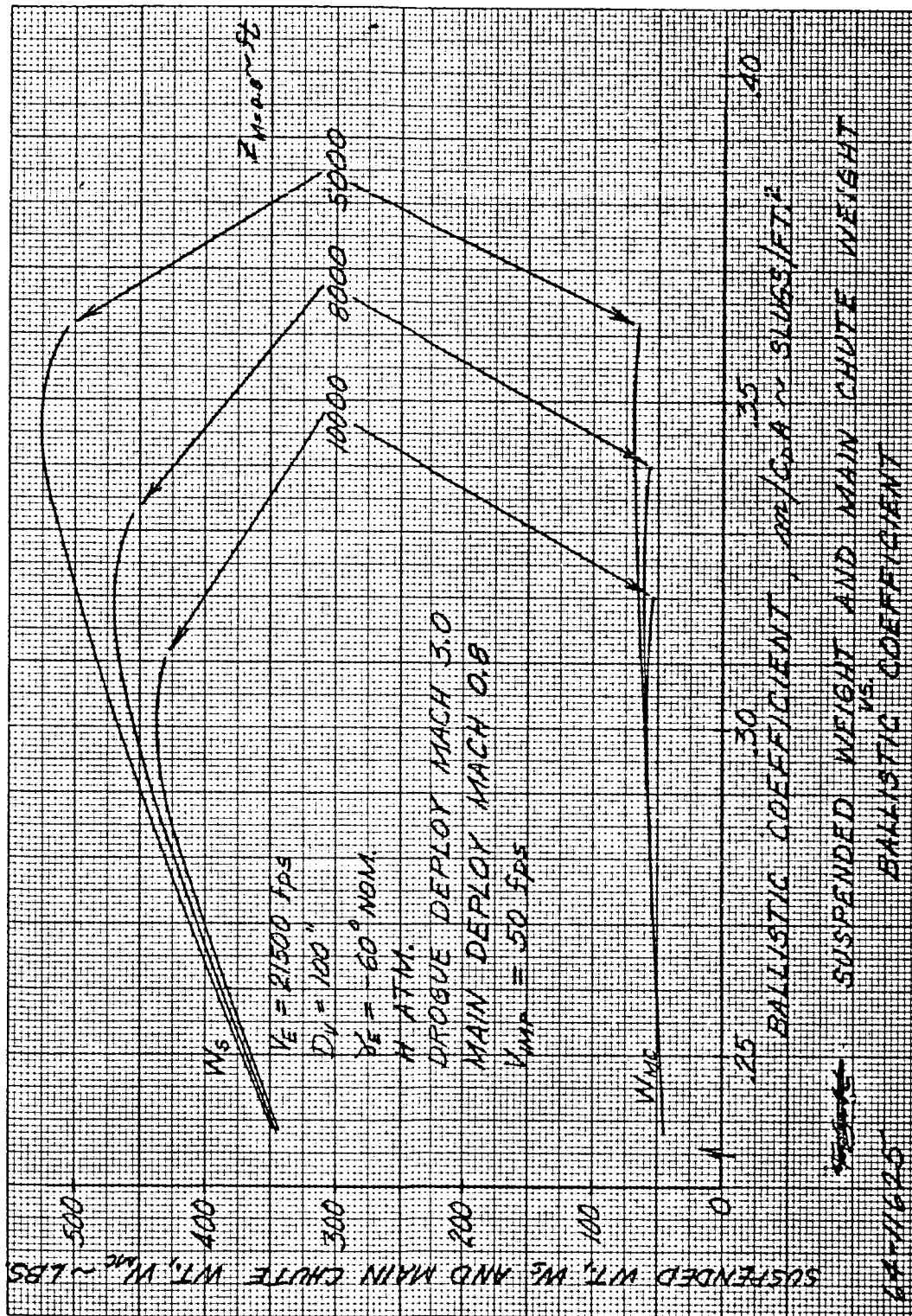


Figure 124 SUSPENDED WEIGHT AND MAIN CHUTE WEIGHT VERSUS M/C_{DA}
 (IMPACT VELOCITY OF 50 FPS, $\gamma_{nominal}$ OF 60 DEGREES AND
 DROGUE DEPLOYMENT AT MACH 3.0)

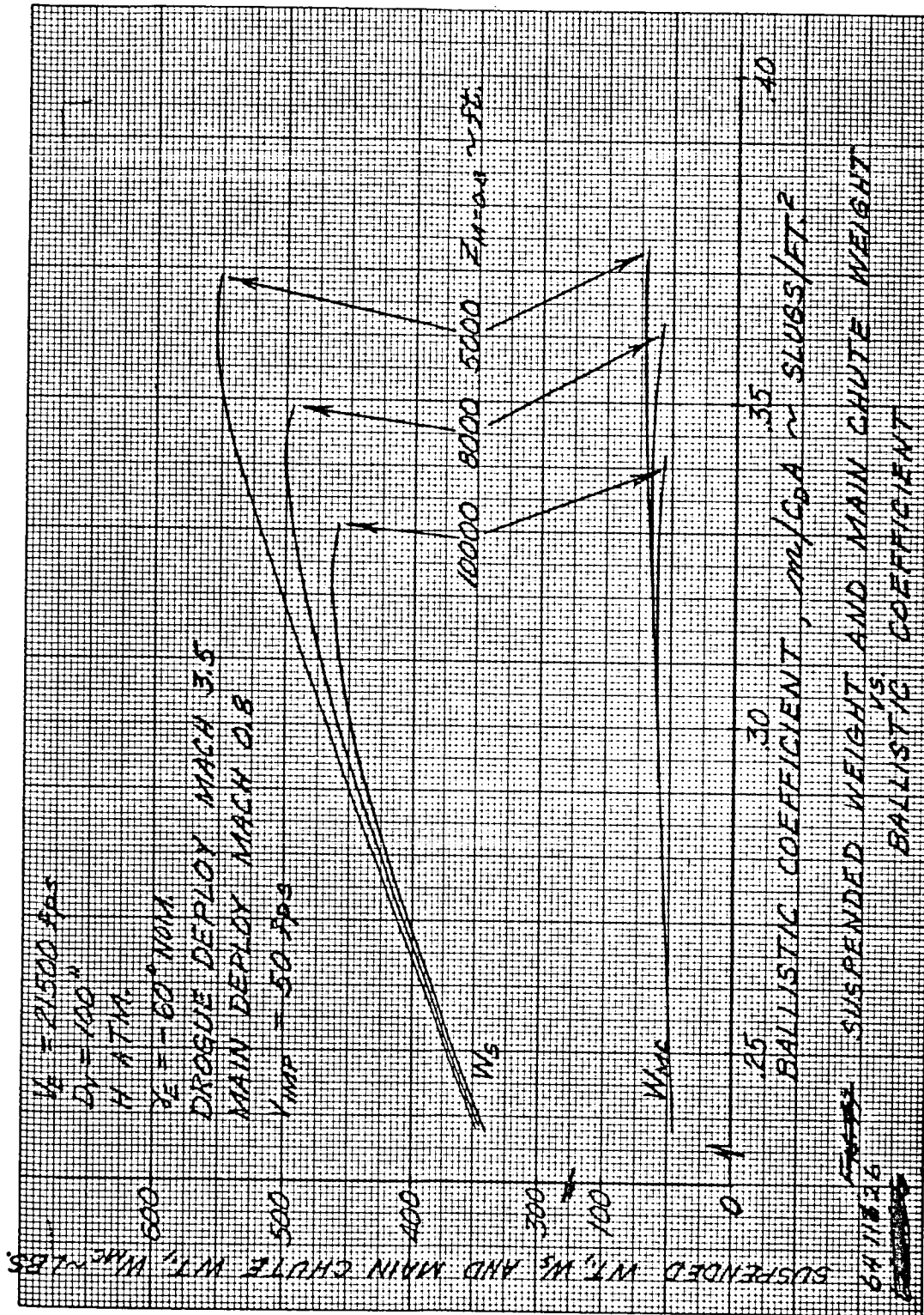


Figure 125 SUSPENDED WEIGHT AND MAIN CHUTE WEIGHT VERSUS $m/C_D A$ (IMPACT VELOCITY OF 50 FPS, γ_{nominal} OF 60 DEGREES AND DROGUE DEPLOYMENT AT MACH 3.5)

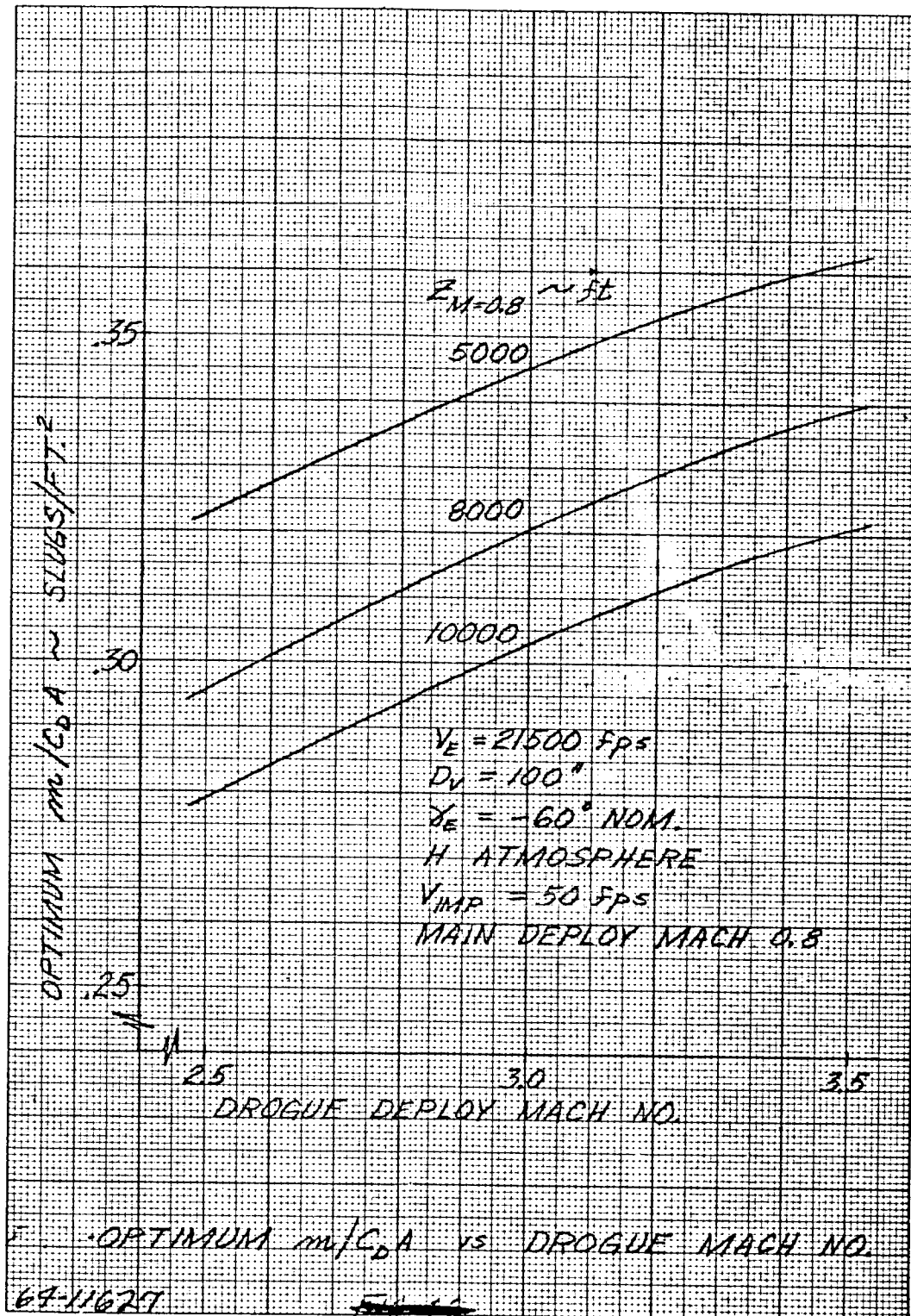


Figure 126 OPTIMUM M/C_{DA} VERSUS DROGUE DEPLOYMENT MACH NUMBER (γ_{nominal} OF 60 DEGREES AND V_{imp} OF 50 FPS)

230

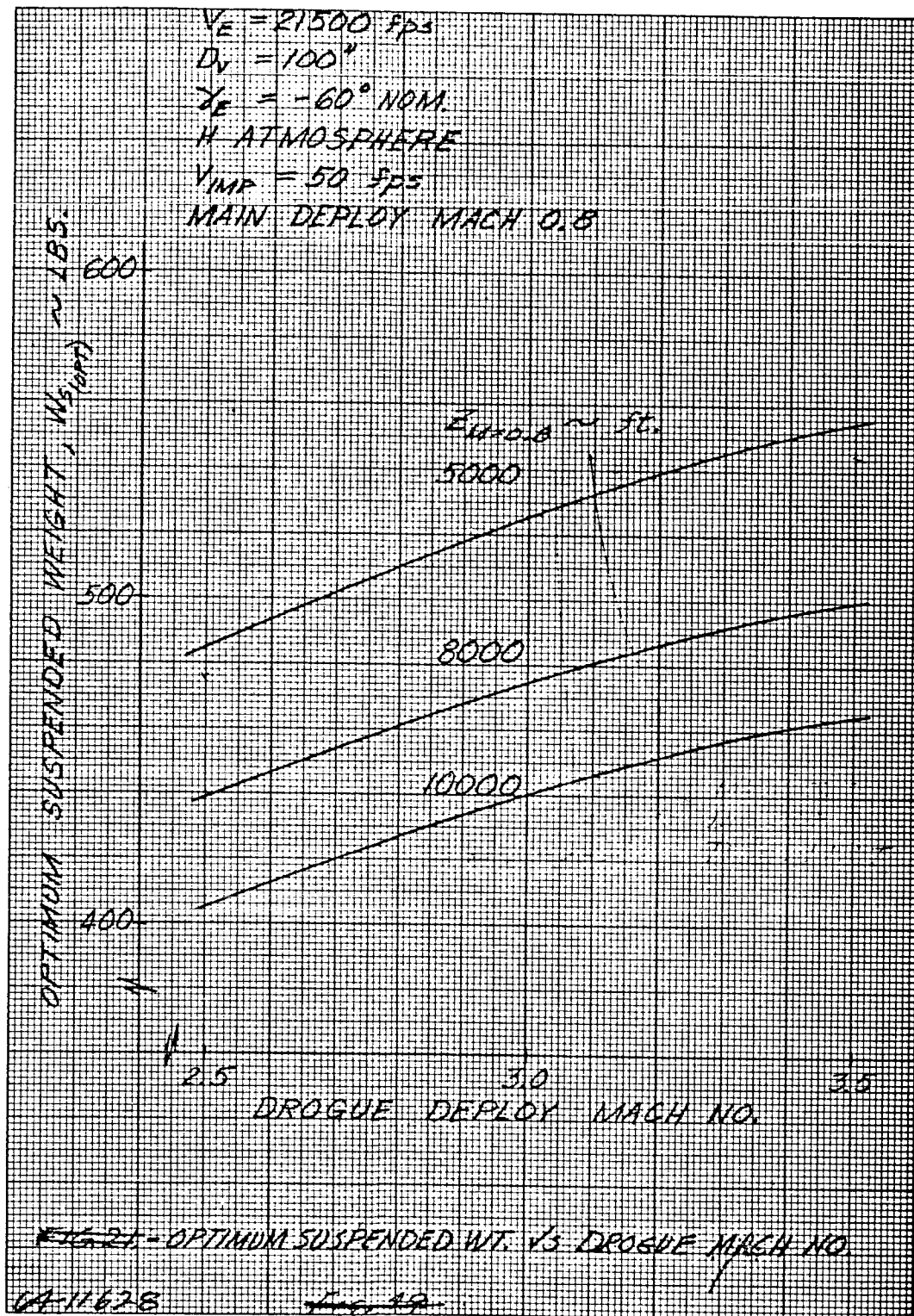


Figure 127 OPTIMUM SUSPENDED WEIGHT VERSUS DROGUE MACH
 NUMBER (γ_{nominal} OF 60 DEGREES AND V_{imp} OF 50 FPS)

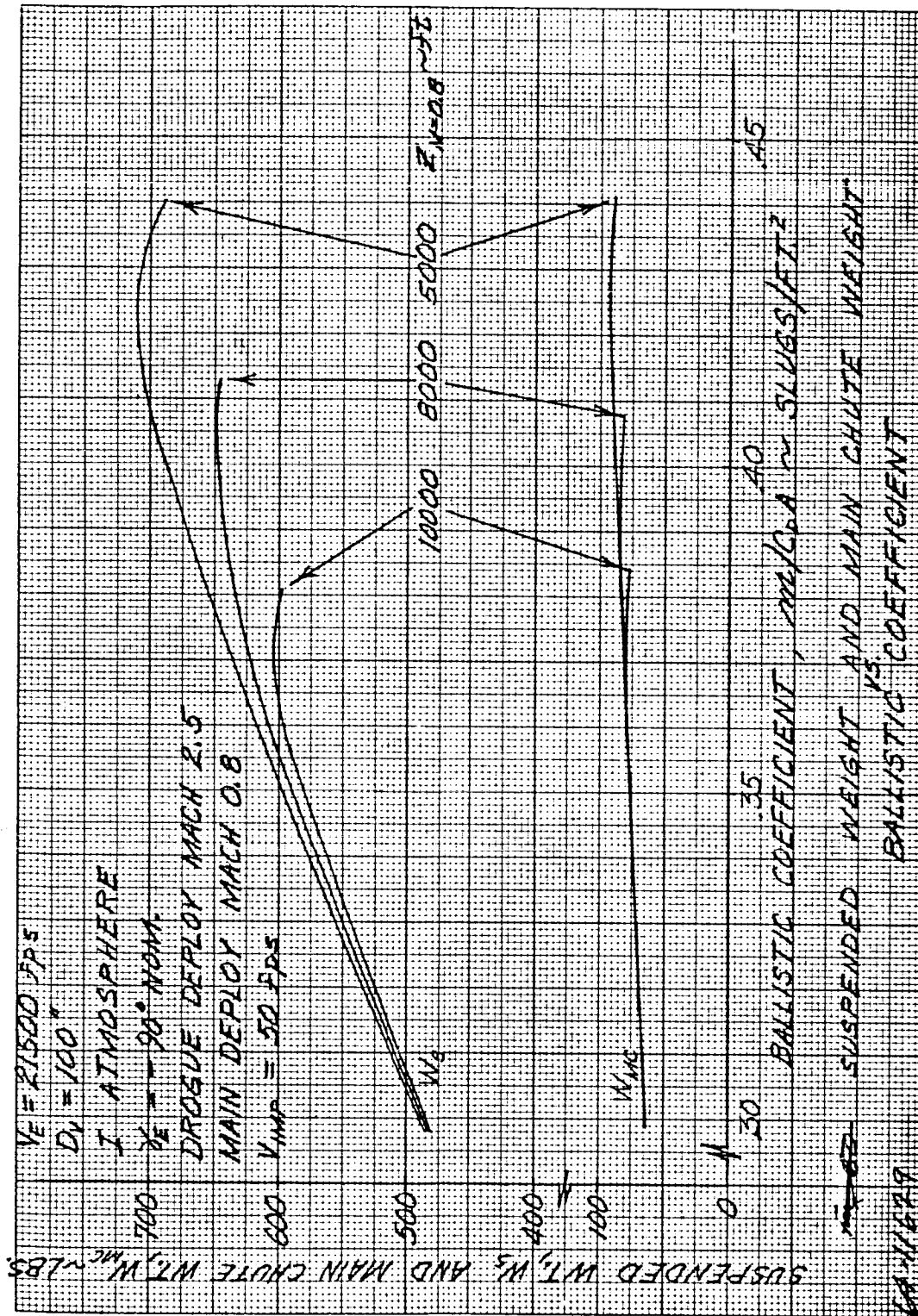


Figure 128 SUSPENDED WEIGHT AND MAIN CHUTE WEIGHT VERSUS M/CDA
 IN THE "T" MODEL ATMOSPHERE (IMPACT VELOCITY OF 50 FPS,
 $\gamma_{\text{nominal}} = 90^\circ$ DEGREES AND DROGUE
 DEPLOYMENT AT MACH 2.5)

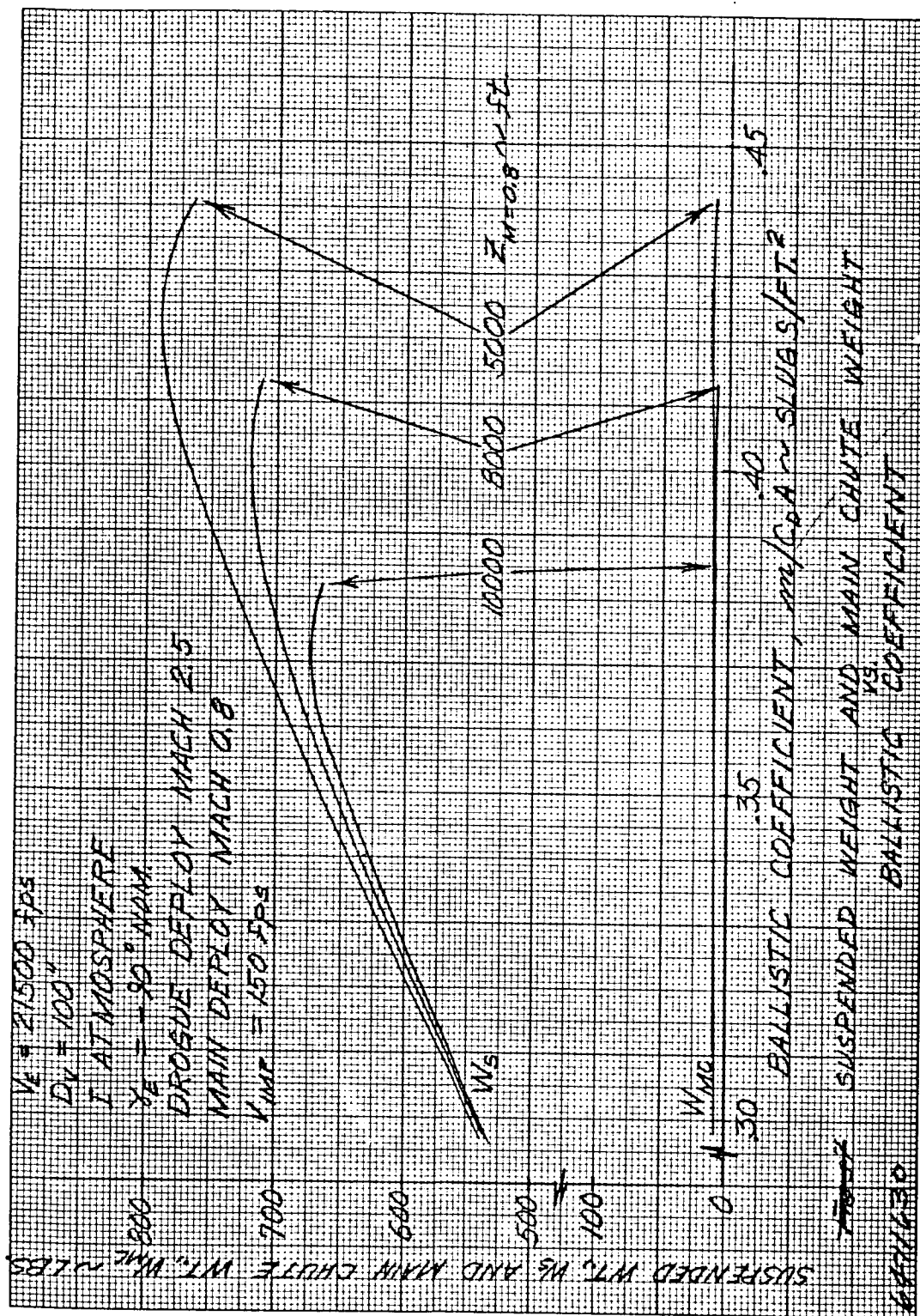


Figure 129 SUSPENDED WEIGHT AND MAIN CHUTE WEIGHT VERSUS m/C_{DA}
 IN THE "I" MODEL ATMOSPHERE (IMPACT VELOCITY OF 150 FPS,
 γ_{nominal} OF 90 DEGREES AND DROGUE
 DEPLOYMENT AT MACH 2.5)

237

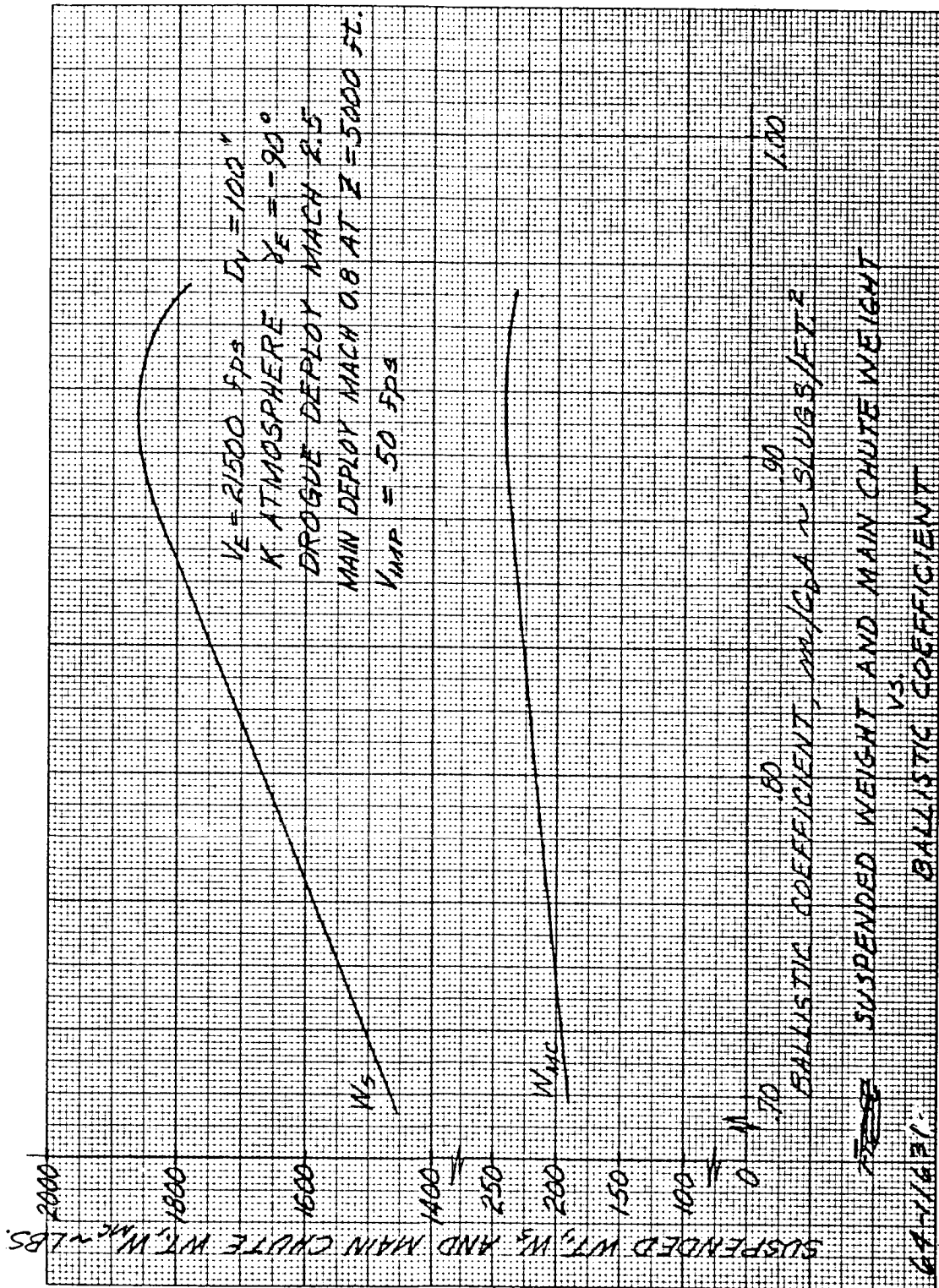


Figure 130 SUSPENDED WEIGHT AND MAIN CHUTE WEIGHT VERSUS m/C_{DA} IN THE "K" MODEL ATMOSPHERE (IMPACT VELOCITY OF 50 FPS, $\gamma_{nominal}$ OF 90 DEGREES AND DROGUE DEPLOYMENT AT MACH 2.5)

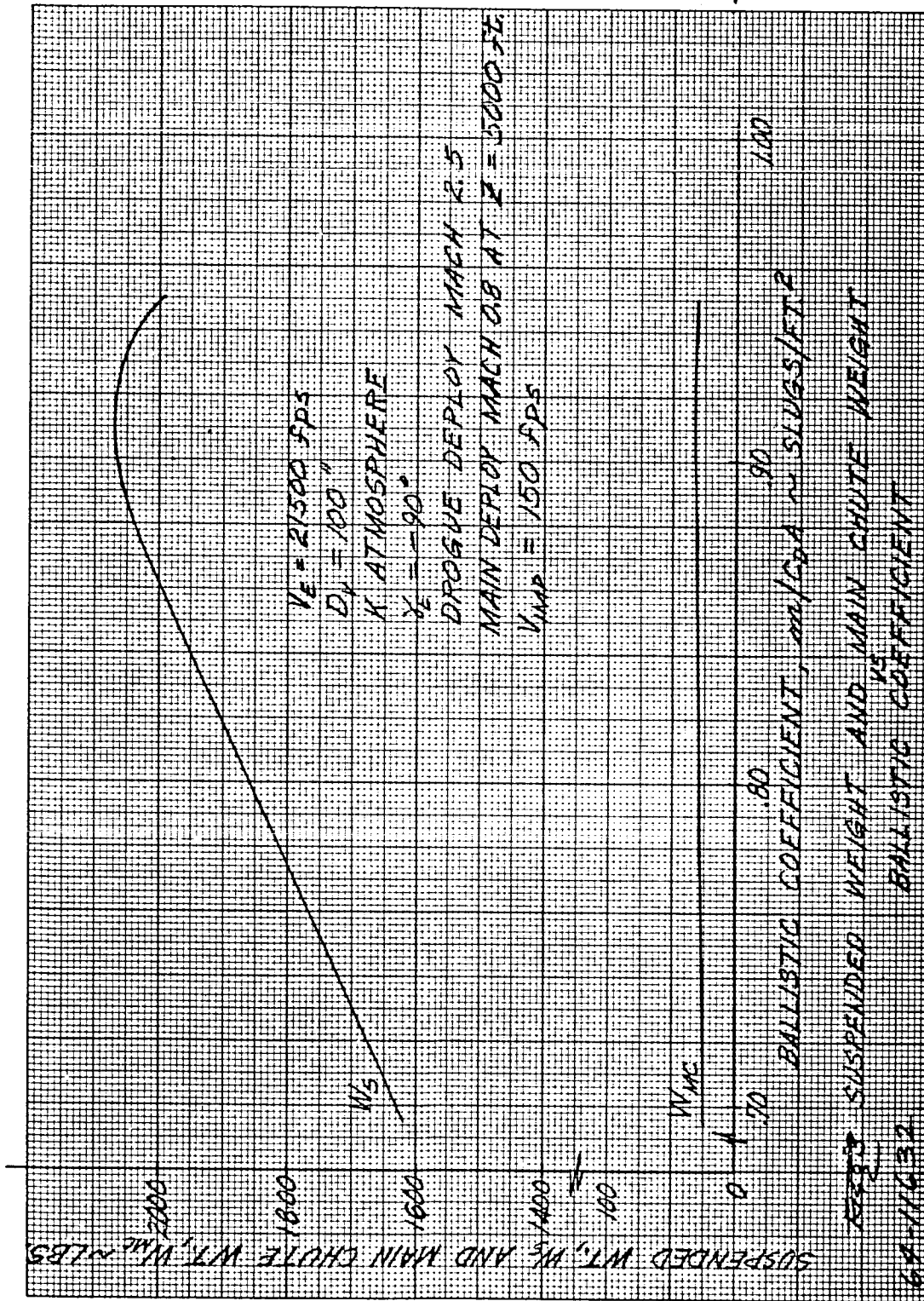


Figure 131 SUSPENDED WEIGHT AND MAIN CHUTE WEIGHT VERSUS M/CDA IN THE "K" MODEL ATMOSPHERE (IMPACT VELOCITY OF 150 FPS, OF 90 DEGREES AND DROGUE DEPLOYMENT AT 2.5)

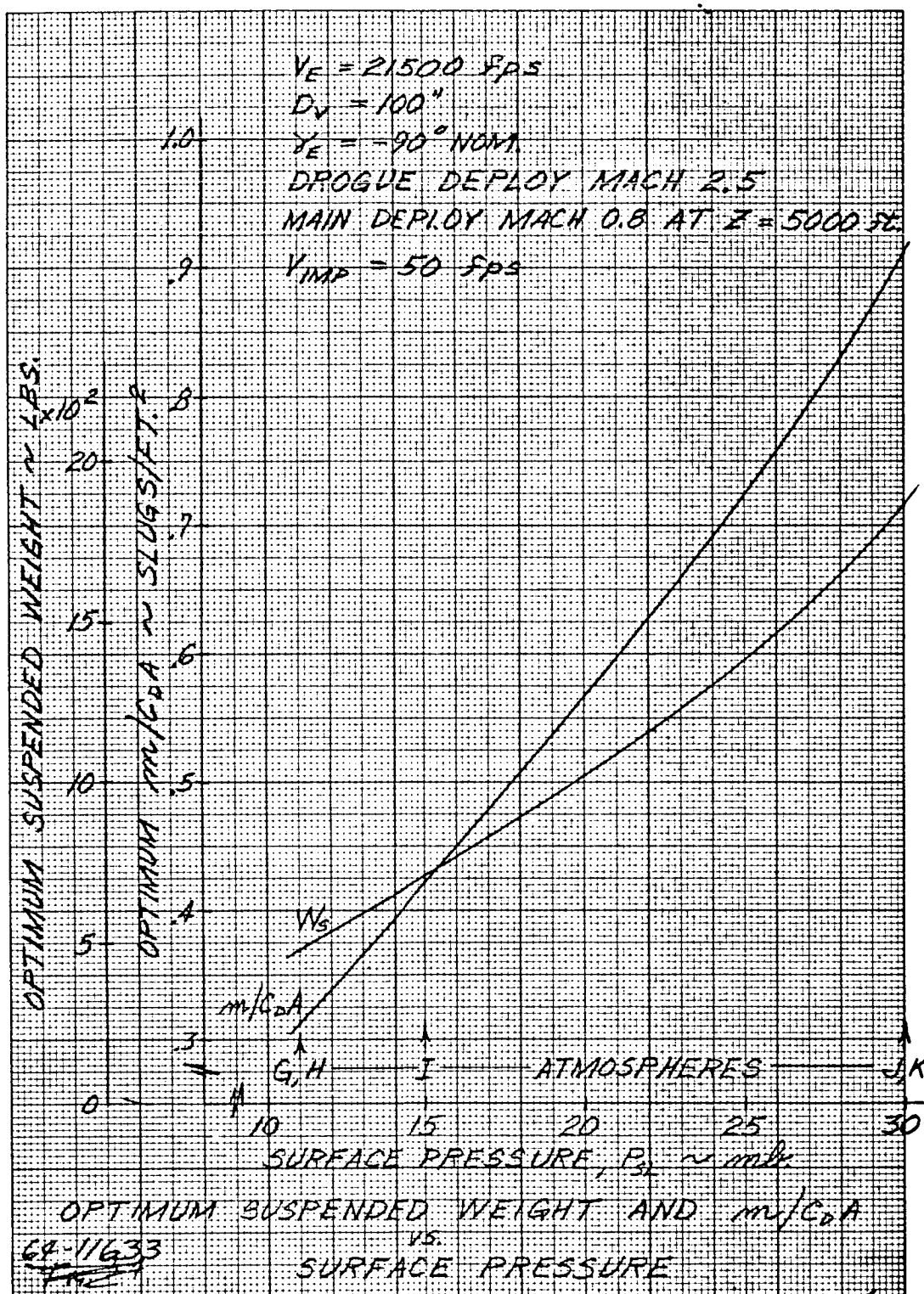


Figure 132 OPTIMUM SUSPENDED WEIGHT AND m/C_{DA} VERSUS SURFACE PRESSURE (IMPACT VELOCITY OF 50 FPS, γ_{nominal} OF 90 DEGREES AND DROGUE DEPLOYMENT AT MACH 2.5)

4. Vehicle Diameter Effects

Results to demonstrate the effect of vehicle diameter are shown on figures 133 through 135. Parametric curves include results for three main chute deployment altitudes, two impact velocities, and the entire entry angle spectrum. Vehicle diameter does not effect the optimum m/CDA but rather only the optimum suspended weight. Figures 133 and 134 show results for a 80 and 90 inch vehicle, respectively, while a summary of the effects of vehicle diameter is shown on figure 135.

7.6 CONCEPTUAL DESIGN ANALYSIS

The following is a detailed analysis and weight breakdown of the parachute descent system. The reference design utilizes a two-chute system consisting of a drogue chute with a nominal deployment of Mach 2.5 and a main chute with a nominal deployment of 0.8. A two-chute system was chosen in lieu of a one-chute system because of the descent time requirements and the difficulty of jettisoning the rear portion of the entry vehicle with a single chute system. It should also be noted that a single chute system would require approximately a 40-foot drogue chute which is beyond the state-of-art development.

The conceptual design input parameters are listed below.

m/CDA	0.244 slugs/ft ²
Vehicle Diameter	90 inches
Modified Apollo Shape	
Drogue Chute Deployment Mach No	2.5
Main Chute Deployment Mach No	0.8
Main Chute Deployment Altitude	8000 feet
Impact Velocity	65 ft/sec
Drogue Area/Vehicle Area $\sim A_D/A_V$	5.3
Main Chute Area/Suspended Wt. A_{mc}/W_s	6.2
Drogue Chute Diameter	17.2 feet
Drogue Chute Area	234.0 ft ²
Main Chute Diameter	50.0 feet
Main Chute Area	1960.0 ft ²
Hyperflo Drogue Chute	
Ring Sail Main Chute	

1. Drogue Chute System

a. Maximum Opening Shock Load

The maximum opening shock on the parachute can be expressed as

$$F_o = kq (C_D A) \text{ (see section 7.3)}$$

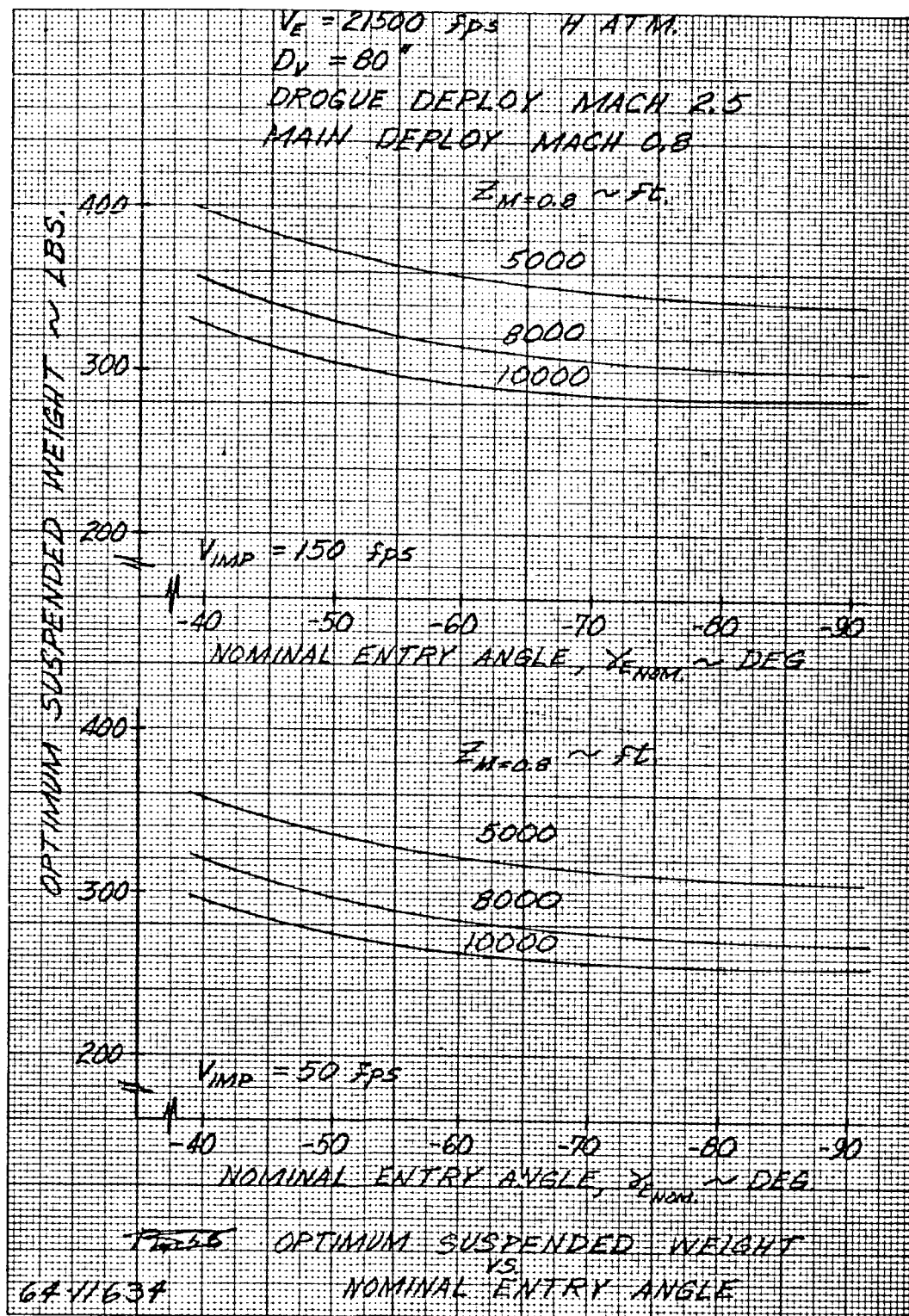


Figure 133 OPTIMUM SUSPENDED WEIGHT VERSUS NOMINAL ENTRY ANGLE FOR AN 80-INCH VEHICLE

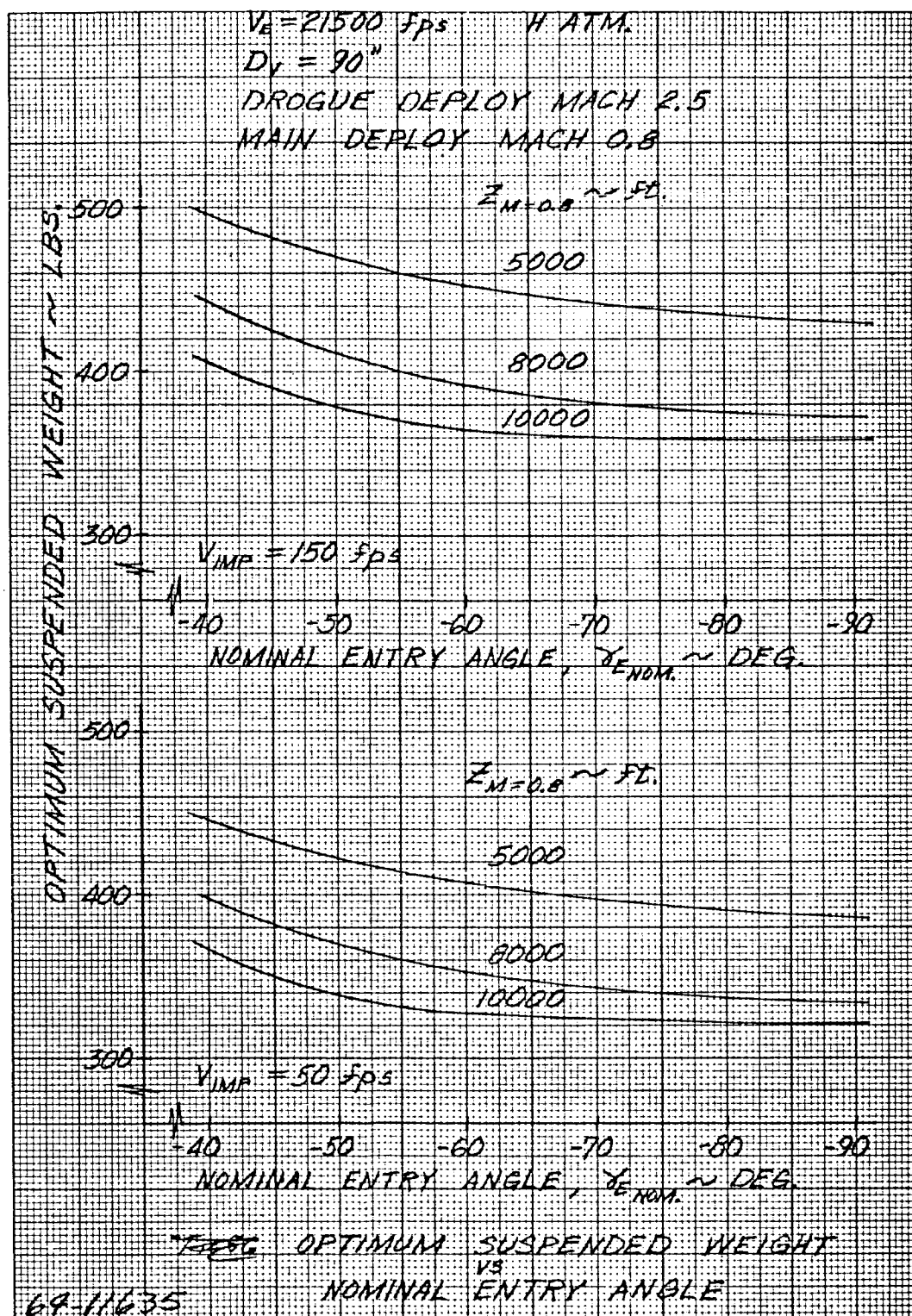


Figure 134 OPTIMUM SUSPENDED WEIGHT VERSUS NOMINAL ENTRY ANGLE
FOR A 90-INCH VEHICLE

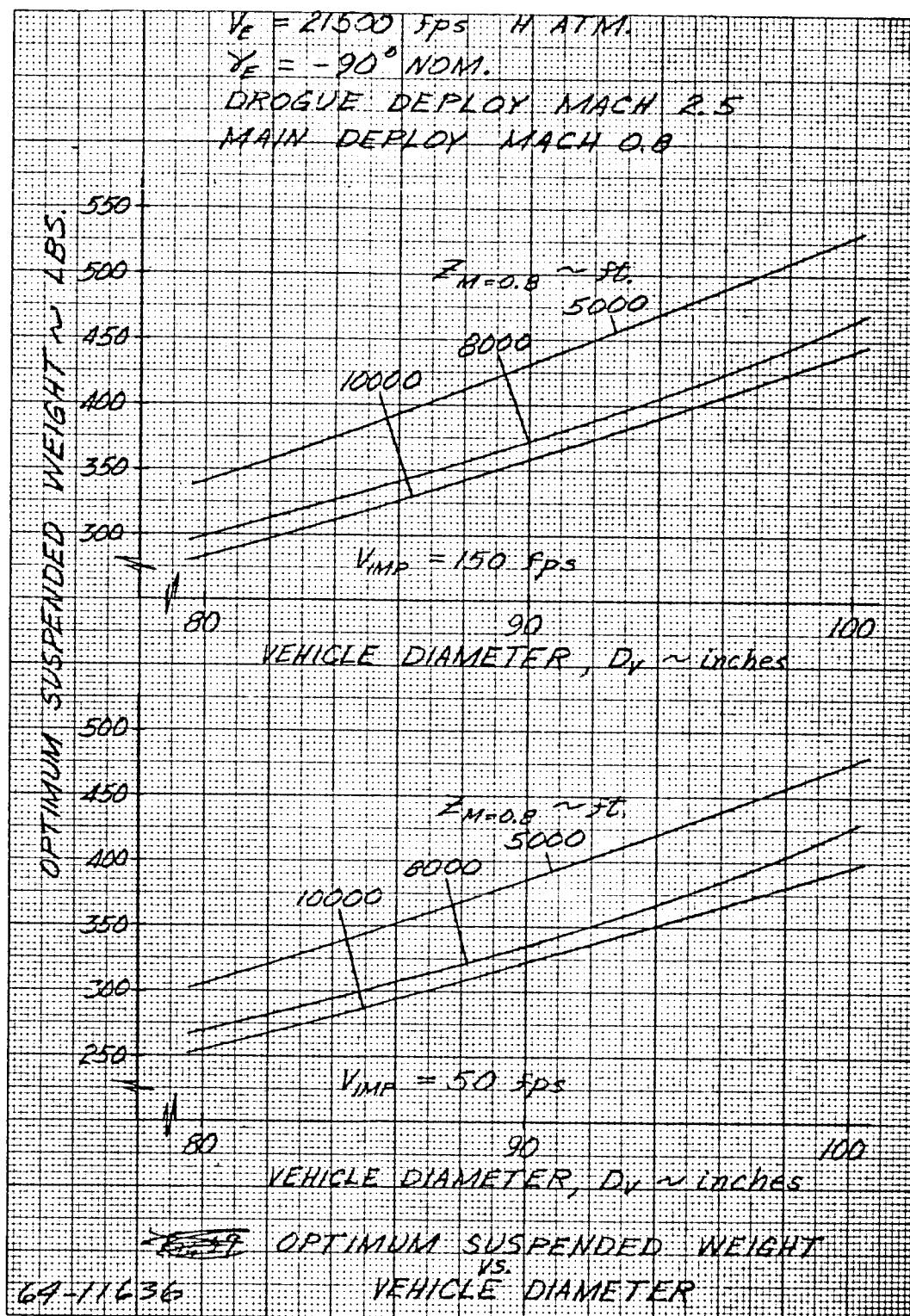


Figure 135 OPTIMUM SUSPENDED WEIGHT VERSUS VEHICLE DIAMETER

For the entry conditions stated above, the dynamic pressure at Mach 2.5 is 70 psf and C_D is 0.6. The amplification factor is 1.85; however, 2.0 will be used for conservatism. Hence,

$$F_o = 2.0 (80) .6 (234)$$

$$= 19,700 \text{ pounds}$$

An "overall design factor" should be applied to the above result. The design factor consists of a safety factor combined with other factors affecting the strength of the chute, e.g., the efficiency of the stitching at the junction of the canopy and the suspension lines. A reasonable design factor of 1.5 is suggested in Reference 3. Hence F_o is approximately 37,000 pounds. This results in 74.0 g at chute opening for a 500-pound vehicle.

b. Suspension Lines and Rise Line Sizing

Canopies should be inflated a minimum of three vehicle diameters behind the primary body in subsonic flow and eight vehicle diameters in supersonic flow. Tests show (reference 4) that the influence of suspension-line length on the inflated shape of the drag producing surface and its performance generally is greatest up to a ratio of L_S/D_o equal to 1.0 (see figure 136).

For L_S/D_o of 1.0, L_S is 17.2 feet, based on a 17.2 foot chute, and

$$L_R = 8 D_V - L_S = 8(8.33) - 17.2 \approx 42.8 \text{ feet.}$$

Table 31 lists the total required weight of the suspension lines.

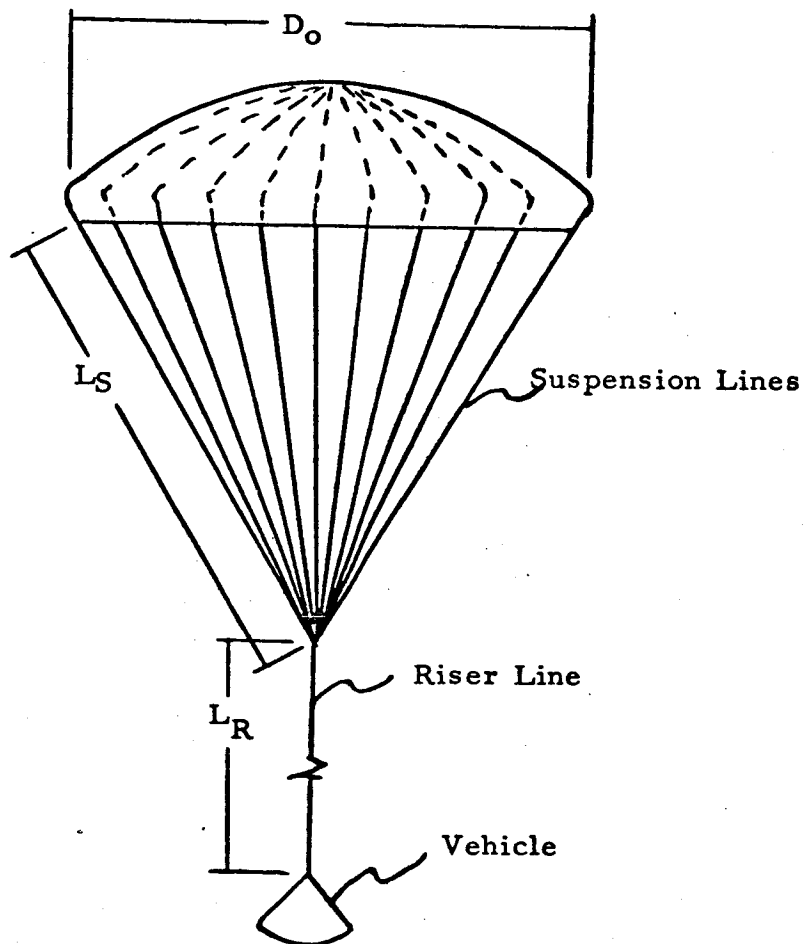
TABLE 31

REQUIRED WEIGHT OF SUSPENSION LINES

Number of Suspension Lines (N)	12	24	36
F_o/N (lbs/line)	3090	1545	1030
Type (ref. 2) MIL-SPEC	W-27657	W-005625C	W-006525C
Break Strength (lbs)	3000	1500	1000
Weigh (oz/yd)	0.9	0.6	0.5
Length Line Required (Ft.)	206	412	618
Total Weight (lbs)	3.86	5.15	6.45

Based on the results of table 31, the design chute will utilize 12 suspension lines which will be 4.5 feet apart on the parachute canopy periphery.

Suspension Line Weight - 3.9 lbs



11637

Figure 136 PARACHUTE CONFIGURATION AND NOMENCLATURE

266

c. Riser Line

The load on the riser line is 37,000 pounds (F_0). Heavy-duty nylon cord Mil-W-5787C, type II (reference 2) has a breaking strength of 40,000 pounds at 18 oz/yd.

Therefore, the total weight for a 42.8-foot riser line is

$$W_r = \frac{42.8 (18)}{48} = 16.1 \text{ pounds}$$

Riser Line Weight - 16.1 pounds

d. Canopy Weight

In calculating the stresses on the canopy of the Hyperflo parachute, a good approximation would be to assume the stress model to be a hemispherical shape. Hence, the stress on the canopy can be calculated by utilizing a thin-wall hemisphere approach, the expression of which is

$$S = \frac{q D_o}{4t} \quad \text{lbs/in}^2 \quad (\text{Reference 2})$$

where q is the pressure acting uniformly on the hemisphere and t is the thickness of the material. A common terminology is to express the loading in lb/in of length of cloth. This yields

$$L = S t = \frac{q D_o}{4}$$

Therefore,

$$L = \frac{70(17.2)}{4(12)} = 25.1 \text{ lb/in.}$$

Nylon cloth fabric with a break strength of 25 lb/in. weighs 0.6 oz/yd². The total canopy weight can now be calculated by approximating the total surface area of the Hyperflo to be hemispherical. Hence

$$A_{\text{surface}} = \frac{\pi D_o^2}{2} = \frac{\pi (17.2)^2}{2} = 465 \text{ ft}^2$$

and

$$W_{\text{canopy}} = \frac{0.6(465)}{144} = 5.8 \text{ pounds}$$

Add a 15 percent weight factor to the total canopy weight to account for doubling, stitching, etc.

$$W_{\text{canopy}} = 1.15(5.8) = 6.7 \text{ pounds}$$

Canopy Weight = 6.7 pounds

e. Other System Components

Bag	1.0 pounds
Aluminum Shell	.75
Pyrotechnic (Charge & Sabot)	.75
Sensing Equipment (Timer & Electrical Devices)	1.0
	<hr/> 3.5 pounds

f. Total Drogue Chute System Weight

Canopy (Including doubling and stitching factor)	6.7 pounds
Suspension Lines	3.9
Riser Line	16.1
Other System Components	3.5
	<hr/> 30.2 pounds

2. Main Chute System

a. Maximum Opening Shock Load

The maximum opening shock load on the ring sail parachute is

$$\begin{aligned}
 F_o &= K_q C_D A \\
 &= 1.05(10)(0.7)(.960) \\
 &= 14,400 \text{ pounds}
 \end{aligned}$$

$$K = 1.05$$

(see section 7.3)

Utilizing an overall design factor of 1.5, the maximum opening shock load is 21,600 pounds.

b. Suspension Lines and Riser Line Sizing

For subsonic flow utilize suspension lines which are $0.85 D_o$. Hence for a 50-foot diameter chute

$$L_s = 0.85 (50) = 42.5 \text{ feet}$$

and

$$L_R = 3 D_V = 3(7.5) = 22.5 \text{ feet}$$

Table 32 lists the total required weight of the suspension lines.

TABLE 32

REQUIRED WEIGHT OF SUSPENSION LINES

Number of Suspension Lines (N)	24	26	48
F ₀ /N (lbs/line)	900	600	450
Type (Ref 2)MIL-SPEC	W-005625C	W-40880	W-4088D
		Type II	Type I
Break Strength	1000	600	500
Weight (oz/yd)	0.5	0.42	0.38
Length Line Required (ft)	1020	1530	2040
Total Weight (lbs)	10.6	13.4	11.9

Based on the results of table 32 the design chute will utilize 24 suspension lines which will be 7.3 feet apart on the parachute canopy periphery.

Suspension Line Weight ~10.6 pounds

c. Riser Line

The load on the riser line is 21,600 pounds (F₀). Heavy-duty nylon cord MIL-N-5787C Type I (reference 2) has a breaking strength of 20,000 pounds at 9 oz/yd.

Therefore, the total weight for a 22.5-foot riser line is

$$W_{\text{Riser}} = \frac{22.5(9)}{48} = 4.2 \text{ pounds}$$

Riser Line Weight ~ 4.2 pounds

d. Canopy Weight

The loading on the main chute canopy is

$$L = \frac{qD_0}{4} = \frac{10(50)}{4(12)} = 10.4 \text{ lb/in.}$$

Hence, utilize nylon cloth fabric of 0.6 oz/yd² which has a break strength of 25 lb/in. The total canopy weight can now be calculated by approximating the total surface area of the ring-sail to be a one-quarter sphere (page 93-reference 2)

$$A_{\text{surface}} = \pi \left(\frac{D_0}{2} \right)^2 = \pi(25)^2 = 1960 \text{ ft}^2$$

$$W_{\text{Canopy}} = \frac{0.6(1960)}{144} = 8.15 \text{ pounds}$$

Add a 15 percent weight factor to the total canopy weight to account for doubling, stitching, etc.

$$W_{T_{\text{Canopy}}} = 1.15(8.15) \approx 9.4 \text{ pounds}$$

Canopy Weight = 9.4 pounds

e. Other System Components

Bag	2.0 pounds
Sensing Equipment (Timer and Electrical Devices)	0.5
	<u>2.5 pounds</u>

f. Total Main Chute System Weight

Canopy	9.4 pounds
Suspension	10.6
Riser Line	4.2
Other System Components	<u>2.5</u>
Total	26.7 pounds

Total Drogue Chute System Weight	30.2 pounds
Total Main Chute System Weight	26.7 pounds

7.7 ACTUATION SYSTEMS

The selection of a sensing system for parachute actuation presents a difficult problem due to the uncertainty of entry conditions and the atmospheric models considered. The sensing system must be capable of deploying a parachute at an acceptable altitude for a "worst" combination of entry angle and model atmosphere. The actuation system must also be such that it assures that the aerodynamic heating and loading remain within the design limits of the canopy fabric. The selected reference actuation system attempts to deploy the drogue chute at a nominal Mach number of 2.5 and the main chute at Mach 0.8.

7.7.1 Drogue Chute Actuation System

The reference system selected utilizes a g switch which senses peak g and a timer which correlates peak g with the time from peak g to the drogue chute deployment Mach number (2.5). The theory of such a system is that the product $G_{MAX} \Delta t$ is a constant from peak g to a given velocity independent of entry angle and atmosphere assuming constant $m/C_D A$, a straight line trajectory, and an isothermal atmosphere. Mach number is the parameter of interest and not velocity; hence a correction is needed for the speed of sound. Figure 137 presents a theoretical curve of time from peak g to Mach 2.5 as a function of max g. Also shown are actual trajectory points for the upper and lower bounds of entry angle and atmosphere combinations. A curve fit of these trajectory points is shown and based on this curve fit,

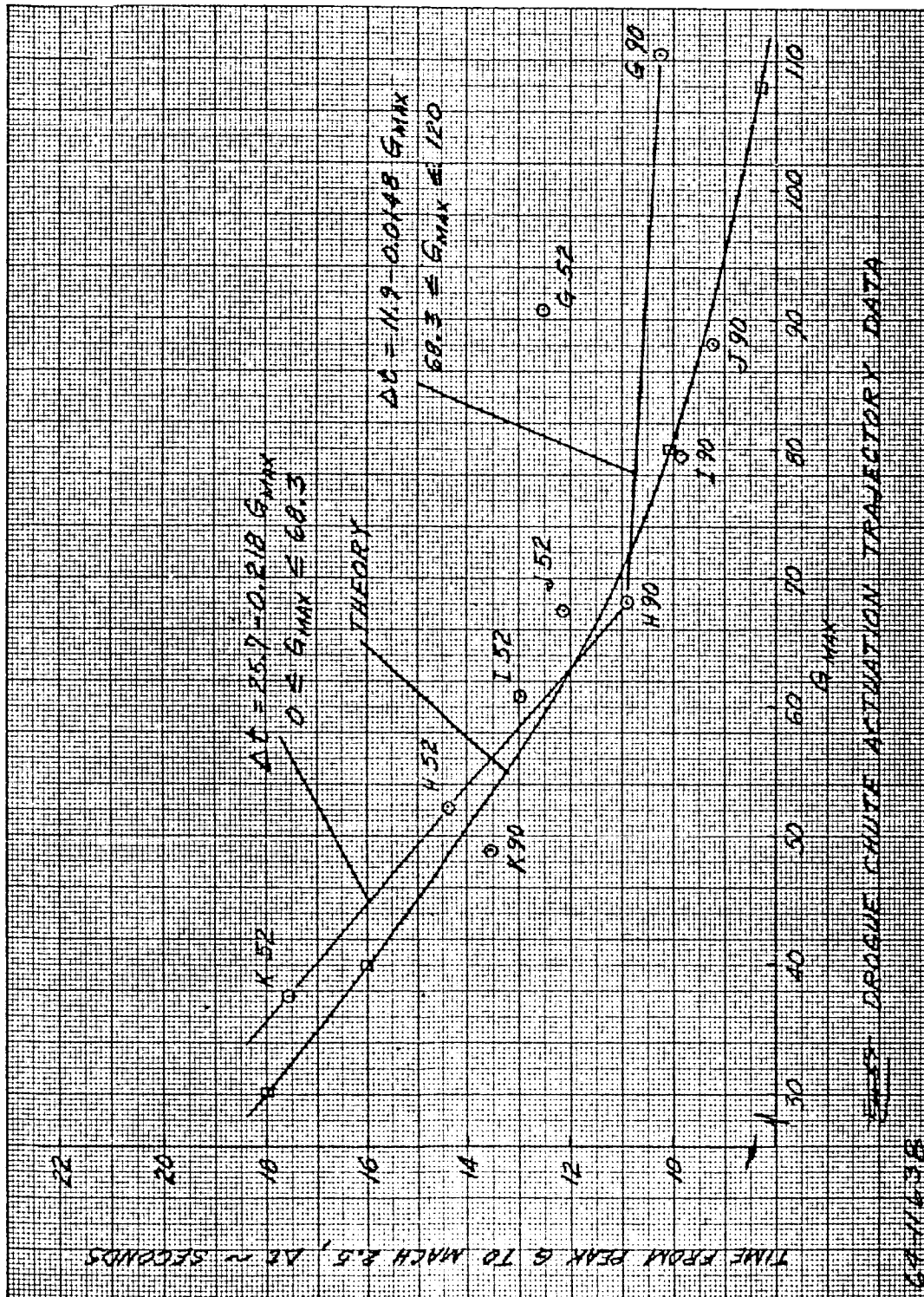


Figure 137 DROGUE CHUTE ACTUATION TRAJECTORY DATA

which relates peak g and Λ_t , it is possible to evaluate the actual drogue chute deployment Mach numbers, altitudes, etc. Table 33 summarizes the predicted drogue chute deployment Mach numbers and altitudes for all the combinations of entry angle and atmosphere based on the reference actuation system. Note that the deployment Mach numbers which are between 2.10 and 3.07 assure fabric wall temperatures that are below the limitations of nylon. Also note that the minimum design drogue deployment altitude of 14,000 feet is satisfied.

Various other sensing methods for the drogue chute actuation have been investigated and are briefly discussed below.

a. Baroswitch

The measured pressure at some point on an entry body can be correlated with experimental data and used to estimate the atmospheric ambient pressure. Utilizing this type of sensing, the parachute deployment would occur at an altitude which would depend on the atmospheric model, experimental simulation accuracy, and the pressure sensing system tolerances. The major problems with this type of sensing system are the angle of attack of the vehicle which makes pressure sensing very difficult and the uncertainty of entry angle and atmosphere which would yield deployment Mach numbers beyond the limits of the nominal design.

b. Axial Accelerometer

A g -switch or axial accelerometer which is set before launch is a simple and common means of sensing for actuation. However, the system has disadvantages for the range of entry angles and atmospheric models under consideration. The g switch setting for deployment is determined by assuring that the altitude for the most severe entry condition namely, H-90 degrees, is no less than what Mach 2.5 deployment would yield. Looking at figures 138 and 139 such a g -switch setting would be approximately 7.9 g . The problem with such a system is that on the other end of the entry angle-atmosphere spectrum (K-52 degrees) the deployment Mach number is bounded by temperature and load limitations on the fabric. However, for this case one can note that the deployment Mach number for the K-52 degrees combination would be approximately 3.11 resulting in a canopy fabric temperature of 1230°R which is within the limit of 1260°R. Hence, this system would serve as a backup to the reference design.

7.7.2 Main Chute Actuation System

The selected reference actuation system for the main chute employs a simple timer. The timer measures time from drogue chute deployment

222

TABLE 33

DROGUE CHUTE ACTUATION PERFORMANCE
(Based on Reference System)

ATM	γ_c (degrees)	M_{ACTUAL}	Z at M = 2.5 (feet)	Z at M_{ACTUAL} (feet)	T_{STAG} (actual) (°R)	(lb/ft ²)	Δt (seconds)
G	52	3.07	24057	27392	1110	78	10.56
	90	2.50	14083	14083	965	72	10.28
H	52	2.51	24588	24599	935	55	14.30
	90	2.50	14289	14289	935	72	10.90
I	52	2.65	33476	34307	780	63	12.40
	90	2.23	24671	22974	695	62	10.73
J	52	2.82	61461	63034	635	69	11.10
	90	2.10	53379	51058	490	57	10.59
K	52	2.51	90885	90915	935	52	17.48
	90	2.39	76868	75368	870	60	14.00

 Δt - time from peak g to Mach 2.5

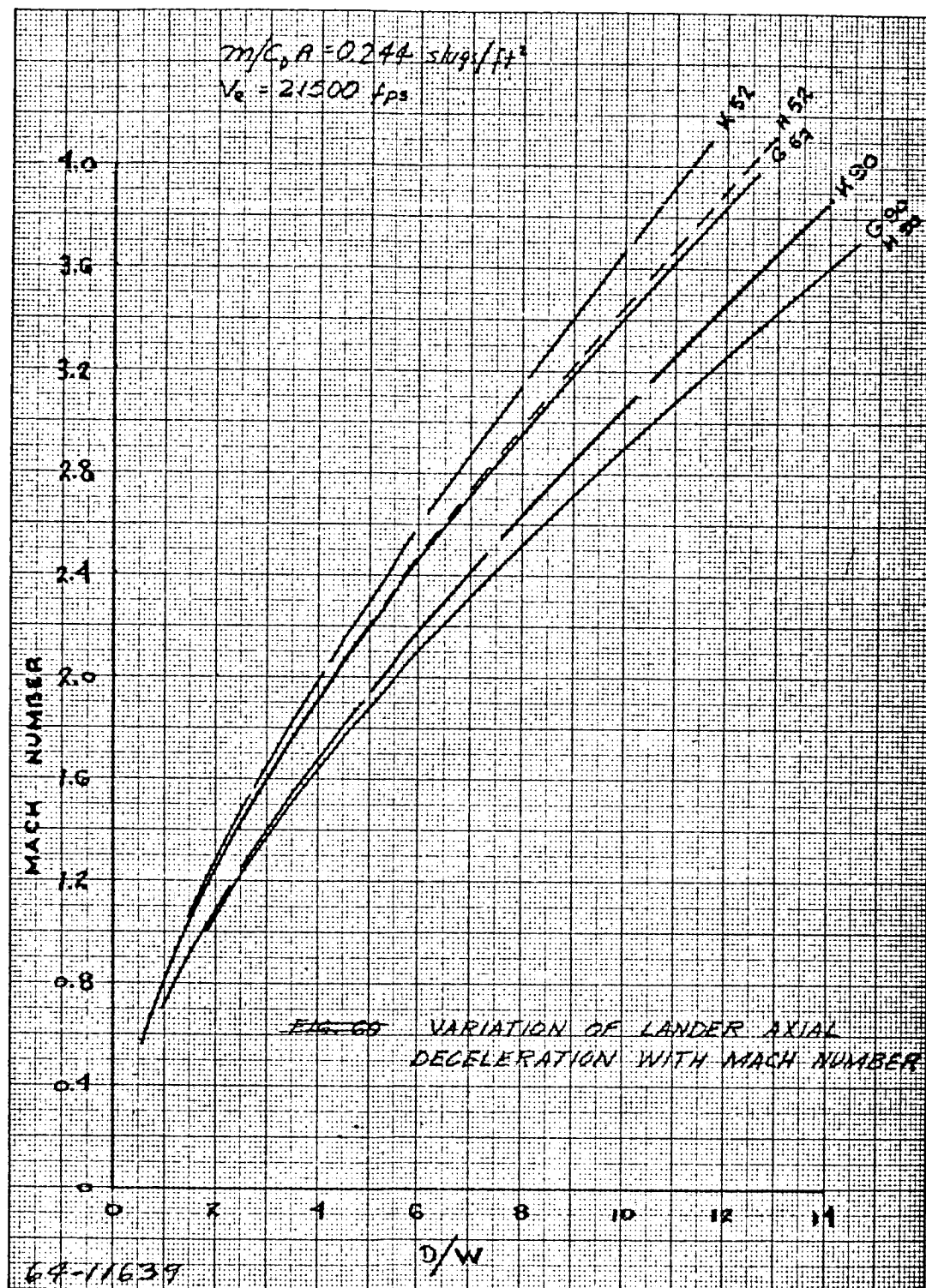


Figure 138 VARIATION OF LANDER AXIAL DECELERATION WITH MACH NUMBER

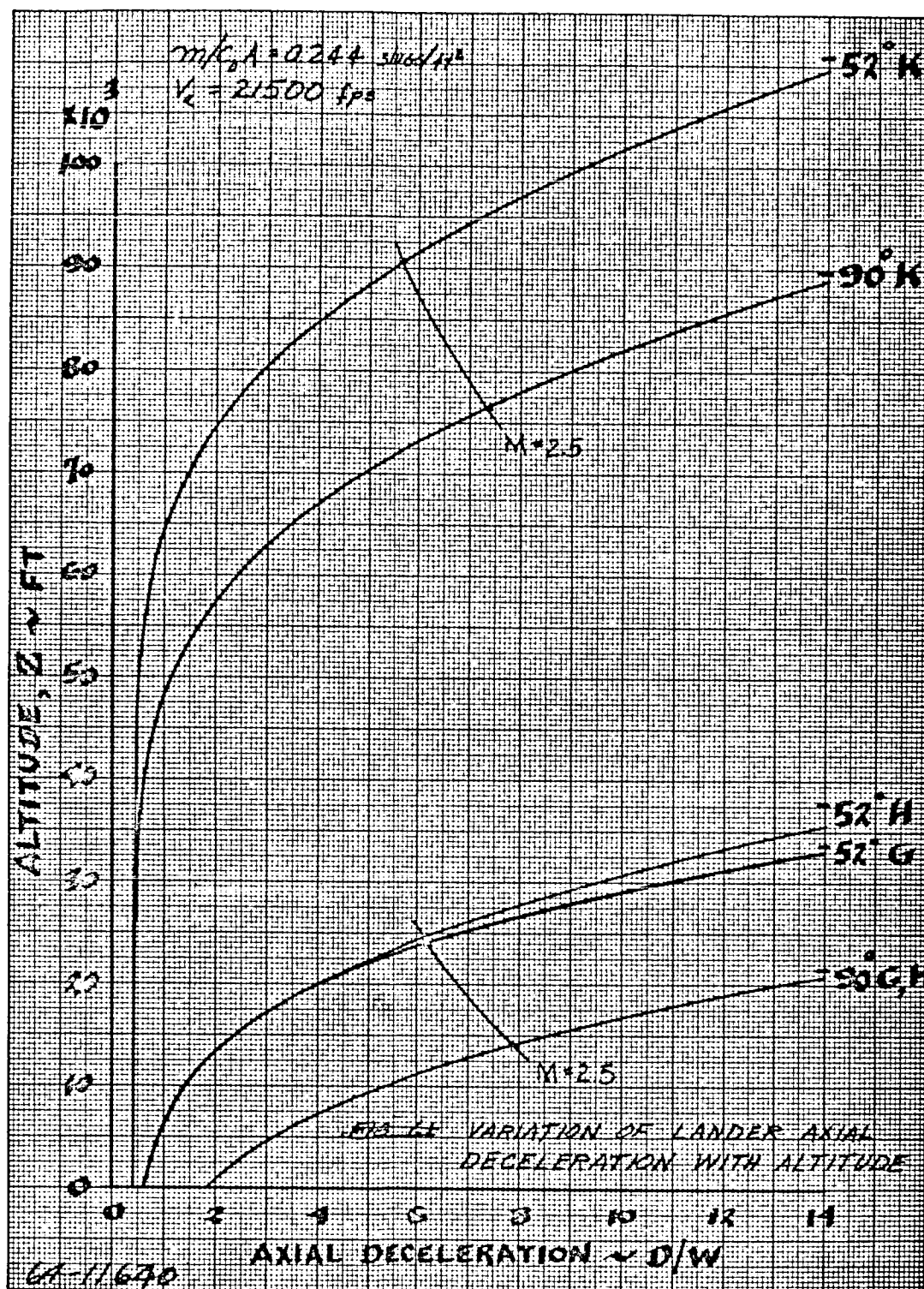


Figure 139 VARIATION OF LANDER AXIAL DECELERATION WITH MACH NUMBER

to main chute deployment. A constant interval of 6.22 seconds is the preset time for all combinations of entry angle and atmospheric models. This system assures actuation of the main chute between Mach 0.61 and 0.88 and the results of such a system are shown on table 34. Also indicated on table 34 are the actual deployment altitudes and one can note that the minimum deployment altitude is approximately 7600 feet, which is within 400 feet of the 8000-foot minimum reference design point. For the range of deployment Mach numbers shown, the temperature and loading limitations of the canopy fabric are easily met.

Other actuation systems were investigated for the main chute. Use of a radar altimeter was investigated, and found unsatisfactory. The major drawback to such a system is complexity and weight. Such a system weighs in the vicinity of 20 to 30 pounds (reference section 10.0).

The use of a baroswitch is unsatisfactory because of the low range of pressure experienced around Mach 0.8 coupled with the sensing system tolerances. Along with the above problem are the effects of the dynamic motions of the vehicle which make interpretation of the measurement difficult.

7.7.3 Actuation System Summary

A sensing system schematic is shown on figure 140. This is the selected reference system and employs a g switch and timer for the actuation of the drogue chute and a timer for the actuation of main chute.

Drogue chute actuation is such that with the use of a jerk meter and g switch, peak g through entry is determined. This value of peak g is correlated with a table of Δt 's and/or time intervals which have been established from the trajectory data curve fits shown on figure 137. Hence, a preset table of peak g versus Δt can be placed within the vehicle in the form of an analog. Note that the timer starts its Δt excursion at peak g and at the end of the prescribed interval, drogue chute actuation takes place. The results of this actuation system are shown on table 33 for all combinations of entry angle and atmosphere.

The main chute actuation system employs a timer which is actuated at drogue chute deployment. A constant interval of 6.22 seconds is the preset interval of time. At the end of this preset time interval, the main chute actuation takes place. This value of time was chosen after thorough examination of the drogue chute trajectory data so as to assure subsonic deployment for a shallow entry in the K atmosphere and to assure a minimum altitude of approximately 8000 feet for a steep entry in either the G or H atmosphere.

In summary a complete flight trajectory sequence from vehicle entry to impact is shown on table 35 for all combinations of entry angle and atmosphere.

TABLE 34

MAIN CHUTE ACTUATION PERFORMANCE

ATM	γ_e	MACTUAL	Z at M = 0.8	Z at MACTUAL
G	52	0.80	20878	20878
	90	0.65	8406	7608
H	52	0.74	19116	18831
	90	0.66	8378	7576
I	52	0.77	29289	28868
	90	0.61	18447	17387
J	52	0.69	58151	57697
	90	0.61	46983	46007
K	52	0.88	83066	83507
	90	0.68	67826	67343

TABLE 35

FLIGHT TRAJECTORY SEQUENCE
(m/CDA = 0.244)

ATM	γ_c degrees	GMAX g's	Drogue Deploy Mach No.	Δt_1 secs	Z at Δt_1 ft	Δt_2 secs	Z at Main Chute Deploy ft	Δt_3 secs	Main Deploy Mach No.	Vimp fps	Δt_{total} sec
G	52	90.8	3.07	55.09	25596	5.22	20878	278.94	0.80	67	339
	90	110.4	2.50	45.13	12340	5.22	7608	100.00	0.65	67	150
H	52	52.3	2.51	59.10	23090	5.22	18831	252.35	0.74	67	317
	90	68.3	2.50	46.39	12266	5.22	7576	99.69	0.66	67	151
I	52	60.8	2.65	56.95	32787	5.22	28868	443.41	0.70	57	506
	90	79.6	2.23	45.93	21349	5.22	17387	274.66	0.61	57	326
J	52	67.6	2.82	54.11	61516	5.22	57697	1071.00	0.69	43	1130
	90	88.3	2.10	44.60	49540	5.22	46007	891.73	0.61	43	942
K	52	37.7	2.51	57.66	89056	5.22	83507	1297.30	0.88	46	1360
	90	49.1	2.39	46.10	73225	5.22	67343	1110.10	0.69	46	1161

Δt_1 - time from entry to drogue chute full open - one second for chute opening

Δt_2 - time from drogue chute full open to main chute deployment

Δt_3 - time from main chute full open to impact

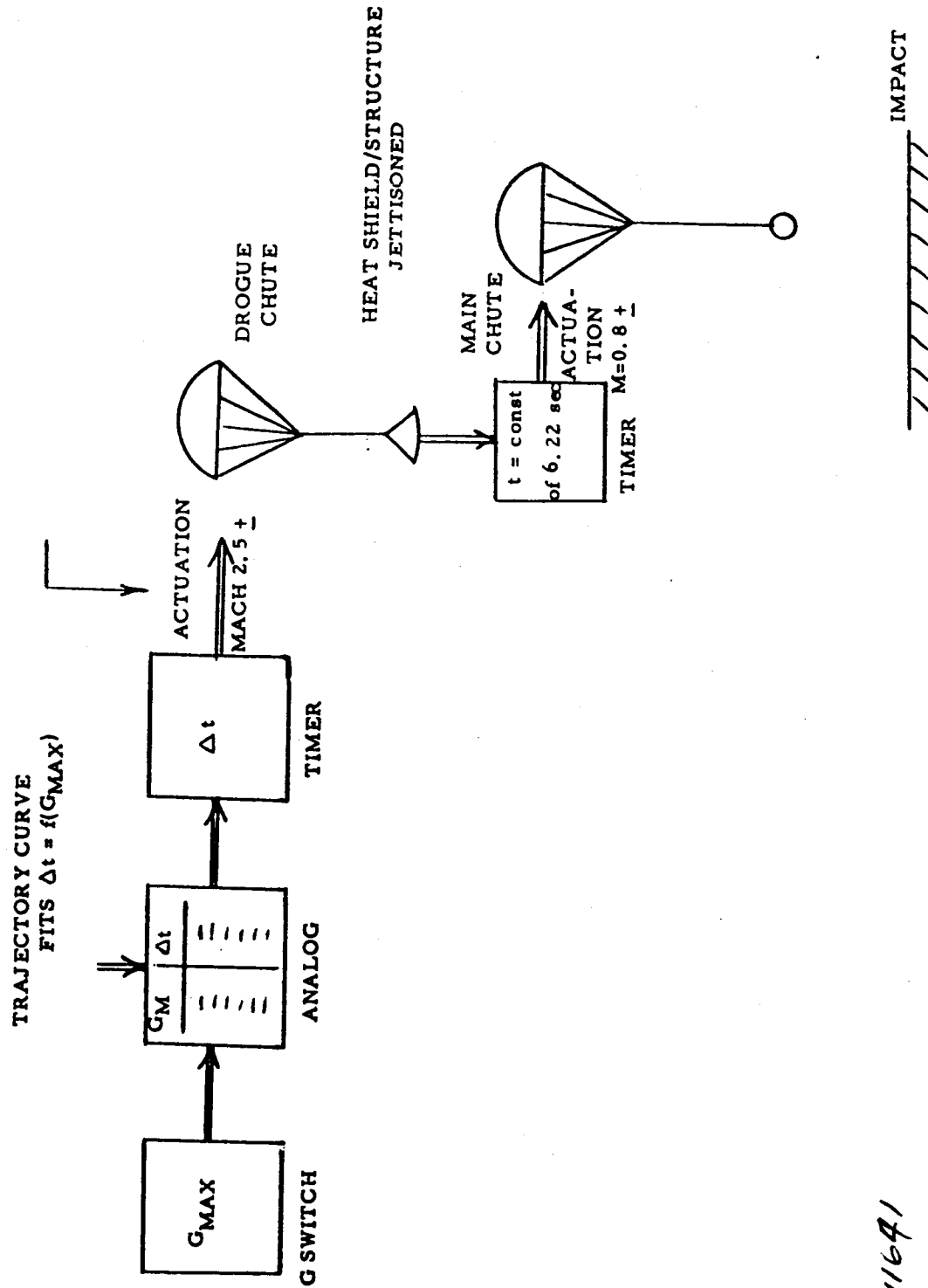


Figure 140 SENSING SYSTEM SCHEMATIC

64-11641

279

7.7.4 Drogue Ejection by Mortar

At a given time interval after peak g (see actuation system) a switch is closed energizing the drogue mortar and initiating drogue deployment as the first event in the descent and landing sequence. The drogue chute is packaged in a small cylinder internally suspended from the afterbody of the entry vehicle.

Mortar operation results as the initiation cartridge pressurizes the volume between the bottom of the small cylinder and a piston-seal sabot which pushes out the drogue chute in its cloth packing bag. A thermal protection cover is required above the drogue chute package and within the cylinder. The compartment and retainer channels are so designed that no sharp edges are presented to the drogue chute harness. Two harness legs are required and should be attached to the outer cylindrical wall of the entry vehicle at diametrically opposite points. As with the drogue chute, thermal protective covers are supplied to provide a flash surface over each channel from the outer attachment points to the mortar cylinder. As the harness becomes taut, the insulated harness covers are deployed. A riser then connects to the drogue chute in its cloth packing bag. An inertia weight in the back end of the bag causes the bag to strip itself off the drogue chute.

A 17.2-foot hyperflo drogue is considered for the above application. A 37,000-pound opening load (maximum) was calculated and the drogue chute weights is about 30.2 pounds.

7.7.5 Heat Shield Structure Jettison and Main Chute Deployment

At a preset time after the drogue chute has been deployed (6.22 seconds) a linear shaped charge is initiated which causes the afterbody heat shield and structure to become separated from the forebody. The drogue chute force then retards the afterbody and in so doing unfolds from its cloth pack a central riser followed by the main parachute canopy. At this point, the drogue chute and afterbody of the lander have separated and hence main chute full deployment takes place.

REFERENCES

1. Parachute Design Study for Mariner B Entry Capsule, Cook Technical Center Report FR-3807A (March 1963).
2. Performance of/and Design Criteria for Deployable Aerodynamic Decelerators, Technical Report No. ASD-TR-61-579 (December 1963).
3. Parachute Recovery Systems, Missile and Drone General Requirements for Development of, Military Specifications MIL-P-25062A (April 1956).
4. Ultra-Fast Opening Personnel Parachute Type XMP-2, WADD TR-60-485 (April 1961).
5. RAD, Mars-Venus Capsule Parametric Study, Avco RAD-TR-64-1, JPL Contract 950262 (21 March 1964).

8.0 IMPACT SYSTEM

The purposes of the parametric study of the impact attenuation system were to investigate basic system choices, making the tradeoff decisions where possible, and to generate general graphs which would be used in the preliminary design of a conceptual spacecraft system. A third purpose was the determination of the effects of small variations in each of the system parameters on a nominal design. In this way "influence coefficients" could be generated to show the relative importance of typical variations in the parameters. A conceptual design analysis was performed also in order to indicate whether or not the breadth and depth of the parametric study were sufficient.

Several basic assumptions were made and several constraints imposed at the start of this study. It was assumed that the ground was a rigid surface (except for a brief look at the possibility of sinking into sand). Overall, omnidirectional protection of the payload by a passive, crushable material energy absorber was also assumed. In all of the parametric work, it was assumed that the usable strain of the impact attenuation material was 75 percent, i. e., an element of material could be crushed $3/4$ of its thickness at constant stress (see appendix A).

The most important constraint imposed was that of designing for a 200-ft/sec horizontal wind velocity. This velocity was always added vectorily to the vertical descent velocity which was assumed or derived. The possibility that the vehicle does not get fully picked up by the wind was investigated, and this investigation is reported in appendix B. However, since the present wind model is not detailed enough to use the results obtained in this appendix, it was assumed in the study that the suspended weight and parachute are moving horizontally at 200 ft/sec at impact.

8.1 PARAMETRIC TRADE-OFF STUDIES

Two distinct parametric studies were performed. The first study started with certain available impact attenuation materials and, using these, attempted to determine other system parameters such as geometry, packaging density, etc. The other study started with certain geometric constraints and sought to define desirable properties of crushable materials.

The notation used in all of the following discussions and graphs is summarized in appendix A.

The equations used to analyze the dynamics of impact were equations (2-3), (2-4), (2-7), (2-8), and (2-9) of appendix A. These equations pertain to a homogeneous, isotropic, energy absorption material; further, the change in total mass being decelerated as a function of time was neglected (see appendix A). The effects of all of these simplifying assumptions were investigated in the section on influence coefficients (section 8.3) and in the conceptual design analysis (section 8.5).

8.1.1. Parametric Evaluation

In the first portion of the study, the velocity of impact was assumed to be 250 ft/sec. The conclusions reached in the initial trade-off studies were not dependent on the particular velocity chosen, at least for velocities between 200 and 300 ft/sec.

As mentioned above, the first study, to which the major effort was applied, involved known impact attenuation materials. Figure 141 is a plot of crushing stress versus bulk density for a number of materials which have been tested. It can be seen that the presently available materials fall into three distinct groupings. One group includes the foamed plastics; the data shown cover several different types, the most widely used being polyurethane. Another group consists of just balsa wood, while the third group includes aluminum honeycombs, truss-grid (a structure built up of layers of corrugated aluminum strip), paper honeycombs, a single data point for a foam-filled fiberglass honeycomb, and glass-cloth reinforced plastic honeycomb. Also, shown on figure 141 are empirical curve fits which provide analytical equations representing each of these three groups. These equations are used in order to obtain analytic results in the study.

The first aspect of the system to be studied parametrically was the geometry. The landed package shapes which were compared are shown on figure 142. Figures 143 through 149 illustrate some of the pertinent parameters plotted versus packaging density of the internal payload, ρ_i . (This value will be typically 1 to 3 slugs/ft³.) Comparing figure 143, which pertains to the lenticular geometry, to the other figures, which all pertain to the spherical geometry, several conclusions were drawn. Although the lenticular shape packages neatly in an Apollo-type entry vehicle, the deceleration levels are very high compared to the sphere, being at least of the order of 5000 g for typical payloads. Since g-level was considered a parameter of primary importance, it was decided to use the spherical geometry as the reference shape.

It is noted on figure 143 that, if plastic foam is used in the lenticular design, the internal payload is only a small fraction of the landed mass. Figure 144 illustrates that this conclusion also holds for the sphere. Because of its inefficiency, plastic foam was eliminated from further consideration.

Figure 145 shows the pertinent parameters for the extremes of the balsa wood data. The g-levels are still very high, so a study was made of the effects of "weakening" the balsa wood, i. e., reducing the density while maintaining the energy absorption capability (ft/lb of kinetic energy absorbed per pound of balsa). Starting with 6 lb/ft³ balsa wood, it was assumed that by coring out the balsa or by using it to partially fill a honeycomb, the bulk density could be as much as halved. The results obtained with these hypothetical materials are shown on figure 146. Some improvement in the g-level

is attained, but for internal payloads of interest, the level is still greater than 3000 g.

Thus, it has been shown that of the three groupings of impact attenuation materials, the aluminum honeycomb class of materials appears to effect an adequate compromise between g-level and material efficiency. Values of the significant parameters of aluminum honeycomb designs are plotted on figures 147, 148, and 149 for various bulk densities. (Here, the actual data for 5052 aluminum honeycomb is used, rather than the curve fit equation.)

The significance of packaging density can also be gleaned from the curves presented. It can be seen, for example, that a very low packaging density could reduce the g-levels, but only at the expense of requiring a very large amount of crushable materials (figure 147). Further, figure 149 shows that the package radius would have to be quite large.

An interesting conclusion gathered from figure 148 is that for packaging densities greater than one slug/ft³, the deceleration parameter is relatively unaffected by increasing packaging density. However, figures 147 and 149 show that increasing packaging density does reduce the amount of crushable material required and also reduces the radius of the landed package.

It should be pointed out here that the internal payload mass has been assumed constant in discussing trends above. If, say, total landed mass were held fixed, then the deceleration level would decrease with higher packaging density. Nevertheless, the general conclusion is that the packaging density of the internal payload ought to be maximized.

8.1.2. Optimum Materials Study

The purpose of this special study was to look at the impact attenuation problem from a new angle. In this case, instead of selecting known energy absorption materials and evaluating their performance, as was done in the basic parametric study, the desired performance was specified and the required material properties derived.

The critical parameter was chosen to be impact decelerations. In order to reduce the g to the minimum possible value, the maximum available stroke ought to be used. Hence, the largest spherical package which can be fitted into a lander constrained by the surveyor shroud (c.f. figure 156), roughly a 3.1-foot radius sphere, was assumed. Further, a payload packaging density of 2 slugs/ft³ was assumed. Using equations (2.3) and (2-10) in appendix A, figure 150 was generated. (The term "minimax" is used to signify the minimum achievable value of the maximum deceleration.)

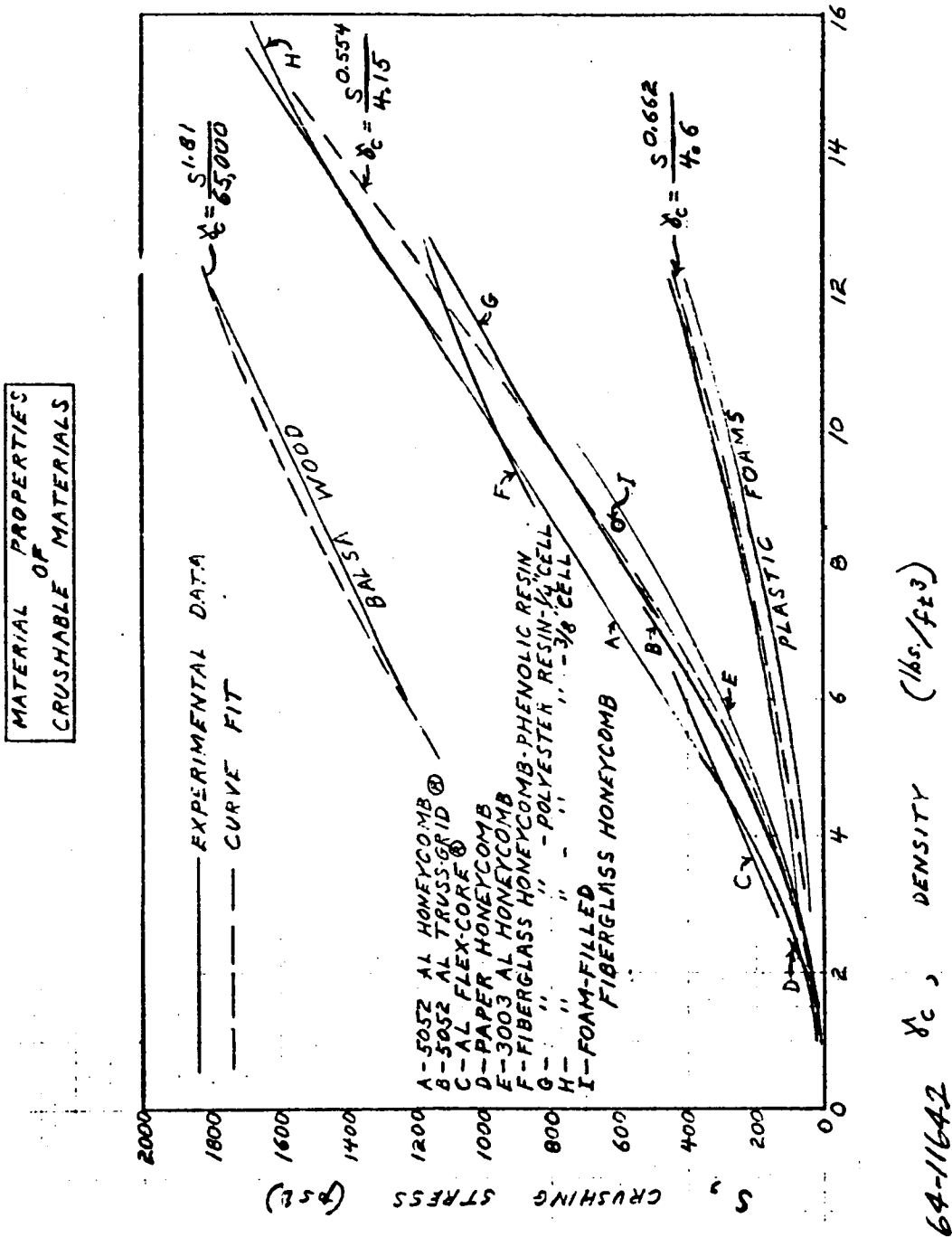
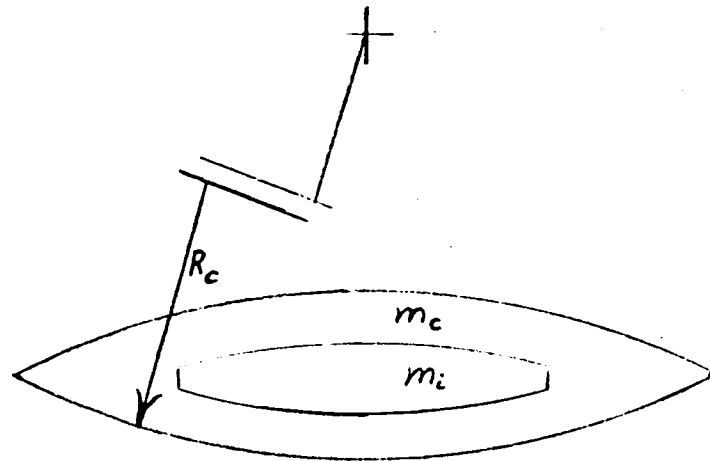
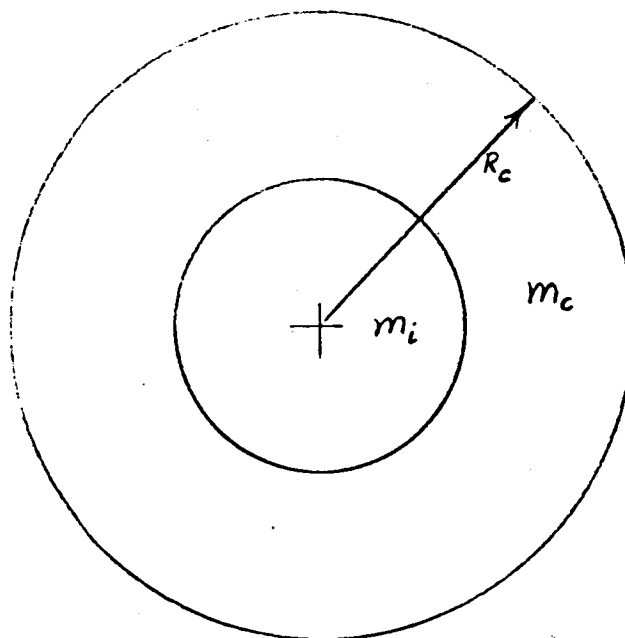


Figure 141 MATERIAL PROPERTIES OF CRUSHABLE MATERIALS



LENTICULAR



SPHERE

64-11643

Figure 142 LANDED PACKAGE SHAPES

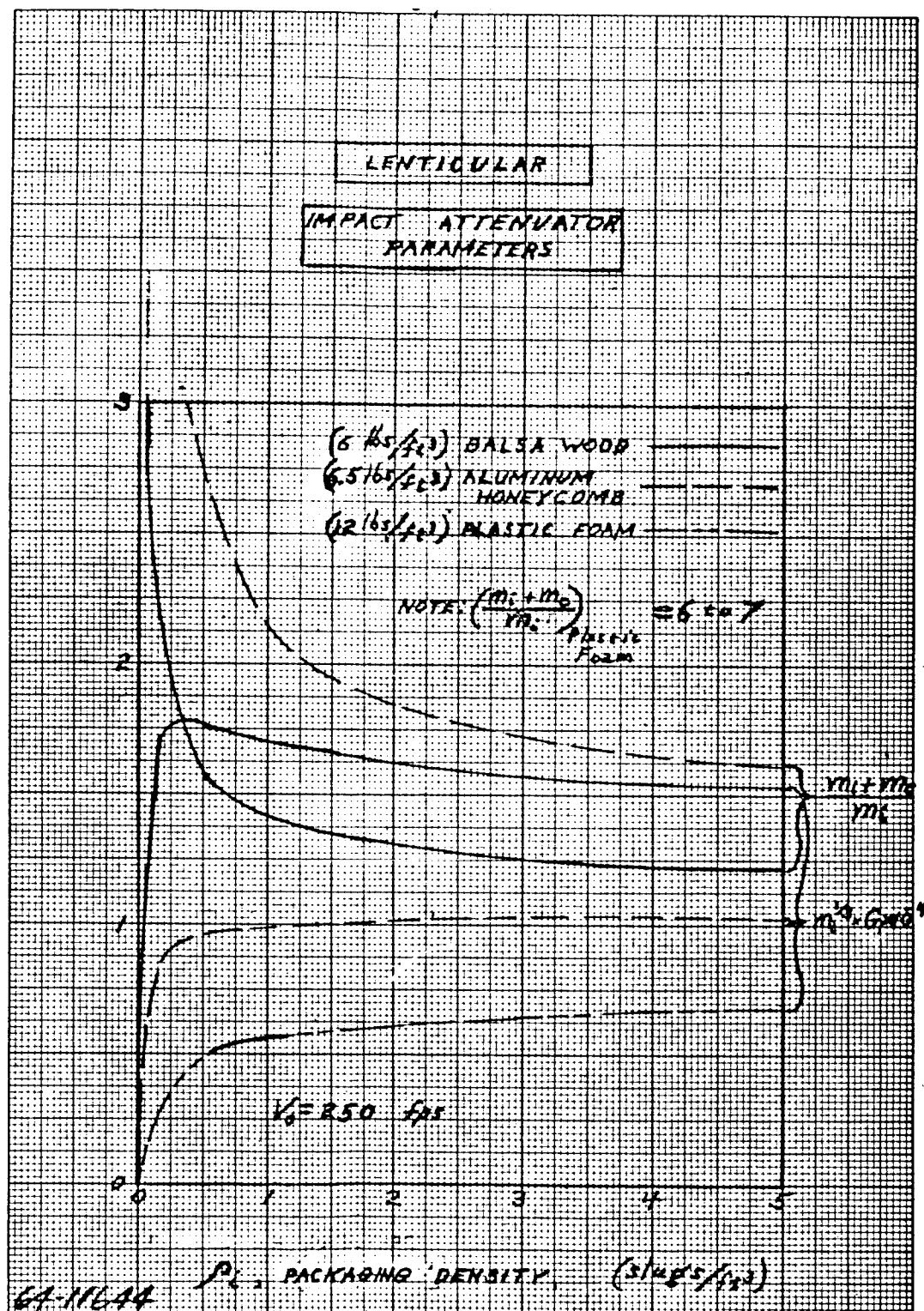


Figure 143 LENTICULAR - IMPACT ATTENUATOR PARAMETERS

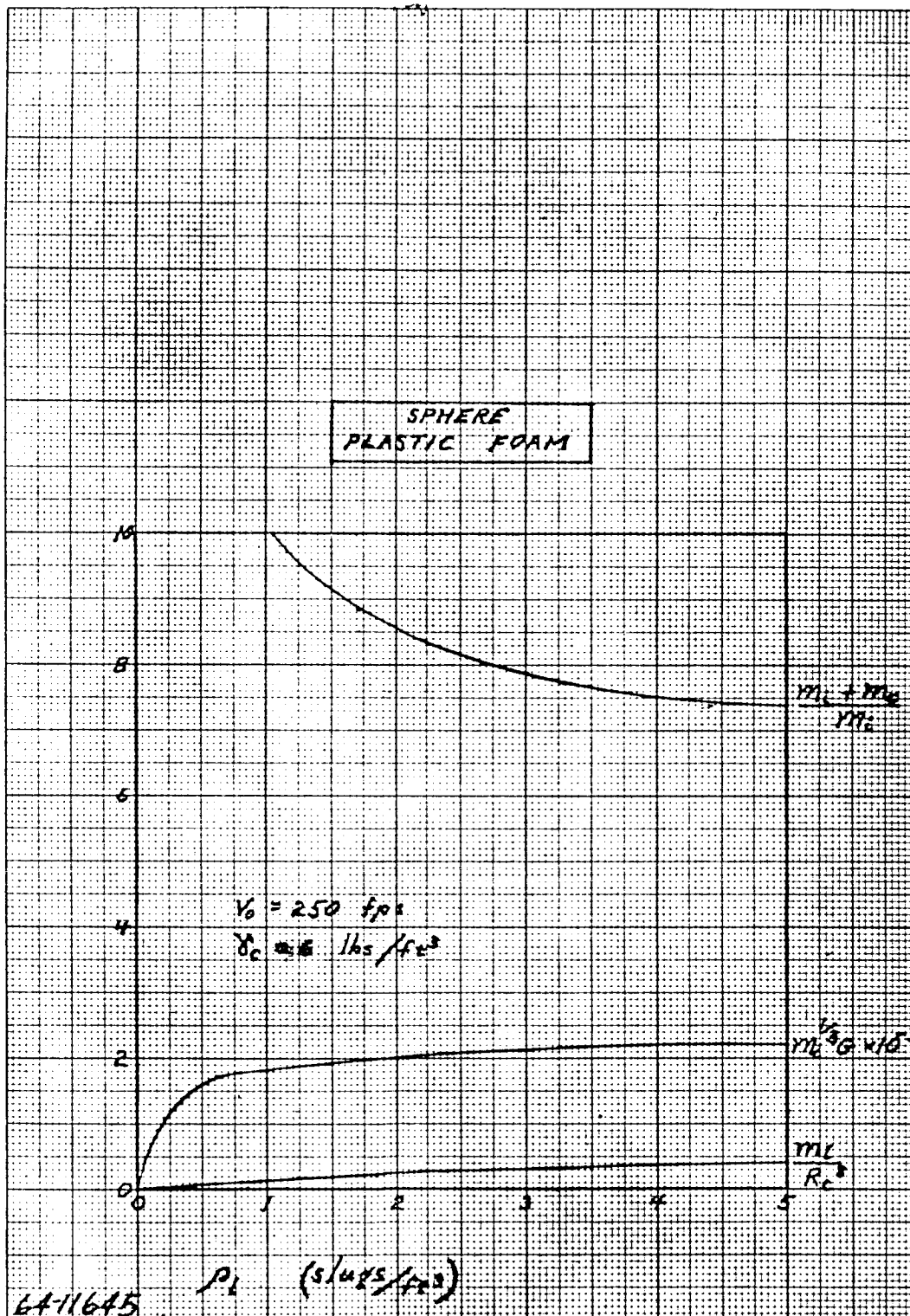
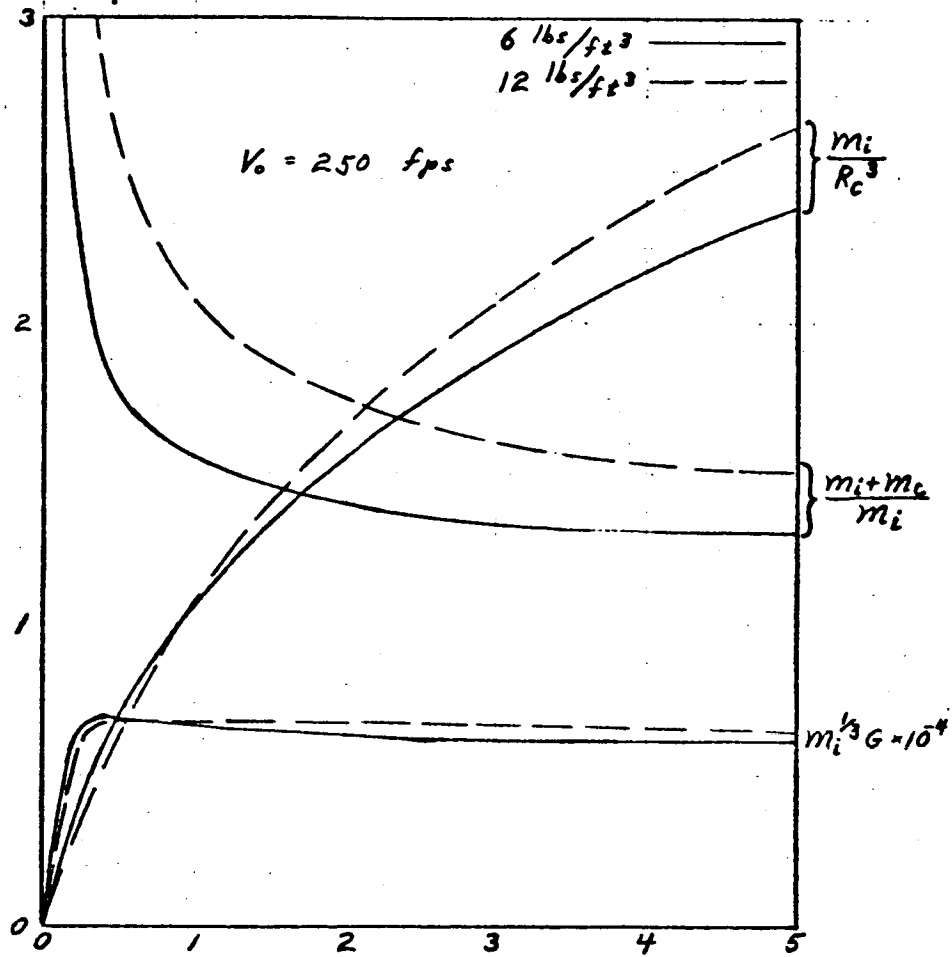
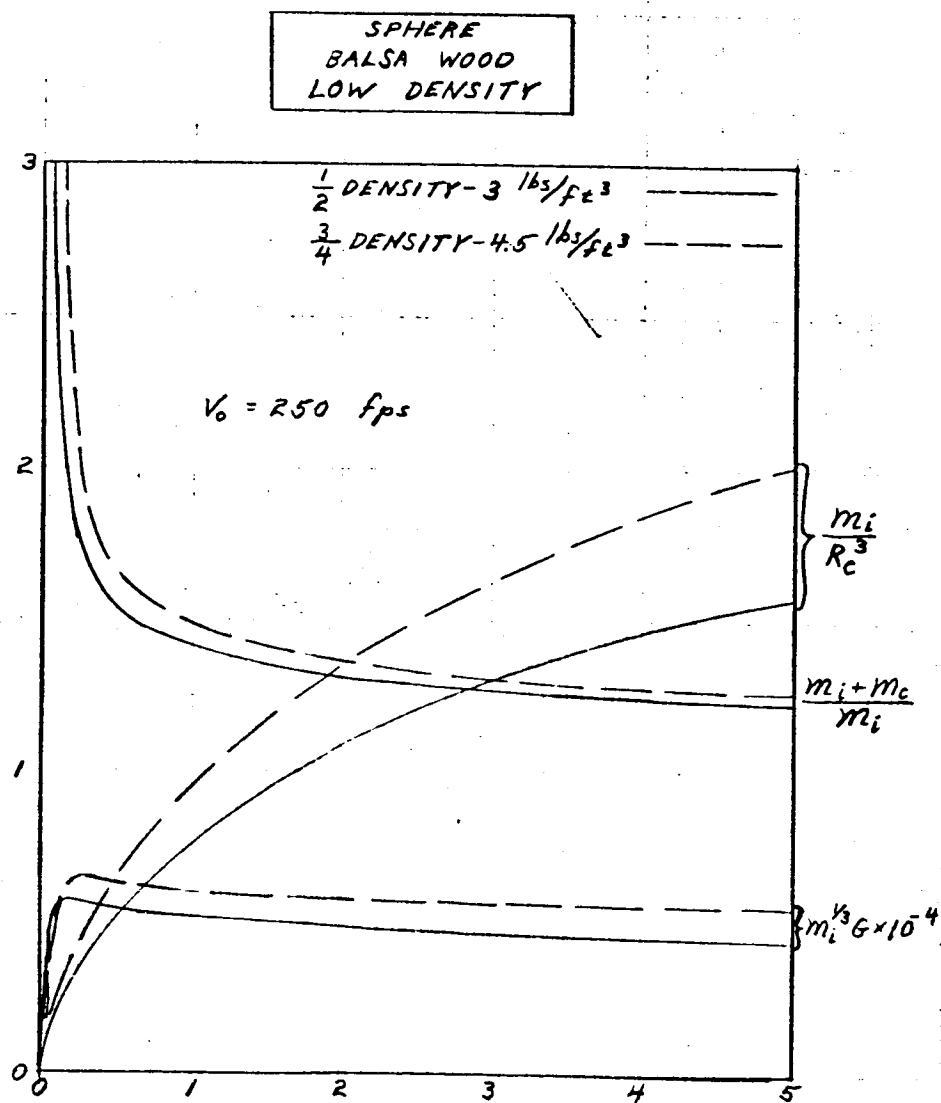


Figure 144 SPHERE - PLASTIC FOAM



64-11646 ρ_i (slugs/ft³)

Figure 145 SPHERE - Balsa WOOD - FULL DENSITY



64-11647 ρ_i (slugs/ft³)

Figure 146 SPHERE - BALSA WOOD - LOW DENSITY

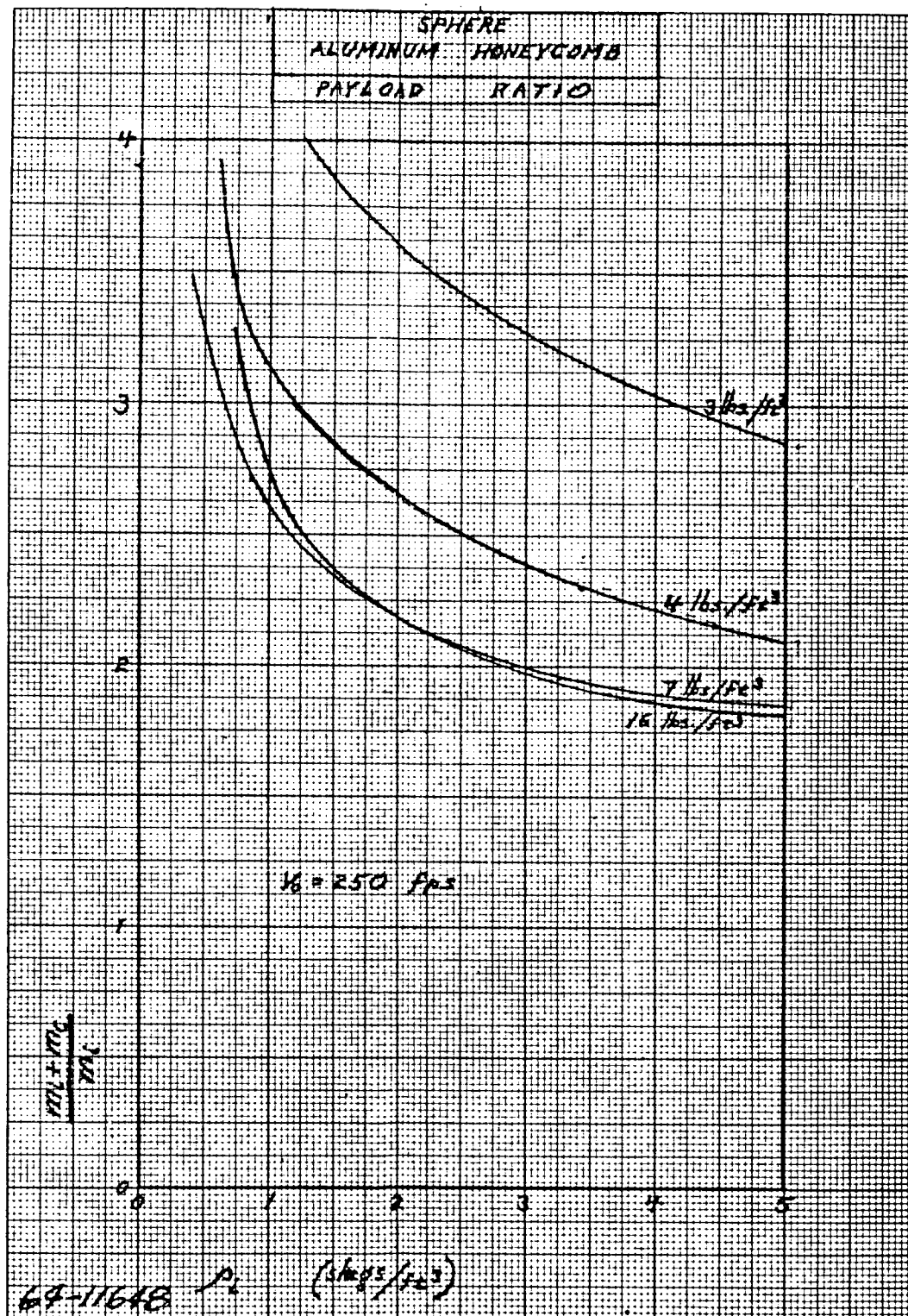


Figure 147 SPHERE - ALUMINUM HONEYCOMB-PAYLOAD RATIO

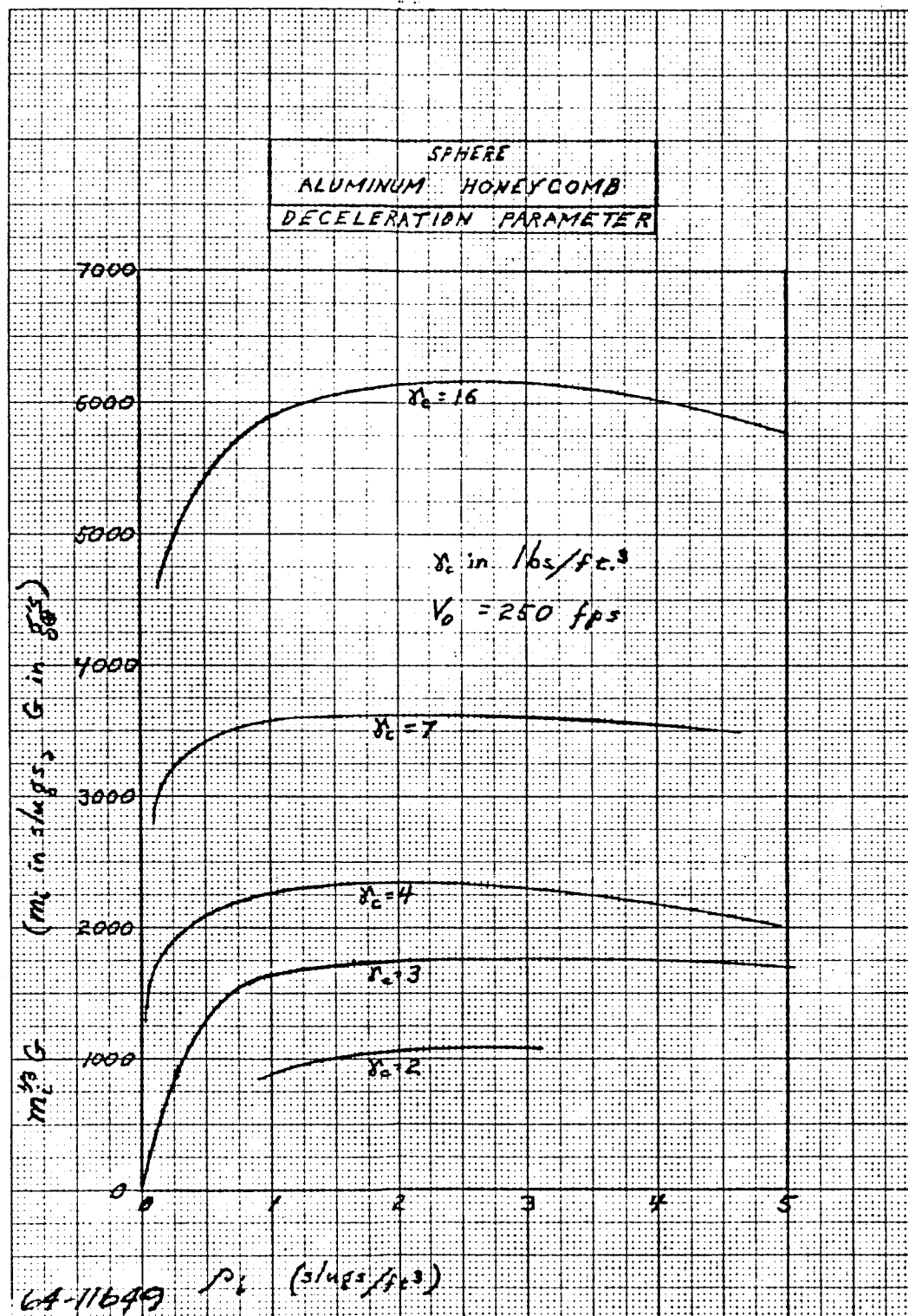


Figure 148 SPHERE - ALUMINUM HONEYCOMB - DECELERATION PARAMETER

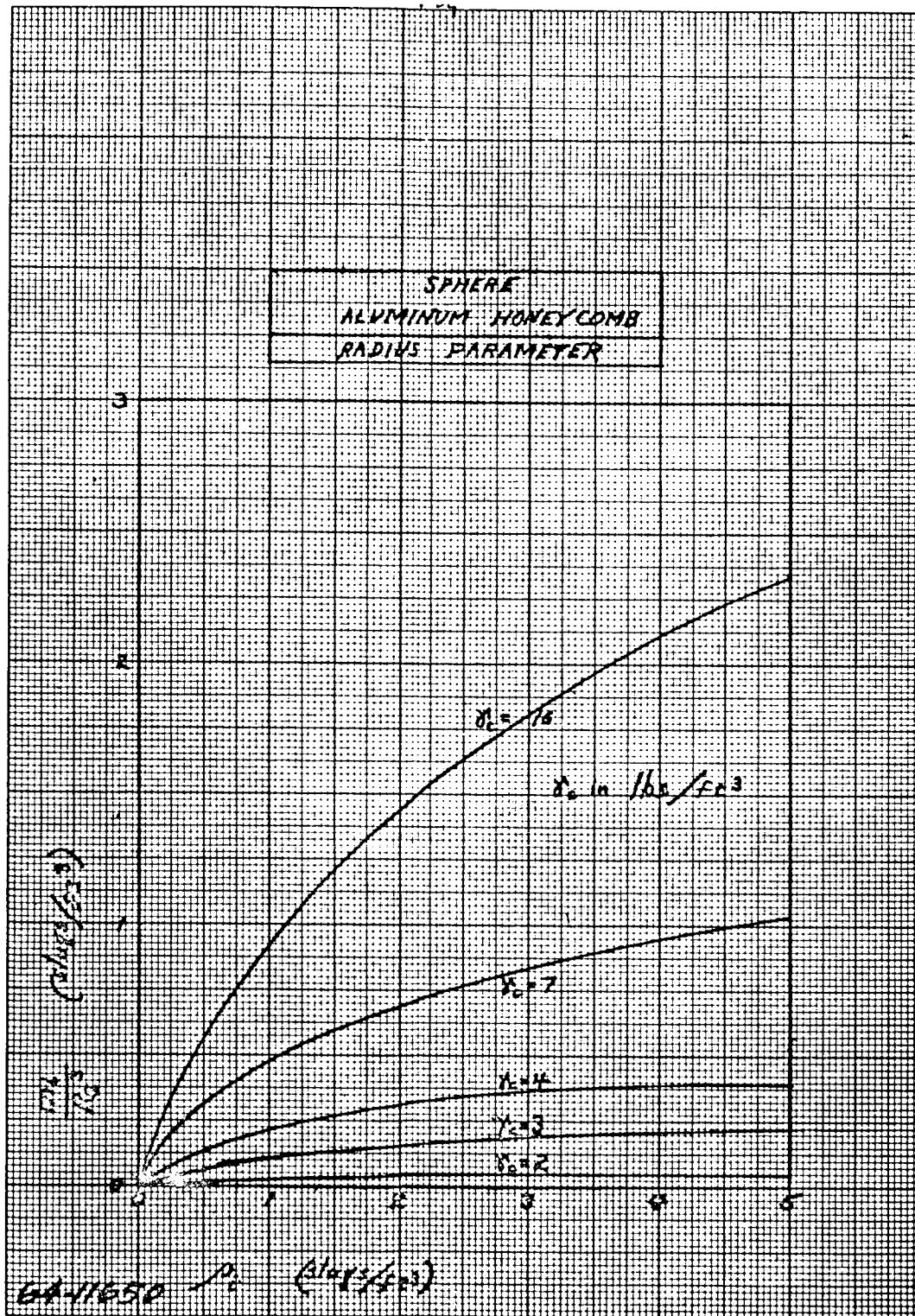


Figure 149 SPHERE - ALUMINUM HONEYCOMB - RADIUS PARAMETER

Equations (2-4), (2-10) in appendix A form a set of equations which can be interpreted as giving the crushing stress and density of a crushable material as a function of its mass and that of the internal payload. This information is plotted in this way on figures 151, 152, and 153 for three values of the impact velocity.

On figure 154, the areas of interest on the previous curves are superimposed onto plots of known material properties (from figure 141). This figure illustrates that for an impact velocity of 250 ft/sec, the minimax condition can be met with the aluminum honeycomb class of materials for some situations. More importantly, this overlay points up the fact that new impact attenuation materials need to be developed, materials which fill in the wide gap in properties between the aluminum honeycomb group and balsa wood. It further serves to point out that several properties must be satisfied, not just one. That is, it is not sufficient in this situation to merely find materials with high energy absorption efficiencies (which is roughly proportional to the stress-density ratio); the materials must also have stress and density values within certain ranges. This is why balsa wood, which possesses the highest energy absorption efficiency of the materials considered, was not recommended for the Advanced Mariner lander. Its crushing stress and density were too high.

8.2 PARAMETRIC DESIGN DATA

8.2.1. Design Curves

The parametric trade-off studies resulted in certain basic systems choices being made. These were that the shape of the landed package should be spherical, that the impact attenuation material ought to be a member of the aluminum honeycomb group of materials (see figure 141), and that the packaging density of the internal payload ought to be made as high as possible. For the purpose of generating design curves, it was assumed that an achievable packaging density was 2 slugs/ft³. The effects of variations in this quantity are described in section 8.3 on influence coefficients.

The optimization studies which are discussed in section 8.4 indicated that the optimum vertical descent velocity for a two-chute system is about 65 ft/sec which yields, with the 200 ft/sec horizontal wind velocity, a total impact velocity of 210 ft/sec. For this condition, figure 155 presents a plot of total landed weight (crushable material plus internal payload) versus outside radius of the landed package. These curves were derived from equations (2.3), (2-4), (2-10), and (2-11) of appendix A, using the curve fit to the aluminum honeycomb group of impact attenuation materials. A typical design overlay of figure 155 is shown on figure 156 to illustrate the constraints on the situation. Thus, for a given $m/C_D A$, the maximum landed weight is fixed. This maximum can be obtained up to a sphere radius

of 2.44 feet, which is the largest sphere which can be placed in the largest Apollo-type vehicle which will fit in the surveyor shroud. For larger radii, a conical section must be added to the entry vehicle after-body, thus reducing the weight available for the lander. The final limit is the largest sphere which can fit in the shroud.

Figure 157, using the same ordinate and abscissa, gives the material properties of the impact attenuator, based on the curve fit to the aluminum honeycomb group of materials. Figures 158 and 159 present the same information except that an impact velocity of 250 ft/sec is used (this would correspond to a vertical descent velocity of 150 ft/sec). A linear interpolation can be used with small error if it is desired to obtain values for velocities between these two.

It was found during the conceptual design effort that by using the actual properties of expanded 5052 aluminum honeycomb instead of the curve fit that there was an appreciable degree of conservatism in using the curve fit to represent this actual material. Because of this, figures 160 and 161 are provided here also. These figures give the same general information which has been presented previously except that actual material properties of 5052 aluminum honeycomb are used. The impact velocities used were 200 and 250 ft/sec, respectively.

8.2.2. Very High Impact Velocity Study

To supplement the data presented thus far, a separate study was made of impact at very high velocities.

The first part of the study was concerned with determining material limitations. For a particular geometry and a particular crushable material, it is possible to determine a limiting velocity, i.e., that at which essentially zero payload can be landed. In other words, for the spherical geometry under consideration here, the limiting velocity is that at which a sphere of crushable material can absorb only its own kinetic energy if a whole hemisphere is crushed. An analytical expression for this velocity can be derived from equation (1-4) of appendix A. If in a spherical lander (or even a lenticular lander) the payload becomes infinitesimal, the volume of material crushed approaches one half of the total volume of crushable material. Thus, if the substitutions

$$V(y_m) = 1/2 \left(\frac{m_c}{\rho_c} \right)$$

and

$$m_i = 0$$

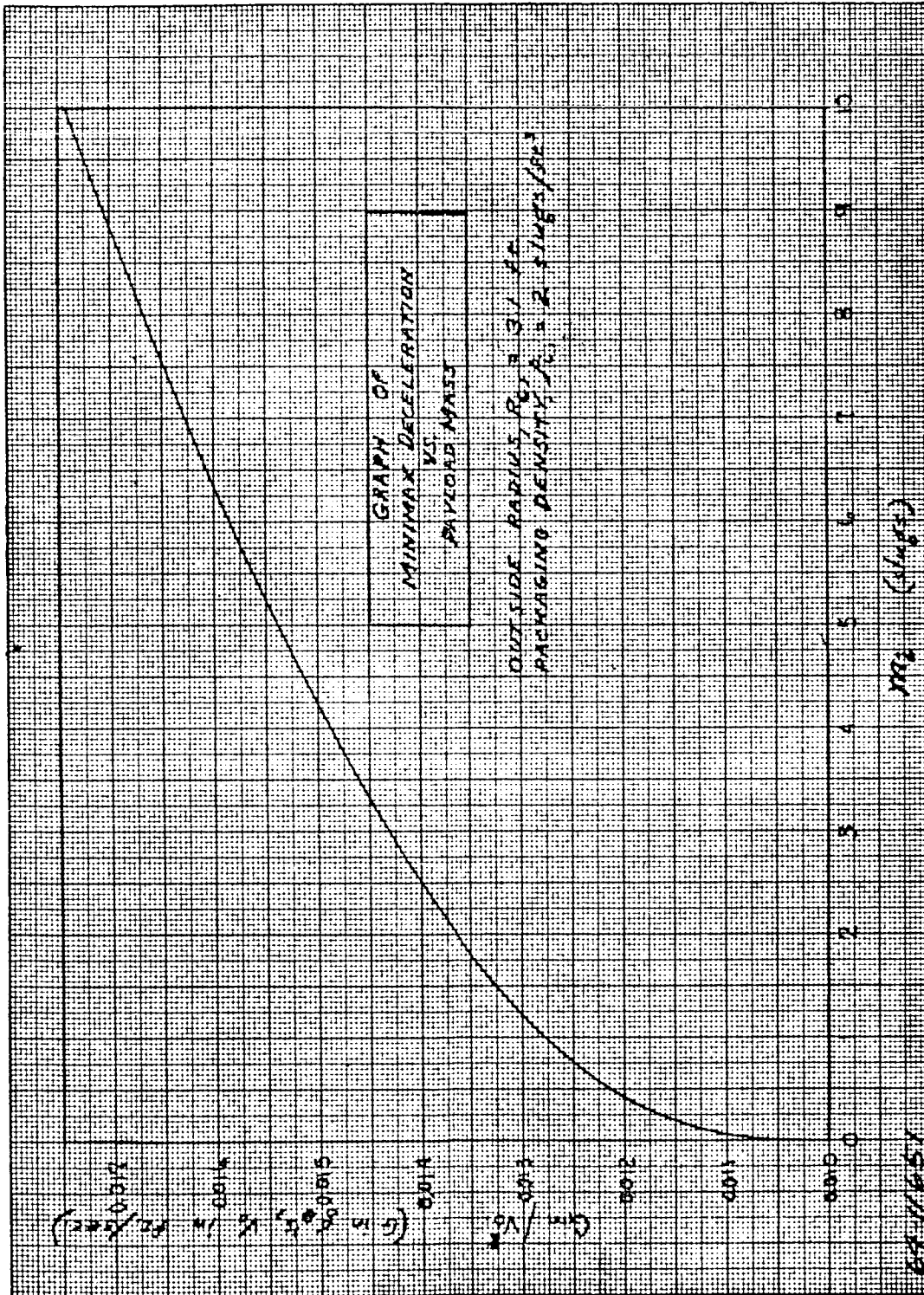
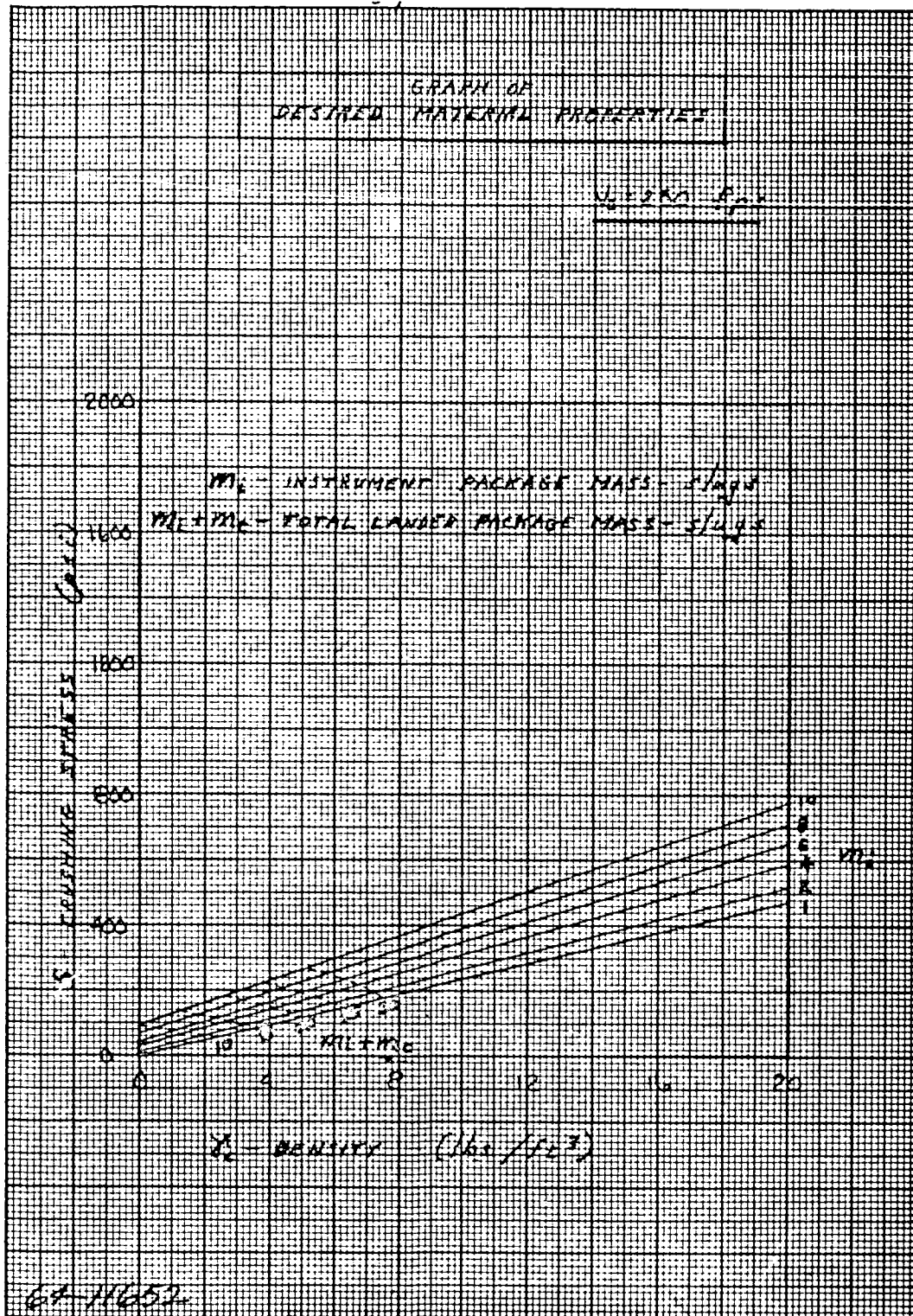
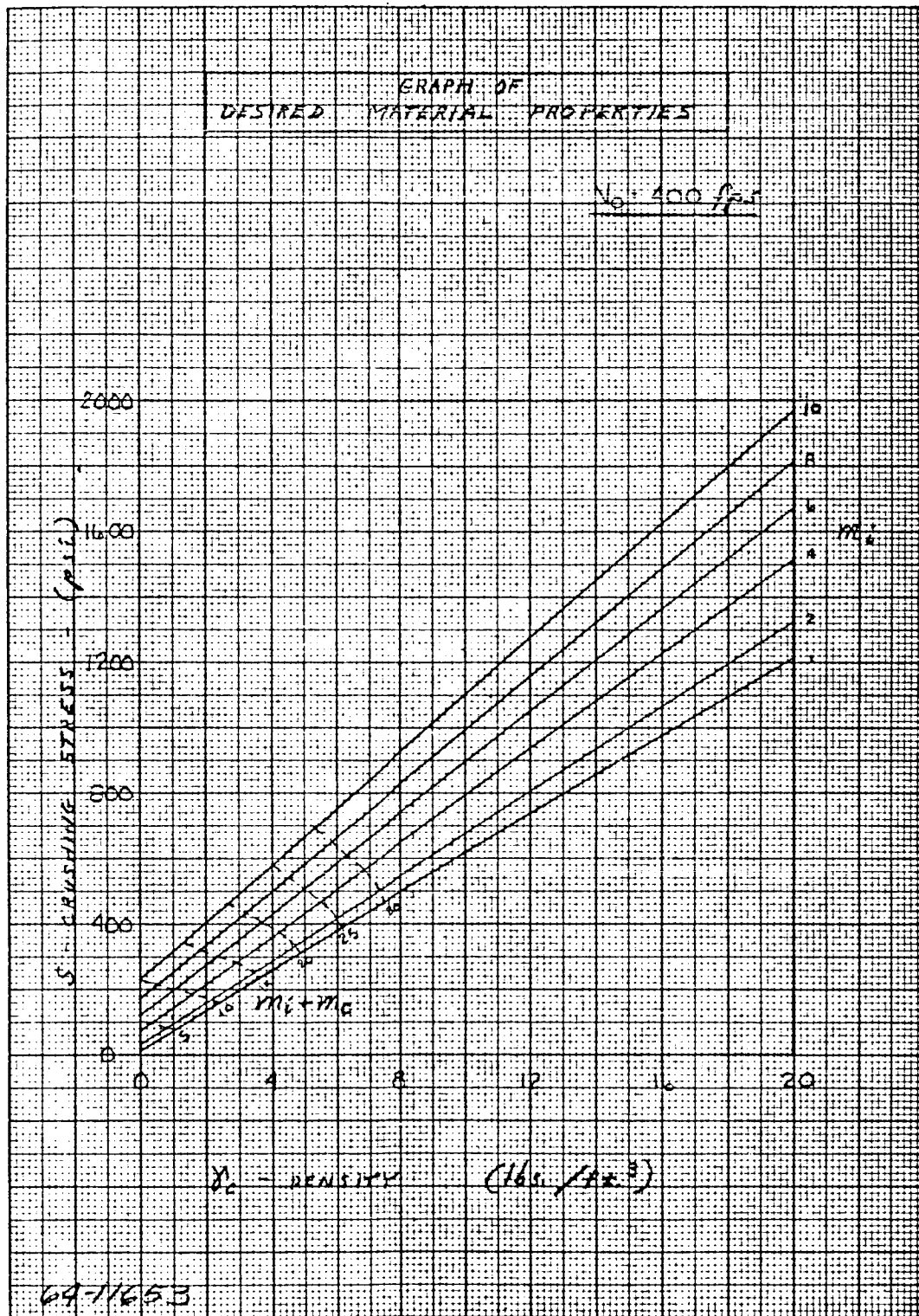


Figure 150 MINIMAX DECELERATION VERSUS PAYLOAD MASS

Figure 151 DESIRED MATERIAL PROPERTIES - $v_0 = 250$ FPS


Figure 152 DESIRED MATERIAL PROPERTIES - $v_0 = 400 \text{ FPS}$

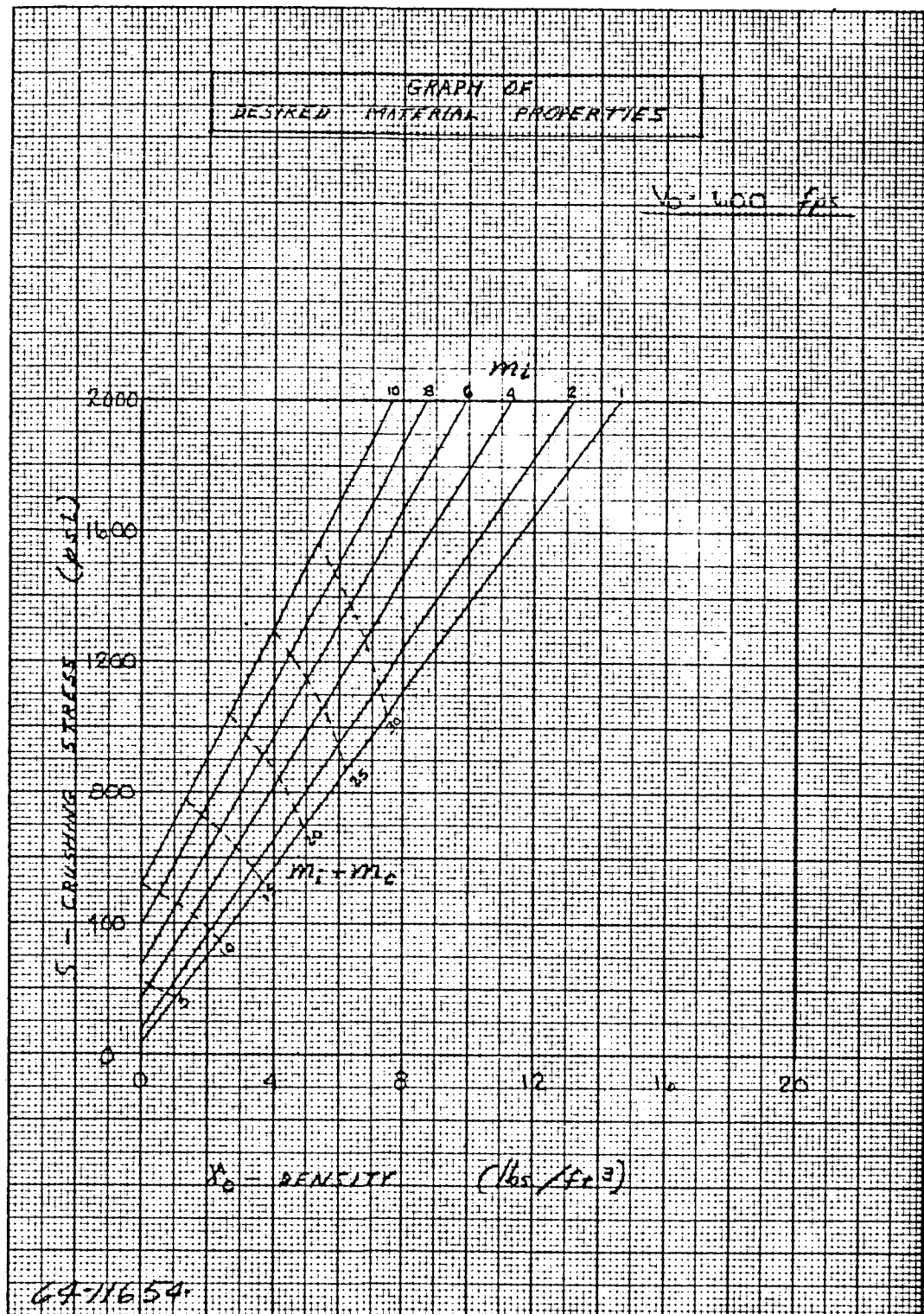


Figure 153 DESIRED MATERIAL PROPERTIES - $v_0 = 600 \text{ FPS}$

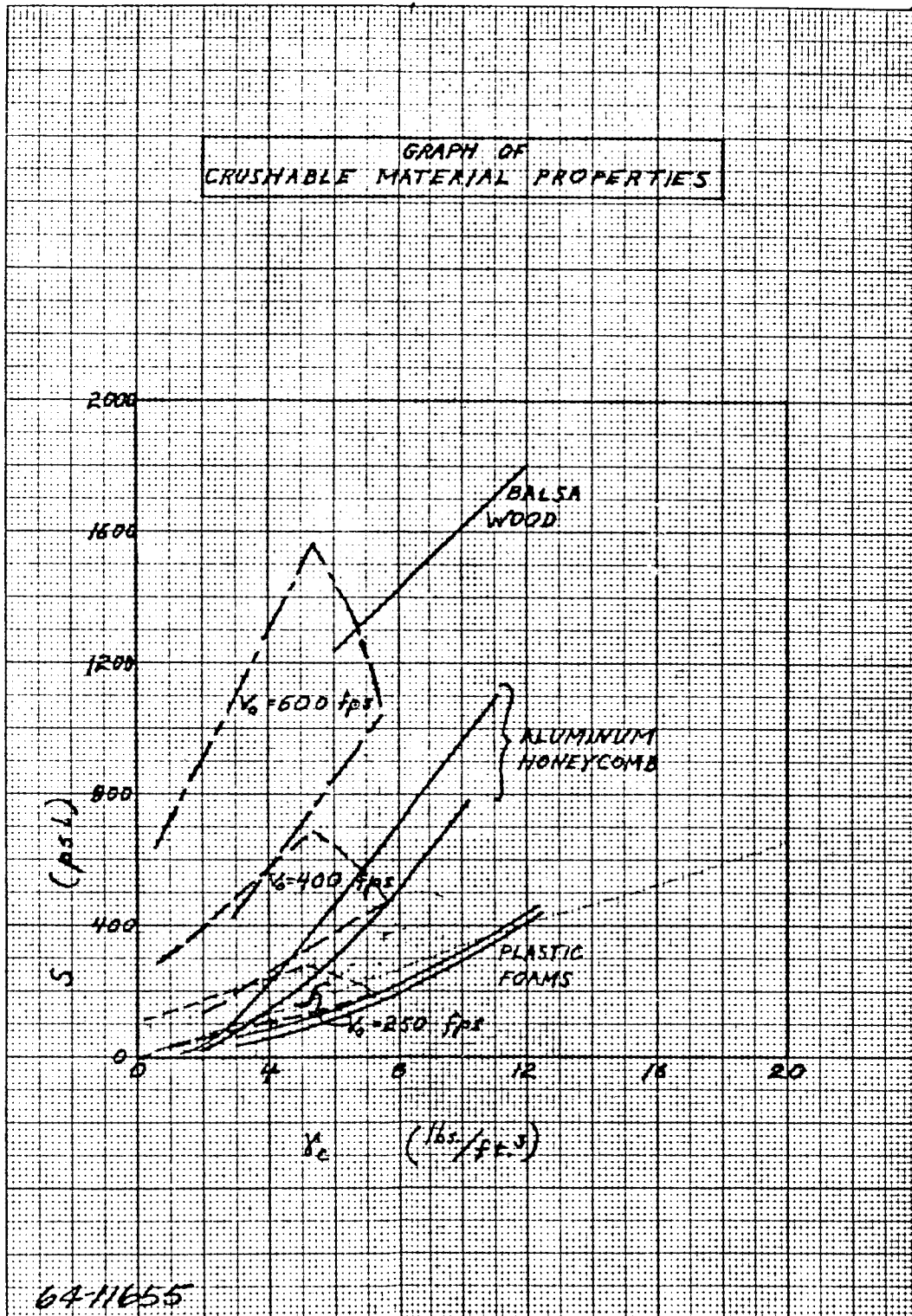


Figure 154 CRUSHABLE MATERIAL PROPERTIES

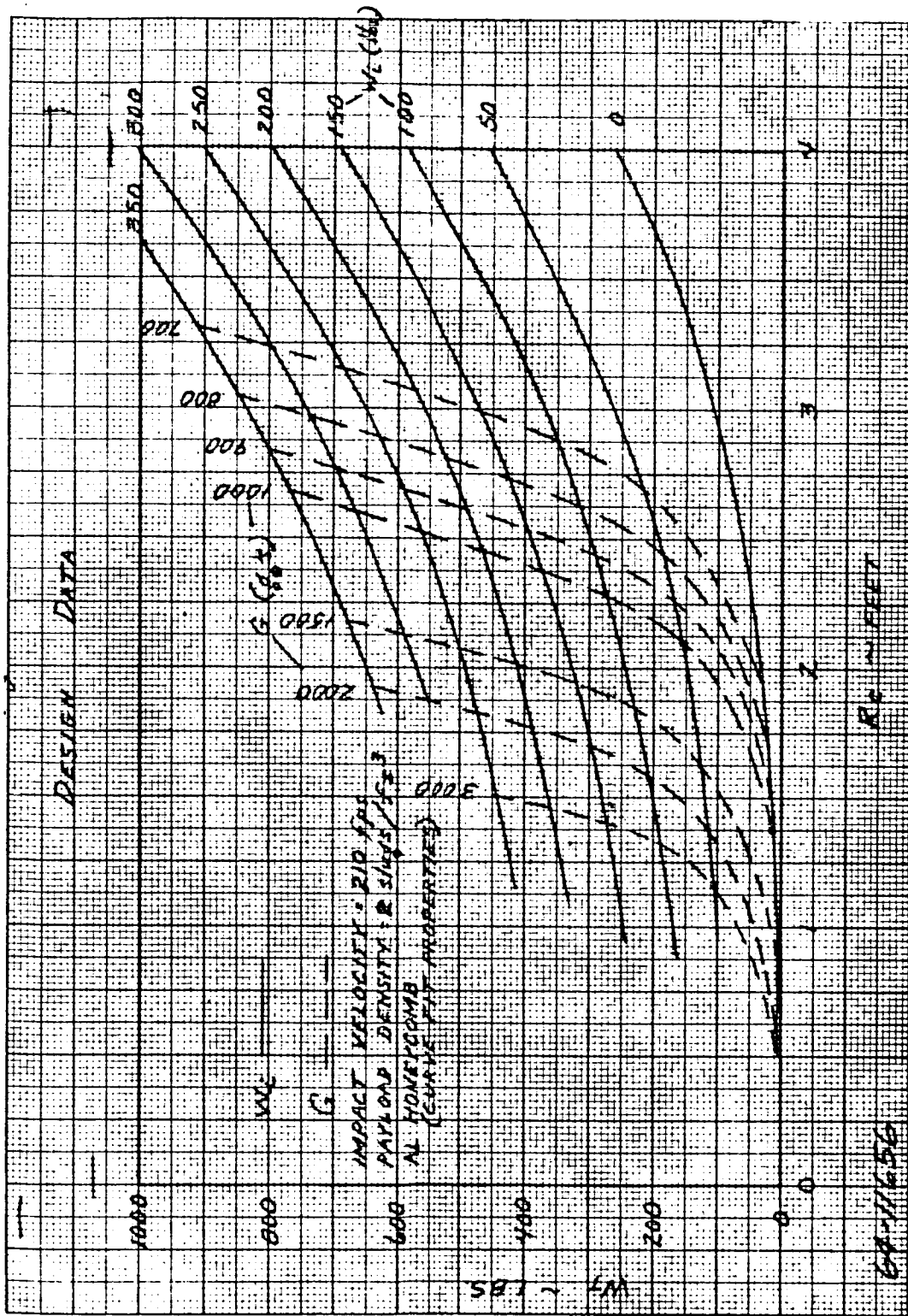


Figure 155 DESIGN DATA - $V_0 = 210$ FPS - ALUMINUM
HONEYCOMB - CURVE FIT

TYPICAL DESIGN CURVE

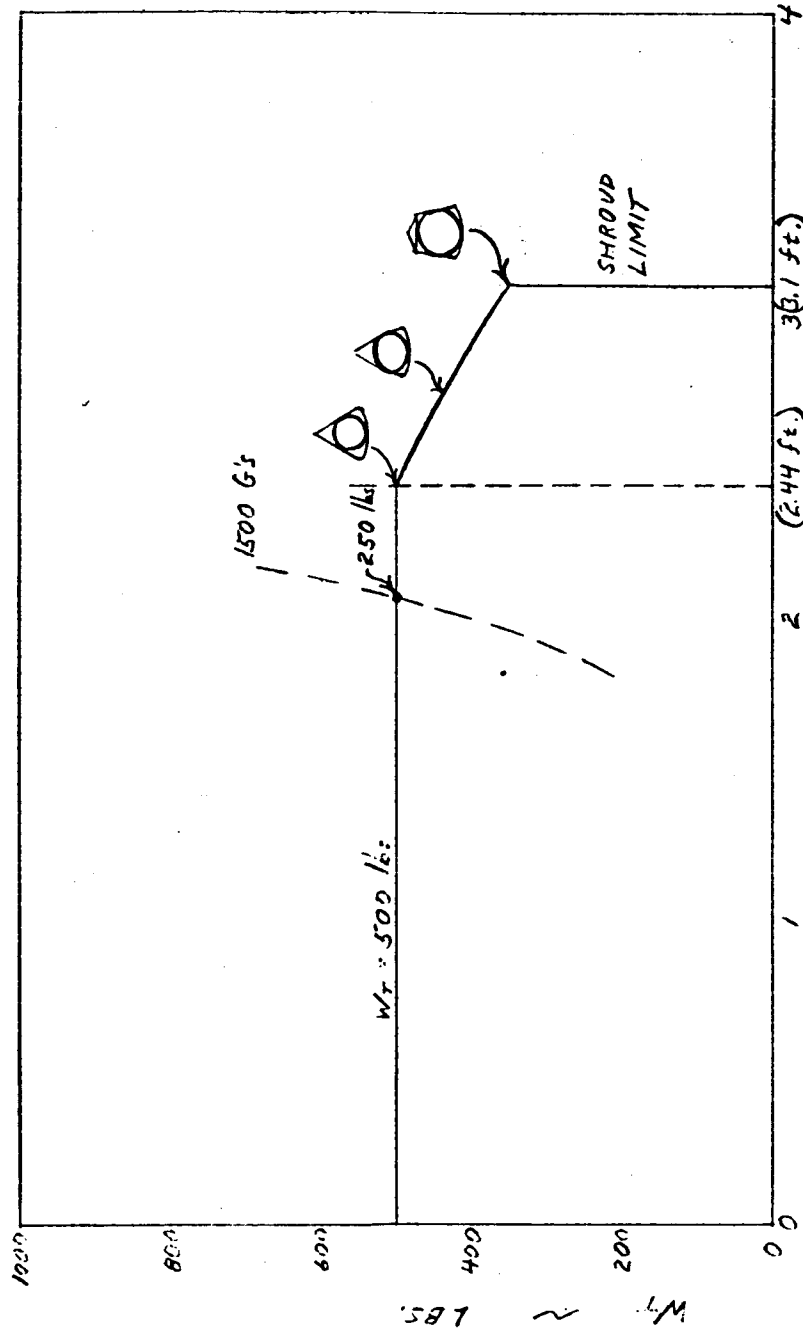


Figure 156 TYPICAL DESIGN CURVE

R_c ~ FEET

64-11657

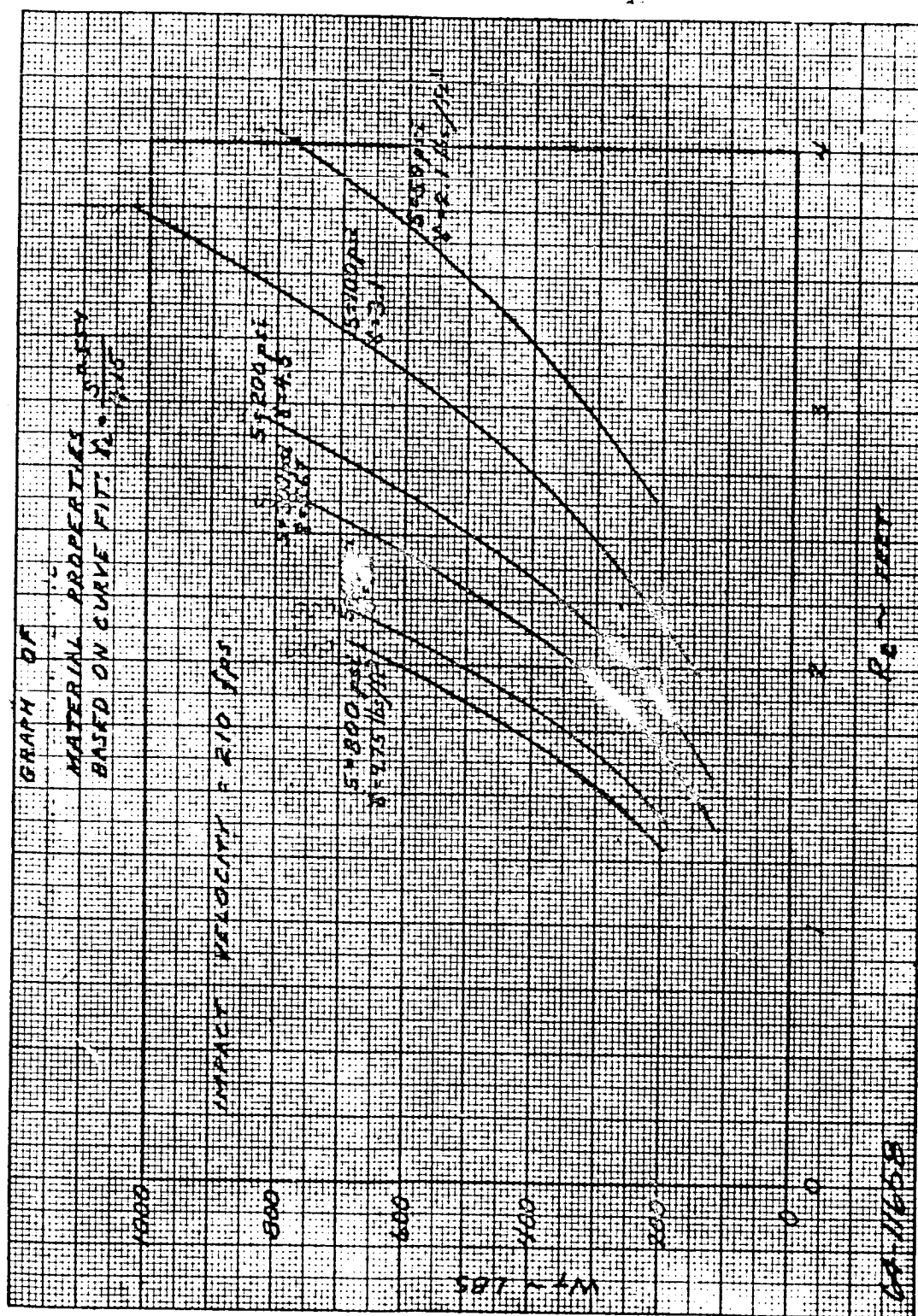


Figure 157 MATERIAL PROPERTIES BASED ON CURVE FIT, -% = 210 FPS

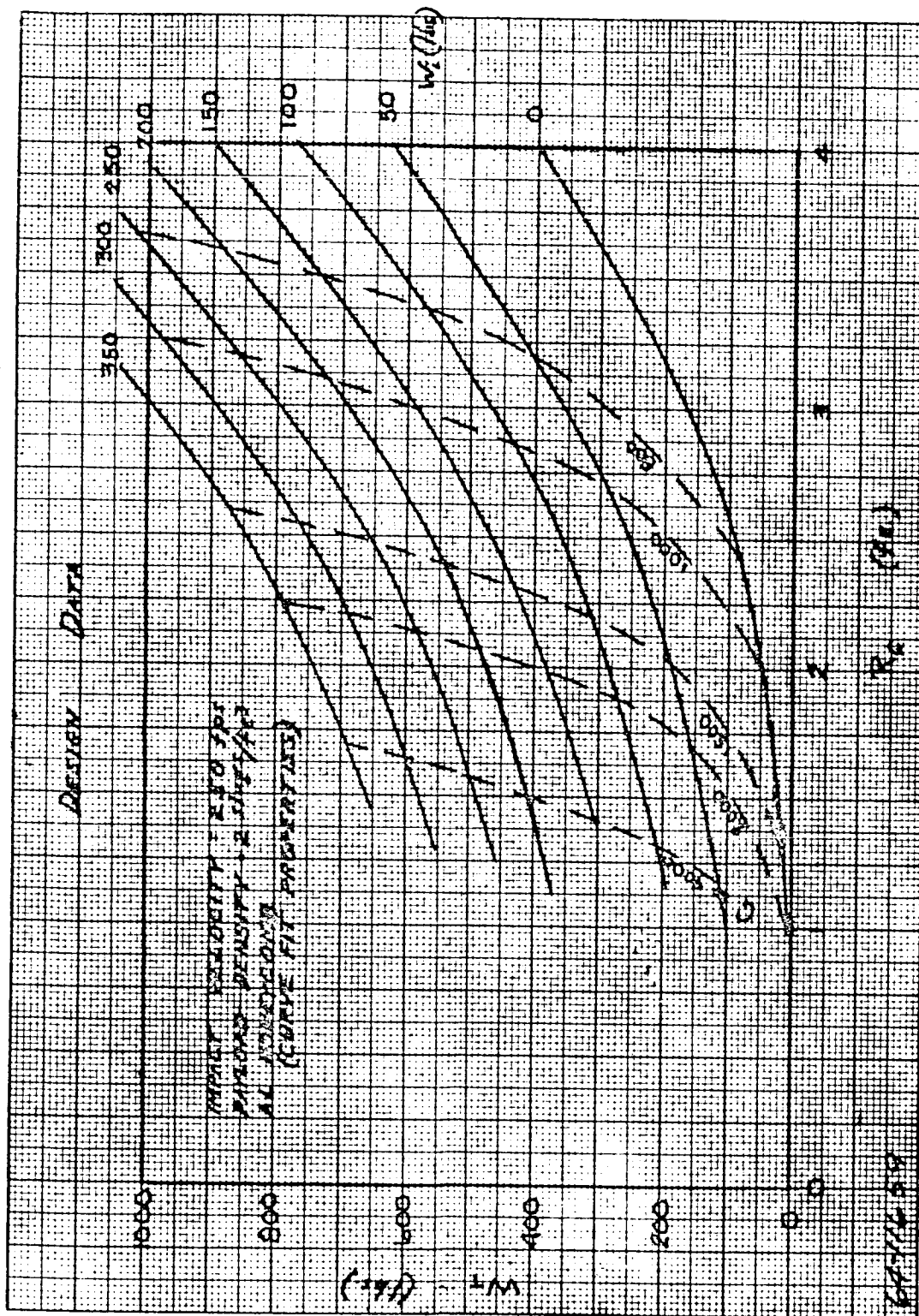


Figure 158 DESIGN DATA - $v_0 = 250$ FPS - AL HONEYCOMB - CURVE FIT

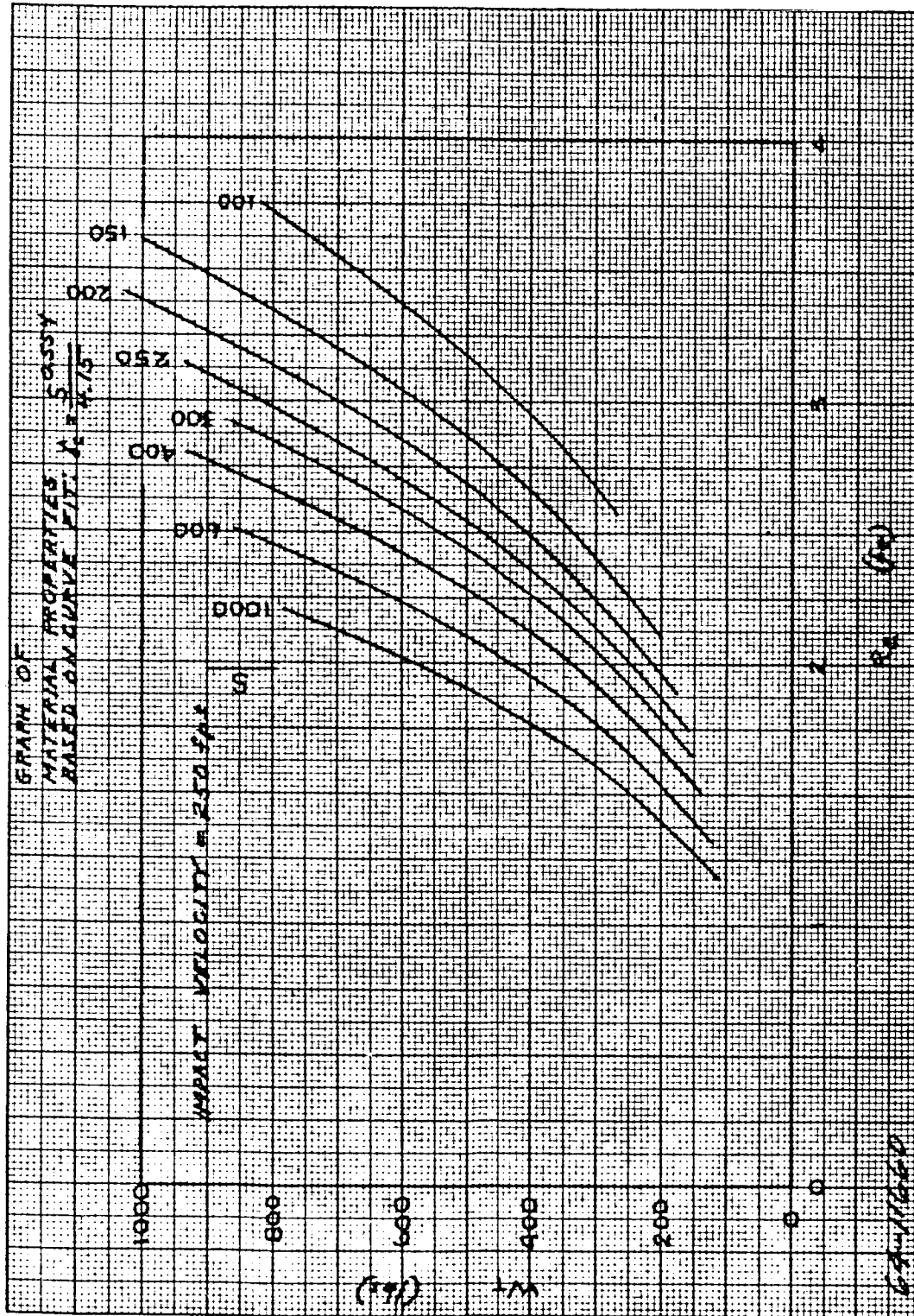


Figure 159 MATERIAL PROPERTIES BASED ON CURVE FIT - $v_0 = 250$ FPS

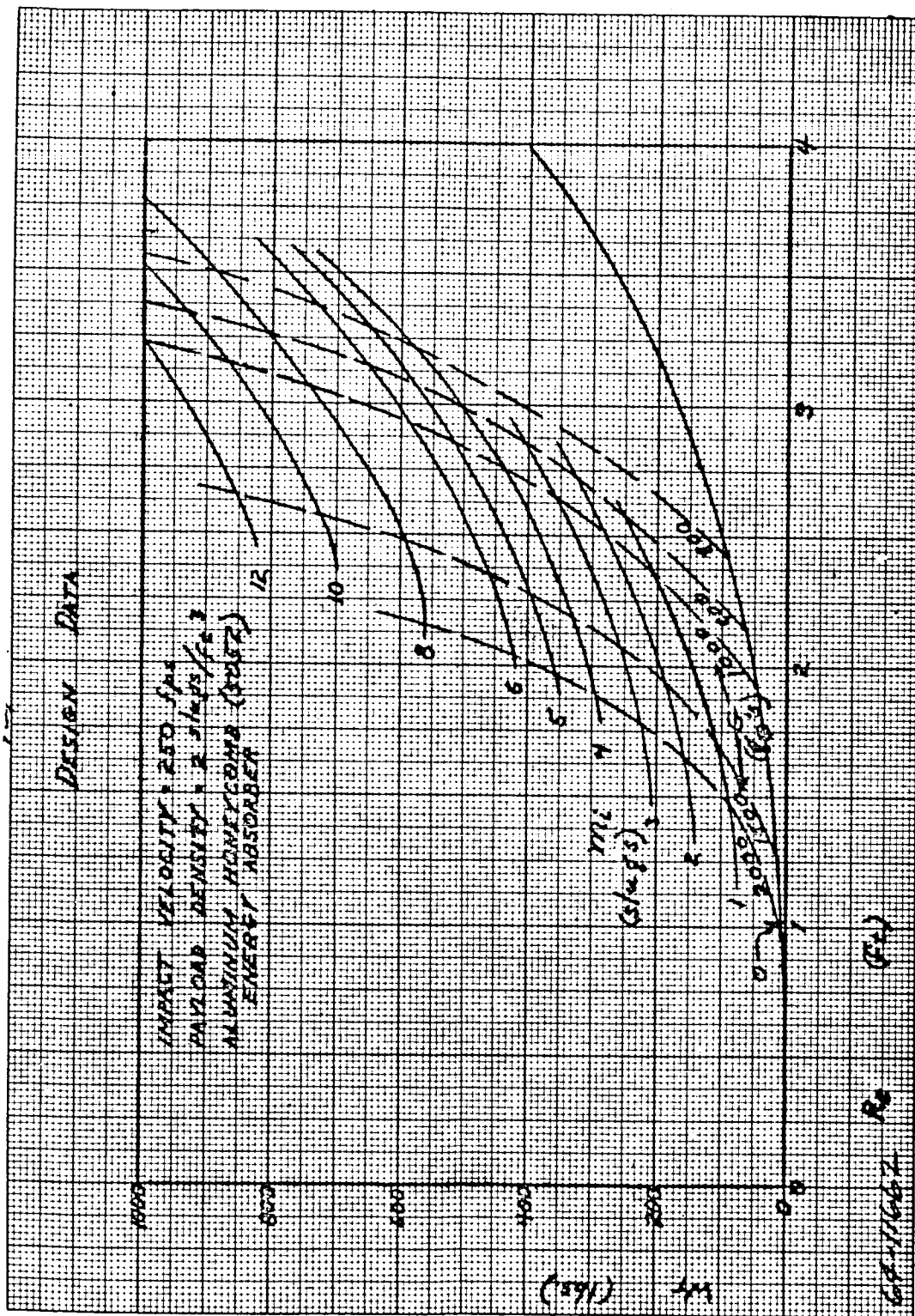


Figure 161 DESIGN DATA - $v_0 = 250$ FPS - AL HONEYCOMB - 5052

are made in equation (1-4), the result is

$$\frac{\rho_c v_o^2}{\epsilon S} = 1.386$$

For balsa wood with a bulk density of six lb/ft³ and a crushing stress of 1230 lb/in.², the limiting impact velocity turns out to be approximately 1000 ft/sec. The other materials investigated all have lower limiting velocities; thus balsa wood seems to hold the greatest promise for very high velocity impact attenuation. This conclusion is also borne out by the optimum materials study summarized on figure 154. It can be seen that for 600 ft/sec, the desired material properties are closer to those of balsa wood than of any other material.

Figures 162, 163, and 164 present the pertinent parameters of an impact system using balsa wood plotted versus the impact velocity.

Figure 164 in particular displays some rather interesting features. Thus if the total landed weight is held fixed, then as the impact velocity increases, the g's increase (and the internal payload decreases of course). However, if the internal payload weight is held fixed, figure 164 shows that as impact velocity increases, the impact decelerations peak at about 500 ft/sec and then decrease. The reason for this paradoxical behavior is that at the very high velocities, an enormous amount of balsa wood is required, much of it just to decelerate itself. Now it can be shown from equation (2-3) of appendix A that to a first approximation, peak deceleration is proportional to velocity squared divided by stroke (or thickness of crushable material). For balsa wood, above 500 fps, the thickness of material is increasing faster than the square of the velocity; so, the g's actually decrease.

The data presented on these curves is used in section 8.4 in the optimization studies of no-chute and one-chute systems.

8.3 INFLUENCE COEFFICIENTS

In this section, the effects of variations in some of the parameters on the design of an impact system are examined. The particular parameters treated herein are velocity of impact, packaging density, and non-homogeneity and anisotropy of the impact attenuation material. In order to present most of this information, nominal conditions were assumed and the variations about these nominals due to the various parameters calculated. In this sense, the graphs can be interpreted as presenting "influence coefficients" which can be used to compute the change in nominal values as a function of the change in the above parameters, taken singularly.

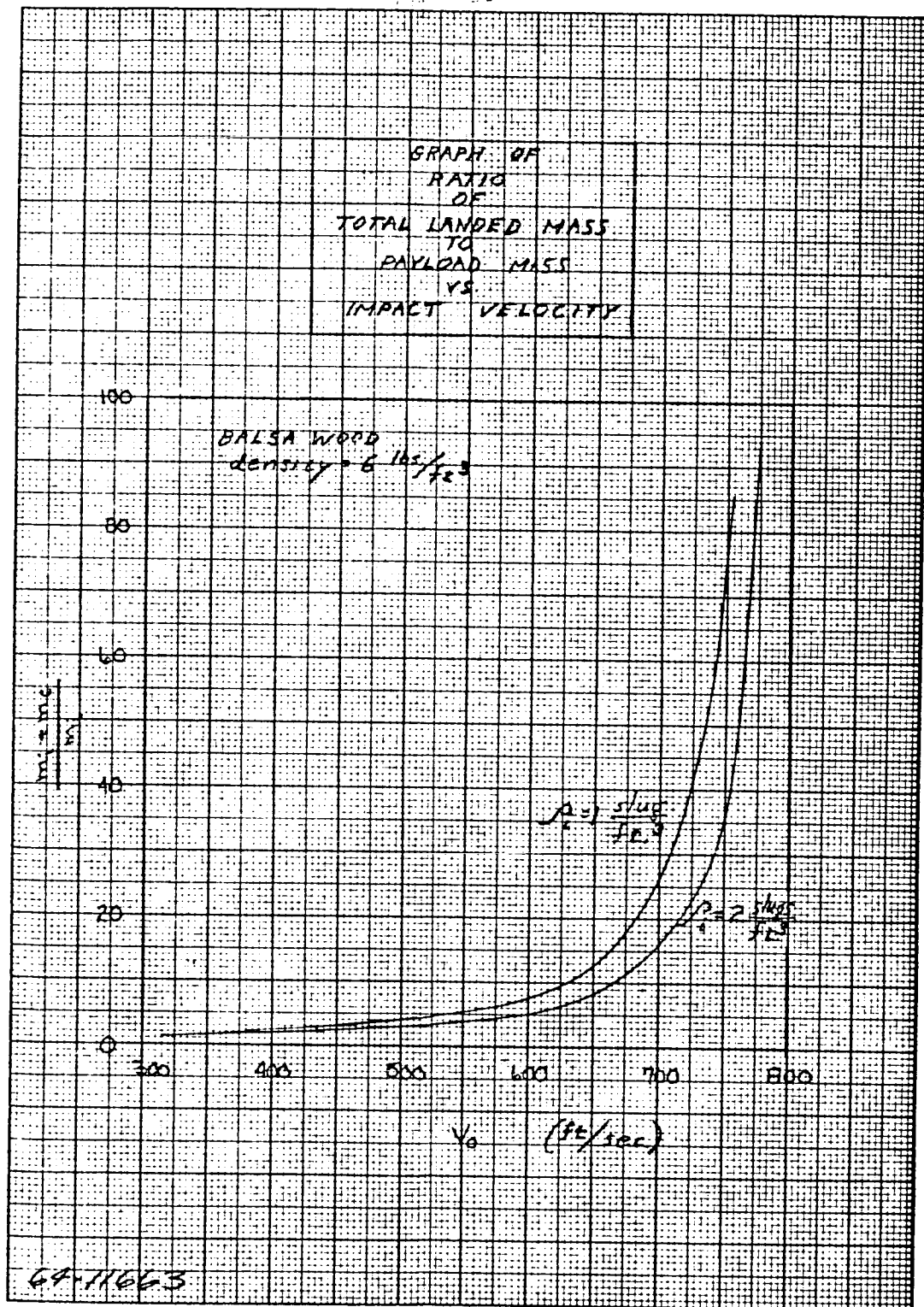


Figure 162 RATIO OF TOTAL LANDED MASS TO PAYLOAD MASS VERSUS
IMPACT VELOCITY - BALSA WOOD

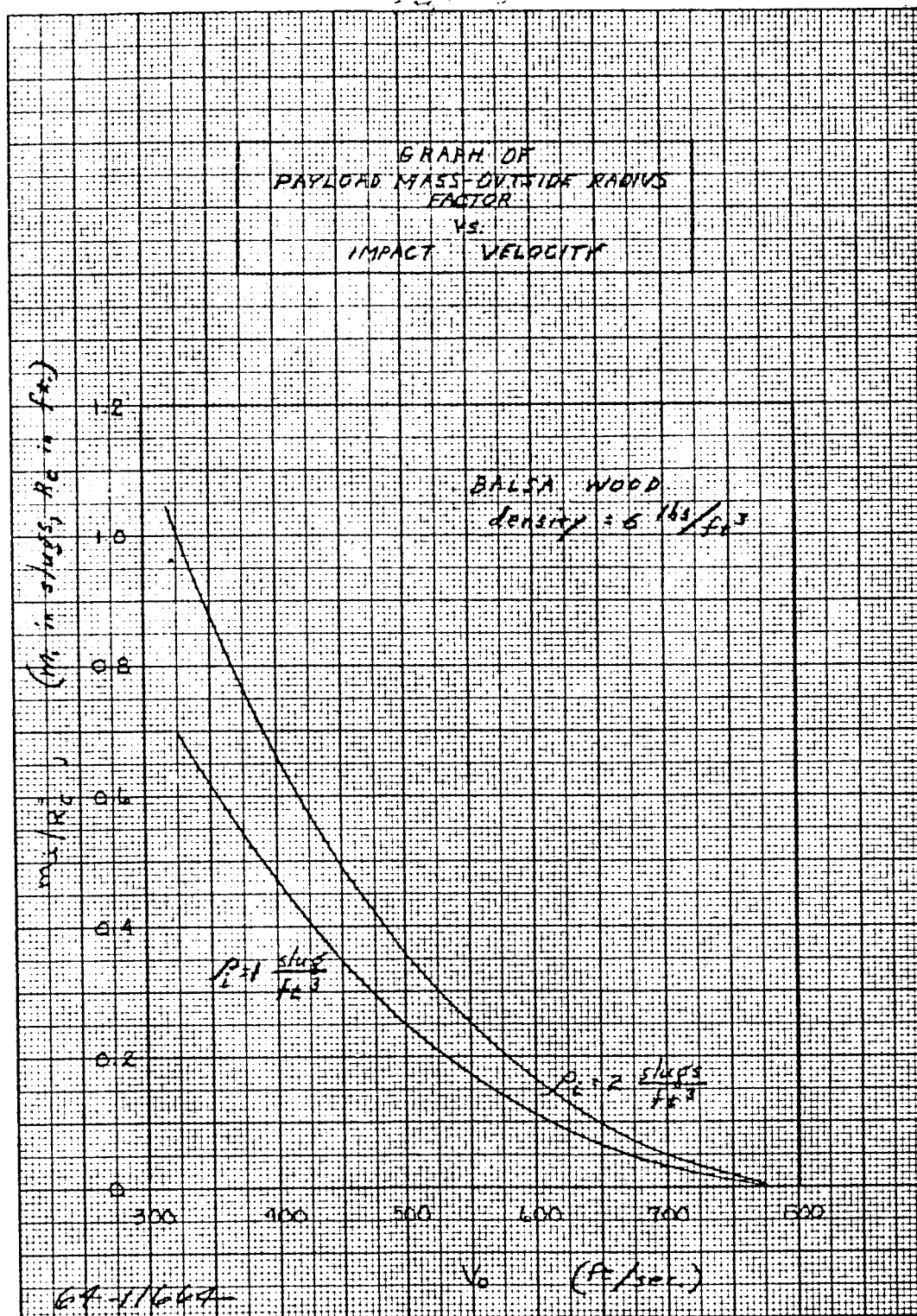


Figure 163 PAYLOAD MASS - OUTSIDE RADIUS FACTOR VERSUS IMPACT VELOCITY - BALSA WOOD

GRAPH OF
IMPACT G PARAMETER
VS.
IMPACT VELOCITY

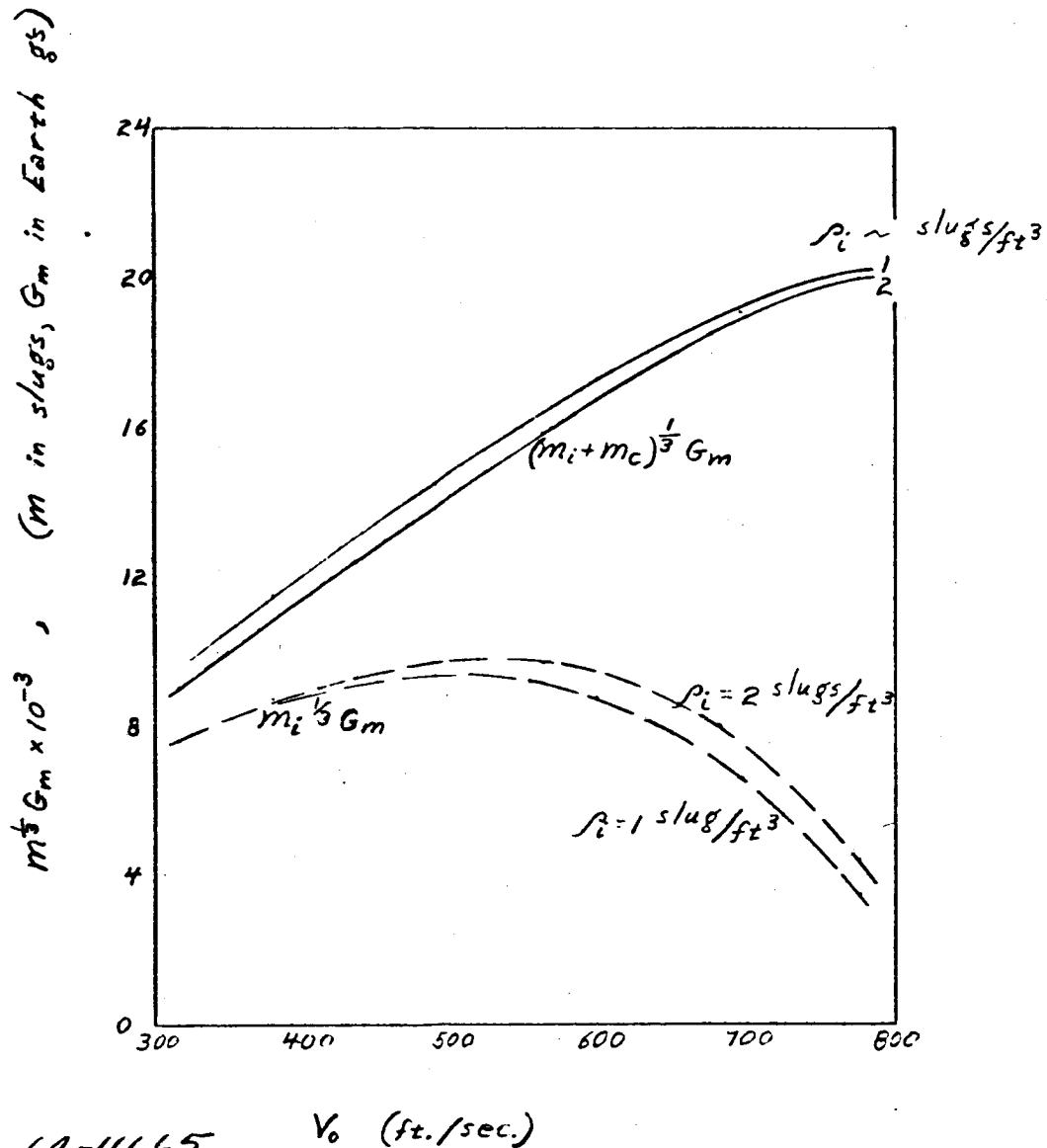


Figure 164 IMPACT G PARAMETER - VERSUS IMPACT VELOCITY - Balsa WOOD

The nominal conditions which were chosen are listed below:

Impact velocity = 200 ft/sec

total landed weight = 500 lbs

peak deceleration = 1500 g

payload packaging density = 2 slugs/ft³

With these values, the internal payload works out to be 267 pounds. The first parameters investigated were impact velocity and packaging density. Using equations (2-3), (2-4), (2-10), and (2-11) of appendix A, together with the nominal aluminum honeycomb curve fit

($y_e = \frac{s^{0.554}}{4.15}$) from figure 141, figure 165 was generated. The nominal

design point described above is pointed out on this figure. It may be noted that the increase in payload in going from a ρ_i of 2 slugs/ft³ to 3 is only about half that gained in going from 1 to 2. This conclusion is fortified by figure 147, which shows that the mass ratio curves are leveling off as packaging densities of 3 or 4 slugs/ft³ are reached.

In section 3 of appendix A, equations are derived for cases involving variable crushing stress of the impact absorber. The first case treated concerns non-homogeneous materials: in this case, the stress is assumed to vary as the radius raised to the n^{th} power. This parameter, n , is used as the measure of nonhomogeneity. The important equations obtained from this analysis are equations (3-8), (3-9), and (3-10). The first figure generated from these equations is figure 166. This curve has the same coordinates as figure 155, but its purpose is to display what happens to a curve of constant payload weight as the parameter n is varied. For a constant total weight, WT , as the exponent n is increased, the landed package radius increases, but the g -level decreases significantly. Alternatively, if the radius of the package is held constant, both the total weight and the g -level can be decreased.

In the next 3 curves, figures 167, 168 and 169, the total weight and the g -level are fixed. It can be seen that significant increases in internal payload weight can be realized with an attendant reduction in package radius. Since aluminum honeycombs can be obtained with crushing stress in excess of 1600 lb/in.² figure 169 indicates that an exponent n of at least 3 is attainable with actual materials.

For the case where the material was assumed anisotropic, where crushing stress was a function of angular orientation, the relevant equations are (3-15), (3-16), (2-10), and (2-11), of appendix A. The stress is now assumed to be proportional to the cosine of the central angle (see figure 254 of appendix A) raised to the m^{th} power; the exponent is used as a measure of anisotropy. Figure 170 shows the loss in payload and the decrease in radius as a function

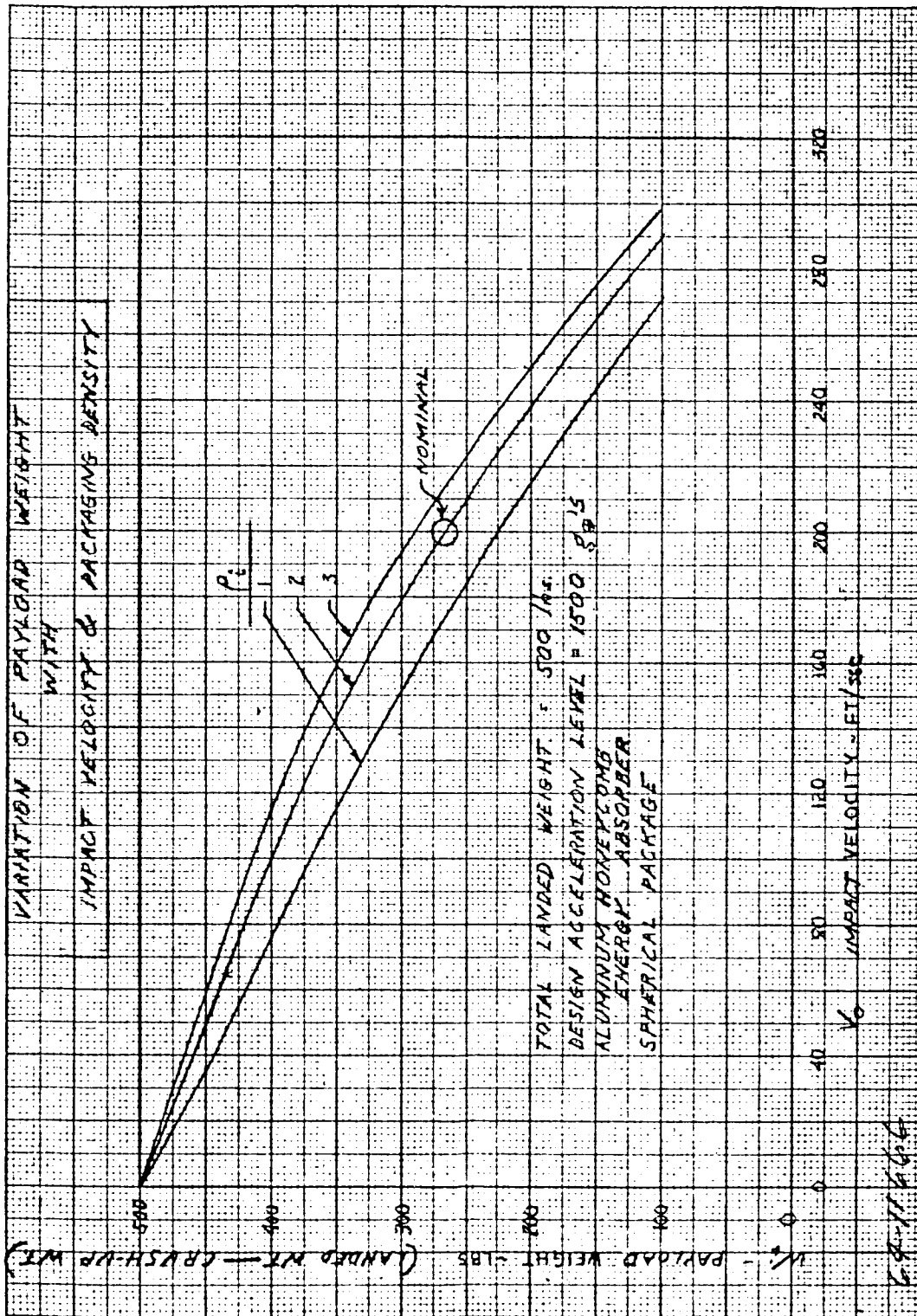


Figure 165 VARIATION OF PAYLOAD WEIGHT WITH IMPACT VELOCITY AND PACKAGING DENSITY

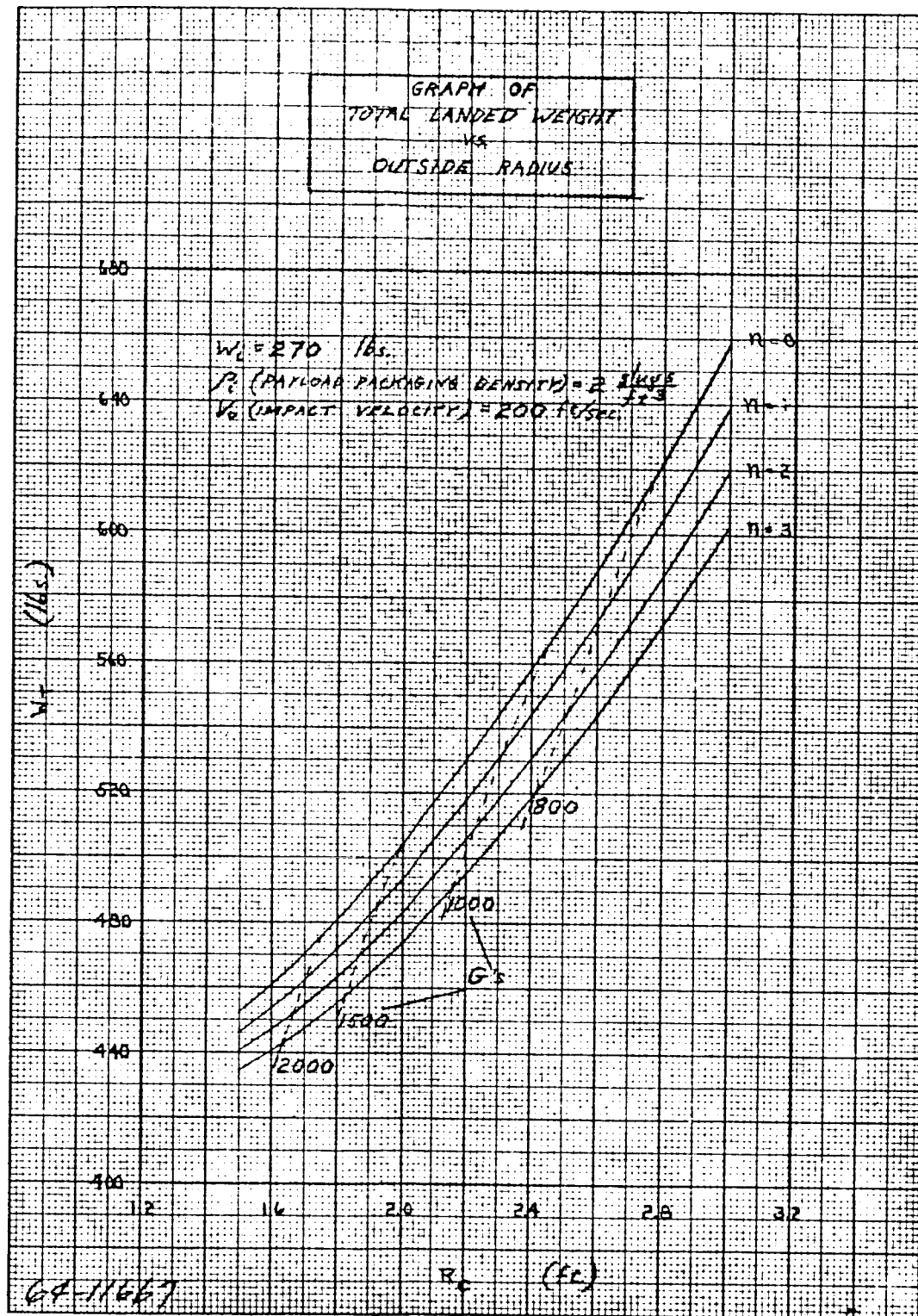


Figure 166 TOTAL LANDED WEIGHT VERSUS OUTSIDE RADIUS

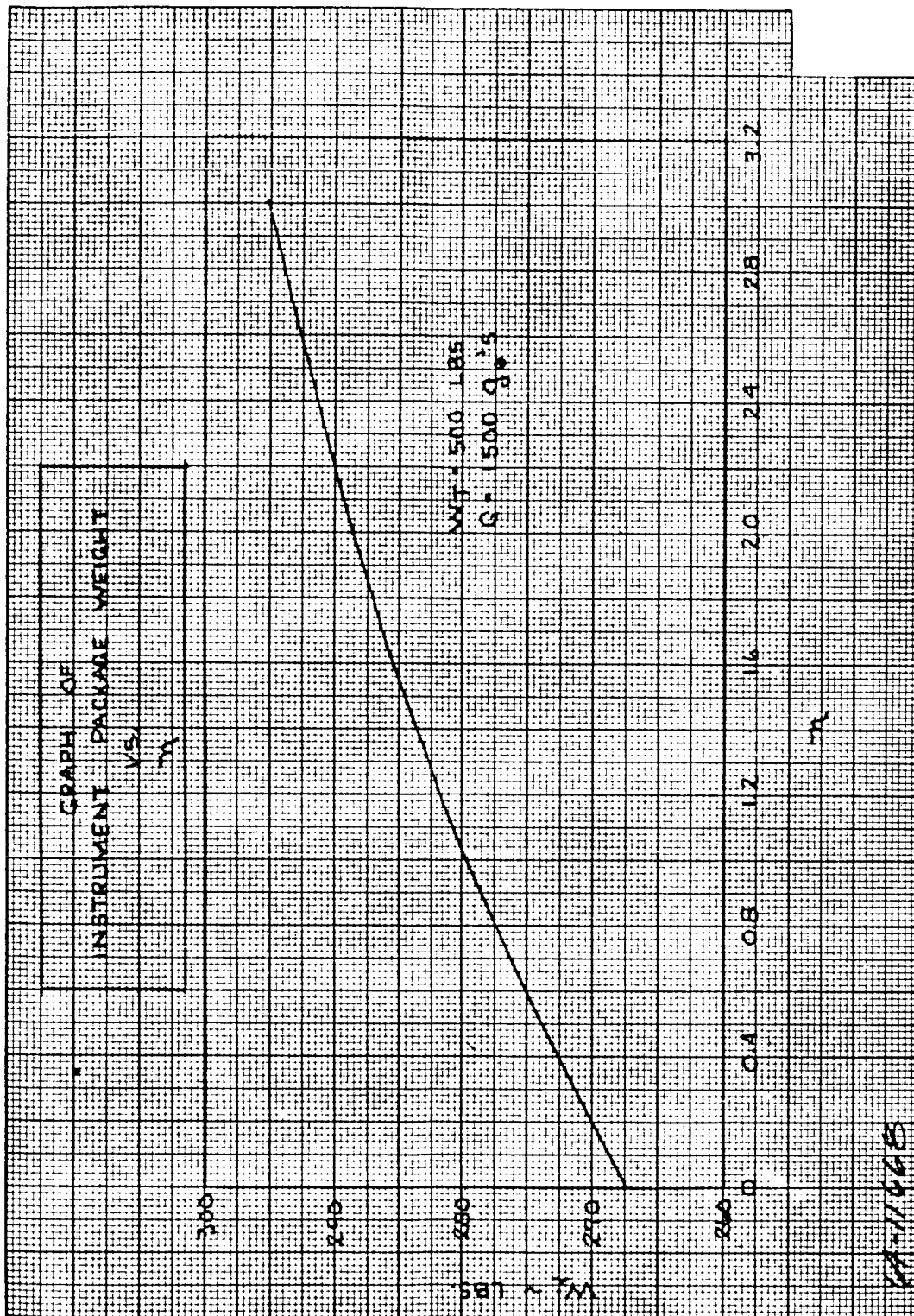


Figure 167 INSTRUMENT PACKAGE WEIGHT VERSUS n

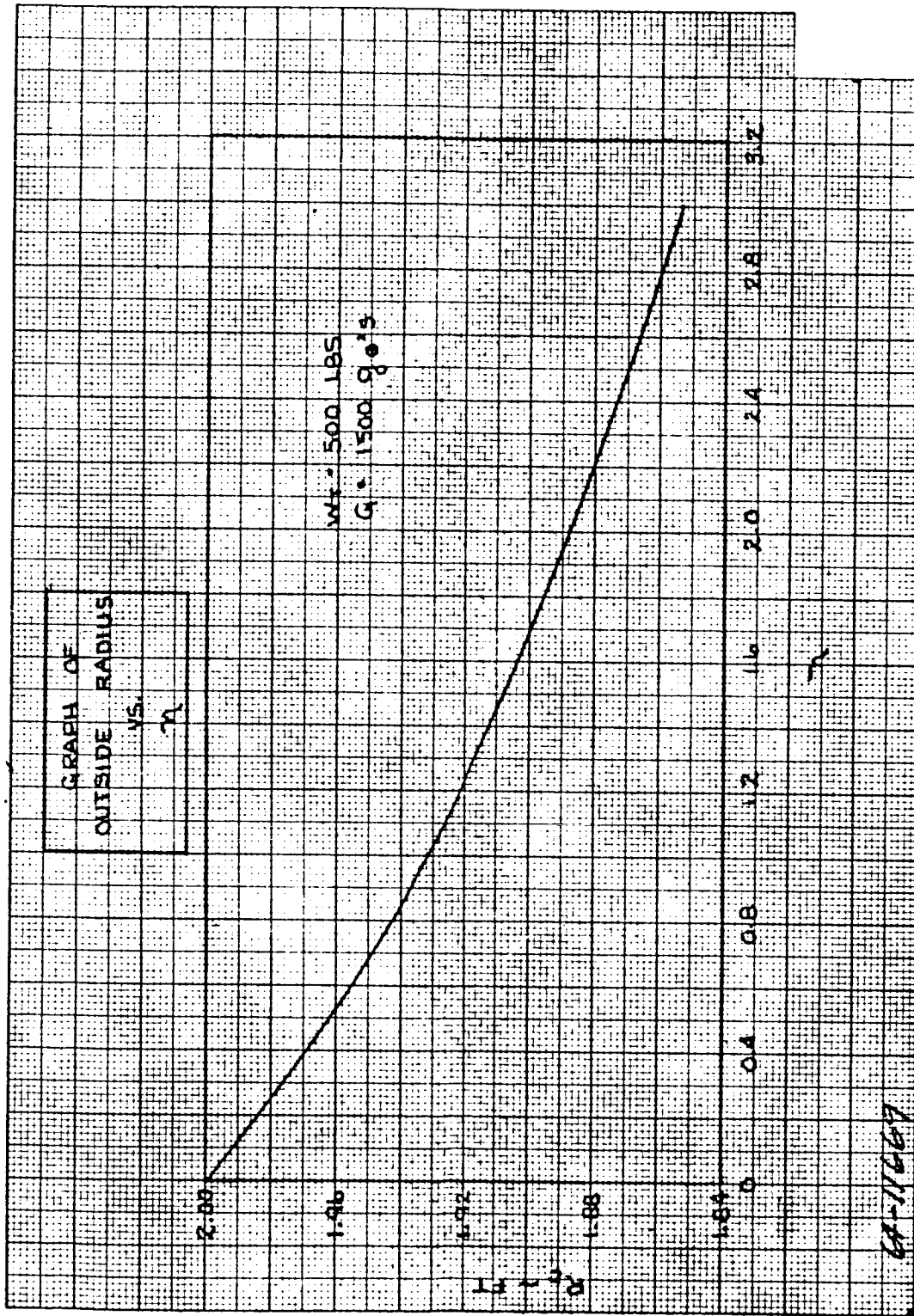


Figure 168 OUTSIDE RADIUS VERSUS n

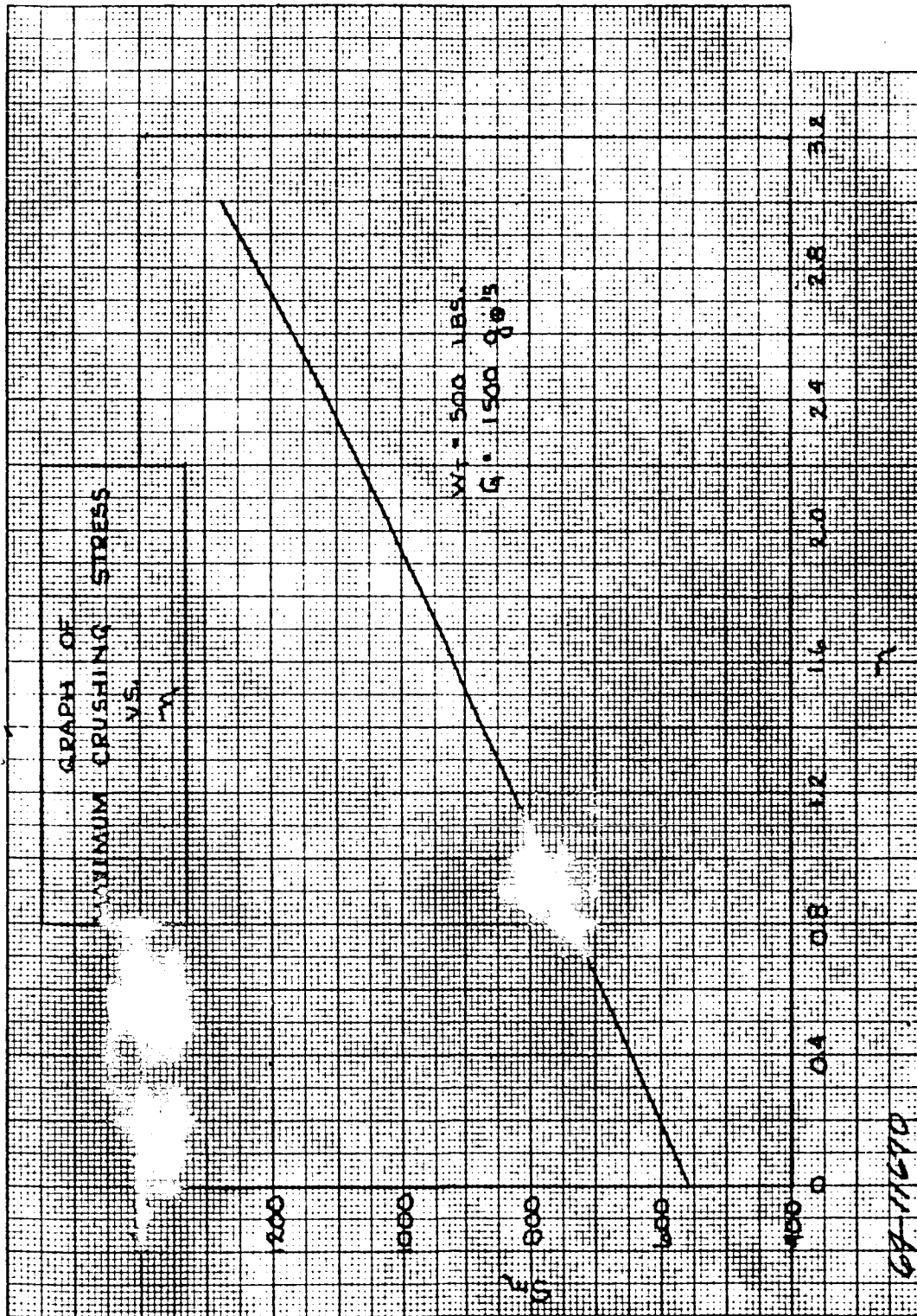


Figure 169 MAXIMUM CRUSHING STRESS VERSUS n

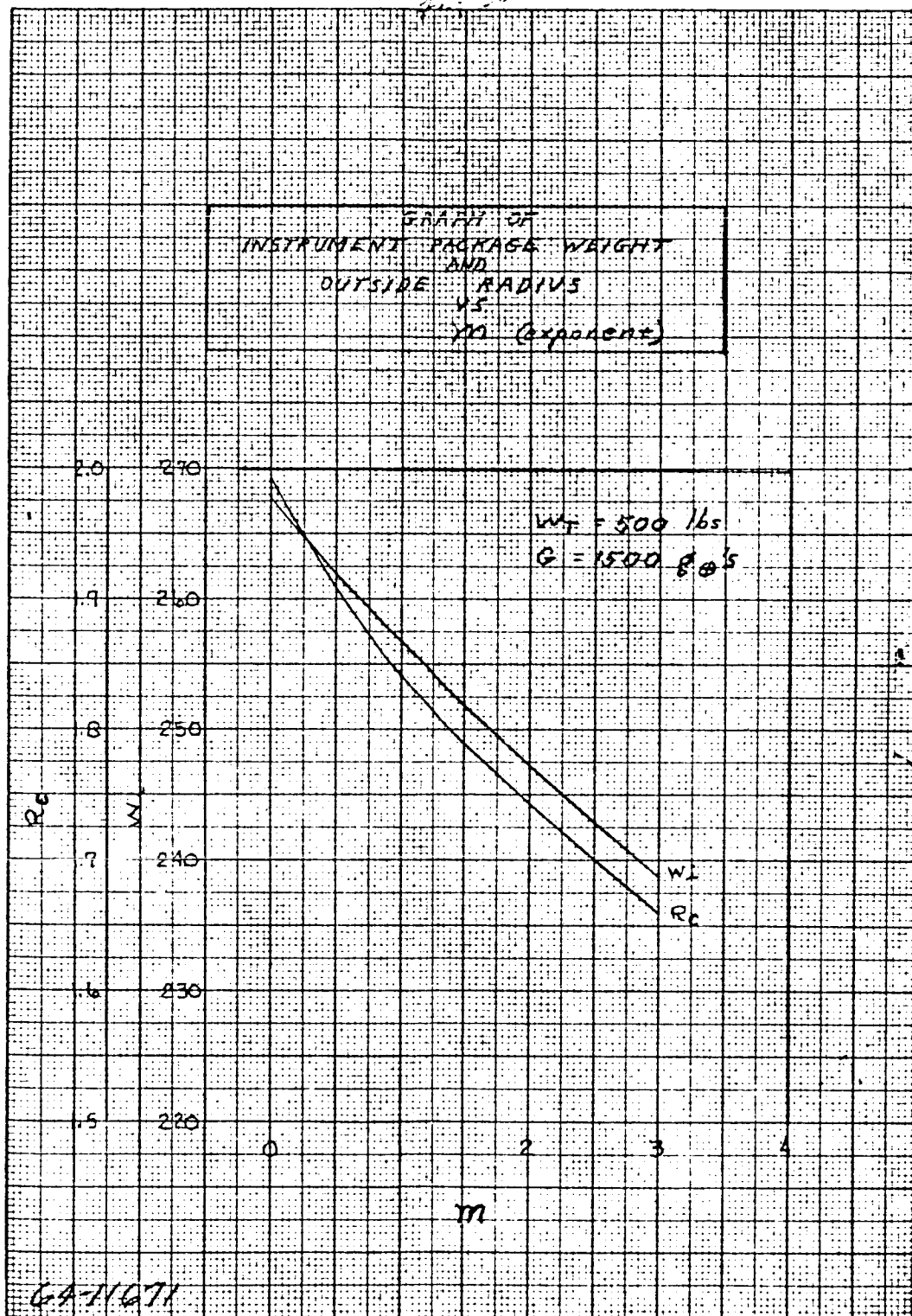


Figure 170 INSTRUMENT PACKAGE WEIGHT AND OUTSIDE RADIUS
VERSUS m

of the exponent m . There is not sufficient test data in existence at this time to allow a valid estimate to be made of the true value of m which ought to be used for any actual material. This determination must await tests performed on materials in the spherical configuration of interest in this study.

In summary, the "influence coefficients" for this particular nominal case are:

$$\frac{\Delta w_i}{\Delta V} \approx 1.65 \text{ lb/ft/sec}$$

$$\frac{\Delta w_i}{\Delta \rho_i} \approx 30 \text{ lb/slug/ft}^3 \approx 1 \text{ lb/lb/ft}^3$$

$$\frac{\Delta w_i}{\Delta n} \approx 13 \text{ lbs/change in } n$$

$$\frac{\Delta w_i}{\Delta m} \approx 10 \text{ lb/change in } m$$

8.4 OPTIMIZATION

Three studies were made involving the maximization of internal payload weight by trading off drag device weight with impact attenuation system weight. The three studies were a no-chute system, a one-chute system using only a drogue chute, and a two-chute system. In the case of no parachute, the trade-off was between vehicle m/CDA and the impact system, while the other cases were basically trade-offs between parachute and impact system weight.

8.4.1 No-Chute Optimization

This section presents parametric results for a lander impacting the planet without the use of an external descent system. For such a case the vehicle itself serves as the primary decelerator; hence an optimization results from a tradeoff between the ballistic coefficient and the impact attenuator material. Figure 171 presents parametric results whereby the payload fraction can be obtained for a particular set of conditions. The first quadrant of figure 171 presents trajectory data of vertical impact velocity plotted against the ratio of gross entry weight over vehicle area (W_G/A) for a range of surface pressures. ¹ With the impact velocity known it is possible to establish the fraction (W_{PL}/W_{IMP}) for a certain type impact attenuator. Quadrant two presents the above mentioned fraction for balsa wood impact attenuation material assuming a 1.0 slug/ft^3 payload packaging density. (See figure 162, section 8.2.2). Shown are curves for horizontal wind velocity components of 0, 100, and 200 ft/sec. Utilizing quadrant one, it is possible to determine the impact weight fraction (W_{IMP}/W_G) for a range of heat shield and structural weight fractions ($W_H/S/S$), where S is the total

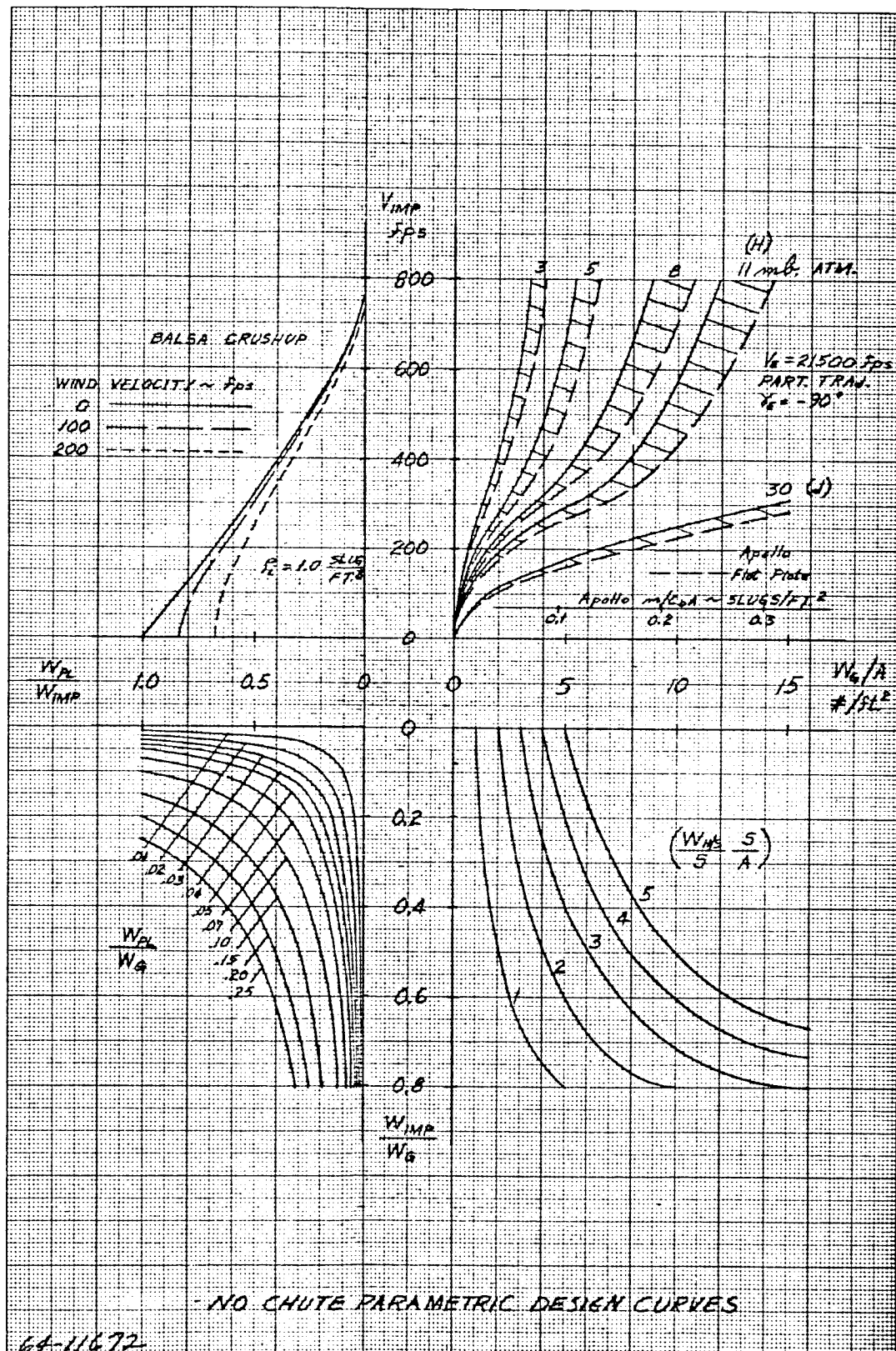


Figure 171 NO-CHUTE PARAMETRIC DESIGN CURVES

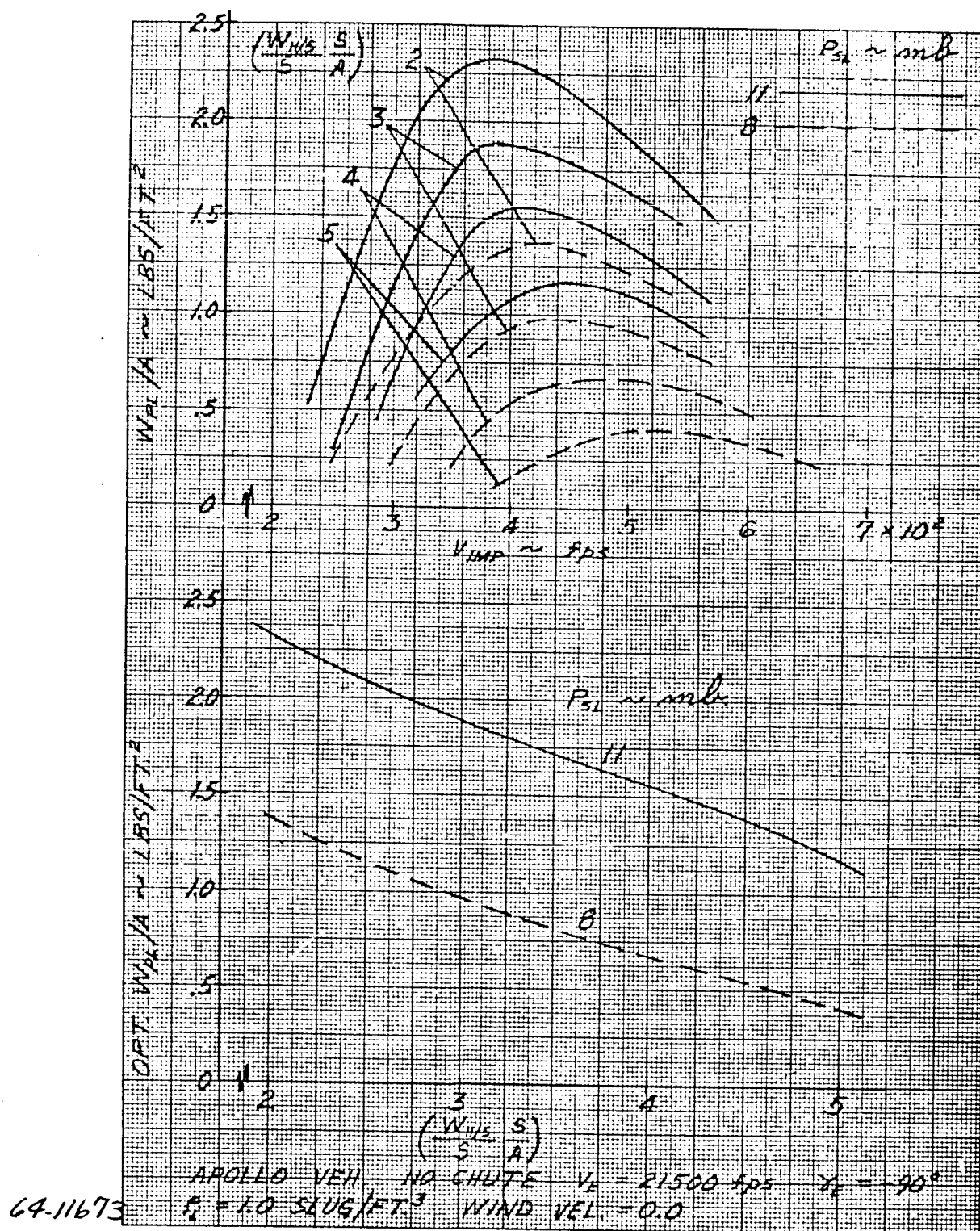


Figure 172 OPTIMUM W_{PL}/A VERSUS W_{HS}/A FOR VARIOUS ATMOSPHERES

surface area of the vehicle. This is shown in quadrant four. The end result of figure 171 is the payload fraction (W_{PL}/W_G) which is evolved by cross plotting quadrants two and four. An example of using the parametric study graph of figure 171 is shown below.

Figure 172 presents payload weight over vehicle area versus impact velocity for a range of ($W_H/S/A$) values. An optimum (W_{PL}/A) is evolved for each value of $W_H/S/A$. The results on figure 172 are for zero horizontal wind velocity and show the effect of surface pressure. Figure 173 is similar to figure 172 and includes results for horizontal wind velocities of 0, 100 and 200 ft/sec.

Sample WPL Solution Using NO CHUTE

PARAMETRIC STUDY Graph

Vehicle

90" diameter Apollo
 $m/CDA = 0.15$
 $W_H/S = 163.7$
 $W_G = 307.0$
 $W_G/A = 7.0$

Assumptions

11 mb. atm.
 wind = 0.0
 $\rho_i = 1.0$

<u>Step</u>	<u>Known Quantities</u>	<u>Solve for</u>	<u>Answer</u>
1.	$W_G/A = 7.0$, 11 mb. atm.	VIMP	356.0
2.	VIMP = 356.0, wind = 0.0, $\rho_i = 1.0$	W_{PL}/W_{IMP}	0.46
3.	$W_H/S = 163.7$, $m/CDA = 0.15$	$\frac{W_H/S}{S} \quad \frac{S}{A}$	3.7
4.	$W_G/A = 7.0$, $\left(\frac{W_H/S}{S} \quad \frac{S}{A}\right) = 3.7$	W_{IMP}/W_G	0.47
5.	$W_{PL}/W_{IMP} = 0.46$, $W_{IMP}/W_G = 0.47$	W_{PL}/W_G	0.22
6.	$W_G = 307.0$, $W_{PL}/W_G = 0.22$	WPL	67.5

8.4.2 One-Chute Optimization

A system using only a drogue parachute to decelerate the vehicle was the next case to be subjected to an optimization study.

The first step was the determination of the amount of weight involved in the drogue chute system, or more correctly, the amount of weight left over after the drogue chute system weight was subtracted out. Figure 174 summarizes this segment of the study. This graph shows the suspended weight versus m/CDA for a number of vertical velocities and for different lander diameters. For the atmosphere used, there is an inverse correlation between the ballistic coefficient and the altitude of drogue chute deployment (i. e., the altitude at which Mach 2.5 is reached). An altitude of 10,000 feet was chosen as the minimum allowable deployment altitude; this corresponds to an m/CDA of 0.32.

With this as the reference m/CDA , the data used to generate figure 162 of section 8.2.2. was used together with the data given on figure 174 in order to obtain figure 175. This figure illustrates the optimization of a one-chute system using a 6 lb/ft³ balsa wood energy absorber. It can be seen that the internal payload weight optimizes at a value of about 325 pounds at a vertical descent velocity of 150 ft/sec. With the wind velocity of 200 ft/sec, this yields a total impact velocity of 250 ft/sec. The peak deceleration experience for this optimum case is of the order of 3000 g.

A similar curve was also drawn for aluminum honeycomb, but in this instance, the g-level was held at a constant 1500 g. The g-level could not be held constant in the case of balsa wood since balsa can be obtained in only a narrow range of densities; hence, for this case, the material density is held fixed and the decelerations which result calculated. Aluminum honeycomb, on the other hand, can be obtained which covers a wide range of densities and crushing stress. Thus, the g-level can be prescribed, and the particular honeycomb required can be determined afterward.

For aluminum honeycomb, the optimum vertical descent velocity was found to be 100 ft/sec. The internal payload was reduced to 185 pounds, but the deceleration level has been halved in comparison to the balsa wood design. The results for aluminum honeycomb are shown on figure 176.

8.4.3 Two-Chute Optimization

The two-chute optimization study proceeded along much the same lines as the one-chute study discussed in the previous section.

Figures 105, 106, and 107 of section 7.5. were used to determine the optimum m/CD values corresponding to various main chute deployment altitudes. (These optimums turn out to be essentially independent of

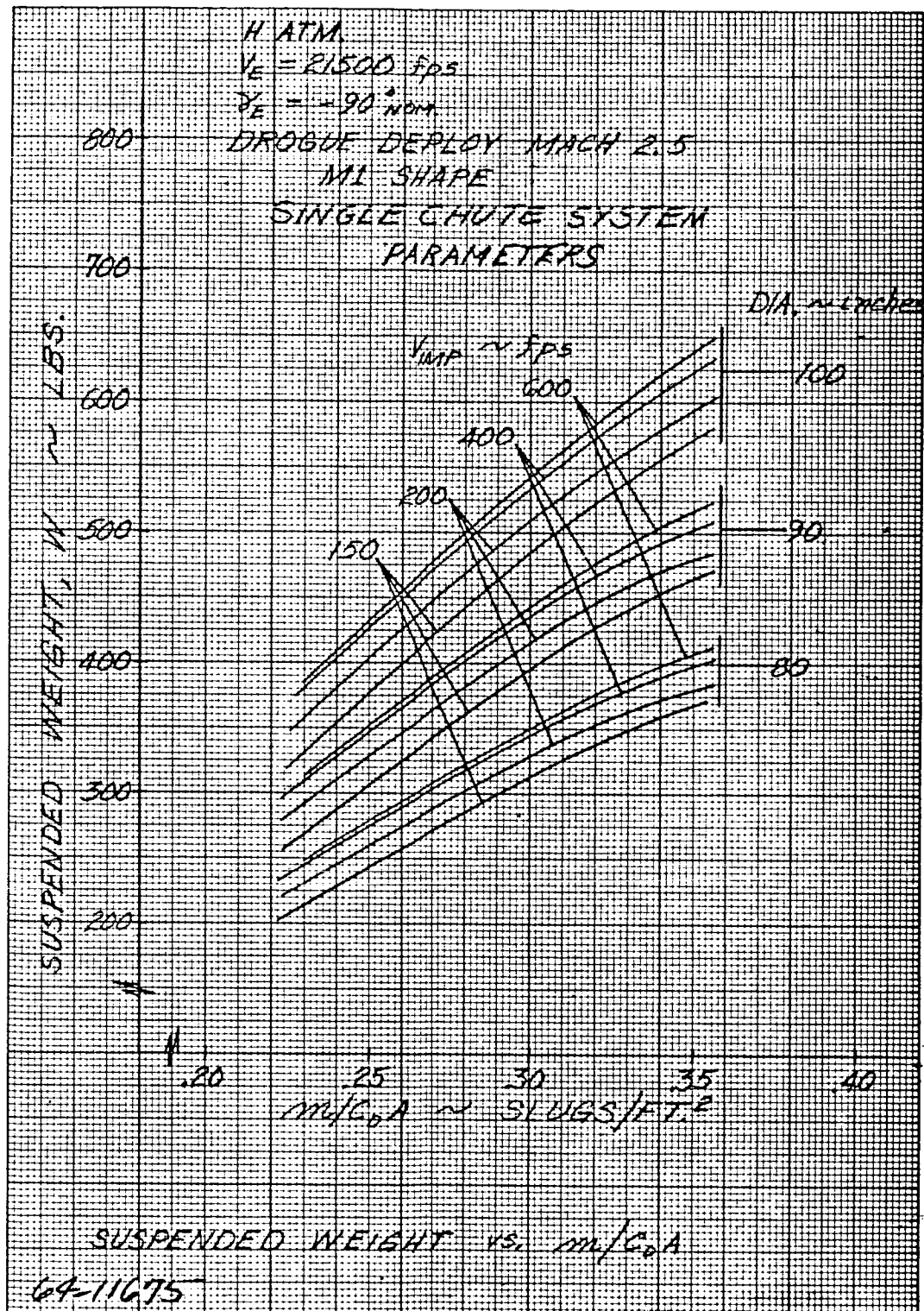


Figure 174 SINGLE CHUTE SYSTEM PARAMETERS

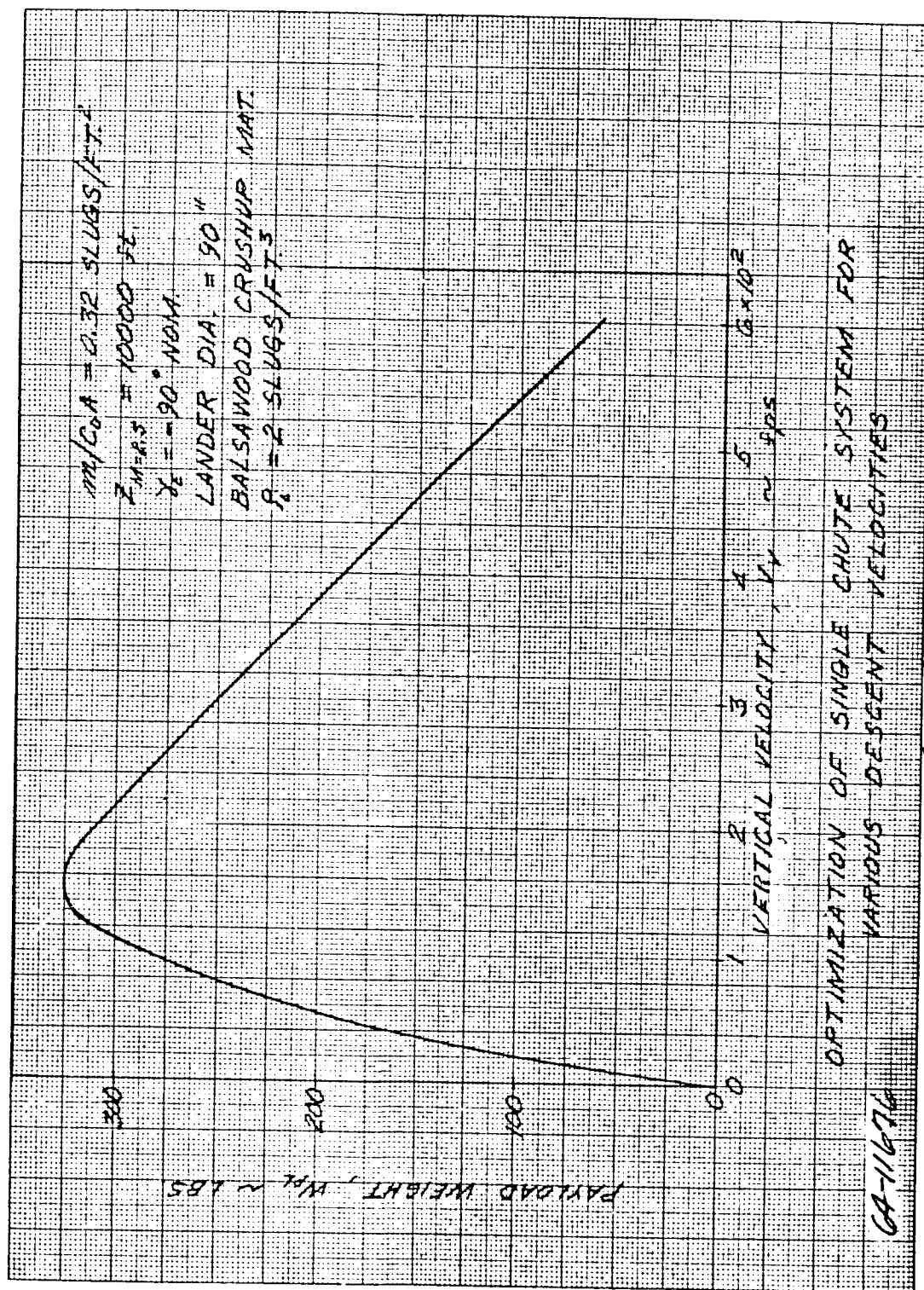


Figure 175 OPTIMIZATION OF SINGLE CHUTE SYSTEM FOR VARIOUS
 DESCENT VELOCITIES - BALSA WOOD

ALUMINUM HONEYCOMB
1500 G IMPACT
M/E.A. = 0.32 (1000 ft)
Z.M. 1.5 = 0.000 ft
 $\gamma_L = 70^\circ$ NOM.
LANDER DIA. = 90"
 $\rho = 2.54 \times 10^{-3}$

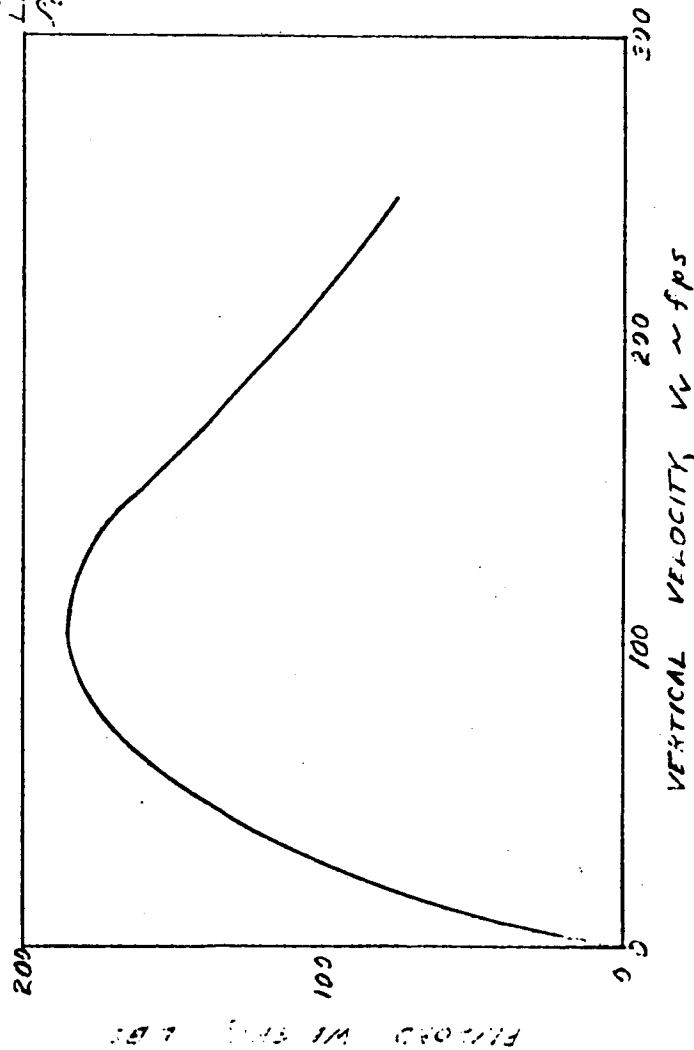


Figure 176 OPTIMIZATION OF SINGLE CHUTE
SYSTEM - ALUMINUM HONEYCOMB

64-11677

desired vertical velocity). These same curves also give the suspended weights as a function of vertical velocity.

Using the equations developed in appendix A (i. e., equations (2-3), (2-4), (2-11), and (2-12)) and assuming aluminum honeycomb impact attenuation material, calculations were made of the residual internal payload weight as a function of vertical descent velocity. These results are depicted on figure 177 for three different main parachute deployment altitudes. It can be seen that the optimum vertical descent velocity is between 60 and 70 ft/sec for all altitudes.

These curves were drawn using the assumption of a 1500 g impact. The effect of g-level was assessed by fixing the deployment altitude and varying the peak deceleration. The results are shown in figure 178; it can be seen that the optimum velocity is still between 60 and 70 ft/sec.

For the purpose of drawing impact system design curves (see figure 155, section 8. 2. 1), a descent velocity of 65 ft/sec was used as the optimum design value. This corresponds to a total impact velocity of 210 ft/sec.

8. 5 CONCEPTUAL DESIGN

In the conceptual design portion of the Advanced Mariner Study, several aspects relating to the actual design of an impact attenuation system were subjected to fairly detailed scrutiny. It should be understood from the first that due to the underdeveloped state-of-the-art of impact attenuation systems in general, an "exact" analysis of an impact attenuator cannot be performed. The effects of various system parameters can be examined in order to indicate whether or not the scope of the parametric study was broad enough.

The material chosen for the conceptual design was 5052 expanded aluminum honeycomb. The reasons for this selection include its past history of extensive development for use as an energy absorber. It possesses a very flat crushing stress versus deflection curve, a characteristic which is desirable in energy absorbers since it absorbs energy most efficiently in this way. Further it has almost zero springback after compression, eliminating the rebound problem which exists with other, nonmetallic absorbers such as plastic foams. Other materials may or may not be able to withstand heat sterilization with no degradation, but this is largely unknown; aluminum can withstand it. Since it is not rf transparent, it must be removed after impact. However, this removal serves the purpose of stabilizing the payload, a function which would have to be performed by another system in a design which uses an rf transparent energy absorber which was not removed. For these reasons and for those discussed in the parametric study, aluminum honeycomb was the reference material.

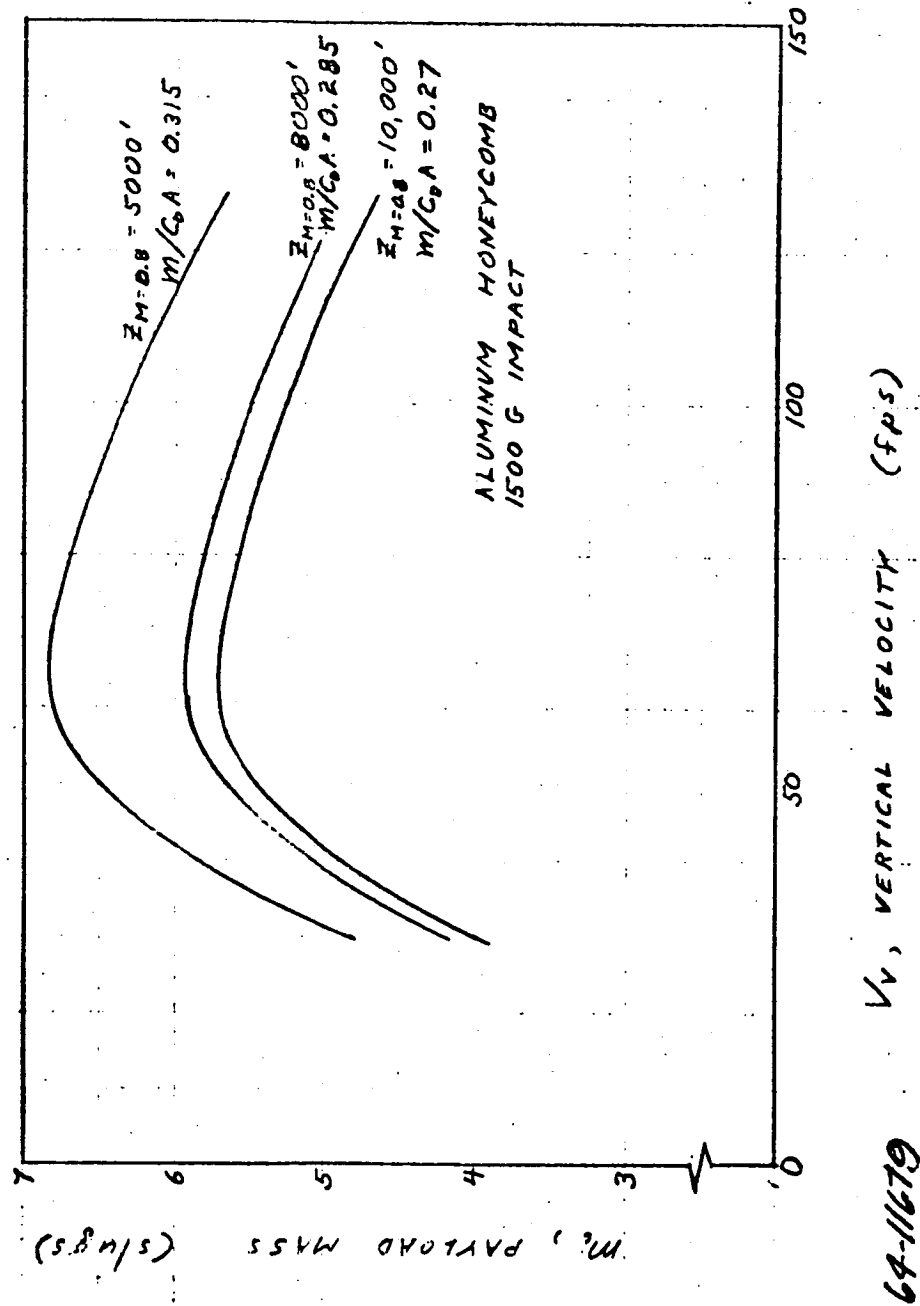


Figure 177 OPTIMIZATION OF DESCENT VELOCITY FOR TWO-CHUTE SYSTEM - FOR VARIOUS ALTITUDES

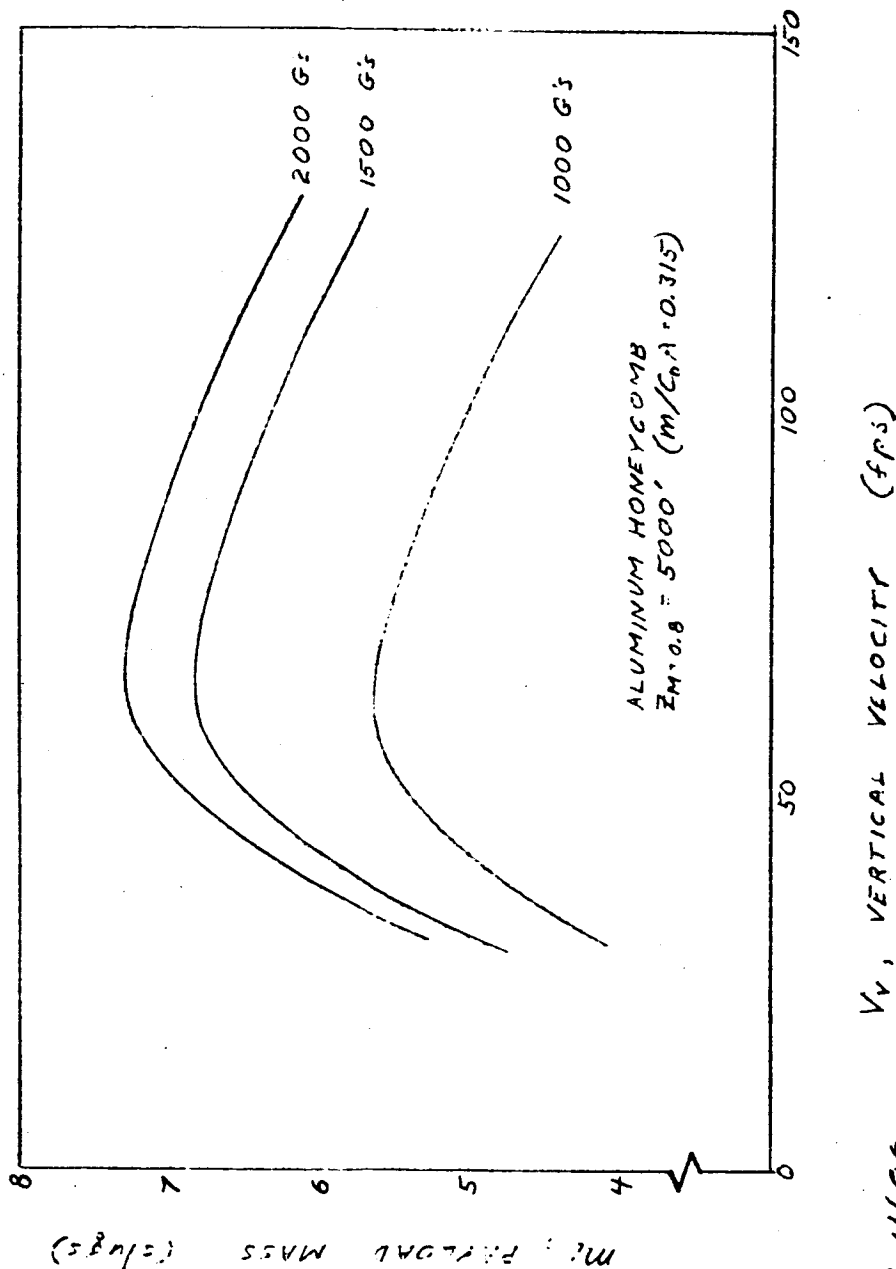


Figure 178 OPTIMIZATION OF DESCENT VELOCITY FOR TWO - CHUTE SYSTEM - FOR VARIOUS G LEVELS

8.5.1 Detailed Design Calculations

An analysis was performed of the impact dynamics in which properties of specific aluminum honeycombs were used. Equations (1-4), (1-5), (2-1), (2-2), and (2-11) of appendix A were used in order to assess the effects of the fact that the mass being decelerated during the impact changes as a function of time. This is due to the fact that in the course of the impact, the impact attenuation material which has been crushed has already been reduced to zero velocity while the rest of the material and the payload are still in motion.

It was decided that a nominal value of peak deceleration of about 1500 g would be used. The reasoning behind this decision can be explained using figure 160 of section 8.2. For internal payloads of 3 to 5 slugs (~96 to 160 pounds), it can be seen that the curves are quite flat for g-levels higher than 1500. This implies that only slight decreases in impact attenuator weight can be attained while much higher decelerations must be accepted. On the other hand, the g-level cannot be decreased significantly without violating geometric constraints imposed by the lander, principal among these being the center-of-gravity constraint.

The properties of the specific aluminum honeycombs used in this study are tabulated in tabulated in table 36.

TABLE 36

ALUMINUM HONEYCOMB PROPERTIES

Honeycomb	Density (lb/ft ³)	Crushing Stress (psi)
Al 1/8 - 5052 - .0010	4.5	253
Al 1/8 - 5052 - .0015	6.1	430
Al 1/8 - 5052 - .0020	8.1	682

The honeycomb designation in this table refers to, in order, the material (aluminum), the cell size (1/8 inch), the particular type of aluminum used (5052), and the foil gage (from 0.001 to 0.002). The density and stress data are based on tests performed by the manufacturer.

Using an impact velocity of 210 ft/sec, a usable strain of 80 percent, an internal payload of 136.1 pounds, and a packaging density of 3.2 slugs/ft³, the equations mentioned above were used to design impact attenuation systems for each material. The results of these calculations are tabulated in table 37.

TABLE 37

CONCEPTUAL DESIGN PARAMETERS

Honeycomb	Outside Radius in.	Crushable Material weight, lbs.	g-Level Earth g
Al 1/8 - 5052 - .0010	21.2	98.5	1450
Al 1/8 - 5052 - .0015	18.5	86.3	1820
Al 1/8 - 5052 - .0020	16.7	80.5	2240

The first row of this table gives a reasonable design. This will now be compared to the design which would be obtained from the parametric study results. Figure 155 of the parametric study (section 8.2) gives a crushable material weight of 154 pounds. Using figure 165 (section 8.3) to correct for the higher packaging density (3.2 compared to 2 slugs/ft³) reduces this weight to approximately 129 pounds.

This weight was obtained using a curve fit to the properties of a number of materials. If the actual properties of this material are used (see figures 160 and 161 of section 8.2), then the resulting impact attenuator weight at a packaging density of 3.2 is 110 pounds, a reduction of 12 percent compared to the curve fit.

This figure, 110 pounds, is what should be compared to the number obtained by the more exact analysis, namely 98.5 pounds. Thus the conceptual design resulted in a weight saving of about 10 percent over the parametric design. This weight saving is due to the effect of a variable mass during impact and to the change in strain used in the analysis from 75 percent in the parametric work to 80 percent in the conceptual design. It appears that each of these factors accounts for about half of the weight saving.

Perhaps it is just as well that the parametric study has a 10 percent conservatism in it to help account for other factors such as anisotropy of the material (which can be compensated for to some extent by designing for a radial variation of crushing stress), manufacturing tolerances, weight of facings, bonds, etc.

8.5.2 Deceleration-Level Factors

One aspect of the entire impact system study deserving of special mention is the peak deceleration level, since it was a strong influence in making several system decisions. It should first be pointed out that deceleration

level is a derived quantity rather than an input. It could actually have been eliminated from the study entirely and the impact system analyzed on the bases of its weight and size only. As it was, the calculation of g-level involved several simplifying assumptions which could be changed in an actual impact. The various factors which affect g-level will be discussed below.

The first factor is the geometric one. The deceleration levels were calculated assuming that crushing always occurs across a plane. However, higher g's could occur in the event of impact into soft sand; the worst case would be when crushing started simultaneously at the surface of the entire downward hemisphere. In this case it can be shown that the total vertical force acting on the payload is equal to the crushing stress of the impact attenuator times the cross-sectional area of the lander sphere. For the present conceptual design this factor could result in increasing the 1520 from the 1450 g given on table 2.

A second source of error could result from the fact that many materials, particularly aluminum honeycomb, exhibit an initial stress peak of as much as twice the crushing stress before actual crushing starts. However, this peak can be eliminated by pre-crushing as part of the manufacturing process.

Another factor which introduces an error is that the g-level calculated in the parametric study ignores the fact that at the end of the stroke, less mass is actually being decelerated than at the beginning. The magnitude of this effect can be determined by comparing the approximate equation, e. g., (1-11) of appendix A, to the "exact" equation, (1-5) of appendix A. For the present conceptual design, this factor leads to an 11 percent increase in peak deceleration.

Temperature could make a difference if the material used had a crushing stress which was a function of temperature (over the temperature range of interest). In this event the system would be designed to absorb all of the impact energy at the highest operating temperature, but the highest g could occur at a lower temperature, at which the material was much stronger.

As far as a particular piece of equipment within the internal payload is concerned, the g-level it experiences could be higher than the nominal calculated due to dynamic response. This aspect of the problem is treated in somewhat more detail in the next section.

8.5.3 Shock Response

A study was made in order to determine some characteristics of the decelerating pulse shape, particularly the possible dynamic load factors which could be felt by a component within the payload.

The deceleration pulse shapes are derived and discussed in appendix A and are summarized on figures 256, 257, and 258 of that appendix.

It now remains to estimate the effect of these types of curves on components mounted in the payload package. This is done through the medium of a shock spectrum. A typical spectrum is shown on figure 179; the important features are the peak in the vicinity of $\omega t_m = 5$ and the subsequent return to a value of unity at higher values of this parameter.

Since no shock spectra have been generated in the past for the particular pulses under consideration here, it was decided to compare these pulses with another class of pulses which has been investigated.² This pulse is illustrated on figures 180 and 181. As an example, the curve for $a = -2\pi$ on figure 181 closely approximates the curve for $n = 1$ on figure 256 of appendix A. The maximum response factor for this pulse (i. e., the value of the peak in the shock spectrum) is plotted on figure 182 for various values of the parameter a .

In summary, for the impact situation under discussion, the duration of the impact will be of the order of 0.01 second, which based on the general discussion of shock spectra above, implies that components whose natural frequencies are of the order of 500 rad/sec (100 cps) will feel more g's than other components. How much more can be estimated from figure 182; a factor of between 1.5 and 2.0, depending on the pulse shape, will have to be applied to the nominal deceleration level to determine the loads felt by these particular components.

8.5.4 Sand Penetration Studies

The question was raised as to whether or not the lander could bury itself upon impact into the sand comprising the Martian desert (even the dark areas of the planet are postulated to be sandy desert spotted with some sort of matter - possibly vegetation, - which gives these areas their dark appearance).

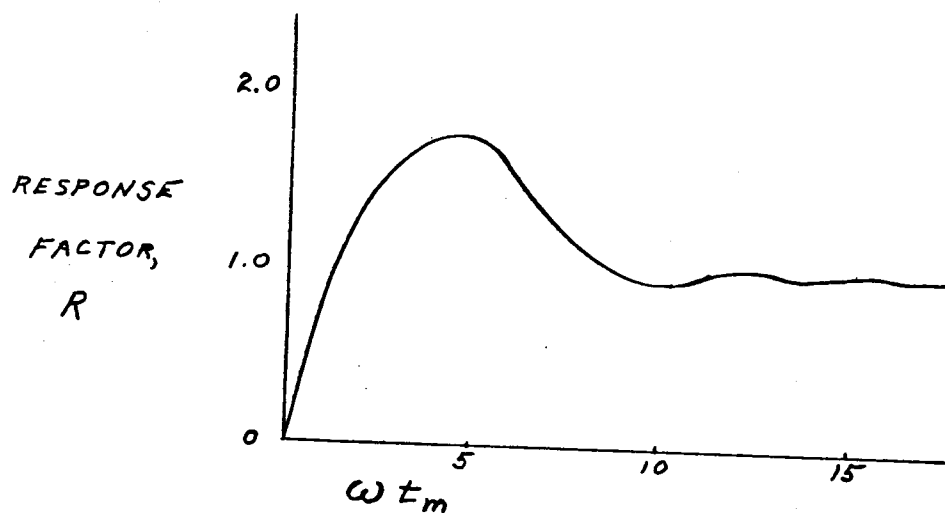
An equation can be derived for this situation in the form

$$S_m = \frac{m}{C_D A \rho} \ln \left[1 + \frac{C_D \rho v_o^2}{2 \left(p_c - \frac{m}{A} g_m \right)} \right] \quad (\text{reference 3})$$

where

S_m = Penetration into sand, feet.

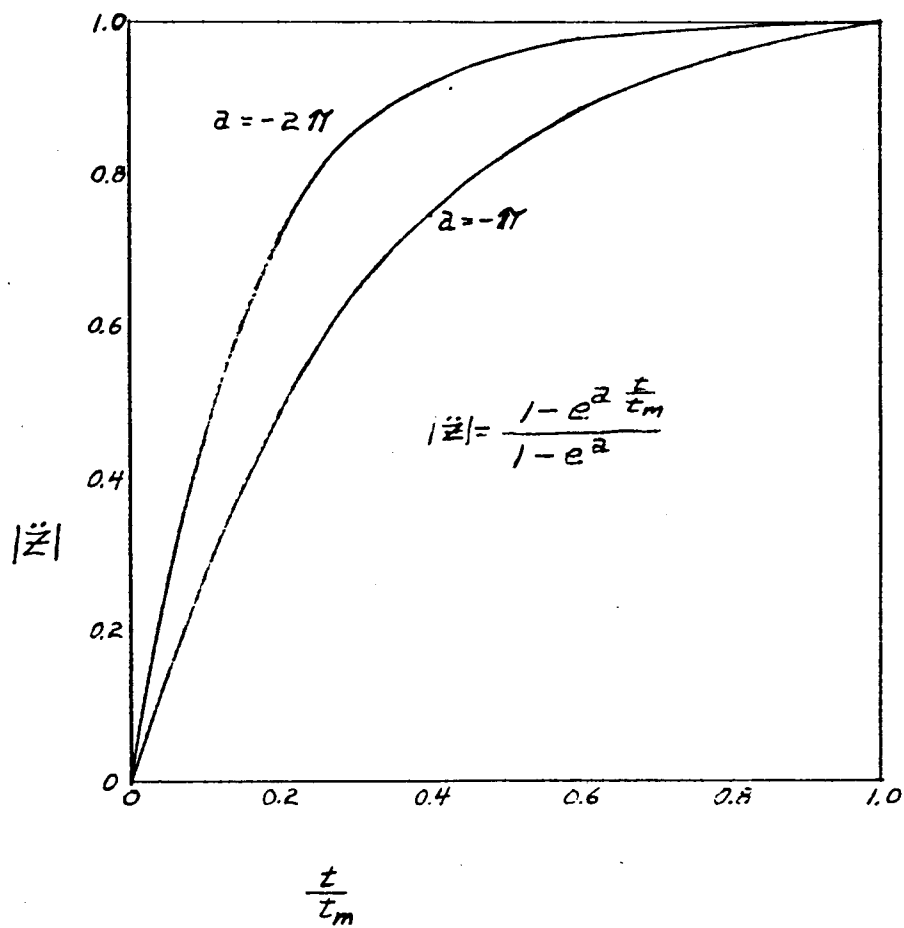
m = Mass, slugs.



ω - natural frequency of component
in radians/sec.
 t_m - duration of acceleration pulse, sec.

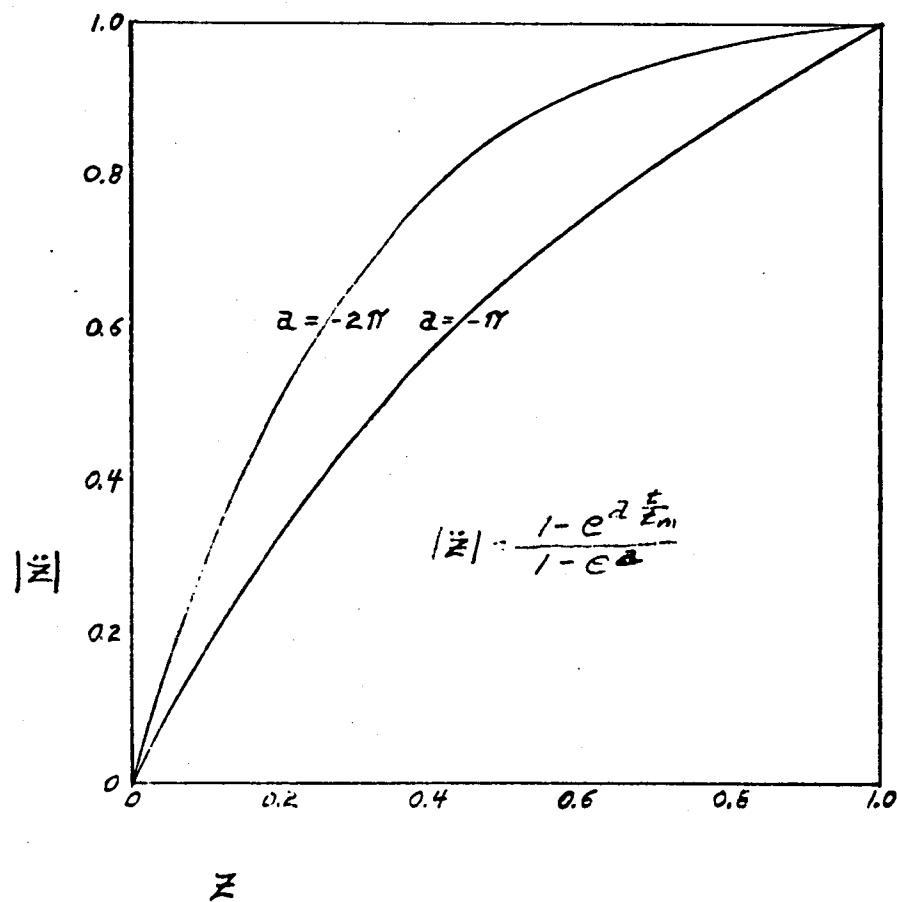
64-11681

Figure 179 TYPICAL SHOCK SPECTRUM



67-11682

Figure 180 ACCELERATION VERSUS TIME FOR EXPONENTIAL PULSE



64-11683

Figure 181 ACCELERATION VERSUS DISTANCE FOR EXPONENTIAL PULSE

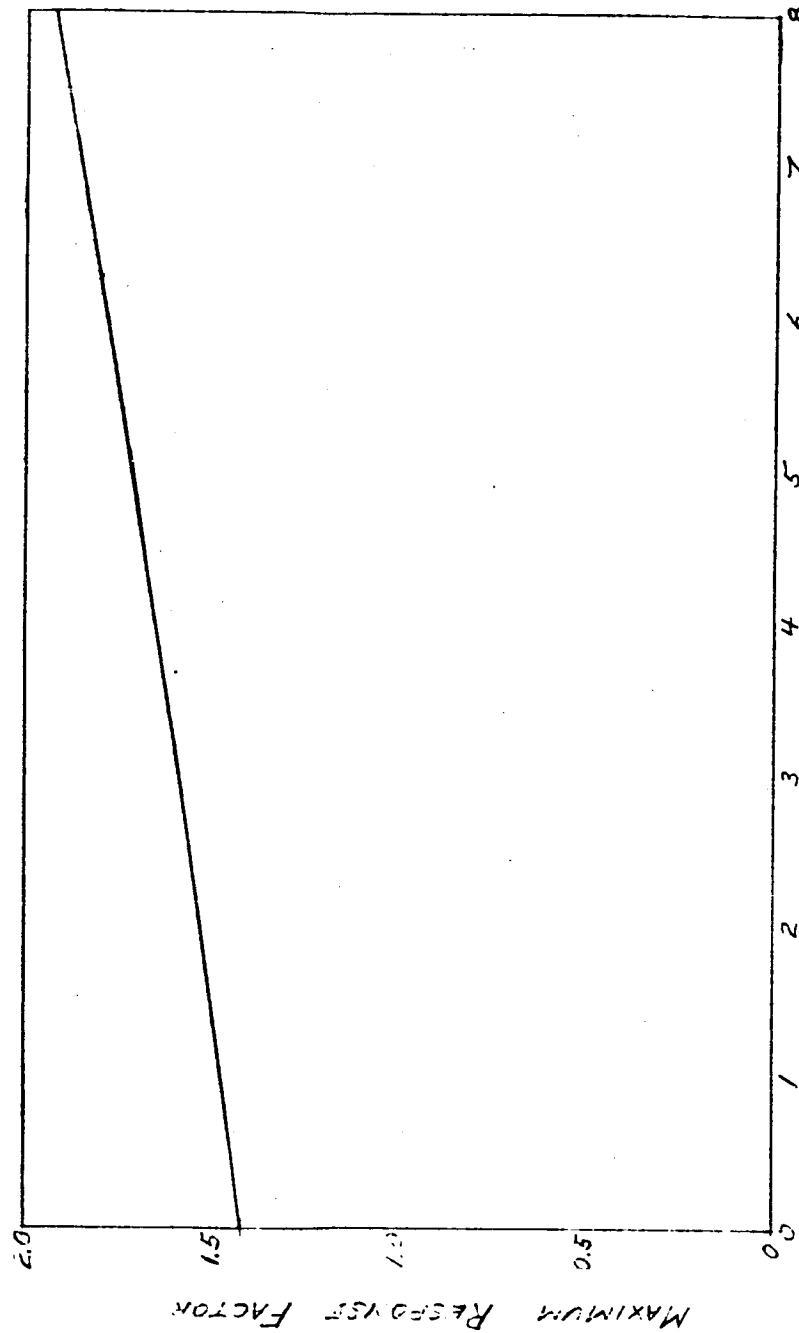


Figure 182 MAXIMUM RESPONSE FACTOR FOR EXPONENTIAL PULSE

64-11684-2

- C_D = Drag coefficient in sand = 2 to 4.
 A = Cross-sectional area of lander, ft^2 .
 ρ = Bulk density of sand, slugs/ft^3
 V_o = Impact velocity, ft/sec .
 P_c = Crushing strength of sand, lb/ft^2 .
 g_m = Martian gravity $12 \text{ ft}/\text{sec}^2$.

Using a C_D of 2, V_o equal to 210 ft/sec , a sand density of 3 slugs/ft^3 (typically, Earth sands of all types, shapes, and sizes give bulk densities between 95 and 105 lb/ft^3) and a minimum Earth sand crushing strength of 5 $\text{lb}/\text{in.}^2$ (720 lb/ft^2) yields

$$S_m = 1/6 \frac{m}{A} \left[11.78 - \ln \left(720 - 12 \frac{m}{A} \right) \right]$$

It is interesting to note that with this minimum strength sand, an $\frac{m}{A}$ of 60 yields $S_m = \infty$, which means that such a projectile would not stop until it reached bedrock. Fortunately, the vehicles under consideration here have much lower values of $\frac{m}{A}$. Current conceptual designs of the landed capsule indicate an $\frac{m}{A}$ ratio in the vicinity of 1.5 slugs/ft^2 which in turn indicates that such a capsule could sink into between 1 and 1-1/2 feet of sand. Since typical capsules are presently at least 1.5 feet in radius, they would sink in no more than halfway. Thus, penetration into sand does not appear to be a problem at present; the lander should not bury itself.

References

1. Mars-Venus Capsule Parametric Study; Avco RAD, TR-64-1, JPL Contract 950626, 21 March, 1964
2. Jacobsen & Ayre; Engineering Vibrations; McGraw-Hill, 1958; p. 175.
3. Allen, Mayfield, and Morrison; Dynamics of a Projectile Penetrating Sand; Journal of Applied Physics; Volume 28, No. 3; March, 1957, pp. 370-376.

9.0 THERMAL CONTROL

The thermal control problem was divided into several phases; 1) near Earth, 2) cruise, 3) post separation, 4) entry, descent and post landing. The individual system requirements for each phase were evolved and the overall compatibility of each phase was determined.

The study approach was to evaluate the severity of the thermal control problem utilizing simplified techniques. The results of these studies were used to estimate the surface infrared absorptivities and emissivities, heater power and insulation requirements. Thereupon, a thermal network was evolved to study the transient temperature variations of critical points within the lander. A conceptual design of the lander thermal control system, including special coatings and fluids, was evolved.

The temperature control requirements on the battery and scientific payload were selected as 40° to 100°F, which is satisfactory for the Nickel Cadmium batteries used for the main lander power supply. The temperature limits on the main propulsion unit of the lander are unknown as a sterilized solid unit has not been built and tested. Currently, small solid rockets will operate satisfactorily down to -60°F; the effect of storage at lower temperatures is unknown. The squibs used in separating the lander from the bus and in separating the sterilization canister will operate down to -60°F. Experience with parachutes at -60°F indicates that this is a satisfactory storage temperature. The ability of the heat shield to tolerate a low temperature depends on its thermal compatibility with the substructure so that large thermal stresses do not arise due to differences in the thermal expansion coefficients of the heat shield and structure. It currently appears feasible to consider temperatures as low as -100°F for the heat shield and structure.

9.1 NEAR EARTH

The significant aspects of the near Earth portion of the flight are the injection, acquisition, and midcourse maneuvers. A simplified study was made to assess the severity of the thermal control problem. The surface coating requirements were evaluated for the case where the lander is exposed to the sun long enough so that steady state conditions exist. Under the assumption of a uniform lander temperature, the required a_s/ϵ ratios to restrict the lander temperatures to below 100°F, to meet the battery and scientific payload limits, were calculated and are shown in figure 183. The results indicate that a low a_s/ϵ ratio is desirable; this is in opposition to the demands for low emissivity on the afterbody during transit and the high values of a_s/ϵ desired near Mars. The effect of using a larger a_s/ϵ near Earth was investigated and the results are shown in figure 184. For the low emissivities desired during cruise, an a_s/ϵ of 2.5 appears feasible which, according to the results shown in figure 184, could

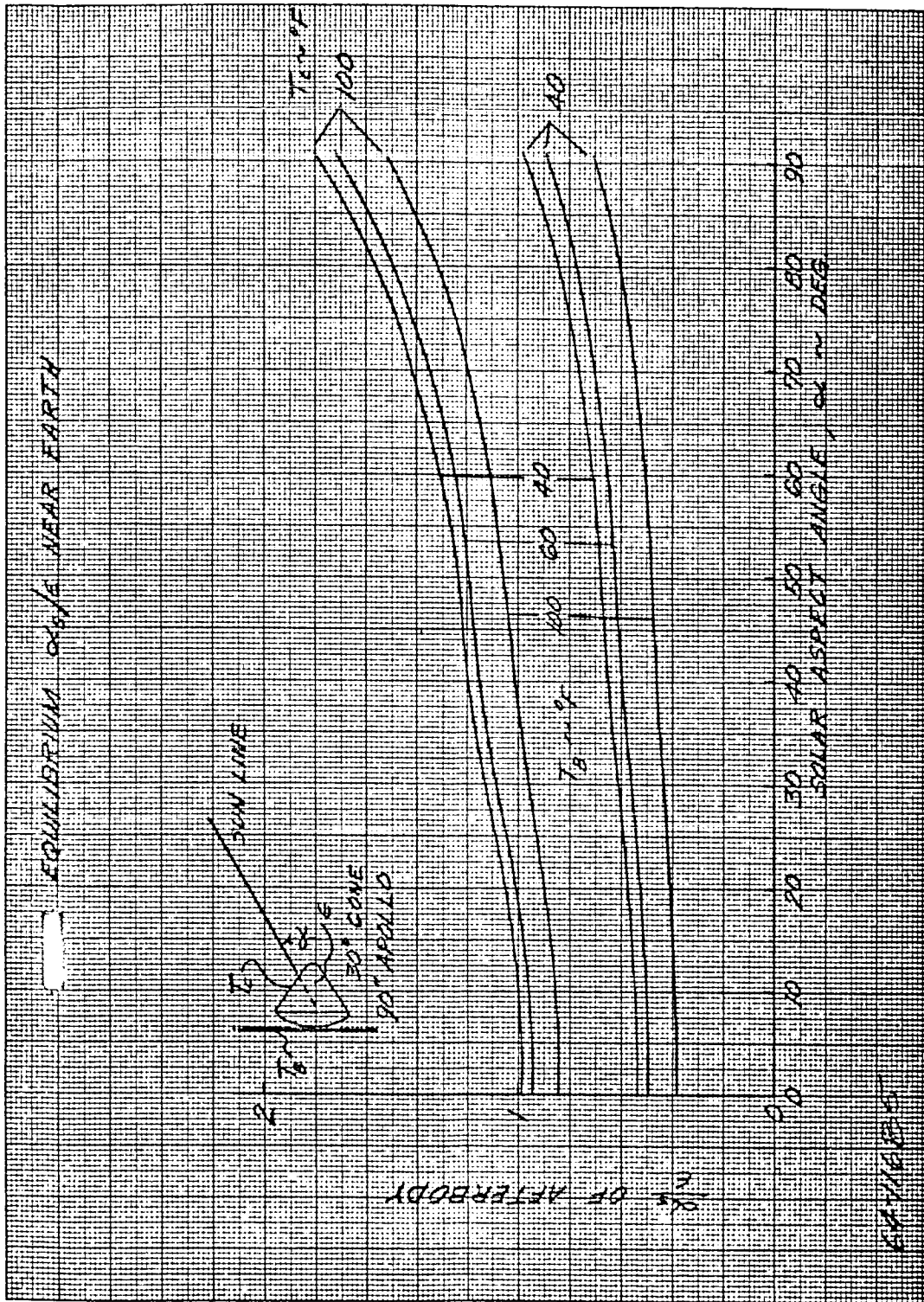
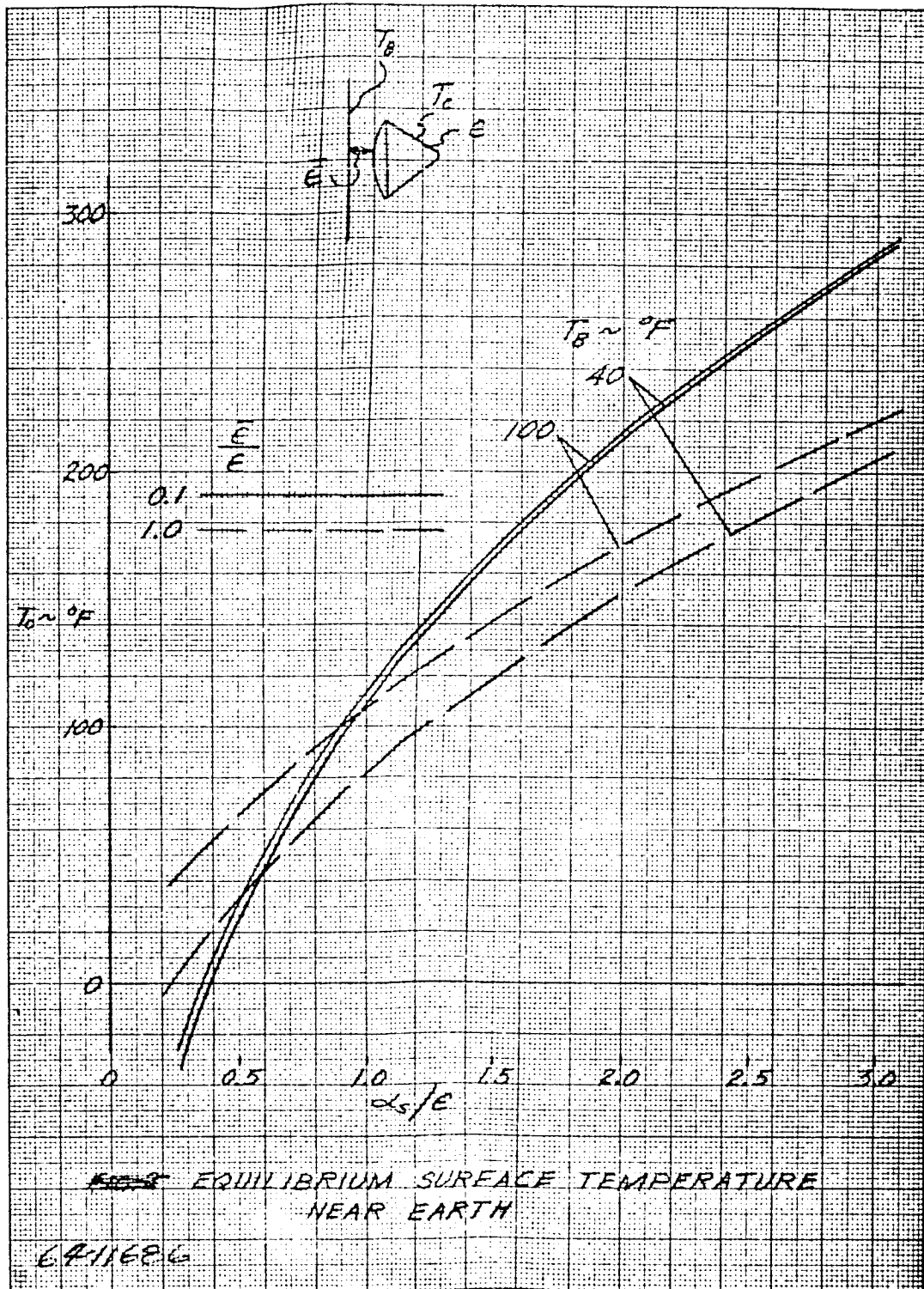


Figure 183 EQUILIBRIUM α_s/ϵ NEAR EARTH



yield equilibrium surface temperatures as high as 200°F. The maneuver times presently considered are on the order of one hour duration and hence the lander is far from complete equilibrium. The nature of the lander time constant was evaluated simply and with a detailed thermal network. The simplified analysis yields a time constant such that

$$\tau = \frac{\Delta X \cdot w c_p}{K}$$

where

- τ = time constant, hrs.
- ΔX = thickness, feet
- w = weight, lbs.
- c_p = specific heat, Btu/lb/°F
- K = conductivity, Btu/hr/ft²/°K/ft.

Considering the insulation requirements for cruise, a time constant of 33 hours exists. Hence, a one hour maneuver time will have a negligible effect on the payload. The surface temperature will rise, however, as its time constant is extremely small.

9.2 CRUISE PHASE

1. External Temperatures

During the cruise phase the lander is mounted on the shaded side of the spacecraft as shown in figure 185. A metal sterilization shroud encloses the lander.

The conductive heat transfer paths between the lander and bus are the three bolted connections and the separation spring assemblies. The amount of heat transferred by these conductive paths can vary by as much as an order of magnitude. The conduction can be varied by the bolting and spring materials and the contact surface pressure distribution at the interface. In a vacuum environment with the mating surfaces at uniform contact pressures of less than 35 lb/in², conductance can vary from 20 to 150 Btu/hr/ft² (reference 1).

For example, consider the contact area between bus and lander as 0.0082 ft², the temperature difference between bus and lander of 85°F and $K = 20$ Btu/hr/ft²/°F/ft. Then $q = KA\Delta T = 4.1$ watts.

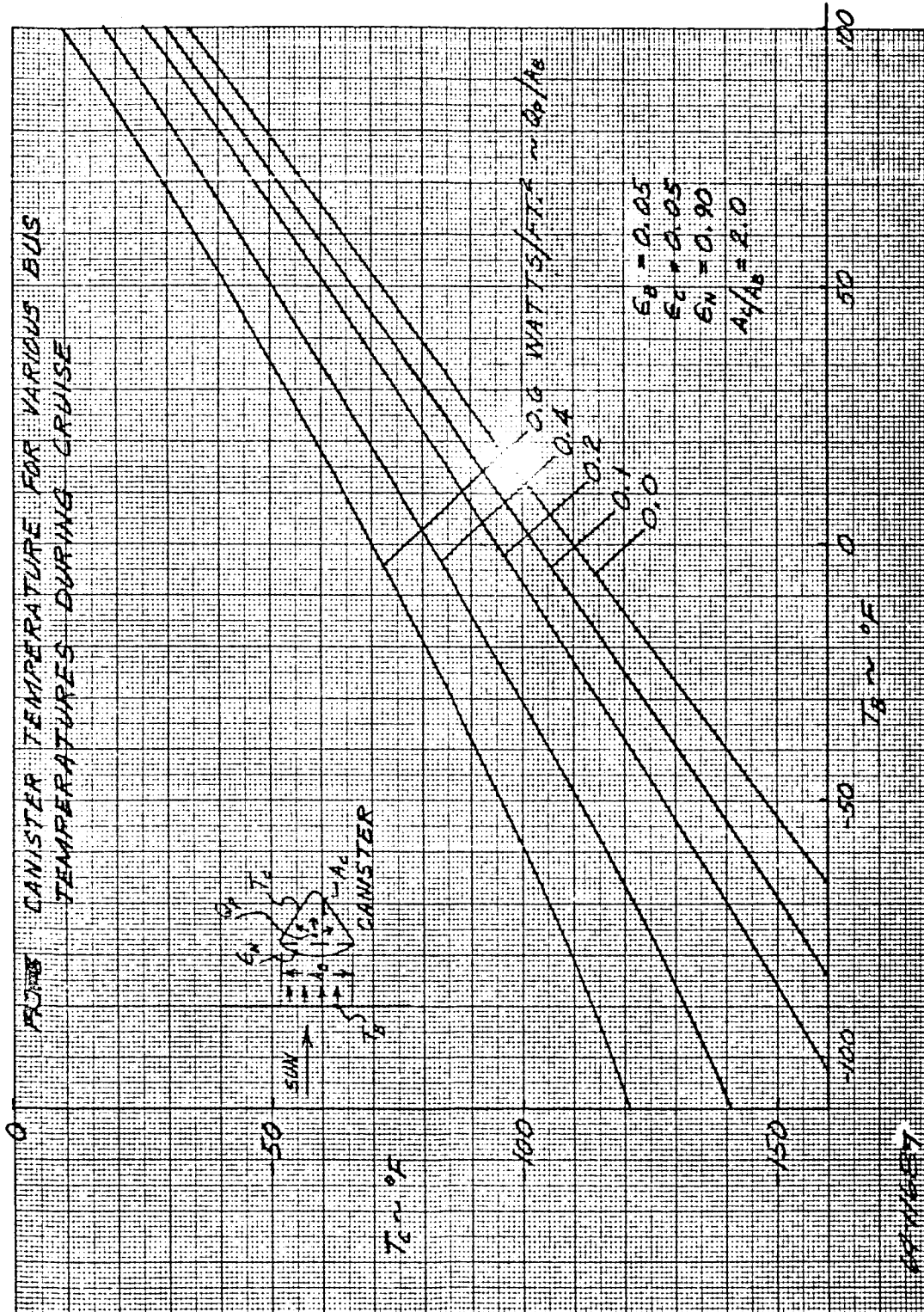


Figure 185 CANISTER TEMPERATURES FOR VARIOUS BUS TEMPERATURES DURING CRUISE

34/2

But for $K = 150 \text{ Btu/hr ft}^2\text{°F/ft}$

Then $q = 31 \text{ watts}$.

Thus it will be necessary to design the conductive heat path from the bus to the lander to match the total heat requirements of the lander and bus.

Radiation interfaces between bus and lander include the main structure, electronic packages, and solar panels. During the cruise mode, the radiation heat exchange between the lander and the back surfaces of the solar panels was considered. Using radiation view factor based on the work of Hamilton and Morgan (reference 2) the temperatures are as follows:

	Near Earth	Near Mars
Solar Panel Backface,	$T = 123^\circ\text{F}$	24°F
Aft portion of Sterilization Can, $T =$	0°F	-90°F

the heat transferred by radiation to the lander from the solar panels is 1) near Earth, 22 watts, and 2) near Mars, 11 watts.

The battery and scientific package requirements are 40° to 100°F . The solid propulsion unit on the lander requires stabilization between 0° and 100°F during cruise phase.

A simplified parametric study of the cruise phase was performed to ascertain the problem areas during the cruise phase. It was assumed that the sterilization cover has uniform temperature (infinite conductivity) and a heat balance was formulated as

$$Q_B + Q_P = \sigma \epsilon A_C T_C^4$$

Neglecting conduction and the solar panels as a radiative source, one has approximately

$$\sigma \bar{\epsilon} A_B (T_B^4 - T_C^4) + Q_P = \sigma \epsilon A_C T_C^4$$

where

σ = Stephan-Boltzmann constant

$\bar{\epsilon}$ = effective emissivity between bus and lander

T_B = temperature of bus

T_C = temperature of sterilization canister

A_B = Projected interface area

A_C = Freespace radiating area

Q_P = internal power dissipated

Q_B = heat supplied by the bus

The results are shown in figure 186 and indicate that the canister will run cold throughout the cruise. Combined bus and lander transient analyses indicate that near Earth the rear of the bus will be at an average temperature of 25°F with a canister temperature of -60°F for 20 watts of power. Near Mars, the bus temperatures facing the lander drops to -20°F with a canister temperature of -90°F.

Mounted on the sterilization canister are the spin rockets and separation squibs. Therefore, it would be highly desirable to limit the sterilization canister to -60°F, the design specification for solid rockets.

In the vicinity of Mars, to maintain the canister temperature at -60°F requires 61 watts. The radiative power supplied by the bus can be obtained from figure 185 and is 25 watts near Mars. Near Mars the solar panels will radiate 11 watts and the interface between the lander and bus will conduct 5 watts. Hence, it appears that through design, test and development, the achievement of a minimum canister temperature of -60°F is very likely attainable, with a maximum of 20 watts supplied electrically from the bus.

2. Science and Battery Package

The science and battery package are enclosed within a multilayered sphere. The solution for the temperature gradient within a sphere with steady state heat generation internally is well known, and is given by:

$$\Delta T = \frac{P (3.41) (b-a)}{4 \pi K a b}$$

where

P = internal power generation; watts

a = outer radius

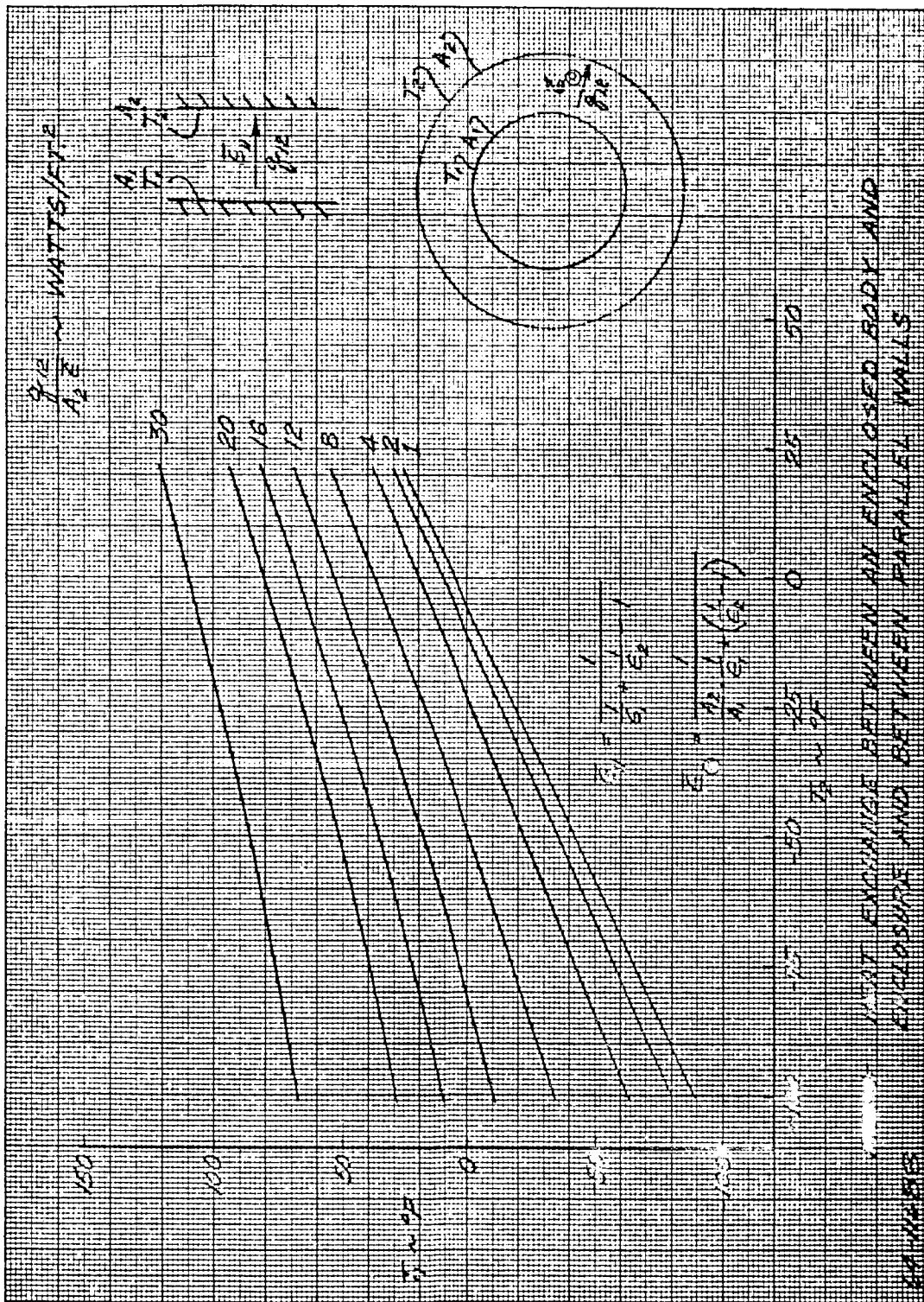


Figure 186 HEAT EXCHANGE BETWEEN AN ENCLOSED BODY AND ENCLOSURE AND BETWEEN PARALLEL WALLS

b = inner radius

ΔT = temperature change

A plot of the above relationship is given in figure 187. Assuming the lander skin temperatures will not be less than -100°F and the battery temperature of 40°F , the maximum temperature drop across the sphere will be 140°F during cruise. Typical values of insulation requirements to maintain the temperature drops across the sphere (assumes negligible thermal resistance between exterior of sphere and lander skin) are tabulated below for a 16 inch inner radius and 20 watts of power.

K Btu/hr- $^{\circ}\text{F}$	$(b-a)$ in.	ρ lbs/ft ³	Weight-lbs
0.001	0.6	18	20
0.0005	0.23	18	8
0.0001	0.056	18	2

The insulation weight requirements can be kept small provided very good thermal isolation is achieved. Data on insulators under high vacuum indicate that these conductivities are achievable.

The above analysis assumes an aluminum honeycomb impact material and neglects its thermal resistance. However, if balsa wood is used, thermal resistance is not negligible. Considering a 10-inch layer of balsa and $K = 0.03$ Btu/hr-ft. $^{\circ}\text{F}$, the temperature drop is found from figure 187. The temperature drop is 50°F across the balsa alone.

9.3 POST-SEPARATION PHASE

The lander is separated from the flyby bus at a distance of 1 to 5 million kilometers from the planet. At an approach asymptote velocity of 3 km/sec, the time from separation to entry can be as long as 15 days. For the 1969 launch, the ZAP angle will be close to 80 degrees; hence the roll axis of the lander when launched from the spacecraft will be nearly aligned with the sun line, with the blunt face towards the sun. Figure 188 depicts the variation in illuminated area with solar aspect angle. At separation, the solar aspect angle is about 10 degrees in 1969.

The variation of the required a_s/ϵ with solar aspect angle and temperature is shown in figures 189 and 190.

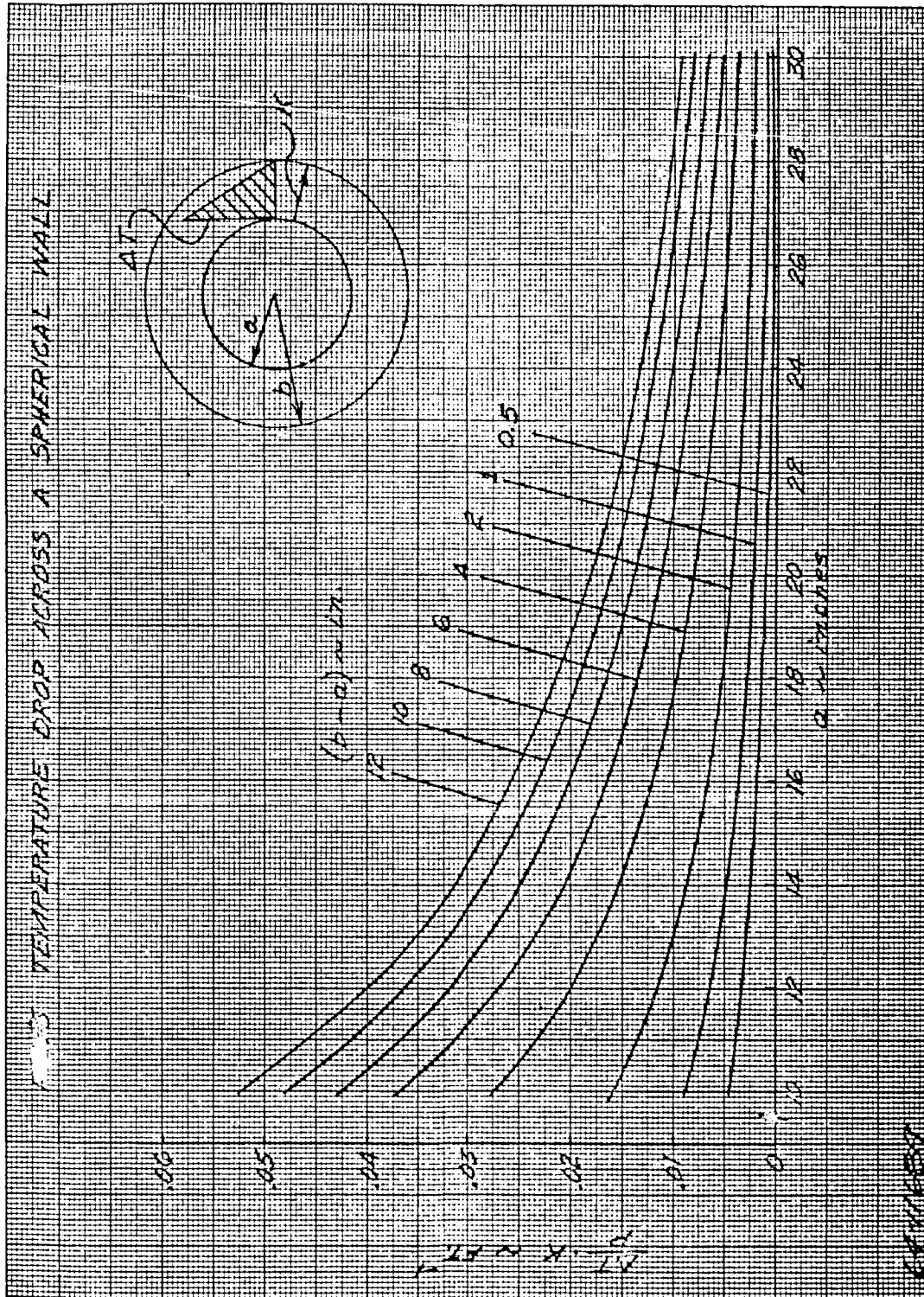


Figure 187 TEMPERATURE DROP ACROSS A SPHERICAL WALL

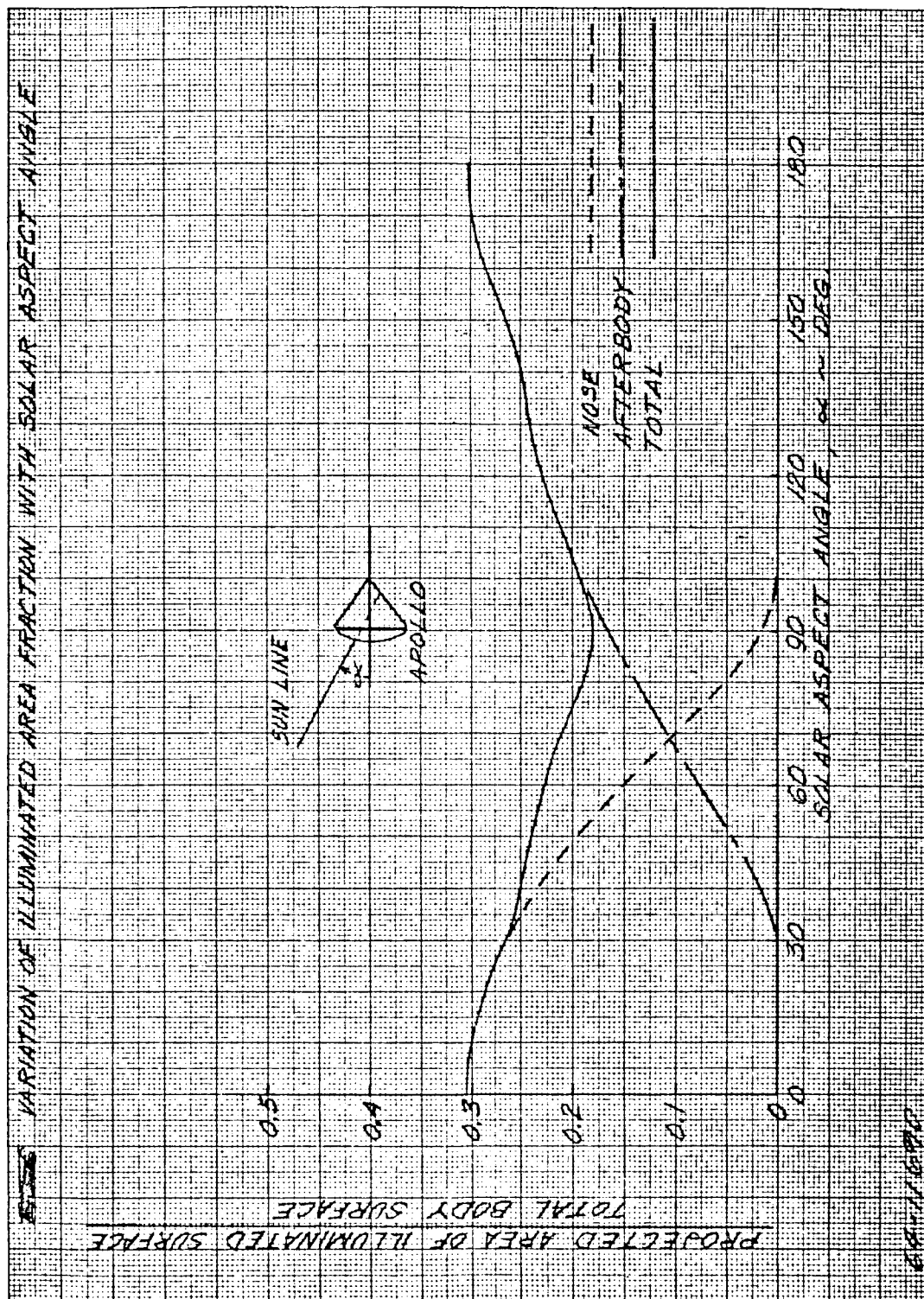


Figure 188 VARIATION OF ILLUMINATED AREA WITH SOLAR ASPECT ANGLE

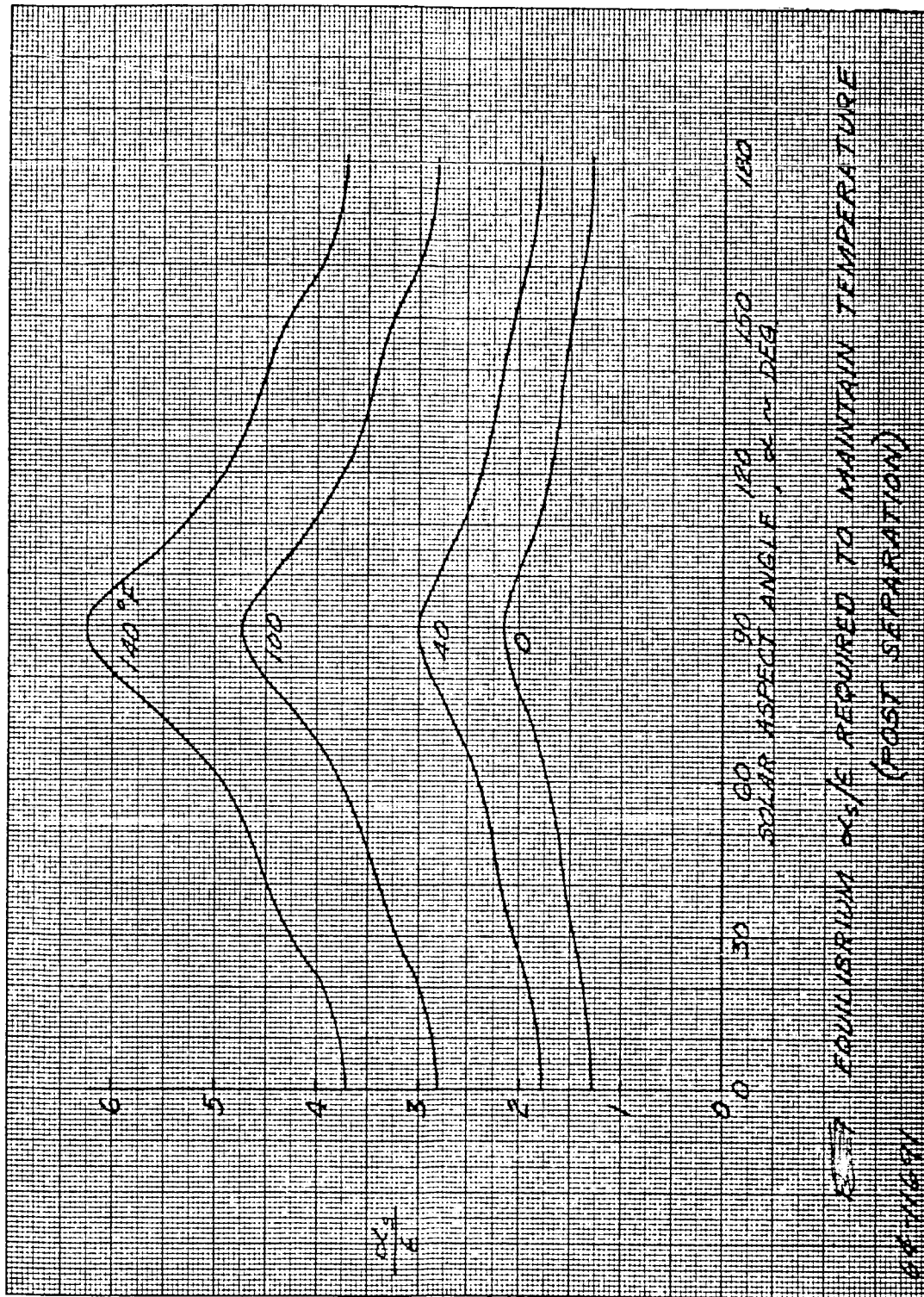


Figure 189 EQUILIBRIUM α_e/E TO MAINTAIN TEMPERATURE

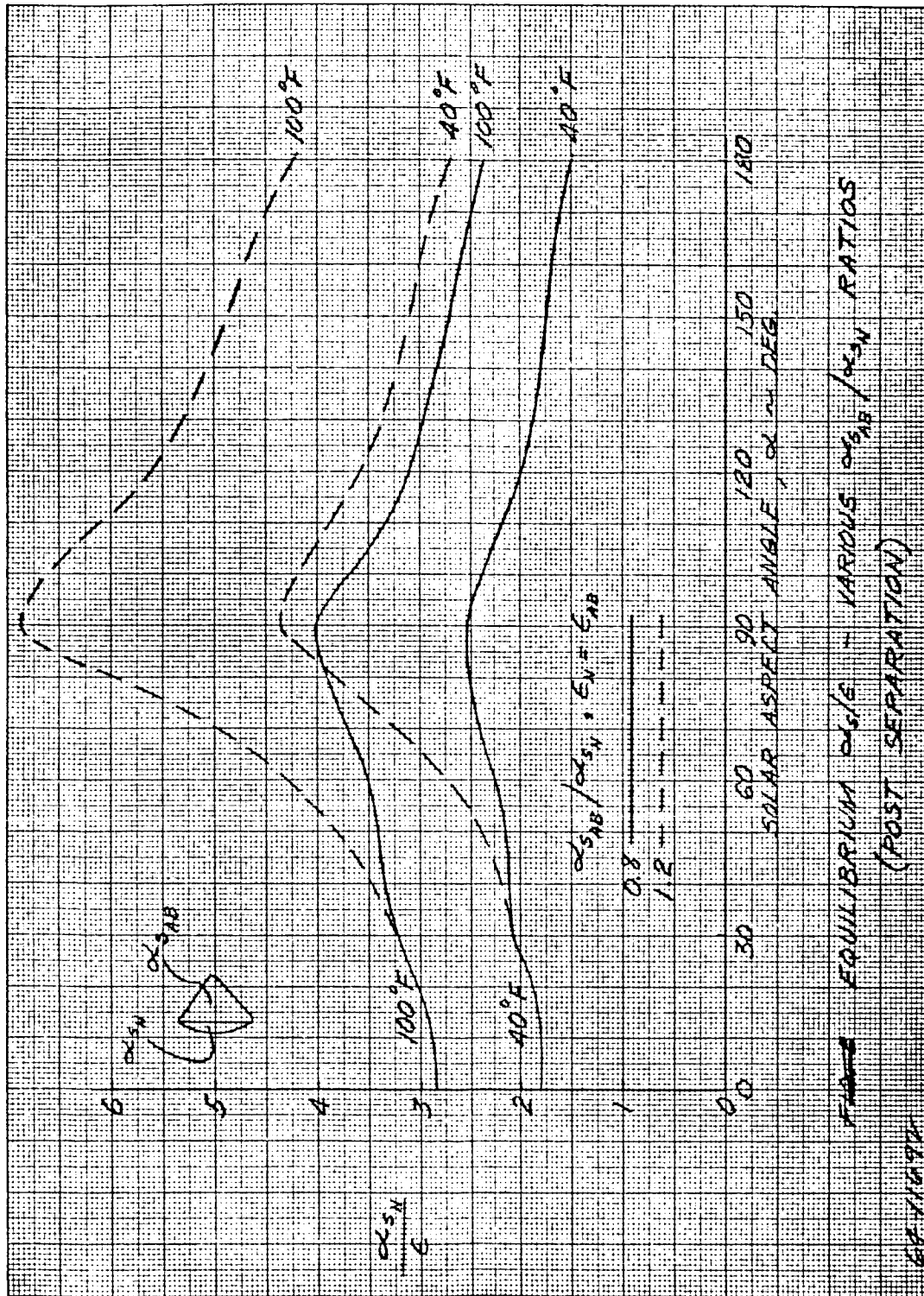


Figure 190 EQUILIBRIUM α_{sN}/ϵ - VARIOUS α_{sAB}/α_{sN} RATIOS

Immediately upon separation, the lander will tend to be in the shade of the bus until it exits from the umbra of the bus. While in the umbra the lander will cool as it now receives negligible heat from the bus and none from the sun. If launched precisely normal to bus and at a ZAP angle of 90 degrees, the length of the umbra cone would be about 2000 feet. If the coast phase of the lander is 1000 feet to minimize plume effects, then part of the lander could be shaded by the bus for a maximum of 15 minutes since the separation velocity increment is 1 ft/sec. Considering the outerskin only, the maximum temperature drop would be given by

$$\Delta T = \frac{A \sigma \epsilon}{W C_p} T^4 .$$

The maximum temperature drop of the skin would be 4 degrees. The internal temperature drop would be negligible.

Following separation, the lander is spin stabilized to facilitate accurate TVC for the lander engine. Hence, the lander is initially attitude stabilized. However, if the values of the moments of inertia in roll, pitch and yaw are close to each other, the vehicle may develop large precession angles and eventually assume another stable attitude.

9.4 ENTRY, PARACHUTE DESCENT, AND POST LANDING PHASES

The afterbody and heat shield reach their peak temperatures during entry phase. The transient temperatures of the afterbody and the backface of the heat shield are shown in figure 191 and 192. The transient temperature of the lander aluminum impact attenuator, assuming infinite conductivity of the aluminum, during entry is shown in figure 193. The temperature rise is considered to be only from radiant heat exchange between the hot afterbody and heat shield and the lander sphere.

During entry several pieces of electronic equipment and the parachutes are exposed to radiant heating from the hot afterbody. These areas present special design problems that can only be solved by coatings and/or insulation.

During descent on the parachute the lander is subjected to cooling on the exterior surface due to the cold atmosphere and internal heating due to operating electronic equipment.

The thermal control concept evolved, was to stabilize the battery and scientific internal payload by thermally isolating it from the external environment. Due to the long time constant of the internal payload, the convective cooling during descent has negligible effect on the internal payload temperature. Since good thermal isolation resulted, it was necessary to provide an internal heat sink to absorb the heat dissipated by the electronics. A number of methods are possible such as eisocane which absorbs 100 Btu/lb at 85°F or vaporizing water is an acceptable means provided the ambient pressure is less than 0.6 lb/in.²

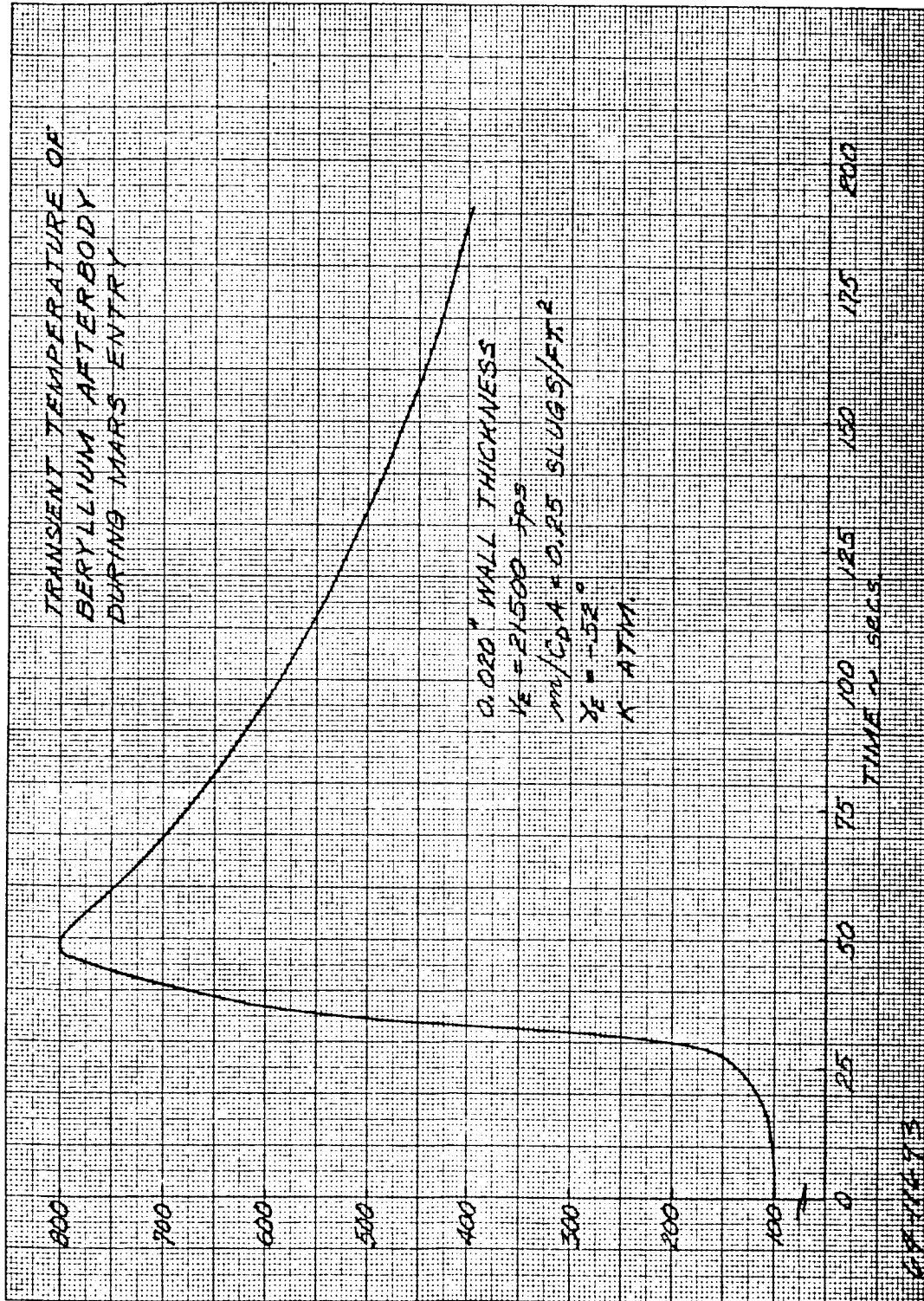


Figure 191 TRANSIENT TEMPERATURE OF BERYLLIUM AFTERBODY
DURING MARS ENTRY

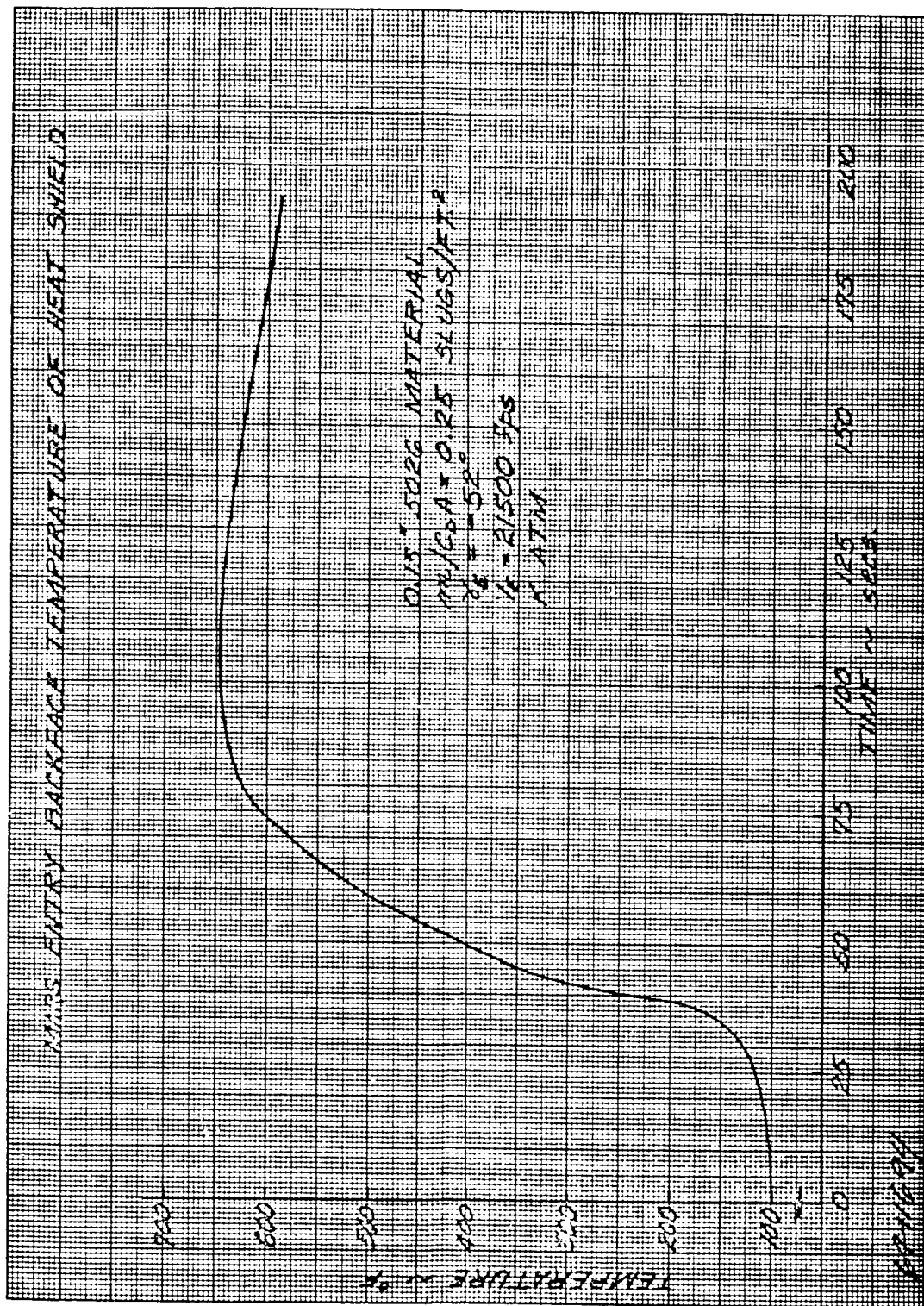


Figure 192 MARS ENTRY, BACKFACE TEMPERATURE HEAT OF HEAT SHIELD

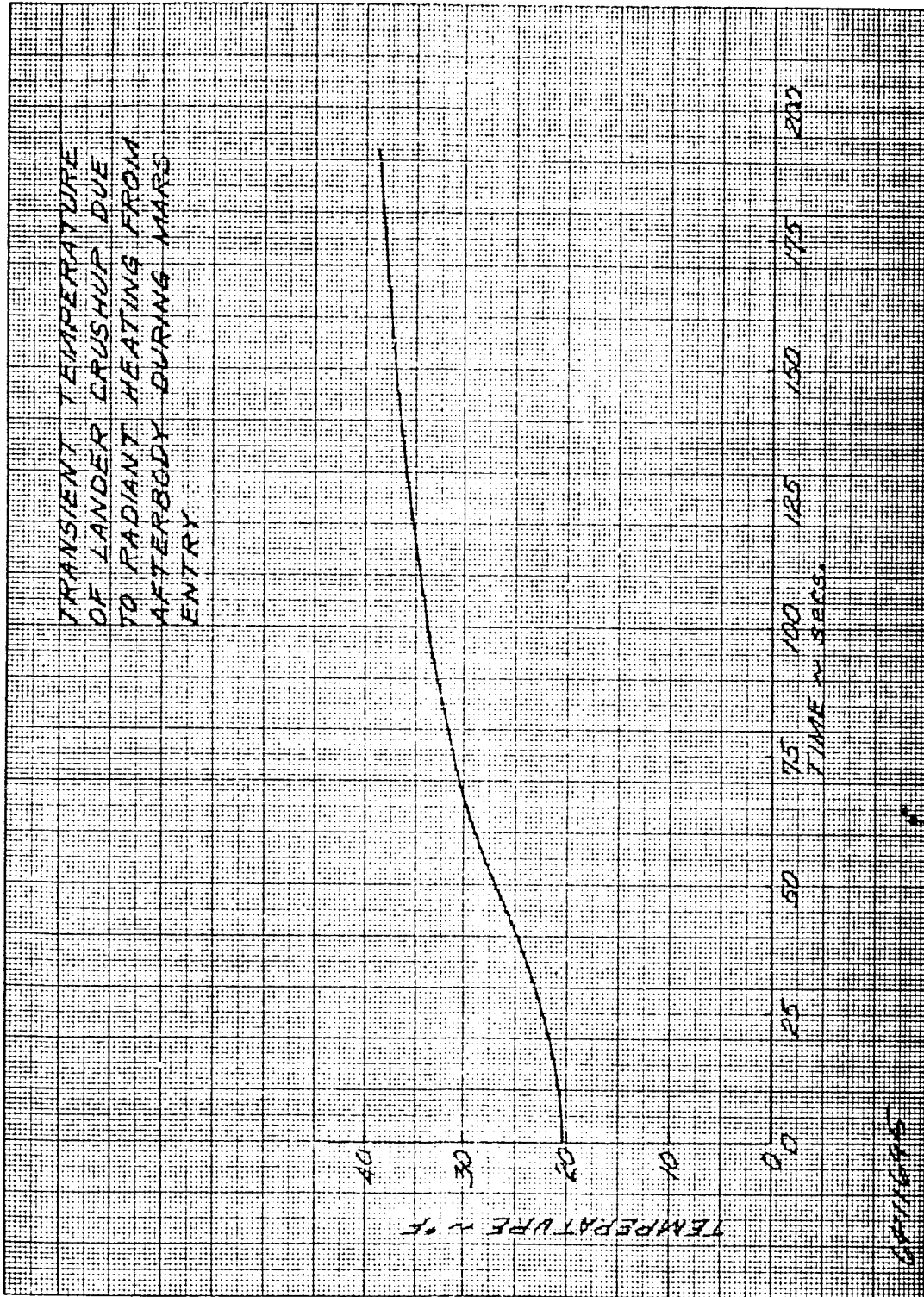


Figure 193 TRANSIENT TEMPERATURE OF LANDER CRUSH-UP DUE TO
RADIANT HEATING FROM AFTERBODY DURING MARS ENTRY

The more important aspects on the descent would be the low temperature effects on the parachute strength, impact attenuator, and scientific sensors and other components located externally to the landed sphere.

For the post landing phase, the mission lifetime requirement of 5 hours is compatible with the thermal control concept of isolating the internal payload. The maximum amount of energy dissipated internally can be determined from the total energy available in the batteries. Twenty-five lbs of batteries are provided which will yield 150 watt-hrs, or roughly 500 Btu's. Hence, 5 pounds of eisocane or 1/2 pound of water would be needed to stabilize the internal payload. The use of water is dependent on the magnitude of the highest pressure expected. If the ambient pressure expected is less than 0.6 lb/in² (41 mb) then the use of water is permissible. Other liquids could be considered, possibly the flotation fluid, to provide the thermal sink. In the final conceptual design water was considered as the thermal control fluid.

The solution for the heat flow through a solid sphere with uniform internal heat generation and a heat sink on the perimeter was examined for the post landing phase, and it was found that the temperature rise from the center to the perimeter would be small (several degrees) for practical choice of conductivities and densities.

9.5 LANDER TRANSIENT ANALYSIS

1. Theory

During the several flight modes of the lander it is necessary to know the temperature-time relationship of the various components of the lander.

The temperature-time relationship is best solved by an electrical analog of the thermal network. The electrical analog is established by lumping sections of the physical system at "nodes", defining thermal resistances between nodes and thermal capacitances at each node. Heat can be added at a node if the problem requires it.

A computer program, based on finite difference methods, is used to solve for the temperature at each node at the end of several time increments.

The heat balance equation which is solved for temperature at a node or each time increment is:

$$T_{\theta+\Delta\theta,i} = \frac{\Delta\theta}{C_i} \left(\sum_j \frac{T_{\theta j}}{R_{ij}} + Q_i - T_{\theta i} \sum \frac{1}{R_{ij}} \right) + T_{\theta i}$$

where:

$T_{\theta + \Delta\theta, i}$ = The temperature of node θ at time $\theta + \Delta\theta$

$T_{\theta, i}$ = The temperature of node i at the time θ

$\Delta\theta$ = Time increment

c_i = The capacitance of node i

\sum_j = The summation overall nodes connected by a resistor to node i

R_{ij} = The resistance between node i and any connected node j .

θ_i = The heat rate into node i from sources other than conduction, convection, or radiation from neighboring nodes.

2. Lander Network

A simplified lander network shown in figure 194 was used to conduct preliminary studies. The surface absorptivities and emissivities used in the network analysis are shown in table 38.

3. Results

The thermal network program was run for three different phases of the lander flight; (1) near Earth, (2) cruise, (3) post separation. The temperature transients of some significant points are plotted for each phase.

Figure 195 is the transient near Earth and indicates that the temperature rise due to solar heating will not be a severe problem for the short one-two hour precruise maneuvering.

Figure 196 is the transient at the start of cruise and indicates a 0.80°F per day decline for the conditions stated, that is, 10 watts from the payload heaters and 20 watts from the backside of the solar panels to the aft portion of the sterilization can. This analysis does not include the heat conduction from the bus which can vary from 4 to 30 watts depending upon mechanical design. By increasing the internal heaters up to 20 watts as required and designing the conductive heat path from bus to the lander for approximately 10 to 15 watts, the lander payload can be maintained above 40°F for the cruise phase.

Figure 197 is the transient after separation from the bus and indicates the extremes of temperature for the lander once it has separated from the bus. The temperature gradient around the afterbody may be due to the assumption that the vehicle is not spinning; for 20 rpm the gradient is negligible for the beryllium.

TABLE 38
SURFACE ABSORPTIVITIES AND EMISSIVITIES

Surface	Emissivity ϵ	Solar Absorbtivity α
Exterior of Sterlization Can		
1. Afterbody portion	0.05	0.125
2. Heatshield portion	0.8	0.15
Interior of Sterilization Can	0.05	
Exterior of Lander		
1. Afterbody portion	0.05	0.125
2. Heatshield portion	0.1	0.15
Interior of Lander		
1. Afterbody portion	0.05	
2. Heatshield portion	0.1	
Exterior of Crushup sphere	0.1	

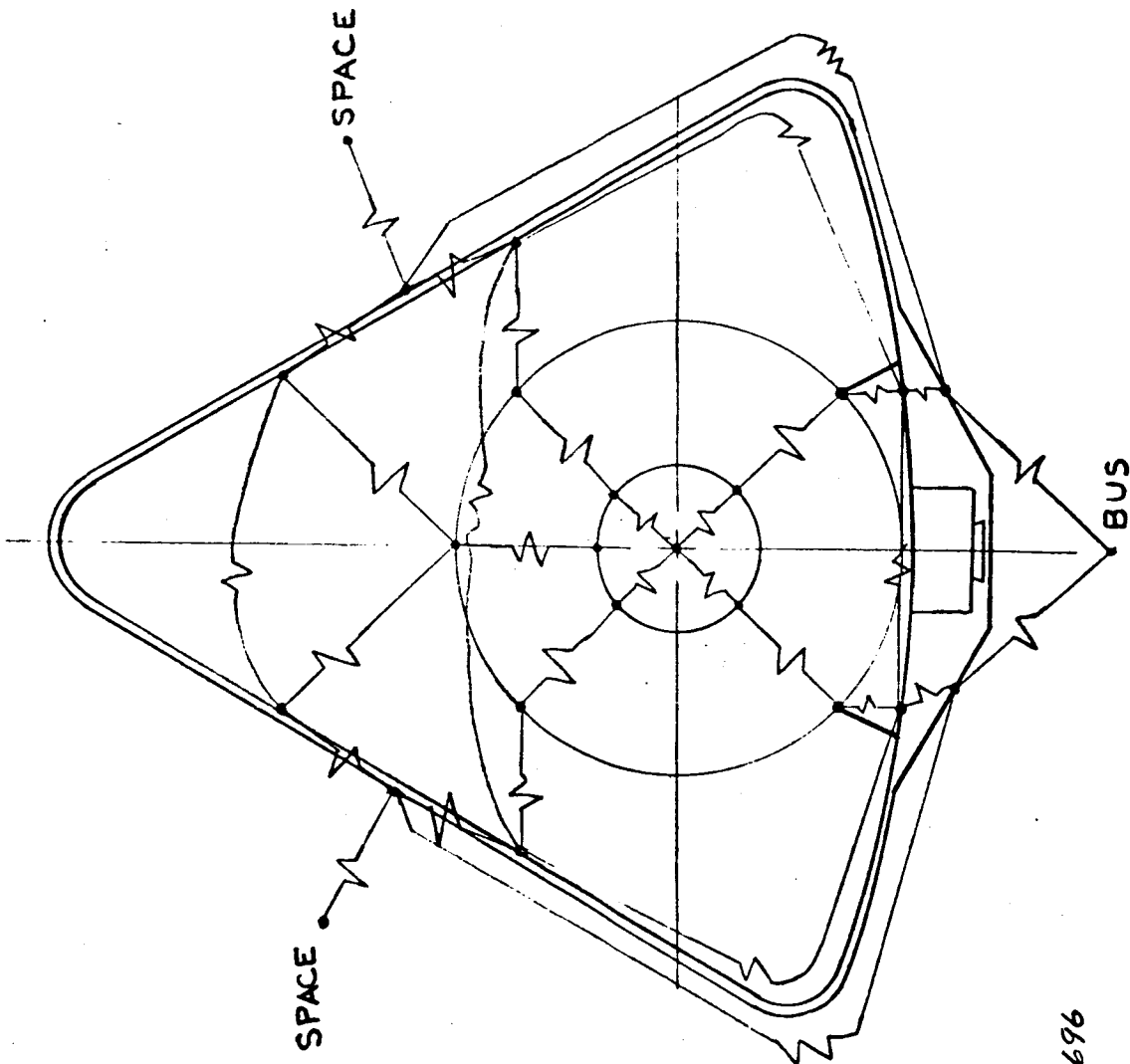


Figure 194 LANDER THERMAL NETWORK

64-11696

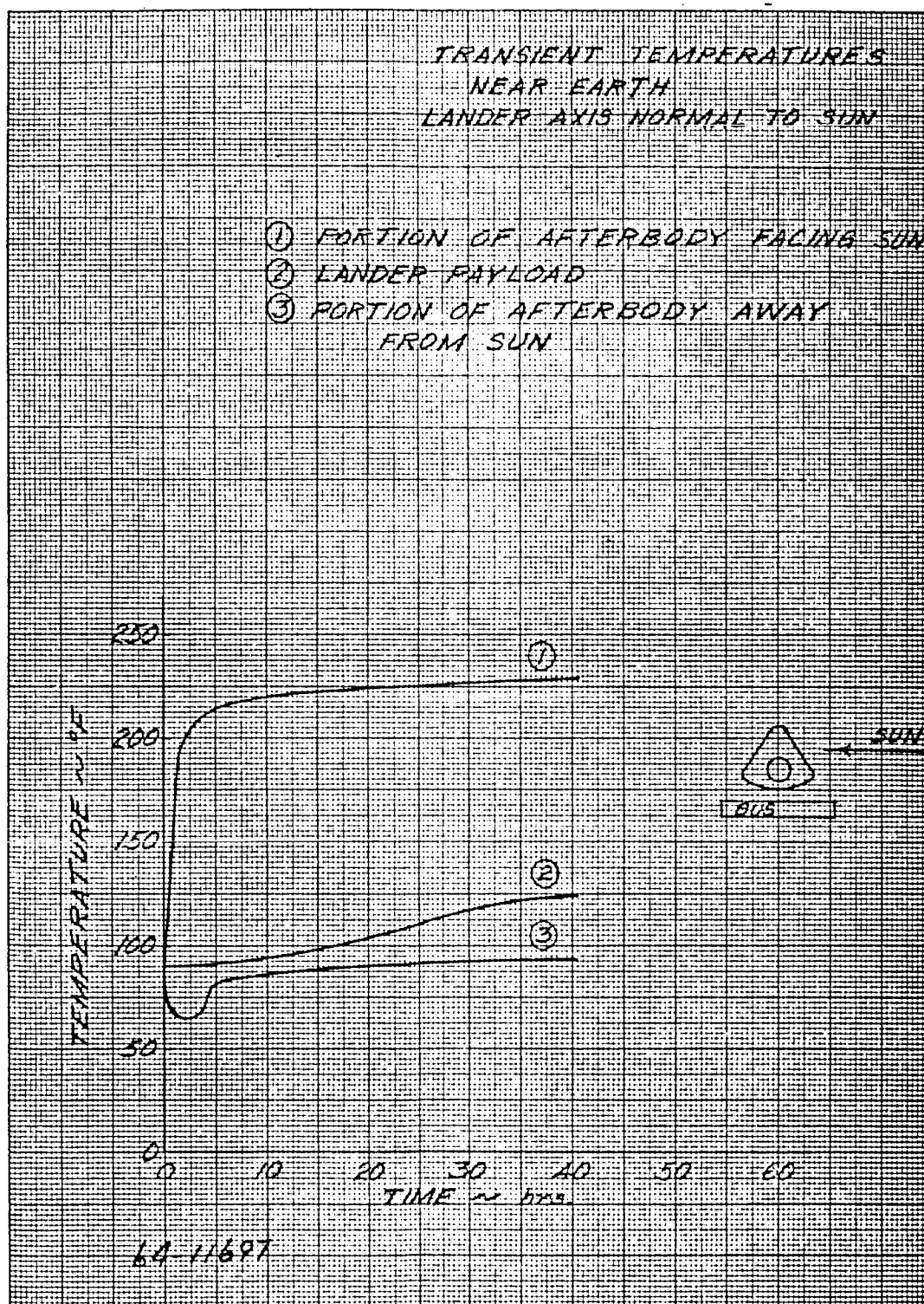


Figure 195 TRANSIENT TEMPERATURES NEAR EARTH

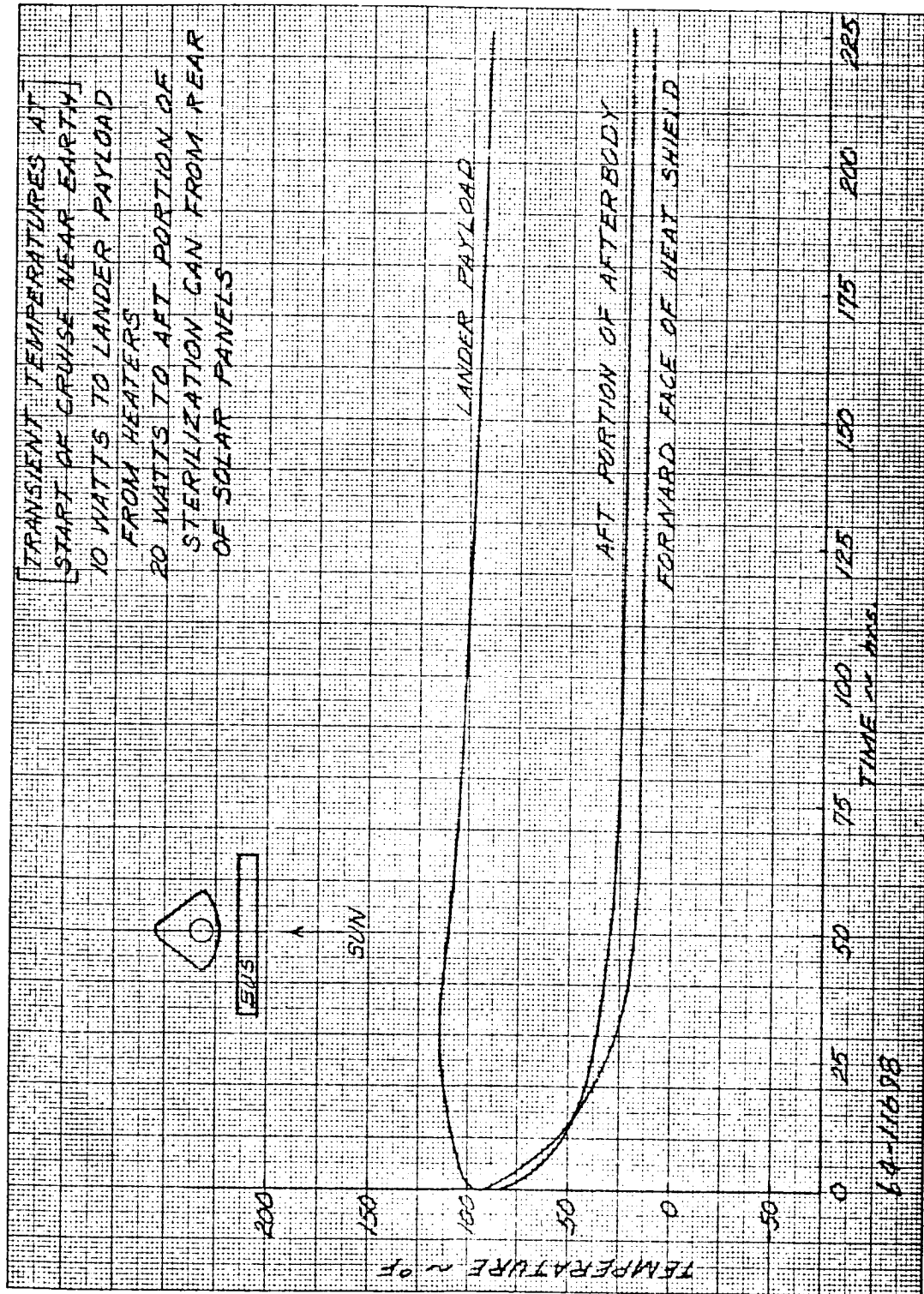


Figure 196 TRANSIENT TEMPERATURES AT START OF CRUISE NEAR EARTH

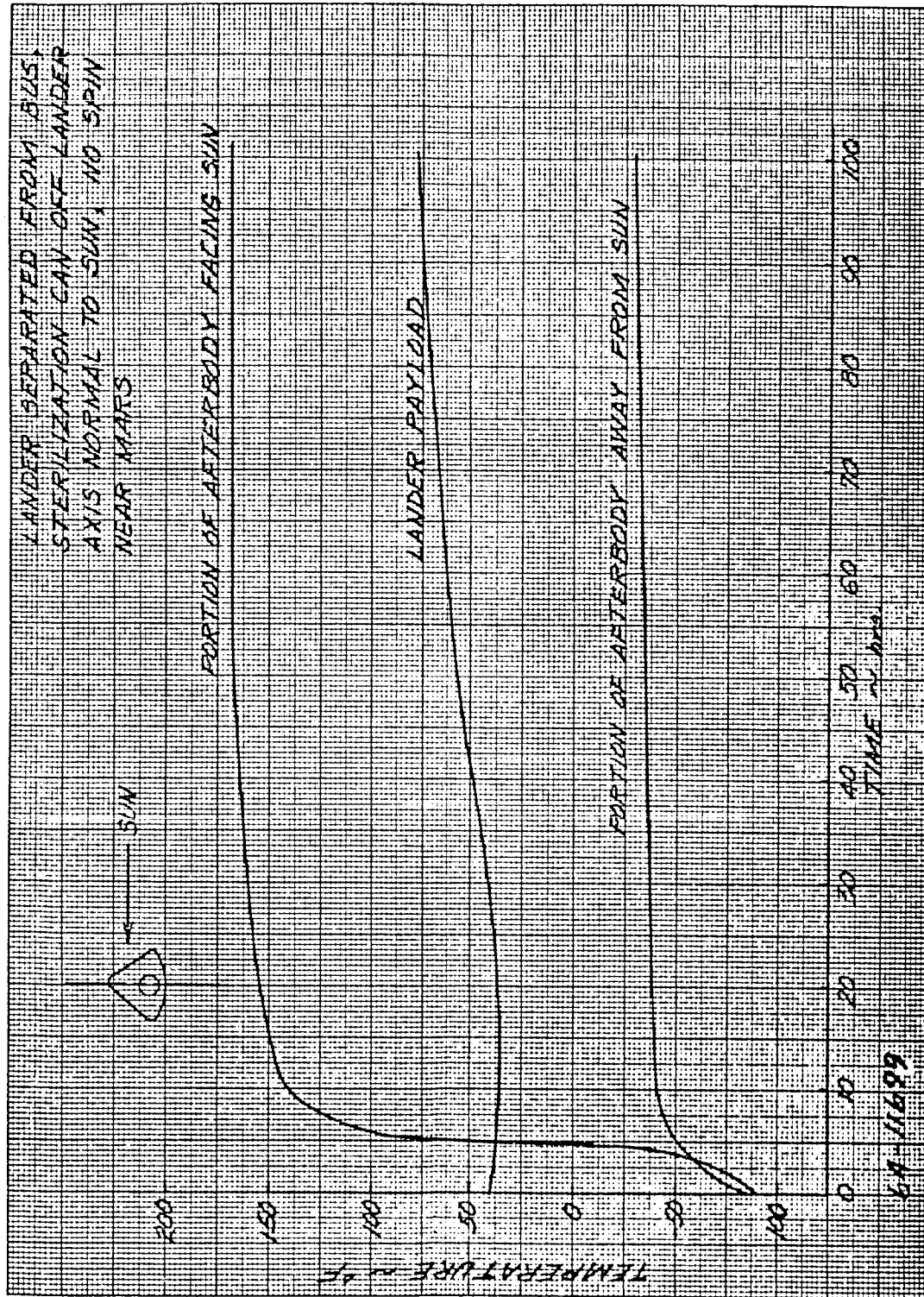


Figure 197 LANDER SEPARATED FROM BUS NEAR MARS

9.6 CONCEPTUAL DESIGN

The exterior surfaces of the sterilization canister and the lander have different requirements for a_s/ϵ depending upon the phase of the flight. Near Earth a low a_s/ϵ (1.0) is best, but due to the short period before cruise acquisition, analysis indicates an a/ϵ of 2.5 will not overheat the payload. During cruise an a_s/ϵ of 2.5 provides the lander with acceptable temperatures.

A sterilization canister fabricated from Alcoa type 1199 (pure) aluminum or United Mineral and Chemical Corp's "Reflectol" (1.5 magnesium and remainder aluminum) can give the desired a_s/ϵ by a combination of mechanical polishing and electropolishing. If a plastic meteoroid bumper is provided on the sterilization can, coatings may be required to achieve the desired a_s/ϵ .

The emissivity and solar absorption properties of beryllium and heat shield material are not known and would have to be determined experimentally. If the required a_s/ϵ are not obtainable with beryllium metal then a coating will have to be used.

The outside surface of the crushable sphere and the internal surfaces of the sterilization canister and lander afterbody must be coated with a low emissivity paint or other applied coating. Low emissivity surfaces are necessary to reduce the radiant heat gain or loss from the crushable sphere to the internal surfaces of the afterbody.

The support ring for the crushable sphere, in order to provide a low thermal conductance path, will be made from a material such as fiberglass or will be insulated from direct contact with the sphere.

The thermal insulation and flotation fluid surrounding the landed payload require materials with K values in the range of 0.0001 - 0.03 Btu/hr ft - °F/ft². The selected flotation fluid is Freon-E3. The insulation will be a material similar to Johns-Manville Min-K 2000.

The overall design concept for the lander payload is to provide a time constant of a least 30-35 hours, so that short time exterior temperature excursions will have little or no effect internally. Temperature inside the lander payload will be maintained between 40°F and 100°F, as this is the allowable temperature range for the batteries.

Electronic equipment, parachutes, and propulsion equipment outside the lander payload will require insulation and/or coatings to maintain satisfactory temperatures.

REFERENCES

1. Fried E., and F. A. Costello, Interface Thermal Contact Resistance Problem in Space Vehicles, ARS Journal, Vol 32, no. 2 (1962) p. 237.
2. Hamilton, D. C., and W. R. Morgan, Radiant-Interchange Configuration Factors NACA TN 2836. (December 1952)

10.0 COMMUNICATIONS AND POWER SUPPLY

Parametric and conceptual design studies were performed on the communication and power system requirements for Advanced Mariner Lander missions in 1969 and 1971. A radar altimeter was considered parametrically as a possible means of parachute deployment but not selected for the conceptual design.

The parametric studies were bounded by assumptions and constraints involving the DSIF capabilities, the landed antenna orientation, the maximum allowable transmitter power, dry heat sterilization, and the expected impact shock level for various impact attenuators. The telemetry link requirements for pre-entry, descent, and landed phases of the lander missions were examined. Both direct (lander to DSIF) and relay (lander to flyby bus) links were examined for the landed phase. Transmitter power, antenna gain, slant range, bit rate, and relay link carrier frequency were the parameters selected for evaluation in the telemetry links. Weight, volume, and power consumption were examined parametrically for the various subsystems in both the communication and power systems. Nickel-Cadmium batteries, fuel cells, and RTG/battery combinations were studied, weight being the parameter selected for comparison.

The conceptual design studies were based on the selection of one of many possible missions payloads. The payload selected (No. 16) required telemetry link operation during all of the previously mentioned phases. The link requirements were examined independently, then modified to simplify the overall design. Typically, the landed relay and direct links use the same transmitter and antenna. Alternate concepts are briefly discussed which further simplify the design.

10.1 ASSUMPTIONS AND CONSTRAINTS

Assumptions were made and constraints imposed which significantly affected the scope of the parametric and conceptual design studies. The most significant constraint imposed early in this study was the requirement to withstand an impact shock pulse of up to 6000 g for 20 milliseconds. The selection of subsystems hardware was based on a 1500 g shock pulse. Others, such as the ability to withstand a dry heat sterilization qualification test of three cycles at 145°C for 36 hours, were of nearly equal significance.

10.1.1 Deep Space Instrumentation Facility

The deep space instrumentation facility (DSIF) characteristics assumed in this study are listed in table 39. The noise bandwidth range assumed is listed in table 11 of JPL Technical Memorandum No. 33-83, March 2, 1962. In Revision 1 of this memorandum, 24 April 1964, table 11 indicates a minimum noise bandwidth of 12 cps. For direct link communications (lander to DSIF) a carrier loop noise bandwidth of 3-5 cps is required to minimize the transmitter power requirements. It is assumed that noise bandwidths in the 3 cps region will be available.

10.1.2 Landed Antenna

A constraint imposed by communications on the lander design is the requirement that after landing, the antenna be pointed vertically upward. Since the lander can assume any orientation after landing, to establish a communication link between the lander and the DSIF or flyby bus would require an antenna subsystem which would a) provide omnidirectional coverage, or b) be a multi-element array in which the element nearest to vertical could be selected by a switching arrangement, or c) be gimballed and use gravity for vertical orientation. Omnidirectional coverage would be a poor selection for three reasons. First, a truly isotropic radiator has no gain (directivity). Second, it is very difficult to achieve an omnidirectional antenna pattern (deep nulls will occur). Third the reflected power from the ground would affect the antenna pattern and also cause multipath (signal fading) problems.

TABLE 39

ASSUMED DSIF CHARACTERISTICS

<u>Receiving Frequency (mc)</u>
2290 -2293 1/3
2293 1/3-2296 2/3
2296 2/3-2300
<u>Reflector Diameter (ft)</u>
210
<u>Reflector Gain (db)</u>
61 ± 1
<u>Circuit Loss (db)</u>
0.03 max.
<u>Noise Temp. ($^{\circ}$K)</u>
28 ± 5
<u>Noise Bandwidth (cps)</u>
(3-250)
<u>Polarization</u>
Right Circ.
<u>Beamwidth (deg)</u>
0.2
<u>Location</u>
All Stations

A multi-element array is also a poor choice. At S-band (required for the direct link) as many as six elements would be required to provide omnidirectional coverage. Selecting the element closest to vertical would require a vertical sensor and an rf switching subsystem. Aside from the fact that a heavy weight and volume penalty would accrue, the switching arrangement would be complicated at best. A gimbaled antenna system appears to be the most logical choice. Either the whole landed payload or the antenna alone would be gimbaled. The advantages of the gimbaled system are simplicity, in that a single radiating element is required, and ability to achieve gain, in that the antenna selection would be a function of the look-angle between the local vertical and target (DSIF or flyby bus).

10.1.3 Transmitter Power Breakdown

Transmitter power breakdown (corona discharge) is a problem experienced at relatively low atmospheric pressures. The Kaplan atmospheric models of Mars indicate the surface pressure to be within the region where this problem could occur. To circumvent this problem will most likely require sealing and pressurizing or evacuating the transmitter, coaxial cables and antenna. In this study the antenna is assumed pressurized with a dielectric window covering the aperture. An arbitrary bound of 100 watts of rf power is assumed to be the upper limit until recent test results can be evaluated by antenna specialists.

10.1.4 Dry Heat Sterilization

Dry heat at 135°C for 24 hours is the assumed sterilization technique. Qualification of hardware is assumed to be 145°C for 36 hours, 3 cycles. This requirement has a great impact on system design e.g., the selection of a Nickel Cadmium (Ni CAD) battery in the parametric studies. Ni CAD batteries are the only types presently known which have been tested successfully in this environment. Similar tests on Silver-Zinc (Ag Zn) cells used in the Mariner C spacecraft have proved negative. A test program has recently been initiated at Avco to study the affects of the dry heat sterilization environment on Ni CAD cell performance. Test results will be available early in 1965.

10.1.5 Impact Shock

Early in this program it was indicated that impact shock levels of up to 6000 g for up to 20 milliseconds in duration would be experienced with some impact attenuators. This requirement is critical in that hardware is not readily available which can survive this environment. Avco has had considerable experience in "hardening" subsystems for various missile reentry vehicle systems. This experience, coupled with discussions and reports from many vendors, indicates the ability to build such equipment. Estimates on weight penalties are in most cases the considered opinions of the vendors.

10.1.6 Telemetry Link Requirements

Communications from the lander will be via a direct link to the DSIF or a relay link through the flyby bus, or both. Figure 198 shows the three links assumed. Pre-entry is that link established between the lander and flyby bus after separation and again just before entry. Descent is the link between the lander and flyby bus while on the main parachute. This link cannot be established on a "no chute" system due to the short time between emergence from blackout and impact. Blackout is the period during entry when a plasma sheath engulfs the entry vehicle and severely attenuates the radiated signal. Post-impact is the link between the lander and the DSIF or the flyby bus established after landing. In all links the parametric data presented in this report are worst cases, i. e., the linear sum of the adverse tolerances is equal to or less than the nominal performance margin. In the direct link the carrier frequency assumed is compatible with table 39. In the relay link frequency is considered parametrically.

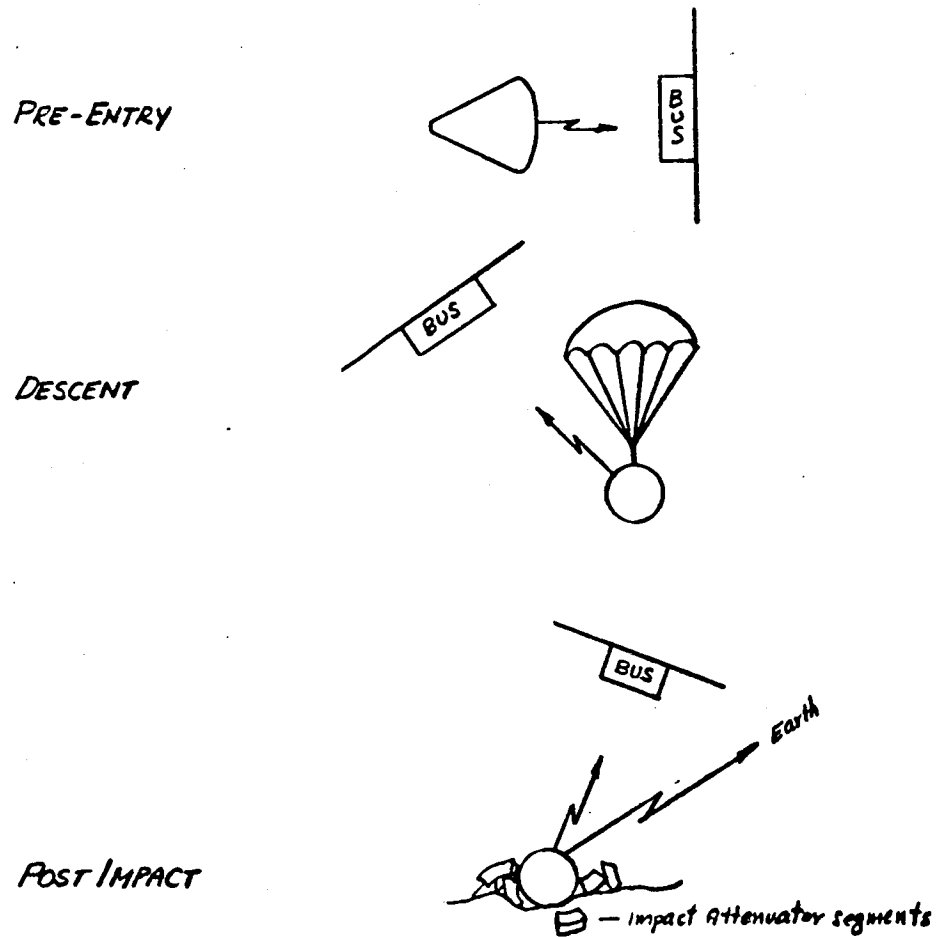
10.2 TELEMETRY LINK STUDIES

In each of the telemetry link parametric studies a design control table similar to the one required by JPL was used. In selecting a modulation scheme prime consideration was given to PCM/PSK/PM as used in the Mariner R Venus flyby experiment and the Mariner C spacecraft. PCM/PSK/PM is pulse code modulation phase shift keying a subcarrier which phase modulates a carrier. A separate synchronization channel using a psuedo-random noise (PN) code for word and bit synchronization was assumed. A dual channel phase-locked loop receiver using synchronous (integrate and dump) detection is assumed. It is recognized that a single channel receiver which combines data and synchronization is being developed.¹ The dual channel receiver was selected for this study since it is readily available.

10.2.1 Telemetry Link Parameters

The design control chart is a tabulation of all parameters affecting the telemetry link performance. In the parametric studies of each link, the parameters selected for variation were transmitter power (P_T), antenna gain (G), slant range (R), and bit rate (\dot{B}). Each of these were assigned reference values in the Design Control Tables. The other parameters were assigned constant values consistent with the respective link.

Using table 42 as a guide, circuit losses consist of all signal attenuations between the power amplifier output and the transmitting antenna output or between the receiving antenna input and the receiver front end. Contributors to these losses and their assumed values are listed in table 40 and figures 199 and 200.



64-11700

Figure 198 TELEMETRY LINK REQUIREMENTS

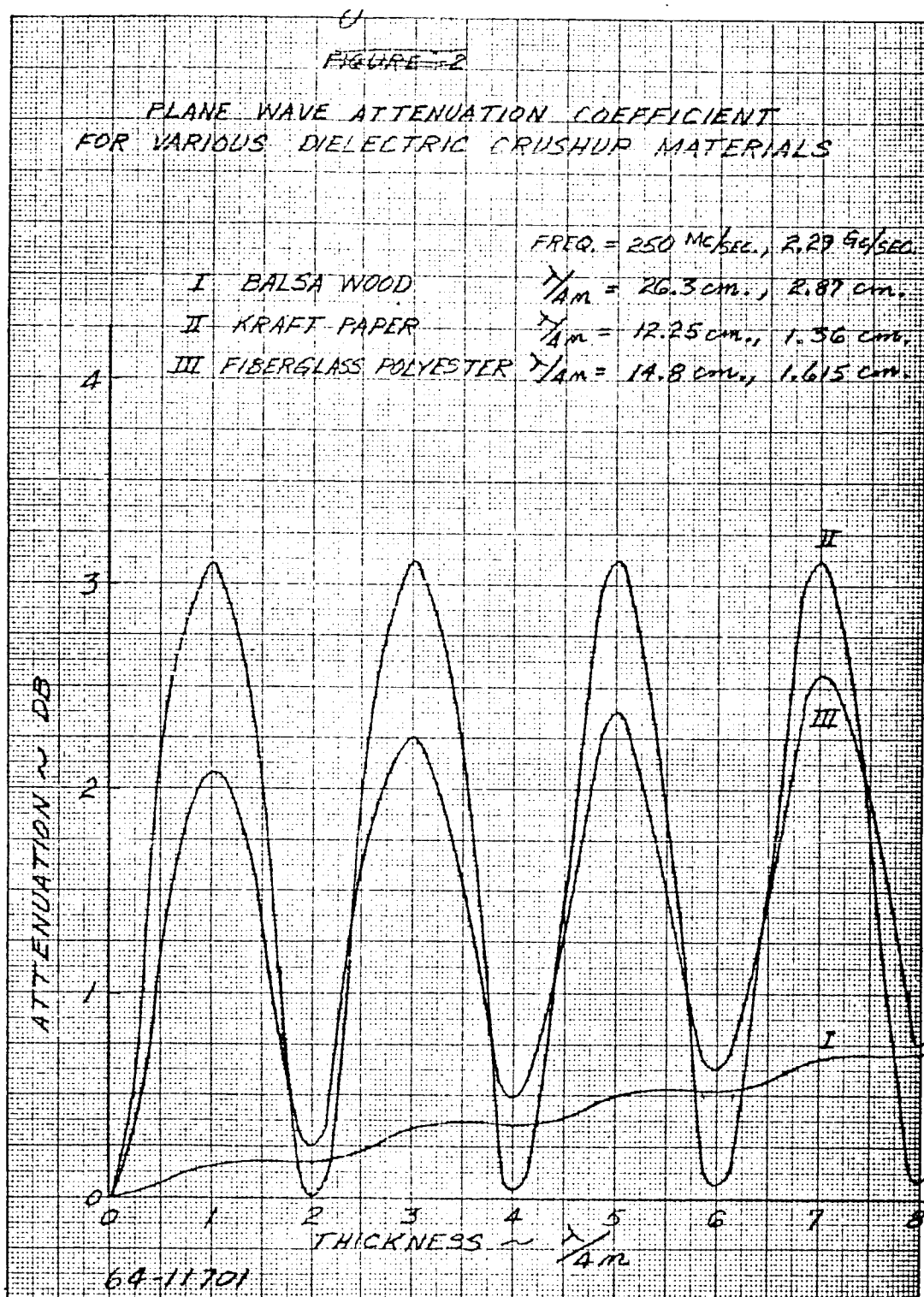


Figure 199 PLANE WAVE ATTENUATION COEFFICIENTS FOR VARIOUS
DIELECTRIC CRUSHUP MATERIALS

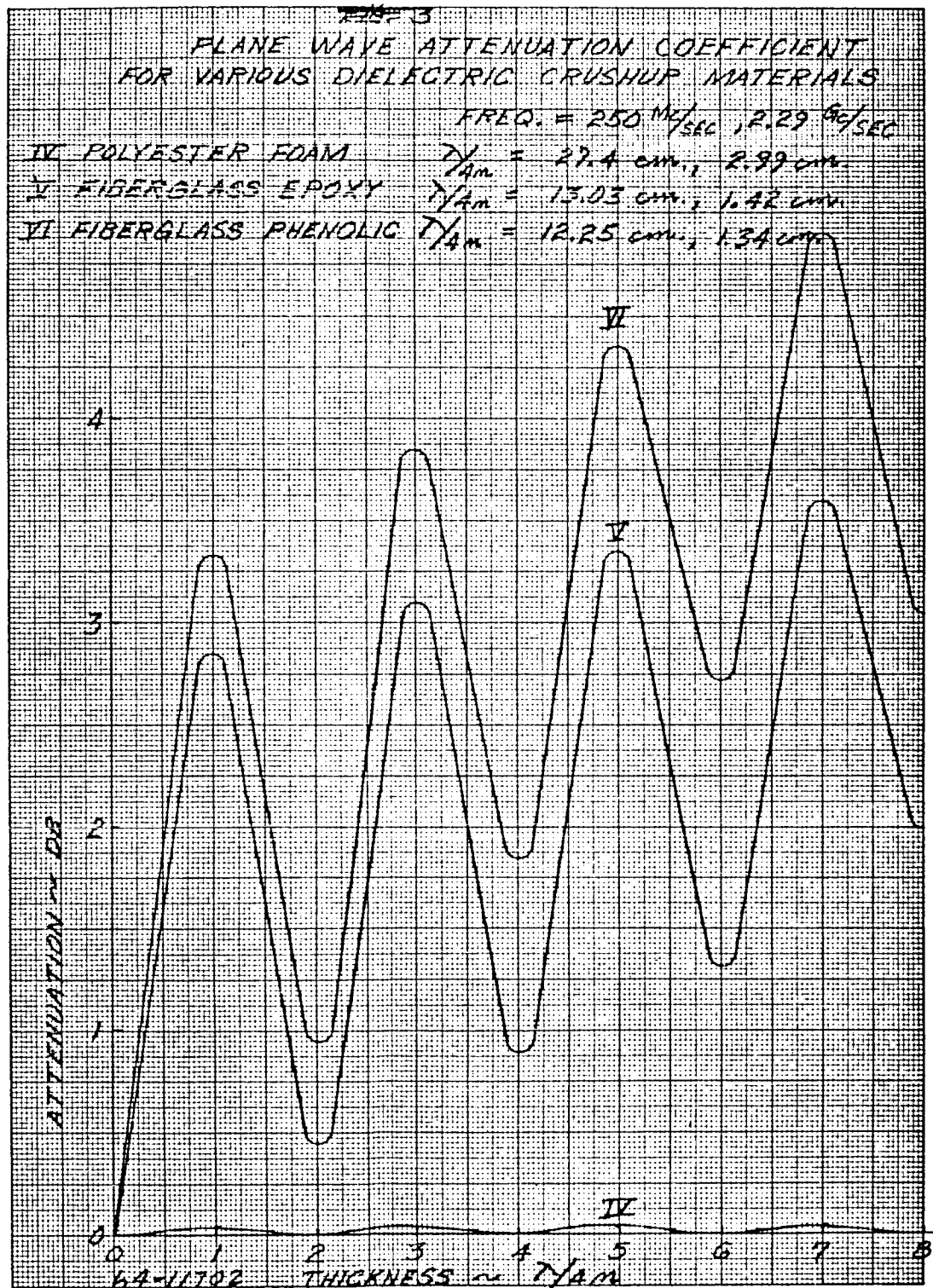


Figure 200 PLANE WAVE ATTENUATION COEFFICIENT FOR VARIOUS
 DIELECTRIC CRUSHUP MATERIALS

The transmitting and receiving antenna gains and pointing losses are treated parametrically in the relay links. In the direct link, the DSIF antenna gain is known and only the transmitting (Lander) antenna gain and pointing loss are treated parametrically. The reference values assigned are 0.0 db.

The space loss for the direct link is calculated for a nominal carrier frequency of 2295 mc and for a reference range of 2×10^8 kilometers. In the relay links, space loss is calculated for a nominal carrier frequency of 2000 mc and for a reference range of 10^4 kilometers. In the relay links, carrier frequency is also examined parametrically, whereas in the direct link, the frequency must be in the band shown in table 39.

Circular polarization was selected for all links in both the transmitting and receiving antennas. The net loss due to off-axis look-angle and Faraday rotation were expected to be no greater than 1 db. In the conceptual design, however, it will be shown that during the landed phase the look-angle is such that this loss will be increased.

Atmospheric absorption loss will be negligible for the frequency band considered.

The system noise temperature was given as $28^\circ\text{K} \pm 5^\circ\text{K}$ for the DSIF receiver. In the bus a pre-amplifier having a $4.5 \text{ db} \pm 0.5 \text{ db}$ noise figure is assumed (available with tunnel diodes at S-band). Also, in determining system noise temperature for the flyby bus receiver the black-body temperature of Mars was assumed to be 218°K .²

The carrier loop noise bandwidth ($2B_{LO}$) required for acquiring and tracking the received carrier is a function of allowable acquisition time and the ability to track the doppler frequency variations. The noise bandwidth required can be determined by considering that initially there will be a frequency offset between the received carrier from the lander and the reference carrier generated by the local oscillator in the flyby bus or DSIF receivers. This frequency offset is caused by drifting (long term instability and temperature affects) of both the transmitter and receiver reference oscillators, and by doppler. The time required to sweep the receiver local oscillator through this offset is the carrier loop acquisition time (Once in phase, the pull-in time will be a small portion of the total acquisition time.) The long term instability quoted in the Mariner C specifications (July 1963) for both the fixed and voltage controlled oscillators is 1 part in 10^6 . It is assumed that at the DSIF the frequency is known at least an order of magnitude better.

If the relative motion between the lander and flyby bus or DSIF remained constant and was known absolutely, the resultant doppler shift could be compensated for by offsetting the receiver local oscillator a corresponding amount. The effective doppler would then be due to the uncertainty in doppler rather than the absolute value. The relative motion between the lander and flyby bus is relatively constant after landing and due primarily to the flyby bus velocity. The rate of change doppler at this time is due to the rotation of the planet and change in the apparent flyby bus velocity (a directional cosine). These effects are negligible. During the descent phase, the rate of change is also small due to the relatively constant descent velocity.

If it is assumed that the frequency drifts in the receiver and transmitter local oscillators are in opposite directions, the worst case frequency offset can be expressed as

$$f_o = 2 f_c / 10^6 + v_u / \lambda \quad (1)$$

where f_c is the carrier frequency, v_u is the velocity uncertainty and λ is the carrier wavelength.

The sweep rate required by the receiver local oscillator is f_o/t , where t is the acquisition time.

It can be shown that the carrier noise bandwidth at threshold is

$$2B_{LO} = w_n \quad (2)$$

where w_n is the loop natural frequency.

Frazier and Page³ show that the maximum allowable rate of change of frequency between the received carrier and the local carrier, for a phase-locked loop receiver and for a probability of capture of 0.9, is

$$R = 0.22 w_n^2 \quad (3)$$

The sweep rate (f_o/t) must therefore be no greater than R , or

$$2B_{LO} \geq (4.5 f_o/t)^{1/2} \quad (4)$$

The descent phase is most critical in terms of allowable acquisition time since the minimum time on the parachute will be approximately 110 seconds and it would be desirable to use 90 to 100 seconds of this time to transmit data acquired during entry. The 10 to 20 seconds available for acquisition would have to be shared between carrier acquisition and sync acquisition. SYNC acquisition is discussed later. Figure 201 shows offset frequency (f_o) as a function of carrier frequency and velocity uncertainty. Figure 202 shows carrier acquisition time as a function of carrier noise bandwidth and frequency offset. It is assumed that the bus receiver will use automatic (swept frequency) acquisition.

The next item in the design control chart is the required threshold signal-to-noise ratio (SNR). The value assumed for all links is 6.0 db which is consistent with existing receivers.

The PN code sync channel is used to provide both word and bit synchronization in the data channel. Bit synchronization is used to control the integrate and dump times for optimum detection. To make bit synchronization easier, the number of PN bits per data bit should be an integer and a multiple of the PN code length. For example, with a 63 bit PN code word and a 7 bit data word there are 9 PN bits per data bit. This is the system used on Mariner R and Mariner C. Table 41 shows the possible values of PN bits per data bit (N) as a function of PN code length (P). A 63 bit PN code word provides the best compromise between allowable values of N and corresponding data word lengths and was used in this study.

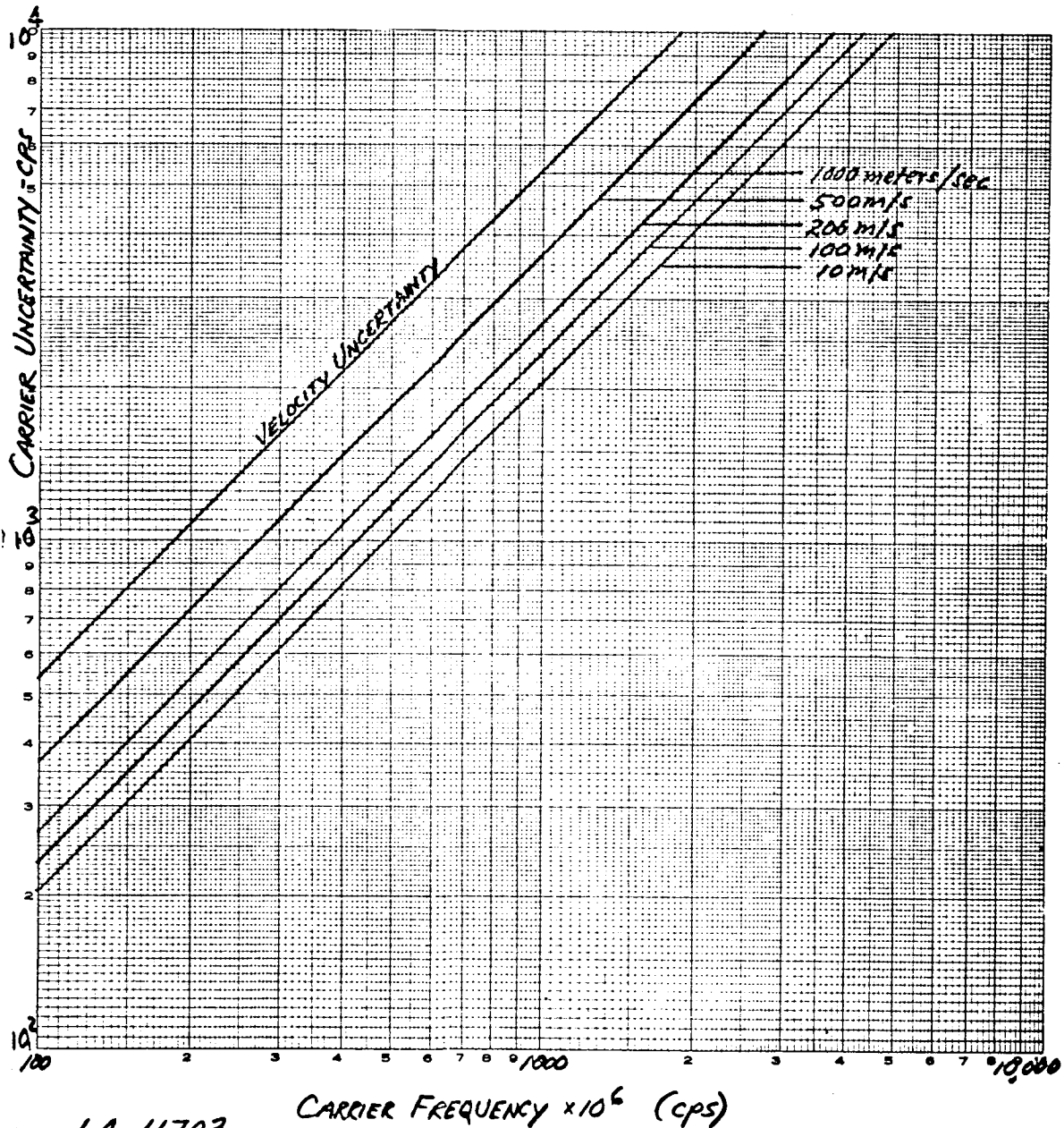
The threshold SNR assumed for the synchronization channel is 8.0 db in all links.

TABLE 40

RF COMPONENT INSERTION LOSSES

Coaxial Cables	-0.22 db	± 0.03 db
VSWR Monitor	-0.22 db	± 0.03 db
Heat Shield (1 inch thick)	-0.25 db	± 0.5 db
Fiberglass (1 inch thick)	-0.25 db	± 0.5 db
Impact Attenuators	See figures 199 and 200.	
DSIF Receiving Circuit Loss	-0.02	± 0.01 db

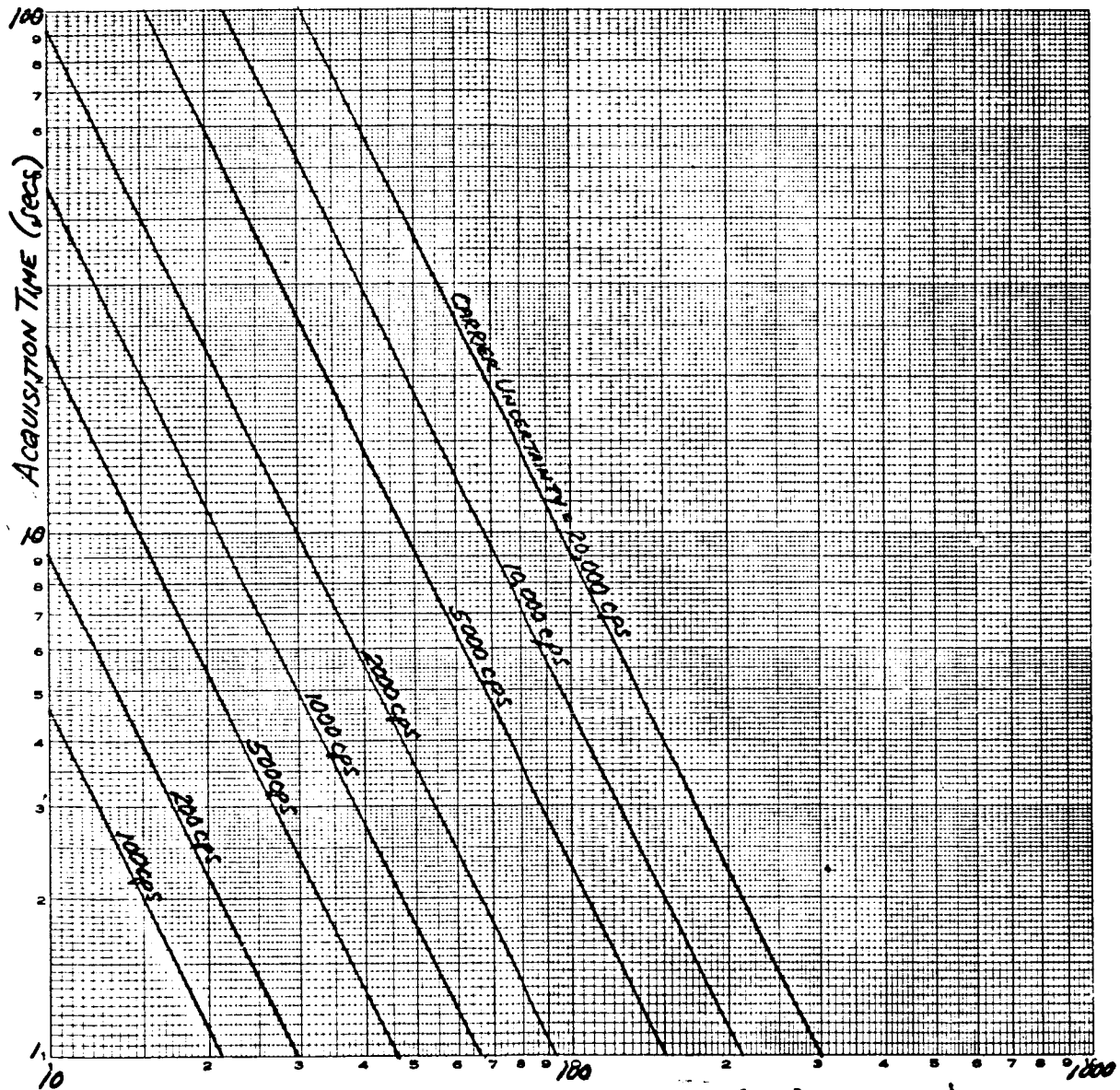
CARRIER UNCERTAINTY
VS.
CARRIER FREQUENCY
VS.
VELOCITY UNCERTAINTY



64-11703

Figure 201 CARRIER UNCERTAINTY VERSUS CARRIER FREQUENCY VERSUS
VELOCITY UNCERTAINTY

ACQUISITION TIME
VS.
CARRIER LOOP NOISE BANDWIDTH
VS.
CARRIER UNCERTAINTY



64-11704 CARRIER LOOP NOISE BANDWIDTH ($2B_L$) - cps

Figure 202 ACQUISITION TIME VERSUS CARRIER LOOP NOISE BANDWIDTH
VERSUS CARRIER UNCERTAINTY

TABLE 41

PN BITS PER DATA BIT VERSUS PN CODE LENGTH

PN CODE LENGTH	PN BITS PER DATA BIT
P = 31 bits	N = 31
63	3, 7, 9, 63
127	127
255	3, 5, 17, 15, 255

10.2.1.1 Lander to Flyby/Bus Telemetry Links

As indicated earlier the lander communicates with the flyby bus shortly after separation, just prior to entry, during descent on the main parachute, and after landing. All parameters affecting the performance of these links are listed in table 42. The assigned values for these parameters are based on the assumptions and calculations discussed previously. A reference carrier noise bandwidth of 20 cps and a sync loop noise bandwidth of 1 cps were selected. These selections were assumed acceptable for the pre-entry and landed links when acquisition time is not critical (compared to the descent link when total playout time is relatively short). The transmitter power required for the reference range frequency, bit rate and antenna gain can be calculated as follows:

1) Carrier Power

$$P_{tc} = \text{Threshold Carrier Power} - \text{Net Circuit Loss}$$

$$= -146.7 \text{ dbm} + 180.9 \text{ db}$$

$$= +34.2 \text{ dbm}$$

$$= 2.63 \text{ watts}$$

2) Data Power

$$P_{td} = \text{Threshold Subcarrier Power} - \text{Net Circuit Loss}$$

$$= -156.7 \text{ dbm} + 180.9 \text{ db}$$

$$= +22.2 \text{ dbm}$$

$$= 166 \text{ milliwatts/bps}$$

TABLE 42

TELECOMMUNICATIONS DESIGN CONTROL CHART

PROJECT: ADVANCED MARINER

CHANNEL: LANDER TO FLYBY/BUS

MODE: TELEMETRY AFTER LANDING (coherent PSK)

NO.	PARAMETER	NOMINAL VALUE (db)	TOLERANCE (db)	WORST VALUE (db)
1	Transmitting circuit loss	-0.5	± 0.2	-0.7
2	Transmitting antenna gain	---	---	0.0
3	Transmitting antenna pointing loss	---	---	0.0
4	Space loss = $32.46 + 20 \log$ $F + 20 \log R$ $F = 2000$ mc, $R = 10,000$ km	-178.5	---	-178.5
5	Polarization loss	0.0	+0.0 -1.0	-1.0
6	Atmospheric absorption loss	---	---	---
7	Receiving antenna gain	---	---	0.0
8	Receiving antenna pointing loss	---	---	0.0
9	Receiving circuit loss	-0.5	± 0.2	-0.7
10				
11				
12	Net circuit loss	-179.5	+0.4 -1.4	-180.9
13	Total transmitter power			
14	Total received power			
15	Receiver noise spectral density (N/B)			
	System Temperature = 1170°K	-167*	± 0.5	-166.7*

*dbm

TABLE 42 (Concl'd)

NO.	PARAMETER	NOMINAL VALUE (db)	TOLERANCE (db)	WORST VALUE (db)
16	Carrier APC noise BW ($2B_{LO} = 20$ cps)	+13.0	---	+13.0
17	Required Threshold SNR in $2B_{LO}$	+6.5	± 0.5	+7.0
18	Threshold carrier power	-147.7*	± 1.0	-146.7*
19	Total received power			
20	Carrier modulation loss			
21	Received carrier power			
22	Performance margin			
DATA CHANNEL				
23	Bit rate ($1/t$) = 1 bps	0.0	---	0.0
24	Required ST/N/B ($P_e = 10^{-3}$)	+7.4	± 0.6	+8.0
25	Threshold subcarrier power	-159.8*	± 1.1	-158.7*
26	Total received power			
27	Modulation loss			
28	Received data subcarrier power			
29	Performance margin			
SYNC CHANNEL				
30	SYNC APC noise BW ($2B_{LO} = 1$ cps)	+0.0	± 0.4	+0.4
31	Threshold SNR in $2B_{LO}$	+8.0	± 1.0	+9.0
32	Threshold subcarrier power	-159.2*	± 1.9	-157.3*
33	Modulation loss			
35	Received SYNC subcarrier power			
36	Performance margin			

* dbm

In the data channel, a reference bit rate of 1 bit per second was selected. Bit rate is treated parametrically. The theoretically required signal energy per unit bandwidth of noise ($ST/N/B$) to achieve a given bit error probability (P_e) for coherent PSK modulation has been tabulated in many references.⁴ Figure 203 shows P_e versus $ST/N/B$ for coherent PSK modulation. Although this curve indicates at $ST/N/B$ of 6.8 db for P_e of 10^{-3} (probability of one bit error per thousand bits), additional signal power should be transmitted to allow for non theoretical performance of the detection equipment. An additional 1.2 db has been allowed for this non theoretical performance.

In the synchronization channel the SYNC loop noise bandwidth ($2B_{LO}$) required is a function of acquisition time, as in the carrier loop. The required bandwidth can be determined by noting that after the PN generator in the flyby/bus or DSIF is in phase with PN the component of the received signal, the synchronizing loop can be treated as a normal phase-locked loop except that pull-in must be fast; no slippage is allowed. The frequency to which the loop locks is always the same; Δf away from the VCO idling frequency. This offset is provided so that the flyby bus or DSIF PN generator, which is driven by the VCO, will run at a different rate than the transmitter PN generator; and the two codes will slip past each other until they come into phase, at which time lock should occur. It is desirable to have the offset frequency as large as possible so that the codes will come into phase quickly. The acquisition time is the time required for the local PN code to slip half its length with respect to the received PN code, since all starting phase discrepancies are equally probable. (The actual pull in time once the PN codes get in phase will be negligible).

It can be shown that the acquisition time can be expressed as

$$t = P/2n \Delta f \quad (5)$$

where P is the length of the PN code in bits and n is the number of PN bits per clock cycle. It can also be shown that

$$f = 0.4 B_{LO} \quad (6)$$

Equation (5) can then be written in the form

$$t = 1.25 P/2B_{LO} \quad (7)$$

where $n = 2$ for non-ambiguous locking

This equation is plotted in figure 204 for $P = 63$ bits.

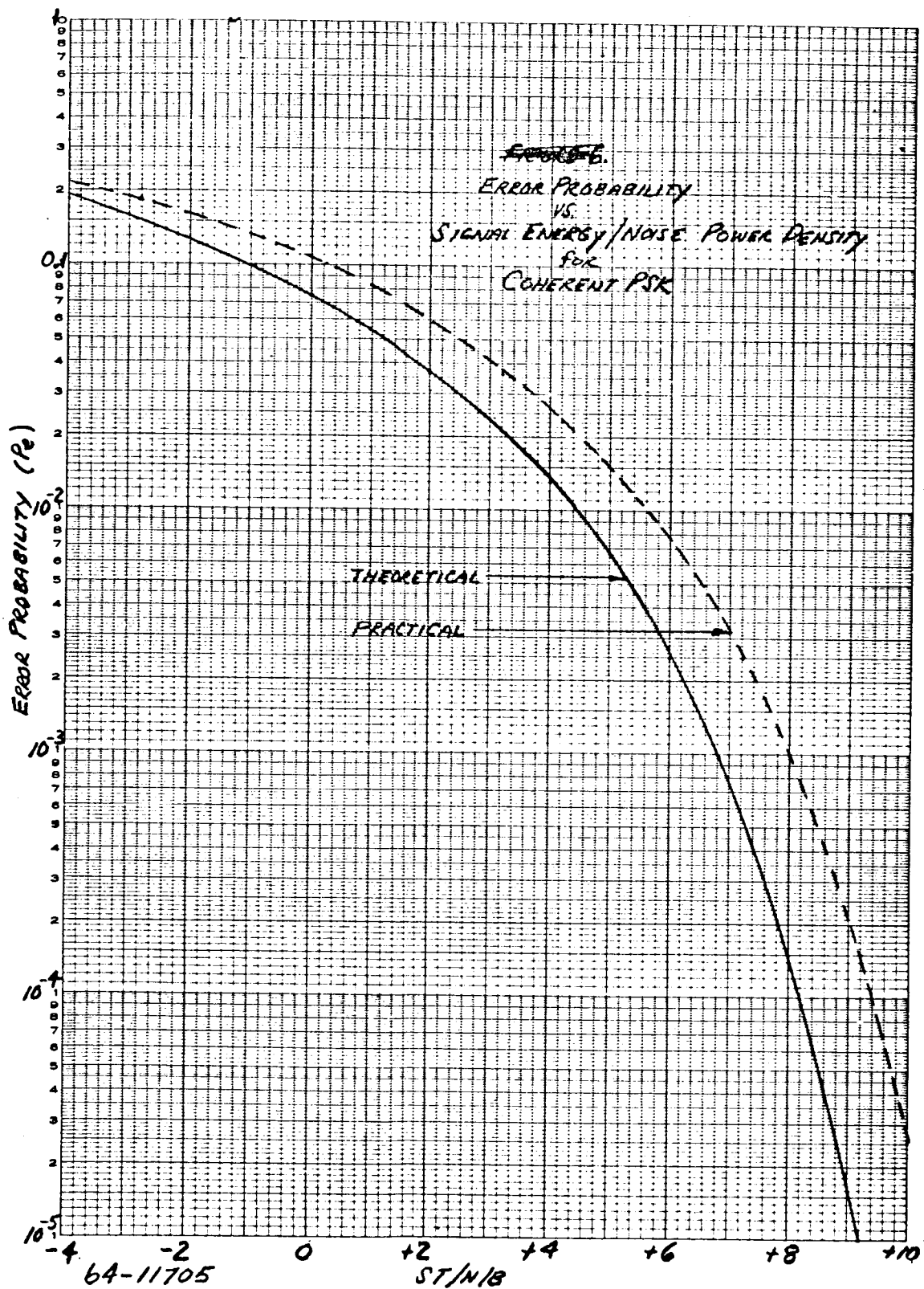


Figure 203 ERROR PROBABILITY VERSUS SIGNAL ENERGY/NOISE POWER DENSITY FOR COHERENT PSK

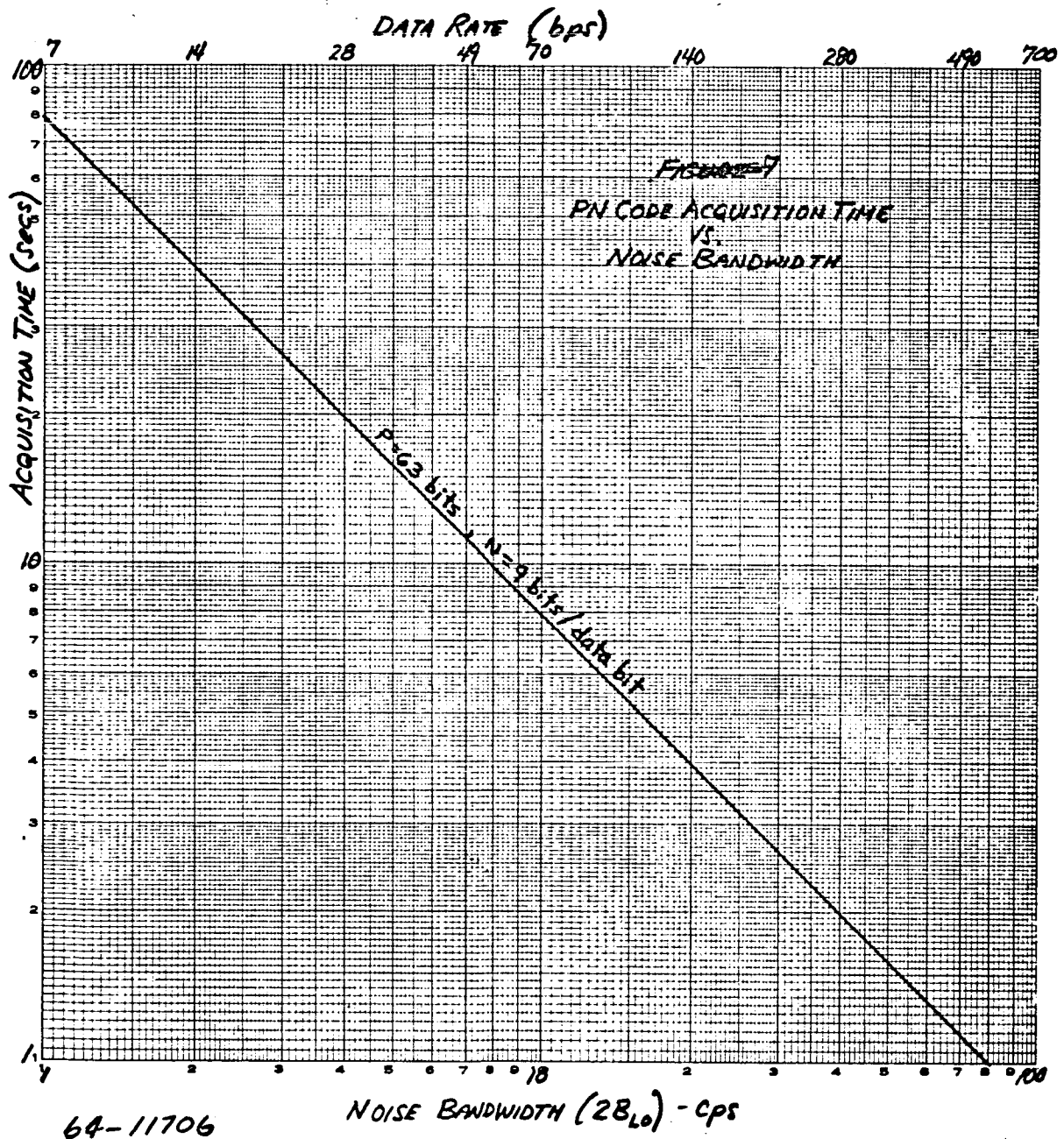


Figure 204 P.N. CODE ACQUISITION TIME VERSUS NOISE BANDWIDTH

3) SYNC Power

P_{ts} = Threshold Subcarrier Power - Net Circuit Loss

$$= -157.3 \text{ dbm} + 180.9 \text{ db}$$

$$= + 23.6 \text{ dbm}$$

$$= 230 \text{ milliwatts}$$

4) Total Power

$$R^P T = P_{tc} + P_{ts} + P_{td}$$

$$= 2.86 + 0.166 \dot{B}$$

Figure 205 shows transmitter power/net antenna gain product (P_{TG}) plotted parametrically as a function of slant range and bit rate. The descent telemetry link requirements can be determined from table 42 with the exception of the carrier and SYNC loop noise bandwidths. Selection of appropriate noise bandwidths is a function of acquisition time allowable as determined from figures 202 and 204. Assuming a 10 cps sync noise bandwidth (8 second acquisition time), figures 206, 207, 208 and 209 show P_{TG} versus range and bit rate for carrier loop bandwidths of 20, 50, 100, and 200 cps. Figure 210 shows variation in P_{TG} as a function of carrier frequency.

10.2.1.2 Lander to DSIF Telemetry Link

All parameters affecting the performance to the direct link are shown in table 43. Proceeding as in the relay link,

$$P_T = 7.45 + 1.66 \dot{B}$$

Figure 211 shows the direct link requirements parametrically.

10.3 RADAR ALTIMETER PARAMETRIC STUDIES

A radar altimeter is a possible candidate for deploying the main parachute. The altimeter requirements were determined parametrically.

The parameters affecting the performance of the radar altimeter are listed in table 44. The assigned values for these parameters are made with regard to typical hardware performance and through direct calculations.

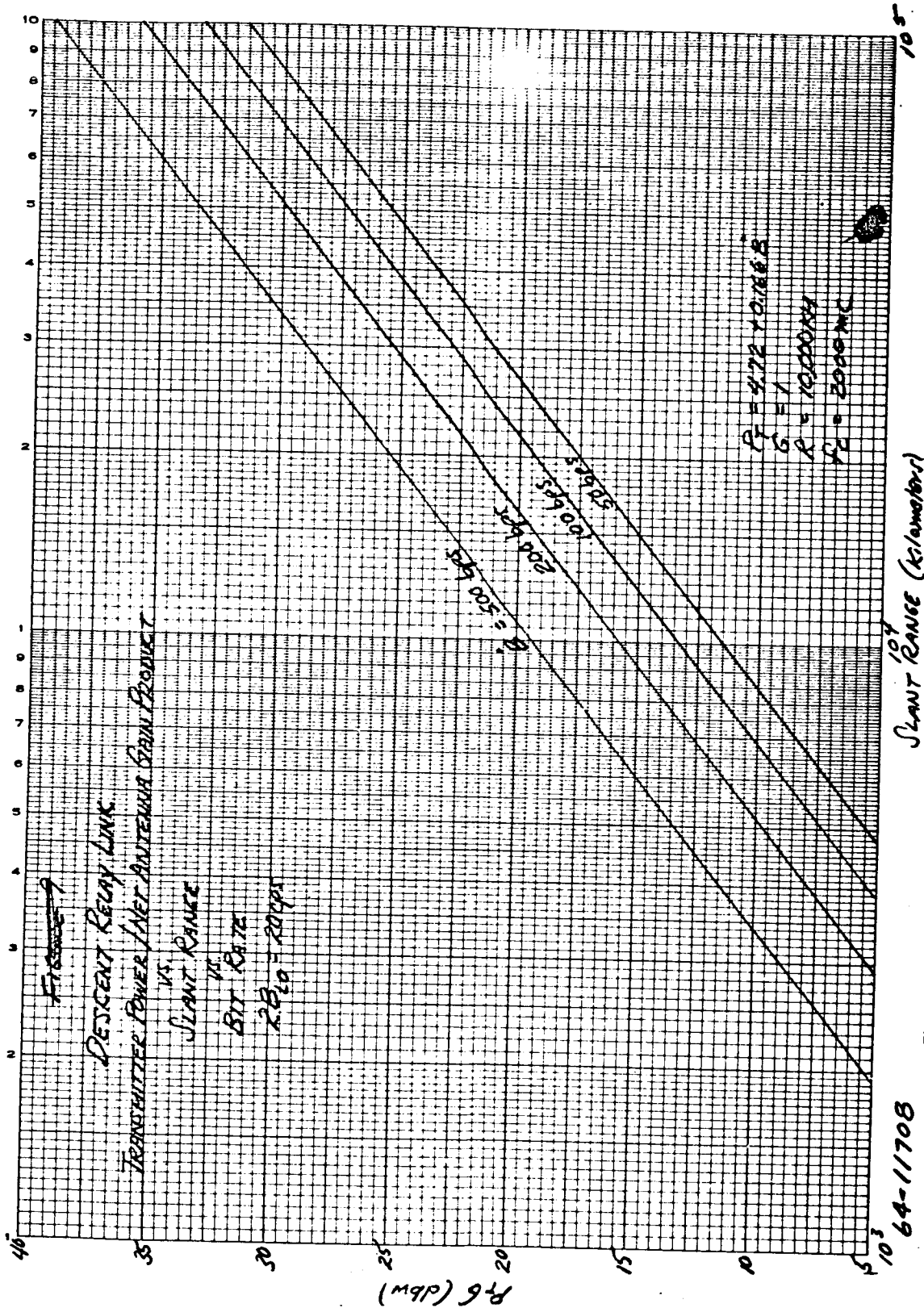


Figure 206 DESCENDING RELAY LINK TRANSMITTER POWER/NET ANTENNA GAIN PRODUCT VERSUS SLANT RANGE
BIT RATE $2 B_{10} = 20 \text{ CPS}$

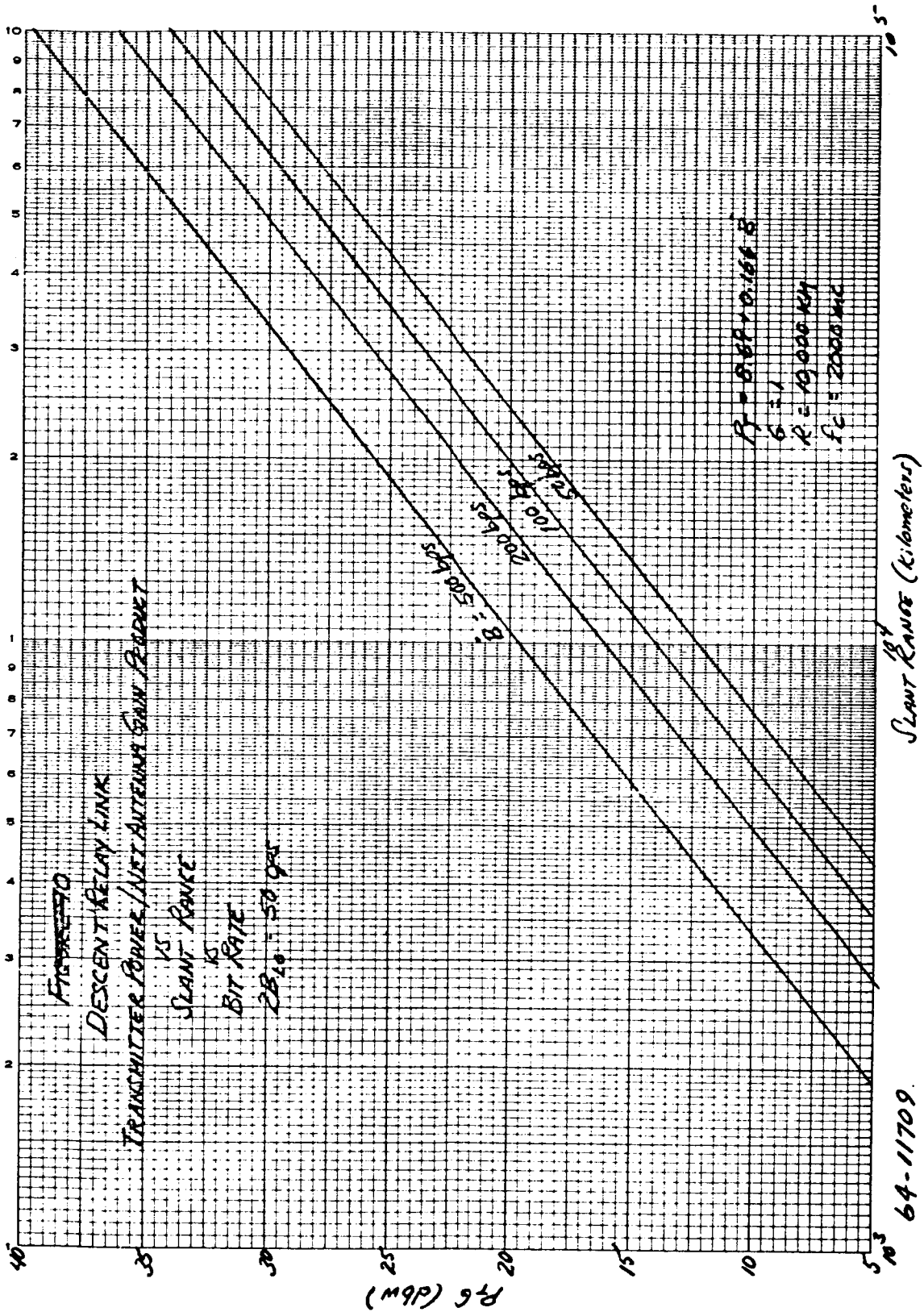


Figure 207 DESCENT RELAY LINK TRANSMITTER POWER/NET ANTENNA GAIN PRODUCT VERSUS SLANT RANGE VERSUS BIT RATE $2 B_{10} = 50 \text{ CPS}$

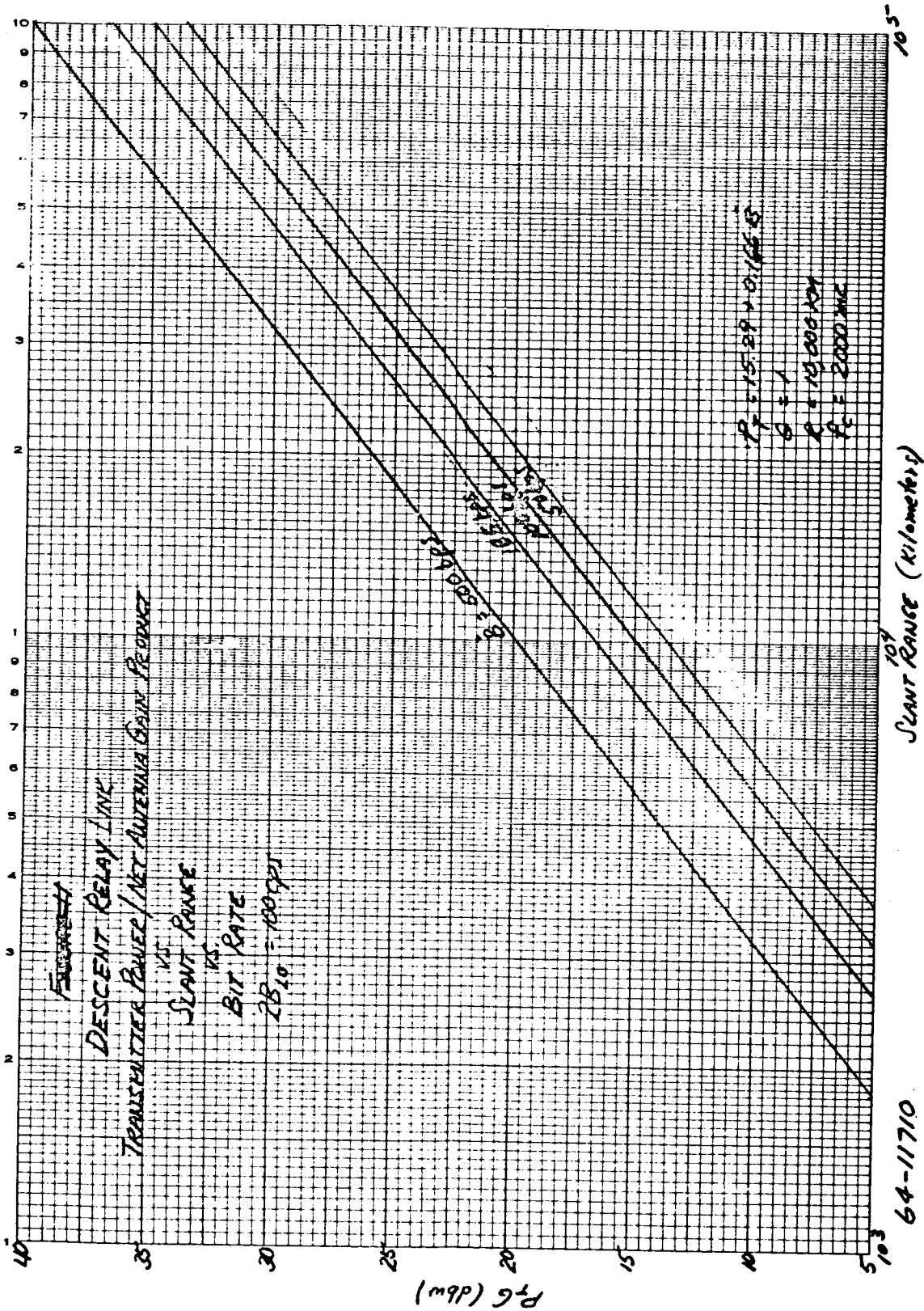


Figure 208 DESCENT RELAY LINK TRANSMITTER POWER/NET ANTENNA GAIN PRODUCT VERSUS SLANT RANGE VERSUS BIT RATE 2 $B_{10} = 100$ CPS

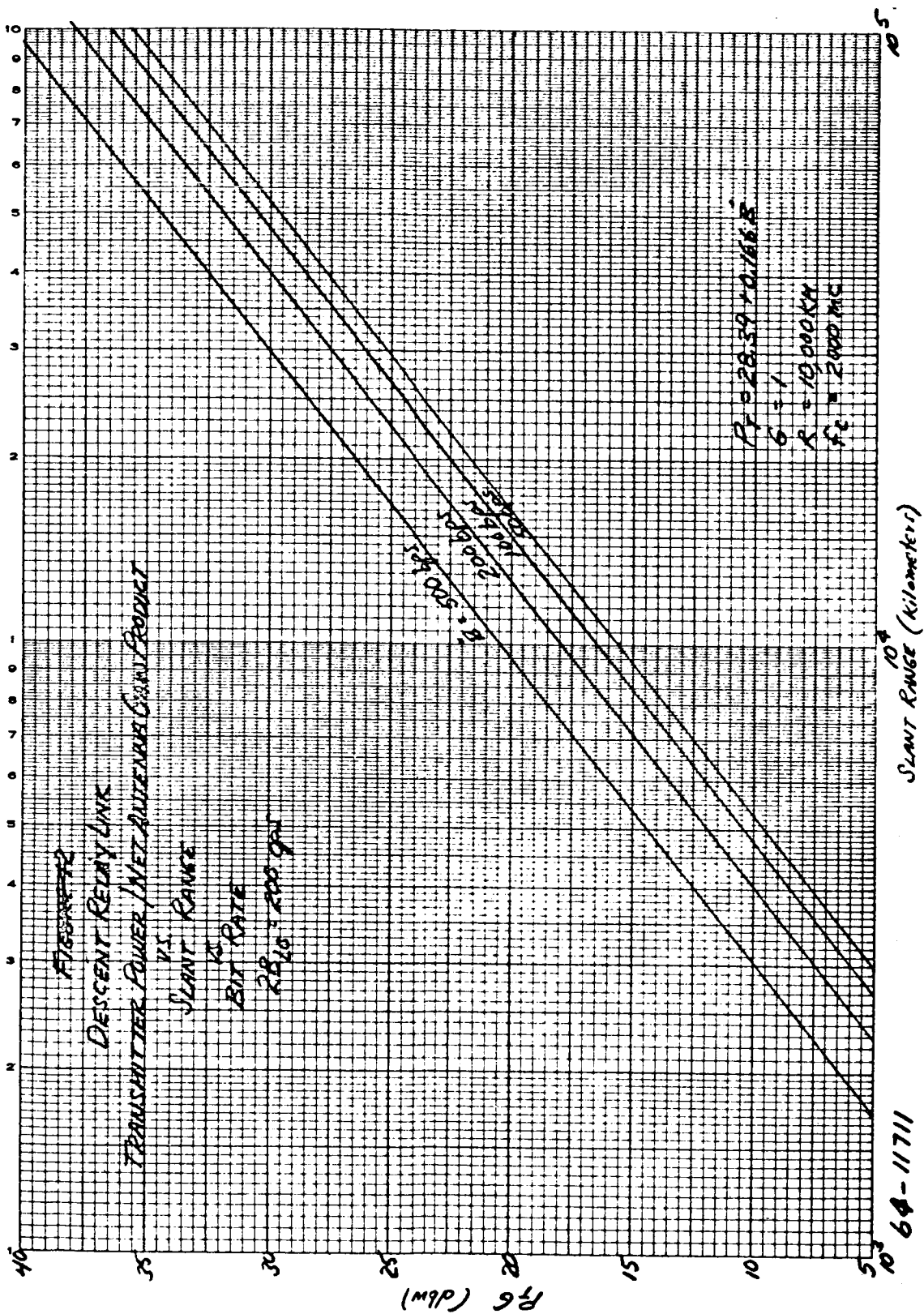


Figure 209 DESCENT RELAY LINK TRANSMITTER POWER/NET ANTENNA GAIN PRODUCT VERSUS SLANT RANGE
 BIT RATE $2 B_{10} = 200 \text{ CPS}$

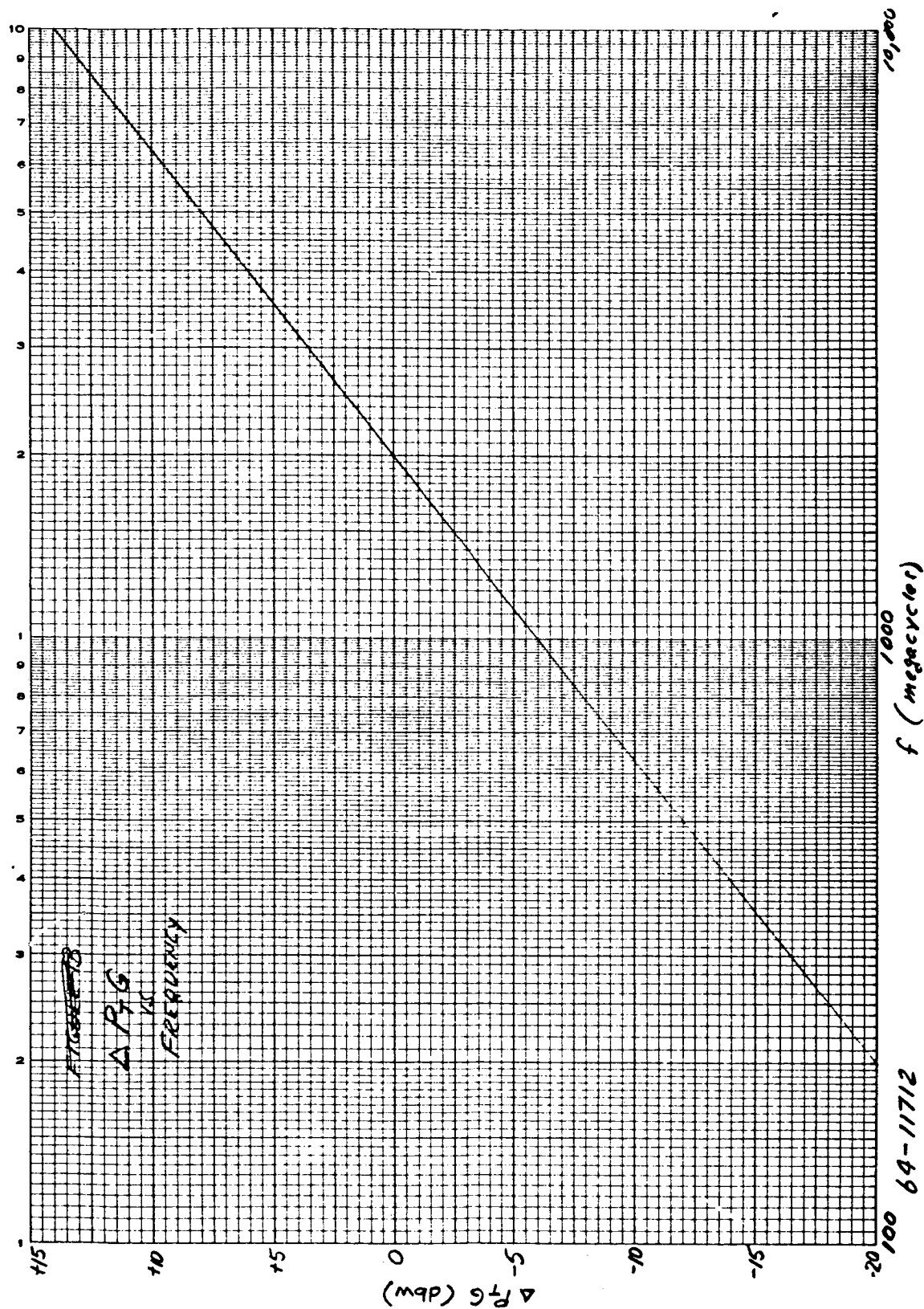


Figure 210 ΔP_G VERSUS FREQUENCY

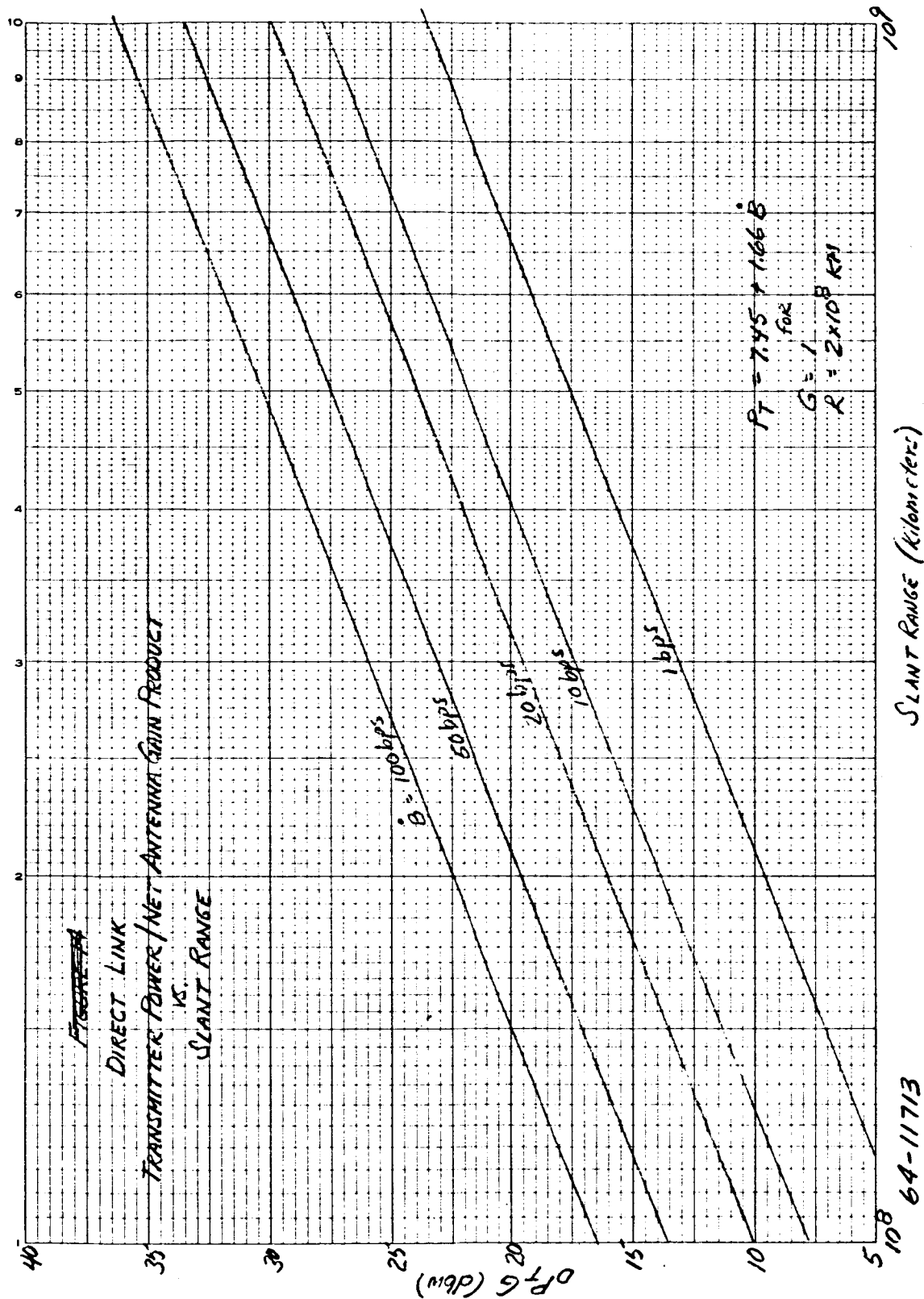


Figure 211 DIRECT LINK TRANSMITTER POWER/NET ANTENNA GAIN PRODUCT VERSUS SLANT RANGE

TABLE 43

TELECOMMUNICATIONS DESIGN CONTROL CHART

SUBJECT: ADVANCED MARINER

CHANNEL: LANDER TO DSIF

MODE: TELEMETRY (coherent PSK)

NO.	PARAMETER	NOMINAL VALUE (db)	TOLERANCE (db)	WORST VALUE (db)
1	Transmitting circuit loss	-0.5	± 0.2	-0.7
2	Transmitting antenna gain	---	---	0.0
3	Transmitting antenna pointing loss	---	---	0.0
4	Space loss = $32.46 + 20 \log F + 20 \log R$ F = 2295 mc, R = 2×10^8 km	-265.7	---	-265.7
5	Polarization loss	0.0	$+0.0$ -1.0	-1.0
6	Atmospheric absorption loss	---	---	---
7	Receiving antenna gain (210' DISH)	+61	± 1.0	+60
8	Receiving antenna pointing loss	---	---	---
9	Receiving circuit loss	-0.02	± 0.01	-0.03
10				
11				
12	Net circuit loss	-205.2	$+1.2$ -2.2	-207.4
13	Total transmitter power			
14	Total receiver power			
15	Receiver noise spectral density (N/B) T System $28^\circ\text{K} \pm 5^\circ\text{K}$ NF _____	-183.9*	± 0.7	-183.2*
16	Carrier APC noise BW ($2B_{LO} = 5$ cps)	7.0	---	+7.0

* dbm

TABLE 43 (Concl'd)

NO.	PARAMETER	NOMINAL VALUE (db)	TOLERANCE (db)	WORST VALUE (db)
17	Required Threshold SNR in $2B_{LO}$	+6.0	± 0.1	+6.1
18	Threshold carrier power	-170.9*	± 0.8	-170.1*
19	Total receiver power			
20	Carrier modulation loss			
21	Receiver carrier power			
22	Performance margin			
DATA CHANNEL				
23	Bit rate (1/t) = 1 bps	0.0	---	0.0
24	Required ST/N/B ($P_e = 10^{-3}$)	+7.4	± 0.6	+8.0
25	Threshold subcarrier power	-176.5*	± 1.3	-175.2*
26	Total receiver power			
27	Modulation loss			
28	Received data subcarrier power			
29	Performance margin			
SYNC CHANNEL				
30	SYNC APC noise BW ($2B_{LO} = 1.0$ cps)	0.0	---	0.0
31	Threshold SNR is $2B_{LO}$	+8.0	± 1.0	+9.0
32	Threshold subcarrier power	-175.9*	± 1.7	-174.2*
33	Total receiver power			
34	Modulation loss			
35	Received SYNC subcarrier power			
36	Performance margin			

*dbm

TABLE 44

TELECOMMUNICATIONS DESIGN CONTROL CHART

PROJECT: Advanced MarinerCHANNEL: Altimeter

NO.	PARAMETER	NOMINAL VALUE (db)	TOLERANCE (db)	WORST VALUE (db)
1.	Transmitting circuit loss	-1.0	± 0.5	-1.5
2.	Transmitting antenna gain	0.0	----	0.0
3.	Transmitting antenna pointing loss	0.0	----	0.0
4.	Space loss = $20 \log F + 30 \log R - 10 \log T - 19.4$ F = 9400 mc, R = 10 km, T = 10^{-6} sec.	-150.3	----	-150.3
5.	Polarization	-3.0	$+0.0$ -0.5	-3.5
6.	Atmospheric absorption loss	-0.0	$+0.0$ -0.1	-0.1
7.	Receiving antenna gain	0.0	----	0.0
8.	Receiving antenna pointing loss	0.0	----	0.0
9.	Receiving Circuit loss	-1.0	± 0.5	-1.5
10.	Reflectivity (0.01)	-20.0	----	-20.0
11.				
12.	Net Circuit Loss	-175.3	$+1.0$ -1.6	-176.9
13.	Total transmitter power			
14.	Total received power			
15.	Receiver noise spectral density (N/B) T System = 2900 °K (NF = 10db)			-163.9*
16.	Receiver noise BW ($2B_{LO} = 3$ mc)	+64.7	----	+64.7
17.	Required Threshold SNR in $2B_{LO}$	+14.5	± 0.5	+15.0
18.	Pulse Integration Improvement	0.0	----	0.0
19.	Threshold Signal Power	-84.7	-0.5	-84.2*

*dbm

The net circuit loss (Item 12) is the summation of Items 1 through 10. The transmitting circuit loss (Item 1) includes all attenuation between the transmitter output and the antenna output. The polarization loss (Item 5) is due to linear polarization of the transmitted signal and circular polarization of the received signal. Atmospheric absorption loss (Item 6) is assigned a two way value of 0.1 db. The receiving circuit loss (Item 9) takes into account the additional losses due to isolation. The transmitting and receiving antenna gain and pointing losses are incorporated in the parametric evaluation. The space loss (Item 4) is calculated for a reference range of 10 km, a reference pulse width of 10^{-6} sec. and a nominal frequency of 9400 mc. For the assigned antenna beamwidth of 20 degrees the cross sectional area illuminated by the radar is pulse-width limited; therefore the space loss is calculated as a function of R^3 .

Reflectivity coefficients (Item 10) of 0.1 and 0.01 have been included in the parametric evaluation. The total transmitter power (Item 13) is determined parametrically.

The receiver noise figure of 10 db was chosen with reference to typical receiver performance curves and also considers the degradation of the S/N ratio due to the target black body temperature. The signal BW of the receiver (Item 16) was selected as 3 mc and the threshold S/N ratio (Item 17) was assigned a value of 15 db. Both these values are consistent with existing technology. It has been assumed that pulse integration improvement (PII) varies as the square root of the number of pulses integrated up to 100 pulses. PII is treated parametrically. The threshold signal power required is the summation of items 15-18.

The following calculations are based on table 44. All results are worst case values and are plotted parametrically in figures 212 and 213, as a function of transmitter power and net antenna gain. The total power required is

$$\begin{aligned}
 P_T &= \text{Threshold Signal Power} - \text{Net Circuit Loss} \\
 &= -84.2 \text{ dbm} + 176.9 \text{ db} \\
 &= +92.7 \text{ dbm} \\
 &= 1.86 \text{ megawatts}
 \end{aligned}$$

The following example illustrates the use of figure 212. At a range of 10 kilometers and with a 100 pulse integration improvement a power gain product of 73 dbm is required. If a horn antenna having a 2.5λ aperture is used the gain is approximately 17 db, or 34 db two way. The resultant peak power required is 39.0 dbm or 7.9 watts.

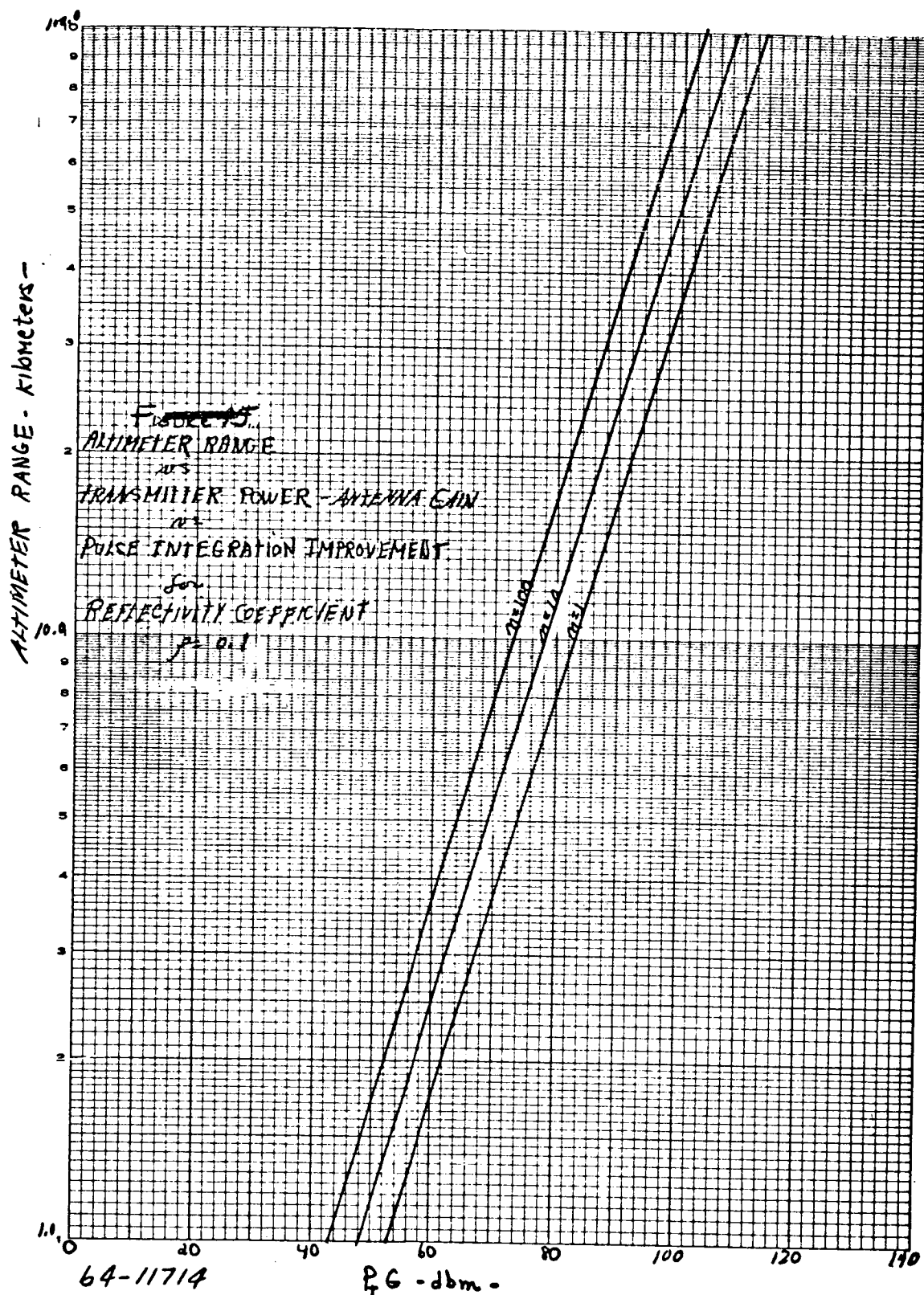


Figure 212 ALTIMETER RANGE VERSUS TRANSMITTER POWER - ANTENNA GAIN VERSUS PULSE INTEGRATION IMPROVEMENT FOR REFLECTIVITY COEFFICIENT

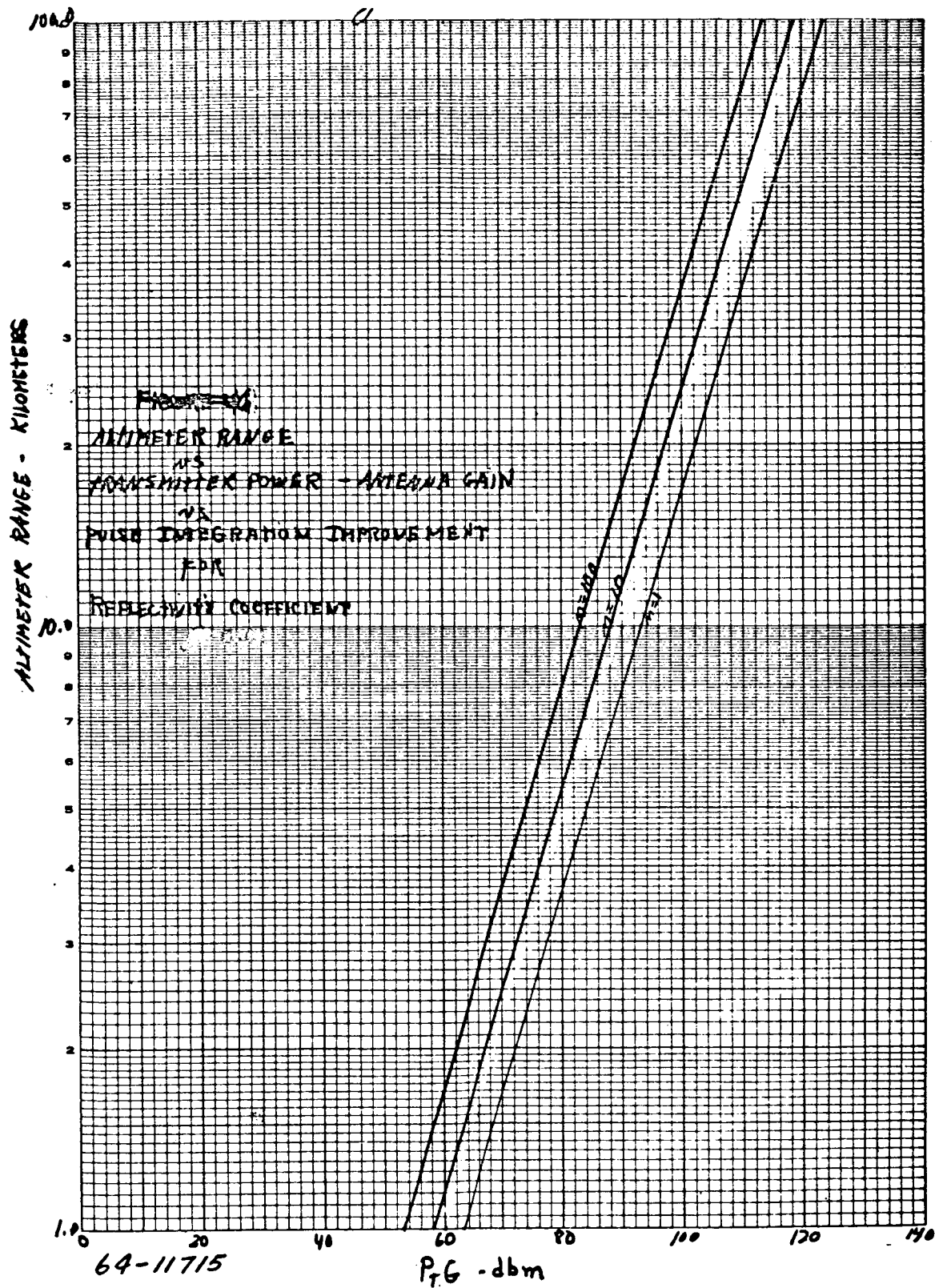


Figure 213 ALTIMETER RANGE VERSUS TRANSMITTER POWER - ANTENNA GAIN VERSUS PULSE INTEGRATION IMPROVEMENT FOR REFLECTIVITY COEFFICIENT

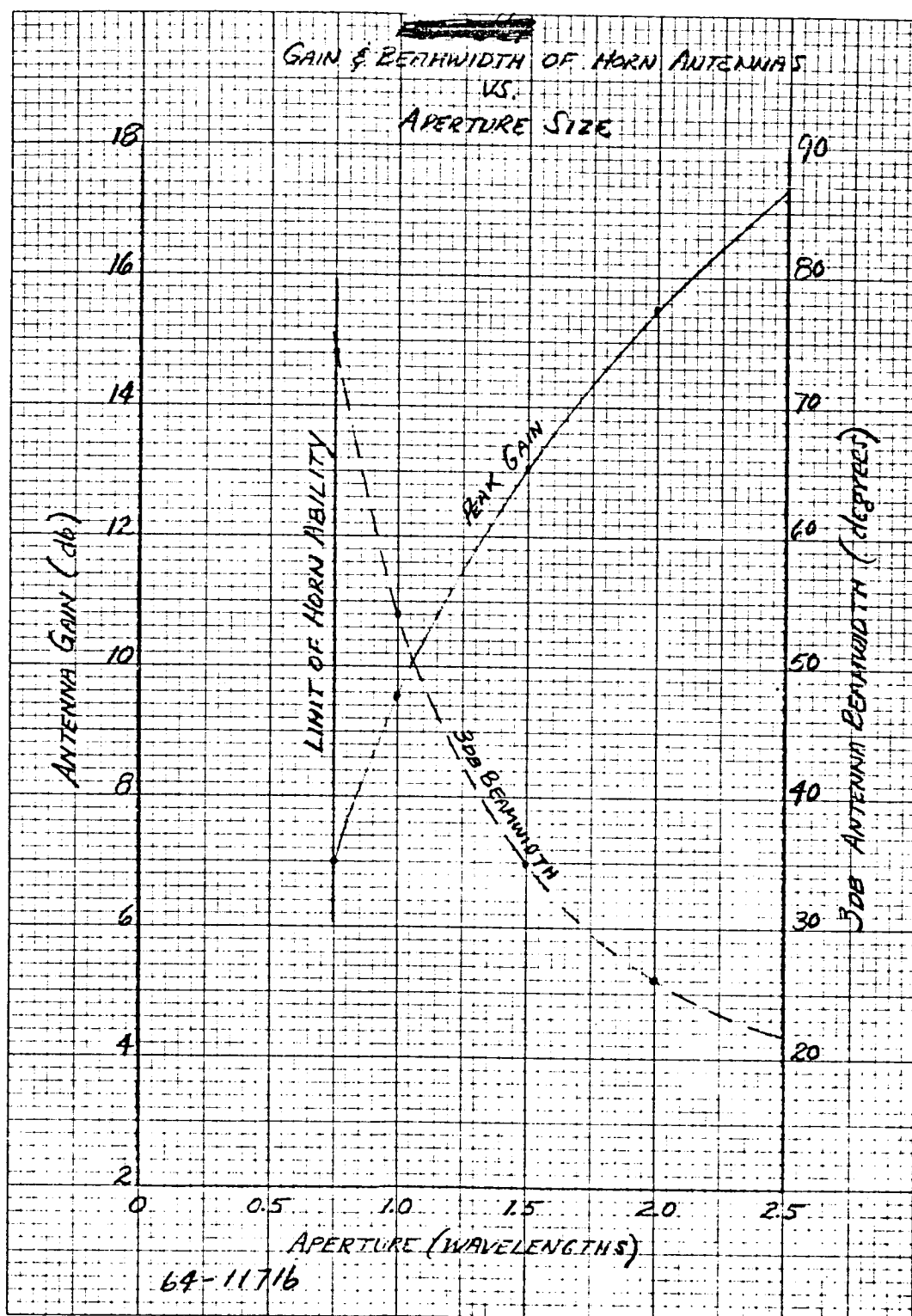


Figure 214 GAIN AND BEAMWIDTH OF HORN ANTENNAS VERSUS APERTURE SIZE

10.4 ANTENNAS

Single slot, slot arrays, parabolic, and horn antennas have been examined parametrically as possible candidates for the lander direct and relay telemetry antennas. The relative merits of each of these antenna types were determined from the points of view of lander dimensional constraints, lander-flyby bus and lander-Earth look-angle requirements, and transmitter power requirements.

10.4.1 Lander Link Antennas

Preliminary studies of lander to DSIF and lander to flyby bus look-angle requirements indicated that a maximum look-angle of approximately 50 degrees would be required in the direct link and 40 degrees in the relay link. These look-angle requirements indicated the possibility of selecting an antenna with directionality (gain). As discussed earlier, the antenna would require orientation after landing. The parabolic antenna was quickly eliminated as a candidate since the feed size would compromise the effective aperture area.

The single slot antenna was also eliminated as a design candidate. Although this antenna easily meets the minimum look-angle requirements, it is inherently a very wide beamwidth antenna and little can be done to narrow this beamwidth without resorting to an array of several slot antennas. This inability to reduce beamwidth results in two distinct disadvantages. First, the net antenna gain is lower at the required look-angle than could be obtained with a different antenna. Second, and most important, the wide beamwidth antenna pattern obtained with this antenna would make multipath fading highly probable in the telemetry link. Since a highly efficient modulation scheme such as PCM/PSK/PM is very susceptible to multipath fading, use of a single slot antenna would force selection of a modulation scheme such as pulsed linear chirp which minimizes this fading. This scheme would require much more transmitter power than PCM/PSK/PM to achieve a given performance level.

An array of slot antennas to narrow the beamwidth was eliminated as a design candidate for packaging and complexity reasons. At least two and most probably four antenna elements would be required in the array, and it would be difficult to achieve good circular polarization with an array. A circularly polarized antenna is desirable for both transmitting and receiving antennas since a 3 db improvement over a linear to circular scheme will be realized.

The horn antenna appears to best satisfy the overall system requirements. Beamwidths up to approximately 75 degrees can be achieved, and designs can be implemented to minimize sidelobes and to maintain good circularity (less than 1 db variation) over beamwidths up to twice the 3 db beamwidth.

The main disadvantage with the horn is its overall length dimension which is greater than one wavelength. Figure 214 shows peak gain and 3 db beam-width of horn antennas versus aperture size in wavelengths. Below an aperture size of 0.75 it is difficult to achieve a good antenna pattern. Figure 215 shows the horn aperture size in inches versus frequency and aperture size in wavelengths. Figure 216 shows the relative gain of the horn antenna versus look-angle.

10.4.2 Pre-entry Link Antenna

Examination of the look-angle requirements between the lander and flyby bus during the pre-entry phase indicated the need for a broadbeam antenna located on the forebody of this lander. A slot antenna was selected for this link.

10.5 POWER SOURCES

Three power sources were considered parametrically as candidates for the lander; a battery, a fuel cell, and an RTG/battery combination. Table 45 is a glossary of terms used in this section. Table 46 is a list of vendors contacted to provide information on the various power sources.

10.5.1 Battery Power Source

A Nickel-Cadmium battery was selected as the battery power source candidate. This type battery is the only one presently available that can withstand dry-heat sterilization at 135°C. Six watt-hours per pound is conservatively estimated to be the attainable conversion factor in making battery weight estimates. Justification for this figure is given at the end of this section. Figure 217 shows battery weight as a function of operating time parametrically as a function of all power users except the relay linked and direct link transmitters. Battery weight required to operate these transmitters is shown in figure 218 as a function of radiated power level and operating time.

a. Fixed Power Users

Fixed power users are defined as all science, all communication subsystems other than the transmitters, and all other users. Figure 217 is used to determine the incremental battery requirements for these users during the different phases of the lander mission. For example, during the entry phase, a certain set of science instruments are on, all communication subsystems are on (as defined above), and possibly some other set of power users is on. This total average wattage level, coupled with the time duration of the entry phase, will result in a battery weight (W_B). Similarly, W_B can be calculated for other phases such as post separation checkout and the

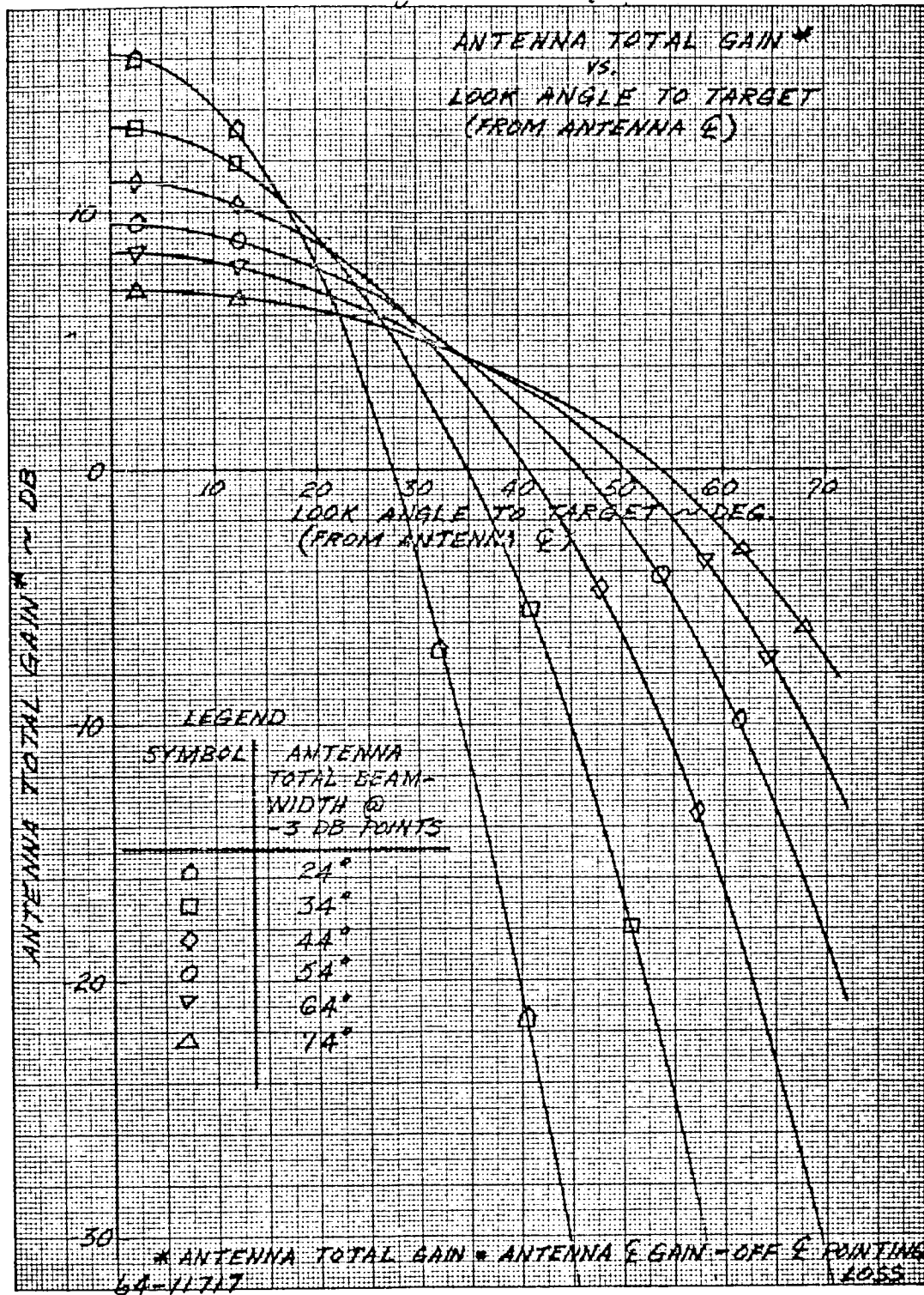


Figure 215 ANTENNA TOTAL GAIN* VERSUS LOOK ANGLE TO TARGET
(FROM ANTENNA E)

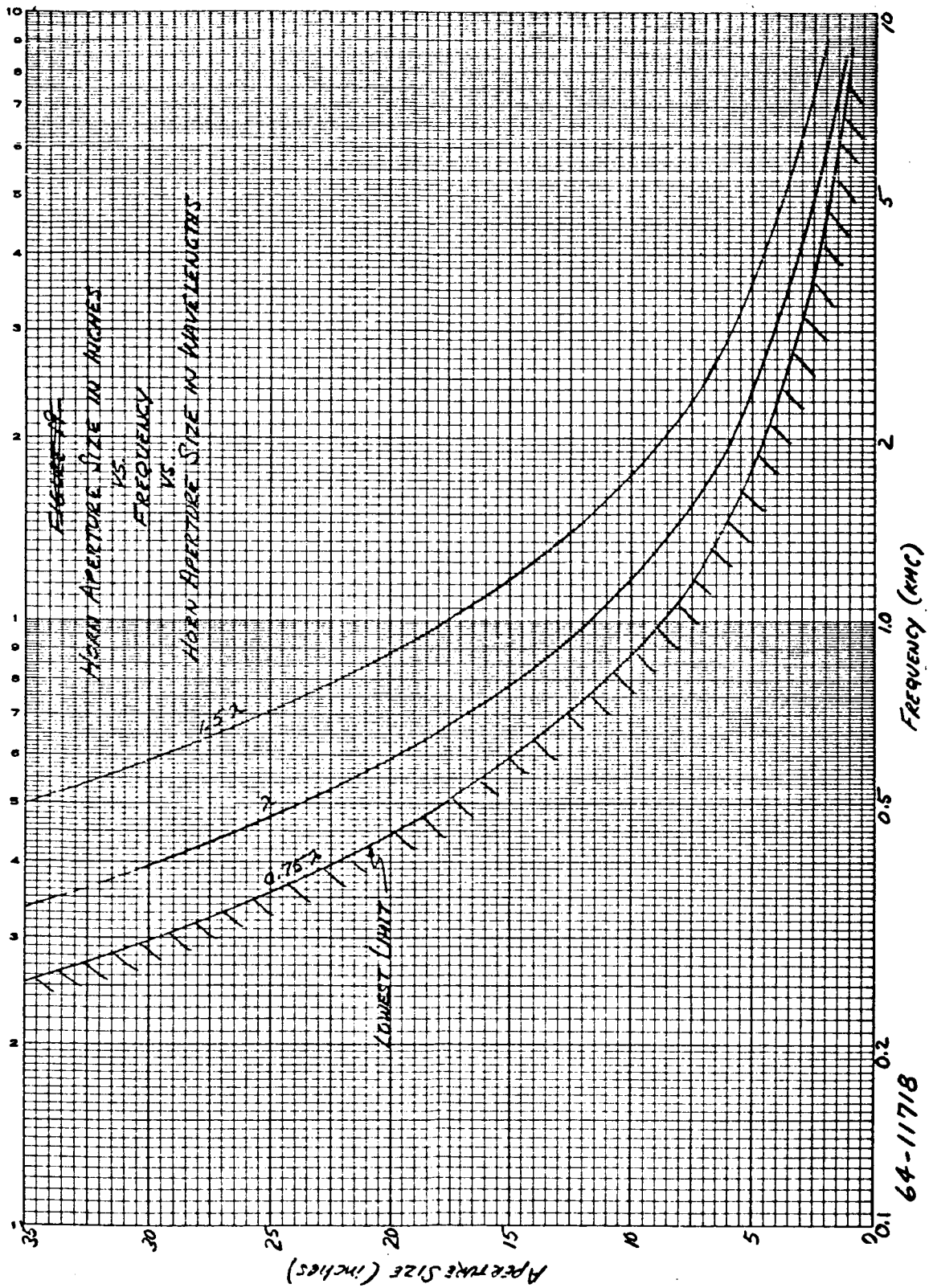


Figure 216 HORN APERTURE SIZE IN INCHES VERSUS FREQUENCY VERSUS
HORN APERTURE SIZE IN WAVELENGTHS

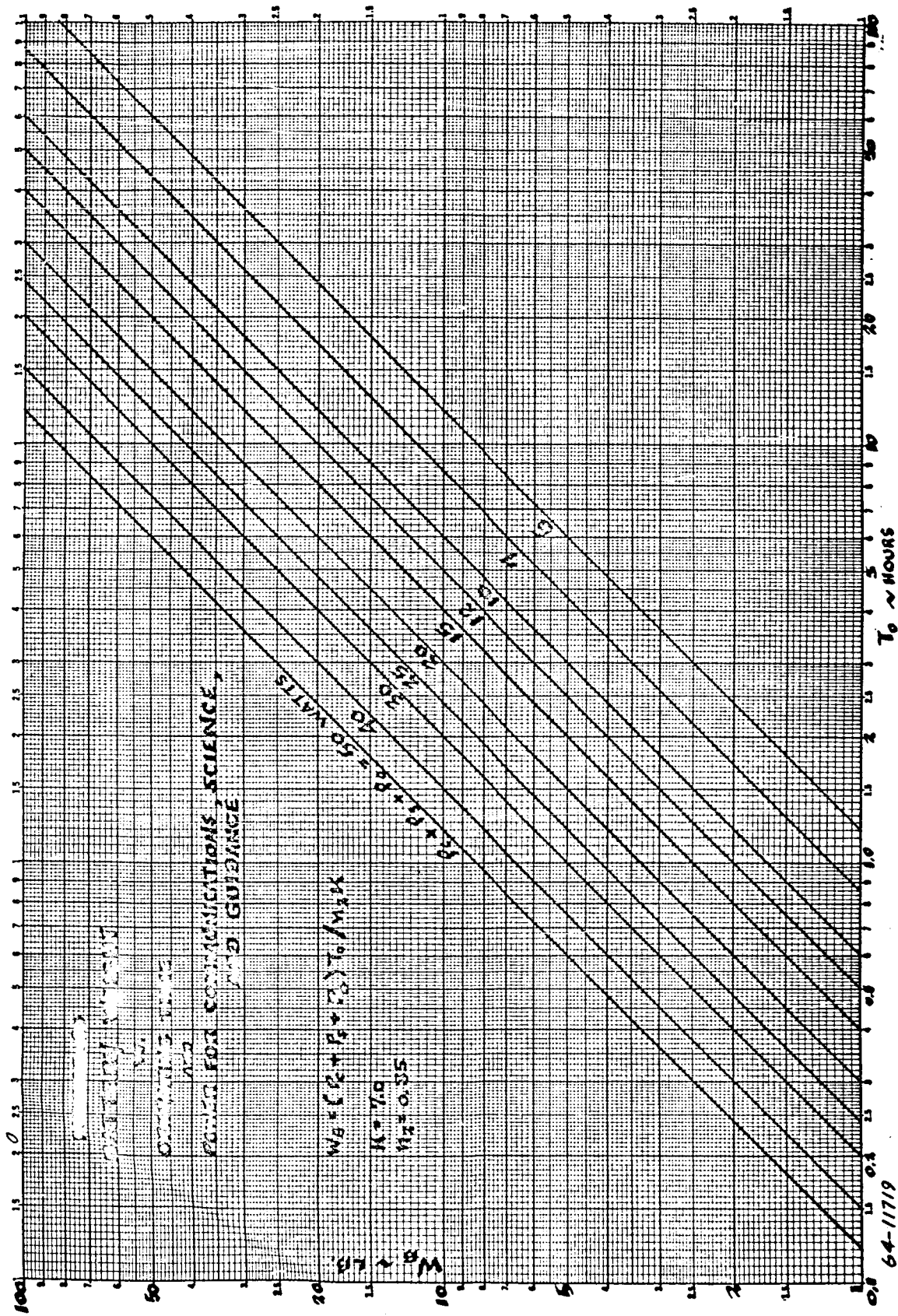


Figure 217 BATTERY WEIGHT VERSUS OPERATING TIME AND POWER FOR COMMUNICATIONS, SCIENCE, AND GUIDANCE

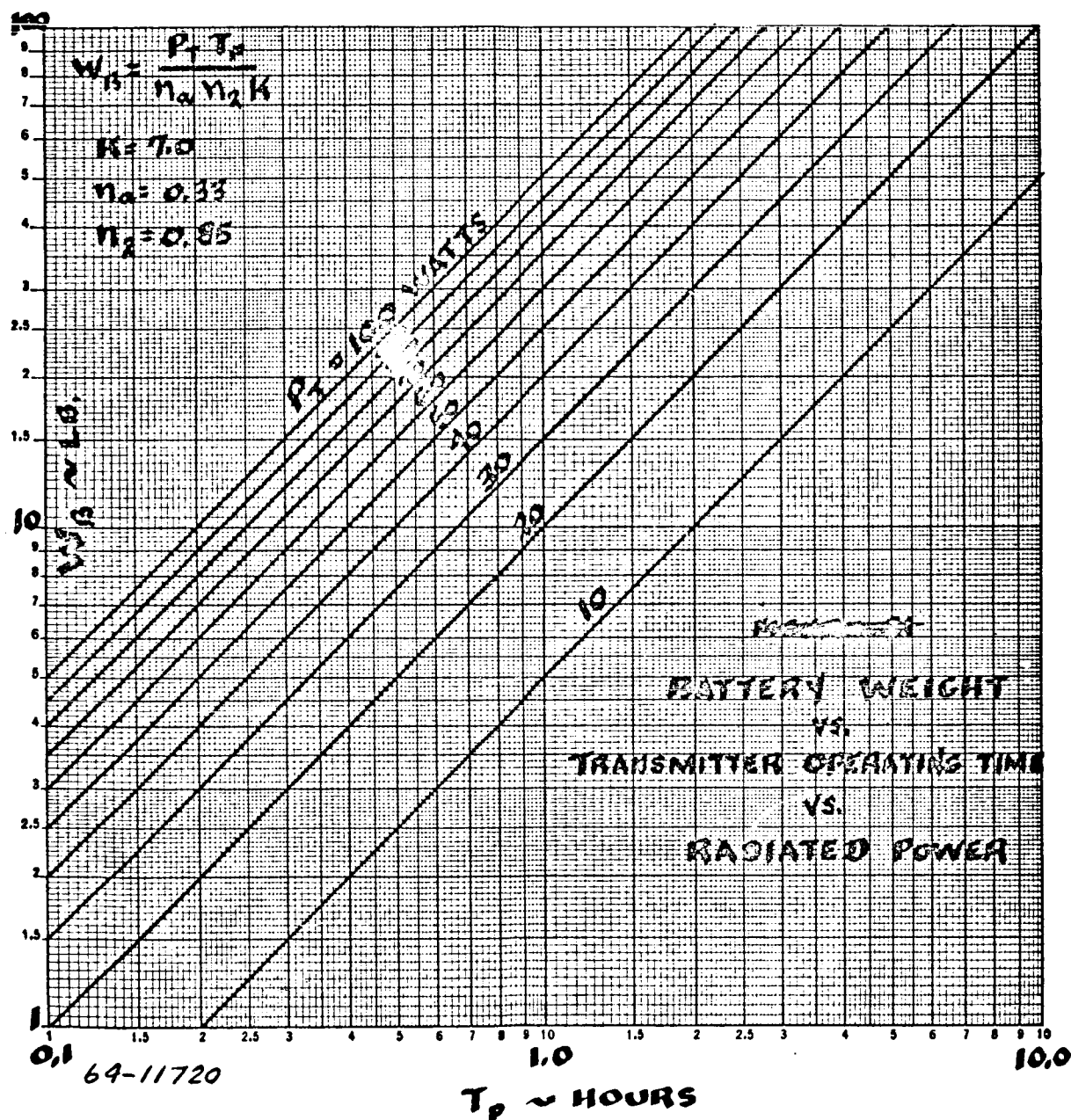


Figure 218 BATTERY WEIGHT VERSUS TRANSMITTER OPERATING TIME
VERSUS RADIATED POWER

TABLE 45
GLOSSARY OF TERMS

K	Battery watt-hour/pound ratio
P _c	Communication power except for transmitters (watts)
P _s	Power for science (watts)
P _o	Power other than P _c P _s P _T (watts)
P _{RTG}	RTG power output (watts)
P _T	Total radiated power from transmitter (watts)
n ₁	Efficiency of converter between RTG and load
n ₂	Battery discharge efficiency
n ₃	Battery charger efficiency
n ₄	Battery charging efficiency
n _a	Power Conversion Efficiency of transmitter
T _c	Recharge time (hours)
T _p	Playout time (hours)
T _o	Operating time for fixed power users (hours)
W _B	Battery weight (pounds)
W _{RTG}	RTG weight (pounds)

TABLE 46

LANDER POWER SYSTEM CONTACTS

<u>ITEM</u>	<u>CONTACT</u>
Nickel - Cadmium Battery	Sonotone Corporation Battery Division Elmsford, New York
Thermo-Electric Converter	A. RCA Electron Tube Division 415 S. Fifth Street Harrison, New Jersey B. Westinghouse Electric Corp. Defense Products Division 32 North Main Street Dayton 2, Ohio C. Minnesota Mining and Mfg. Co. 400 McKnight Road St. Paul 19, Minnesota
Thermionic Converter	Thermo-Electron Eng'g Corp. 85 First Ave. Waltham 54, Mass.
Radioisotopes	Monsanto Research Corp. Mound Lab. Miamisburg, Ohio
RTG System	Martin Co. (Marietta) Nuclear Division Baltimore 3, Md.
Fuel Cell	Electro-Optical Systems Inc. 300 N. Halstead St. Pasadena, Calif.

landed phase. The total battery weight for all phases is the summation of those incremental battery weights.

$$W_B = (P_c + P_s + P_o) T_o / \eta_2 K$$

In figure 217 K is 7 watt-hours/ pound and η_2 is 0.85.

b. Relay and Direct Link Transmitters

The battery weight required to operate each telemetry link transmitter is shown in figure 218. For each operation of a given transmitter (post separation, entry or post landing) allow approximately (2) minutes for warm-up.

$$W_B = P_T T_P / \eta_2 \eta_a K$$

In figure 21, K is 7 watt-hours/pound, η_a is 0.33 and η_2 is 0.85.

The energy storage device selected for use in the lander is a nickel cadmium battery. Nickel cadmium was chosen because it is the only battery presently capable of being heat sterilized at 135°C. (Sonotone Corp.).

Seven watt-hours per pound is used in the foregoing calculations of system weight for the following reasons:

The nominal maximum energy density of a nickel cadmium battery - measured at the battery terminals and with a depth of discharge of 100 percent - is 11 watt hours per pound. This is based upon a cylindrical configuration and magnesium packaging (Sonotone). A sterilized battery may lose as much as 10 percent of its capacity (Sonotone) and a depth of discharge of 70 percent brings the useable energy density to 7 watt-hours per pound. A 70 percent depth of discharge is consistent with high reliability for hundreds of cycles. The attainable energy density is a function of the battery discharge rate. In all battery calculations, the battery discharge efficiency (η_2) is assumed to be 85 percent. This results in an effective energy density of 6 watt-hours per pound.

10.5.2 A fuel cell is being considered as an alternative energy storage device to the nickel cadmium battery for the lander.

The fuel cell referred to is the hydrogen-oxygen regenerative system being developed by Electro Optical Systems Inc. In a letter dated 6/4/63 E. O. S. said "regarding the sterilization question, we feel that with little difficulty, materials which would not be adversely affected by the 300°F soak could be substituted where necessary."

Various values are given for the energy density, from a low of 18 w-hr/lb (SPS 37-17 confidential) for the prototype to a high of 38 w. hr/lb for the

design goal. Assuming the lowest value, the fuel should offer a factor of $\frac{18 \text{ wh}}{6 \text{ wh}}$ improvement in weight over the nickel cadmium system. However, the need for good voltage regulation is expected to reduce the minimum to 15 w. hr/lb resulting in an overall improvement of 2.5 (reduction of 0.4) over nickel cadmium batteries.

10.5.3 RTG/Battery Source

For extended life lander missions (many hours or days), the total energy required to operate the various subsystems will quickly rise to a point where a power storage device (such as a battery) will consume a major portion of the total payload weight. In these cases, a constant power device such as a radioisotope-thermoelectric (or thermionic) -generator (RTG) or a combination of constant power and power storage devices would be contenders for the lander power system. A survey has been made of radioisotope materials and both thermoelectric and thermionic converters to determine the feasibility of such a power system for the lander. The results of this study are given at the end of this section. The power storage device selected is the Ni Cad battery considered previously.

A general load profile for an extended lander mission employing both relay and direct telemetry links is shown in figure 219. It is assumed with this load profile that the power required by all communication and science subsystems is relatively constant and will be supplied in total by the RTG. During data transmission it is assumed that all power required by the transmitter is supplied by batteries. Figure 220 shows a simplified block diagram of the power system during data transmission; figure 221 shows the system during data acquisition when battery recharge occurs.

With these assumptions, the battery weight required to operate the transmitter is

$$W_B = P_T T_P / n_2 K \quad (8)$$

The watt-hours to be replaced, referred to the RTG, are

$$WH = W_B K / n_3 n_4 \quad (9)$$

The watt-hours available from the RTG to recharge the battery are

$$WH = [P_{RTG} - (P_c + P_s) / n_1] T_c \quad (10)$$

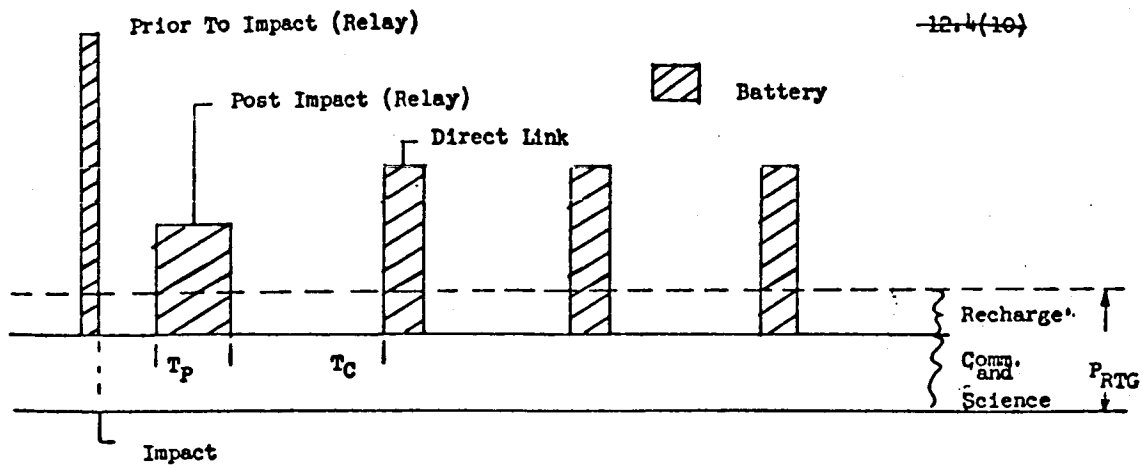


Figure 219 GENERAL LOAD PROFILE

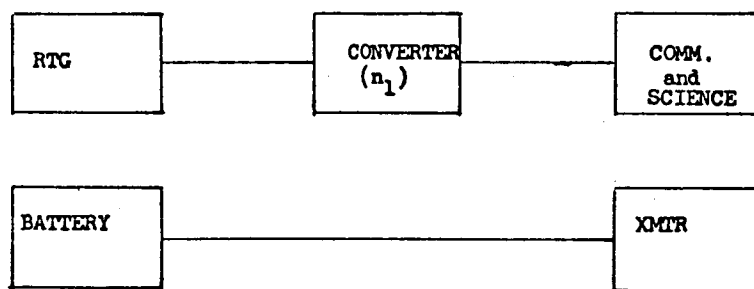


Figure 220 POWER SYSTEM DURING DATA TRANSMISSION

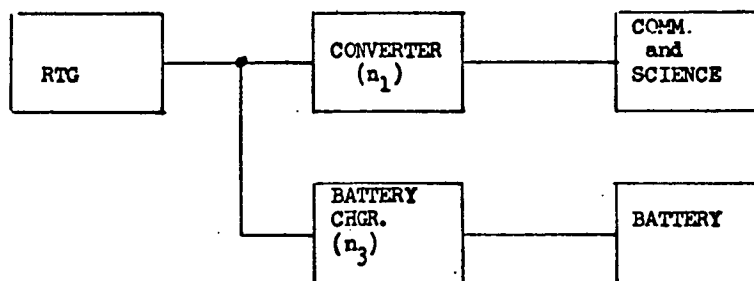


Figure 221 POWER SYSTEM DURING DATA ACQUISITION

To satisfy equation 2,

$$[P_{RTG} - (P_c + P_s)/n_1] T_c \geq W_B K/n_3 n_4 \quad (11)$$

$$P_{RTG} \geq W_B K/n_3 n_4 T_c + (P_c + P_s)/n_1 \quad (12)$$

Equation (8) is plotted in figure 218. Figure 222 shows the RTG power required to satisfy the fixed communication and science subsystem requirements. Figure 223 shows the added RTG power required to recharge the battery.

The general load profile in figure 219 indicates three different transmitter power levels, one associated with a relay telemetry link prior to landing, one with a relay telemetry link after landing, and one with a direct link after landing. The battery size required to operate these transmitters will of course be dictated by the larger of the three energy requirements. This battery weight can be determined from figure 218. The total RTG output power required can be determined as follows:

- a. For $P_c = 20$ watts and $P_s = 15$ watts, figure 222 shows that 39 watts of RTG power are required for $n_1 = 0.9$.
- b. If a 30-watt transmitter operating for 1 hour is the largest energy consumer in the three telemetry links, figure 218 shows that a 7.5 pound battery is required.
- c. If this battery must be recharged in 15 hours, figure 223 shows that $\Delta P_{RTG} = 7$ watts.
- d. Total RTG power is therefore 46 watts.

The weight of the RTG (less shielding) is shown in figure 241.

The major criteria for selection of a suitable RTG model for this study involved selection of a suitable converter and radioisotope. Selection was based on the following:

- 1) 1965 Technology
- 2) Availability
- 3) Mission Life
- 4) Weight

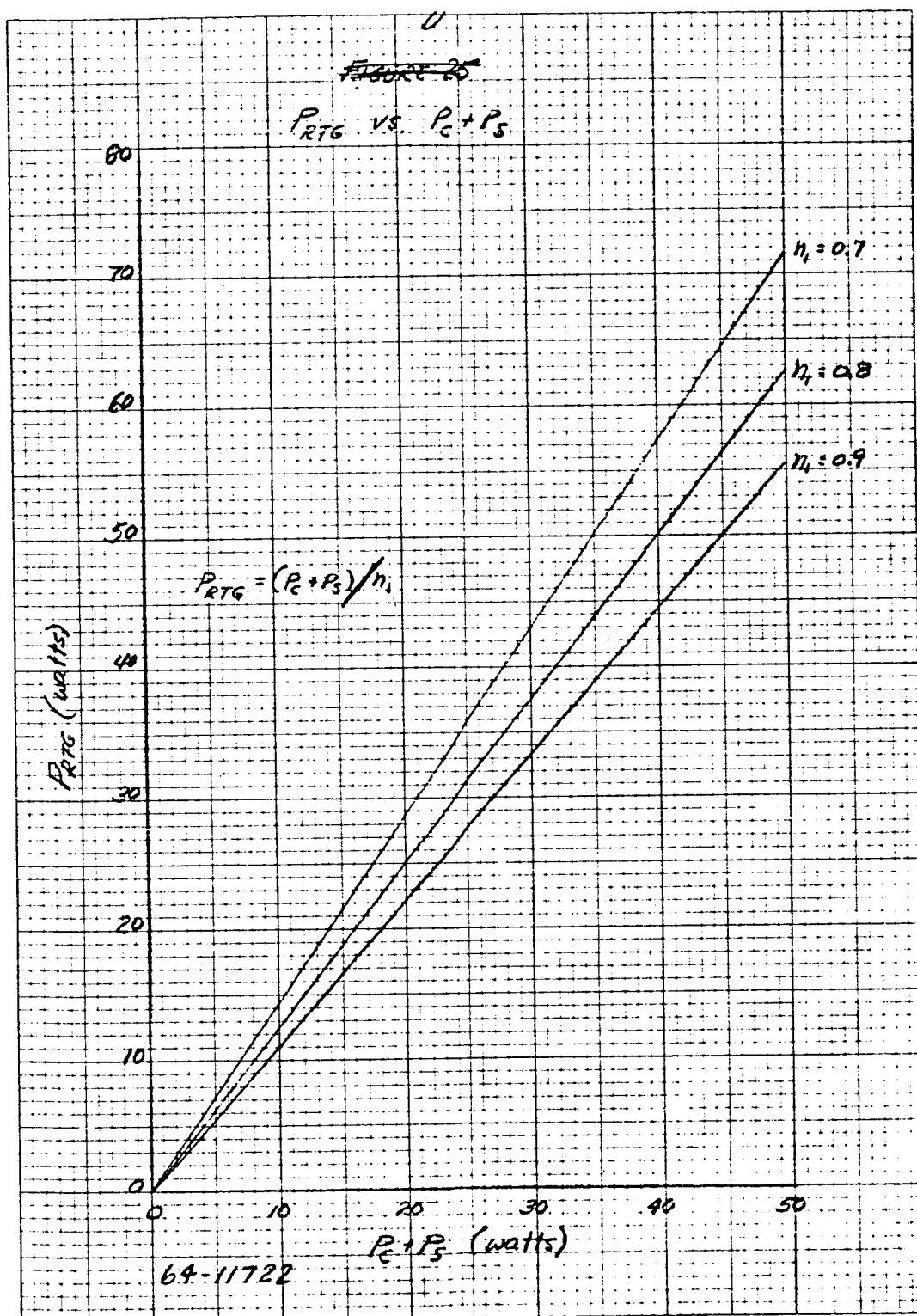
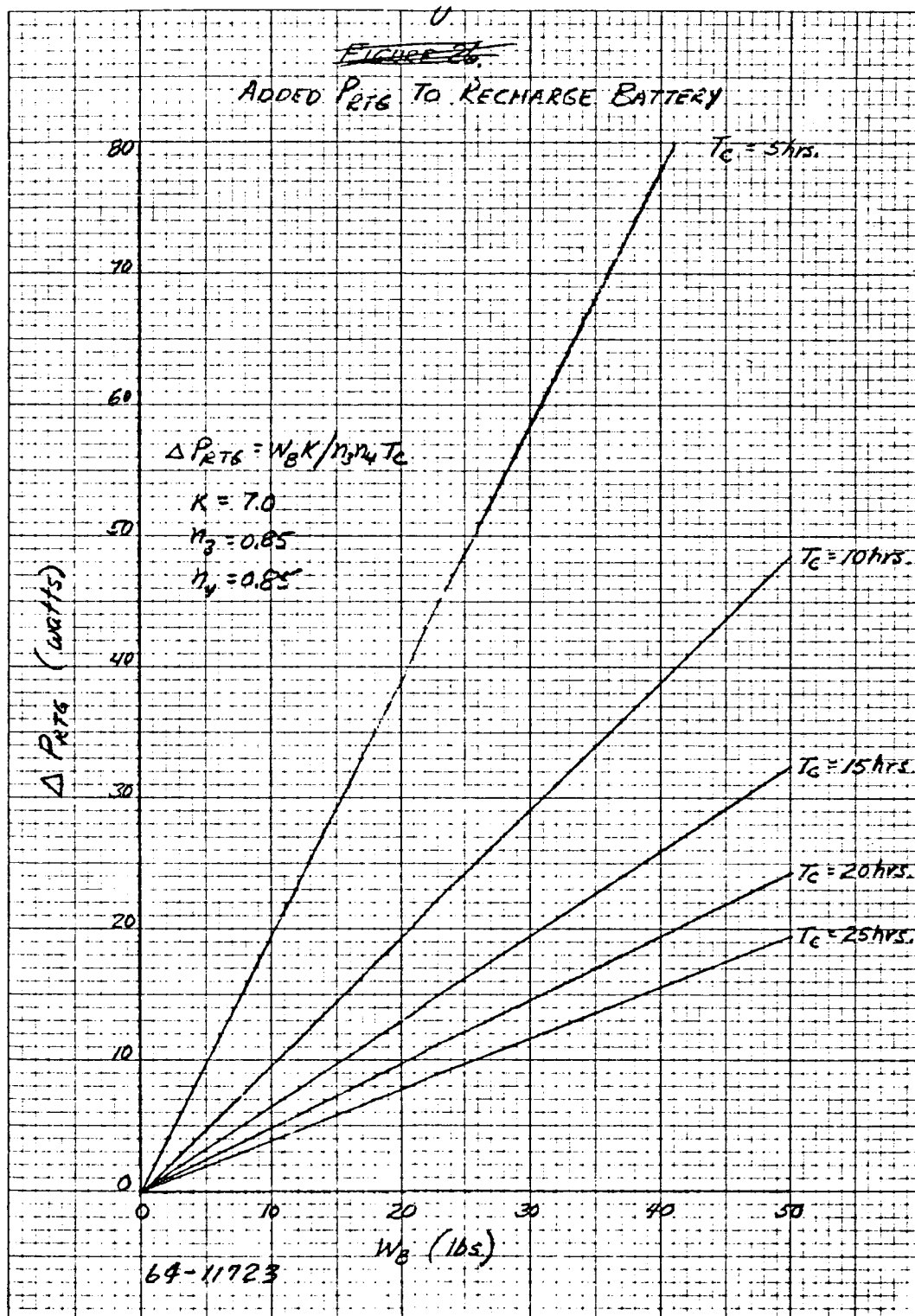


Figure 222 PRTG VERSUS P_C + P_S

411


Figure 223 ADDED P_{RTG} TO RECHARGE BATTERY

5) Volume

6) Cost

a. Converter Selection:

Both thermoelectric and thermionic converters were considered as design candidates. The following study results indicate that a thermoelectric converter is the only real choice at this time.

1) 1965 Technology

Both Lead Telluride ($P_b - T_e$) and Silicon-Germanium ($Si - Ge$) thermoelectric devices have received considerable environmental testing. In particular, $Si - Ge$ thermocouples have been subjected to shock tests up to 200 g without failure, acceleration up to 10 g, and many thermal shock tests. No environmental testing to the same degree has been reported on thermionic devices in 1964; however, some are scheduled for early 1965. The outcome is expected to be good.

2) Availability

According to RCA, manufacture of $Si - Ge$ thermoelectric modules will be on a production basis in 1965. Thermionic converters (for RTG application) are still in a laboratory development stage and are not expected to be in any production status until 1966 or later.

3) Mission Life

The required life of an RTG power source will be on the order of one year (approximately 9000 hours). Thermoelectric systems using Lead-Telluride have exceeded this requirement and as of May 1964 Silicon - Germanium has exceeded 7000 hours without failure.

All information in the open literature relating to life testing indicate thermionic generator failure before 1000 hours. Classified test programs are known to have exceeded this figure but not by a substantial amount.

4) Weight

RTG systems using thermionic converters are expected to achieve about 5 watts per pound at 500 watt outputs when fully developed. This compares with 2 to 4 watts per pound at this level for the best

thermoelectric devices. At the 100 watt output level the range for thermoelectrics is 1 to 2 watts/lb. as compared to 3-4 watts/lb. for the thermionic converter. However, the apparent superiority of the thermionic converter is based on operating temperatures in the order of 1600° to 1800°K. At this temperature level serious material problems occur which have not apparently been solved yet. At the lower and more practical operating temperatures of 1000°K there is no particular weight advantage for either converter.

5) Cost

The predicted cost per watt of electrical output is given as 10 to 15 dollars for Silicon - Germanium thermoelectric converter.⁵ Lead-Telluride is expected to be slightly higher. A thermionic converter will cost at least 10 to 20 times this amount.

b. Isotope Selection

1) Mission life

Because of the required minimum life of 1 year, only the following current reduction radio-isotopes were considered:

Cesium 137, Curium 244, Plutonium 238, Promethium 147, Strontium 90 and Cobalt 60.

2) Availability

The assumption is made that sufficient quantities of a radio-isotope must be available no later than the middle or end of 1967. Calculations based on projected new production facilities cannot be considered.

Using a value of 10 percent efficiency, for a 100 watt electrical output, at least a 1000 thermal watt input must be available after one year of operation. The original amount required varies with the isotope half-life.

Promethium 147 is heavily dependent on construction of new production facilities so this eliminates this highly desirable radio-isotope.

3) Weight and volume

Strontium 90 and Cobalt 60 require heavy shielding against gamma radiation. For example, at least 15 cm of Uranium shielding

would be needed to produce a dose of 10^{-2} millirads/hr. 100 cm from the isotope source center. At the 1000 thermal watt level, Cesium 137 also requires relatively heavy shielding. This is due to its large volume (in excess of 4200 cm^3) and high weight (in excess of 1400 gms). This large volume coupled with considerable gamma and X radiation requires shielding exceeding that for Strontium 90. For these reasons Strontium 90, Cobalt 60 and Cesium 137 were eliminated as possible candidates.

4) Comparison of Curium 244 and Plutonium 238

Of the two remaining candidates, table 47 lists the salient characteristic of each.

TABLE 47
COMPARISON OF CURIUM 244 AND PLUTONIUM 238

	Cm 244	Pu 238
Approx. Weight required for 1 KW (thermal) source	350 gm	2400 gm
Approx. Volume required for 1 KW (thermal source)	90 cm^3	550 cm^3
Safety (Biological) Rating	$10^{-9} \text{ } \mu\text{C/cc}$	10^{-12} C/cc
Gamma Shielding Req'd (10^{-2} milli rads/hour 100 cm from source)	10 cm Uranium	4 cm Uranium
Dollars/Thermal Watt	>Pu 238	\$200-\$1000

In spite of the thicker lead shielding required for Cm 244 as compared with Pu 238, the total volume (and weight) required is comparable because of the smaller volume of Cm 244 isotope material needed. However, the neutron penetration depth is so much greater for Cm 244 that for transistorized instruments restricted to a maximum dose of 10^4 reps, the required thickness of shielding would be too great.

This must be weighed against the fact that Pu 238 is poor from the handling (inhalation) point of view. If availability and expected cost per thermal watt is further compared, then Pu 238 is chosen as the candidate radio-isotope.

The form of radio-isotope is Plutonium Dioxide PuO_2 having a specific power of 0.396 watts/gm, thermal Density of 3.6 watts/cm^3 .

10.6 COMMUNICATION SYSTEM HARDWARE

The lander communication system includes the radar altimeter and all subsystem associated with the collection, storage and transmission of data. These subsystems include the antennas, transmitters, storage subsystem, data handling subsystem and programmer. The parametric data accumulated on these subsystems was obtained from the manufacturers listed in table 48.

10.6.1 Antennas

A horn antenna was selected for the landed phase direct and relay links and for the radar altimeter. Figure 224 shows horn dimensions in wavelengths, (λ). The L dimension must be greater than 0.75λ . Figure 225 shows horn antenna weight as a function of frequency for three materials; steel, aluminum and magnesium. The horn will be pressurized to prevent power (corona) breakdown. For this reason a factor of two is included in the weight estimates to allow for a dielectric radome over the horn aperture.

10.6.2 Transmitters

The transmitter in this study is assumed to consist of an exciter and a power amplifier. The exciter includes a stable oscillator, varactor frequency multiplier, phase modulator, and power amplifiers up to the drive level needed by the main power amplifier. The main power amplifier includes the amplifier tube and power converter.

a. Exciter

An all solid state exciter was selected as a model for this study. Figure 226 shows exciter weight, volume, power conversion efficiency (ratio of rf power output to total dc power input) and maximum useful power output attainable as a function of frequency. As an example, if the required direct link (2295 mc) outpower power from the main power amplifier is 20 watts, and this amplifier has 20 db power gain, the drive power required from the exciter is 200 milliwatts. As indicated in figure 226, this power level is well within the 2.5 watt maximum power available at this frequency. The exciter will have a weight of approximately 4.5 pounds, volume of 80 in.³, and will consume approximately 5 watts.

b. Power Amplifier

At frequencies above 200 megacycles, the power available from solid state devices diminishes rapidly. For applications such as the lander, the choice of suitable vacuum tube amplifiers to achieve a required output level is limited. For the direct link (2295 mc), the Amplitron amplifier manufactured by Raytheon Company has been used as a

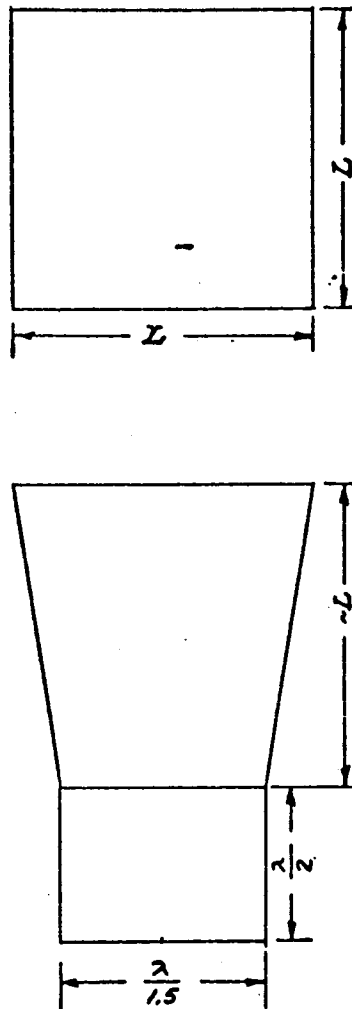
TABLE 48

LANDER COMMUNICATION SUBSYSTEM CONTACTS

<u>Subsystem</u>	<u>Manufacturer</u>
Antennas	Avco RAD Wilmington, Mass.
Transmitter	
a. Exciter	Avco, Electronics Division 2630 Glendale-Milford Road Cincinnati 41, Ohio
b. Power Amplifier	Raytheon Company Hartwell Road Bedford, Mass.
	General Electric Receiving Tube Dept. Owensburg, Kentucky
	Watkins-Johnson Co. Palo Alto, California
	Hughes Microwave Tube Division Los Angeles, California
Solid State Memories	
a. Core Memory	Electronic Memories, Inc. 12621 Chadron Ave. Hawthorne, California
b. Thin Film Memory	International Business Machines Federal Systems Division 7220 47 th Street Bethesda, Maryland
c. Plated Wire Memory	Sperry Rand Corporation Univac Division P. O. Box 500 Blue Bell, Pennsylvania

TABLE 48 (Concl'd)

<u>Subsystem</u>	<u>Manufacturer</u>
Tape Recorders	Electronic Specialty Co. Electronics Division 5121 San Fernando Road Los Angeles, California
	Leach Corporation Controls Division 717 N. Coney Ave. Azusa, California
	Borg Warner Control P. O. Box 1679 Santa Ana, California
Data Handling Subsystem and Programmer	Texas Instruments Inc. Apparatus Division 6000 Lemon Avenue P. O. Box 6015 Dallas 22, Texas



64-11724

Figure 224 HORN ANTENNA DIMENSIONS IN WAVELENGTHS

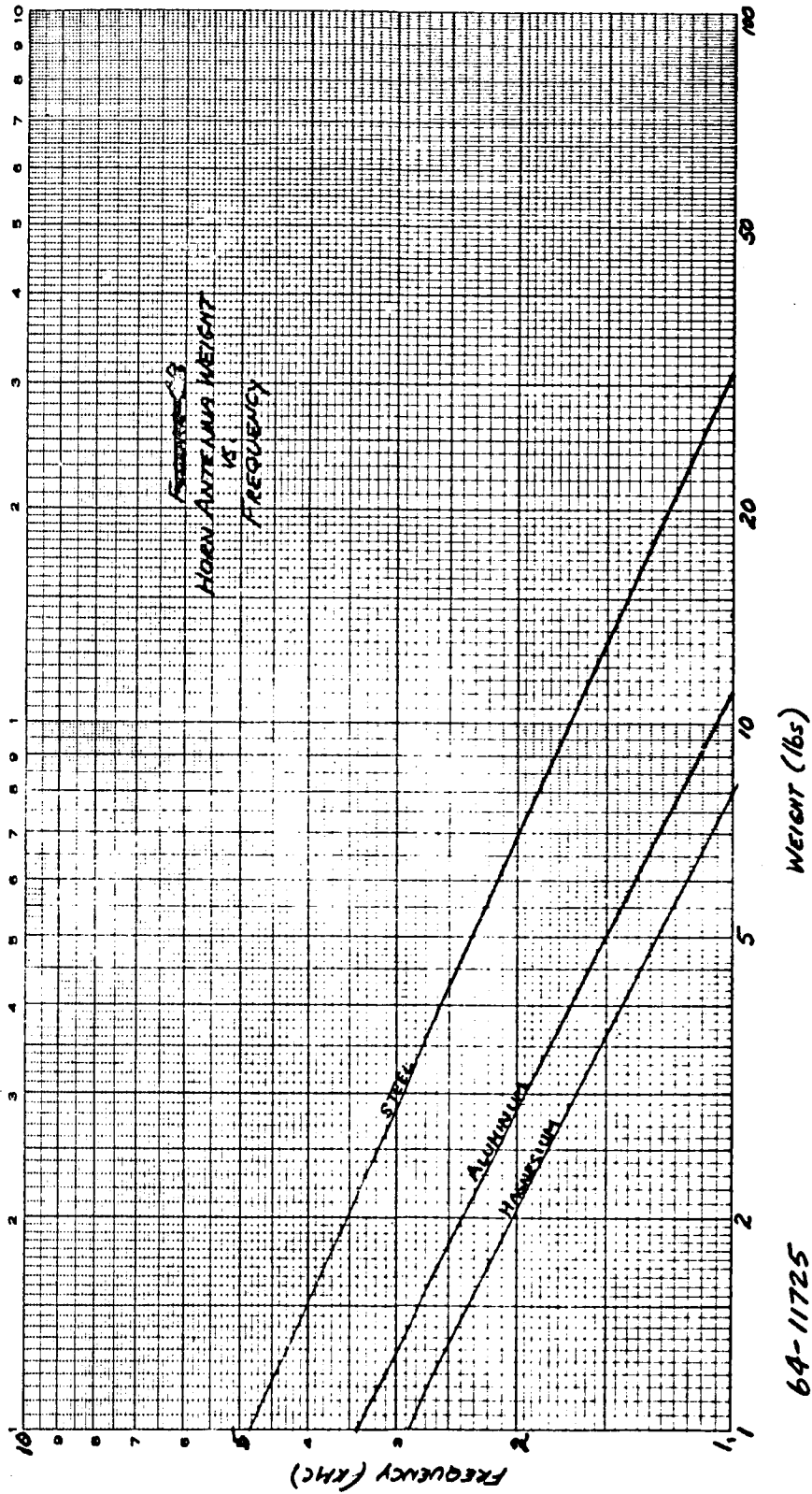
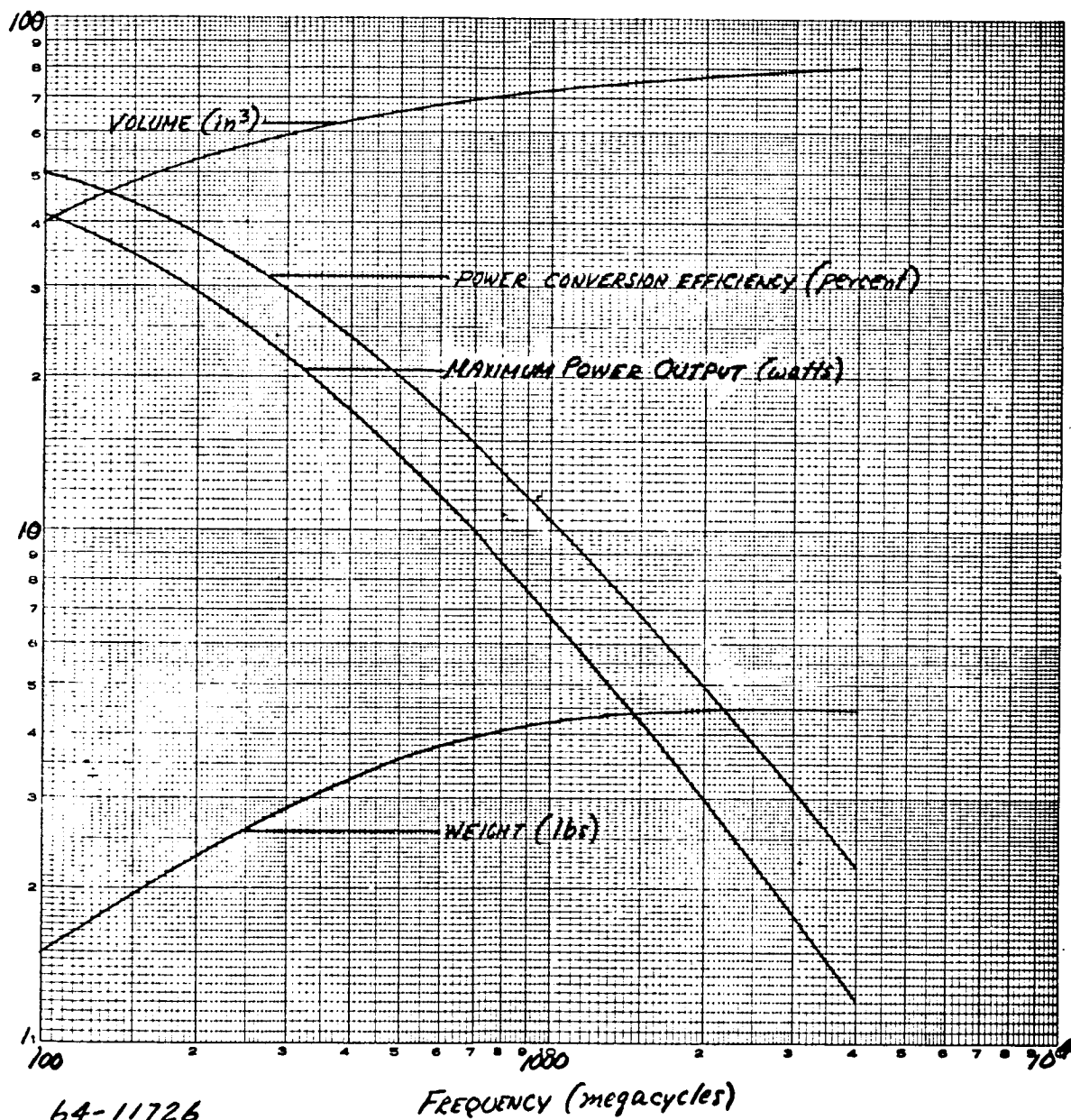


Figure 225 HORN ANTENNA WEIGHT VERSUS FREQUENCY

64-11725



64-11726

Figure 226 SOLID STATE EXCITER WEIGHT, VOLUME, POWER CONVERSION EFFICIENCY, AND MAXIMUM POWER OUTPUT VERSUS FREQUENCY

421

reference in this study. Other tubes such as planar ceramic triodes manufactured by General Electric Company have also been considered. Figures 227, 228, 229, and 230 show Amplitron weight, volume efficiency and drive power required, respectively, as a function of output power for the 3 amplifier configurations shown in figure 231. Configuration A is simply an amplitron operating at the required output power. Configuration B is a redundant mode. In the event of failure of the normal amplifier, the emergency amplifier would be turned on. The normal amplifier would then appear as a lossy (2.2 db) waveguide. Configuration C is a high power mode in that one amplitron is used to drive the succeeding stage. An isolator is required between amplifiers in this mode. For a 30-watt amplifier, figure 229 shows that 37 percent conversion efficiency is achievable with configuration A. Figure 230 shows that approximately 0.5 watt of drive power is required for this amplifier. Figure 226 shows that the exciter efficiency would be on the order of 4.5 percent. The total transmitter efficiency would then be approximately 33 percent. This efficiency has been assumed in all transmitter power consumption calculations.

Figure 232 shows amplifier efficiency as a function of frequency for 10-20- and 70-watt amplitrons.

10.6.3 Storage Subsystems

Both solid state memories and magnetic tape recorders were considered as possible storage system candidates. Study results indicate that the solid state memory is preferable. At the higher g levels, the problems associated with recorder design are considerable; also, with dry heat sterilization at 135°C, there is some doubt that a suitable tape can be obtained.

a. Solid State Memories

Ferrite core and plated wire memories were selected as possible candidates for a solid state storage system. Ferrite Core and plated wire memories have approximately the same bit density and specific gravity figures, but the plated wire memory consumes less power. The storage environment of the plated wire memory is over 150°C, while the ferrite core memory has a maximum storage temperature of 125°C.

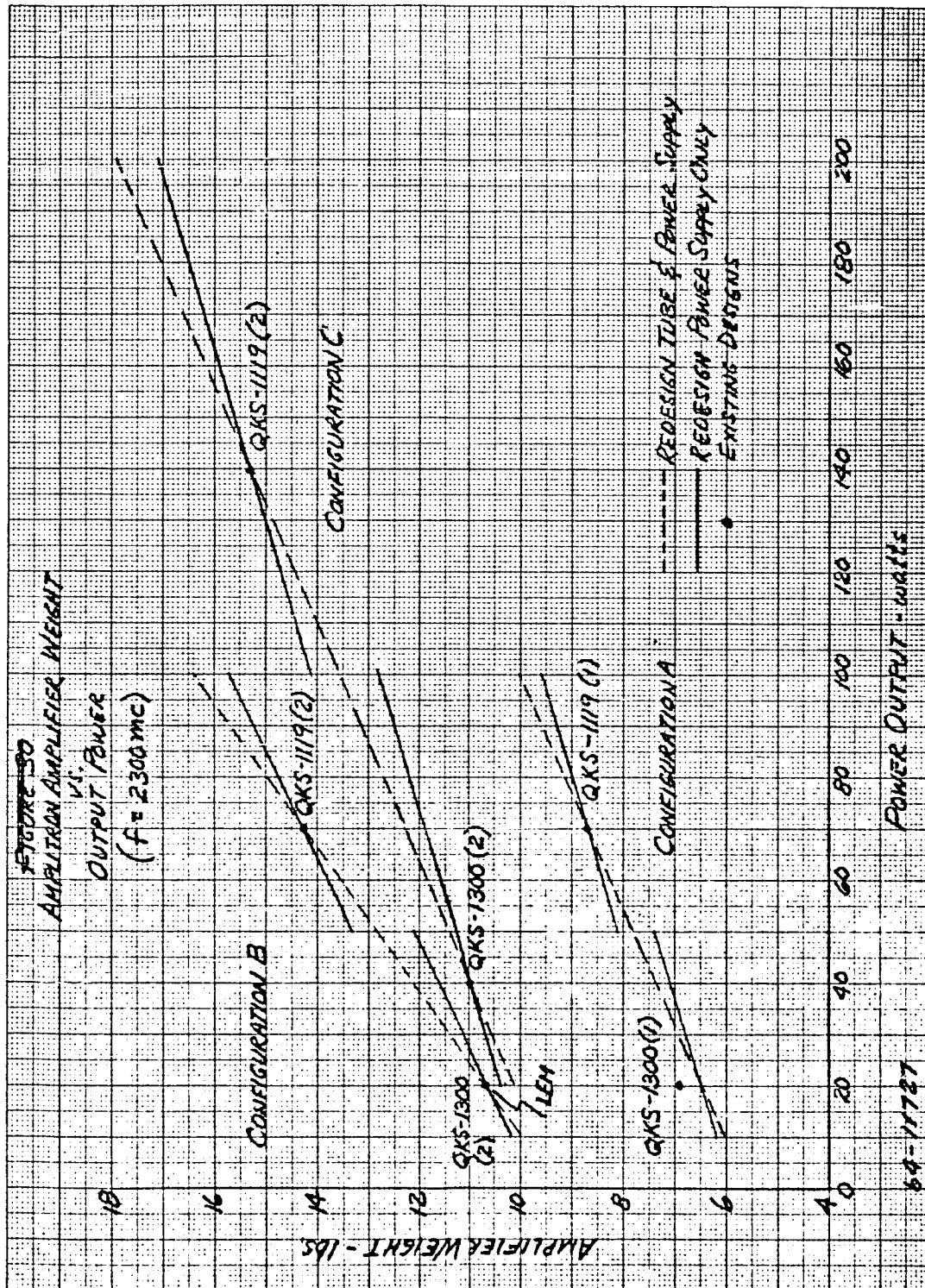


Figure 227 AMPLITRON AMPLIFIER WEIGHT VERSUS OUTPUT POWER

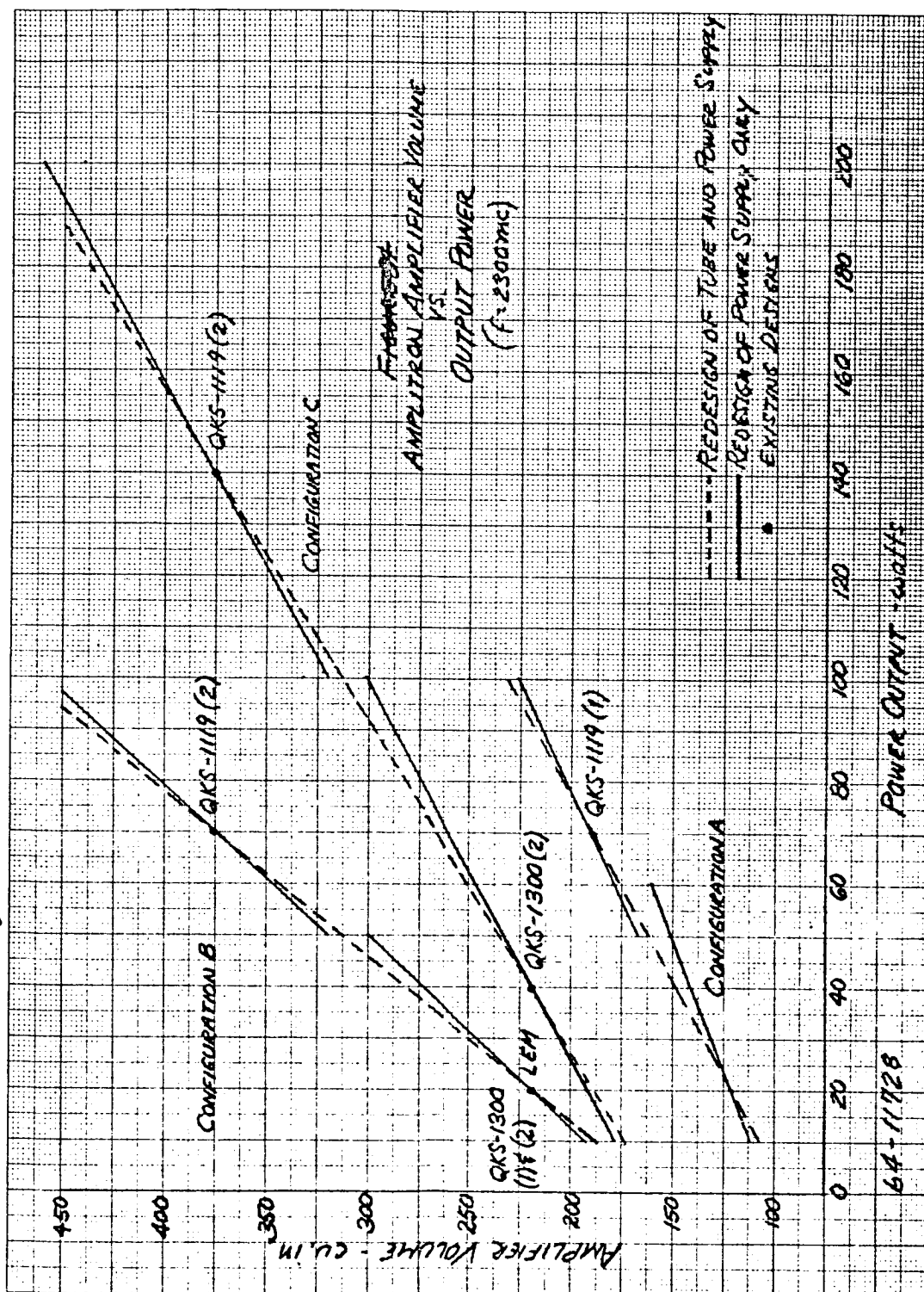


Figure 228 AMPLITRON AMPLIFIER VOLUME VERSUS OUTPUT POWER

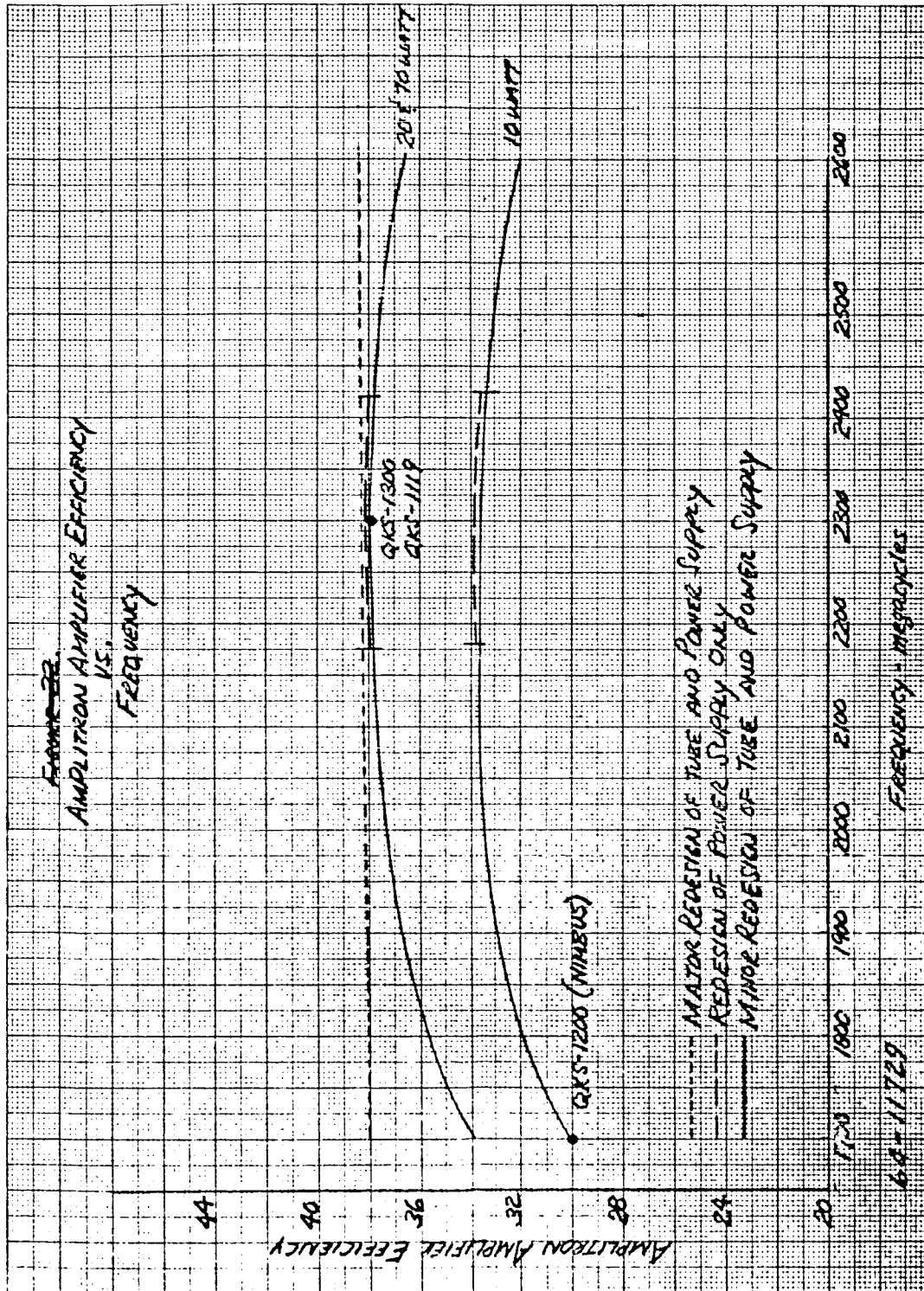


Figure 229 AMPLITRON AMPLIFIER EFFICIENCY VERSUS FREQUENCY

1/2.5

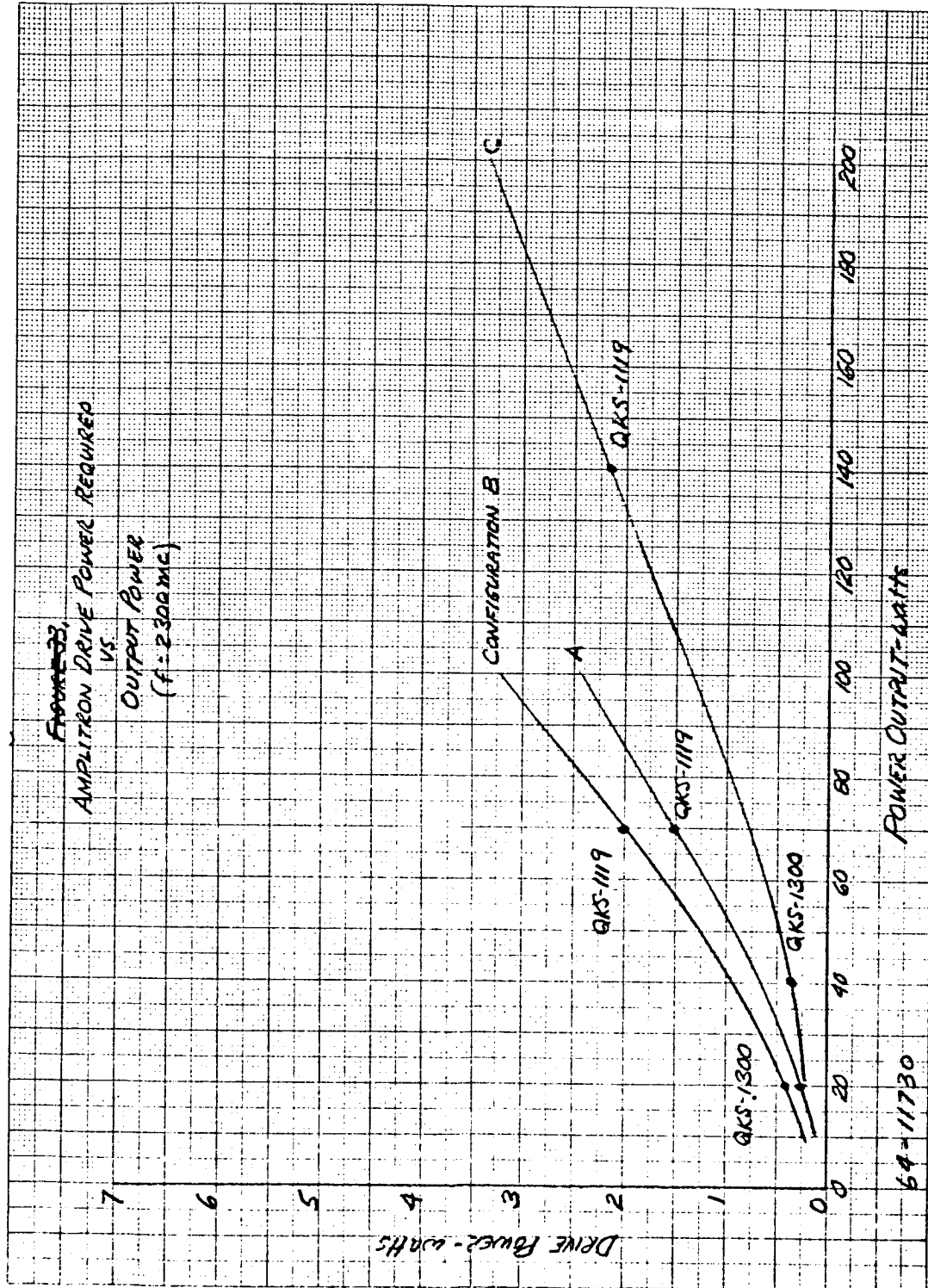
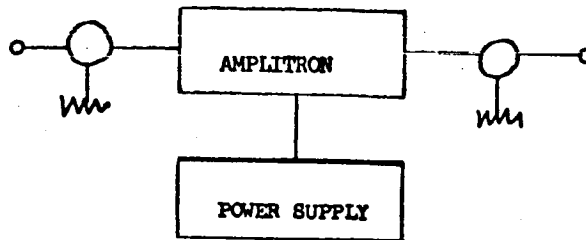
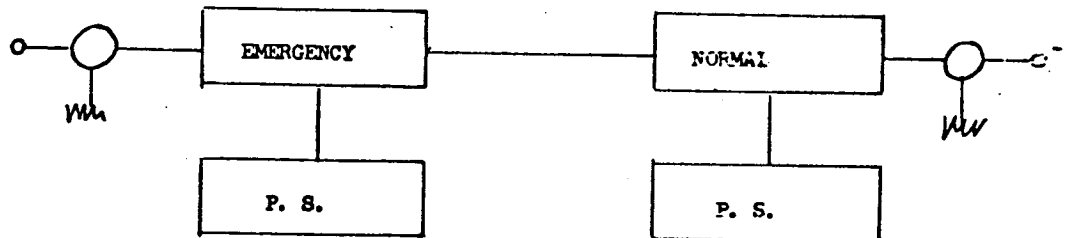


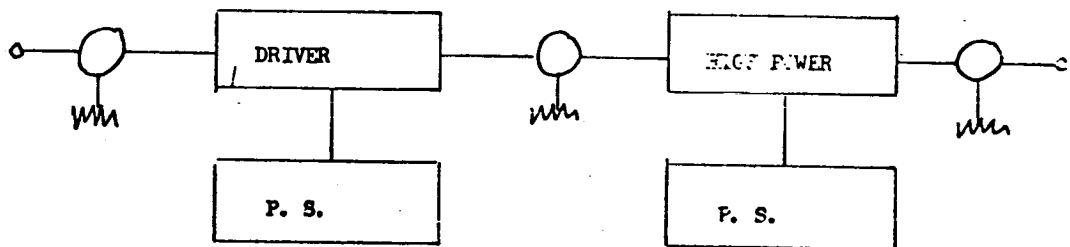
Figure 230 AMPLITRON DRIVE POWER REQUIRED VERSUS OUTPUT POWER



CONFIGURATION A



CONFIGURATION B



CONFIGURATION C

64-11731

Figure 231 AMPLITRON CONFIGURATIONS

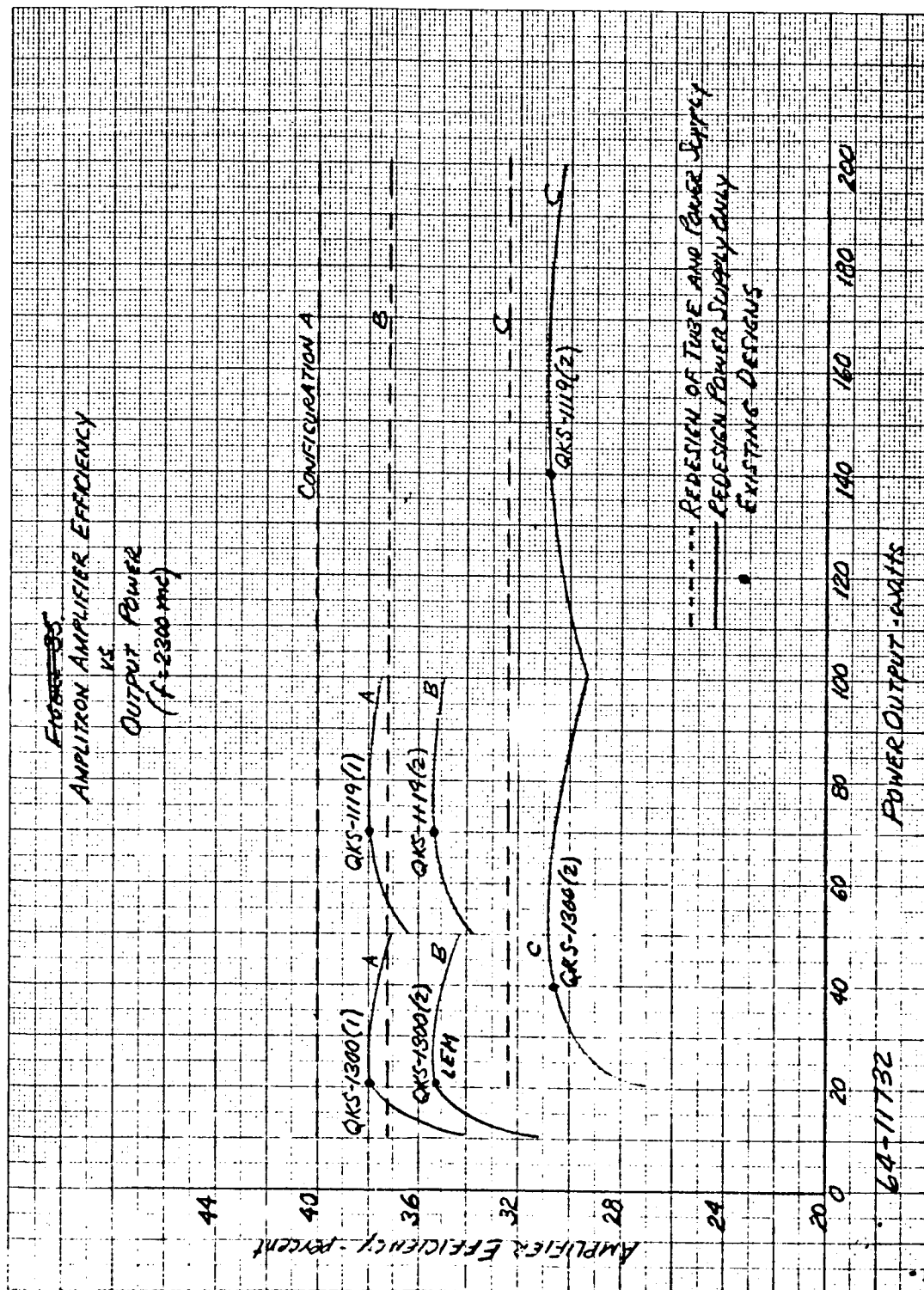


Figure 232 AMPLITRON AMPLIFIER EFFICIENCY VERSUS OUTPUT POWER

1) Ferrite core memories

The data on ferrite core memories were supplied by Electronic Memories Inc. of Hawthorne, California. At the present time, EMI has built a 100,000 bit memory to operate a 100 g, a 1440 bit memory system to survive a 3000 g shock for 3 ms, and they are presently developing a 1/4 million bit memory. The estimated values for larger memories and more severe environments have been provided from EMI on the basis of their experience in the design and manufacture of satellite core memories. The information has been recorded on figures 233, 234, 235, and 236, which indicate volume, weight, power, and budgetary costs versus storage capacity and shock level. Break off points of existing memories and in-house development programs have been indicated on the figures.

From the curves it can be determined that a 100 kilobit memory in Class 1 shock level would weight approximately 4 1/2 pounds, occupy 100 cubic inches, and consume about 5 watts of power, EMI models SEMS-IR and 3R aerospace core memory systems are 10⁵ bit memories available in an operating temperature environment of -55°C to 100°C and a storage environment of -65°C to 125°C. Discrete components comprise the electronics portion of the system but trends to integrated circuits within the next year have been predicted.

2) Plated wire memories

Univac Division of Sperry Rand Corporation has supplied technical information on thin film plated wire spacecraft memories. These non-destructive readout memories have been built to capacities of 1 million bits. The data supplied by Sperry Rand has been plotted in figures 237, 238, and 239 and from these figures, the approximate weight, volume, and power requirements can be determined for the various memories. Univac has also built memories utilizing integrated circuits; the effect of integrated circuitry on the basic parameters is also shown. Information on integrated circuits has been provided by Sperry Rand for Class 1 shock memories only. Univac has not tested a memory to exceed 100 g shock, and their estimated values for class 2 and 3 memories employing discrete components are based on existing memories undergoing redesigned potting and packaging techniques. They indicated that the more realizable design concept for high shock environment memories would be one using integrated circuits since the weight and volume requirements are decreased considerably. These memories can operate reliably within a temperature range of -45°C to +125°C, and they can sustain storage temperatures in excess of 150°C.

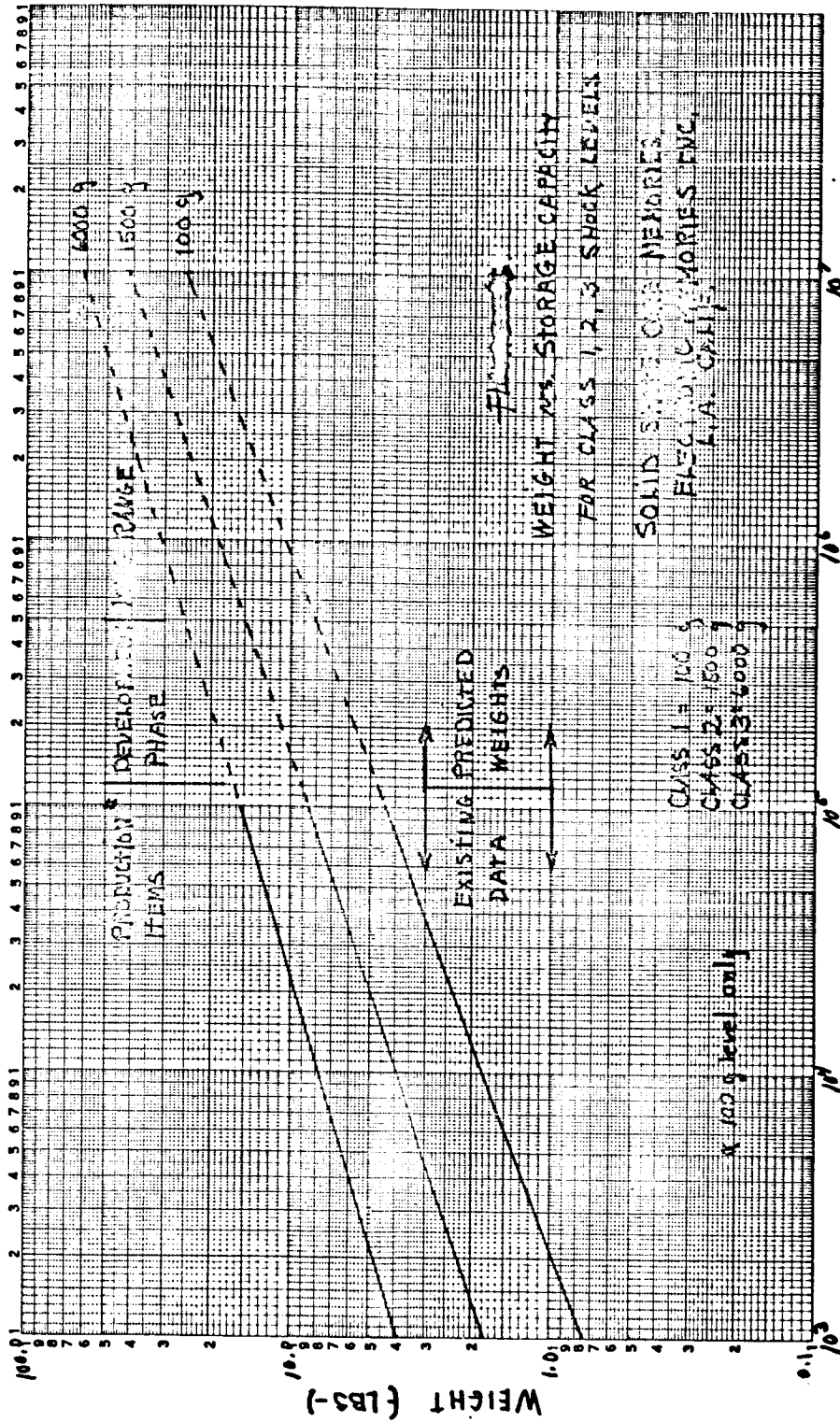


Figure 233 WEIGHT VERSUS STORAGE CAPACITY FOR CLASS 1, 2, 3 SHOCK LEVELS

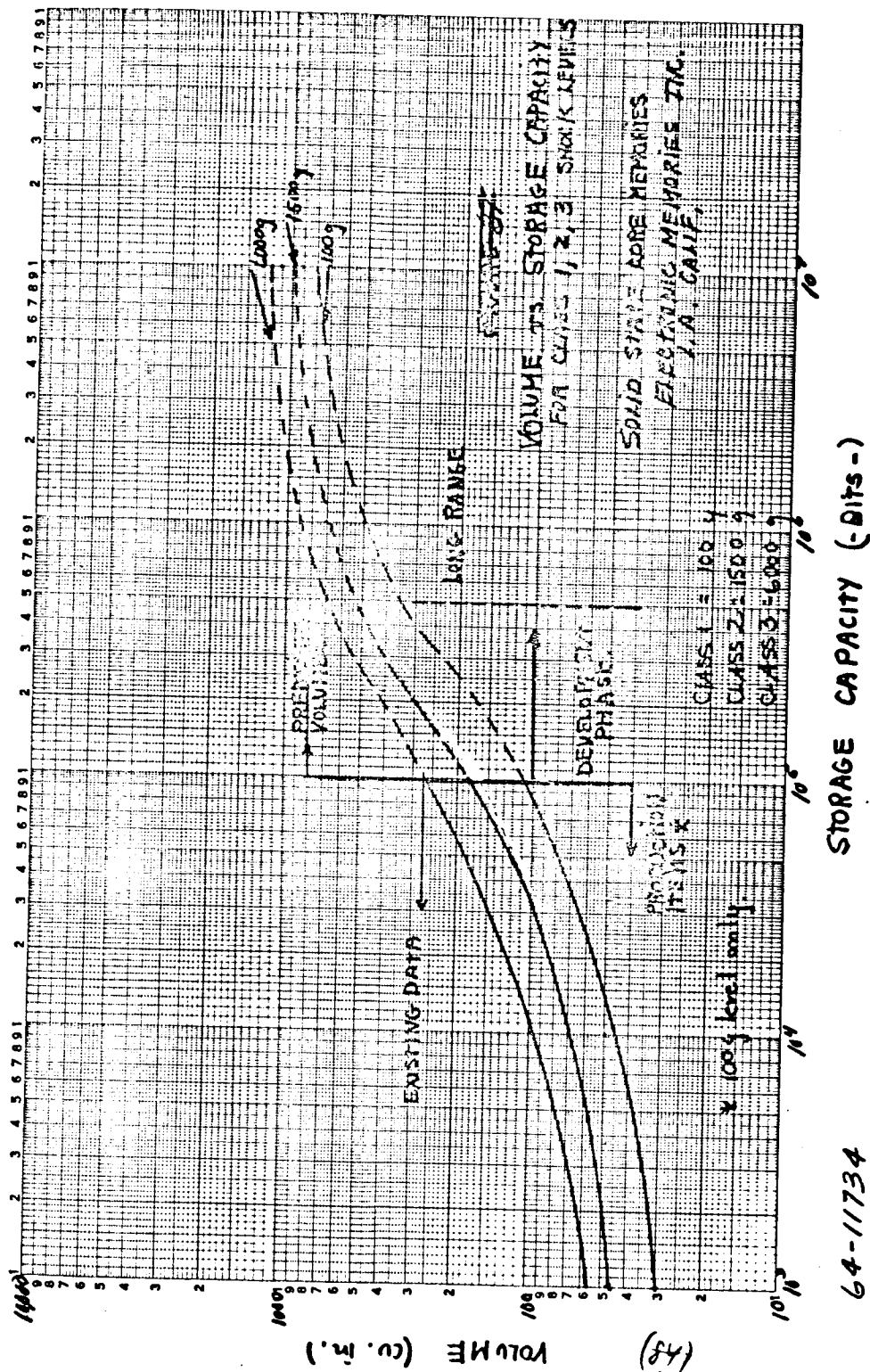
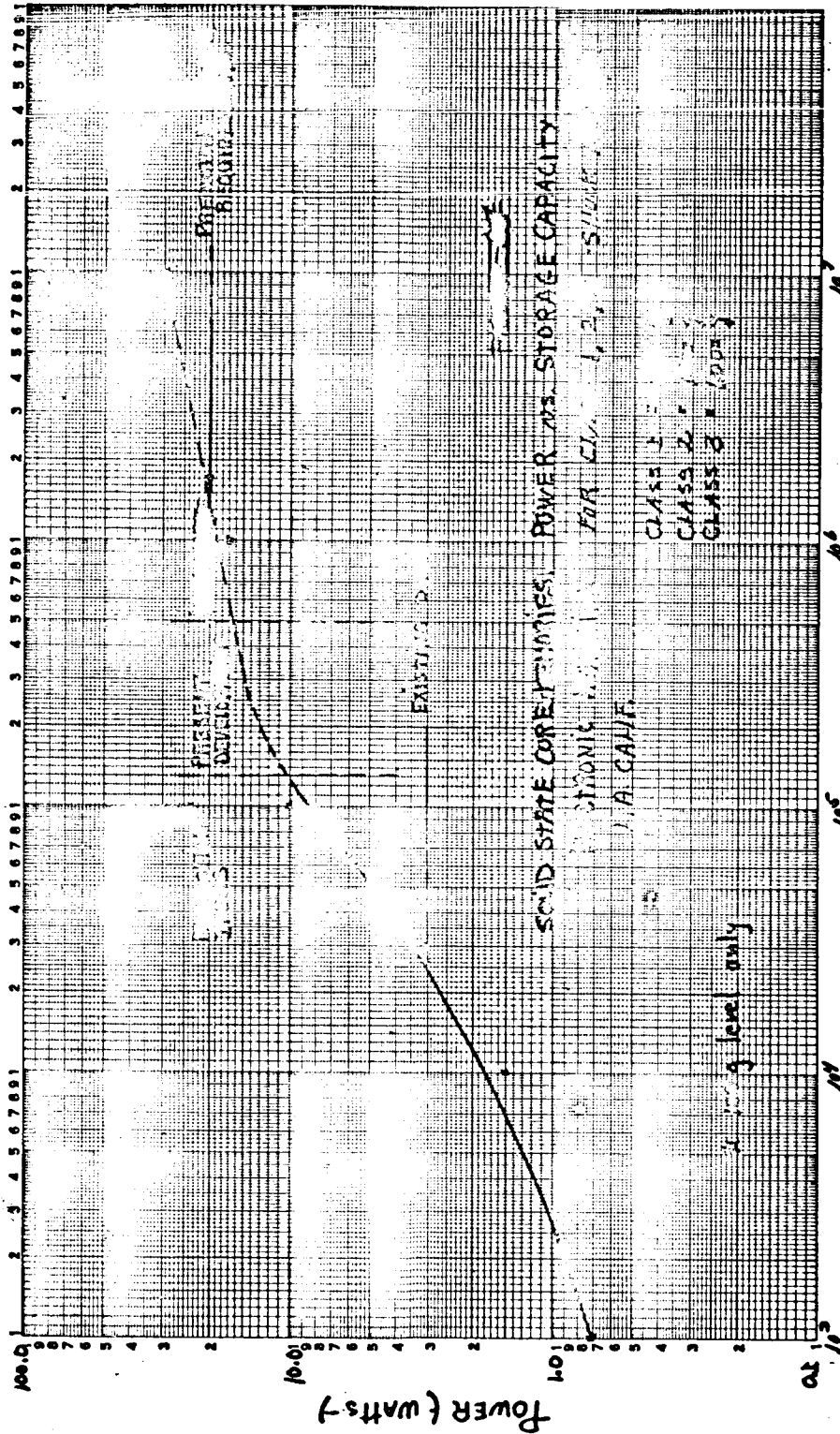


Figure 234 VOLUME VERSUS STORAGE CAPACITY FOR CLASS 1, 2, 3 SHOCK LEVELS



STORAGE CAPACITY - (bits)

64-11735

Figure 235 POWER VERSUS STORAGE CAPACITY FOR CLASS 1, 2, 3 SHOCK LEVELS

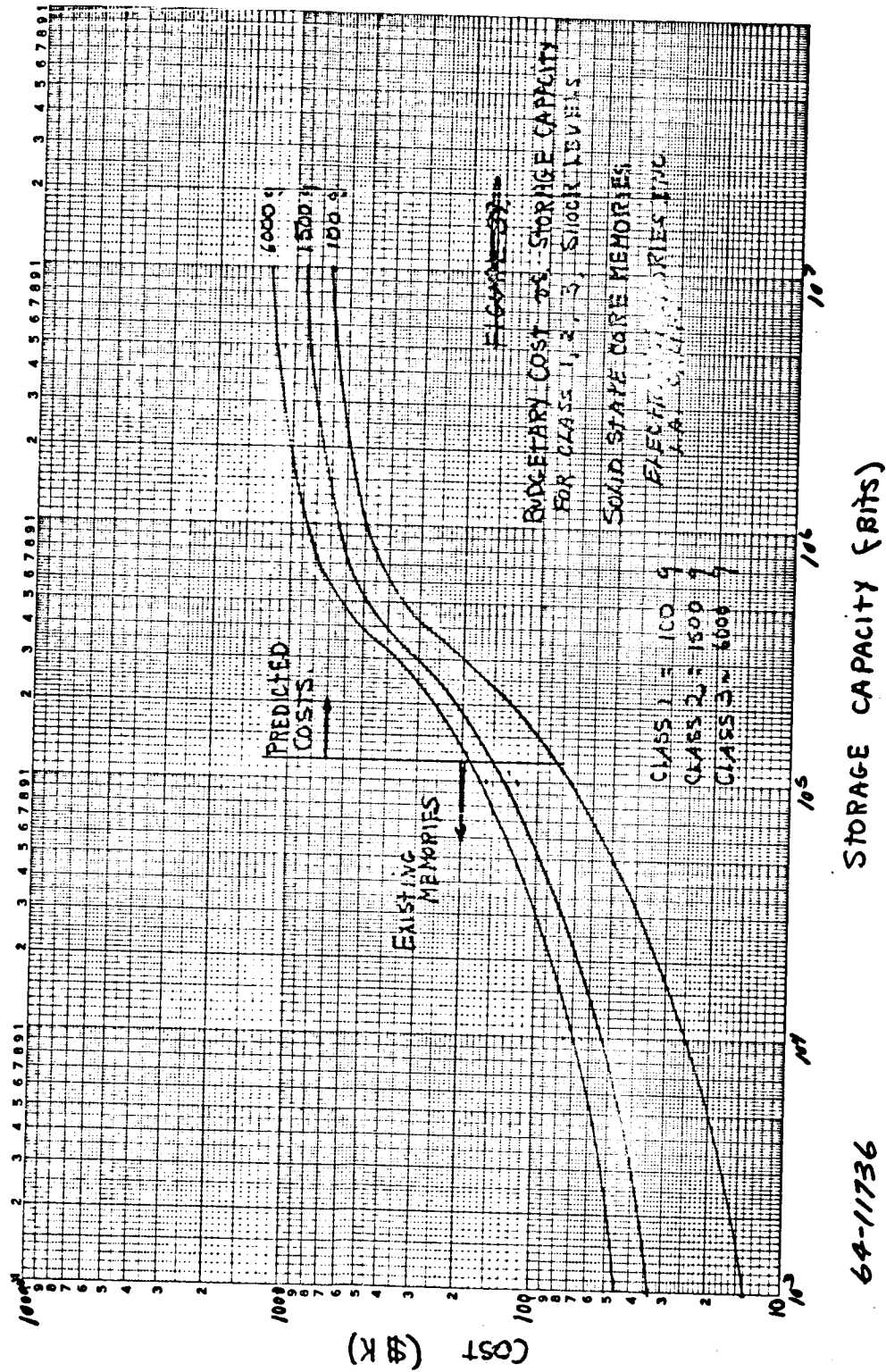


Figure 236 BUDGETARY COST OF STORAGE CAPACITY FOR CLASS 1, 2, 3 SHOCK LEVELS

64-11736

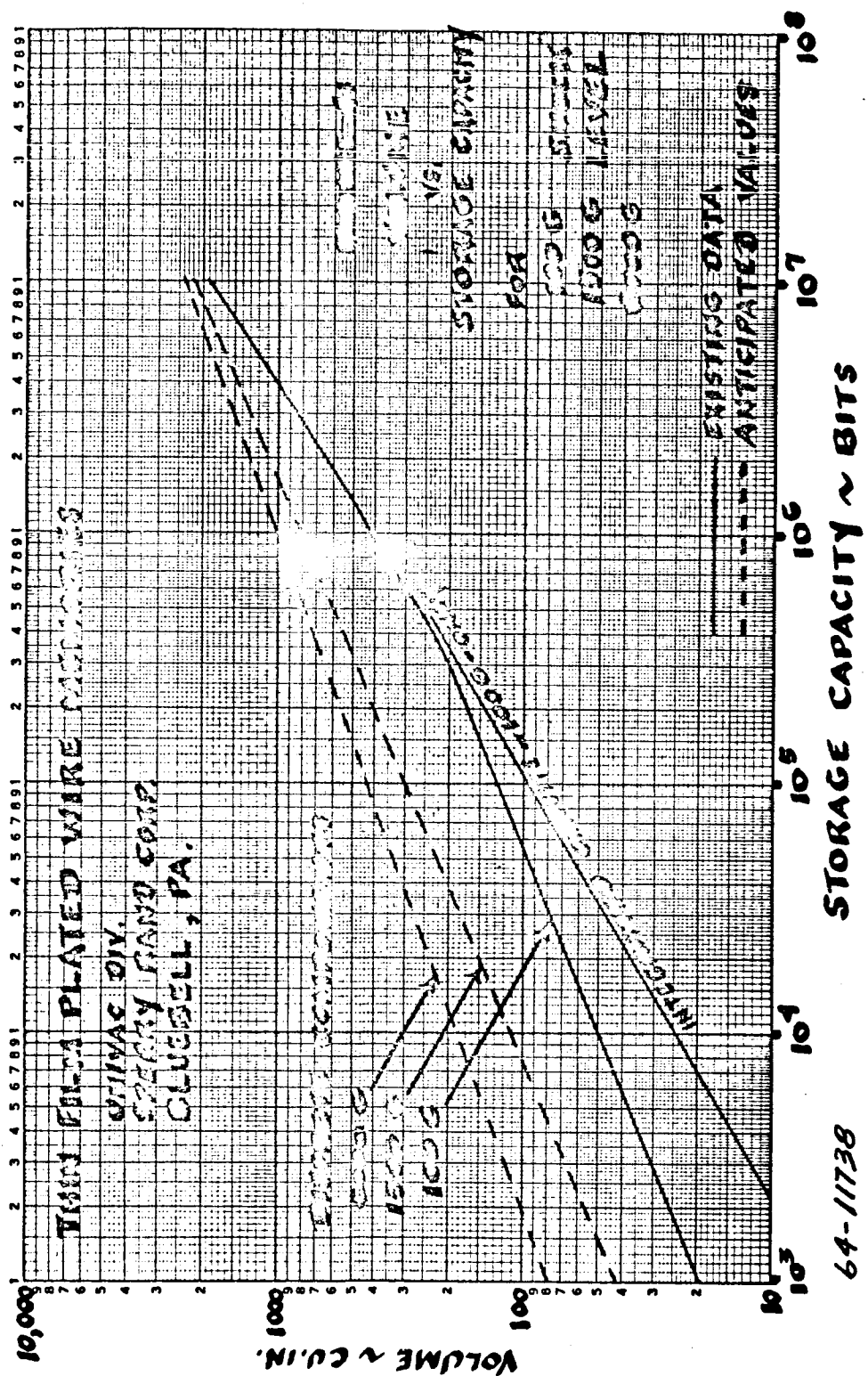


Figure 238 VOLUME VERSUS STORAGE CAPACITY FOR 100 g, 1500 g, 6000 g SHOCK LEVELS

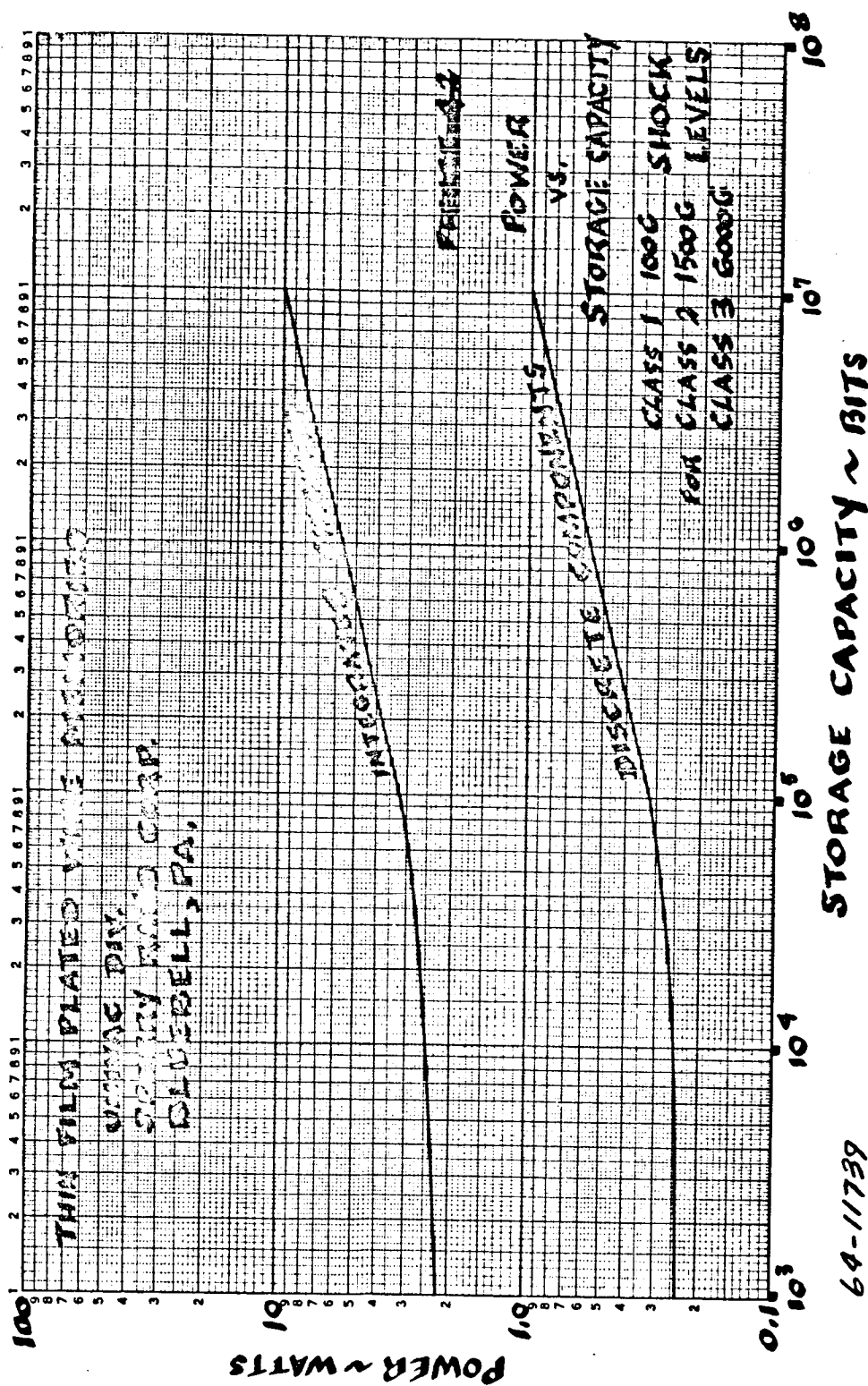


Figure 239 POWER VERSUS STORAGE CAPACITY FOR CLASS 1, 100 g, CLASS 2, 1500 g, CLASS 3, 6000 g SHOCK LEVELS

b. Tape Recorders

The data received on tape recorders indicates that the temperature environment of 145°C will cause permanent deformation of mylar backed tapes. At high capacities, tape recorders have the best bits/in.³ ratio, but below 100 kilobits, solid state storage systems are competitive. Three sources supplied technical information on tape recorders and are listed below.

1) Electronic Specialty Co. (ESC)

Electronic Specialty Co. of Los Angeles, California has submitted technical information on Model DR-300 tape recorder/ reproducer which will survive a 1500 g shock level of up to 20 milliseconds duration. The recorder is designed to be hermetically sealed, completely self-contained, and to operate from a 30 volt \pm 10 percent dc source.

Model DR-300 has a capacity of 3.6×10^6 bits/channel and up to 40 channels may be utilized in any standard IRIG configuration on 1-inch tape. As shown in figure 240, the weight and volume quoted by ESC for this recorder will not increase considerably with increasing capacities. Model DR-300 weighs 8 pounds, occupies 140 in.³ and consumes 8 watts. This model has more tape than is required so the size and weight of the unit could be reduced somewhat through a redesign. However, the sterilization temperature of the tape recorder is a critical problem. The best specification to date for mylar backed instrumentation tape is 120°C.

ESC reports that the DR-300 is a good intermediate step toward a design goal of a unit to survive 6000 g shock and that is reasonable to assume that a unit which has to survive a 6000 shock load can be packaged at approximately the same weight and power which is now required.

2) Borg warner controls

Borg Warner Controls of Santa Ana, California has designed a recorder/reproducer, Model R-201, that will operate during and survive a 1000 g shock environment. They are presently under contract from a major contractor to develop a recorder which will operate successfully during a 3000 g shock. They do not feel at the present time that they have sufficient information that can be presented. Model R-304 recorder/reproducer, which is a Class 1 shock machine, is comparable to other tape recorders at the shock level.

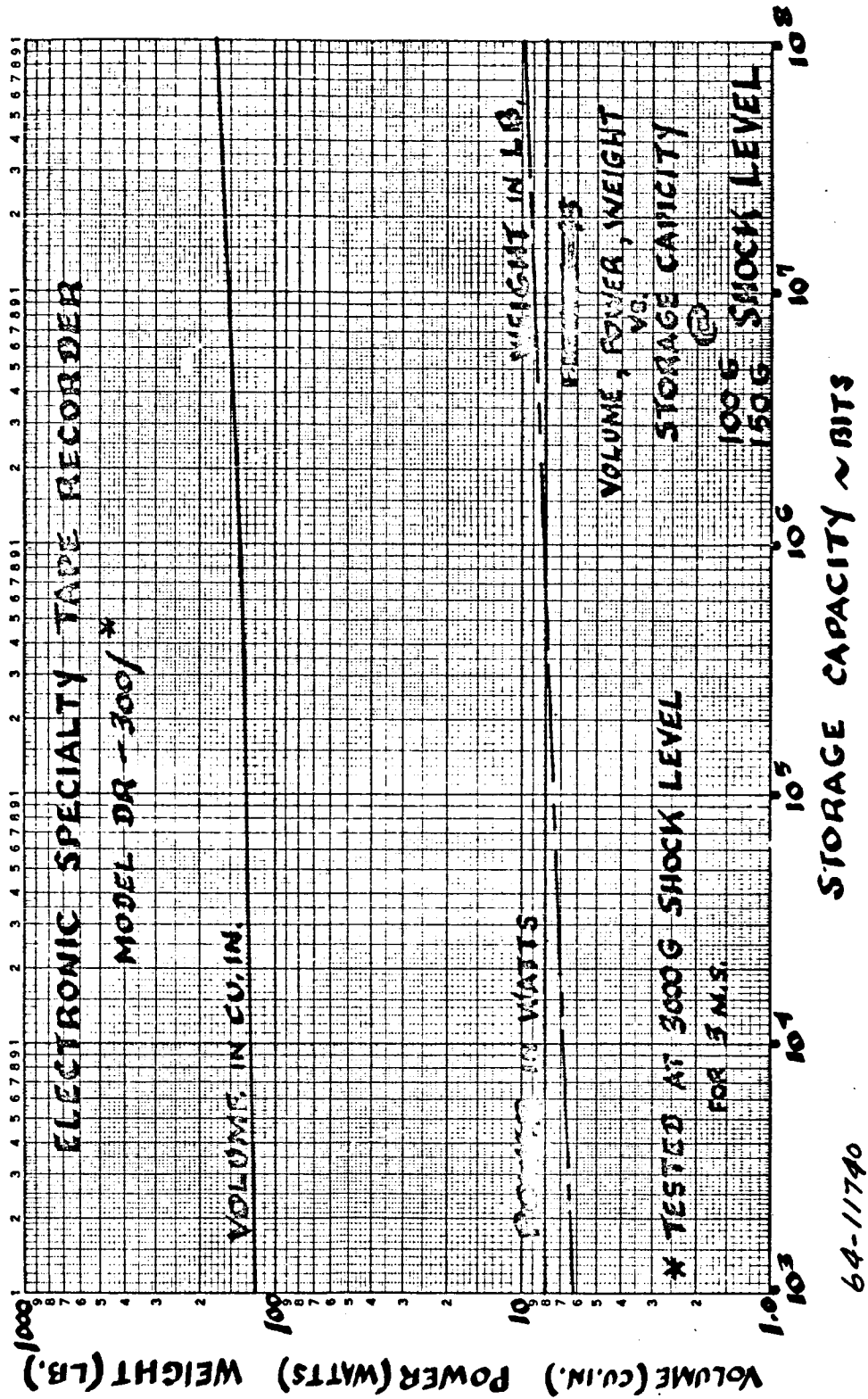


Figure 240 VOLUME, POWER, WEIGHT, VERSUS STORAGE CAPACITY AT 100 g, 150 g SHOCK LEVELS

Borg Warner reports, however, that they cannot supply a machine that will operate after a dry heat sterilization cycle of 145°C for 36 hours. The mylar backing will take a permanent deformation if exposed to temperatures in excess of 140°F for extended periods.

3) Leach corporation

Leach Corporation, Controls Division of Azusa, California has designed Magnetic Tape Recorders/Reproducers to survive severe shock environments. The 75 foot tape capacity model, MTR-362, is capable of withstanding 2000 g for 3 ms on any axis. The MTR 800 with a 300 foot tape capacity is capable of surviving an impact of 750 g. Up to 14 channels of 1-inch tape in any standard IRIG configuration is possible. The weight and volume of the recorder are consistent with competitive types, but the power consumption is approximately 50 percent higher. The temperature environment is from -50°F to 200°F, which is well below the qualification temperature of 145°C for dry heat sterilization.

10.6.4 Data Handling Subsystem and Programmer

The data handling subsystem and programmer were assumed to be of integrated circuit design. The characteristics of these subsystems, as shown in table 49, were not treated parametrically. The assigned values cover a wide enough design range to preclude a requirement for parametric study.

TABLE 49

DATA HANDLING SUBSYSTEM AND PROGRAMMER CHARACTERISTICS

	Weight	Volume	Dimensions	Power
Data Handling Subsystem				
a. Simple Missions	4.0 lbs.	60 in ³	4 x 5 x 3(in)	4.0 watts
b. Complex Missions	7.0	120	4 x 5 x 6	8.0
Programmer				
a. Simple Missions	2.0	30	3 x 5 x 2	2.0
b. Complex Missions	4.0	60	4 x 5 x 6	4.0

10.6.5 Radar Altimeter

The characteristics of the X-band radar altimeter are shown in table 50. Over the expected range of system requirements the assigned values are applicable. The weight estimate does not include the antenna.

TABLE 50

RADAR ALTIMETER CHARACTERISTICS

Weight	5.0 lbs
Volume	60 in ³
Dimensions	5 x 6 x 3 (in)
Power Consumption	20 watts

10.6.6 Power System

a. Battery

An effective energy density of 6 watt-hours per pound was assumed in the battery parametric studies. Assuming a 28-volt terminal voltage, a 300-watt-hour battery would occupy a volume of approximately 600 in.³. As a rough approximation this relationship can be considered linear.

b. RTG

Figure 44 shows total RTG weight versus output power for three types of fuel and three types of thermoelectric couple.⁶

The radio-isotopes are Plutonium 238 (Pu 238), Curium 244 (Cm 244) and Strontium 90 (Sr 90). The thermocouples are Lead Telluride (PbTe), Germanium-Silicon (Ge-Si) and a cascaded arrangement of Ge-Si and PbTe with the Ge-Si couples occupying the hotter section of the temperature gradient.

The following assumptions have been made in calculating weights.

- 1) The generators are designed for intact entry of the isotope capsule.
- 2) 100 percent void volume is allowed within the fuel capsule for the alpha emitters (Pu 238, and Cm 244) in order to take care of Helium production.
- 3) Only the optimum cold junction temperatures are assumed for each case.
- 4) Hot Junction temperature of 1500°F (for thermo couples)
- 5) Minimum weight for a given electrical output. This is not necessarily the maximum efficiency.
- 6) A rectangular fuel block is used with thermoelectric elements on two parallel flat sides.
- 7) Heat rejection is solely by radiative fins.
- 8) No shielding is allowed for in the design. In general the attenuation provided by the generator structure will reduce the dose rates by a factor of two, at most.

Shielding for nuclear radiation is then, for the most part, external to the generator, and its weight depends on the area to be shielded as well as the permissible dose rate, material to be used, etc.

In figure 241 the RTG weight required as a function of power level, for the isotope candidate selected for this study (Pu 238), is shown for PbTe, SiGe, and SiGe-PbTe cascaded thermoelectric converters.

Figure 242 shows a configuration with a hexagonal fuel block. Overall dimensions are shown in table 51.

TABLE 51

RTG DIMENSIONS -INTACT ENTRY

Power Level (watts)	Cm244		Fuel Pu238		SR 90	
	A	B	A	B	A	B
50	23 in.	14 in.	25 in.	15 in.	26 in.	16 in.
100	24	14	25	16	26	18
300	25	23	26	23	27	23

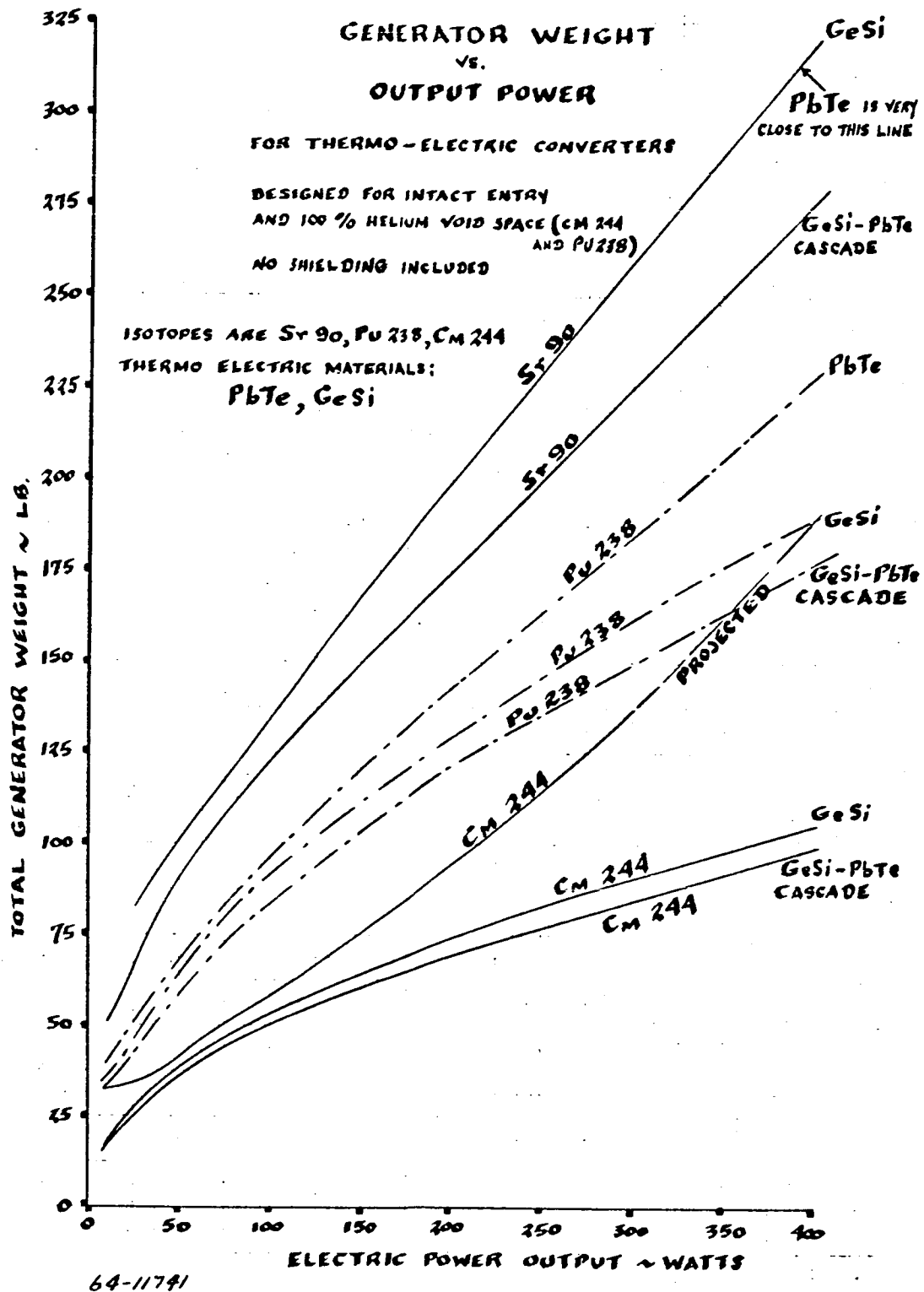
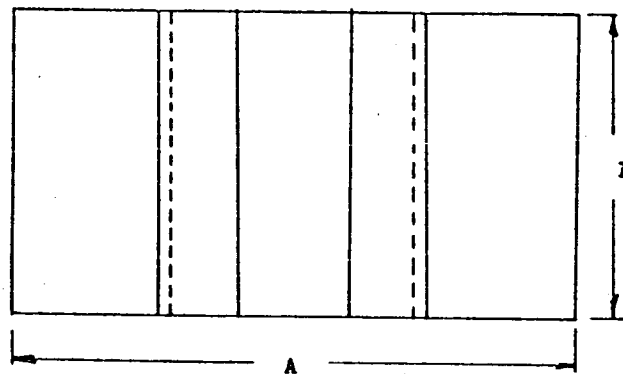
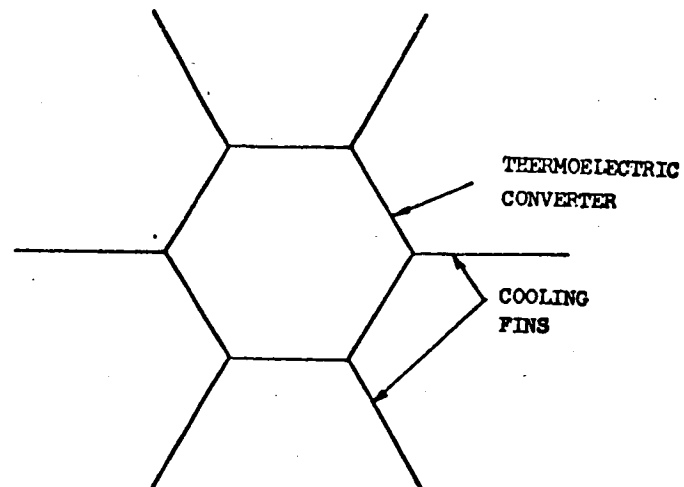


Figure 241 GENERATOR WEIGHT VERSUS OUTPUT POWER



64-11742

Figure 242 CHARACTERISTIC SHAPE OF A THERMOELECTRIC GENERATOR

4/43

10.7 COMMUNICATION AND POWER SYSTEM CONCEPTUAL DESIGN

Payload 16 was selected for the conceptual design study. This payload requires data transmission during the pre-entry phase, descent phase and landed phase of the mission. The conceptual design of the communication system evolved primarily from mission data requirements and lander packaging constraints. Other constraints such as dry heat sterilization had a strong influence on subsystem selection. Each telemetry link will be discussed to indicate how the parametric data were used to arrive at the conceptual design. A block diagram of the conceptual design is shown in figure 243 and a parts list in table 52.

10.7.1 Landed Telemetry Links

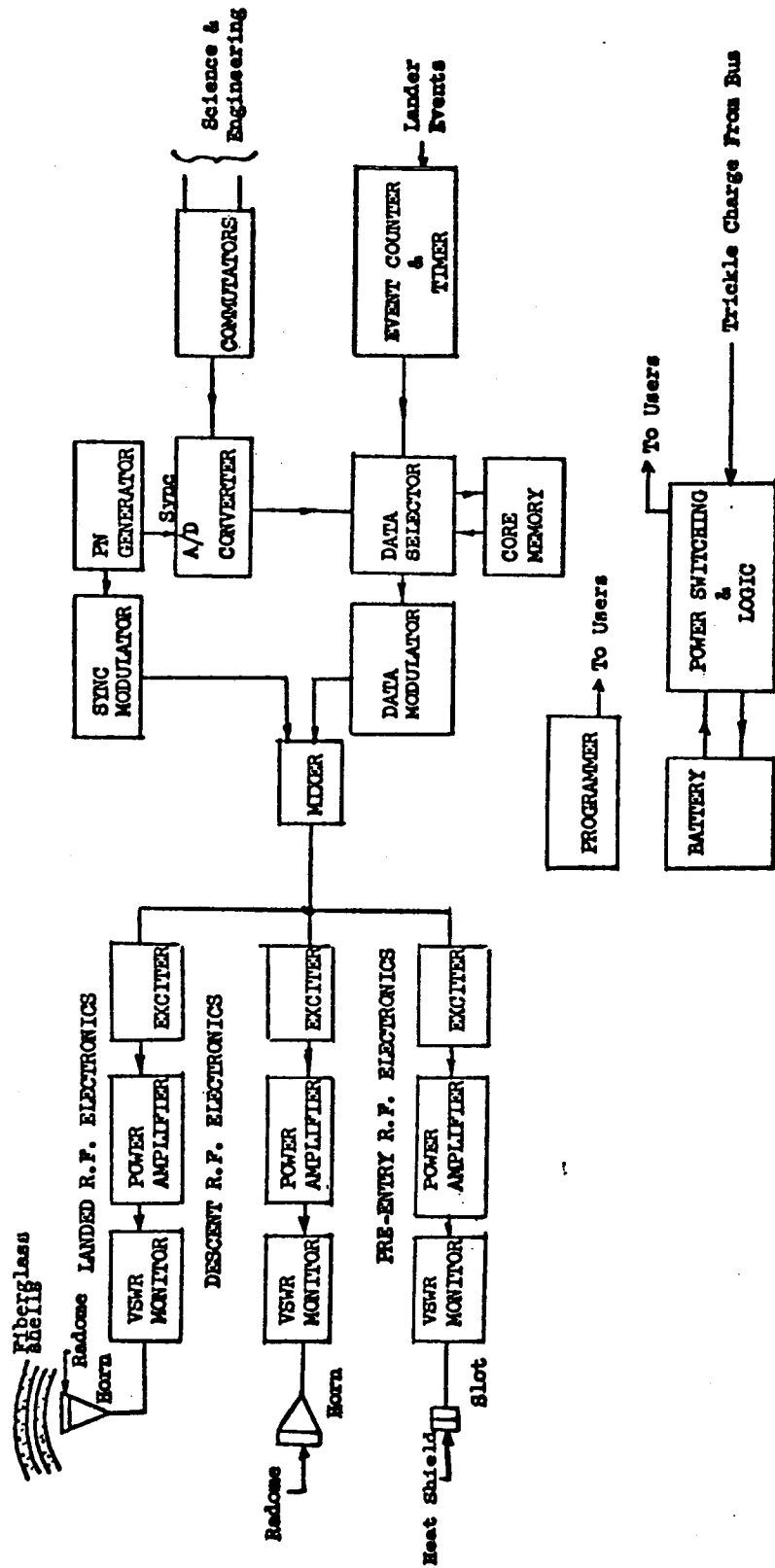
The strongest impact on system design, from the points of view of communication system constraints on the lander design and packaging constraints on the communication system, is felt by the telemetry link requirements after landing. From a reliability point of view, a direct link to the DSIF is considered mandatory. A back-up link to the flyby/bus is considered highly desirable. As discussed earlier, a gimballed antenna was considered a requirement by communications to minimize the antenna system complexity.

10.7.1.1 Direct Link

After landing, engineering diagnostic data and data generated by the lander scientific instruments are stored. In addition, the data generated during the entry to impact phase have been stored (nondestructive read-out is used during the descent phase). The transmitter power required to transmit this data is obtained from the parametric data shown in figure 211 and the following considerations:

- 1) Carrier frequency --- From table 39; 2295 mc
- 2) Slant range ---- From the 1969 and 1971 trajectory parameters, the maximum slant range is 1.76×10^8 km for a 2 November 1969 arrival date. The minimum slant range is 90.4×10^6 km for a 15 October 1971 arrival date.
- 3) Impact point
 20° North latitude, 280.4° longitude---selection based on 3 sigma dispersion for 150 km tracking error of $3 \times 3.24^\circ = 9.70^\circ$ latitude dispersion and $3 \times 3.20^\circ = 9.60^\circ$ longitude dispersion about an aim impact point of 10° N. latitude and 290° longitude (Syrtis Major).

4/44



64-11743

Figure 243 ADVANCED MARINER LANDER - COMMUNICATIONS AND POWER SUBSYSTEM BLOCK DIAGRAM

445

TABLE 52

ADVANCED MARINER LANDER COMMUNICATIONS AND
POWER SUBSYSTEM PARTS LIST

	Weight (pounds)	Volume (in. ³)	Power Cons. (watts)
Pre-Entry R. F. Electronics			
Slot Antenna	1.0	---	---
Heat Shield Window	0.5	---	.20 db*
VSWR Monitor	0.5	---	.25 db*
Power Amplifier	6.8	130	79.0
Exciter	4.5	80	10.5
Coaxial Cable (Antenna/VSWR Monitor)	0.5	---	.25 db*
Coaxial Cable (VSWR Monitor/Pwr. Amp)	0.25	---	.25 db*
Coaxial Cable (Pwr/Amp/Exciter)	0.25	---	---
Descent R. F. Electronics			
Horn Antenna	1.0	---	---
Radome	0.6	---	.20 db*
VSWR Monitor	0.5	---	.25 db*
Power Amplifier	9.4	215	237.0
Exciter	4.5	80	49.0
Coaxial Cable (Antenna/VSWR Monitor)	0.5	---	.25 db*
Coaxial Cable (VSWR Monitor/Pwr. Amp)	0.25	---	.25 db*
Coaxial Cable (Pwr. Amp/Exciter)	0.25	---	---

*Insertion Loss

TABLE 52 (Concl'd)

	Weight (pounds)	Volume (in. 3)	Power Cons. (watts)
Landed R. F. Electronics			
Horn Antenna	1.0	---	---
Radome	0.6	---	.20 db*
VSWR Monitor	0.5		.25 db*
Power Amplifiers (2)	11.6	205	79.0
Exciter (2)	9.0	160	10.5
Coaxial Cable (Antenna/VSWR Monitor)	0.25	---	.25 db*
Coaxial Cable (VSWR Monitor/Pwr. Amp)	0.25	---	.25 db*
Coaxial Cable (pwr. Amp/Exciter	0.25	---	---
Telemetry Subsystem			
Commutators	4.5		
A/D Converter	1.6	120	8.0
Event Counter and Timer	1.5		
PN Generator and Sync Modulator	1.0		
Data Selector			
Data Modulator and Mixer			
Core Memory			
Descent Memory	8.3	100	2.0
Landed Memory			
Programmer (2)	8.0	120	4.0
Battery	25.3	200	---
Temperature Transducer	0.1	---	---
Power Switching and Logic	2.0	80	1.5
Non-RF Cabling	2.0	---	---

*Insertion Loss

4) Earth Elevation Above Martian Equator

13. 2° South latitude--worst angle possible during launch window.

5) Look-angle to earth

56° maximum, 33° minimum, during mission with entry at a longitude corresponding to 0.75 hour after sunrise assuming zero time for descent (worst case).

6) Antenna selection

A horn antenna was selected for the lander antenna for the reasons stated earlier. To maximize the gain at the worst case look-angle of 56°, a 74 degree 3 db beamwidth horn was selected which is the practical limit of the horn ability.

7) Antenna gain

From figure 215, at a 56° look-angle the gain of 74° horn is -0.8 db. However, an additional 0.5 db polarization loss can be expected at this look-angle, therefore net gain is -1.3 db. At the minimum look-angle (33°) the gain is +4.6 db.

8) Power-gain product

From figure 211, at a 1.76×10^8 Km slant range and a bit rate of 11.5 bps (to maintain a binary relationship between bit rates in pre-entry and descent phases) the Power-Gain required is +13.3 dbw.

9) Transmitter power

From items 7 and 8 above,

$$P_T(56^\circ) = +13.3 \text{ dbw} - (-1.3 \text{ db}) = +14.6 \text{ dbw}$$

$$\approx 30 \text{ watts}$$

$$P_T(33^\circ) = +13.3 \text{ dbw} - 4.6 \text{ db} = +8.7 \text{ dbw}$$

10) Performance margins

Figure 211 is drawn for worst case values on all tolerances in the associated design control chart. Table 53 shows nominal, best and worst case performance margins for the two range extremes assuming a 30 watt transmitter.

TABLE 53
DIRECT LINK PERFORMANCE MARGINS

Range (km)	Look-Angle (deg)	Performance Margin (db)		
		Best	Nominal	Worst
1.76×10^8	56	6.17	3.67	0.17
	33	12.07	9.57	6.07
	56	11.97	9.47	5.97
	33	17.87	15.37	11.87

10.7.1.2 Relay Link

This link is a back-up to the direct link. Unlike the direct link there is no restriction on carrier frequency selection. As indicated in figure 216 horn aperture size is shown parametrically as a function of aperture size in wavelengths and carrier frequency. Studies on allowable aperture size that could be accommodated in the landed payload package indicated a maximum size of approximately 5.5 inches. For a 0.75λ aperture (74 degrees) this would correspond to a carrier frequency of approximately 1550 mc. If this carrier frequency was used, there would be a requirement for separate relay and direct link systems, an impossible situation from the point of view of packaging two antennas and transmitters. Studies showed that if the direct link system was also used for relay, a significant performance margin would be obtained in the relay link. Studies of the lander to flyby bus look-angle requirements showed a variation as a function of initial intercept latitude, flyby bus trajectory inclination, and time after impact. Table 54 was prepared assuming a nominal minimum inclination range of 40 to 45 degrees to allow for the window effect, a 900 ft/sec bus slowdown, and a nominal 10^6 km separation distance.

10.7.2 Descent Relay Link

During atmospheric entry, data concerning the temperatures, pressures and acceleration sensed by the lander is collected and stored. This data is then played back to the flyby bus during descent on the main parachute. To simplify the bus receiving equipment the carrier frequency selected for this phase is also 2295 mc. The minimum descent time as determined for the "H" atmosphere, $\gamma_e = -90^\circ$ and $M/C_D A = 0.244$, is 110 seconds. The

TABLE 54

POST IMPACT RELAY LINK

Initial intercept latitude ($^{\circ}$ N)	30	30	30	40	40	40
Bus trajectory inclination (deg)	45	45	45	40	40	40
Time from entry (hours)	0	3	5	0	3	5
Periapsis altitude (km)	10^4	10^4	10^4	10^4	10^4	10^4
Slant Range (km $\times 10^3$)	74.6	34.3	11.8	75.0	34.5	11.0
$P_T G$ at $B^{\circ} = 11.5$ (figure 205)	24.2	17.2	8.2	24.2	17.4	7.5
$P_T G$ at 2295 mc (figure 210)	1.2	1.2	1.2	1.2	1.2	1.2
Net $P_T G$	25.4	18.4	9.4	25.4	18.6	8.7
Lander Bus Look Angle (deg)	17.1	28.0	44.5	33.1	32.9	2.6
74 degree antenna gain (figure 215)	6.5	5.4	2.5	4.6	4.7	7.0
Bus Lander Look angle (deg)	0.8	2.4	9.5	1.9	2.8	0.6
34 degree Antenna gain (figure 215)	13.3	13.2	12.4	13.2	13.2	13.3
Net Antenna gain (db)	19.8	18.6	14.9	17.8	17.9	20.3
P_T required	5.6	-0.2	-5.5	7.6	0.7	-11.6
P_T selected (direct link)	14.8	14.8	14.8	14.8	14.8	14.8
Performance margin (db)	9.2	15.0	20.3	7.1	14.1	26.4

descent velocity uncertainty expected is no greater than 100 m/sec. In order to have as much time as possible for data transmission, the total acquisition time (carrier plus sync) should be as fast as possible. A major assumption is made concerning the flyby bus receiver; it is assumed that the receiver is capable of automatic acquisition, i.e., it is frequency swept and will lock onto the received carrier when in-phase. Using figures 201 and 201 for approximately 3 second carrier acquisition, $2B_{LO} = 100$ cps. From figure 204 for 7 second acquisition of the sync loop, $2B_{LO} = 10$ cps. Total acquisition time is therefore approximately 10 seconds. To be compatible with the direct link telemetry system (11.5 bps) a bit rate of 184 bps is selected. Table 55 shows the descent link requirements. From the lander/bus look-angle requirements, a 74 degrees beamwidth horn antenna is selected for the lander. A 34 degree beamwidth horn is used on the bus.

Relay Link - Separation to Entry Phase

The separation to entry phase of relay communication will be accomplished by a system similar to the direct/relay system selected for the post impact phase, except for the antenna selection. A slot antenna was selected and placed on the forebody of the lander. The antenna gain (worst case) will be approximately -1 db. Using figures 205 and 210, at 11.5 bits per second a power-gain product of +26.2 dbw is required at a worst case range of 75,000 km. The bus antenna gain is +13.2 db resulting in a transmitter power requirement of +14.0 dbw, or 25 watts. A 30 watt transmitter was selected for the conceptual design.

10.7.3 Hardware Selection

10.7.3.1 RF Subsystem

The preceding discussion indicated that the direct link telemetry requirements are dictated by the 1969 opportunity and that a minimum transmitter power of 30 watts would be required using a 74 degree beamwidth horn antenna. It is significant to note that in 1971, the minimum transmitter power is approximately 8 watts due to the shorter range. In the landed relay link, table 54 shows a minimum performance margin of 7.1 db for a 30 watt transmitter. The minimum landed relay link power is therefore approximately 6 watts. In 1971, then, acceptable performance in both the direct and relay landed links could be obtained with a 10 watt transmitter rather than the 30 watts selected for 1969. In the pre-entry and descent links, the 30 watt and 90 watt transmitter would be required for both 1969 and 1971 unless additional antenna gain can be obtained. (A possible technique to accomplish this is discussed later in the alternate concepts section).

TABLE 55
DESCENT RELAY LINK

Planetocentric Latitude (deg)	30 N	40N
Flyby Bus Inclination (deg)	45	40
Nominal Flyby Bus Slowdown (ft/sec)	900	900
Time from Separation (hrs)	68.3	68.3
Slant Range (km)	74,625	75,041
Bit Rate (bps)	184	184
P _T G from figures 208 and 210	+35.2	+35.2
Lander to Bus Look Angle (deg)*	27.1	43.1
Lander Antenna Gain (db)	+5.5	+2.8
Bus to Lander Look Angle (deg)	0.8	1.4
Bus Antenna Gain (db)	13.2	13.2
Net Antenna Gain (db)	+18.7	+16.0
P _T Required (dbw)	+16.5	+19.2
P _T Selected (dbw)	+19.5 (90W)	+19.5 (90W)
Performance Margin (db)	+3.0	+3

*Assuming ± 10 degree swing on parachute

The antenna selected for the pre-entry telemetry link is a crossed-slot type. A sketch of this antenna is shown in figure 244. Figure 245 shows a typical radiation pattern for this type of antenna. The slots would be fed off-axis and 90 degrees out of phase to obtain circular polarization. The feed would consist of a printed circuit power divider and phase shifter. Circularity is predicted to be 0.25 db on axis and 1 db at the 3 db points.

The antenna selected for both the descent and landed links is a horn. A sketch of this antenna is shown in figure 246. Figure 247 shows a typical radiation pattern. A coax to rectangular waveguide transition is used since circular polarization is obtained by rotating the waveguide 45 degrees to excite the TE_{01} and TE_{10} modes in the transition section. The phase of one mode is changed 90° to obtain circular polarization. Circularity is predicted to be 0.25 db on axis, 1 db at the 3 db points and 1.5 db at 56° off-axis.

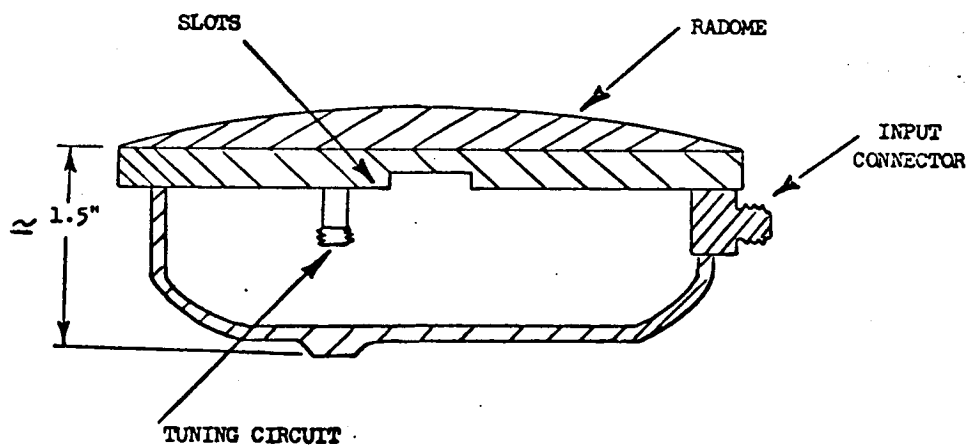
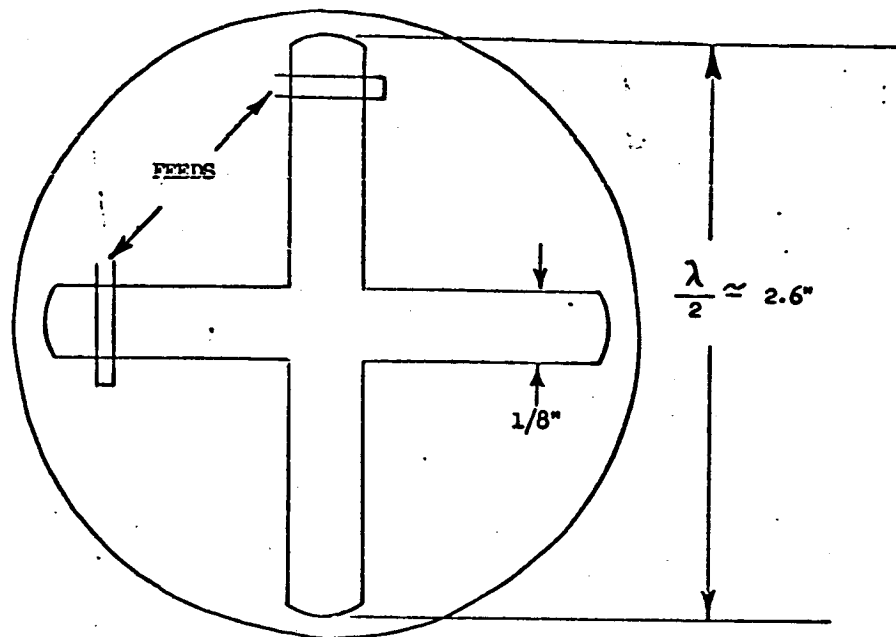
The transmitters selected for the three links are amplatron types, manufactured by Raytheon Company. Other amplifier types such as ceramic triodes or traveling wave tubes (TWT's) could also be used. The parametric data obtained from Raytheon reflected the variation in weight, power, and volume of a complete power amplifier including the associated dc-dc converter and was therefore easily adaptable to the conceptual design study. Data obtained on ceramic tubes and TWT's is given for the power tubes only. If these tubes were used, it is assumed that the weight figures would be consistent with those shown for amplitrans. The volume, and efficiency would be different since a crossed-field device such as the amplatron is theoretically more efficient than the other types and the shape factor for TWT's is different. In the pre-entry and descent links, a non-redundant amplifier was selected (Configuration A in figure 231). In the landed link, a redundant amplifier (Configuration B in figure 231) was selected. The redundant amplifiers and converters would be oriented 90 degrees with respect to each other to minimize a possible failure mode at impact.

The exciters selected for the three power amplifier would be solid state varactor multiplier types.

The weights, volumes, and power consumptions for these items as listed in the parts list (table 52) were taken from the corresponding figures in the parametric studies.

10.7.3.2 Digital Subsystems

The telemetry subsystem and programmer are assumed to be of integrated circuit design. The data shown in table 49 are estimates based on work done for Avco by Texas Instruments, Inc. on past

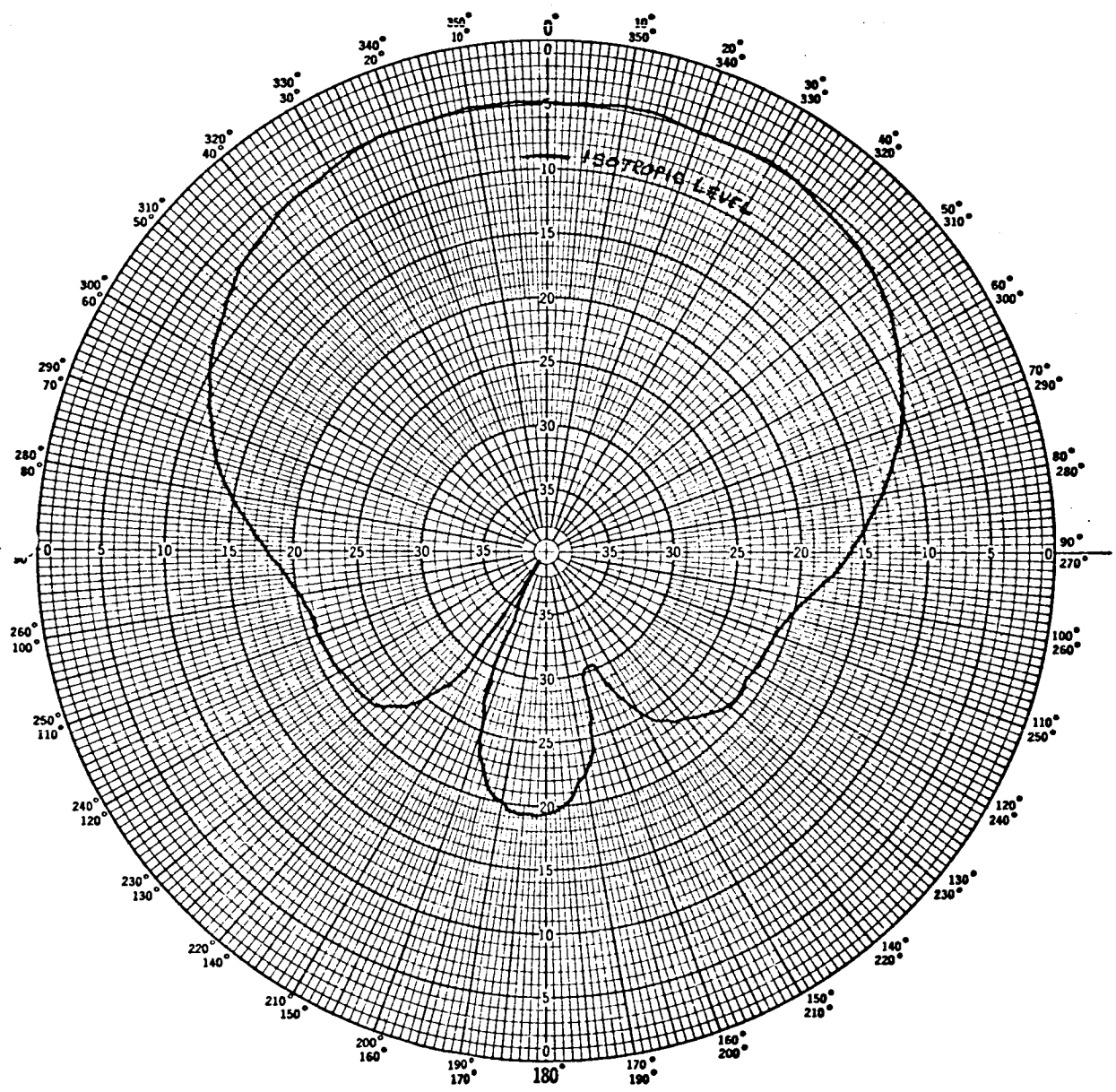


64-11744

Figure 244 SLOT ANTENNA

454

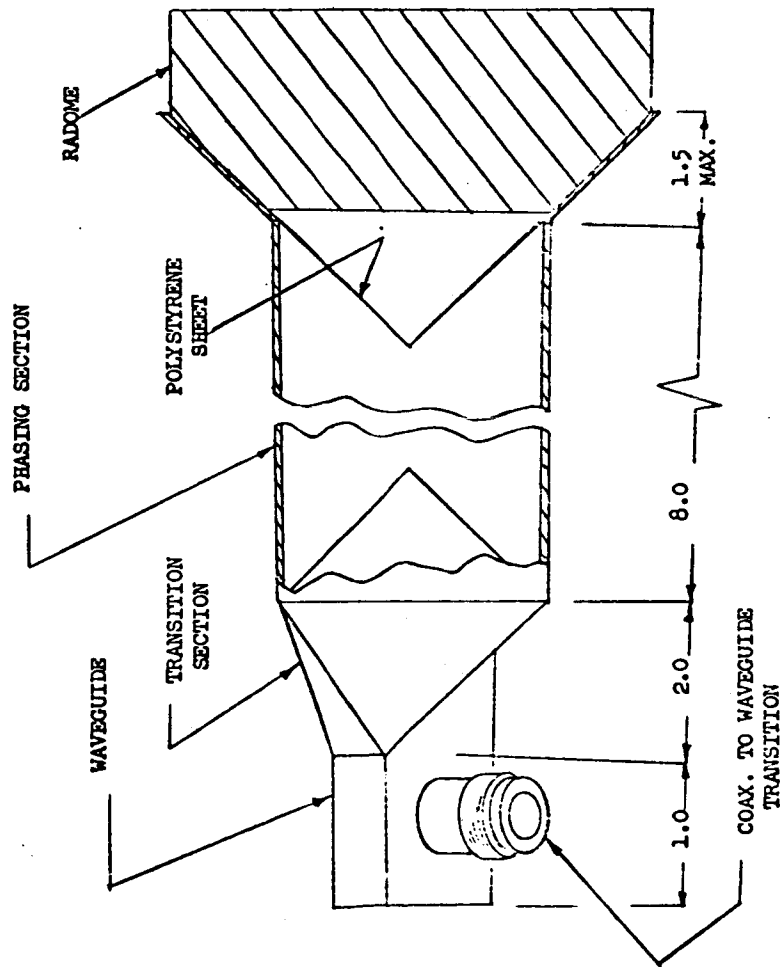
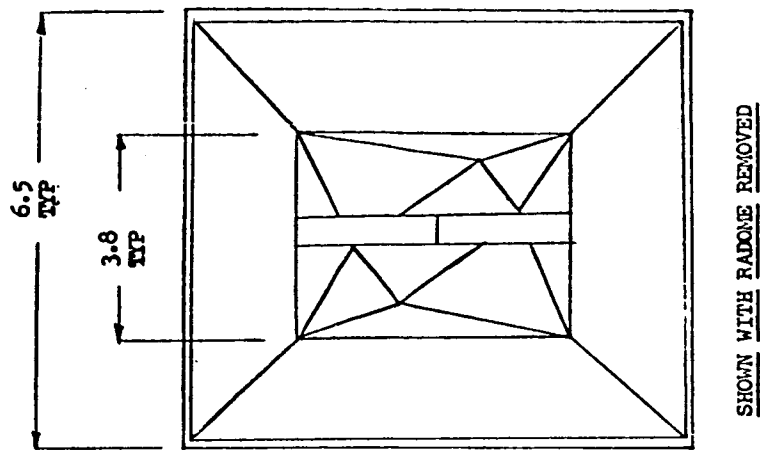
TYPICAL RADIATION PATTERN - SLOT ANTENNA



64-11745

Figure 245 TYPICAL RADIATION PATTERN - SLOT ANTENNA

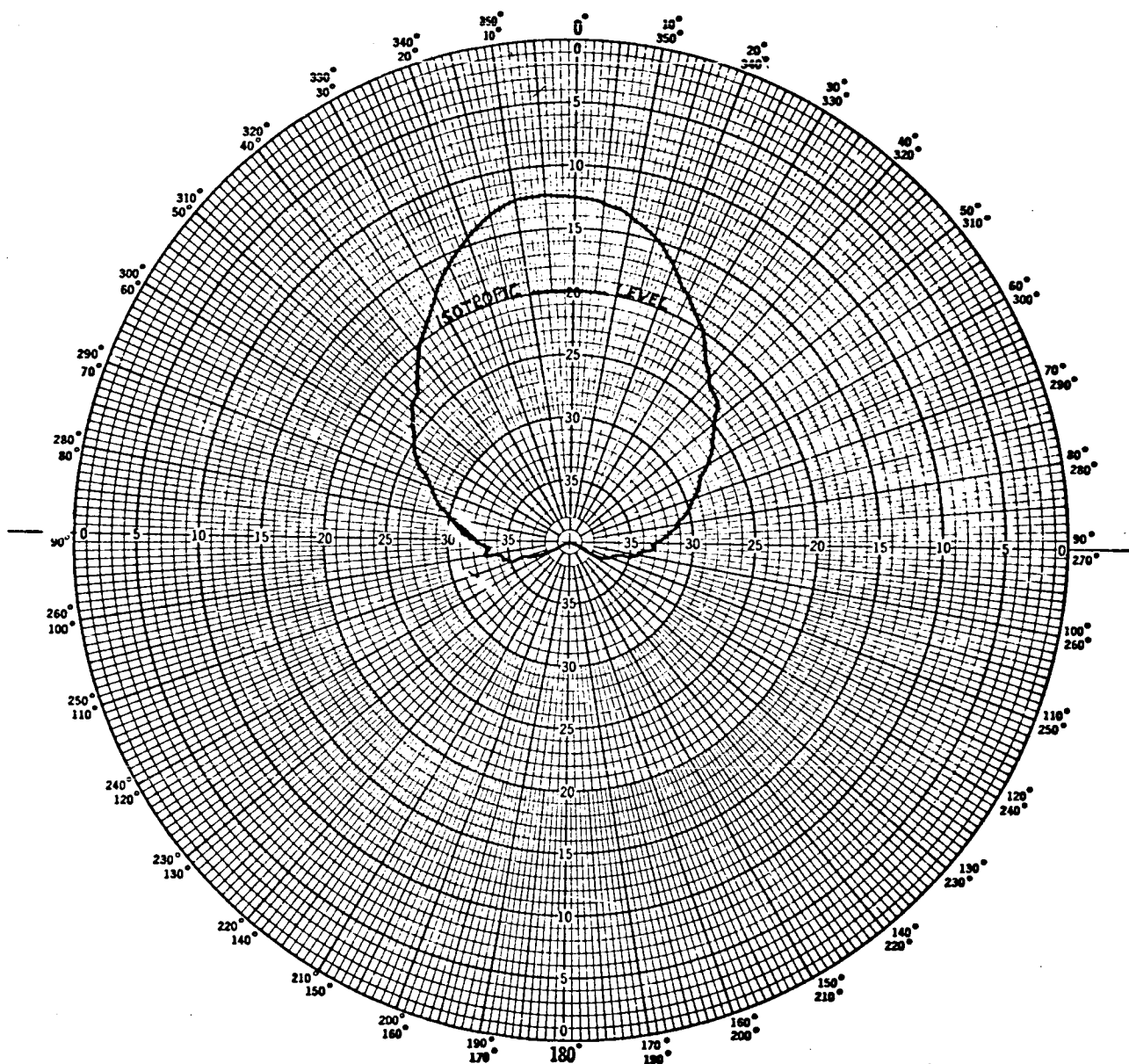
455



NOTE: Dimension in Inches

Figure 246 CIRCULARLY POLARIZED HORN

64-11746



64-11747

TE_{01} & TE_{10} modes

Figure 247 TYPICAL RADIATION PATTERN - HORN ANTENNA*

programs (typically, the Mariner 66 Capsule Proposal). The storage subsystem selected for the conceptual design was a solid state design. As indicated earlier, tape recorders were considered marginal from the dry heat sterilization and impact shock level points of view. Either plated wire or core memories could be used. However, the core memory may need some development work to withstand the dry heat qualification cycle. The data shown in table 52 for these items was obtained from the corresponding figures in the parametric studies.

10.7.3.3 Power Subsystem

Due to the short life of the landed mission, an energy storage device such as a battery is a logical selection for the power source. The RTG/battery combination would only be competitive for much longer missions. Also there would be a severe thermal control problem with an RTG of any significant output power. The NiCAD battery was selected for the conceptual design for the reasons stated earlier on its ability to withstand dry heat sterilization. The fuel cell is considered acceptable from an energy density point of view; however, it has not exhibited the ability to withstand dry heat sterilization. The power switching and logic subsystem is a simple power routing device controlled by the programmer. The battery size was determined from table 56.

10.7.3.4 Payload Package

The communication and power system is split into landed payload and payload external to the landed package as indicated in table 57.

10.8 Alternate Concepts

Three alternate concepts have been given a cursory study. One involves a method to reduce the relatively high transmitter powers required (especially in the descent link) and the other two simplify the rf Electronics Subsystem.

10.8.1 Alternate Concept 1

Figure 247 showed the radiation pattern obtained with a horn antenna excited in the TE_{01} and TE_{10} modes. Figure 248 shows a typical radiation pattern obtained by exciting the TM_{01} mode in a circular horn. Polarization in this case is linear. The shaded area indicates the variation in lander to DSIF look-angle for the direct link. A circular horn antenna could be designed to maximize the gain in this shaded area. Instead of the -0.8 db net gain obtained in the conceptual design, the gain would be on the order of +7 db. Due to linear instead of circular polarization, there would be a 3 db loss giving a net improvement over the conceptual design of approximately 5 db. This would reduce the power required in the direct link for 1969 from 30 watts to approximately 10 watts. Other factors such as look angle variation in the landed relay link would affect the ultimate selection. A similar technique could be employed with the descent antenna.

TABLE 56

PAYLOAD NO. 16 - POWER USAGE BREAKDOWN FOR LANDED PAYLOAD

Subsystem	Item	Mission Phase	Watts		Watt-hrs.	Multiple Unit Usage Multiplier	Total Watt hrs.
			Hours	Watts			
Science/protected /external	Pressure Sensor	Post impact	0.10	0.10	0.50	1	0.50
	Radio Isotope Growth Detector	Post impact	3.00	3.00	15.00	1	15.00
	Anemometer	Post impact	0.07	0.07	0.35	1	0.35
	Accelerometer	Entry to impact	1.00	1.00	0.10	3	0.30
	IR radiometer	Entry to impact	7.00	7.00	0.14	1	0.14
Communications Pre-entry relay	Pressure Sensor	Entry to impact	0.10	0.10	>0.01	3	0.01
	Temp. Sensor	Entry to impact	0.10	0.10	>0.01	3	0.01
			Science Subsystem Total				16.31
	P _{tot} = 3.0 P _{trans} B = 11.5 bps f = 2.295	Warm up (2 X missions) transmitting	9.00	9.00	0.07	1	0.63
	P _{trans} = 30 w P _{tot} = 3.0 P _{trans} B = 18 bps f = 2.295	(2 X missions) Warm up (1 X mission) transmitting	90.00	90.00	0.09	1	8.10
Descent relay			27.00	27.00	0.02	1	0.54
	P _{trans} = 90 w P _{tot} = 3.0 P _{trans} B = 11.5 bps f = 2.295	(1 X mission) transmitting	270.00	270.00	0.03	1	8.10
		Warm up (3 X missions) transmission	9.00	9.00	0.10	1	0.90
			90.00	90.00	0.37	1	33.10
			Communications Subsystem Total				51.37
Landed relay/ Data	Handling	Sep. to impact	8.00	8.00	0.25	1	2.00
	Programming	Post impact	8.00	8.00	5.00	1	40.00
		Sep. to impact	4.00	4.00	0.25	1	1.00
	Storage (12,000 bits)	Post impact	4.00	4.00	5.00	1	20.00
	Diagnostics	Separation thru post impact	2.00	2.00	5.50	1	11.00
			2.00	2.00	5.50	1	11.00
			Data Subsystem Total				85.00
			Watt-Hour Power Totals				152.68
			at 6 watt-hrs/lb. - Battery Wt. = 25.40 lbs.				
			at 7.66 in ³ /lb. - Battery Vol. = 200 in ³				

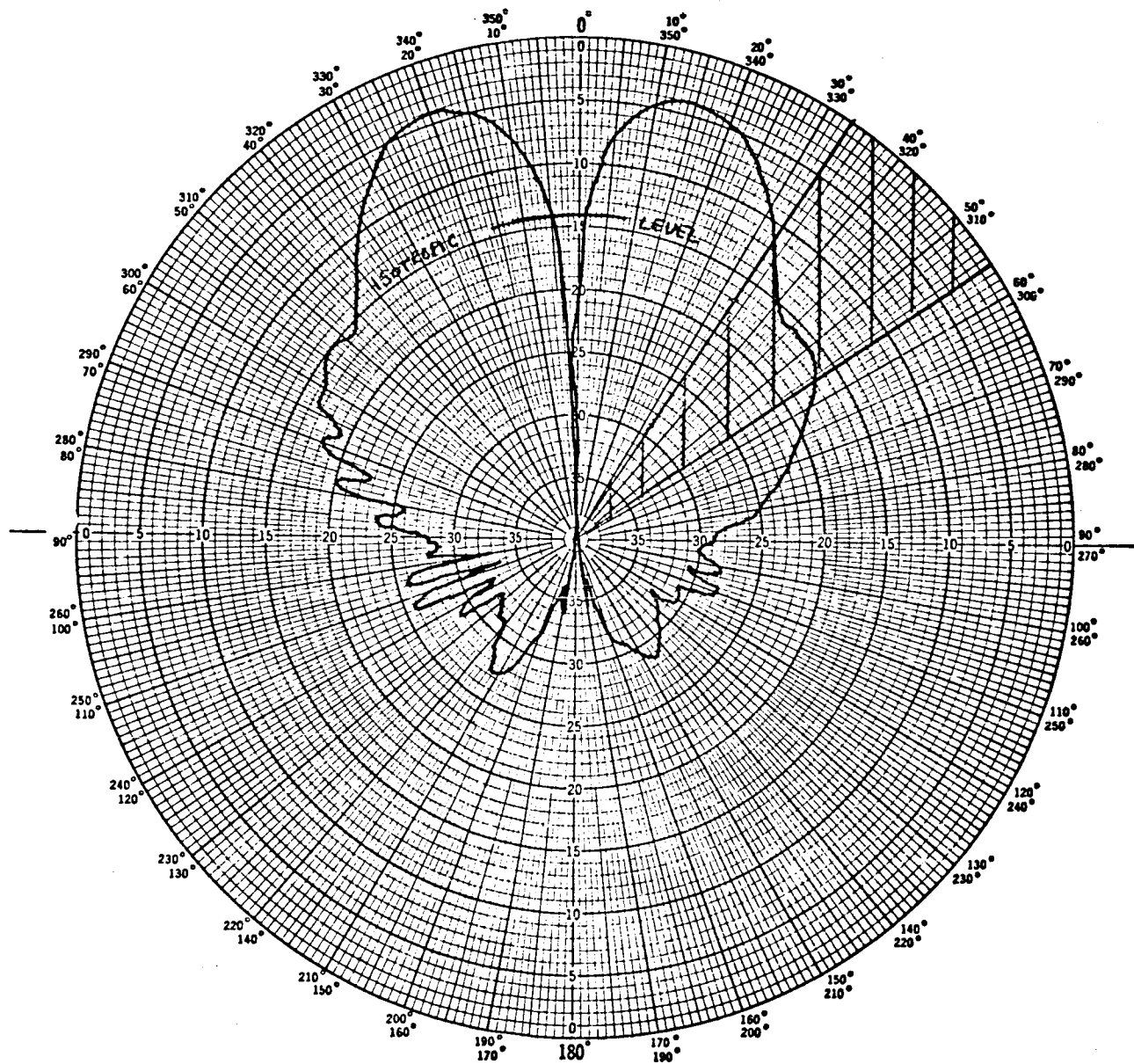
TABLE 57Landed Communication and Power Payload

	Weight (lbs)	Volume (in. ³)
Landed rf Electronics	23.4	445
Telemetry Subsystem	8.6	120
Core Memory	8.3	100
Programmer	8.0	120
Battery	25.4	200
Power Switching and Logic	2.0	80
Non rf Cabling	2.0	--
Total	77.7	1065

External Communication Payload

Pre-Entry rf Electronics	14.3	510
Descent rf Electronics	17.0	375
Total	31.3	885

TYPICAL RADIATION PATTERN - HORN ANTENNA *



64-11748 * TM_{01} mode

Figure 248 TYPICAL RADIATION PATTERN - HORN ANTENNA*

10.8.2 Alternate Concept 2

Circulator switches have been built to withstand at least 500 g impact shocks (Rantec Corp.). The rf signals in the pre-entry and descent modes could be routed by means of a circulator switch and thereby eliminate one exciter.

RF switching in general was not considered favorable in the conceptual design because of the high g impact. Another alternative with rf switching would be to use the power amplifier configuration shown in figure 231 (configuration C). The high power amplifier would be excited during descent. During pre-entry this amplifier would act as a lossy waveguide and only the driver amplifron would be excited. A circulator switch would route the power to the appropriate antenna.

10.8.3 Alternate Concept 3

The section of impact attenuator in front of the landed payload antenna could be made of balsa wood (dielectric) so that during descent, this antenna could be used for telemetry instead of the external one used in the conceptual design. Again, by suitable amplifier selection and using circulator switching, the pre-entry and descent transmitters could be eliminated.

REFERENCES

1. Proceedings of the 1962 National Telemetry Conference, Volume II, Session 8-4 Command Techniques for the Remote Control of Interplanetary Space craft, J. C. Springett.
2. Skolnik, Introduction to Radar Systems, McGraw-Hill Book Company, Inc. (1962).
3. Frazier and Page, Phase-Lock Loop Frequency Acquisition Study, IEE Transactions on Space Electronics and Telemetry (September 1962).
4. Becher, H. O. and J. G. Lawton, Theoretical Comparison of Binary Data Transmission Systems, Cornell Aeronautical Laboratory, Inc. Report No. CA-1172-S-1 (May 1958).
5. Van Heyst, H. P. and T. M. Cunningham, Si-Ge Thermoelectric Power Modules, Presented at 18th Annual Power-Sources Conference, Atlantic City, N. J. (May 21 1964).
6. Radioisotope-Fueled Generator Compendium and Parametric Study, MND 2994 (June 1963), Martin Company Nuclear Division Conf. Doc. No. 28451. Prepared for J. P. L.

APPENDIX A
IMPACT DYNAMICS ANALYSIS

This appendix is concerned with analyses of the impact dynamics of planetary landing systems which utilize material deformation to absorb and dissipate the kinetic energy of the falling body.

Three separate sections are included in this appendix. The first section presents the derivation of general equations applicable to any arbitrary geometry of a landing system. In the second section, the equations which have been derived are applied to the particular case where the crushable material is in the shape of a spherical segment. The third section is concerned with investigations of the effects of nonhomogeneity and anisotropy of the crushable material for the same special case of a spherical segment geometry.

Symbols

F	Force
m	Mass
v	Velocity
S	Crushing Stress
t	Thickness
A	Area
V	Volume
W	Earth Weight
ρ	Mass Density
R	Radius
g	Acceleration of Gravity
ϵ	Total Useable Strain
θ	Angle
α β	Constants

Subscripts

- ()_i Instrument Package
- ()_c Crushup
- ()_m Maximum

1. General Equations

Some of the important parameters for this study are illustrated in figure 249. The surface upon which the mass is impacting is considered to be flat, smooth, and infinitely rigid. The crushup material is assumed to have a stress-strain curve similar to that shown in figure 250; i.e., it crushes at approximately constant stress, S , up to a strain, ϵ , at which point abrupt bottoming occurs.

The cross-hatched area on figure 250 is the area under the unloading portion of the stress-strain diagram. It represents the energy which is stored elastically and which is returned to the impacting mass after it has stopped, causing it to rebound. An obvious requirement for a crushup material is that this rebound energy be a small fraction of the total energy absorbed.

Since the material does not crush completely, the area over which crushing is occurring at a given time will not be at the ground surface, but will be some distance above it, as shown on figure 249. This area of crushing is assumed to increase monotonically with time. Initially, the mass of crushup will be included in the analysis.

a. General Analysis

The starting point of the analysis is Newton's second law,

$$F = - \frac{d}{dt} (m\dot{y}) = - m\ddot{y} - \dot{m}\dot{y}$$

where F is the reactive force which the surface exerts on the mass.

This force has two components, one of which acts to decelerate an incremental mass of crushup material to zero velocity, while the other component acts on the remaining mass. Thus, one component is

$$F_1 dt = - dm \cdot \dot{y}$$

$$F_1 = - m \ddot{y}$$

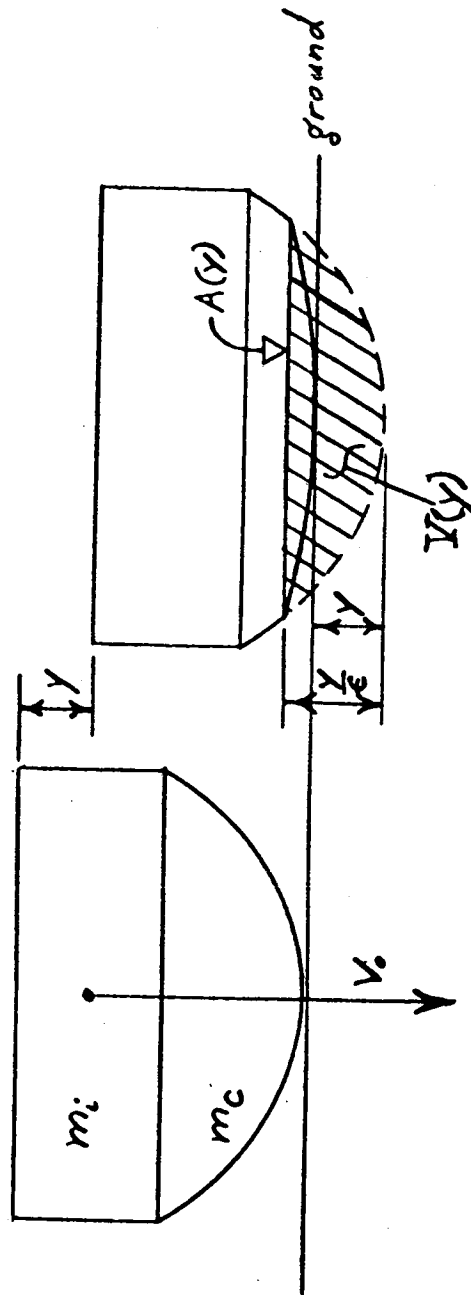
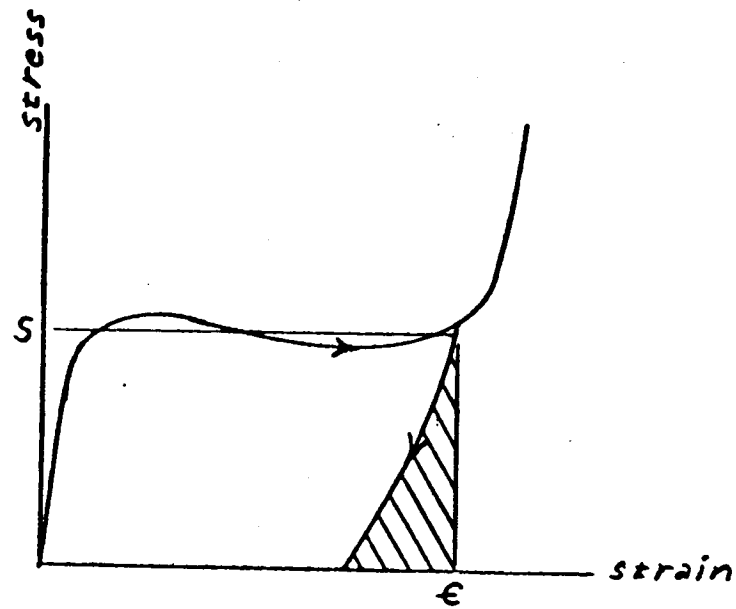


Figure 249 IMPACT DYNAMICS PARAMETERS

64-11749



TYPICAL STRESS-STRAIN CURVE

64-11750

Figure 250 TYPICAL STRESS STRAIN CURVE

and from equilibrium considerations, the other force is equal to the crushing stress times the area over which crushing is occurring, or

$$F_2 = S \cdot A(y)$$

So, with

$$m = m_i + m_c - \rho_c V(y)$$

(see table of notation)

$$S \cdot A(y) = -[m_i + m_c - \rho_c V(y)] \quad (1-1)$$

Since

$$\ddot{y} = \dot{y} \frac{d\dot{y}}{dy}, \quad \frac{-A(y) dy}{m_i + m_c - \rho_c V(y)} = \frac{1}{S} \dot{y} d\dot{y}$$

Referring to figure 249, it can be seen that

$$\int_0^{y/\epsilon} A(y) d\left(\frac{y}{\epsilon}\right) = V(y)$$

or

$$\frac{dV(y)}{dy} = \frac{A(y)}{\epsilon}$$

Integrating,

$$\ln [m_i + m_c - \rho_c V(y)] = \frac{\rho_c}{2 \epsilon S} \dot{y}^2 + c \quad (1-2)$$

The initial conditions are

$$y(0) = 0, \dot{y}(0) = v_0, V(0) = 0$$

$$\therefore c = \ln(m_i + m_c) - \frac{\rho_c v_0^2}{2 \epsilon S}$$

then

$$1 - \frac{\rho_c V(y)}{m_i + m_c} = e^{-\frac{\rho_c}{2\epsilon s} (v_o^2 - \dot{y}^2)} \quad (1-3)$$

The maximum value of y occurs when $\dot{y} = 0$.

$$V(y_m) = \frac{m_i + m_c}{\rho_c} \left[1 - e^{-\frac{\rho_c v_o^2}{2\epsilon s}} \right] \quad (1-4)$$

Combining this with the above equation for acceleration,

$$-\ddot{y}_m = \frac{S \cdot A(y_m)}{m_i + m_c} e^{-\frac{\rho_c v_o^2}{2\epsilon s}} \quad (1-5)$$

The last two equations relate the initial velocity, maximum acceleration, and crushup material geometry. These would be the equations used in a detailed analysis of a crushup system in which the crushup mass is a significant percentage of the total mass.

For those design situations in which all of the crushable material is utilized to absorb the impact energy, the crushup mass can be expressed as

$$m_c = \rho_c V(y_m) \quad (1-6)$$

which leads to

$$m_c = m_i \left[e^{\frac{\rho_c v_o^2}{2\epsilon s}} - 1 \right] \quad (1-7)$$

and

$$-\ddot{y}_m = \frac{S \cdot A(y_m)}{m_i} \quad (1-8)$$

In many situations, however, all of the material may not be used because of odd geometries or other considerations. The relation between total mass of crushable material and the volume of material crushed during impact may be quite complex in these cases.

470

Simplified Equations

Some simplification of the above equations is possible for cases in

which $\frac{\rho_c v_o^2}{2\epsilon S} \ll 1$

Then

$$e^{\pm \frac{\rho_c v_o^2}{2\epsilon S}} = 1 \pm \frac{\rho_c v_o^2}{2\epsilon S} \quad (1-9)$$

and the equations become

$$V(y_m) = \frac{\frac{1}{2}(m_i + m_c) v_o^2}{\epsilon S} \quad (1-10)$$

$$-\ddot{y}_m = \frac{S \cdot A(y_m)}{m_i + m_c} \quad (1-11)$$

When all of the crushup mass is used, it is given by

$$m_c = \frac{\rho_c m_i v_o^2}{2\epsilon S} \quad (1-12)$$

The simplification of these equations has put them into a much more recognizable form. Thus, equation (1-10) states that, to a first approximation, the energy absorbed per unit volume of material crushed (ϵS) times the total volume crushed is equal to the kinetic energy of the system immediately prior to impact. By comparison, equation (1-4) states that, in actuality, less volume need be crushed. This is due to the fact that the material being crushed does not have to absorb all of its own kinetic energy; the rigid ground performs some of this work. Therefore, the simplified equation, (1-10), errs on the side of conservatism.

On the other hand, equation (1-11) slightly underestimates the peak decelerations since the actual mass being decelerated is the total mass ($m_i + m_c$) minus the mass which has already been crushed.

471

2. Spherical Geometry

The preceding equations will now be applied to the case where the crushup material is shaped in the form of a spherical segment. For this particular case,

$$A(y) = \pi \left[2R_2 \frac{y}{\epsilon} - \left(\frac{y}{\epsilon} \right)^2 \right] \quad (2-1)$$

$$V(y) = \pi \left[R_2 \left(\frac{y}{\epsilon} \right)^2 - \frac{1}{3} \left(\frac{y}{\epsilon} \right)^3 \right] \quad (2-2)$$

where R_2 is the radius of the segment.

Substituting these relations into equations (1-10) and (1-11) and writing the results in dimensionless form leads to

$$-\frac{\ddot{y}_m R_2}{v_o^2} = \frac{3 \left[2 - \frac{y_m}{\epsilon R_2} \right]}{2 \epsilon \left(\frac{y_m}{\epsilon R_2} \right) \left[3 - \frac{y_m}{\epsilon R_2} \right]} \quad (2-3)$$

$$\frac{\pi S R_2^3}{(m_i + m_c) v_o^2} = \frac{3}{2 \epsilon \left(\frac{y_m}{\epsilon R_2} \right)^2 \left(3 - \frac{y_m}{\epsilon R_2} \right)} \quad (2-4)$$

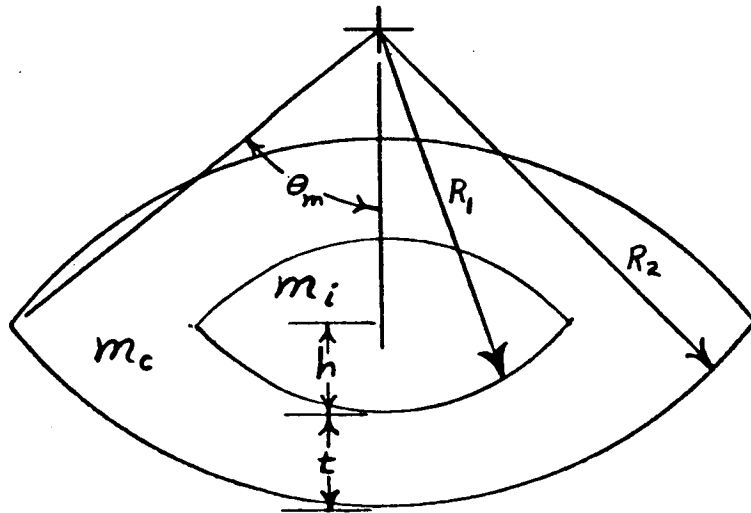
For the case of a shallow sphere, for which $\frac{y_m}{\epsilon R} \ll 1$ the equations become

$$-\ddot{y}_m = \frac{v_o^2}{y_m} \quad (2-5)$$

$$\frac{2 \pi R_2 S}{\epsilon (m_i + m_c)} = \frac{v_o^2}{y_m^2} \quad (2-6)$$

Geometric Relations

The general lander shape under consideration in this section is shown on figure 251. It is composed of spherical segments butted against one another.



64-11751

Figure 251 LANDED PACKAGE GEOMETRY

The volume of the internal package is

$$V_i = 2 \left[\frac{1}{3} \pi h^2 (3R_1 - h) \right]$$

and the volume of crushable material is

$$V_c = 2 \left\{ \frac{1}{3} \pi (h+t)^2 [3R_2 - (h+t)] \right\} - V_i$$

or, since $h+t = R_2(1 - \cos \theta_m)$,

$$V_i = \frac{2\pi}{3} R_2^3 \left[1 - \frac{t}{R_2} - \cos \theta_m \right]^2 \left[2 \left(1 - \frac{t}{R_2} \right) + \cos \theta_m \right] \quad (2-7)$$

$$V_c = \frac{2\pi}{3} R_2^3 (1 - \cos \theta_m)^2 (2 + \cos \theta_m) - V_i \quad (2-8)$$

The masses of the internal package and of the crushable material are merely

$$m_i = \rho_i V_i \quad (2-9)$$

$$m_c = \rho_c V_c$$

assuming a homogeneous crushup material.

For the special case where $\theta_m = 90$ degrees, the lander is a sphere and the equations for mass are

$$m_i = \frac{4}{3} \pi \rho_i R_2^3 \left(1 - \frac{t}{R_2} \right)^3 \quad (2-10)$$

$$m_c = \frac{4}{3} \pi \rho_c R_2^3 \left[1 - \left(1 - \frac{t}{R_2} \right)^3 \right] \quad (2-11)$$

3. Variable Stress Analyses

In this section, departures from the ideal, homogeneous, isotropic crushable material assumed in all of the foregoing are examined. The variations of mass involved during the impact are neglected; the purpose of these equations is to indicate the extent to which nonhomogeneity or anisotropy affect the design of an impact attenuation system.

474

a. Nonhomogeneous Material

This situation is one which is more likely to be introduced on purpose by the designer rather than being an inherent property of these crushable materials. Any natural deviations from homogeneity should be random and localized. The particular situation analyzed herein assumes that the material is spherically symmetric and isotropic; this implies that the stress is a function of the radial coordinate only. This type of behavior could be obtained by manufacturing the impact attenuator by laying up successive spherical shells of material of different crushing stresses.

Now, the elemental area is an annular strip dx wide at a distance x from the mid-axis (figure 252)

$$dA = 2\pi x dx$$

but, since

$$x^2 = R^2 - \left(R_2 - \frac{y}{\epsilon}\right)^2$$

then

$$2\pi x dx = 2\pi R dR$$

hence

$$dA = 2\pi R dR \quad (3-1)$$

The differential force acting over this area is

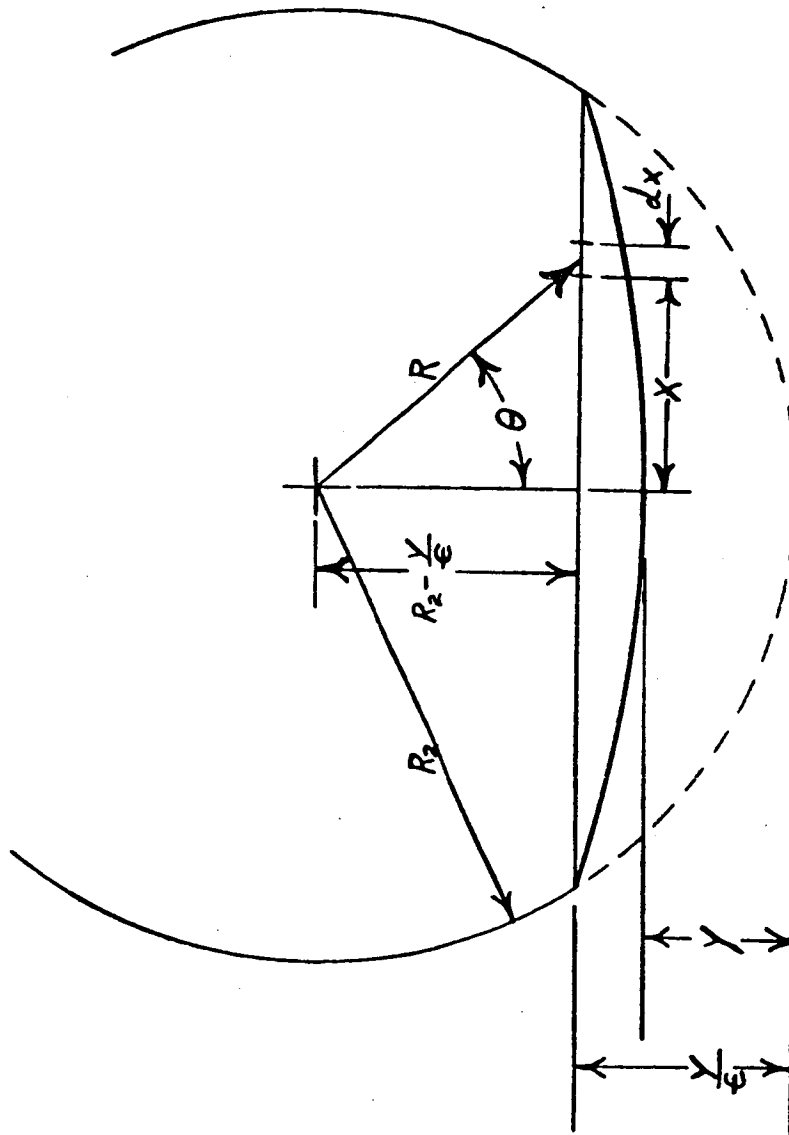
$$dF = S(R) dA$$

and the total force acting over the entire plane of crushing is

$$F = \int_{R_2 - y/\epsilon}^{R_2} 2\pi R \cdot S(R) dR \quad (3-2)$$

Using Newton's Law;

$$F = (m_i + m_c) \ddot{y} = 2\pi \int_{R_2 - \ddot{y}/\epsilon}^{R_2} R \cdot S(R) dR \quad (3-3)$$



VARIABLE CRUSHING STRESS PARAMETERS

— GENERAL —

64-11752

Figure 252 VARIABLE CRUSHING STRESS PARAMETERS - GENERAL

then, since

$$\ddot{y} = \dot{y} \frac{d\dot{y}}{dy}, \quad \frac{1}{2} (m_i + m_c) \dot{y}^2 = 2\pi \int \left[\int_{R_2 - y/\epsilon}^{R_2} R S(R) dR \right] dy \quad (3-4)$$

Now setting the value of y in the integrals equal to y_{\max} will yield the maximum acceleration and the total velocity which can be dissipated.

Thus; with $\frac{y_{\max}}{\epsilon} = t$

$$\ddot{y}_m = \frac{2\pi}{m_i + m_c} \int_{R_2 - t}^{R_2} R S(R) dR \quad (3-5)$$

$$v_o^2 = \frac{4\pi}{m_i + m_c} \int_0^{y_m} \left[\int_{R_2 - y/\epsilon}^{R_2} R S(R) dR \right] dy \quad (3-6)$$

In order to obtain some idea of how the stress variation affects the results, a particular function for $S(R)$ was chosen, as shown on figure 253.

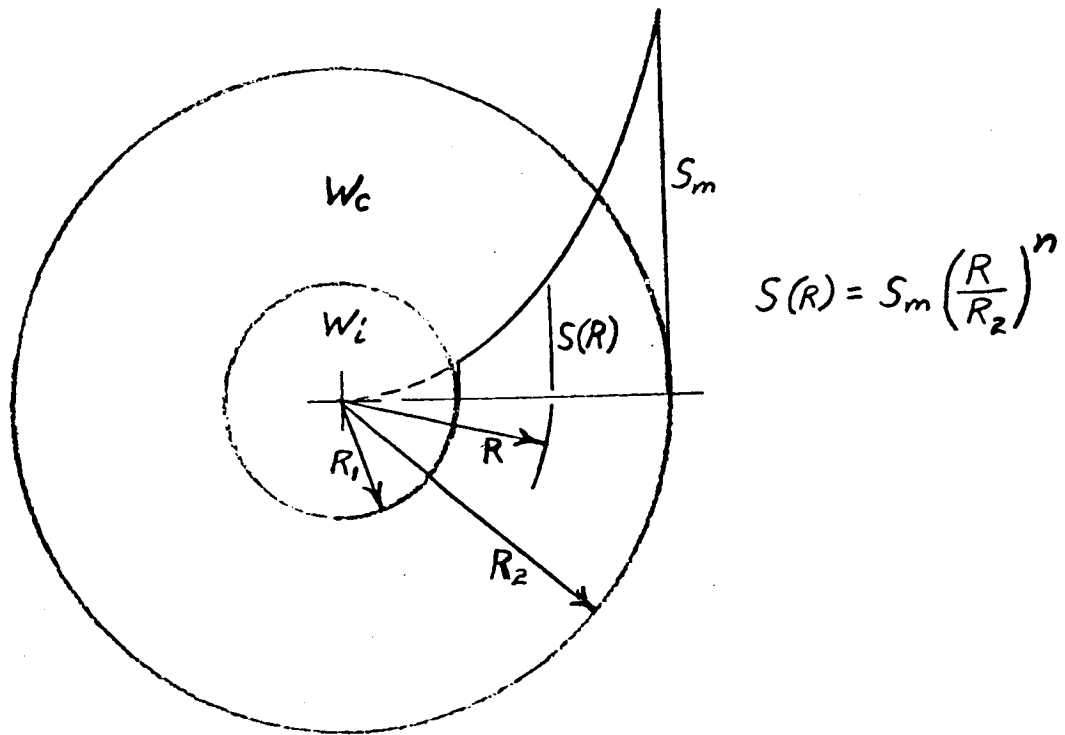
$$S = S_m \left(\frac{R}{R_2} \right)^n \quad (3-7)$$

Substituting into the above equations yields

$$\ddot{y}_m = \frac{2\pi S_m R_2^2}{(n+2)(m_i + m_c)} \left[1 - \left(1 - \frac{t}{R_2} \right)^{n+2} \right] \quad (3-8)$$

$$v_o^2 = \frac{4\pi \epsilon S_m R_2^3}{(n+2)(m_i + m_c)} \left[\frac{t}{R_2} - \frac{1 - \left(1 - \frac{t}{R_2} \right)^{n+3}}{n+3} \right] \quad (3-9)$$

Now, assuming that the lander is a complete sphere, the mass of the crushup can be calculated. The incremental mass of a spherical shell of thickness dR is



64-11753

Figure 253 VARIABLE CRUSHING STRESS PARAMETERS - NON-HOMOGENEOUS MATERIAL

$$dm_c = 4\pi\rho_c R^2 dR$$

If a single type of crushable material is used, such as aluminum honeycomb, it is possible to fit a curve to the plot of material properties. It has been found, in fact, that a curve of the form

$$\rho_c = \frac{S^\beta}{a'}$$

can be fit to all of the materials of interest. Using this equation, the total crushup mass is (using equation 3-7)

$$m_c = 4\pi \frac{S_m^\beta}{a'} \frac{1}{R_2^{\beta_n}} \int_{R_2-t}^{R_2} R^{\beta_n+2} dR$$

which gives

$$m_c = 4\pi\rho_{cm} R_2^3 \frac{\left[1 - \left(1 - \frac{t}{R_2}\right)^{\beta_n+3}\right]}{\beta_n+3} \quad (3-10)$$

where ρ_{cm} is the mass density corresponding to the maximum crushing stress, S_m .

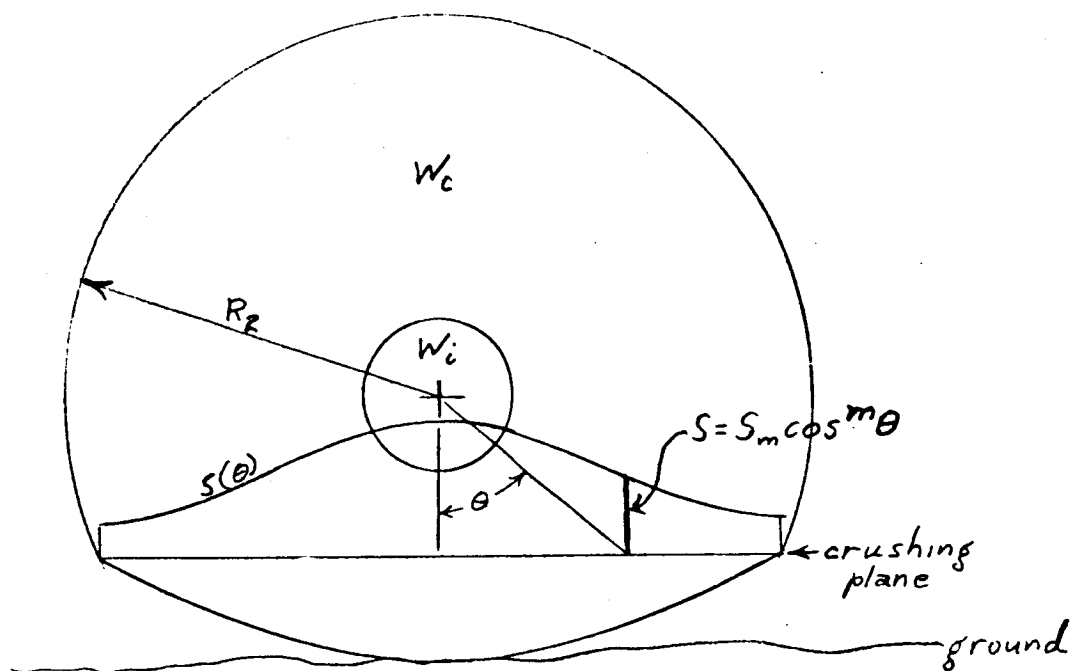
Thus, equations (3-8), (3-9), and (3-10), together with the equation for payload mass, equation (2-10), form the basis for parametric studies of the effect of using nonhomogeneous impact attenuation materials.

b. Anisotropic Material

All of the commonly used crushable materials exhibit anisotropic behavior to some degree. Honeycombs are strongest when loaded in a direction parallel to the cell axes, and balsa wood is strongest under loads aligned with the grain. Even plastic foams tend to be a bit stronger in the direction in which the foam rose.

In this analysis, the anisotropic material was assumed to be arranged with its "strongest" direction radial. Thus, the crushing stress was assumed to be a function of the coordinate θ (see figure 254). The particular function chosen for the analysis was

$$S = S_m \cos^m \theta \quad (3-11)$$



VARIABLE CRUSHING STRESS PARAMETERS
— ANISOTROPIC MATERIAL —

64-11754

Figure 254 VARIABLE CRUSHING STRESS PARAMETERS - ANISOTROPIC MATERIAL

Figure 255 illustrates several members of this family of curves and shows the variation possible.

Since

$$\cos \theta = \frac{R_2 - \frac{y}{\epsilon}}{R}$$

then

$$S = S_m \left(\frac{R_2 - \frac{y}{\epsilon}}{R} \right)^m \quad (3-12)$$

Now, since S is expressed as $f(R)$, the analysis of the preceding section is applicable up to equations (3-5) and (3-6). So, substituting equation (3-12) into these relations and performing the indicated integrations

yields, with $\frac{y_m}{\epsilon} = \tau$,

$$\ddot{y}_m = \frac{2\pi S_m R_2^2}{(2-m)(m_i + m_c)} \left(1 - \frac{\tau}{R_2}\right)^m \left[1 - \left(1 - \frac{\tau}{R_2}\right)^{2-m}\right] \quad (3-13)$$

$$v_o^2 = \frac{4\pi\epsilon S_m R_2^3}{(2-m)(m_i + m_c)} \left[\frac{1 - \left(1 - \frac{\tau}{R_2}\right)^{m+1}}{m+1} - \frac{1 - \left(1 - \frac{\tau}{R_2}\right)^3}{3} \right] \quad (3-14)$$

except for the special case $m = 2$, in which event the results are

$$\ddot{y}_m = \frac{2\pi S_m R_2^2}{m_i + m_c} \left(1 - \frac{\tau}{R_2}\right)^2 \ln \frac{1}{\left(1 - \frac{\tau}{R_2}\right)} \quad (3-15)$$

$$v_o^2 = \frac{4\pi\epsilon S_m R_2^3}{9(m_i + m_c)} \left[\left(1 - \frac{\tau}{R_2}\right)^3 \ln \left(1 - \frac{\tau}{R_2}\right)^3 - \left(1 - \frac{\tau}{R_2}\right)^3 + 1 \right] \quad (3-16)$$

Since the material was assumed to be homogeneous in this analysis, the density is a constant and the masses of the crushup and of the internal package are given by previously derived relationships, i.e., equations (2-10) and (2-11).

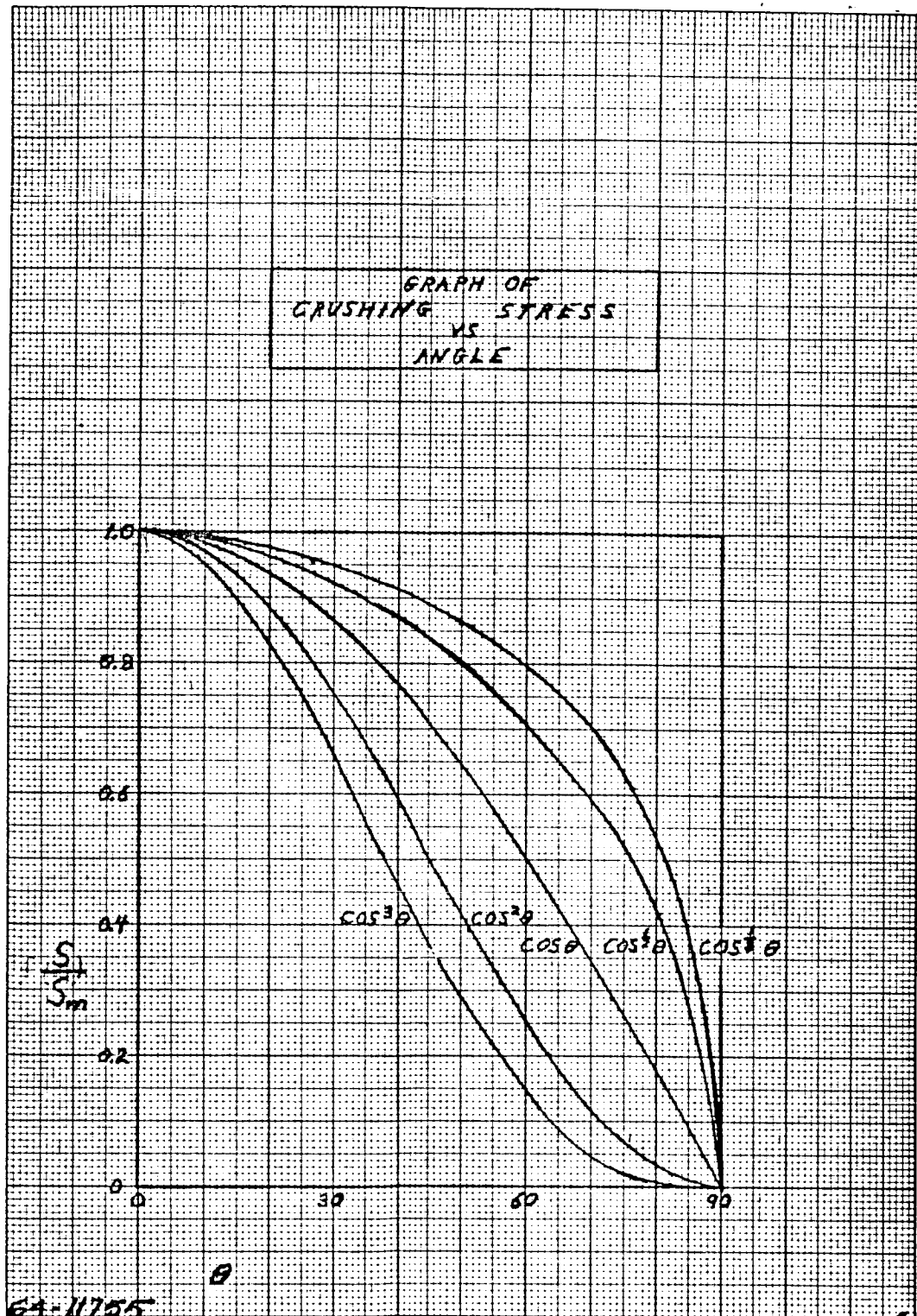


Figure 255 CRUSHING STRESS VERSUS ANGLE-ANISOTROPIC MATERIAL

c. Some Discussion of Pulse Shapes

The equation for deceleration for the nonhomogeneous case, equation (3-3), can be written in the nondimensional normalized form

$$\ddot{z} = 1 - (1 - z)^{n+2} \quad (3-17)$$

This equation is plotted on figure 256 for various value of the parameter n . For the case of an anisotropic material, the non-dimensional equation is

$$\begin{aligned} \ddot{z} &= k(1-z)^m [1 - (1-z)^{2-m}] & m \neq 2 \\ \ddot{z} &= k(1-z)^2 \ln \frac{1}{1-z}, & m = 2 \end{aligned} \quad (3-18)$$

and is plotted on figure 257. However, in this instance, the curves are somewhat misleading. If an accelerometer were mounted on a payload and if its readings were plotted versus stroke during an actual impact, the resulting curve would not look like figure 257. The reason for this is shown on figure 258. The bottom part of this figure schematically represents a capsule. Crushing begins at the left and proceeds to the right until the deceleration level reaches point P on the curve (the particular \ddot{z} versus z curve shown corresponds roughly to the $m = 2$ curve on figure 257). At this stage, the deceleration level is the same as at point Q, which corresponds to a plane situated just beneath the payload. This implies, since $F = ma$ (and since the difference in mass for the two cases is assumed ignorable), that the same total force which causes crushing to occur across plane 1 (see figure 258) also causes crushing across plane 2. Thus, "double-crushing" would take place, and the actual load-deflection curve which would be recorded by an accelerometer mounted on the payload would be close to that illustrated by the solid line on figure 258 instead of following the theoretical dashed curve shown.

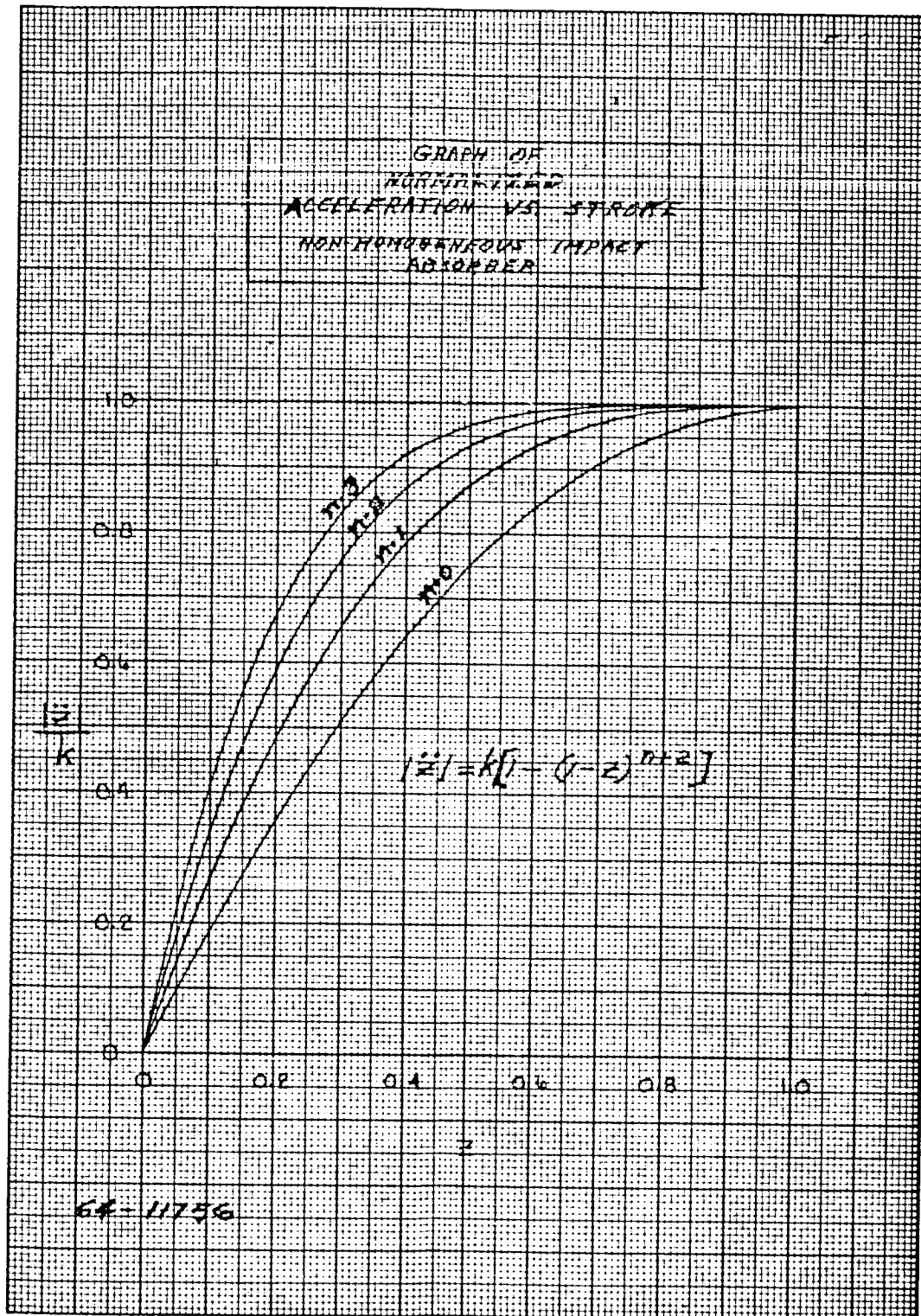


Figure 256 NORMALIZED ACCELERATION VERSUS STROKE - NON-HOMOGENEOUS
IMPACT ABSORBER

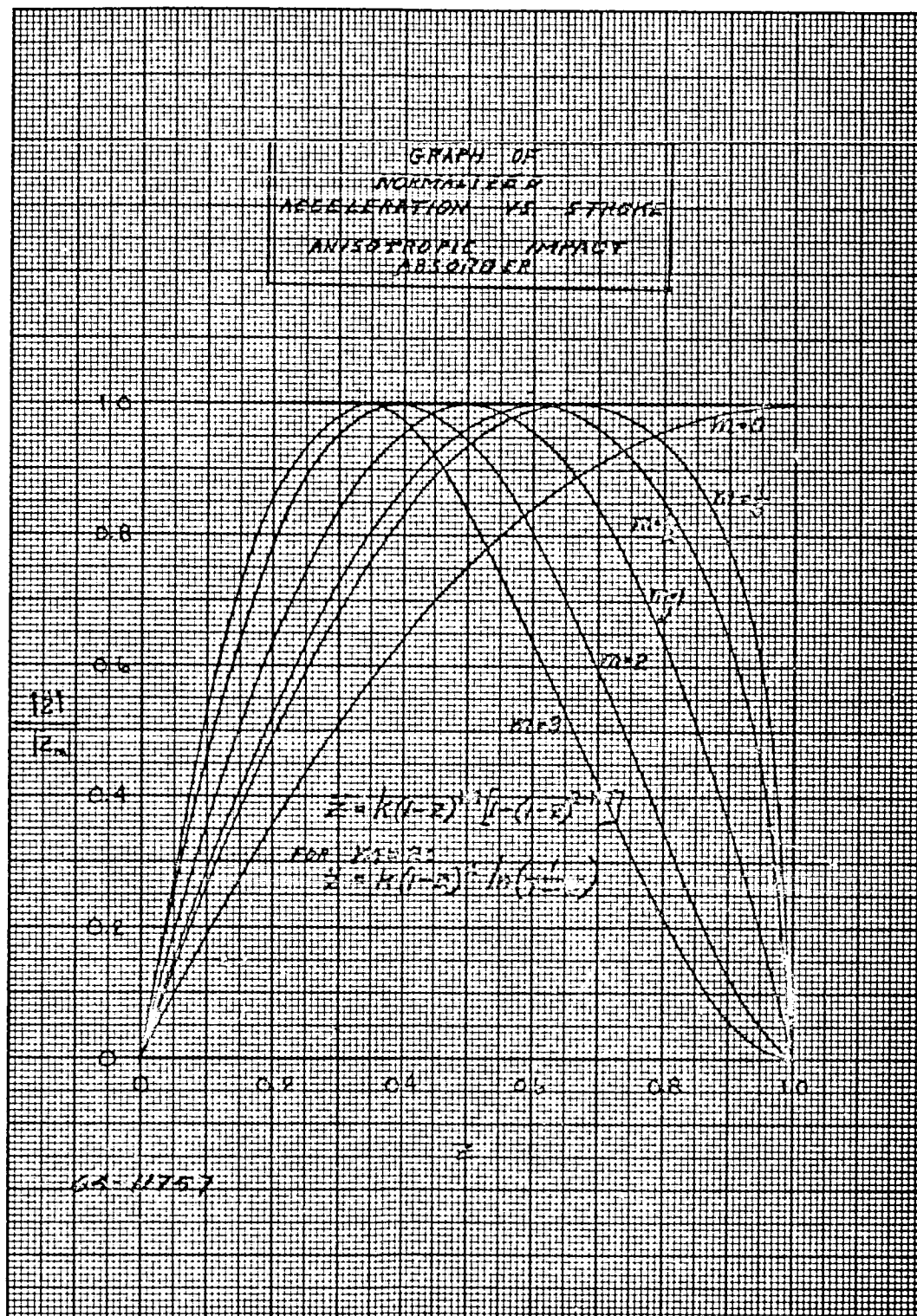
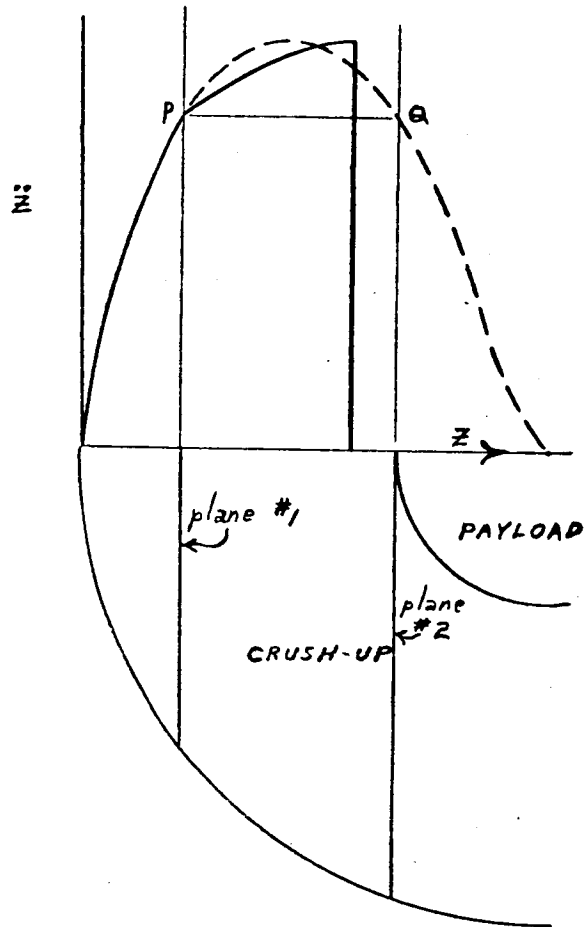


Figure 257 NORMALIZED ACCELERATION VERSUS STROKE - ANISOTROPIC IMPACT ABSORBER



"DOUBLE-CRUSHING"

64-11758

Figure 258 "DOUBLE-CRUSHING"

APPENDIX B

WIND DYNAMICS ANALYSIS

An analysis was made of the dynamics of a vehicle under a parachute falling through a finite thickness wind layer. The purpose of this investigation was to indicate that a more detailed model of the surface wind profile on Mars may allow some reduction in the severity of the constraints which the present model imposes on the design of the lander.

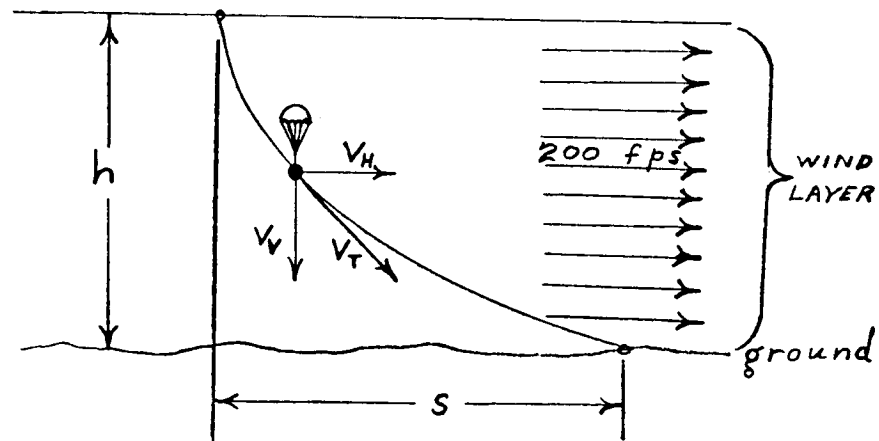
The wind velocity was assumed to be a constant 200 ft/sec through a layer of atmosphere extending from the surface of the planet to some altitude, h . Further, this altitude was assumed to be small enough so that the variation in atmospheric density with altitude could be neglected. The vehicle was assumed to be always at terminal vertical velocity under the parachute, and the drag coefficient of the parachute was assumed the same in the horizontal and vertical directions.

Some of the important parameters are shown on figure 259; others include:

- A - area, ft.
- C_D - drag coefficient
- g - acceleration of gravity, ft/sec²
- m - mass, slugs
- ρ - mass density, slugs/ft³

subscripts;

- ()_H - horizontal
- ()_V - vertical
- ()_W - wind
- ()_T - total
- ()_m - Mars



64-11759

Figure 259 WIND DYNAMICS PARAMETERS

Newton's law in the horizontal direction gives

$$\frac{1}{2} \rho_m C_{DH} A_H (V_W - V_H)^2 = m \frac{dV_H}{dt} \quad (1)$$

Let $\frac{1}{2} \rho_m C_{DH} A_H / m = B$:

$$B dt = \frac{dV_H}{(V_W - V_H)^2}$$

Integrating, using the initial condition that at $t = 0$, the horizontal velocity of the system is zero,

$$\frac{V_H}{V_W} = \frac{1}{1 + \frac{1}{BV_W t}} \quad (2)$$

Now, Newton's law applied to equilibrium vertical descent yields

$$mg_m = \frac{1}{2} \rho_m C_{DV} A_V V_V^2 \quad (3)$$

If equation (3) is submitted into the equation defining the parameter B, the result is

$$B = \frac{C_{DH}}{C_{DV}} \cdot \frac{A_H}{A_V} \cdot \frac{g_m}{V_V^2} \quad (4)$$

Finally, it is evident that to reach the surface takes a period of time

$$t = \frac{h}{V_V} \quad (5)$$

Substituting equations (4) and (5) into equation (2) yields

$$V_H = \frac{1}{1 + \frac{C_{DV}}{C_{DH}} \frac{A_V}{A_H} \frac{V_V^3}{V_W} \frac{1}{hg_m}} V_W \quad (6)$$

If it is assumed that the parachute is roughly in the shape of a hemisphere, then $A_V = 2 A_H$. If the assumption that the drag coefficient is the same in both directions is also used, equation (6) reduces to

$$V_H = \frac{1}{1 + 2 \frac{V_V^3}{V_W hg_m}} V_W \quad (7)$$

Figure 260 is a graph of this equation, showing how closely the horizontal velocity, V_H , approaches the wind velocity as a function of V_V and h .

The total impact velocity is obtained by vector addition of the vertical and horizontal velocities. Figure 261 is a plot of this total velocity versus vertical velocity for a number of values of altitude. By plotting the graph in this way, an interesting feature can be observed. This is the fact that the total velocity can be minimized for altitudes below 7200 feet.

If these data are replotted as shown on figure 262, the problem is put into better perspective. This figure illustrates that if the wind layer thickness is 5000 feet or less, then any vertical velocity between 100 and 150 ft/sec will yield a total impact velocity which is about as low as can be achieved. With vertical velocities less than 100 ft/sec, the vehicle will be picked up by the wind very quickly; for the velocities greater than 150 ft/sec, the total velocity is already high, and the wind just makes it go higher.

Referring to figure 165 in section 8.3 of this volume, it can be seen that significant increases in payload weight could be realized if the impact velocity were lowered. For example, if a wind profile model were postulated which set a maximum altitude of 2000 feet, then it would be possible to obtain (from figure 262) a total impact velocity of 170 ft/sec. If the nominal design point were 210 ft/sec (at a packaging density, $\rho_i = 2$ slugs/ft³), then this would result in the internal payload being increased from 50 percent of the landed weight to 63 percent. This is an increase in payload weight of greater than 25 percent. A further benefit in this example is that the parachute would actually be made smaller than that corresponding to the 210 ft/sec initial nominal design (which implied a vertical velocity of 65 ft/sec) in order to make the vehicle drop faster. Thus, still more weight savings could be realized.

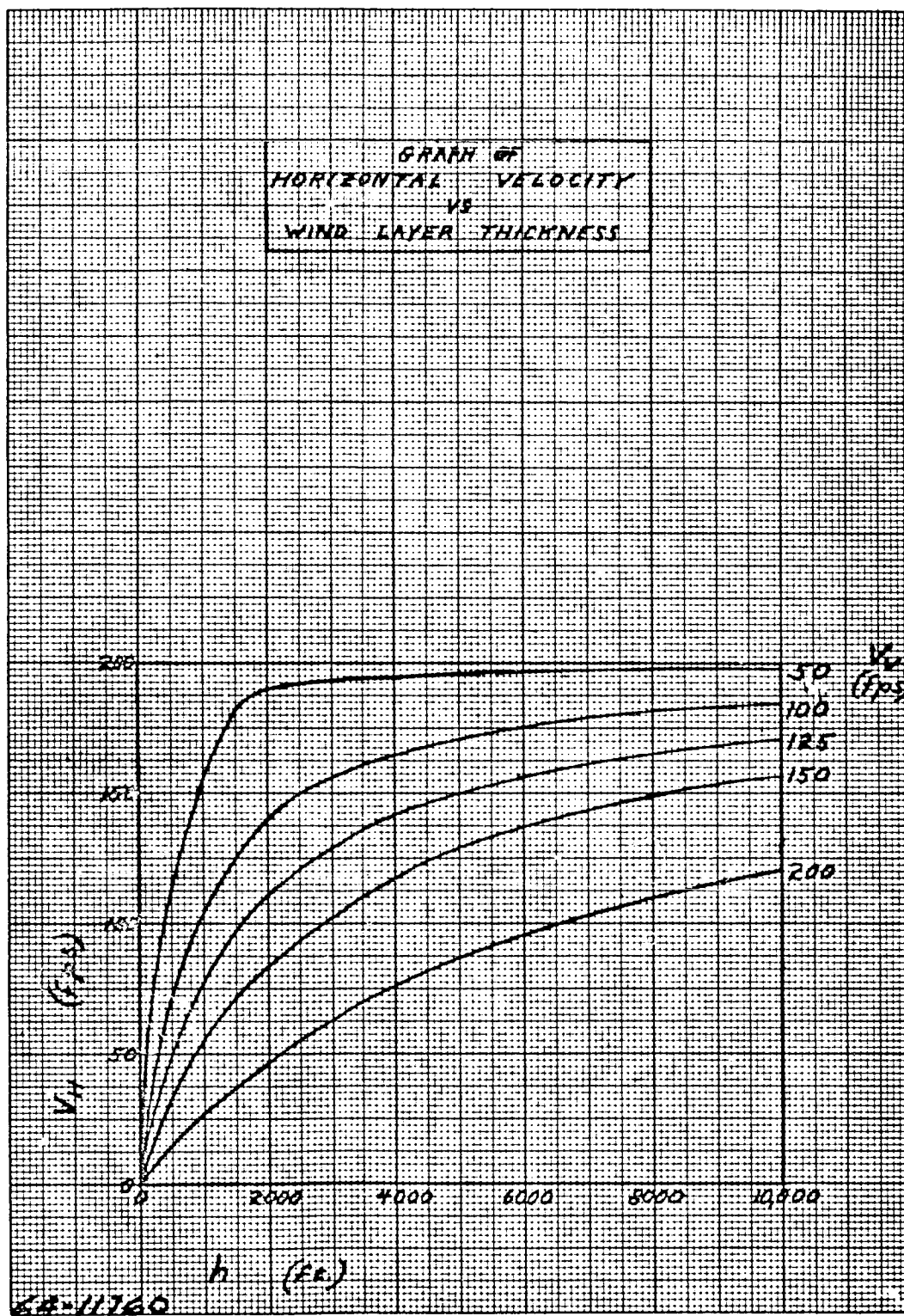
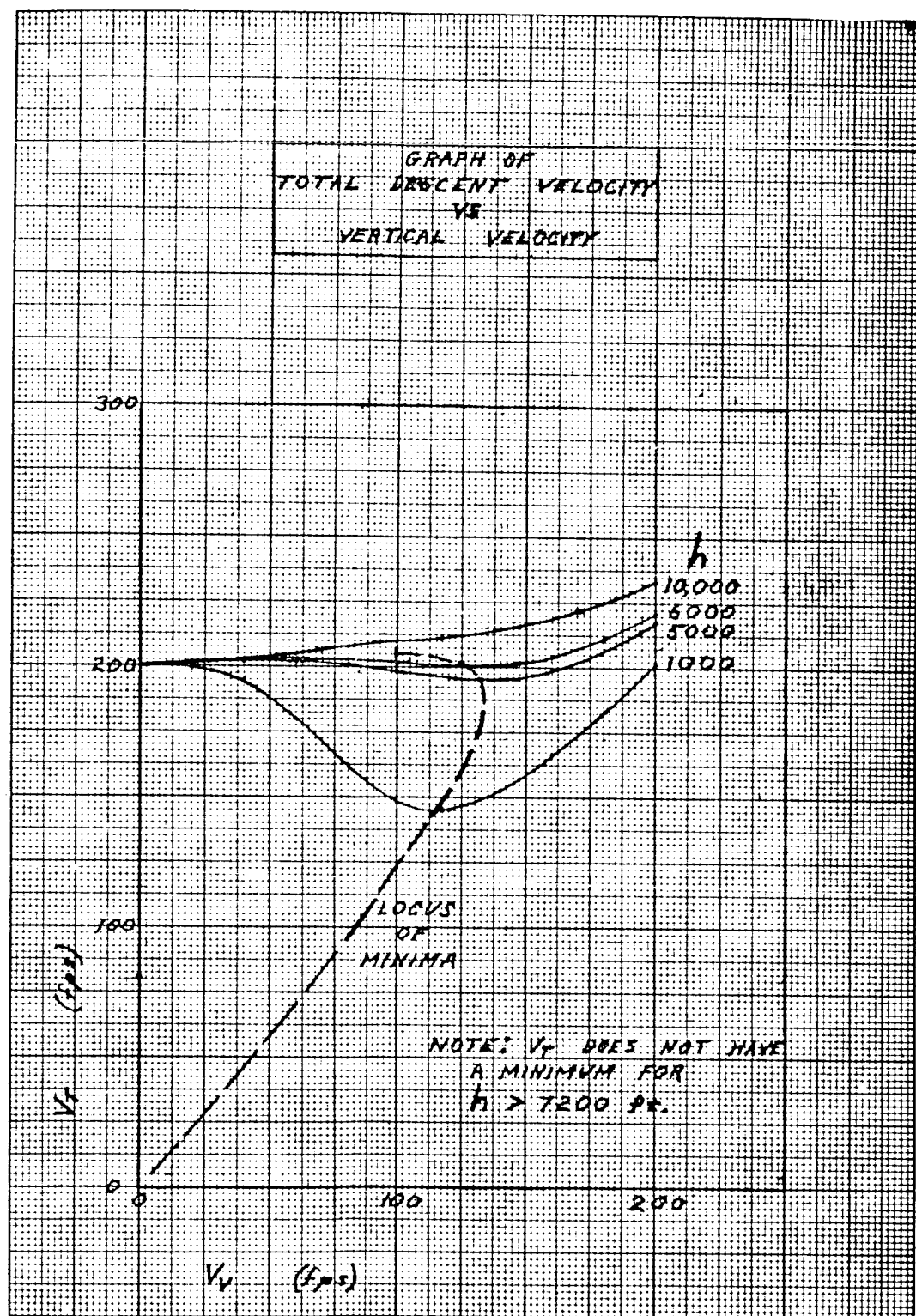
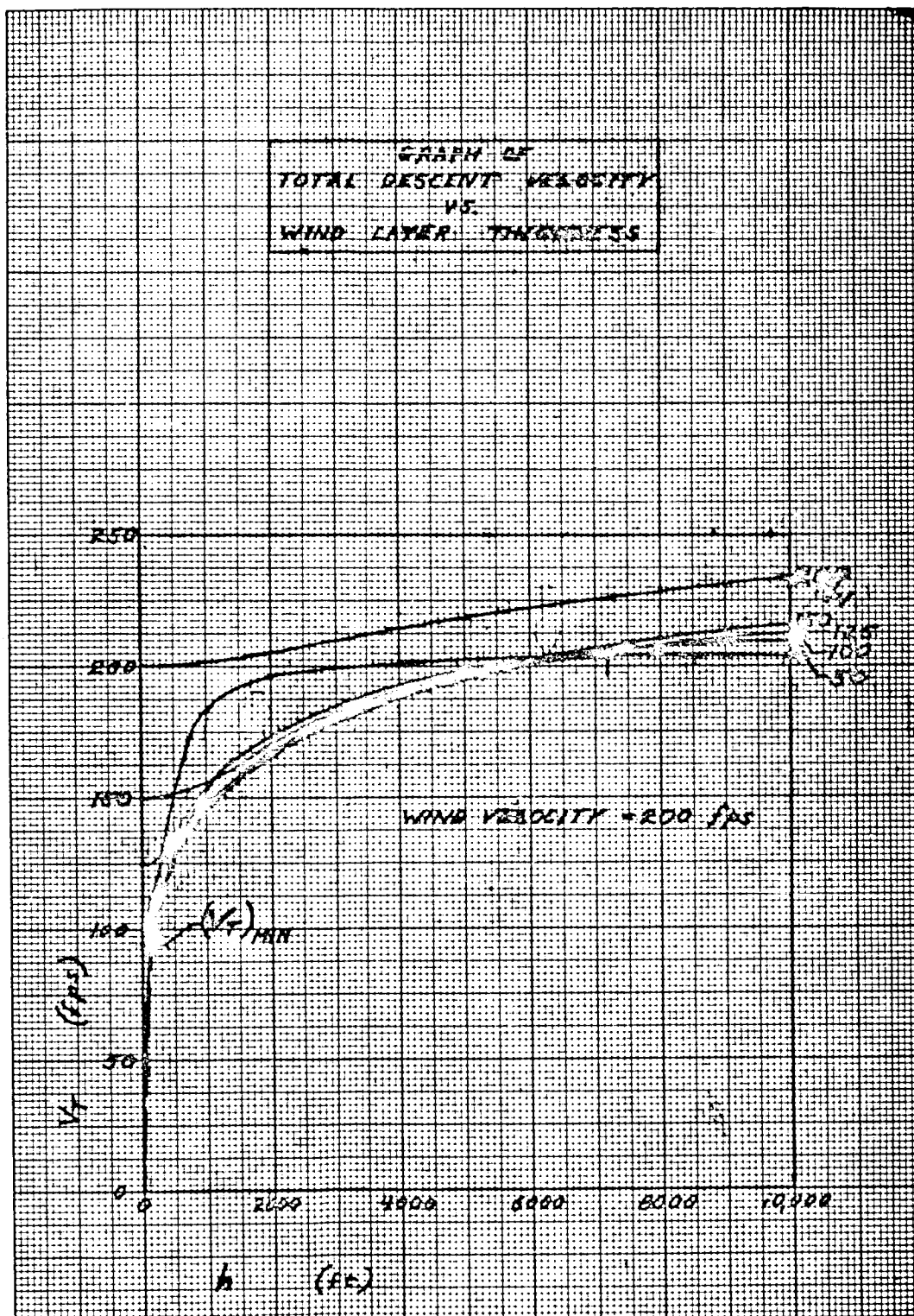


Figure 260 HORIZONTAL VELOCITY VERSUS WIND LAYER THICKNESS



64-11761

Figure 261 TOTAL DESCENT VELOCITY VERSUS VERTICAL VELOCITY



64-11762

Figure 262 TOTAL DESCENT VELOCITY VERSUS WIND LAYER THICKNESS

APPENDIX C

DENSITY PROFILE DETERMINATION

A. INSTRUMENTATION

A system utilizing 3 axis accelerometers mounted at, or very near, the vehicle c.g. was investigated to evaluate the following:

1. Instrument Accuracy Requirements
2. Sampling Rate Requirements
3. Effects of Vehicle Dynamics

It was presumed that the sampling begins when the deceleration of the vehicle becomes significant. A preset axial accelerometer reading of G_0 was used to initiate the sampling. Single and dual range accelerometers were considered.

Estimated accuracies for servo and strain gauges were factored into the study. However, other aspects as weight, volume, warmup time, and mounting have to be considered in selecting the proper instrument.

B. ANALYSIS

The accelerations felt by each accelerometer are given by

$$a_x = \frac{C_x A q}{m} (Q^2 + R^2) + y(\dot{R} - PQ) - z(\dot{Q} + PR)$$

$$a_y = -\frac{C_n A q}{m} \frac{\sin \beta}{\sin \alpha'} - x(\dot{R} + PQ) + y(P^2 + R^2) + z(\dot{P} - RQ)$$

$$a_z = \frac{C_n A q}{m} \frac{\sin \alpha}{\sin \alpha'} + x(\dot{Q} - PR) - y(\dot{P} + QR) + z(P^2 + Q^2)$$

where

C_x = axial force coefficient

C_n = normal force coefficient

x, y, z = coordinate location of accelerometers

A = reference area

q = dynamic pressure

P, Q, R = Roll, Pitch, Yaw Rates

α, β = components of total angle of attack as defined in RAD-TR-64-1, Page 157

α' = total angle of attack

The actual measured data will differ from the ideal values due to system errors which are assumed to be proportional to the full scale value of the accelerometer. The actual measured quantities can then be written as,

$$a'_x = a_x + \delta x a_{xpn}$$

$$a'_y = a_y + \delta y a_{ypn}$$

$$a'_z = a_z + \delta z a_{zpn}$$

where

$\delta x, \delta y, \delta z$ = error in accelerometer reading as a fraction of peak value

$a_{xpn}, a_{ypn}, a_{zpn}$ = peak values of each accelerometer for each range.

Three ranges of accelerometers may be selected in which case the selection on which accelerometer to use will be done using the smallest value of a_{xpn} , a_{ypn} , a_{zpn} such that

$$a_x \leq a_{xpn}, a_y \leq a_{ypn}, a_z \leq a_{zpn}.$$

The drag and lift equations using the measured data have the form,

$$\dot{V}' = -a'_D - g_{sl} \left(\frac{RSL}{RSL + Z} \right)^2 \sin \gamma'$$

$$\dot{\gamma}' = \frac{V' \cos \gamma'}{(RSL + Z')} - \frac{g_{sl}}{V'} \left(\frac{RSL}{RSL + Z} \right)^2 \cos \gamma'$$

$$\dot{Z}' = V' \sin \gamma'$$

where

$$a'_D = a'_x \cos \alpha'' + \sqrt{(a'_y)^2 + (a'_z)^2} \sin \alpha''$$

V' = measured or otherwise deduced velocity

γ' = measured or otherwise deduced flight path angle

Z' = deduced altitude

g_{sL} = acceleration due to gravity at surface

R_{SL} = radius of planet at the surface

The lift term has been omitted from the lift equation as the orientation of the lift vector cannot be deduced from the limited instrumentation package being considered.

For a sphere, it should be noted that

$$a_D' = \sqrt{a_x'^2 + a_y'^2 + a_z'^2}$$

C. RESULTS

Initial studies were performed to ascertain the effect of sampling interval. For these calculations, zero angle of attack was assumed and no accelerometer errors were introduced. The sampling was initiated at one g(Earth value). The results are tabulated below.

ΔT	ρ'/ρ	P'/P
0.10	1.545	1.081
0.50	1.541	1.055
1.0	1.536	1.054
2.0	1.506	1.054
3.0	1.462	0.985

where

ΔT = sampling interval; seconds

ρ'/ρ = ratio of deduced to actual density at surface

P'/P = ratio of deduced to actual density at surface

The effect of sample rate on the results was found to be insignificant, for the zero angle of attack case. The discrepancies between the deduced and actual values arose due to the assumption that at the time sampling began, namely at one-g deceleration, the velocity was identical with the entry velocity at 800,000 feet. It was subsequently observed that the velocity decreased by approximately one percent from 800,000 feet to the point at which one g occurred, causing a significant error in the density predictions at the surface.

Other factors affecting the choice of the sampling rate are the altitude change between intervals and the fact that constant sampling time interval yields a density profile at low altitude much more detailed than at high altitude, the angle of attack motions of the vehicle, and the data handling storage and transmission limitations.

Angle of attack studies required a method for estimating the angle of attack, in order to deduce the drag. The drag acceleration is given by

$$a_D = a_X \cos \alpha + a_N \sin \alpha$$

where

$$a_N = \sqrt{a_Z^2 + a_Y^2}$$

Since $C_N/C_X = a_N/a_X$ a relationship was evolved where

$$\alpha' = f(C_N/C_X)$$

in the form

$$(\alpha')^2 = C_2(C_N/C_X) + C_3(C_N/C_X)^2$$

where

$$\alpha' = \text{deduced angle of attack.}$$

$$C_3, C_2 = \text{empirical constants.}$$

The angle of attack analysis was limited to $\alpha < 60$ degrees as the axial force coefficient changes sign beyond this point. Utilizing the above approach to estimate the angle of attack, a study was performed for large angles of attack at entry. Three axis accelerometers were employed with a dual range of 400 and 4200 ft/sec², and accuracies of 0.1 percent fullscale based on capabilities of pendulous servo accelerometers. The initiation of the sampling rate was set for 10 g to insure that the angle of attack would be less than 60 degrees. The results are tabulated below for conditions at Mach 2.5, (time of parachute deployment).

Sample Rate Interval Seconds	α_c^*	ATM	γ_c	ρ'/ρ	P'/P
1.0	179	G	-90	0.92	0.99
1.0	179	G	-40	0.91	0.99
0.1	179	G	-90	1.25	1.04
0.1	179	G	-40	0.95	1.01
1.01	179	G	-90	0.93	0.99
1.01	179	G	-40	0.96	1.01
1.01	20	G	-90	1.03	0.99

*Zero rates at entry.

The results shown above indicate that the sampling rate has a weak effect on the predicted density or pressure. Evidently compensating effects occur where the sampling time is long; e. g., one second, due to randomness as the samples are being taken during the vehicle oscillations. The vehicle has a peak frequency of 6 cps. Hence, the detail of the motion is being followed only in the case of sampling rates interval on the order of 0.01 second, yet the predicted pressures and densities were good for a low sample rate of once per second. The angle of attack envelopes observed never exceeded 20 degrees beyond the 10 g actuation point down to Mach 2.5. Hence, part of the results can be explained by the fact that the angle of attack was low during the sampling period, although the data used give the following variation in drag coefficient with angle of attack, which indicates a significant variation.

α (degrees)	$C_D/C_{D_{\alpha=0}}$
0	1.00
10	0.961
20	0.871

The variation in drag coefficient even at small angles of attack appears significant. A calculation was performed to ascertain the feasibility of a single axis accelerometer which assumed that the drag coefficient was equal to its zero angle of attack level. The results are

Sample Rate Interval Seconds	α_c	ATM	γ_c	ρ'/ρ	P'/P
1.0	179	G	-90	1.66	1.04

The results indicate adequate prediction of the pressure, but rather poor prediction of the density.

The effects of measurement accuracy were studied and are summarized below

α_c	Atm	γ_c	Sample Interval Seconds	Error percent Full Scale	ρ'/ρ	P'/P
0	G	-90	1	0.1	1.14	1.02
0	G	-90	1	0.25	1.23	1.03
0	G	-40	1	0.1	1.11	1.08
0	G	-40	1	0.25	1.24	1.10
0	K	-90	1	0.1	0.92	1.00
0	K	-40	1	0.1	0.90	1.03

The tabulated results are for conditions at Mach 2.5 and zero angle of attack flight. The 0.25 percent error is representative of strain gauge accelerometers.

The effects of locating the accelerometer off the c.g. was investigated.

The offset examined was 0.01 foot, for which a negligible effect was found.

A number of trends are apparent from the results of the above analyses, although caution should be exercised in using the results due to the limited nature of the study. The trends indicate that:

1. A three axis system with final data accuracies on the order of 0.1 percent is necessary to deduce the density profile.

2. The accelerometer requirements to deduce the pressure are much less stringent than those required to deduce the density. This can be seen from elementary straight line gravity free analyses, as the ratio of deduced to actual density is

$$\frac{\rho'}{\rho} = \frac{v^2}{(v')^2}$$

and for an error $\delta a_D/a_D$, the ratio of deduced to actual velocity is

$$\frac{\delta v}{v} \approx \frac{\delta a_D}{a_D} \left(\frac{v_e}{v} \right)$$

Near the end of the flight (v_e/v) can be as high as 20 and hence a one percent error yields a 20 percent error in velocity and a 40 percent error in density. On the other hand the ratio of the deduced to the actual pressure is

$$\frac{p'}{p} = \frac{\ln v_e/v'}{\ln v_e/v}$$

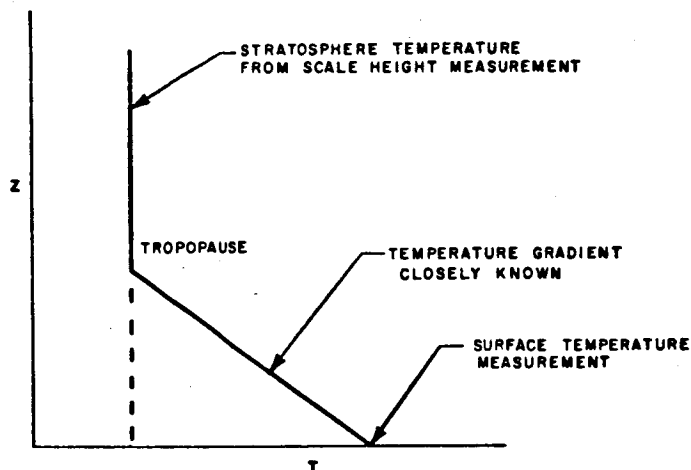
Hence, for $v_e/v = 20$ and $v_e/v' = 24$, $p'/p = 1.06$

The results therefore indicate that the three axis or possibly even a single axis system is well suited to deducing the pressure of the atmosphere at low altitudes or at impact.

3. A sampling rate of one sample per second provides adequate pressure data. The sampling rate necessary for accurate density determination is presently unclear. Results were obtained that indicated one sample a second was adequate for the density profile; however, if during the oscillations, the sampling was consistently biased (i.e., if the sample rate were an exact multiple of the frequency and occurred at zero or maximum angle of attack consistently) then large errors would be introduced into the density results; however the probability of this occurring is small.

4. Since dynamic trajectory results on the conceptual design indicate a maximum variation of 3 percent in peak deceleration due to angle of attack effects, the simple measurement of peak deceleration is suited to the determination of scale height.

5. The combined results of items 2, 3, 4 above indicate that for a small data capacity system a three axis accelerometer system sampling every second provides a worthwhile experiment. A complete first cut at the density profile could be obtained from these data. Provided composition (molecular weight) and surface temperature were also determined, the construction of the density profile, would also be based on the assumption of a temperature profile shown in the sketch below, to provide redundant use of the data.



SKETCH OF ATMOSPHERIC TEMPERATURE PROFILE

6. If a parachute is used, the molecular weight of the atmosphere can be found by measuring pressure and temperature with time. This follows as it can be shown that

$$\rho = - \left(\frac{1}{g} \frac{dp}{dt} \right)^2 \frac{1}{2g} \left(\frac{C_D A}{m} \right) \text{ (Chute Descent)}$$

Since P , ρ , T can be deduced, the molecular weight follows from the equation of state.